UC Berkeley
UC Berkeley Electronic Theses and Dissertations

Title

Synthesis and Study of Heterometal-Cobalt Oxo Cubanes

Permalink

https://escholarship.org/uc/item/9k8075bx

Author

Wheeler, Thomas Alexander

Publication Date

2024

Peer reviewed|Thesis/dissertation

eScholarship.org Powered by the California Digital Library
University of California

Synthesis and Study of Heterometal-Cobalt Oxo Cubanes

By

Alex Wheeler

A dissertation submitted in partial satisfaction of the
requirements for the degree of
Doctor of Philosophy
in
Chemistry
in the
Graduate Division
of the
University of California, Berkeley

Committee in Charge:
Professor T. Don Tilley
Professor John Arnold
Professor Alexis T. Bell

Spring 2024

Abstract

Synthesis and Study of Heterometal-Cobalt Oxo Cubanes

by

Thomas Alexander Wheeler

Doctor of Philosophy in Chemistry

University of California, Berkeley

Professor T. Don Tilley, Chair

Solar energy storage is critical to combatting anthropogenic climate change and transitioning to renewable sources of energy. Billions of years ago, plants evolved the ability to harvest and store energy from the sun in a process initiated by Photosystems I and II, wherein the oxygen evolving complex oxidizes water to produce dioxygen. This heterocubane $CaMn_4O_5$ cluster serves as a source of inspiration for the Tilley group's investigations into the chemistry of water oxidation by cobalt oxo cubanes. Chapter 1 briefly describes the current understanding of the mechanism for water oxidation by the oxygen evolving complex, and the challenges posed to synthetic inorganic chemists by this system. Chapter 2 details the first approach attempted to synthesize new heterometallic cobalt oxo cubanes starting from simple tricobalt precursors. While the primary aim of this study was to find rational synthetic routes to a wide library of MCo_3O_4 clusters, the electronic structure of the Co_3O_4 fragment provides insight into the role of the fourth cobalt in the parent cluster. Chapter 3 presents a near complete investigation into the metal-metal exchange reaction between the Co_4O_4 cubane and $Mn^{II/III}$ complexes to give the $MnCo_3O_4$ cubane. This study provides mechanistic evidence for a pendant metal intermediate during the exchange process, details reactions with Co^{III} and Co^{IV} materials, and also reports an array of substituted benzoate and pyridine ligated cobalt oxo cubanes. This manuscript is available publicly on ChemRxiv. Chapter 4 details the synthesis and properties of a vanadium-cobalt oxo cubane through the principles outlined in the metal-metal exchange study. The isostructural vanadium and ruthenium cobalt oxo cubanes allow for interrogation of the role of the tricobalt framework. This chapter continues to describe the oxidative reactivity of the vanadium-cobalt oxo system and attempts to observe the oxidized intermediate spectroscopically with in situ methods. Theory and experiment suggest a more localized hole compared to the all-cobalt system, which may have implications for vanadium-cobalt oxide materials

Acknowledgements

I would not be here without the support of my partner Cecelia, my family, my friends, my lab mates, my advisor Don, and all of the teachers that encouraged me along the way. I am certain that I will forget someone here, so in advance of that, know that at some point on this journey I thought of an appreciated you. I will try to go chronologically, but the first person I want to thank is the reader. I hope you find that everything in this work is in order, and for the most part grammatically correct. If you have any questions, I would be happy to answer you.

Mom, you did it. It is difficult to remember a time before you telling me that one day I would be here. Even as I brushed you off, you never stopped supporting me on this journey I was only certain I wanted much later. Dad, thank you for reminding me that at the end of the day, nobody is going to read this and for as long as I'm proud of it, I should spend more time biking to get drinks with people. Nana, thank you for always thinking of me and making me laugh. Stephanie and CJ, thank you for messaging me even when I forget to respond constantly. Elizabeth (Lizza, Cat), thank you for always being there and for picking up all of my phone calls, even if just to tell me that you were too busy petting untrained therapy animals. I wish we had spent more time together while you were in the Bay Area.

To all of the excellent public-school teachers I had, thank you for patience encouraging an exuberant kid with a short attention span. I want to thank those at New Trier that imparted more than just academic knowledge but personal wisdom, and to Dr. Hendren for allowing me to 'TA' for his chemistry class. I probably wasn't a very good TA back then so if you have any burning chemistry questions I definitely owe you. Jack, Charlie, Lily, Emry, Ben, thanks for staying in touch, I miss all of you.

To all of the wonderful people I met at Minnesota, thank you for doing so much to shape the person I am today. One of the best decisions I ever made was to live in Taylor House, where I had the privilege to meet an incredible group of genuine, kind, and hilarious people. When I was able to work there as a CA next year I was once again unbelievably fortunate; Sean Smallwood thank you for teaching me how to connect with students and helping me be more empathetic. Kris and Allie, I think I would've been unbelievably lonely if you two hadn't insisted on studying in my room, 'forcing' me to get coffee –or Kowloon – with you, and all of the morning Al's runs. To the rest of the CAs, working with you was truly a pleasure. To my Taylor House crew that ended up becoming APROBE house, and then those that became CASIJ (?) house, thank you for your patience with the most annoying housemate. To the Rivera family, you have been unbelievably supportive of Cecelia and I, for which I am grateful. I appreciate you keeping us both in your prayers, and always asking about us. Olivia, Micah, Abigail, and Joshua, you are all wonderful people, and I am excited to spend more time with you. Frank and Margot, your hospitality is unmatched and we couldn't have done any of this without you.

I would be remiss not to thank the person that really set me off on this journey, Professor Ian Tonks. Ian, your organic chemistry class was the first college classroom I ever entered, and within the month I was already pretty confident that, despite telling my mom I would never do it, I wanted to go to graduate school. When I had the opportunity to do research in your group I was overjoyed.

Your group was a second family to me, and I wore the moniker ‘undergrad’ with pride. In hindsight, I must have really annoyed all of you, so allow me to emphasize that because of you all, I will look back on those times as some of the best of my life.

Zach, everything I really know about science is because of you. From how to google, to how to clean a column, to how to assess how air-free a reaction needs to be, to what music to blast, to how to give a good presentation, to kinetics. I hope your eyes have adjusted to be able to read papers in journals with impact factors lower than ten! Peter, thank you for teaching me how basic NP is, and how a real chemist makes EtMgBr. Jimmy (Hsin-Chun), thank you for showing me how you should work your hardest when things are working, and demonstrating how to properly vac transfer a cork ring. Abby, thank you for being the realest Minnesotan in the group and converting me to a MN lover, and for often not kicking me out of the lab when I was there way later than I should’ve been. Adam, I still remember excited you were when you figured out the MeI addition product to your hydrazido; I think that was the first time I felt like someone was addressing me as a scientist. Xin Yi, I wish I could say I learned how to replicate your beautiful lab notebook but I think my handwriting doomed me from the start. I will always appreciate your sense of humor, your determination, and the way you could brutally take people down – even unintentionally. Evan, if Zach taught me everything I know about science, you humanized it, put it all into perspective, and gave me a deep appreciation for creative, thorough science. Additionally, the way you devour the literature is incredible. I know for a fact I would’ve lost my mind, and probably quit, if I hadn’t been able to call you on the weekends walking into the lab or working in the glovebox. Being a part of your wedding was unironically an honor and a privilege. You and Caitlin showed me that chemists can actually be cool, and are truly among the best people I’ve ever met. I don’t have a segue into this one but I will never forget the story of you two spilling vegetable oil on your kitchen floor and telling each other to bring some hexanes in from the lab to clean it up before Zach asked, “Have you guys ever heard of soap?” Letitia, on behalf of the Tonks group from that era, thank you for being an incredible facility manager and part of the family. Whenever I catch myself feeling frustrated in a meeting to write something, I remind myself of your story about working for a whole day on a figure that didn’t even make it into the SI. Vic Young, thanks for giving Evan an additional nickname for me, for giving me a deep appreciation of wallpapers, and for the confidence to do crystallography. John Ellis, thank you for taking a rare chance on an eager undergrad into your inorganic class. Your classes irrevocably altered the way I think of inorganometallic chemistry; I still have (and check) all of your notes!

Which brings me to the Tilley group, my cohort of graduate students from 2018, and the staff at Berkeley. Don, I will forever appreciate the freedom you gave me, and the faith you put in me. I would do it again. Hasan, Simon, Nick, Miao, Chithra, and Cooper, thank you for not only forming the backbone of the university, but for your immense patience and kindness. Hasan and Simon especially, your advice and expertise were critical to my studies. To my fellow 12A GSIs, you all are incredible scientists and friends. Andre I am so excited to see where your career takes you because I know you’ll be crushing it. Hopefully now that I’m less busy I can actually call you more often. Trevor, thank you for joining us on some incredible camping trips. Josh, as my original cube coworker it was tough to have you go, but hopefully seeing me spend so many years struggling has convinced you it was the right call. With my newfound free time I am always down to bonk

on a ridiculous ride with you. Patrick, I barely overlapped with you, but I have learned so much from you in the couple of days we spent doing EPR together. Irene, I wish I was able to interact with you more but it sounds like you're killing it. Ben, I should have listened to you way way way more: kinetics was a terrible idea, and I finally understand why you were always cautious about gerunds. Your students will appreciate your dedication to both good writing and thorough science. Ryan, you embody "cool as a cucumber," right until you've had two beers by the campfire, at which point nobody could be as animated about insurance. Thanks to you I will never trust the color of a compound again. Amelie, somehow whenever you were in the 571 box we were always discussing something ridiculous; I hope you continue the passion for discussing the differences between messy and unclean (it just struck me that unclean itself is a naphthyridine neurosis). Jom, you are the nicest, most excited chemist I have ever had the pleasure of working with. I am still blown away by how indefatigable you always seemed to be. I look forward to seeing all the progress your group will make in Alberta! Harry, some of my biggest regrets in grad school are having never been to any of your house parties, or getting crushed by you in tennis. I will never forget the way you transformed the knot story from an accident into a target and the way that conversion made all of the difference. I am excited to not be able to understand your independent publications. Rex, nothing I could write here could properly express my gratitude for you; if I could properly convey anything to you, I would want you to know that I wouldn't have had any fun in grad school if it weren't for you. You are a true role model and because of that, I am certain your students will grow tremendously as people and scientists. Whenever I feel lost in the sauce, I ask myself what you would be doing in that moment. I am so excited to attend your wedding and to visit Vancouver with you again. You and Katherine are a blast to hang out with and . Love you dude. Elle, I'm sorry you didn't get to pick up where you left off on the cubane project. I hope your graduation goes smoother than mine. Matt, I can tell you really are growing as a scientist, even though it's often driving you crazy. Thanks for always teaching me the hip new lingo. Oh, and thank goodness there was another midwestern coffee nerd in the group or I would have truly lost it. August, thanks for roaming the corridors with Rex and me searching for scrap late at night. I hope you keep in touch about what you're planning after all of this. Jose, it was super fun to work with you to make that soluble iodosylbenzene derivative. I am really impressed with how much you've learned since then, and I hope you continue that trajectory. Vincent, I am so happy to have had you become a legacy of team cubane. You took the skeleton of a project idea and turned it into incredible science in no time. You have to end up teaching one day because you would be such a fun professor to have as an undergraduate. Robert, thank you for joining the cubane team, and for making time to pick up Ti! I know it's brutally difficult at the moment, but I'm optimistic that very soon you'll have a better understanding of this wild mechanism than I do. Rhett, the Tilley-Canada connection must go on. You are clearly a very capable chemist and I hope to see you ramp up to Rex level soon. Nathalie, I really enjoy talking to you about science, you always sound excited! Now for the Tilley post-docs: Raul, I have never met you but thank you for the endless stories you gave everyone before me. Addison, congratulations on everything you've achieved since I first met you in Ian's group. I can't think of someone more passionate about the true advances in chemistry. Yang-Jin, (John) thank you for being a part of team cubane. Dawson, I really appreciate the way you were able to go with the flow: "you'll do." Pablo (and Valle), you arrived at probably the worst possible moment to start a post-doc, but also probably when the Tilley lab needed you

the most. Without you the Tilley group would've languished for much longer, but seeing the way you threw yourself into it every day really lit fires under us. You also have a great sense of humor that I appreciate, and I hope to visit you two and Olivia soon! Stefan, as the most recent member of team cubane, I wish I had been a better and more focused student back then, and that I'd taken the advice of Whitesides when you sent his paper on papers over to me. I will never forget your attitude toward bad beer, it belongs in the sink. Laurent, thank you for teaching me so many tips and tricks for echem and for your patience when I was slow solving structures for you. Tyler, you are the only person I've ever met who I've wanted to strangle so often, but that I would still consider a friend. I am excited to hear about your program, and I hope that research starts to improve in Regensburg. Thanks for being the group id. There were many incredible undergraduates in the group I would like to acknowledge but my interactions with many of you were exceptional. To all of my 12A undergrads, you were so much fun and a great introduction to Cal. Peiqiao Xie (Jocelyn), thank you for being my guinea pig and learning with me as I learned how to mentor. Sammy, I wish things had been more straightforward and we could've pushed that substituted cubane project further. Shilin, I appreciate the way you listened to my 'sage' advice and took my 'homework' assignments so seriously, even if they didn't pan out. I have high expectations for you in John Anderson's lab and the next time I'm in Chicago you are my #1 priority visit. Qinchuan (Max), these words are meaningless now but you were such an inspiration and I had never been so positive before that an undergrad deserved to be a PI before I met you.

NL, thank you for the constant reminder to enjoy pushing the rock up the hill.

I need to thank some very special individuals Cece and I encountered on our myriad walks through Berkeley. Camper, 2622 Benvenue roof boy, Penny, Prince, Ring, Claremont steps, Mochi, Derrick, Sammy (RIP), Charlie, Sky, Tux & Edo, Snorf, Mercury, Stumpy, Cleo, Meowy, pudge faces, Sid, and Flüf (Satsuma). "They are cats; they are fluffy."

Finally, Cece, you took a leap of faith moving out here with me after having only known me for a year and a half. I could not have been luckier to have met you at such a pivotal moment in my life. Over the last six years, you have taught me so much about who I am. Thank you for your support, for pushing yourself constantly, for going on thousands of walks with me, for appreciating my hobbies and finding amusement in my amusement. I will always love and appreciate you.

Chapter 1

Facets of the Oxygen Evolving Complex Relevant to Synthetic Inorganic Chemists

Overview.

Bioinorganic chemists are motivated by the study of the myriad enzymatic active sites that contain metal ions. These studies help to elucidate the spectroscopic properties and reactivity patterns of biomimetic complexes, which are useful tools for probing the hypotheses generated by biochemists studying native enzymes. This interplay between the development of biomimetic models and advances in enzymatic chemistry has proven fruitful to both inorganometallic and biochemists. As the power of the spectroscopic techniques available for metalloenzymes improve, the biomimetic complexes must begin to address more precise questions about the active site. In order to synthesize models capable of answering these questions, inorganic chemists must understand the increasingly sophisticated domain of the target enzyme. The goal of this chapter is to describe diagrammatically the current understanding of one such enzyme active site, the oxygen evolving complex, as it is relevant to synthetic inorganic chemists. This brief overview cannot express the nuances of biological water oxidation. The intent is to provide a foundation to understand the many excellent reviews available in the literature, which the reader should examine.[1-11]

A Potential Remedy to Anthropogenic Climate Change.

Photosystem II is a membrane pigment-protein found in bacteria and plants that absorbs solar radiation to perform charge separation, from which energy can be stored in the form of chemical bonds. In doing so, photosystem II (PSII) harvests the electrons from water to generate dioxygen and protons in a process known as the oxygen evolution reaction (OER).[1, 2, 12] Aerobic life depends on this ability of photosynthetic organisms to efficiently catalyze the OER, and in turn humanity has become dependent on the fossil fuel energy that was stored in those chemical bonds billions of years ago.[13-15]

At the present moment, the accumulation of atmospheric CO_2 derived from the burning of fossil fuels is the root cause of anthropogenic climate change, the consequences of which are likely to be devestating.[16, 17] In order to limit a climate change driven catastrophe, it is therefore necessary to look to new sources of energy.[18, 19] One such alternative could involve production of fuel by way of solar driven water splitting.[13] Indeed, several devices that utilize solar (or solar derived) energy to convert water into fuels have been fabricated, but a barrier to their widespread adoption is the low efficiency due to energy lost catalyzing the OER.[20-22] The most promising and scalable OER catalysts are based on metal oxides, which are difficult to rationally optimize. The efficient active site of PSII, known as the oxygen evolving complex (OEC), is one source of inspiration to the challenge of an efficient OER.

Structure and Overview of the OEC.

The OEC is a calcium-manganese oxo cluster composed of a $CaMn_3O_4$ heterocubane, with an additional pendent metal ion known as "the dangler" (Figure 1); it is only recently that high resolution X-ray diffraction (XRD) data capable of precisely determining the connectivity of the OEC became available.[23-26] Prior to the availability of high resolution data from X-ray diffraction analysis of PSII, numerous studies were key to developing a mechanistic hypothesis and model for the $CaMn_4O_4$ cluster, and several of these studies are also important for understanding the language used to describe the OEC.[2] The studies that established the Mn and Ca ion requirement for OER activity, isotopic labeling studies, and early EPR measurements were critical, but the keystone experiments were polarographic measurements that related the number of light flashes to the yield of oxygen produced by isolated chloroplasts.[9,27-29] In these experiments, an electrochemical method was used to precisely determine the concentration of oxygen following successive flashes of light which could be repeated at short intervals. These remarkable experiments demonstrated that oxygen was first produced following three flashes, after which point oxygen was produced every four flashes. These studies led to the proposal of the Kok cycle, which uses S_i-states (i = 0-4) as a notation to describe the mechanism by which the OEC oxidizes water.[30,31]

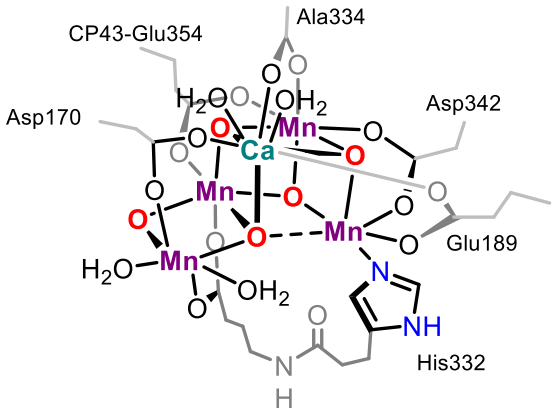


Figure 1. Schematic representation of the oxygen evolving complex in the S_1 state. Amino acid side chains truncated, ambiguous μ-oxo hydrogen atoms not shown. The core structure is a $CaMn_3O_4$ heterocubane, with an additional Mn ion appended by a μ_2-oxo ligand. The dashed line reflects the possibility of a bonding interaction between Mn and the μ_3-oxo ligand, although current crystallographic and computational analysis suggests that there is no bond.

In the Kok cycle, the OEC is progressively oxidized by a tyrosine radical, known as Y_z, to accumulate the charge required to oxidize water.[1,32-34] The electron transfer events to produce this Y_z radical are not critical to this discussion. The OER initiates from the S_1-state, from which only three oxidations are required to reach the transitive S_4 state (Figure 2). After the collapse of the S_4 state to generate O_2, the OEC returns to the S_0 state, now requiring four flashes to turnover. The Kok cycle starts in the S_1 state because the S_2 and S_3 states, in the absence of the oxidizing conditions (light), eventually decay back to the S_1 state, and the S_1 state is indefinitely stable under these conditions. Thus, the S_1 state is known as the dark-stable state.[9,28]

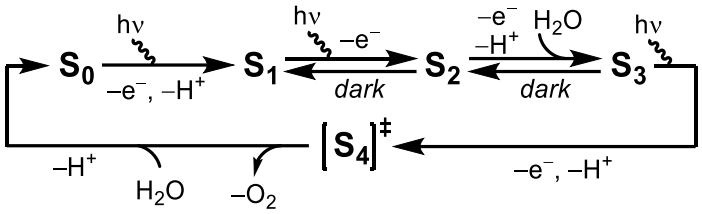


Figure 2. The Kok cycle as it is currently understood. The use of hν substitutes for a full description of the light induced oxidation relay; alternatively, the active oxidant could be represented by the tyrosine radical (Y_z).

Historically, two proposals were made for the oxidation states of the Mn ions throughout the Kok cycle, referred to as the low- and high-valent schemes, however the latter scheme is so widely favored in the literature that the low-valent paradigm will not be considered in this discussion.[35] In the S_0 state, the oxidation states of the Mn ions in OEC are distributed as $(Mn^{III})_3(Mn^{IV})$. The Mn^{III} ions are successively oxidized to Mn^{IV} until the S_3 state, at which point all of the Mn ions are Mn^{IV}. A variety of oxidation states have been proposed for the transitive S_4 state, including $[Mn^{IV}_4]^+$ (oxyl radical), $(Mn^{IV})_3(Mn^{V})$, and even $(Mn^{III})_3(Mn^{VII})$, but the consensus is increasingly that the $[Mn^{IV}_4]^+$ oxyl radical proposal is most likely. The Mn ion proposed to access these high oxidation states is the pendent "dangler" Mn4, while the oxyl radical is believed to be either O5, or a transiently formed terminal oxyl ligand (Figure 3). As the oxidizing equivalents required for the OER are stored by the Mn ions, the positive charge is balanced by dissociation of protons into proton channels in a 1:0:1:2 stoichiometry following each flash.[3,36-38] As depicted in Figure 3, it may be more accurate to describe this as a 1:0:1:1:1 process, because the protons are all lost in one of the five transitions in the Kok cycle.

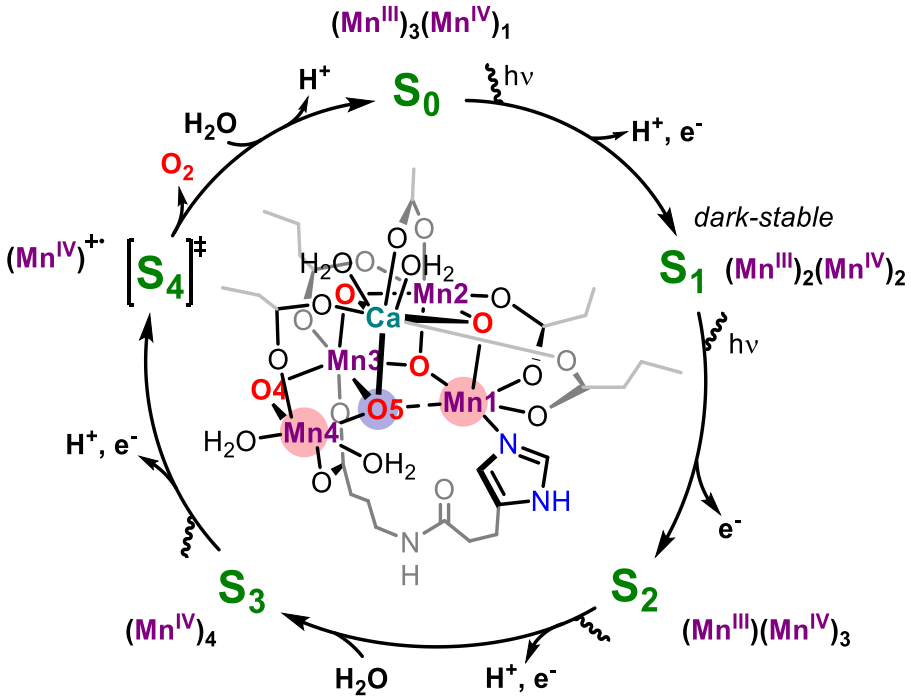


Figure 3. Depiction of the key features of the Kok cycle with structure of the OEC in the S_0, S_1 or S_2 states inset.

A few possibilities exist for the timing of the introduction of substrate waters. In one class of proposed mechanisms, both substrate waters are replenished as ligands bound to Mn and or Ca immediately following oxygen evolution. In the other class of mechanisms, the water molecules bind to the OEC during two different S state transitions. The first water binds in the $S_4 \rightarrow S_0$ transition after O_2 is formed, at which point water is inserted into the Mn cluster. The second water binds during the $S_2 \rightarrow S_3$ transition and is believed to insert between O5 and Mn1, the crystallographic labels used to describe the OEC core (Figure 3).

The above is the necessary background to understand the following discussion of the Kok cycle based on protein crystallography studies using X-ray free electron lasers (XFEL). XFEL are sources of coherent, high power, X-ray pulses with extremely fast, tunable pulse lengths.[39,40] These factors make XFEL ideally suited for the study of short-lived metalloenzyme intermediates such as the S-states in the Kok cycle.[41,42]

Intermediates Observed by X-ray Diffraction Analysis with Free Electron Laser Sources.

Macromolecular X-ray crystallographic studies require X-ray flux only achievable using synchrotron radiation. Unfortunately, the X-ray intensities required for protein crystallography can also damage the sample, which leads to an averaging of the damaged and undamaged samples in the refined solid-state molecular structure. For PSII in particular, radiation damage introduces varying amounts (depending on factors such as the dose intensity) of a reduced OEC cluster that, on the basis of bond distances, is more consistent with the presence of Mn^{II} ions. This photoreduction process by conventional synchrotron radiation sources can be mitigated, but not completely eliminated. In contrast, XFEL delivers significantly higher doses of radiation in an ultrafast pulse (on the order of femtoseconds) to generate diffraction images before any photoreduction can occur.

The first studies of PSII using XFEL demonstrated the feasibility of the XFEL approach, and a dataset with a resolution of 6.5 Å was obtained.[43] This resolution is sufficient to determine the protein structure, but not of high enough quality to precisely define the OEC. The subsequent study collected X-ray emission spectroscopy (XES) and XRD data in tandem to determine the Mn ion oxidation states and extent of damage in the S_1- and S_2-states. The OEC can be enriched with S-states higher than the S_1 state by saturating the sample with well-timed flashes from a laser or LED. The extent of each S-state can be measured by difference FTIR spectroscopy and by optimizing the O_2 yield from samples of PSII. With these data, the contributions to the solid-state structure from each of the S-states can be determined, and the data subtracted to examine a singular S_i-state. Data for the S_1 state was collected at a resolution of 5.7 Å, with some analysis done on data cutoff at 4.1 Å.[44] Notably, the X-ray emission spectroscopic data demonstrated that the extent of photoreduction was significantly lower in these datasets. Attempts to examine the S_2 state were also made, and the tandem spectroscopic techniques indicated that at this resolution, structural variations in the active site and photoreduction were minimal. This was shortly followed by a study of PSII in the S_1-, S_3-, and S_0-state which concluded that, at resolutions higher than 4.5 Å, significant changes (> 0.5 Å) in the OEC geometry were not observable.[45] The simultaneously collected XES data of PSII advancing from $S_3 \rightarrow (S_4) \rightarrow S_0$ at 250 μs supported prior findings that

Mn is not oxidized in this time frame, which was taken as evidence for slow formation of a Mn^{V} intermediate, or an oxyl radical.

The next study reexamined the S_1 state at a resolution of 5.0 Å, and endeavored to collect data on the S_3-state, with a dataset at a resolution of 5.5 Å.[46] In the S_1 state at this resolution, compared to conventional X-ray datasets, a slight contraction of the OEC bond distances was observed. The authors report that the solid-state molecular structure of the OEC in the putative S_3 state reveals an increase in the distance between Mn4 and Mn1, which had been computationally proposed.[47-49] However, subsequent commentary has indicated that caution should be taken as to the significance of this observation.[50]

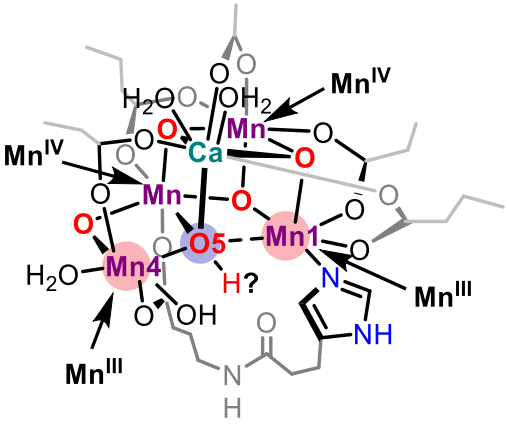


Figure 4. Solid-state molecular structure of the OEC in the S_1 state determined by XFEL at cryogenic temperatures.[51] Proposed O5–H moiety included.

The subsequent report achieved a significant enhancement in the resolution, to 1.95 Å, by collecting data on larger isomorphous crystals of PSII in the S_1 state at cryogenic temperature, once again revealing that previous structures suffered from some degree of photoreduction as the Mn—Mn distance was observed to be contracted in the structure obtained using XFEL.[51] The formal oxidation states of the Mn ions in this state were assigned on the basis of the Jahn-Teller distortion of Mn^{III} and the Mn–O bond distances. The long Mn4–O5 bond distance was taken as evidence that O5 may be a hydroxide ligand (Figure 4).

The next advance was a room-temperature study of PSII in the S_1-, and S_3-state, in addition to an ammonia enriched sample in the S_3 state, with resolutions of 3.0 Å, 2.8 Å, and 2.25 Å respectively.[52] In comparison to the structure measured at cryogenic temperature, significant changes were observed in the protein framework and unit cell dimensions, but the OEC itself was practically unchanged throughout these transitions. Comparison of the S_1- and S_3-states in this study provided evidence that the cubane undergoes distortion in this transition, as Mn4 was observed to be contorted away from the cubane, along with O5 (Figure 5).

Ammonia can bind to the OEC without halting OER activity, which suggests that sites where ammonia can bind are not necessarily the sites of OER substrate waters. In the ammonia enriched S_3 state, the data weakly support ammonia binding to a Mn4 site (Figure 5), and strongly imply

that O5 is not substituted. This suggests that both substrate waters do not necessarily originate on Mn4.

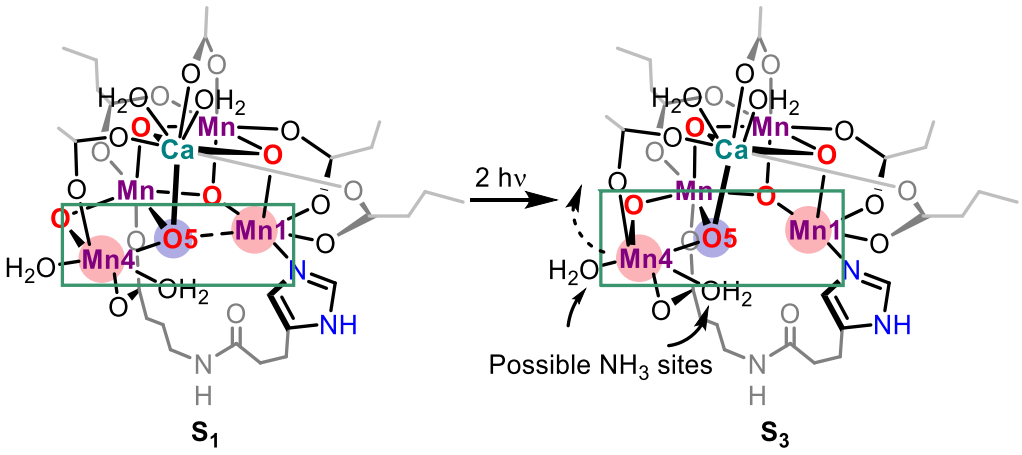


Figure 5. Change in the OEC structure observed from S_1- to S_3-state, with dashed arrow shown to indicate direction of distortion.[52]

At nearly the same time, a study of S_3-state enriched PSII using highly optimized conditions at a resolution of 2.35 Å provided evidence for a mechanistic pathway for O–O bond formation.[53] In this case, similar to the previous study, Mn4 was observed to move further away from the cubane. In addition, the Ca—Mn4 distance increases, and electron density for a never before observed oxygen ligand (O6) between O5 and Mn1 was located; the proposed O5—O6 distance of 1.5 Å is suggestive of bonding character. However, formation of an O–O bond in the S_3 state would run counter to the manganese oxidation states assigned by prior studies.

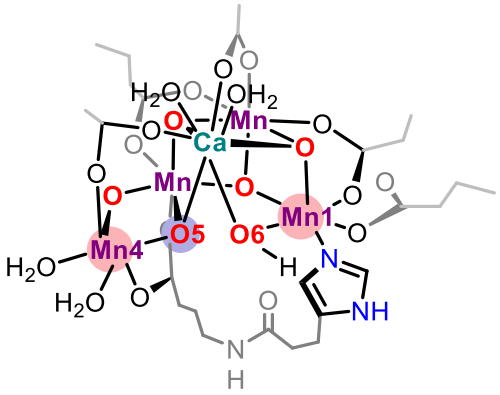


Figure 6. Proposed structure of the OEC with additional oxygen, O6, observed in the S_3-state.

The complete investigation into all of the S-states using XFEL at high resolution (ca. 2 Å) provided additional clarification.[54] In contrast to the prior study, the O5—Ox (O6 in Suga *et. al.*[53]) distance of 2.1 Å is consistent with two μ_2-oxo ligands without any bonding interaction. This observation is more consistent with prior experimental probes of the Mn oxidation states in the S3 state, and the measured XES data. The data also support a role for one of the water ligands on Ca (W3) being involved in substrate delivery. Thorough reexamination at cryogenic temperature supported these observations, i.e., that the O5—O_X/O6 distance is consistent with oxyl and oxo ligands, not a

peroxide intermediate in the S_3 state.[55] However in this case, the role of the Ca in water substrate delivery was proposed to be related to the dissociation of a Ca ligand (Glue 189), and not docking of a substrate water.

Investigation into the mechanism of water insertion during the $S_2 \rightarrow S_3$ transition (at resolutions between 2.01-2.27 Å) revealed that a carboxylate ligand bridging Ca and Mn1 plays a key role.[56] Additionally, while water insertion from one of the water channels (O1 channel) cannot be ruled out, the conformational changes required suggest that the involvement of a water ligand from Ca is more likely. Snapshots of the $S_2 \rightarrow S_3$ transition between 50 µs and 200 ms after illumination reveal that the carboxylate residue that chelates Ca and Mn1 (Glu 189) dissociates from Ca, and after this, the oxidation to Mn^{IV} and the insertion of O_X/O6 occur near simultaneously. The dissociated carboxylate possibly stabilizes the inserted hydroxide ligand through a hydrogen bonding interaction. This would be in contrast to proposals wherein O5 stabilizes the O_X/O_6 hydroxide by hydrogen bonding.[49,55]

Snapshots of the $S_3 \rightarrow [S_4]^{\ddagger} \rightarrow S_0$ state transition were examined to elucidate the timeline of O_2 evolution.[57] A lag between the reduction of Y_Z radical by the OEC and movement of moieties associated with the proton gate were observed, which may indicate that proton release proceeds oxidation to the $[S_4]^{\ddagger}$ transition. After the proton transfer and oxidation, a second delay was observed before a shortening of the Mn1—Mn4 distance, which is in line with a peroxide intermediate, followed by elimination of O_2, rather than a direct four electron reductive elimination of O_2. These data also support that the proposed O–O bond forming event occurs between O5 and O_X/O_6. Throughout the $S_3 \rightarrow S_0$ transition, the oxygen density for O5 remained observable, which suggests that displacement of O_2 is highly concerted, and that an open $CaMn_4O_4$ cluster is not an intermediate.

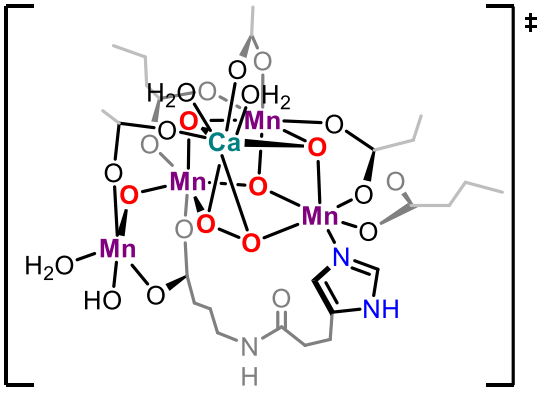


Figure 7. A possible peroxide intermediate,

Most recently, 14 datasets with resolutions between 2.15 and 2.30 Å at timepoints between flash advancement of the S_1-state were compared to examine the S_1-S_3 transitions.[58] In the $S_1 \rightarrow S_2$ transition, oxidation of the OEC results in an increase in the Mn4—Ca distance, followed by movement of Mn1 further away from the OEC core. The $S_2 \rightarrow S_3$ transition that follows revealed electron density that was suggested to support coordination of a hydroxide ligand to Ca, followed

by rapid delivery to Mn1 to form the bridging hydroxide O6. In this case, the water ligands of Ca did not appear to be likely to form the substrate ligand O6.

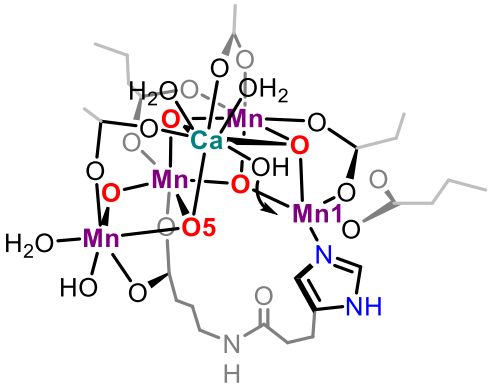


Figure 8. Structurally consistent proposal for the insertion of the hydroxide ligand onto Mn1.

The above (and Figure 9) summarizes the current understanding of the mechanism of OER by the OEC as determined by XFEL.[43-46,51-58] Absent from this overview of XFEL studies of PSII is a summary of the subtler changes to the protein framework that support much of the proposed mechanism. Finally, it should be noted that, in spite of the power of the technique, XFEL studies are far from definitive.[59]

To narrow the focus of this overview and emphasize structural motifs to be targeted, many of the most challenging questions about the OEC were unaddressed here, such as the structural isomers in the S_2 state observed by EPR spectroscopy,[10,60-63] and studies of substrate waters examined by time-resolved mass spectrometry.[64-66] Additionally, though fundamental to the mechanistic understanding of the OEC, computational studies were also not be discussed.[67-70]

Questions for Synthetic Inorganic Chemists.

Although synthetic chemists have been successful in modeling many of the unique bonding features of the OEC, several features have been difficult to replicate.[71,72] Notably, a synthetic model for Mn4 bridged by a μ_2-oxo has not been reported. Many of the remaining tasks for synthetic models relate to mimicking the observed reactivity of the OEC. Models should address the ability of Glu189 to assist in deprotonation of an aquo ligand, and to stabilize the resulting hydroxide ligand by hydrogen bonding. The exchange of $H_2{}^{18}O$ labeled water for the bridging oxo ligands of synthetic models has been investigated, but the interplay between the oxidation state of the Mn ions in the presence of a Mn4 mimic could prove useful to studies examining substrate water exchange rates.[73] Model systems targeting peroxide intermediates would also prove invaluable to understanding the OEC, especially if these peroxide structures eject O_2 in the presence of another ligand such as water. Finally, a frontier that has seen little exploration are model systems that replicate the OEC assembly process. The PSII framework that supports the active site is fairly rigid and helps to guide the synthesis and repair of the OEC, which is also photochemically driven and thought to occur through several distinct intermediates.[74-80]

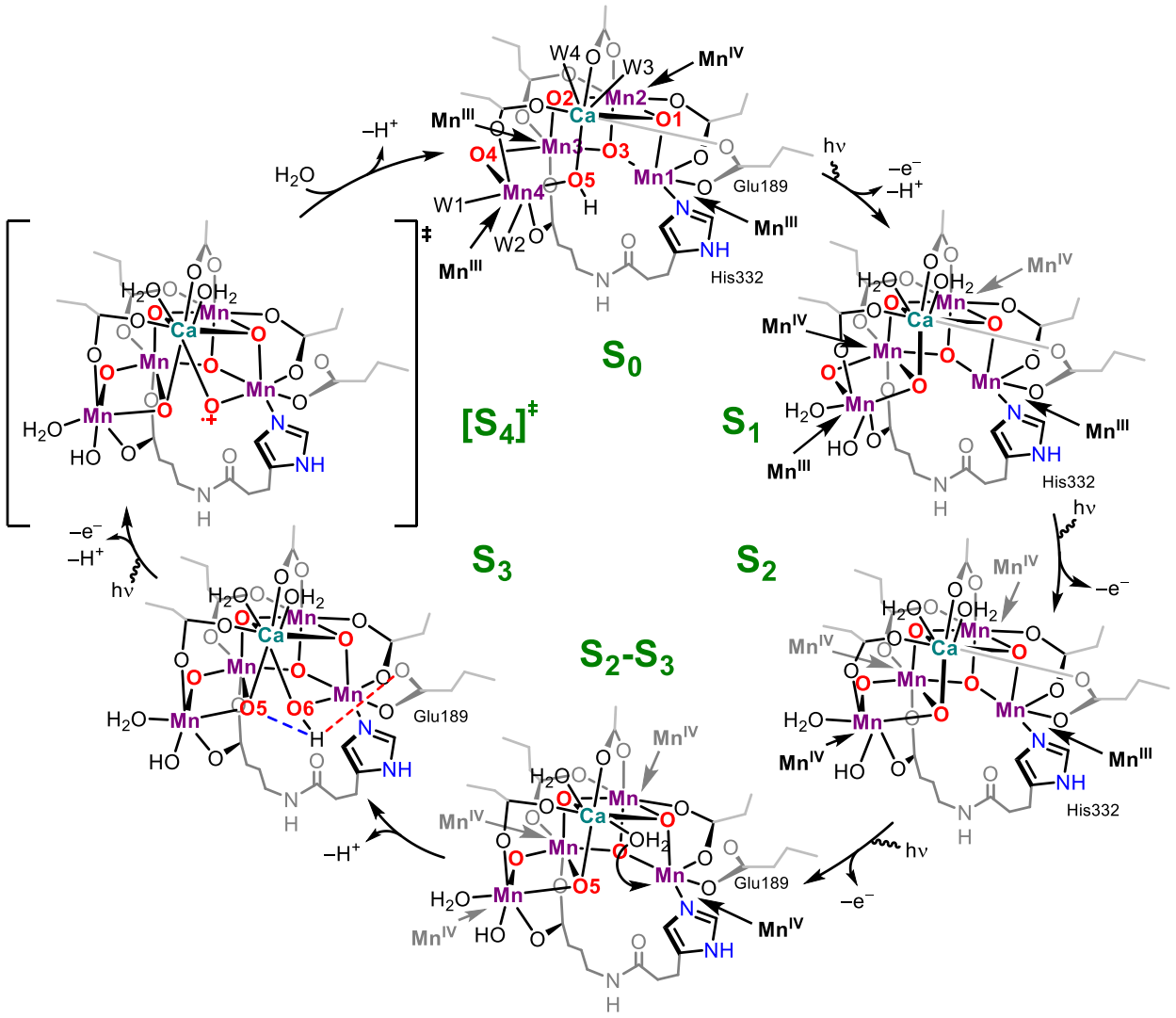


Figure 9. Depiction of the Kok cycle as determined by XFEL studies, with several steps that remain a part of the mechanistic debate selected. In the $S_2 \rightarrow S_3$ transition, the role of the Ca ion in regulating the insert of W3, or a hydroxide from the bulk solvent is still unclear. It is also possible that Glu189 assists in this insertion. In the S_3-state, both O5 and Glu189 have been proposed to hydrogen bond the O6 hydroxide proton, as indicated by the dashed lines. In the S_4-state, O6 is proposed to have significant oxyl radical character, but the O–O bond forming steps and the egress of O_2 from the OEC are not well-understood.

Concluding Remarks.

Synthetic OEC model systems are still relevant to the OEC.[5,81-84] This overview seeks to rationalize the following synthetic studies and provide context as to the mechanistic questions that are of interest to bioinorganic chemists. The synthesis of "open" Co_3O_4 cubanes that may be relevant to the biosynthesis of the OEC is examined in Chapter 2. In Chapter 3, the interaction of exogeneous metal atoms with Co_4O_4 cubanes, similar to Mn4 with the OEC, and the metal-metal redox-exchange chemistry that ensues is detailed. Then, metal-metal redox exchange chemistry is used to synthesize a VCo_3O_4 cubane and the reactivity of this cluster is investigated in Chapter 4.

References:

1. Yano, J.; Yachandra, V., Mn_4Ca Cluster in Photosynthesis: Where and How Water is Oxidized to Dioxygen. *Chem. Rev.* **2014,** *114*, 4175-4205.
2. Yachandra, V. K.; Sauer, K.; Klein, M. P., Manganese Cluster in Photosynthesis: Where Plants Oxidize Water to Dioxygen. *Chem. Rev.* **1996,** *96*, 2927-2950.
3. Cox, N.; Pantazis, D. A.; Lubitz, W., Current Understanding of the Mechanism of Water Oxidation in Photosystem II and Its Relation to XFEL Data. *Annu. Rev. Biochem* **2020,** *89*, 795-820.
4. Pantazis, D. A., Missing Pieces in the Puzzle of Biological Water Oxidation. *ACS Catalysis* **2018,** *8*, 9477-9507.
5. Paul, S.; Neese, F.; Pantazis, D. A., Structural models of the biological oxygen-evolving complex: achievements, insights, and challenges for biomimicry. *Green Chemistry* **2017,** *19*, 2309-2325.
6. Pérez-Navarro, M.; Neese, F.; Lubitz, W.; Pantazis, D. A.; Cox, N., Recent developments in biological water oxidation. *Curr. Opin. Chem. Biol.* **2016,** *31*, 113-119.
7. Simon, P. S.; Makita, H.; Bogacz, I.; Fuller, F.; Bhowmick, A.; Hussein, R.; Ibrahim, M.; Zhang, M.; Chatterjee, R.; Cheah, M. H.; Chernev, P.; Doyle, M. D.; Brewster, A. S.; Alonso-Mori, R.; Sauter, N. K.; Bergmann, U.; Dobbek, H.; Zouni, A.; Messinger, J.; Kern, J.; Yachandra, V. K.; Yano, J., Capturing the Sequence of Events during the Water Oxidation Reaction in Photosynthesis using XFELs. *FEBS Lett.* **2023,** *597*, 30-37.
8. Shevela, D.; Kern, J. F.; Govindjee, G.; Messinger, J., Solar Energy Conversion by Photosystem II: Principles and Structures. *Photosynth. Res.* **2023,** *156*, 279-307.
9. Joliot, P., Period-four Oscillations of the Flash-induced Oxygen Formation in Photosynthesis*. *Photosynth. Res.* **2003,** *76*, 65-72.
10. Cox, N.; Pantazis, D. A.; Neese, F.; Lubitz, W., Biological Water Oxidation. *Acc. Chem. Res.* **2013,** *46*, 1588-1596.
11. Huang, H. L.; Brudvig, G. W., 8.22 - Oxygen Evolution of Photosystem II. In *Comprehensive Coordination Chemistry III*, Constable, E. C.; Parkin, G.; Que Jr, L., Eds. Elsevier: Oxford, 2021; pp 569-588.
12. Barber, J., *Oxygen Production and Reduction in Artificial and Natural Systems*. WORLD SCIENTIFIC: 2018; p 436.
13. Barber, J., How Biology Solved Its Energy Problem and Implications for the Future of Humankind. In *Oxygen Production and Reduction in Artificial and Natural Systems*, WORLD SCIENTIFIC: 2018; pp 1-30.
14. Kutcherov, V. G.; Krayushkin, V. A., Deep-seated Abiogenic Origin of Petroleum: From Geological Assessment to Physical Theory. *Reviews of Geophysics* **2010,** *48* .
15. Tissot, B.; Welte, D., Petroleum Formation and Occurrence, 2nd edn, 699 pp. Springer, Berlin: 1984.
16. Lewis, N. S.; Nocera, D. G., Powering the Planet: Chemical Challenges in Solar Energy Utilization. *Proc. Natl. Acad. Sci. U.S.A.* **2006,** *103*, 15729-15735.
17. Lee, H.; Calvin, K.; Dasgupta, D.; Krinner, G.; Mukherji, A.; Thorne, P.; Trisos, C.; Romero, J.; Aldunce, P.; Barrett, K., Climate Change 2023: Synthesis Report. Contribution of Working Groups I, II and III to the Sixth Assessment Report of the Intergovernmental Panel on Climate Change. **2023**.
18. Blankenship, R. E.; Tiede, D. M.; Barber, J.; Brudvig, G. W.; Fleming, G.; Ghirardi, M.; Gunner, M. R.; Junge, W.; Kramer, D. M.; Melis, A.; Moore, T. A.; Moser, C. C.; Nocera, D.

G.; Nozik, A. J.; Ort, D. R.; Parson, W. W.; Prince, R. C.; Sayre, R. T., Comparing Photosynthetic and Photovoltaic Efficiencies and Recognizing the Potential for Improvement. *Science* **2011,** *332*, 805-809.
19. Lewis, N. S., Research Opportunities to Advance Solar Energy Utilization. *Science* **2016,** *351*, aad1920.
20. Ifkovits, Z. P.; Evans, J. M.; Meier, M. C.; Papadantonakis, K. M.; Lewis, N. S., Decoupled Electrochemical Water-splitting Systems: a Review and Perspective. *Energy & Environmental Science* **2021,** *14*, 4740-4759.
21. Barber, J., Photosynthetic Water Splitting Provides a Blueprint for Artificial Leaf Technology. *Joule* **2017,** *1*, 5-9.
22. Nocera, D. G., The Artificial Leaf. *Acc. Chem. Res.* **2012,** *45*, 767-776.
23. Kawakami, K.; Umena, Y.; Kamiya, N.; Shen, J.-R., Structure of the Catalytic, Inorganic Core of Oxygen-evolving Photosystem II at 1.9Å resolution. *Journal of Photochemistry and Photobiology B: Biology* **2011,** *104*, 9-18.
24. Umena, Y.; Kawakami, K.; Shen, J.-R.; Kamiya, N., Crystal Structure of Oxygen-evolving Photosystem II at a Resolution of 1.9 Å. *Nature* **2011,** *473*, 55-60.
25. Zouni, A.; Witt, H.-T.; Kern, J.; Fromme, P.; Krauss, N.; Saenger, W.; Orth, P., Crystal Structure of Photosystem II from Synechococcus elongatus at 3.8 Å Resolution. *Nature* **2001,** *409*, 739-743.
26. Ferreira Kristina, N.; Iverson Tina, M.; Maghlaoui, K.; Barber, J.; Iwata, S., Architecture of the Photosynthetic Oxygen-Evolving Center. *Science* **2004,** *303*, 1831-1838.
27. Joliot, P., Kinetic Studies of Photosystem II in Photosynthesis*. *Photochem. Photobiol.* **1968,** *8*, 451-463.
28. Kok, B.; Forbush, B.; McGloin, M., Cooperation of Charges in Photosynthetic O_2 Evolution–I. A Linear Four Step Mechanism. *Photochem. Photobiol.* **1970,** *11*, 457-475.
29. Joliot, P.; Joliot, A., A Polarographic Method for Detection of Oxygen Production and Reduction of Hill Reagent by Isolated Chloroplasts. *Biochimica et Biophysica Acta (BBA) - Bioenergetics* **1968,** *153*, 625-634.
30. Joliot, P.; Joliot, A.; Kok, B., Analysis of the Interactions between the Two Photosystems in Isolated Chloroplasts. *Biochimica et Biophysica Acta (BBA) - Bioenergetics* **1968,** *153* (3), 635-652.
31. Law, N. A.; Caudle, M. T.; Pecoraro, V. L., Manganese Redox Enzymes and Model Systems: Properties, Structures, and Reactivity. In *Adv. Inorg. Chem.*, Sykes, A. G., Ed. Academic Press: 1998; Vol. 46, pp 305-440.
32. Blakemore, J. D.; Crabtree, R. H.; Brudvig, G. W., Molecular Catalysts for Water Oxidation. *Chem. Rev.* **2015,** *115*, 12974-13005.
33. McEvoy, J. P.; Brudvig, G. W., Water-Splitting Chemistry of Photosystem II. *Chem. Rev.* **2006,** *106*, 4455-4483.
34. Brudvig, G. W., Water Oxidation Chemistry of Photosystem II. *Philosophical Transactions of the Royal Society B: Biological Sciences* **2007,** *363*, 1211-1219.
35. Krewald, V.; Retegan, M.; Cox, N.; Messinger, J.; Lubitz, W.; DeBeer, S.; Neese, F.; Pantazis, D. A., Metal oxidation states in biological water splitting. *Chem. Sci.* **2015,** *6*, 1676-1695.
36. Schlodder, E.; Witt, H. T., Stoichiometry of Proton Release from the Catalytic Center in Photosynthetic Water Oxidation: Reexamination by a Glass Electrode Study at pH 5.5–7.2. *J. Biol. Chem.* **1999,** *274*, 30387-30392.

37. Dau, H.; Haumann, M., Eight Steps Preceding O–O Bond Formation in Oxygenic Photosynthesis—A Basic Reaction Cycle of the Photosystem II Manganese Complex. *Biochimica et Biophysica Acta (BBA) - Bioenergetics* **2007,** *1767*, 472-483.
38. Suzuki, H.; Sugiura, M.; Noguchi, T., Monitoring Proton Release during Photosynthetic Water Oxidation in Photosystem II by Means of Isotope-Edited Infrared Spectroscopy. *J. Am. Chem. Soc.* **2009,** *131*, 7849-7857.
39. Margaritondo, G.; Rebernik Ribic, P., A Simplified Description of X-ray Free-electron Lasers. *Journal of Synchrotron Radiation* **2011,** *18*, 101-108.
40. Bergmann, U.; Kern, J.; Schoenlein, R. W.; Wernet, P.; Yachandra, V. K.; Yano, J., Using X-ray free-electron lasers for spectroscopy of molecular catalysts and metalloenzymes. *Nature Reviews Physics* **2021,** *3*, 264-282.
41. Neutze, R.; Wouts, R.; van der Spoel, D.; Weckert, E.; Hajdu, J., Potential for Biomolecular Imaging with Femtosecond X-ray Pulses. *Nature* **2000,** *406*, 752-757.
42. Chapman, H. N.; Fromme, P.; Barty, A.; White, T. A.; Kirian, R. A.; Aquila, A.; Hunter, M. S.; Schulz, J.; DePonte, D. P.; Weierstall, U.; Doak, R. B.; Maia, F. R. N. C.; Martin, A. V.; Schlichting, I.; Lomb, L.; Coppola, N.; Shoeman, R. L.; Epp, S. W.; Hartmann, R.; Rolles, D.; Rudenko, A.; Foucar, L.; Kimmel, N.; Weidenspointner, G.; Holl, P.; Liang, M.; Barthelmess, M.; Caleman, C.; Boutet, S.; Bogan, M. J.; Krzywinski, J.; Bostedt, C.; Bajt, S.; Gumprecht, L.; Rudek, B.; Erk, B.; Schmidt, C.; Hömke, A.; Reich, C.; Pietschner, D.; Strüder, L.; Hauser, G.; Gorke, H.; Ullrich, J.; Herrmann, S.; Schaller, G.; Schopper, F.; Soltau, H.; Kühnel, K.-U.; Messerschmidt, M.; Bozek, J. D.; Hau-Riege, S. P.; Frank, M.; Hampton, C. Y.; Sierra, R. G.; Starodub, D.; Williams, G. J.; Hajdu, J.; Timneanu, N.; Seibert, M. M.; Andreasson, J.; Rocker, A.; Jönsson, O.; Svenda, M.; Stern, S.; Nass, K.; Andritschke, R.; Schröter, C.-D.; Krasniqi, F.; Bott, M.; Schmidt, K. E.; Wang, X.; Grotjohann, I.; Holton, J. M.; Barends, T. R. M.; Neutze, R.; Marchesini, S.; Fromme, R.; Schorb, S.; Rupp, D.; Adolph, M.; Gorkhover, T.; Andersson, I.; Hirsemann, H.; Potdevin, G.; Graafsma, H.; Nilsson, B.; Spence, J. C. H., Femtosecond X-ray Protein Nanocrystallography. *Nature* **2011,** *470*, 73-77.
43. Kern, J.; Alonso-Mori, R.; Hellmich, J.; Tran, R.; Hattne, J.; Laksmono, H.; Glöckner, C.; Echols, N.; Sierra, R. G.; Sellberg, J.; Lassalle-Kaiser, B.; Gildea, R. J.; Glatzel, P.; Grosse-Kunstleve, R. W.; Latimer, M. J.; McQueen, T. A.; DiFiore, D.; Fry, A. R.; Messerschmidt, M.; Miahnahri, A.; Schafer, D. W.; Seibert, M. M.; Sokaras, D.; Weng, T.-C.; Zwart, P. H.; White, W. E.; Adams, P. D.; Bogan, M. J.; Boutet, S.; Williams, G. J.; Messinger, J.; Sauter, N. K.; Zouni, A.; Bergmann, U.; Yano, J.; Yachandra, V. K., Room Temperature Femtosecond X-ray Diffraction of Photosystem II Microcrystals. *Proc. Natl. Acad. Sci. U.S.A.* **2012,** *109*, 9721-9726.
44. Kern, J.; Alonso-Mori, R.; Tran, R.; Hattne, J.; Gildea, R. J.; Echols, N.; Glöckner, C.; Hellmich, J.; Laksmono, H.; Sierra, R. G.; Lassalle-Kaiser, B.; Koroidov, S.; Lampe, A.; Han, G.; Gul, S.; DiFiore, D.; Milathianaki, D.; Fry, A. R.; Miahnahri, A.; Schafer, D. W.; Messerschmidt, M.; Seibert, M. M.; Koglin, J. E.; Sokaras, D.; Weng, T.-C.; Sellberg, J.; Latimer, M. J.; Grosse-Kunstleve, R. W.; Zwart, P. H.; White, W. E.; Glatzel, P.; Adams, P. D.; Bogan, M. J.; Williams, G. J.; Boutet, S.; Messinger, J.; Zouni, A.; Sauter, N. K.; Yachandra, V. K.; Bergmann, U.; Yano, J., Simultaneous Femtosecond X-ray Spectroscopy and Diffraction of Photosystem II at Room Temperature. *Science* **2013,** *340*, 491-495.
45. Kern, J.; Tran, R.; Alonso-Mori, R.; Koroidov, S.; Echols, N.; Hattne, J.; Ibrahim, M.; Gul, S.; Laksmono, H.; Sierra, R. G.; Gildea, R. J.; Han, G.; Hellmich, J.; Lassalle-Kaiser, B.; Chatterjee, R.; Brewster, A. S.; Stan, C. A.; Glöckner, C.; Lampe, A.; DiFiore, D.; Milathianaki, D.; Fry, A. R.; Seibert, M. M.; Koglin, J. E.; Gallo, E.; Uhlig, J.; Sokaras, D.; Weng, T.-C.;

Zwart, P. H.; Skinner, D. E.; Bogan, M. J.; Messerschmidt, M.; Glatzel, P.; Williams, G. J.; Boutet, S.; Adams, P. D.; Zouni, A.; Messinger, J.; Sauter, N. K.; Bergmann, U.; Yano, J.; Yachandra, V. K., Taking Snapshots of Photosynthetic Water Oxidation using Femtosecond X-ray Diffraction and Spectroscopy. *Nat. Commun* **2014,** *5*, 4371.
46. Kupitz, C.; Basu, S.; Grotjohann, I.; Fromme, R.; Zatsepin, N. A.; Rendek, K. N.; Hunter, M. S.; Shoeman, R. L.; White, T. A.; Wang, D.; James, D.; Yang, J.-H.; Cobb, D. E.; Reeder, B.; Sierra, R. G.; Liu, H.; Barty, A.; Aquila, A. L.; Deponte, D.; Kirian, R. A.; Bari, S.; Bergkamp, J. J.; Beyerlein, K. R.; Bogan, M. J.; Caleman, C.; Chao, T.-C.; Conrad, C. E.; Davis, K. M.; Fleckenstein, H.; Galli, L.; Hau-Riege, S. P.; Kassemeyer, S.; Laksmono, H.; Liang, M.; Lomb, L.; Marchesini, S.; Martin, A. V.; Messerschmidt, M.; Milathianaki, D.; Nass, K.; Ros, A.; Roy-Chowdhury, S.; Schmidt, K.; Seibert, M.; Steinbrener, J.; Stellato, F.; Yan, L.; Yoon, C.; Moore, T. A.; Moore, A. L.; Pushkar, Y.; Williams, G. J.; Boutet, S.; Doak, R. B.; Weierstall, U.; Frank, M.; Chapman, H. N.; Spence, J. C. H.; Fromme, P., Serial Time-resolved Crystallography of Photosystem II using a Femtosecond X-ray Laser. *Nature* **2014,** *513*, 261-265.
47. Isobe, H.; Shoji, M.; Yamanaka, S.; Umena, Y.; Kawakami, K.; Kamiya, N.; Shen, J. R.; Yamaguchi, K., Theoretical illumination of water-inserted structures of the $CaMn_4O_5$ cluster in the S_2 and S_3 states of Oxygen-evolving Ccomplex of Photosystem II: Full Geometry Optimizations by B3LYP Hybrid Density Functional. *Dalton Trans.* **2012,** *41*, 13727-13740.
48. Siegbahn, P. E. M., Mechanisms for proton release during water oxidation in the S2 to S3 and S3 to S4 transitions in photosystem II. *PCCP* **2012,** *14*, 4849-4856.
49. Siegbahn, P. E. M., Structures and Energetics for O2 Formation in Photosystem II. *Acc. Chem. Res.* **2009,** *42*, 1871-1880.
50. Sauter, N. K.; Echols, N.; Adams, P. D.; Zwart, P. H.; Kern, J.; Brewster, A. S.; Koroidov, S.; Alonso-Mori, R.; Zouni, A.; Messinger, J.; Bergmann, U.; Yano, J.; Yachandra, V. K., No Observable Conformational Changes in PSII. *Nature* **2016,** *533*, E1-E2.
51. Suga, M.; Akita, F.; Hirata, K.; Ueno, G.; Murakami, H.; Nakajima, Y.; Shimizu, T.; Yamashita, K.; Yamamoto, M.; Ago, H.; Shen, J.-R., Native Structure of Photosystem II at 1.95 Å Resolution Viewed by Femtosecond X-ray Pulses. *Nature* **2015,** *517*, 99-103.
52. Young, I. D.; Ibrahim, M.; Chatterjee, R.; Gul, S.; Fuller, F. D.; Koroidov, S.; Brewster, A. S.; Tran, R.; Alonso-Mori, R.; Kroll, T.; Michels-Clark, T.; Laksmono, H.; Sierra, R. G.; Stan, C. A.; Hussein, R.; Zhang, M.; Douthit, L.; Kubin, M.; de Lichtenberg, C.; Vo Pham, L.; Nilsson, H.; Cheah, M. H.; Shevela, D.; Saracini, C.; Bean, M. A.; Seuffert, I.; Sokaras, D.; Weng, T.-C.; Pastor, E.; Weninger, C.; Fransson, T.; Lassalle, L.; Bräuer, P.; Aller, P.; Docker, P. T.; Andi, B.; Orville, A. M.; Glownia, J. M.; Nelson, S.; Sikorski, M.; Zhu, D.; Hunter, M. S.; Lane, T. J.; Aquila, A.; Koglin, J. E.; Robinson, J.; Liang, M.; Boutet, S.; Lyubimov, A. Y.; Uervirojnangkoorn, M.; Moriarty, N. W.; Liebschner, D.; Afonine, P. V.; Waterman, D. G.; Evans, G.; Wernet, P.; Dobbek, H.; Weis, W. I.; Brunger, A. T.; Zwart, P. H.; Adams, P. D.; Zouni, A.; Messinger, J.; Bergmann, U.; Sauter, N. K.; Kern, J.; Yachandra, V. K.; Yano, J., Structure of Photosystem II and Substrate Binding at Room Temperature. *Nature* **2016,** *540*, 453-457.
53. Suga, M.; Akita, F.; Sugahara, M.; Kubo, M.; Nakajima, Y.; Nakane, T.; Yamashita, K.; Umena, Y.; Nakabayashi, M.; Yamane, T.; Nakano, T.; Suzuki, M.; Masuda, T.; Inoue, S.; Kimura, T.; Nomura, T.; Yonekura, S.; Yu, L.-J.; Sakamoto, T.; Motomura, T.; Chen, J.-H.; Kato, Y.; Noguchi, T.; Tono, K.; Joti, Y.; Kameshima, T.; Hatsui, T.; Nango, E.; Tanaka, R.; Naitow, H.; Matsuura, Y.; Yamashita, A.; Yamamoto, M.; Nureki, O.; Yabashi, M.; Ishikawa,

T.; Iwata, S.; Shen, J.-R., Light-induced Structural Changes and the Site of O=O Bond Formation in PSII Caught by XFEL. *Nature* **2017,** *543*, 131-135.
54. Kern, J.; Chatterjee, R.; Young, I. D.; Fuller, F. D.; Lassalle, L.; Ibrahim, M.; Gul, S.; Fransson, T.; Brewster, A. S.; Alonso-Mori, R.; Hussein, R.; Zhang, M.; Douthit, L.; de Lichtenberg, C.; Cheah, M. H.; Shevela, D.; Wersig, J.; Seuffert, I.; Sokaras, D.; Pastor, E.; Weninger, C.; Kroll, T.; Sierra, R. G.; Aller, P.; Butryn, A.; Orville, A. M.; Liang, M.; Batyuk, A.; Koglin, J. E.; Carbajo, S.; Boutet, S.; Moriarty, N. W.; Holton, J. M.; Dobbek, H.; Adams, P. D.; Bergmann, U.; Sauter, N. K.; Zouni, A.; Messinger, J.; Yano, J.; Yachandra, V. K., Structures of the Intermediates of Kok's Photosynthetic Water Oxidation Clock. *Nature* **2018,** *563*, 421-425.
55. Suga, M.; Akita, F.; Yamashita, K.; Nakajima, Y.; Ueno, G.; Li, H.; Yamane, T.; Hirata, K.; Umena, Y.; Yonekura, S.; Yu, L.-J.; Murakami, H.; Nomura, T.; Kimura, T.; Kubo, M.; Baba, S.; Kumasaka, T.; Tono, K.; Yabashi, M.; Isobe, H.; Yamaguchi, K.; Yamamoto, M.; Ago, H.; Shen, J.-R., An Oxyl/Oxo Mechanism for Oxygen-oxygen Coupling in PSII Revealed by an X-ray Free-electron Laser. *Science* **2019,** *366*, 334.
56. Ibrahim, M.; Fransson, T.; Chatterjee, R.; Cheah, M. H.; Hussein, R.; Lassalle, L.; Sutherlin, K. D.; Young, I. D.; Fuller, F. D.; Gul, S.; Kim, I.-S.; Simon, P. S.; de Lichtenberg, C.; Chernev, P.; Bogacz, I.; Pham, C. C.; Orville, A. M.; Saichek, N.; Northen, T.; Batyuk, A.; Carbajo, S.; Alonso-Mori, R.; Tono, K.; Owada, S.; Bhowmick, A.; Bolotovsky, R.; Mendez, D.; Moriarty, N. W.; Holton, J. M.; Dobbek, H.; Brewster, A. S.; Adams, P. D.; Sauter, N. K.; Bergmann, U.; Zouni, A.; Messinger, J.; Kern, J.; Yachandra, V. K.; Yano, J., Untangling the Sequence of Events During the $S_2 \rightarrow S_3$ Transition in Photosystem II and Implications for the Water Oxidation Mechanism. *Proc. Natl. Acad. Sci. U.S.A.* **2020,** *117*, 12624-12635.
57. Bhowmick, A.; Hussein, R.; Bogacz, I.; Simon, P. S.; Ibrahim, M.; Chatterjee, R.; Doyle, M. D.; Cheah, M. H.; Fransson, T.; Chernev, P.; Kim, I.-S.; Makita, H.; Dasgupta, M.; Kaminsky, C. J.; Zhang, M.; Gätcke, J.; Haupt, S.; Nangca, I. I.; Keable, S. M.; Aydin, A. O.; Tono, K.; Owada, S.; Gee, L. B.; Fuller, F. D.; Batyuk, A.; Alonso-Mori, R.; Holton, J. M.; Paley, D. W.; Moriarty, N. W.; Mamedov, F.; Adams, P. D.; Brewster, A. S.; Dobbek, H.; Sauter, N. K.; Bergmann, U.; Zouni, A.; Messinger, J.; Kern, J.; Yano, J.; Yachandra, V. K., Structural Evidence for Intermediates during O_2 Formation in Photosystem II. *Nature* **2023,** *617*, 629-636.
58. Li, H.; Nakajima, Y.; Nango, E.; Owada, S.; Yamada, D.; Hashimoto, K.; Luo, F.; Tanaka, R.; Akita, F.; Kato, K.; Kang, J.; Saitoh, Y.; Kishi, S.; Yu, H.; Matsubara, N.; Fujii, H.; Sugahara, M.; Suzuki, M.; Masuda, T.; Kimura, T.; Thao, T. N.; Yonekura, S.; Yu, L.-J.; Tosha, T.; Tono, K.; Joti, Y.; Hatsui, T.; Yabashi, M.; Kubo, M.; Iwata, S.; Isobe, H.; Yamaguchi, K.; Suga, M.; Shen, J.-R., Oxygen-evolving Photosystem II Structures during S_1–S_2–S_3 Transitions. *Nature* **2024,** *626*, 670-677.
59. Drosou, M.; Comas-Vilà, G.; Neese, F.; Salvador, P.; Pantazis, D. A., Does Serial Femtosecond Crystallography Depict State-Specific Catalytic Intermediates of the Oxygen-Evolving Complex? *J. Am. Chem. Soc.* **2023,** *145*, 10604-10621.
60. Chatterjee, R.; Lassalle, L.; Gul, S.; Fuller, F. D.; Young, I. D.; Ibrahim, M.; de Lichtenberg, C.; Cheah, M. H.; Zouni, A.; Messinger, J.; Yachandra, V. K.; Kern, J.; Yano, J., Structural Isomers of the S_2 State in Photosystem II: Do they Exist at Room Temperature and are they Important for Function? *Physiol. Plant.* **2019,** *166*, 60-72.
61. Pantazis, D. A.; Ames, W.; Cox, N.; Lubitz, W.; Neese, F., Two Interconvertible Structures that Explain the Spectroscopic Properties of the Oxygen-Evolving Complex of Photosystem II in the S_2 State. *Angew. Chem.* **2012,** *51*, 9935-9940.

62. Shiau, A. A.; Lee, H. B.; Oyala, P. H.; Agapie, T., Coordination Number in High-Spin–Low-Spin Equilibrium in Cluster Models of the S_2 State of the Oxygen Evolving Complex. *J. Am. Chem. Soc.* **2023,** *145*, 14592-14598.
63. Lee, H. B.; Oyala, P. H.; Agapie, T., Synthesis, Electronic Structure, and Spectroscopy of Multinuclear Mn Complexes Relevant to the Oxygen Evolving Complex of Photosystem II. In *Oxygen Production and Reduction in Artificial and Natural Systems*, World Scientific: 2018; pp 259-283.
64. Chernev, P.; Aydin, A. O.; Messinger, J., On the simulation and interpretation of substrate-water exchange experiments in photosynthetic water oxidation. *Photosynth. Res.* **2024**.
65. Huang, H.-L.; Ghosh, I.; Banerjee, G.; Brudvig, G. W., Progress Towards Unraveling the Water-Oxidation Mechanism of Photosystem II. In *Oxygen Production and Reduction in Artificial and Natural Systems*, World Scientific: 2018; pp 285-306.
66. Hillier, W.; Wydrzynski, T., The Affinities for the Two Substrate Water Binding Sites in the O_2 Evolving Complex of Photosystem II Vary Independently during S-State Turnover. *Biochemistry* **2000,** *39*, 4399-4405.
67. Cox, N.; Retegan, M.; Neese, F.; Pantazis, D. A.; Boussac, A.; Lubitz, W., Electronic Structure of the Oxygen-evolving Complex in Photosystem II prior to O-O bond Formation. *Science* **2014,** *345*, 804-808.
68. Shoji, M.; Isobe, H.; Shigeta, Y.; Nakajima, T.; Yamaguchi, K., Concerted Mechanism of Water Insertion and O_2 Release during the S_4 to S_0 Transition of the Oxygen-Evolving Complex in Photosystem II. *J. Phys. Chem. B* **2018,** *122*, 6491-6502.
69. Lohmiller, T.; Krewald, V.; Navarro, M. P.; Retegan, M.; Rapatskiy, L.; Nowaczyk, M. M.; Boussac, A.; Neese, F.; Lubitz, W.; Pantazis, D. A.; Cox, N., Structure, Ligands and Substrate Coordination of the Oxygen-evolving Complex of Photosystem II in the S_2 state: a Combined EPR and DFT Study. *PCCP* **2014,** *16* , 11877-11892.
70. Ames, W.; Pantazis, D. A.; Krewald, V.; Cox, N.; Messinger, J.; Lubitz, W.; Neese, F., Theoretical Evaluation of Structural Models of the S_2 State in the Oxygen Evolving Complex of Photosystem II: Protonation States and Magnetic Interactions. *J. Am. Chem. Soc.* **2011,** *133*, 19743-19757.
71. Kanady, J. S.; Tsui, E. Y.; Day, M. W.; Agapie, T., A Synthetic Model of the Mn_3Ca Subsite of the Oxygen-Evolving Complex in Photosystem II. *Science* **2011,** *333*, 733-736.
72. Zhang, C.; Chen, C.; Dong, H.; Shen, J.-R.; Dau, H.; Zhao, J., A synthetic Mn_4Ca-cluster Mimicking the Oxygen-evolving Center of Photosynthesis. *Science* **2015,** *348*, 690-693.
73. Kanady, J. S.; Mendoza-Cortes, J. L.; Tsui, E. Y.; Nielsen, R. J.; Goddard, W. A., III; Agapie, T., Oxygen Atom Transfer and Oxidative Water Incorporation in Cuboidal Mn_3MO_n Complexes Based on Synthetic, Isotopic Labeling, and Computational Studies. *J. Am. Chem. Soc.* **2013,** *135*, 1073-1082.
74. Dasgupta, J.; Ananyev, G. M.; Dismukes, G. C., Photoassembly of the Water-oxidizing Complex in Photosystem II. *Coord. Chem. Rev.* **2008,** *252*, 347-360.
75. Nixon, P. J.; Michoux, F.; Yu, J.; Boehm, M.; Komenda, J., Recent Advances in Understanding the Assembly and Repair of Photosystem II. *Annals of Botany* **2010,** *106*, 1-16.
76. Bao, H.; Burnap, R. L., Photoactivation: The Light-Driven Assembly of the Water Oxidation Complex of Photosystem II. *Front. Plant Sci.* **2016,** 7:578.
77. Zhang, M.; Bommer, M.; Chatterjee, R.; Hussein, R.; Yano, J.; Dau, H.; Kern, J.; Dobbek, H.; Zouni, A., Structural insights into the light-driven auto-assembly process of the water-oxidizing Mn4CaO5-cluster in photosystem II. *eLife* **2017,** *6*, e26933.

78. Murray, J. W.; Rutherford, A. W.; Nixon, P. J., Photosystem II in a State of Disassembly. *Joule* **2020,** *4* (10), 2082-2084.
79. Zabret, J.; Bohn, S.; Schuller, S. K.; Arnolds, O.; Möller, M.; Meier-Credo, J.; Liauw, P.; Chan, A.; Tajkhorshid, E.; Langer, J. D.; Stoll, R.; Krieger-Liszkay, A.; Engel, B. D.; Rudack, T.; Schuller, J. M.; Nowaczyk, M. M., Structural insights into photosystem II assembly. *Nat. Plants.* **2021,** *7*, 524-538.
80. Sato, A.; Nakano, Y.; Nakamura, S.; Noguchi, T., Rapid-Scan Time-Resolved ATR-FTIR Study on the Photoassembly of the Water-Oxidizing Mn_4CaO_5 Cluster in Photosystem II. *J. Phys. Chem. B* **2021,** *125*, 4031-4045.
81. Cady, C. W.; Crabtree, R. H.; Brudvig, G. W., Functional Models for the Oxygen-evolving Complex of Photosystem II. *Coord. Chem. Rev.* **2008,** *252*, 444-455.
82. Mullins, C. S.; Pecoraro, V. L., Reflections on Small molecule Manganese Models that Seek to Mimic Photosynthetic Water Oxidation Chemistry. *Coord. Chem. Rev.* **2008,** *252*, 416-443.
83. Wieghardt, K., The Active Sites in Manganese-Containing Metalloproteins and Inorganic Model Complexes. *Angewandte Chemie International Edition in English* **1989,** *28*, 1153-1172.
84. Dismukes, G. C.; Brimblecombe, R.; Felton, G. A. N.; Pryadun, R. S.; Sheats, J. E.; Spiccia, L.; Swiegers, G. F., Development of Bioinspired Mn_4O_4−Cubane Water Oxidation Catalysts: Lessons from Photosynthesis. *Acc. Chem. Res.* **2009,** *42*, 1935-1943.

Chapter 2

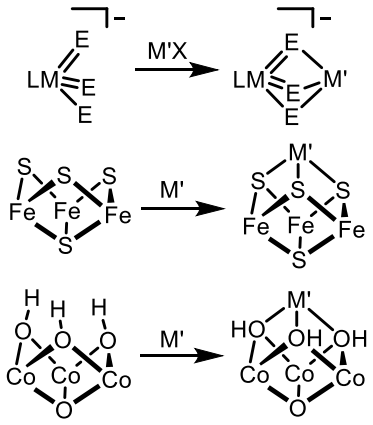
Open cobalt-oxo cubanes as potential synthons for heterometal-cobalt oxo cubanes

Introduction:

Trimetallic tetrachalcogenide [M_3E_4] clusters are important catalytic centers for iron-sulfur proteins and are also critical subunits of the [$CaMn_4O_4$] oxygen evolving complex (OEC) and [$NiFe_4S_4$] carbon monoxide dehydrogenase (CODH).[1-5] These enzyme active sites catalyze challenging reactions at low overpotential and with impressive turnover frequencies.[6, 7] The pentametallic active sites may be subdivided into an open cubane ([Mn_3O_4]/[Ni_3S_4]) cluster, a heterometal (Ca/Fe) within said cluster, and an exogeneous metal ion (Mn/Ni) that are all believed to play a distinct role in the catalytic transformations.[8, 9] Currently, the Ca^{II} ion in the OEC is believed to tune both the oxidation potential of the cluster, and the distance to substrate water ligands from the Mn reaction centers.[10, 11] Synthetic models for the OEC that probe the role of the Ca^{II} ion have been instrumental to this understanding, especially cubane models that have been constructed from open cubane precursors, because the role of the heterometal can be decoupled from the influence of the trimetallic complex.[12-15] In this sense, open cubanes platforms may be thought of as precisely defined (pro)ligands for the study of heterometal containing metallo chalcogenido cubanes similar to the group 6 compounds $[LME_3]^-$ (L = tris(3,5-dimethyl-1-pyrazolyl)borate, pentamethylcyclopentadiene; M = Mo, W; E = O, S, Te) (Scheme 1).[16-21]

One barrier to further investigation is that open cubane complexes often require tri(substitutedaryl)benzene ligands to enforce the trimetallic framework because the preference for the open cubane arrangement of the [M_3E_4] cluster over other [M_xE_y] oligomers appears to be low.[1, 22, 23] For example, an open cobalt oxo cubane was one of the numerous [$Co_n(OAc)_xO_y$] oligomers isolable in low yield from solutions of $Co(OAc)_2(H_2O)_4$ and pyridine oxidized by ozone or H_2O_2.[24-29] Likewise, there are only a few reports of iron sulfur clusters without rigid ligand frameworks.[1] While there are a few examples of Co_3O_4 open cubanes, the reported yield, purification, and solubility properties suggested that generating appreciable amounts of these open cubanes for further derivatization would be difficult. Thus, investigation began into the synthesis of more convenient open cobalt oxo cubane precursors.

Scheme 1. Metallo-chalcogenido ligand precursors to heteroatom cluster models.

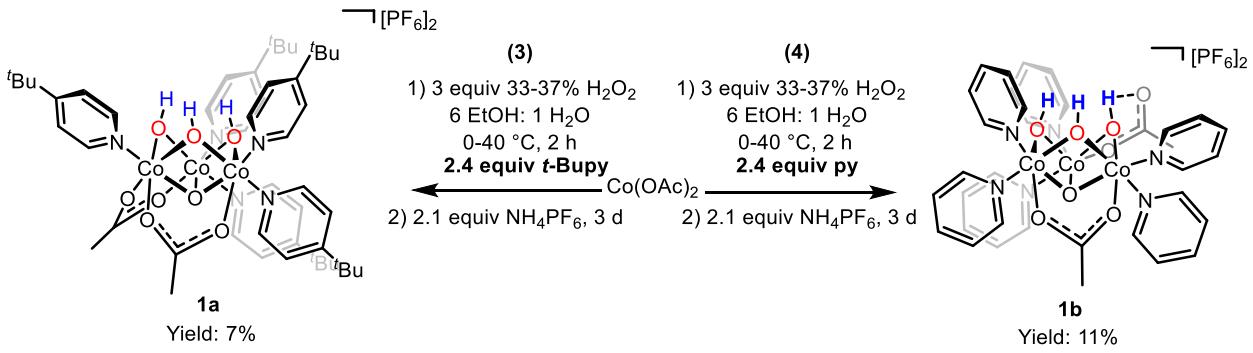


Described is the synthesis and characterization of a previously reported open cobalt oxo cubane and a new open cobalt oxo cubane, in addition to the unsuccessful metalation attempts of the latter cluster. The open cubane reported herein has solubility and spectroscopic properties that make it ideal for further studies into the role of the heteroatom on the electronic structure of metal oxo cubanes. Reaction of said open cubane with $Cp^*Hf(CH_2Ph)_3$ results in a known cobalt oxo acetate oligomeric structure that is consistent with metalation reactivity, followed by extensive decomposition. These complexes may pave way for the synthesis of heterometallic cobalt oxo cubanes.

Results and Discussion:

Initial investigations into open tricobalt clusters began with reactions of $Co(OAc)_2(H_2O)_4$ and H_2O_2, with 4-*tert*butylpyridine (*t*-Bupy) as the pyridine source for both the added solubility and ^1H NMR spectroscopic handles. Treatment of a deep purple 6:1 EtOH:H_2O solution of $Co(OAc)_2(H_2O)_4$ with 2.4 equiv of *t*-Bupy, and then 33-37% H_2O_2 added dropwise to keep the temperature close to 25 °C, resulted in darkening of the solution and effervescence (Scheme 2). After the addition of H_2O_2 was complete, NH_4PF_6 was added in one portion as a solid, following which the solution was stirred at 25 °C for 30 minutes. After resting for 72 hours, the resulting dark black, tacky solids were collected on a medium porosity frit. The solids were transferred to a solution of hot ^{i}PrOH containing NH_4PF_6, and after vigorous stirring for 30 minutes, the solids and crystalline precipitate of the mother liquors were collected on a medium frit, to give open cubane $[Co_3(\mu_3\text{-}O)(\mu_2\text{-}OH)_3(\kappa^2\text{-}OAc)_2(t\text{-}Bupy)_5][PF_6]_2$ **1a** as the ethanol solvate (Scheme 2) in a combined yield of 17%. This composition was confirmed by high-resolution electrospray ionization mass spectrometry (HR-ESI-MS) analysis, which revealed the anticipated mass for both the dicationic and monocationic species.

Scheme 2. Synthetic Scheme to prepare open cobalt oxo cubanes.



The ^1H NMR spectrum of **1a** in acetonitrile-d_3 revealed three unique pyridine environments, in a 1:2:2 ratio. Two upfield resonances in a 2:1 ratio at –1.54 and –2.86 ppm respectively suggested the presence of hydroxide ligands without any hydrogen bonding interactions from an acetate ligand.[28] In accordance, a broad O–H stretch at 3518 cm^{-1} in the solid-state IR spectrum of **1a** further suggested the presence of hydroxide ligands. X-ray diffraction quality crystals were grown by layer diffusion of hexanes into a CH_2Cl_2 solution of **1a** at –5 °C over several days. The solid-state molecular structure of **1a** consists of the tricobalt unit, two PF_6 anions, and two equivalents of residual EtOH; a truncated model is shown in Figure 1. The residual EtOH present in the solid-state structure is within hydrogen bonding contact distance of two of the hydroxide ligands of the cobalt trimer, but hydrogen atoms for these hydroxide ligands could not be located in the difference

map (Figure **1**). The presence of this residual solvent in the solid-state structure is consistent with the tenacity with which EtOH binds to samples **1a**. The bonding metrics for **1a** are not substantially different from that of the $Co_4(\mu_3\text{-}O)_4(OAc)_4(py)_4$ cobalt cubane,[30] however the Co1–O2 and Co2–O2 distances are marginally longer than any of the cobalt cubane oxo bonds. The observed symmetry in the solid-state structure of **1a** is consistent with the symmetry observed in solution by ^{1}H NMR spectroscopy.

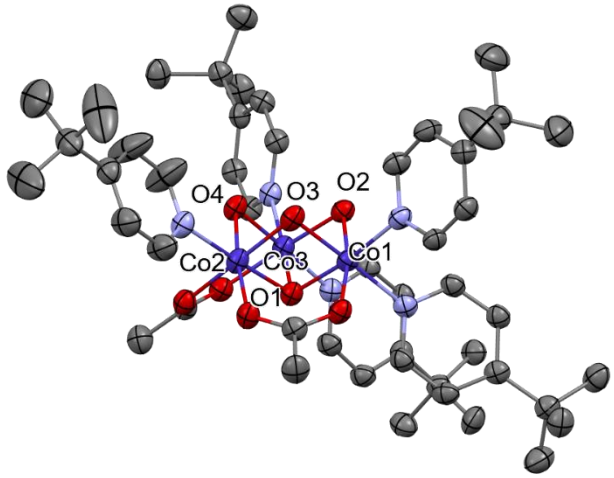


Figure 1. Solid-state molecular structure of **1a**. Thermal ellipsoids are shown at 50% probability level. Hydrogen atoms and counteranions removed for clarity. Selected bond distances (Å) and angles (°): Co1–O1: 1.859(2), Co1–O2: 1.937(2), Co1–O3: 1.900(3), Co2–O1: 1.862(2), Co2–O3: 1.854(3), Co2–O4: 1.885(2), Co3–O2: 1.920(2), O4–F: 3.028(3) Co2–O1–Co3: 94.68(9), Co2–O1–Co1: 94.21(9), Co3–O1–Co1: 101.2(1); Co1–O3–Co2: 93.1(1).

The conditions for the synthesis of **1a** were also applied with py in place of *t*-Bupy to give $[Co_3(\mu_3\text{-}O)(\mu_2\text{-}OH)_3(2\kappa^2,3\,\kappa^3\text{-}OAc)(1\kappa^1\text{-}OAc)(py)_6][PF_6]_2$ (**1b**) in 7% yield, the composition of which was confirmed by HR-ESI-MS analysis. Note that complex **1b** was previously reported without a given yield.[27] The ^{1}H NMR spectrum of **1b** matches the previous report and is consistent with six inequivalent pyridine ligands, three unique hydroxide ligands, and two unique acetate ligands. The solid-state molecular structure of **1b** determined crystallographically reveals the same open cubane core structure observed for **1a**, but with a different arrangement of acetate ligands and an additional pyridine ligand. The asymmetry of hydrogen bonding environments is consistent with the three distinct environments observed in acetonitrile-d_3 by ^{1}H NMR spectroscopy at 5.21, –.32, and –2.78 ppm respectively. Presumably, the hydroxide proton that is hydrogen bonding with the κ^1-OAc ligand is the most downfield resonance.[31, 32] The three O–H stretches at 3667, 3507, and 3377, cm^{-1} observed in the FTIR spectrum of **1b** are also suggestive of unique hydroxide ligand proton environments. The solubility and spectroscopic properties of **1b** were unfavorable, and for these reasons complex **1a** was chosen for further studies of the open tricobalt oxo cubane.

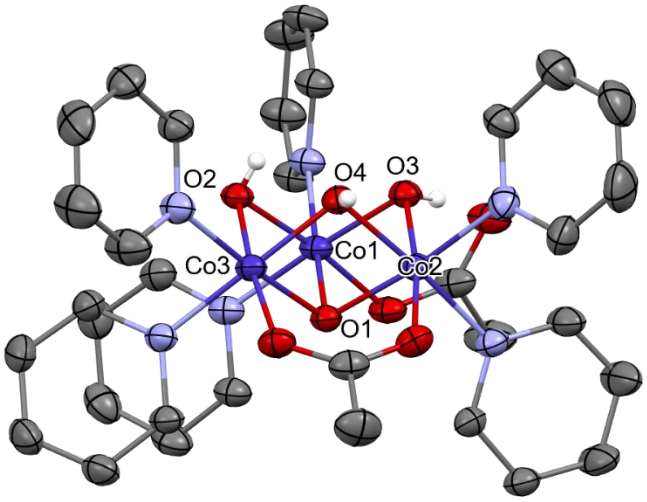
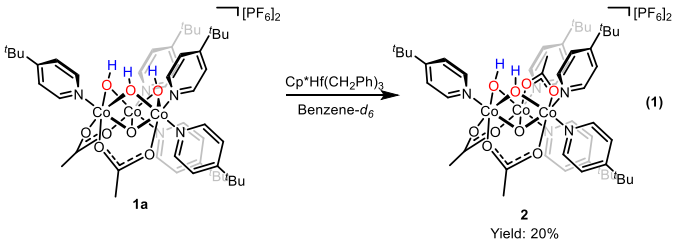


Figure 2. Solid-state molecular structure of **1b**. Thermal ellipsoids are shown at 50% probability level. Hydrogens placed with a riding model, counterions, and solvent of recrystallization removed for clarity. Hydroxide protons were located in the difference map. Selected bond distances (Å) and angles (°): Co1–O1: 1.890(2), Co1–O2: 1.899(2), Co1–O4: 1.927(2), Co3–O1: 1.872(2), Co3–O4: 1.908(2), Co1–O1–Co2: 97.57(9), Co1–O1–Co3: 99.13(9), Co3–O1–Co2: 93.37(9)

Heterogeneous cobalt oxide water oxidation catalysts have been proposed to bear similar structure to that of the open cubanes synthesized,[24] and so an electrochemical study of the open cubane **1a** was undertaken. Unfortunately, compound **1a** displays no reversible electrochemical features and instead irreversible oxidation at potentials above 0.88 V, and irreversbile reduction to Co^{II} at potentials below –0.64 V, vs. Fc/Fc^{+}. The bridging hydroxide ligands and trimetallic nature of **1a** likely limit the communication between the Co ions of **1a** in comparison to the cobalt oxo cubane, destabilizing higher-oxidation states.[33, 34] Thus, the absence of a well-defined and reversible oxidation event is not entirely surprising.

Numerous examples of heterometal installation into synthetic Fe_3S_4 clusters are known, and encouragingly, the reported solid-state molecular structure of a Ca^{II} ion bound to a tricobalt cluster suggested that it may be possible to install a heterometal into **1a** with either a tribasic metal fragment, or the appropriate source of metal cation.[21,35-37] For preliminary investigation, deprotometalation strategies with the fragment **1a** were investigated.



The tribasic d^0 complex $Cp^*Hf(CH_2Ph)_3$ was selected for preliminary studies of the deprotometalation of **1a** for the basic benzyl ligands and Cp* capping group.[38] Treatment of a benzene-d_6 solution of **1a** with 1 equiv of $Cp^*Hf(CH_2Ph)_3$ produced an intractable mixture of products over 10 minutes by ^1H NMR spectroscopy. Over 2 days at room temperature, small brown orthorhombic crystals of $[Co_3(\mu_3\text{-}O)(\mu_2\text{-}OH)_2(\kappa^2\text{-}OAc)_3(t\text{-}Bupy)_5][PF_6]_2$ (**2**) resulted (eq 1), which were isolated by filtration in 20% yield. The speciation of **2** was confirmed by HR-ESI-MS analysis. In the ^1H NMR spectrum, an additional resonance at 2.51 ppm corresponding to a unique

new acetate ligand is present, and the resonance for the hydroxide proton of **1a** at –2.86 ppm is absent, indicating ligand exchange occurred at the tricobalt cluster. The solid-state molecular structure of **2** determined by single-crystal X-ray diffraction analysis revealed a known Co(OAc)(O) oligomeric structure (Figure 3).[26] Because the yield of **2** is low, and the additional acetate ligand present necessitates redistribution of ligands from other clusters, a mechanistic hypothesis for the formation of **2** is unclear. However, it is speculated that complex **2** is the result of metalation, followed by decomposition of the tetrametallic intermediate with loss of the oxo ligand. Reactions of **1a** with similar basic metal sources resulted in similar mixtures and yields of **2**.

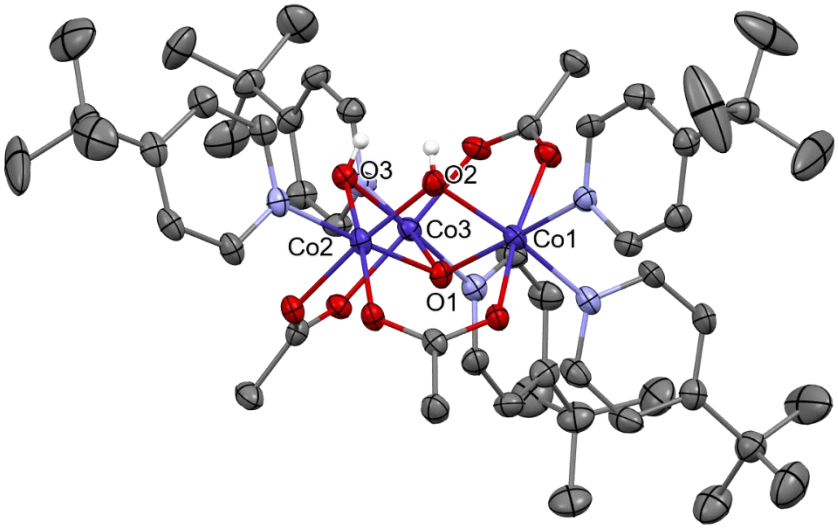


Figure 3. Solid-state molecular structure of **2**. Thermal ellipsoids are shown at 50% probability level. Hydrogens placed with a riding model, counterions, and solvent of recrystallization removed for clarity. Selected bond distances (Å) and angles (°): Co1–O1: 1.886(2), Co2–O1: 1.884(2), Co3–O1: 1.882(2), Co1–Co3–3.3441(7), Co1–O1–Co2: 95.4(1), Co2–O1–Co3: 95.6(1), Co1–O1–Co3: 125.1(1).

A final attempt at the direct deprotometalation of **1a** was made with $VO(O^iPr)_3$ as the source of tribasic heterometal. Interest in the generation of a vanadium-cobalt oxo cubane in this manner stems from questions about the synthesis of a vanadium-cobalt oxo cubane by way of metal-metal exchange (Chapter 4). In the metal-metal exchange reaction between the cobalt oxo cubane and $VCl_4(THF)_2$, a proton source is required to achieve appreciable yields of the vanadium-cobalt oxo cubane, and the mechanism is believed to go through an inner-sphere electron transfer mechanism. An alternative to the proposed electron transfer mechanism might involve the partial decomposition of the cobalt cubane into an oligomer such as **1a**, which could then bind a vanadium ion to give the $[VCo_3O_4]$ product. Treatment of a benzene-d_6 solution of **1a** with one equiv of $VO(O^iPr)_3$ did not result in any reaction after 16 h at 23 °C by ^{1}H NMR spectroscopy. As monitored by ^{1}H NMR spectroscopy, heating this solution at 55 °C for 24 h depleted the resonances associated with the hydroxyl protons of **1a** and resulted in an intractable mixture of products that did not match for a $[VCo_3O_4]$ cubane. Likewise, HR-ESI-MS analysis of an aliquot from these solutions provided no evidence for the formation of a $[VCo_3O_4]$ cubane. Thus, deprotometalation of the open cobalt oxo cubane was not readily achieved, even with heterometals known to form stable MCo_3O_4 products.

The ability of **1a** to coordinate Ca^{II} ions was next investigated. Treatment of an acetonitrile-d_3 solution of **1a** with 1 equiv of $CaCl_2$, $Ca(OAc)_2$ or Ca(cyclohexylbutyrate)$_2$ and heating to 55 °C for 16 h resulted in depletion of the equivalent hydroxide resonances of **1a** by ^{1}H NMR spectroscopy, suggesting that there may be an interaction between the hydroxide ligands and Ca. However, HR-ESI-MS analysis of this reaction solution and comparison of the IR spectrum of **1a** with the solids obtained after removal of the solvent from these reaction solutions indicated that no calcium coordination complex was formed. Similarly, the change in chemical shift of the equivalent hydroxide protons observed in a benzene-d_6 solution of **1a** treated with $Ca(OBz)_2$ and heated at 55 °C for 16 h suggested some interaction of the Ca source with **1a**, but IR and HR-ESI-MS analysis indicated that **1a** was unchanged. Similar unpromising reactivity was observed with reagents such as $Sc(OTf)_3$.

Concluding Remarks:

This study describes models for $[M_3E_4]$ (E = O, S) cluster subunits that are critical to the function of enzymes such as CODH and the OEC, for which few models exist.[24, 26, 29] Specifically, trimetallic clusters with the open cubane structure without tri(substituted-arene)aryl ligands are rare because of challenges associated with selectivity for the trimetallic oligomer, with only a few reported examples.[1] The described report presents a general synthetic scheme and the bonding metrics of the open cubane clusters **1a,b** ($[Co_3O(OH)_3(OAc)_2(t\text{-Bupy})_5][PF_6]_2$, $[Co_3O(OH)_3(OAc)_2(py)_6][PF_6]_2$). Notably, open cubane **1a** has an arrangement of acetate ligands that more strongly resembles the cobalt oxo cubane and the OEC, which contributes to the superior solubility and spectroscopic properties of **1a** compared to **1b**. The spectroscopic properties and solid-state metrics suggest that these tricobalt clusters are less capable of charge distribution than the cobalt oxo cubane.

The precise way the group II metal tunes the reactivity of the OEC remains the subject of intense research, motivating investigations into model complexes.[39, 40] Open cubanes based on the MCo_3O_4 framework are expected to be precursors to functional model complexes that could only be prepared previously using strong metal oxidants.[41, 42] Preliminary reactivity studies with **1a** emphasized deprotometalation and coordination of heterometals; neither pathway led to metalation of **1a**. Complex **2**, $[Co_3(\mu_3\text{-}O)(\mu_2\text{-}OH)_2(\kappa^2\text{-}OAc)_3(t\text{-Bupy})_5][PF_6]_2$ was isolated following treatment of **1a**, a product that suggests deprotonation of **1a**, decomposition, and redistribution the ligands.

Future investigations into the heterometal within the heteroatomic cubanes may help unravel the specific effects of the Ca^{II} ion within the OEC. Although the open cobalt oxo cubanes presented were not metalated under the explored conditions, future studies into heterometal cobalt oxo cubanes are expected to benefit from the availability of soluble, well-defined trimetallic tetrachalcogenido materials. These heterometallic cubanes may be expected to have superior water oxidation reactivity and or stability that may also be relevant to doped materials.

References:

1. Brown, A. C.; Suess, D. L. M., An Open-Cuboidal [Fe_3S_4] Cluster Characterized in Both Biologically Relevant Redox States. *J. Am. Chem. Soc.* **2023,** *145*, 2075-2080.
2. Barber, J., A Mechanism for Water Splitting and Oxygen Production in Photosynthesis. *Nat. Plants.* **2017,** *3*, 17041.
3. Brown, A. C.; Suess, D. L. M., - Synthetic Iron-Sulfur Clusters. In *Comprehensive Coordination Chemistry III*, Constable, E. C.; Parkin, G.; Que Jr, L., Eds. Elsevier: Oxford, 2021; pp 134-156.
4. Bigness, A.; Vaddypally, S.; Zdilla, M. J.; Mendoza-Cortes, J. L., Ubiquity of Cubanes in Bioinorganic Relevant Compounds. *Coord. Chem. Rev.* **2022,** *450*, 214168.
5. Beinert, H.; Holm, R. H.; Münck, E., Iron-Sulfur Clusters: Nature's Modular, Multipurpose Structures. *Science* **1997,** *277*, 653-659.
6. Yano, J.; Yachandra, V., Mn_4Ca Cluster in Photosynthesis: Where and How Water is Oxidized to Dioxygen. *Chem. Rev.* **2014,** *114*, 4175-4205.
7. Jeoung, J.-H.; Dobbek, H., Carbon Dioxide Activation at the Ni,Fe-Cluster of Anaerobic Carbon Monoxide Dehydrogenase. *Science* **2007,** *318*, 1461-1464.
8. Cox, N.; Pantazis, D. A.; Lubitz, W., Current Understanding of the Mechanism of Water Oxidation in Photosystem II and Its Relation to XFEL Data. *Annu. Rev. Biochem* **2020,** *89*, 795-820.
9. Cox, N.; Rapatskiy, L.; Su, J.-H.; Pantazis, D. A.; Sugiura, M.; Kulik, L.; Dorlet, P.; Rutherford, A. W.; Neese, F.; Boussac, A.; Lubitz, W.; Messinger, J., Effect of Ca^{2+}/Sr^{2+} Substitution on the Electronic Structure of the Oxygen-Evolving Complex of Photosystem II: A Combined Multifrequency EPR, ^{55}Mn-ENDOR, and DFT Study of the S_2 State. *J. Am. Chem. Soc.* **2011,** *133*, 14149-14149.
10. Ibrahim, M.; Fransson, T.; Chatterjee, R.; Cheah, M. H.; Hussein, R.; Lassalle, L.; Sutherlin, K. D.; Young, I. D.; Fuller, F. D.; Gul, S.; Kim, I.-S.; Simon, P. S.; de Lichtenberg, C.; Chernev, P.; Bogacz, I.; Pham, C. C.; Orville, A. M.; Saichek, N.; Northen, T.; Batyuk, A.; Carbajo, S.; Alonso-Mori, R.; Tono, K.; Owada, S.; Bhowmick, A.; Bolotovsky, R.; Mendez, D.; Moriarty, N. W.; Holton, J. M.; Dobbek, H.; Brewster, A. S.; Adams, P. D.; Sauter, N. K.; Bergmann, U.; Zouni, A.; Messinger, J.; Kern, J.; Yachandra, V. K.; Yano, J., Untangling the Sequence of Events during the $S_2 \rightarrow S_3$ Transition in Photosystem II and Implications for the Water Oxidation Mechanism. *Proc. Natl. Acad. Sci. U.S.A.* **2020,** *117*, 12624-12635.
11. Lionetti, D.; Suseno, S.; Shiau, A. A.; de Ruiter, G.; Agapie, T., Redox Processes Involving Oxygen: The Surprising Influence of Redox-Inactive Lewis Acids. *JACS Au* **2024,** *4*, 344-368.
12. Kanady, J. S.; Tsui, E. Y.; Day, M. W.; Agapie, T., A Synthetic Model of the Mn_3Ca Subsite of the Oxygen-Evolving Complex in Photosystem II. *Science* **2011,** *333*, 733-736.
13. Lin, P.-H.; Takase, M. K.; Agapie, T., Investigations of the Effect of the Non-Manganese Metal in Heterometallic-Oxido Cluster Models of the Oxygen Evolving Complex of Photosystem II: Lanthanides as Substitutes for Calcium. *Inorg. Chem.* **2015,** *54*, 59-64.
14. Zhang, C.; Chen, C.; Dong, H.; Shen, J.-R.; Dau, H.; Zhao, J., A synthetic Mn_4Ca-cluster mimicking the oxygen-evolving center of photosynthesis. *Science* **2015,** *348*, 690-693.
15. Yao, R.; Li, Y.; Chen, Y.; Xu, B.; Chen, C.; Zhang, C., Rare-Earth Elements Can Structurally and Energetically Replace the Calcium in a Synthetic Mn_4CaO_4-Cluster Mimicking the Oxygen-Evolving Center in Photosynthesis. *J. Am. Chem. Soc.* **2021,** *143*, 17360-17365.

16. Lang, J.-P.; Kawaguchi, H.; Tatsumi, K., Synthesis and structures of a triply-fused incomplete-cubane cluster [{(η^5-C_5Me_5)WS_3}$_3$$Cu_7$(MeCN)$_9$]($PF_6$)$_4$ and a 2D polymer [(η^5-C_5Me_5)WS_3Cu_3Cl(MeCN)(pz)]PF_6 (pz = pyrazine). *Chem. Commun.* **1999,** 22, 2315-2316.
17. Lang, J.-P.; Tatsumi, K., Aggregation of the Half-Sandwich Trisulfido Complex of Tungsten with Silver Ions: Synthesis of a Cyanide-Bridged Helical Polymer {[(η^5-C_5Me_5)WS_3]$_2$$Ag_3$(CN)}∞ and a Cyclic Cluster [(η^5-C_5Me_5)WS_3Ag]$_4$. *Inorg. Chem.* **1999,** *38*, 1364-1367.
18. Xu, G.; Wang, Z.; Ling, R.; Zhou, J.; Chen, X.-D.; Holm, R. H., Ligand Metathesis as Rational Strategy for the Synthesis of Cubane-type Heteroleptic Iron–sulfur Clusters Relevant to the FeMo Cofactor. *Proc. Natl. Acad. Sci. U.S.A.* **2018,** *115*, 5089-5092.
19. Scott, A. G.; Agapie, T., Synthesis of a Fe_3–Carbyne Motif by Oxidation of an Alkyl Ligated Iron–Sulfur (WFe_3S_3) Cluster. *J. Am. Chem. Soc.* **2023,** *145*, 2-6.
20. Le, L. N. V.; Joyce, J. P.; Oyala, P. H.; DeBeer, S.; Agapie, T., Highly Activated Terminal Carbon Monoxide Ligand in an Iron–Sulfur Cluster Model of FeMco with Intermediate Local Spin State at Fe. *J. Am. Chem. Soc.* **2024,** *146*, 5045-5050.
21. Ama, T.; Yonemura, T.; Morita, S.; Yamaguchi, M., Penta-aqua-tri-mu(3)-hydroxido-tris-(imino-diacetato)-mu(3)-oxido-tetra-hedro-calcium(II)tricobalt(III) 2.54-hydrate. *Acta Crystallogr Sect E Struct Rep Online* **2010,** *66*, m483-4.
22. Lee, S. C.; Lo, W.; Holm, R. H., Developments in the Biomimetic Chemistry of Cubane-Type and Higher Nuclearity Iron–Sulfur Clusters. *Chem. Rev.* **2014,** *114*, 3579-3600.
23. McSkimming, A.; Sridharan, A.; Thompson, N. B.; Müller, P.; Suess, D. L. M., An [Fe4S4]3+–Alkyl Cluster Stabilized by an Expanded Scorpionate Ligand. *J. Am. Chem. Soc.* **2020,** *142* (33), 14314-14323.
24. Dimitrou, K.; Folting, K.; Streib, W. E.; Christou, G., Dimerization of the [Co_2III$(OH)_2$] Core to the First Example of a [Co_4IIIO_4] Cubane: Potential Insights into Photosynthetic Water Oxidation. *J. Am. Chem. Soc.* **1993,** *115*, 6432-6433.
25. Beattie, J. K.; Hambley, T. W.; Klepetko, J. A.; Masters, A. F.; Turner, P., The Chemistry of Cobalt Acetate: The Isolation and Crystal Structure of the Symmetric trimer, Hexakis(μ-acetato)-μ3-oxo-Tris(pyridine)tricobalt(III) Perchlorate Water Solvate, [$Co_3O(CH_3CO_2)_6(C_5H_5N)_3$][$ClO_4$]·$H_2O$. *Polyhedron* **1996,** *15*, 2141-2150.
26. Beattie, J. K.; Hambley, T. W.; Klepetko, J. A.; Masters, A. F.; Turner, P., The Chemistry of Cobalt Acetate—IV. The Isolation and Crystal Structure of the Symmetric cubane, Tetrakis[(μ-acetato)(μ3-oxo) (pyridine)cobalt(III)] · Chloroform Solvate, [Co_4(μ3-O)$_4$(μ-CH3CO2)4(C_5H_5N)$_4$] · 5$CHCl_3$ and of the Dicationic Partial Cubane, Trimeric, [(μ-acetato)(acetato)tris(μ-hdyroxy(μ$_3$-oxo) Hexakispyridinetricobalt(III)]hexafluorophosphate · Water Solvate, [Co_3(μ$_3$-O)(μ-OH)$_3$(μ-CH_3CO_2(CH_3CO_2(C_5H_5N)$_6$[PF_6]$_2$ · 2H_2O. *Polyhedron* **1998,** *17*, 1343-1354.
27. Beattie, J. K.; Klepetko, J. A.; Masters, A. F.; Turner, P., The chemistry of cobalt acetate. VIII. New members of the family of oxo-centred trimers, [Co_3(μ$_3$-O)(μ-O_2CCH_3)$_5$–p(μ-OR)pL_5]$^{2+}$ (R=H, alkyl, L=ligand, p=0–4). The Preparation and Characterisation of the Trimeric Tetrakis(μ-acetato)-(μ-hydroxo)-μ$_3$-oxo-pentakis(pyridine)-tri-cobalt(III) Hexafluorophosphate, [Co3(μ3-O)(μ-O2CCH3)4(μ-OH)(C5H5N)5][PF6]2, and the Preparation and Crystal Structure of the Trimeric Tris(μ-acetato)-(μ-hydroxo)-(μ-methoxo)-μ3-oxo-pentakis(pyridine)-tri-cobalt(III) Hexafluorophosphate·Methanol·Water Solvate [Co_3(μ3-O)(μ-O_2CCH_3)$_3$(μ-OH)(μ-OCH_3)(C_5H_5N)$_5$][PF_6]$_2$·CH_3OH·0.25H_2O. *Polyhedron* **2003,** *22*, 947-965.

28. Beattie, J. K.; Beck, C. U.; Lay, P. A.; Masters, A. F., Chemistry of Cobalt Acetate. 7. Electrochemical Oxidation of μ3-Oxo-Centered Cobalt(III) Acetate Trimers. *Inorg. Chem.* **2003,** *42*, 8366-8370.
29. Ama, T.; Yonemura, T.; Yamaguchi, M., Trinuclear Complexes Containing Incomplete Cubane $CoIII_3O_4$ Cores. Structures of the Isomers of theN-(2-Pyridylmethyl)glycinato Complex. *Bull. Chem. Soc. Jpn.* **2006,** *79*, 1063-1065.
30. Chakrabarty, R.; Bora, S. J.; Das, B. K., Synthesis, Structure, Spectral and Electrochemical Properties, and Catalytic Use of Cobalt(III)−Oxo Cubane Clusters. *Inorg. Chem.* **2007,** *46*, 9450-9462.
31. Ann DeLucia, A.; Khadanand, K. C.; Olshansky, L., Impact of hydrogen-bonding interactions on the properties of biomimetic $Co_2(\mu\text{-}OH)_2$ complexes. *Inorg. Chim. Acta* **2024**, 121931.
32. DeLucia, A. A.; Kelly, K. A.; Herrera, K. A.; Gray, D. L.; Olshansky, L., Intramolecular Hydrogen-Bond Interactions Tune Reactivity in Biomimetic Bis(μ-hydroxo)dicobalt Complexes. *Inorg. Chem.* **2021,** *60*, 15599-15609.
33. Amtawong, J.; Skjelstad, B. B.; Balcells, D.; Tilley, T. D., Concerted Proton–Electron Transfer Reactivity at a Multimetallic Co_4O_4 Cubane Cluster. *Inorg. Chem.* **2020,** *59*, 15553-15560.
34. Amtawong, J.; Nguyen, A. I.; Tilley, T. D., Mechanistic Aspects of Cobalt–Oxo Cubane Clusters in Oxidation Chemistry. *J. Am. Chem. Soc.* **2022,** 144, 1475-1492.
35. Ciurli, S.; Ross, P. K.; Scott, M. J.; Yu, S. B.; Holm, R. H., Synthetic Nickel-containing Heterometal Cubane-type Clusters with $NiFe_3Q_4$ cores (Q = sulfur, selenium). *J. Am. Chem. Soc.* **1992,** *114*, 5415-5423.
36. Zhou, J.; Scott, M. J.; Hu, Z.; Peng, G.; Munck, E.; Holm, R. H., Synthesis and comparative reactivity and electronic structural features of $[MFe_3S_4]^{z+}$ Cubane-type Clusters (M = Iron, Cobalt, Nickel). *J. Am. Chem. Soc.* **1992,** *114*, 10843-10854.
37. Lee, S. C.; Holm, R. H., The Clusters of Nitrogenase: Synthetic Methodology in the Construction of Weak-Field Clusters. *Chem. Rev.* **2004,** *104*, 1135-1158.
38. Castillo, I.; Don Tilley, T., Hafnium Imido Complexes Containing Silyl Ligands. *J. Organomet. Chem.* **2002,** *643-644*, 431-440.
39. Paul, S.; Cox, N.; Pantazis, D. A., What Can We Learn from a Biomimetic Model of Nature's Oxygen-Evolving Complex? *Inorg. Chem.* **2017,** *56*, 3875-3888.
40. Pantazis, D. A., Missing Pieces in the Puzzle of Biological Water Oxidation. *ACS Catalysis* **2018,** *8*, 9477-9507.
41. Amtawong, J.; Balcells, D.; Wilcoxen, J.; Handford, R. C.; Biggins, N.; Nguyen, A. I.; Britt, R. D.; Tilley, T. D., Isolation and Study of Ruthenium–Cobalt Oxo Cubanes Bearing a High-Valent, Terminal RuV–Oxo with Significant Oxyl Radical Character. *J. Am. Chem. Soc.* **2019,** *141*, 19859-19869.
42. Nguyen, A. I.; Suess, D. L. M.; Darago, L. E.; Oyala, P. H.; Levine, D. S.; Ziegler, M. S.; Britt, R. D.; Tilley, T. D., Manganese–Cobalt Oxido Cubanes Relevant to Manganese-Doped Water Oxidation Catalysts. *J. Am. Chem. Soc.* **2017,** *139*, 5579-5587.

Supporting Information for Chapter 1.

Experimental:

General Considerations

Unless specified otherwise, all reactions were performed in the presence of air and atmospheric water. Room temperature is defined as 22 °C ± 4 °C. Yields for self-assembled reactions are reported with respect to the cobalt reagent regardless of the stoichiometry required to produce the final cluster *i.e.* to produce **2, 3, 5**. All reagents were used as purchased without further purification. $Co(OAc)_2 \cdot 4H_2O$ and $Cu(OAc)_2$ were purchased from Alfa-Aesar (Tewksbury, MA), 1,3,5-trimethoxybenzene (TMB), 4-*tert*butylpyridine, H_2O_2 (33-37% in water), NH_4PF_6, $Mn(OAc)_2$, pyridine (spectrophotometric grade), $AgNO_3$ (analytical grade), and $N(Bu)_4PF_6$ (analytical grade) were purchased from Millipore-Sigma-Alrich (Milwaukee, WI), solvent (HPLC grade) was purchased from Fischer Scientific (Hampton, NH), deuterated solvents were purchased from Cambridge Isotope Labs (Tewksbury, MA). When air-free techniques were applied, solvents were degassed with argon, dried and collected with a JC Meyers SDS solvent purification system, and stored over 3 Å molecular sieves in an N_2 filled glovebox. Acetonitrile-d_3 was dried over calcium hydride for greater than one week before undergoing three freeze-pump-thaw cycles and being vacuum transferred to a Schlenk bomb where it was stored.

All ^1H, $^{13}C\{^1H\}$, $^{19}F\{^1H\}$, and $^{31}P\{^1H\}$ experiments were performed using Bruker Avance-300, Avance-400, Avance-400, Avance-500, or Avance III-600 MHz spectrometers at room temperature. ^1H and $^{13}C\{^1H\}$ NMR experiments were calibrated to residual monoprotio-isotopomer relative to tetramethylsilane (CD_2HCN = 1.94 ppm, C_6D_5H = 7.16 ppm) . $^{19}F\{^1H\}$ NMR were calibrated externally to 1,4-difluorobenzene, calibrated to trifluoroacetic acid ($C_6H_4F_2$ = -120.94 ppm). $^{31}P\{^1H\}$ experiments were calibrated externally to triphenylphosphine (PPh_3 = -5.0 ppm). Electrospray ionization mass spectrometry (ESI-MS) experiments were performed using a PerkinElmer time-of-flight mass spectrometer AxION 2 TOF tuned and calibrated in the positive ion range, ATR IR experiments were performed using a Bruker Vertex 80 Time-resolved FTIR. Calculated *m/z* shown assumes neutral charge. Solution magnetic susceptibilities were determined by ^1H NMR using the method of Evans.[1] Elemental analyses were performed at the Microanalytical Facility at the University of California, Berkeley.

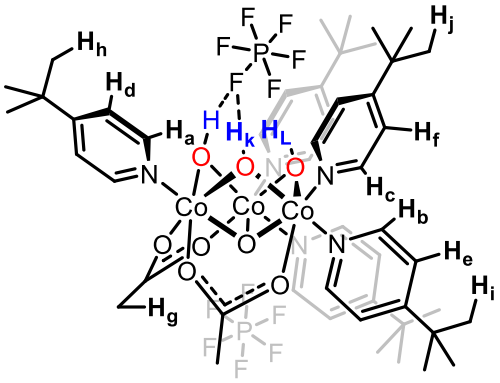
Single crystal X-ray diffraction for **2** was performed at UC Berkeley CheXRay crystallographic facility. Data collection was performed using a Rigaku XtaLAB P200 equipped with a MicroMax 007HF rotating anode and a Pilatus 200k hybrid pixel array detector using Mo Kα radiation (λ = 0.71073 Å) monochromated by a graphite monochromator. All other diffraction studies were collected at the Advanced Light Source beamline 12.2.1 using a Bruker D85 three-circle diffractometer equipped with a PHOTON II CCD area detector using synchrotron radiation (λ = 0.7288 Å) monochromated using a channel-cut Si(111) monochromator. Structure solution, modeling, and refining was performed using both the OLEX2[2] and SHELX[3,4] software suite.

Elecrochemical experiments

Electrochemical experiments were performed at ambient temperature using a BASi EC Epsilon potentiostat/galvanostat and a PWR-3 Power Module. A 3 mm diameter glassy carbon electrode was used as the working electrode, which was polished with 0.30 μm alumina, rinsed with deionized water, followed by 0.05 μm alumina, rinsed with water, and dried before use. Platinum

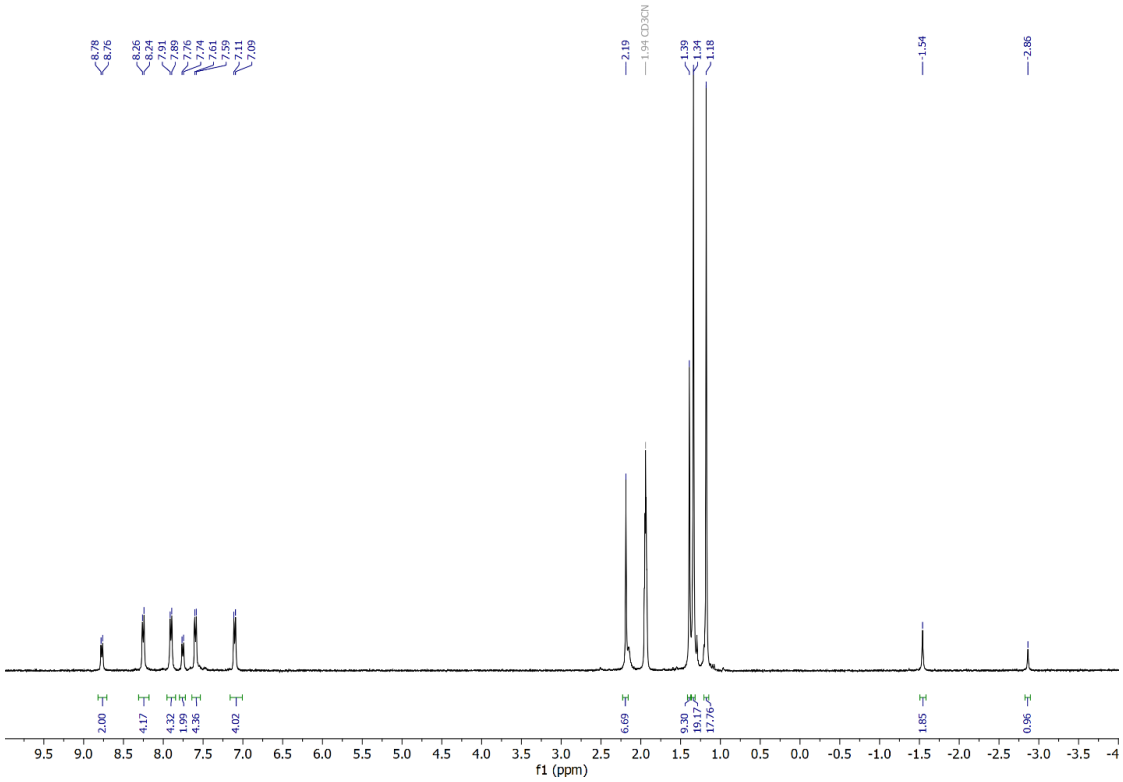
and silver wires were used the counter and reference electrodes respectively. Analytical grade tetrabutylammonium hexafluorophosphate (0.1 M) was used as the electrolyte in HPLC grade acetonitrile. Ferrocene was added at the end of each experiment as an internal reference against the half-potential of $[Cp_2Fe]^0/[Cp_2Fe]^+$ (Fc/Fc^+). Internal resistance compensation was carried out for each experiment to correct for solution resistance. Analyte concentration was 1.0 mM in the case of **1a** and 0.18 mM in the case of **3**. The E° values reported are the midpoints of the anodic (E_{pa}) and cathodic peak potentials, calculated as (E_{pc}) $E^\circ = (E_{pa} + E_{pc})/2$. The reversibility of the redox events was determined by the peak-to-peak separations and ($\Delta E_p = E_{pa} - E_{pc}$). The peak currents were determined by EC Lab software.

Synthesis and Characterization:

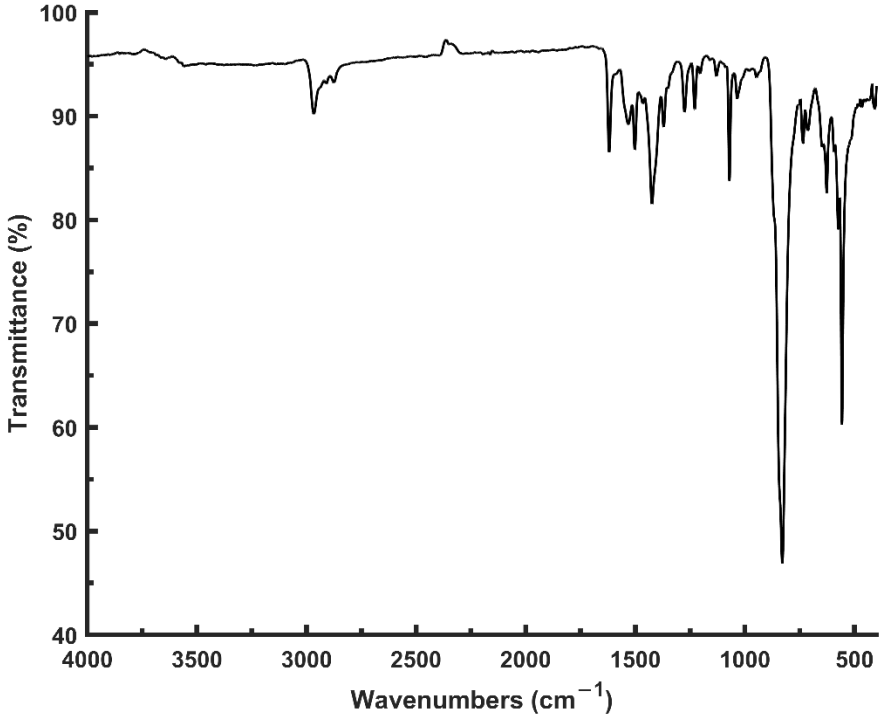


Preparation of $[Co_3O(OH)_3(OAc)_2(^tBuPy)_5][PF_6]_2$ (1a):

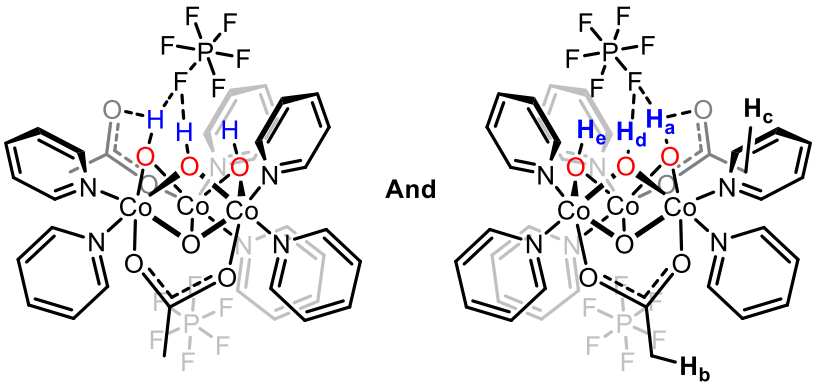
A 100 mL round-bottom flask was charged with $Co(OAc)_2 \cdot 4H_2O$ (4.0 g, 16 mmol) 4-*tert*butylpyridine (5.2 g, 38 mmol), 6:1 EtOH : deionized water (10 mL), and a stir bar. The solution was allowed to stir at room temperature until complete dissolution of the $Co(OAc)_2$ to a dark purple solution. The flask was placed in a room-temperature water bath, before addition of H_2O_2 (5.0 mL, 51 mmol) dropwise over 15 min, accompanied by darkening of the solution to a red/brown. The solution was stirred for 30 min, followed by addition of NH_4PF_6 (1.8 g, 11 mmol) in one portion as a solid. Stirring was continued for 1 h. The solution was allowed to rest undisturbed and unsealed at room temperature for 72 h. The red/brown solids formed were collected on a medium sintered frit, and the supernatant discarded. The crude solids were transferred to a vigorously stirred, refluxing solution of ^{i}PrOH (100 mL), containing NH_4PF_6 (1 g). The solution was stirred hot for 30 min before being filtered through a medium frit to collect the solid brown **1a** as the ethanolate. Removal of ethanol required heating to 80 °C *in vacuo* for several days. The supernatant may be allowed to evaporate undisturbed for several days to produce additional crops of crude **1a**. Crude **1a** was purified *via* recrystallization from layered CH_2Cl_2/Hexanes at –35 °C to produce black blocks. Yield: 0.55 g; 7%. Further crops increased the yield significantly; Yield: 1.40 grams; 17%. Characterization data: ^{1}H NMR (300 MHz, Acetonitrile-d_3) δ 8.77 (d, J = 6.1 Hz, 2H), 8.25 (d, J = 6.0 Hz, 4H), 7.90 (d, J = 6.1 Hz, 4H), 7.75 (d, J = 6.0 Hz, 2H), 7.60 (d, J = 5.9 Hz, 4H), 7.10 (d, J = 6.0 Hz, 4H), 2.19 (s, 6H), 1.39 (s, 9H), 1.34 (s, 18H), 1.18 (s, 18H), –1.54 (s, 2H), –2.86 (s, 1H). ^{13}C{^{1}H} NMR (101 MHz, Acetonitrile-d_3) δ 189.2, 165.7, 165.4, 164.9, 153.7 152.0, 151.4, 123.6, 123.4, 122.7, 35.8, 35.5, 30.43, 30.40, 30.37, 25.84. ^{19}F{^{1}H} NMR (376 MHz, Acetonitrile-d_3) δ –72.68 (d, J_{FP} = 706.1 Hz). ^{31}P{^{1}H} NMR (162 MHz, Acetonitrile-d_3) δ –141.39 (septet, J_{PF} = 706.5 Hz). Anal. Calcd. for $C_{49}H_{74}Co_3F_{12}N_5O_8P_2$: C, 44.32; H, 5.62; N, 5.27. Found: C, 44.91; H, 6.35; N, 4.71. We attribute the somewhat high hydrogen and carbon content to the very hygroscopic nature of the complex. IR (cm^{-1}): 3518 (w, *broad*) 2964 (w), 2873 (w), 1618 (m), 1529 (w), 1501 (m), 1422 (m), 1370 (w), 1227 (w), 1070 (m), 828 (s, *broad*), 626 (m), 556 (s). HRMS (ESI) *m/z*: Calcd. for $[C_{49}H_{74}Co_3F_6N_5O_8P]^+$:1182.3107 Found: 1182.3337 $([Co_3O(OH)_3(OAc)_2(^tBuPy)_5][PF_6])^+$



S1. ^{1}H NMR spectrum of **1a** (400 MHz, acetonitrile-d_3).

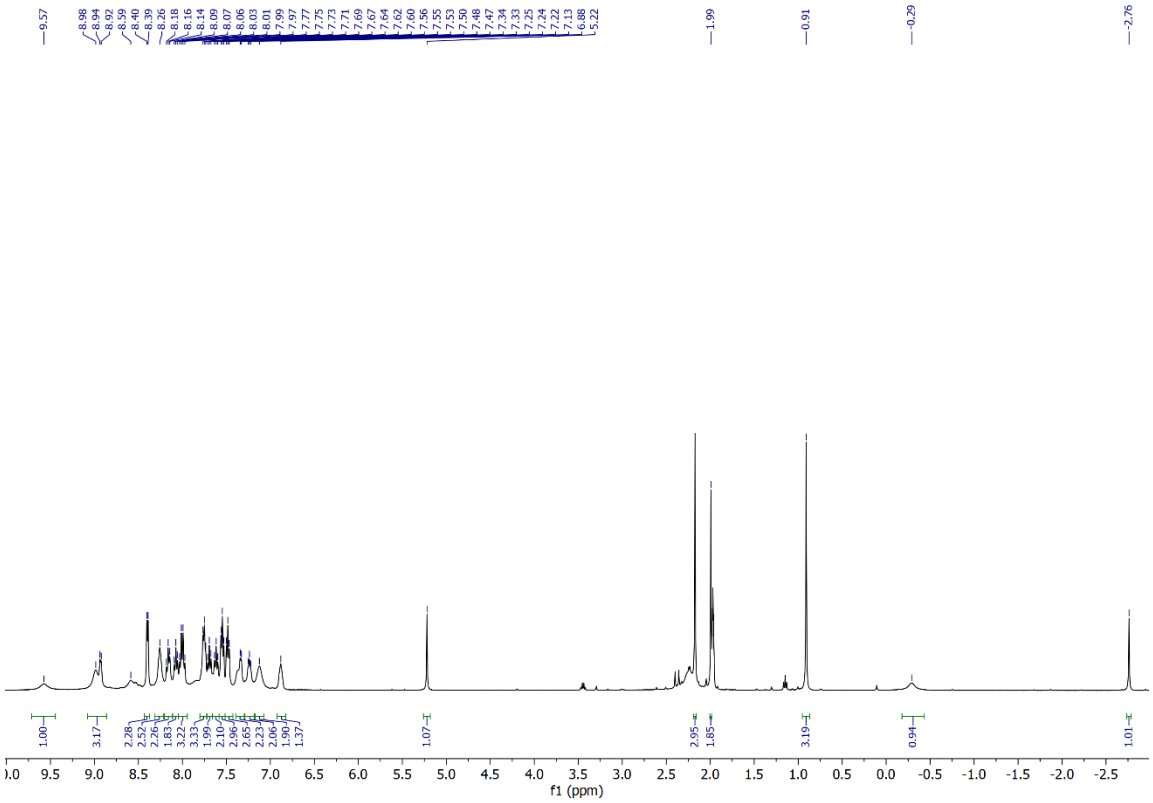


S2. FTIR spectrum of **1a**.

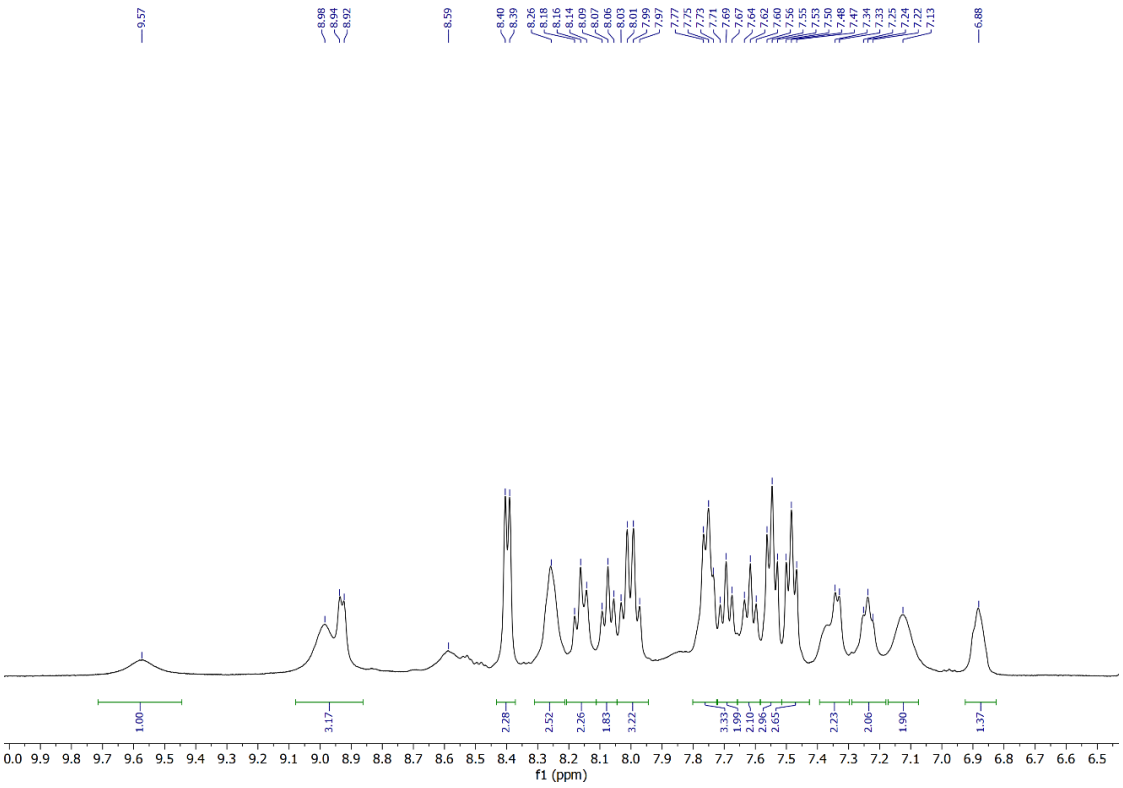


Preparation of $[Co_3O(OH)_3(OAc)_2(Py)_6][PF_6]_2$(Rac) (1b):

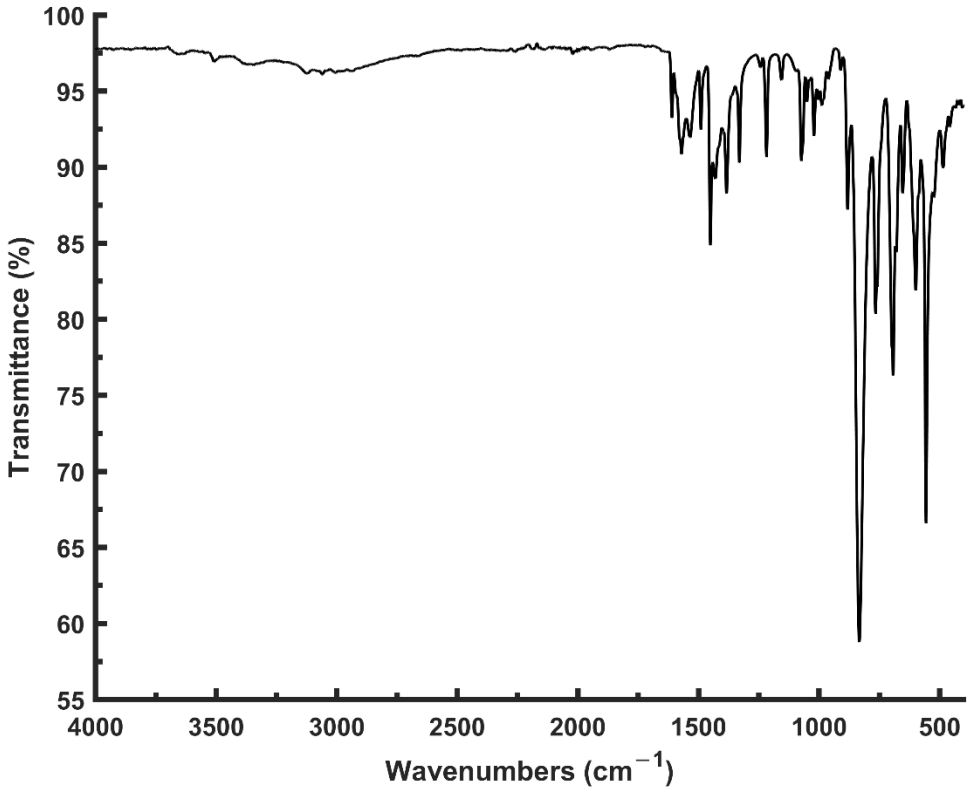
The synthesis of **2b** from $[Co(OAc)_2 \cdot 4H_2O$, (1.4 g, 5.8 mmol), pyridine (1.8 g, 23 mmol), H_2O_2 (5.0 mL, 50 mmol) and NH_4PF_6 (1.5 g, 9.2 mmol)] are the same as that for **1a**, but the brown/red solids collected on the frit were treated with a different procedure. The solids were extracted with CH_2Cl_2 (2 x 100 mL) from the frit into a fresh filter flask, and the residual solids discarded; the solvent was then removed *in vacuo*. The crude material was dissolved in minimal CH_2Cl_2 and cooled to -35 °C before layering with hexanes prechilled to -35 °C. After 40 h, a dark black oil was deposited. The oil was collected on a fine frit, washed with chilled hexanes, and dried with gentle airflow. The resulting solids were then collected, dissolved in MeCN, and chilled to -35 °C. The MeCN solution was then layered with Et_2O chilled to -35 °C and allowed to diffuse at -35 °C for an additional 40 h. Dark red-black blocks suitable for X-ray diffraction result, and the crystals were collected on a medium frit. Yield: 0.238 g; 11%. Characterization data: Because **1b** exists as a racemic mixture likely in equilibrium, the ^1H and $^{13}C\{^1H\}$ NMR are exceedingly complicated with 6 unique pyridine environments and total molecular asymmetry. ^1H NMR (500 MHz, Acetonitrile-d_3) δ 9.68 - 6.80 (multiplets and broad peaks overlapping, 32H, PyHs) 5.21 (s, $1H_a$), 2.14 (s, $3H_b$), 0.88 (s, $3H_c$) –0.32 (broad s, $1H_d$), –2.78 (s, $1H_e$) $^{13}C\{^1H\}$ NMR (101 MHz, Acetonitrile-d_3) δ 189.7, 184.8, 156.3, 155.7, 155.2, 154.5, 153.7, 152.7, 151.8, 151.7, 140.9, 140.7, 140.5, 140.3, 126.6, 126.3, 126.1, 126.0, 25.4, 24.6. $^{19}F\{^1H\}$ NMR (376 MHz, Acetonitrile-d_3) δ –72.68 (d, J = 706.7 Hz). $^{31}P\{^1H\}$ NMR (162 MHz, Acetonitrile-d_3) δ –141.25 (septet, J = 707.0 Hz). Anal Calcd. for $C_{34}H_{39}Co_3F_{12}N_6O_8P_2$: C, 36.25; H, 3.49; N, 7.46. Found: C, 37.68; H, 3.76; N, 8.17. Further combustion analysis is underway; the higher than anticipated CHN content are likely residual pyridine and acetonitrile, which hydrogen bond to the O-H in the solid-state molecular structure. IR (cm^{-1}): 3507 (w, *broad*), 3209 (w), 1609 (m), 1569 (w), 1534 (w), 1489 (w), 1450 (w), 1429 (w), 1383 (w), 1329 (w), 1217 (m), 1154 (w), 1072 (m), 832 (s), 765 (m), 692 (s), 653 (w), 598 (m), 556 (s). HRMS (ESI) *m/z*: Calcd. for $C_{34}H_{39}Co_3F_6N_6O_8P^+$: 981.0462 Found: 981.0356 $([Co_3O(OH)_3(OAc)_2(Py)_6][PF_6])^+$



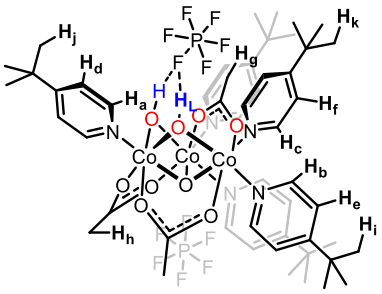
S3. ^{1}H NMR spectrum of **1b** (400 MHz, acetonitrile-d_3).



S4. Enhanced view of the aromatic region in **S3**.

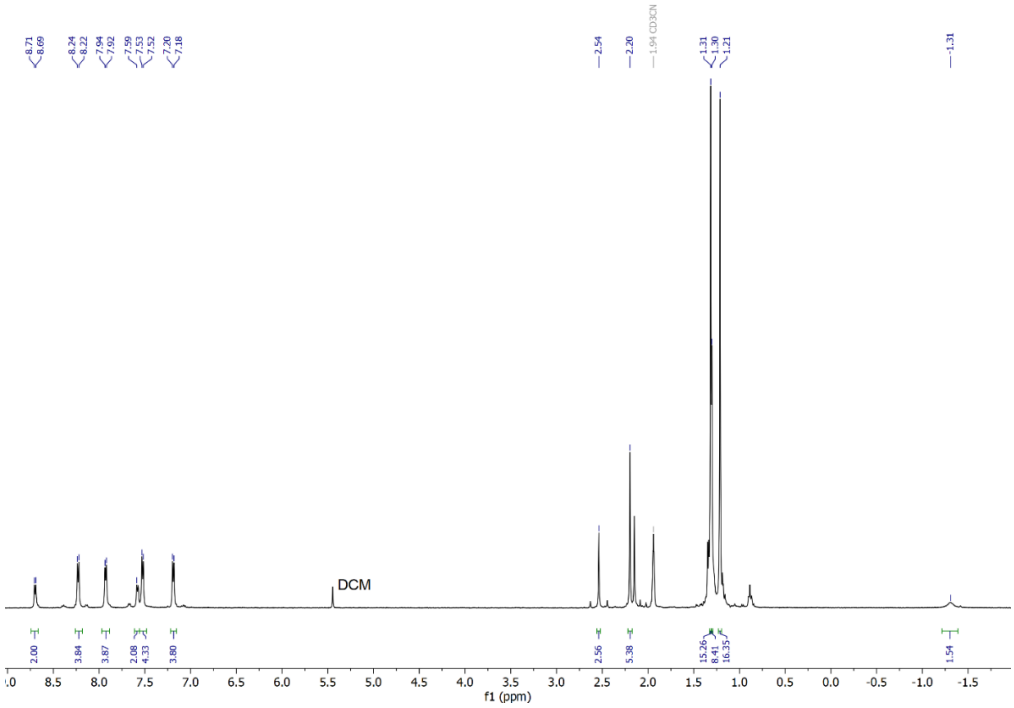


S5. FTIR spectrum of **1b**.



Preparation of $[Co_3O(OH)_2(OAc)_3(^tBuPy)_5][PF_6]_2$ (2):

In an N_2 filled glovebox, **1a** (30 mg, 0.02 mmol) was dissolved in benzene-d_6 (0.55 mL) and transferred to a J-Young NMR tube. Cp*Hf(Bnz)$_3$ (14 mg, 0.02 mmol) was dissolved in benzene-d_6 (0.20 mL), and the Cp*Hf(Bnz)$_3$ solution was added in one portion to the NMR tube; the NMR tube was sealed and removed from the glovebox to monitor the reaction progress. Over 30 h, brown blocks suitable for X-ray diffraction appeared. In an N_2 filled glovebox the resulting solution was washed from the J-Young tube using toluene (2 mL) and the solvent removed *in vacuo*. The solids were washed with toluene (3 x 5 mL) and the toluene solution transferred to a separate vial. The residual solids were dissolved in THF (5 mL), and toluene was added (~2 mL). The solution was chilled to -35 °C to produce crystals of **2**, which were collected on a medium frit. Yield 33 mg, 20%. Characterization data: ^{1}H NMR (400 MHz, Acetonitrile-*d3*) δ 8.70 (d, *J* = 6.2 Hz, 2H), 8.23 (d, J = 6.2 Hz, 4H), 7.93 (d, J = 6.0 Hz, 4H), 7.58 (d, J = 6.0 Hz, 2H), 7.52 (d, *J* = 6.1 Hz, 4H), 7.19 (d, *J* = 6.1 Hz, 4H), 2.54 (s, 3H), 2.20 (m, 6H), 1.31 (s, 18H), 1.30 (s, 9H), 1.21 (s, 18H), -1.30 (s, 2H) ^{13}C{^{1}H} NMR (101 MHz, Acetonitrile-*d3*) δ 189.07, 165.11, 153.51, 152.35, 152.13, 143.1, 123.17, 122.92, 122.51, 35.72, 35.59, 30.48, 30.42, 26.48, 24.76. HRMS (ESI) *m/z* calcd. for: $[C_{51}H_{76}Co_3F_6N_5O_9P]^+$: 1224.3275 ($[Co_3O(OH)_3(OAc)_3(tBuPy)][PF_6]$)$^+$Found: 1224.3285



S6. ^{1}H NMR spectrum of **2** (400 MHz, acetonitrile-d_3).

Crystallographic Information.

Identification code	**2**	**1b**	**1a**
Empirical formula	$C_{69}H_{94}N_5O_9F_{12}P_2Co_3$	$C_{34}H_{39}N_6O_8F_{12}P_2Co_3$·Py/$CH_3CN$	$C_{49}H_{74}N_5O_8F_{12}P_2Co_3$·2EtOH
Crystal system	orthorhombic	monoclinic	orthorhombic
Space group	Pbca	$P2_1/c$	Pbca
a (Å)	23.7906(5)	20.0414(8)	21.9073(9)
b (Å)	19.7071(4)	12.8820(5)	22.4597(9)
c (Å)	32.5642(8)	20.2103(8)	26.4944(12)
α (°)	90	90	90
β (°)	90	114.034(2)	90
γ (°)	90	90	90
Volume ($Å^3$)	15267.5(6)	4765.4(3)	13036.1(10)
Z	8	4	8
Density (g/cm^3)	1.396	2.171	2.167
Absorption coefficient (mm^{-1})	0.771	3.902	4.147
F(000)	6672.0	2993.0	8176.0
Crystal size/mm^3	0.4 × 0.3 × 0.2	0.1 × 0.08 × 0.05	0.15 × 0.15 × 0.1
Reflections collected	107994	72651	192643
Independent reflections	17960 [R_{int} = 0.1000, R_{sigma} = 0.0898]	10572 [R_{int} = 0.0583, R_{sigma} = 0.0371]	14538 [R_{int} = 0.0848, R_{sigma} = 0.0483]
Goodness-of-fit on F^2	1.025	1.053	1.036
Final R indexes [I>=2σ (I)]	R_1 = 0.0673, wR_2 = 0.1307	R_1 = 0.0427, wR_2 = 0.1097	R_1 = 0.0538, wR_2 = 0.1432
Final R indexes [all data]	R_1 = 0.1207, wR_2 = 0.1510	R_1 = 0.0521, wR_2 = 0.1163	R_1 = 0.0714, wR_2 = 0.1552
Largest diff. peak/hole / e $Å^{-3}$	0.78/-0.69	1.08/-0.60	1.10/-0.50

Acknowledgements:

The author would like to acknowledge Jaruwan Amtawong (Jom) and Josh Tang for helpful discussion and support. Prof. Rittle made the excellent suggestion that the PF_6—H interaction was abnormally strong. Rex Handford, Ben Suslick, and Jom provided helpful, critical feedback. J.T. and T.A.W. both made **4** independently for separate studies, but the compound has not been prepared before otherwise. This work was funded by the National Science Foundation under grant no. CHE-1566538. UC Berkeley ChexRay is funded by the National Institutes of Health under grant no. S10-RR027172. This research used resources of the Advanced Light Source beamline 12.2.1, which is a DOE Office of Science User Facility under contract no. DE-AC02-05CH11231. UC Berkeley College of Chemistry NMR facility is partially funded by the NSF: NSF grant CHE-0130862, CHE-911557, CHE-8703048, and NIH: S10-RR-03353-01, 1S10-RR-016634-01, SRR023679A.

References for Supporting Information of Chapter 2:

1. Evans, D. F., The determination of the paramagnetic susceptibility of substances in solution by nuclear magnetic resonance. *Journal of the Chemical Society (Resumed)* **1959**, 2003-2005.
2. Dolomanov, O. V.; Bourhis, L. J.; Gildea, R. J.; Howard, J. A. K.; Puschmann, H., OLEX2: a complete structure solution, refinement and analysis program. *J. Appl. Crystallogr.* **2009,** *42*, 339-341.
3. Sheldrick, G., Crystal structure refinement with SHELXL. *Acta Cryst. C* **2015,** *71*, 3-8.
4. Sheldrick, G., SHELXT - Integrated space-group and crystal-structure determination. *Acta Cryst. Section A* **2015,** *71*, 3-8.

Chapter 3:

Metal-Metal Redox Exchange to Produce Manganese-Cobalt Oxo Cubanes via a "Dangler" Intermediate

Introduction:

Tetrametallic tetrachalcogenide [M_4E_4, E = O, S] heterocubane clusters (M_4E_4, E = O, S) are important reaction centers that can effectively mediate proton-coupled, multi-electron chemical processes in biological systems.[1-4] Prominent examples include [Fe_4S_4] iron sulfur clusters that are essential electron-transfer cofactors for a range of enzymes.[5-7] The $CaMn_4O_4$ cluster known as the oxygen evolving complex (OEC, Figure 1a) of Photosystem II, and the $NiFe_4S_4$ active site of carbon monoxide dehydrogenase (CODH) are structurally similar heterocubane complexes that play an important role in enzymatic catalysis.[8] The importance of this structural motif in biology has motivated significant research into the role of the tetrametallic assembly, and much of this effort has benefited from the use of synthetic models that mimic structural and spectroscopic aspects of the appropriate cubane.[5,9-11] Indeed, synthetic models were instrumental in understanding the geometry of the OEC before high resolution X-ray diffraction enabled determination of the active site arrangement.[12-14] Current OEC model systems effectively replicate EPR spectra observed for the S_2 and S_3 state of the OEC, and structurally reproduce nearly all of the key OEC bonding motifs (Figure 1b).[15-24] Despite the progress made from these studies, the synthesis of cubane models that accurately mimic biological function remains a significant challenge, in part due to a limited understanding of cubane assembly mechanisms. Investigations into the assembly and metal-metal exchange reactivity of iron sulfur clusters has demonstrated that these clusters can readily undergo Fe-Fe exchange, as shown by isotopic labeling studies.[25-29] However, general synthetic methods that allow construction of heterometallic cubanes analogous to those observed in biology are quite limited, and the mechanisms by which heterocubanes assemble remain poorly understood.[30-34]

An interesting feature of certain cubane active sites is their close association with an additional redox-active metal ion that is directly involved in the function of the enzyme.[8] In the OEC, a $CaMn_3O_4$ oxo cubane is associated with a pendent Mn ion referred to as the "dangler" (Figure 1a), whereas an Fe_3NiS_4 cubane of the CODH active site is bound to an Fe ion.[35, 36] In proposed catalytic mechanisms for both the OEC and CODH, these exogenous metal ions directly assist in utilizing accumulated redox equivalents of the cubane to perform difficult reactions at low overpotentials.[37-43] Despite clear indication that these dangler ions are essential, a detailed mechanistic understanding of their specific role is lacking. Therefore, an important research objective is the preparation and study of cubane model systems that possess redox-active, dangler metal centers. Only a few such dangler-cubane assemblies have been synthesized (e.g., Figure 1b,c), including a manganese-cobalt oxo cubane synthesized by complexation of "$Co^{II}(NO_3)(OAc)$" to the oxo cubane $MnCo_3(\mu_3\text{-}O)_4(OAc)_5(py)_3$ (OAc = acetate, py = pyridine).[19, 20,44-46] In this synthesis, an acetate migration assists in complexation of the incoming metal ion to produce a new, κ^1,κ^1-(OAc)MOM' binding mode that supports the dangler structure (Figure 1c). Thus, it appeared that a reasonable starting point for the synthesis of other danglers could involve established cobalt, oxo cubanes such as $Co_4(\mu_3\text{-}O)_4(OAc)_4(py)_4$ in reactions of acetate-containing sources of a dangler ion.[47]

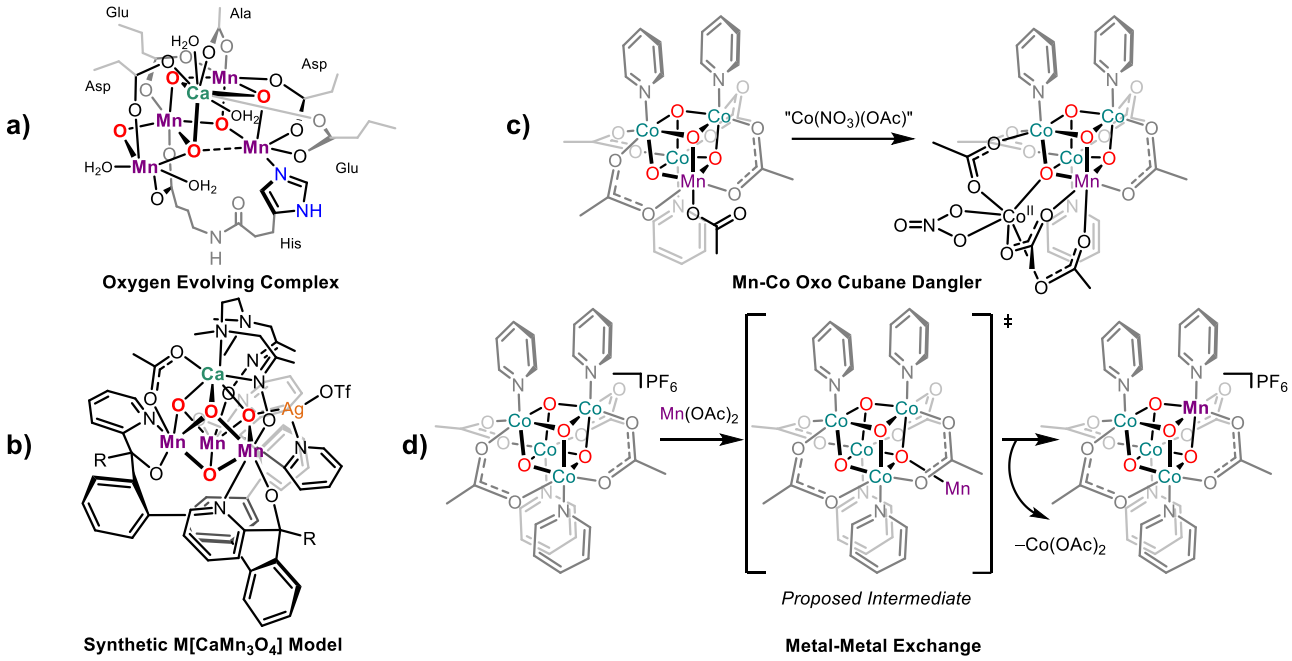


Figure 1. Established metal oxo cubane "dangler" complexes. (a) The oxygen evolving complex (OEC) of Photosystem II. (b) A pentametallic structural analogue of the OEC. (c) A pentametallic model of the OEC complex. (d) Generalized exchange reaction described in this contribution.

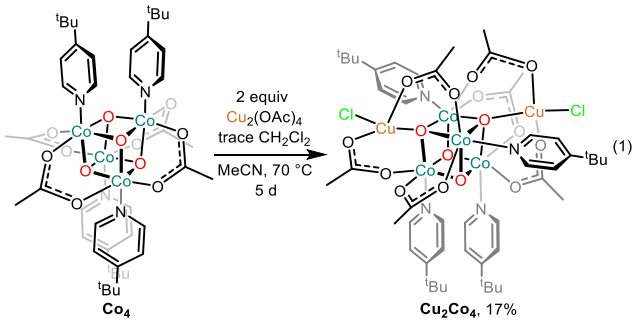
This contribution describes the application of this strategy to investigate incorporation of divalent metal ions as danglers onto a cobalt oxo cubane ([Co_4O_4]) core (Figure 1 1d). A dangler complex containing two Cu^{II} ions has been discovered, as well as an unexpected metal-metal (Co-Mn) exchange reaction that provides a convenient route to heterometallic oxo cubanes with a manganese-cobalt oxo cubane ([$MnCo_3O_4$]) core.[44] As shown herein, this exchange likely occurs through a dangler intermediate possessing acetate-bridged Co and Mn centers. This redox-based exchange process incorporating a Mn^{IV} ion is possibly relevant to the mechanism of biosynthesis of the OEC, which is believed to require multiple Mn^{II} ion oxidation events and a conformational rearrangement in order to generate a Mn_2Ca OEC precursor.[27,30,48,49] This process may generally point the way to synthesis of new heterometallic cubane complexes, and may also serve as a molecular model for "Galvanic exchange" processes used for doping metal oxide nanoparticles and bulk materials.[50-54]

Results and Discussion:

Synthesis of an Oxo Cubane with Pendent Copper Centers. The possible binding of a monometallic "dangler" metal ion to the oxo cubane cluster, $Co_4O_4(OAc)_4$(*t*-Bupy)$_4$ (**Co_4**, *t*-Bupy = 4-*tert*butylpyridine), was investigated by screening its reactions with divalent transition metal acetates. This approach was motivated by the prior observation that "Co(OAc)(NO_3)" adds to a [$MnCo_3O_4$] cubane to produce the $MnCo_4O_4(OAc)_6(NO_3)(py)_3$ dangler complex (Figure 1c).[44] In the latter process, a bridging acetate ligand detaches from the cubane core to capture the additional metal ion, and this hemilability serves as a pathway to the dangler complex.

Treatment of cubane **Co_4** with $Ca(OAc)_2$, $Fe(OAc)_2$, $Ni(OAc)_2$, or $Zn(OAc)_2$ in MeCN solution at 23 °C or 55 °C led to complex reaction mixtures that did not appear to contain a dangler complex, as determined by ^{1}H NMR spectroscopy and high-resolution electrospray ionization mass

spectrometry (HR-ESI-MS). However, when a solution of **Co4** and $Cu_2(OAc)_4(H_2O)_2$ in MeCN solution (with trace CH_2Cl_2 as solvent of crystallization for **Co4**) was heated at 70 °C for 16 h, followed by cooling to 23 °C, dark green crystals of paramagnetic $Cu_2Co_4(\mu_4\text{-}O)_2(\mu_3\text{-}O)_2(OAc)_6Cl_2(t\text{-}Bupy)_4$ (**Cu2Co4**) were obtained in 17% yield (eq 1). Single-crystal X-ray diffraction (SC-XRD) analysis enabled determination of the solid-state molecular structure, which may be described as a "double dangler" complex, with each copper atom bound to a bridging oxo ligand of the cubane (to create two μ_4-oxos) and linked to the cubane core by two bridging acetates. Presumably the chloride ligands on copper originate from the CH_2Cl_2 present in samples of **Co4**. Thus, the reaction results in retention of the original cubane ligands, and formal addition of two "CuCl(OAc)" units to adjacent corners of the cubane. The resulting cluster displays approximate C_2 symmetry that relates the two four-coordinate Cu centers.



The ^{1}H NMR spectrum of complex **Cu2Co4** in acetonitrile-d_3 is consistent with the desymmetrization of **Co4** (Figure S6); however, the broad paramagnetic resonances cannot definitively confirm the structure. This bonding arrangement is accompanied by exchange of acetate and pyridine coordination sites for two of the Co centers, to produce the observed heterobimetallic CoOCu(1κ^2,2κ^2-OAc) chelate rings. Binding of the Cu ions results in slight elongation of the Co–O(oxo) bonds (1.89(2)Å) with respect to those for $Co_4(\mu_3\text{-}O)_4(OAc)_4(py)_4$ (1.86(2) Å), and all Co–(μ_4-O) distances are elongated to an average of 1.906(6) Å. The solution magnetic moment of 3.3 μ_B (Evans method[55]) is consistent with two isolated Cu^{II} centers.

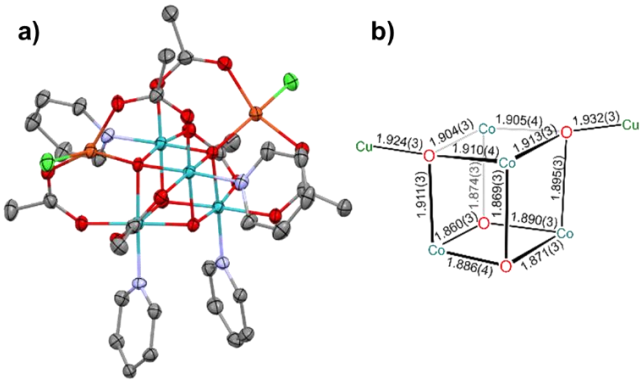
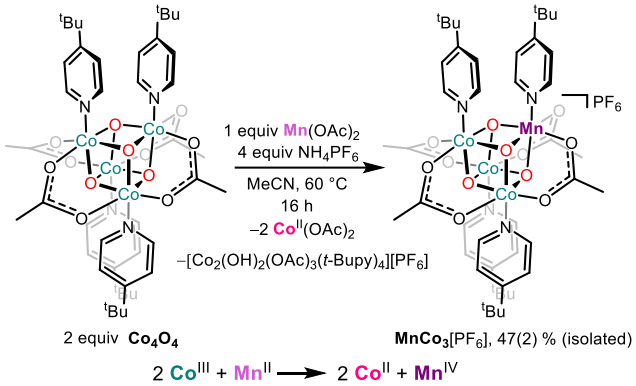


Figure 2. (a) Solid-state molecular structure of complex Cu_2Co_4. Solvent of recrystallization, other equiv of Cu_2Co_4 in the asymmetric unit, and *tert*-butyl groups removed for clarity. (b) Cluster bond distances.

Cyclic voltammetry of compound **Cu2Co4** in MeCN reveals a reversible oxidation at 1.05 V vs. ferrocene/ferrocenium (Figure S8). Interestingly, the binding of the copper fragments increases the oxidation potential of the parent cubane **Co4** by 0.77 V. Sweeping cathodically reveals a host of overlapping, irreversible reduction events that could not be assigned.

Mn-Co Exchange in Cobalt Oxo Cubane Co4. The isolation of complex **Cu2Co4** suggested that other metal acetates could generate dangler complexes, and a Mn dangler would be most relevant as a model for the OEC. Addition of $Mn(OAc)_2$ to a solution of **Co4** in MeCN at 60 °C resulted in a color change from green to brown over 16 h, and in the presence of two equiv of NH_4PF_6 (to enhance solubility), a red homogeneous solution was obtained (Scheme 1). Analysis of this crude reaction mixture by HR-ESI-MS indicated the presence of a tetra(*t*-Bupy)-substituted cubane cation analogous to the previously reported $[MnCo_3(\mu_3\text{-}O)_4(OAc)_4(py)_4]^+$, as well as several Co^{III} acetate oligomers, most notably the dicobalt complex $[Co_2(\mu\text{-}OH)_2(OAc)_3(t\text{-}Bupy)_4]^+$ which was also identified by ^{1}H NMR spectroscopy (*vide infra*; Scheme 1).[44,56] Generation of the formally $Mn^{IV}Co^{III}_3$ cubane corresponds to a redox reaction whereby Mn^{II} is oxidized by two equiv of Co^{III}, with one equiv of Co^{III} acting as a sacrificial oxidant (Scheme 1).

Scheme 1. Metal-metal Exchange between Co4 and Mn(OAc)2 with the Corresponding Formal Redox Equation.



Workup of the reaction mixture involved filtration to separate the precipitated byproduct, pink $Co(OAc)_2$ powder (*vide infra*), followed by crystallization from CH_2Cl_2/pentane to give red crystals of $[MnCo_3(\mu_3\text{-}O)_4(OAc)_4(t\text{-}Bupy)_4][PF_6]$ (**MnCo3**$[PF_6]$, 47(2)% isolated yield) that were suitable for single-crystal X-ray diffraction. The solid-state molecular structure indicates retention of the basic oxo cubane framework, and the refinement improved when the metal vertex was modeled as partially occupied by Mn. Similar to what was previously observed for an analogous tetrapyridine $[MnCo_3]$ cubane system (with py ligands), **MnCo3**$[PF_6]$ crystallizes as an inversion-twin in the $P\bar{4}n2$ space group, such that ¼ of the cubane resides in the asymmetric unit, making determination of the precise location of the Mn atom impossible.[44] The ^{1}H NMR spectrum of **MnCo3**$[PF_6]$ in acetonitrile-d_3 contained broad resonances consistent with a paramagnetic species, as confirmed by an Evans method measurement (3.31 μ_B, S = 3/2). The identity of the $[Co_2(\mu\text{-}OH)_2(OAc)_3(t\text{-}Bupy)_4][PF_6]$ byproduct (10% yield by ^{1}H NMR spectroscopy) was confirmed by isolation and characterization by ^{1}H NMR spectroscopy and HR-ESI-MS.[56,57] Other Co^{III} acetate *t*-Bupy species present (by ^{1}H NMR spectroscopic and mass spectrometric analysis) appear to correspond to oligomeric species.[58, 59]

The reaction depicted in Scheme 1 was monitored by ^{1}H NMR spectroscopy to establish the overall stoichiometry. Addition of $Mn(OAc)_2$ to a solution of **Co4** in acetonitrile-d_3 resulted in the immediate appearance of several unassigned, low-intensity resonances with no evidence for formation of **MnCo3**$^+$, and after 24 h at room temperature no further change was observed. The solution was then heated to 50 °C for 24 h, which resulted in complete conversion of **Co4** and appearance of resonances corresponding to paramagnetic **MnCo3**$^+$ along with the aforementioned cobalt byproducts. The limited solubility of $Mn(OAc)_2$ in organic solvents made determination of

the stoichiometry by NMR spectroscopy difficult, and motivated use of the more soluble Mn^{II} starting material $Mn(OTf)_2$. Acetonitrile-d_3 solutions with various **Co4**:$Mn(OTf)_2$ ratios were heated to 50 °C for 24 h and the reaction was monitored by ^1H NMR spectroscopy, with 1,3,5-trimethoxybenzene (TMB) as an internal standard (Figure S94). When the **Co4**:$Mn(OTf)_2$ molar ratio was lower than 2:1, **Co4** was completely converted to several diamagnetic species, presumably Co^{III} oligomers (as substantiated by HR-ESI-MS), and broad paramagnetic resonances for **MnCo3**$^+$ were observed. Consistent with the expected stoichiometry for this redox reaction, the isolated yield of **MnCo3**$[PF_6]$ from the reaction of **Co4** with 1 equiv of $Mn(OTf)_2$ and NH_4PF_6 was 40(5)%.

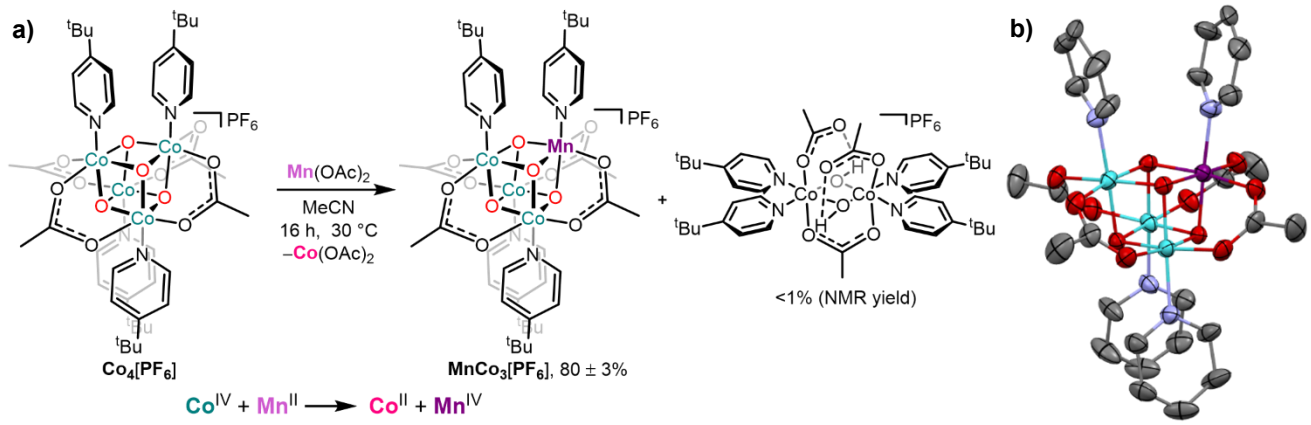
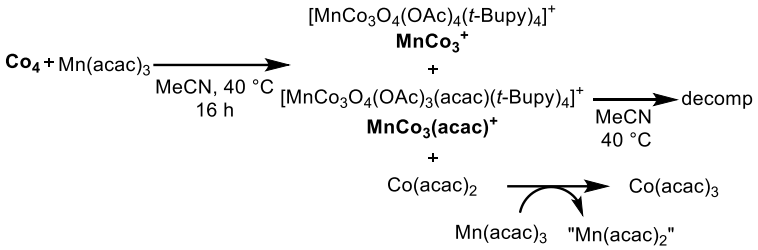


Figure 3. (a) Synthesis of **MnCo3**$[PF_6]$ from **Co4**$^+[PF_6]$. (b) Solid-state molecular structure of **MnCo3**$[PF_6]$ with 50% probability thermal ellipsoids shown and one metal ion arbitrarily assigned as Mn (see main text). Hydrogen atoms, *tert*-butyl groups, and counterion removed for clarity.

Since the product of this metal-metal exchange reaction contains a Mn^{IV} center, the reaction of $Mn(OAc)_2$ with the oxidized and formally Co^{IV}-containing $[Co^{IV}Co_3(\mu_3\text{-}O)_4(OAc)_4(^t\text{BuPy})_4][PF_6]$ (**Co4**$^+[PF_6]$) was also examined. A vigorously stirred solution of $Mn(OAc)_2$ and **Co4**$^+[PF_6]$ (1:1) in MeCN at 30 °C resulted in a slow color change from brown/olive green to red over 16 h (Figure 3). Removal of the solvent *in vacuo* and extraction with CH_2Cl_2 resulted in a dark brown-red solution and a pink solid (presumably $Co(OAc)_2(L)_n$,) that was separated by filtration. Layer diffusion of pentane into the dichloromethane solution at –5 °C over 48 h produced red blocks of **MnCo3**$[PF_6]$ (80(3)% yield) and accordingly, HR-ESI-MS analysis of the crystalline material indicated the presence of a single cation corresponding to **MnCo3**$^+$. The pink solid byproduct was analyzed by HR-ESI-MS, ^1H NMR, and FTIR spectroscopy, all of which suggest the presence of $Co(OAc)_2(L)_n$ (L = *t*-Bupy, H_2O, Figure S110). The stoichiometry of this exchange, initiated from either $Mn(OAc)_2$ or $Mn(OTf)_2$ in acetonitrile-d_3, was examined by ^1H NMR spectroscopy, and in both cases one equivalent of Mn^{II} per equivalent of Co^{IV} was required for the complete consumption of **Co4**$^+[PF_6]$ (Figure S96). A trace amount (<1% yield vs internal standard) of $[Co_2(\mu\text{-}OH)_2(OAc)_3(^t\text{BuPy})_4][PF_6]$ in the product mixture may be attributed to reaction of residual unoxidized **Co4** in the sample of **Co4**$^+[PF_6]$ (Figure S89). Monitoring the metal-metal exchange of **Co4** or **Co4**$^+[PF_6]$ with $Mn(OAc)_2$ by ^1H NMR spectroscopy in dry, degassed acetonitrile-d_3 in a sealed J-Young NMR tube under an N_2 atmosphere indicated that the reactions are not influenced by water and air, since the product distributions and qualitative reaction rates were unaffected. A balanced redox equation for this metal-metal exchange reaction requires one equivalent of Co^{IV} and one equivalent of Mn^{II} to give Co^{II} and Mn^{IV} in a two-electron redox process (Figure 3).

Reactions of Co_4 with Mn^{III} sources. To probe the possible participation of intermediate Mn^{III} species in the above processes, redox reactions of **Co_4** with $Mn^{III}(acac)_3$ were investigated by ^1H NMR spectroscopy, with yields determined by comparison to TMB as an internal standard. An acetonitrile-d_3 solution of equimolar $Mn(acac)_3$ and **Co_4**, heated at 40 °C for 16 h, gave complete conversion of $Mn(acac)_3$, 95% conversion of **Co_4**, formation of both **$MnCo_3^+$** and $[MnCo_3(\mu_3\text{-}O)_4(OAc)_3(acac)(t\text{-}Bupy)_4]^+$ (**$MnCo_3(acac)^+$**; by HR-ESI-MS and ^1H NMR spectroscopy), and a 27% yield of $Co(acac)_3$ in addition to other unidentified paramagnetic side products. Use of two equiv of $Mn(acac)_3$ led to complete conversion of **Co_4** and a 92% yield of $Co(acac)_3$ by ^1H NMR spectroscopy, along with the same $[MnCo_3O_4]$ cubane products according to the idealized stoichiometry outlined in Scheme. Note that an accurate determination of the yield and product ratios associated with **$MnCo_3^+$** and **$MnCo_3(acac)^+$** is difficult to establish due to very broad ^1H NMR resonances for these paramagnetic complexes.

Scheme 2. Idealized reaction of Co_4 with $Mn(acac)_3$.



Presumably, one equiv of $Mn(acac)_3$ is also consumed in the production of $Co(acac)_3$ (Scheme 2). The $[MnCo_3O_4]$ cubane products (**$MnCo_3^+$** and **$MnCo_3(acac)^+$**) produced in this transformation were isolated as PF_6^- salts by chromatographic separation following the reaction of **Co_4** with $Mn(acac)_3$ and NH_4PF_6 which gave the coeluting products **$MnCo_3$**$[PF_6]$ and **$MnCo_3(acac)$**$[PF_6]$ in a combined yield of 33%.

Presumably, one equiv of $Mn(acac)_3$ is also consumed in the production of $Co(acac)_3$ (Scheme 2). The $[MnCo_3O_4]$ cubane products (**$MnCo_3^+$** and **$MnCo_3(acac)^+$**) produced in this transformation were isolated as PF_6^- salts by chromatographic separation following the reaction of **Co_4** with $Mn(acac)_3$ and NH_4PF_6 which gave the coeluting products **$MnCo_3$**$[PF_6]$ and **$MnCo_3(acac)$**$[PF_6]$ in a combined yield of 33%.

Another possible secondary reaction involves radical processes of the acac ligands, as this has been reported for other $Mn(acac)_3$ systems.[60-63] Indeed, a dichloromethane-d_2 solution of equimolar $MnCo_3(\mu_3\text{-}O)_4(OAc)_5(py)_3$ and acetylacetone heated to 35 °C for 16 h resulted in partial (ca. 33%) decomposition of the $[MnCo_3O_4]$ cubane and formation of $Co^{III}(acac)$ products by ^1H NMR spectroscopy and HR-ESI-MS. Likewise, heating a solution containing a mixture of purified **$MnCo_3$**$[PF_6]$ and **$MnCo_3(acac)$**$[PF_6]$ to 40 °C resulted in depletion of **$MnCo_3(acac)^+$** by 25% relative to **$MnCo_3^+$** after 16 h (HR-ESI-MS, Figure S185). Thus, radical-based reactions of acac ligands appear to contribute to a lower stability of the **$MnCo_3(acac)^+$** cubane and may contribute to the greater than stoichiometric consumption of **Co_4** by $Mn(acac)_3$ (Table 1, entries 1-3). Overall, the data in Table 1 are consistent with the stoichiometry outlined in Scheme 2.

Table 1. Investigation of Mn^{III} Reagents.

[Mn] Source	Equiv	Conversion of Co_4 (%)[a]	Yield Co^{III} (%)[a]
$Mn(acac)_3$	0.5	80	7
	0.75	91	11
	1	95	14
	1.5	100	29
	2	100	45
Mn^{III}(*t*-Bupy)$[PF_6]$	0.5	44	13
	0.75	58	17
	1	69	25
	1.5	83	38
	2	100	63

[a]Yields determined by ^1H NMR spectroscopy vs 1,3,5-trimethoxybenzene as an internal standard as the sum of potential Co^{III} products.

To limit possible side products involving acac-induced decomposition, reactions with $[Mn(acac)_2(t\text{-Bupy})_2][PF_6]$ (**Mn^{III}(*t*-Bupy)**$[PF_6]$), a Mn^{III} source with one less acac ligand, were also investigated. An acetonitrile-d_3 solution of equimolar **Mn^{III}(*t*-Bupy)**$[PF_6]$ and **Co_4**, heated at 40 °C for 16 h, resulted in full conversion of **Mn^{III}(*t*-Bupy)$^+$**, 69% conversion of **Co_4**, a 50% yield of $[Co(acac)_2(t\text{-Bupy})_2][PF_6]$ (**Co^{III}(*t*-Bupy)**$[PF_6]$, Table 1) and an undetermined amount of **$MnCo_3^+$/$MnCo_3$(acac)$^+$** (observed by ^1H NMR and HR-ESI-MS). The reaction of **Co_4** and **Mn^{III}(*t*-Bupy)$^+$** to give **$MnCo_3^+$/$MnCo_3$(acac)$^+$** and **Co^{III}(*t*-Bupy)$^+$** obeyed a 1:2 (**Co_4**:Mn^{III}) stoichiometry (Table 1), following a pathway analogous to that depicted in Scheme 2. Note that, unlike the reaction of **Co_4** with $Mn(acac)_3$, this reaction does not lead to overconsumption of **Co_4** at lower **Co_4**:Mn^{III} ratios. The conversion of **Co_4** to **Co^{III}(*t*-Bupy)$^+$** suggests that one equiv of Mn^{III} undergoes metal-metal exchange with **Co_4**, and another equiv of Mn^{III} oxidizes the putative $Co(acac)_2$ byproduct to form one equiv of Co^{III}. In agreement with this hypothesis, the reaction of equimolar $Co(acac)_2$ and **Mn^{III}(*t*-Bupy)** in acetonitrile-d_3 resulted in quantitative conversion to **Co^{III}(*t*-Bupy)** by ^1H NMR spectroscopy.[64] On a synthetic scale, the reaction of two equiv of **Mn^{III}(*t*-Bupy)**$[PF_6]$ with **Co_4** gave an unoptimized yield of 11% for the mixture of **$MnCo_3^+$/$MnCo_3$(acac)$^+$**, while red crystals of **Co^{III}(*t*-Bupy)**$[PF_6]$ were isolated in 42% yield.

By ^1H NMR spectroscopy, no reaction occurred for an acetonitrile-d_3 solution of $MnCo_3(\mu_3\text{-}O)_4(OAc)_5(py)_3$ and $[Mn(acac)_2(py)_2][PF_6]$ (**Mn^{III}(py)**$[PF_6]$) heated to 40 °C for 16 h. This indicates that a secondary reaction of the $[MnCo_3O_4]$ cubane product with **Mn^{III}(py)$^+$** does not influence the observed product distributions under these conditions. Additionally, monitoring the reaction of **Co_4** with **Mn^{III}(*t*-Bupy)$^+$** by ^1H NMR spectroscopy indicates that a non-oxidative ligand exchange does not compete with metal-metal exchange for the consumption of **Co_4** in the reaction of **Co_4** and **Mn^{III}(*t*-Bupy)$^+$**. Thus, the Co-Mn exchange involving **Co_4** and **Mn^{III}(*t*-Bupy)$^+$** more closely follows the idealized stoichiometry of **Scheme** and early in this reaction there are no significant, competing processes that consume **Co_4**. The reduced 63% yield of Co^{III} in the 1:2 reaction of **Co_4** with **Mn^{III}(*t*-Bupy)$^+$** is likely due to radical-induced processes.

Metal-Metal Exchange Kinetics Involving Mn^{III}. To probe the mechanism of cobalt-manganese exchange, kinetic studies involving $[Co_4O_4]$ cubanes and Mn^{III} complexes were conducted, using initial rate data collected from reactions monitored by UV-vis spectroscopy. The cobalt oxo cubanes chosen for study are benzoate derivatives that allow tuning of the cubane electronic properties with *para* substituents in the pyridine and benzoate ligands. These substituted pyridine and benzoate complexes, e.g., $Co_4(\mu_3\text{-}O)_4(OBz)_4(py)_4$ (**Co_4(py-H)**) and $Co_4(\mu_3\text{-}O)_4(OBz)_4(\underline{t\text{-}Bupy})_4$ (**$Co_4(O_2CC_6H_4\text{-}H)$**), were readily prepared by the known procedure involving $Co(OAc)_2(H_2O)_4$ and the corresponding pyridine with H_2O_2, or by ligand-exchange reactions of a benzoic acid derivative with **Co_4** (see SI).[65-67] The Mn^{III}-based reactant $[Mn(acac)_2(py)_2][PF_6]$ **Mn^{III}(py)**$[PF_6]$ was chosen due to its favorable solubility properties and slow rates of ligand-exchange side reactions. As determined by ^1H NMR spectroscopy, no reaction was observed within 0.5 h of combining equimolar solutions of **$Mn^{III}(py)^+$** and **Co_4(py-H)**. The Mn-Co exchange proceeds in a manner similar to that involving **Co_4** and **Mn^{III}(*t*-Bupy)$^+$**, to give $[MnCo_3(\mu_3\text{-}O)_4(OBz)_4(py)_4][PF_6]$ (**$MnCo_3$(py)**$[PF_6]$) and $[Co(acac)_2(py)_2][PF_6]$ (**Co^{III}(py)**$[PF_6]$). Critically, there are no side reactions that occur before metal-metal exchange in the reaction with Mn^{III} sources and **Co_4(py-H)**, and it is assumed that the measured initial rates are minimally affected by competing secondary processes. Note that ligand exchange was observed in other cases; for example, $Mn(OTf)_2$ reacts rapidly with **Co_4** by initial ligand exchange, to give triflate-containing cobalt cubane complexes (by ^1H NMR and ESI-MS; Figure S99) before metal-metal exchange occurred. Ligand exchange was also observed in the transfer of an acac ligand in the reaction of **Co_4** with $Mn(acac)_3$ (eq 2), which suggests operation of an inner-sphere electron-transfer process.

Equimolar MeCN solutions of **Co_4(py-H)** and **$Mn^{III}(py)^+$** were combined in a sealed cuvette and the resulting reaction mixture was heated to 40 °C for 350 minutes. Monitoring by UV-vis spectroscopy revealed an approximate isosbestic point at 308 nm (Figure 4), indicating a linear relationship between the concentrations of products and reactants. Generally, in further kinetics experiments, the entire UV-vis spectrum was collected at each timepoint, and rate data was determined simultaneously in triplicate to estimate the experimental error. Attempts to fit the data to an integrated rate law did not cleanly delineate between various mechanistic possibilities, likely due to the aforementioned background oxidation reaction of $Co(acac)_2$ to give **Co^{III}(py)**.

Kinetics for the metal-metal exchange reaction were followed by UV-vis spectroscopy, with an excess of **Co_4(py-H)** or **$Mn^{III}(py)^+$** to establish pseudo first-order conditions. The slope of the log/log plot of $[\mathbf{Mn^{III}(py)^+}]_0$ vs. k_{init} indicated a reaction order of 0.8(2), while the log/log plot of $[\mathbf{Co_4(py\text{-}H)}]_0$ vs. k_{init} indicated a reaction order of 0.55(3) (Figure S143). Although the fractional reaction orders are difficult to interpret, the concentration dependence of the rate on both **$Mn^{III}(py)^+$** and **Co_4(py-H)** concentrations indicates that both species are involved in a rate-determining step. This behavior is consistent with both outer- and inner-sphere electron-transfer mechanisms, but an inner-sphere redox process in an intermediate adduct formed by coordination of **$Mn^{III}(py)^+$** to a μ_3-oxo ligand of **Co_4(py-H)** seems likely. Note that in the observations described above, ligand transfer often, but not always, accompanies metal-metal exchange (*vide supra*).

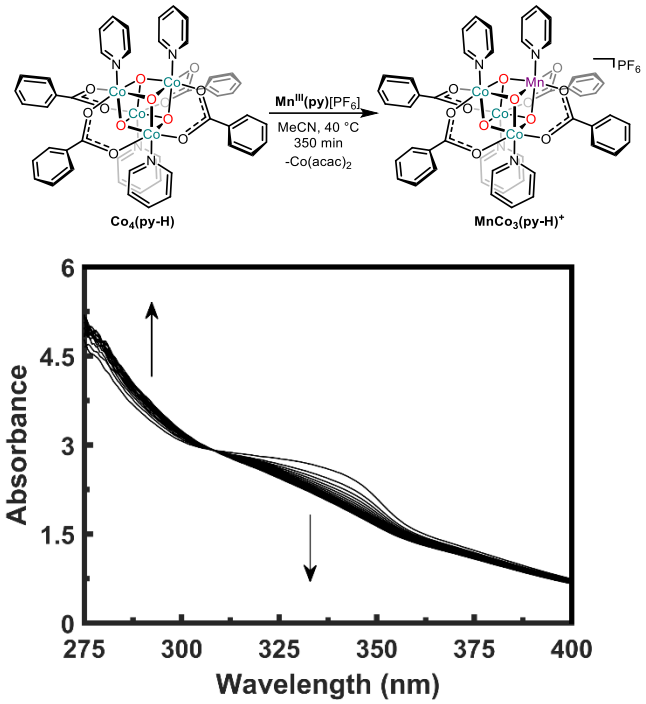


Figure 4. Representative UV-vis spectra tracking the metal-metal exchange reaction between equimolar $Mn^{III}(py)^+$ and Co_4(py-H) over 350 min.

Given the apparent lability of the complexes in this process, the role of added ligands on the reaction kinetics was investigated by monitoring the reaction of **Co4(py-H)** and **$Mn^{III}(py)^+$** in the presence of added pyridine or benzoate (as ^{n}Bu$_4$NOBz). Additional pyridine had no discernible effect on k_{init} (Figure S145), indicating that pyridine ligand dissociation does not significantly influence the rate of metal-metal exchange. Additional benzoate inhibited the rate of metal-metal exchange, as indicated by the –1.0(3) order dependence of k_{init} on [^{n}Bu$_4$NOBz]$_0$; this inhibitory effect could result from binding of benzoate to **$Mn^{III}(py)^+$** to render it less reactive. Alternatively, benzoate might add to the cubane via coordination to a cobalt center, to form an anionic complex. While a solution of ^{n}Bu$_4$NOBz and **Co4** (1:1) remained unchanged after 16 h (by ^{1}H NMR spectroscopy), addition of ^{n}Bu$_4$NOBz (1 equiv) to a solution of **$Mn^{III}(py)^+$** in acetonitrile-d_3 immediately resulted in several new products, as indicated by broad resonances in the ^{1}H NMR spectrum. It is presumed that benzoate adds to **$Mn^{III}(py)^+$** to generate one or more less-reactive (likely less electrophilic) Mn complexes. The rate of metal-metal exchange was also examined in CH_2Cl_2, *ortho*-difluorobenzene, DMSO, 1,1,2,2-tetrachloroethane, and THF; however, no relationship between the solvent dielectric constant and k_{init} was discerned across this series.

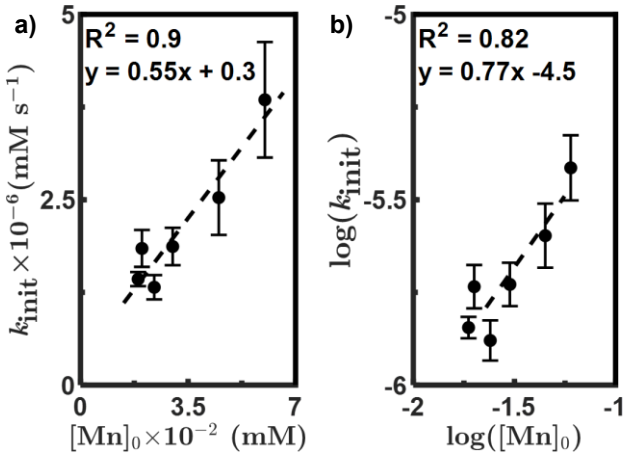


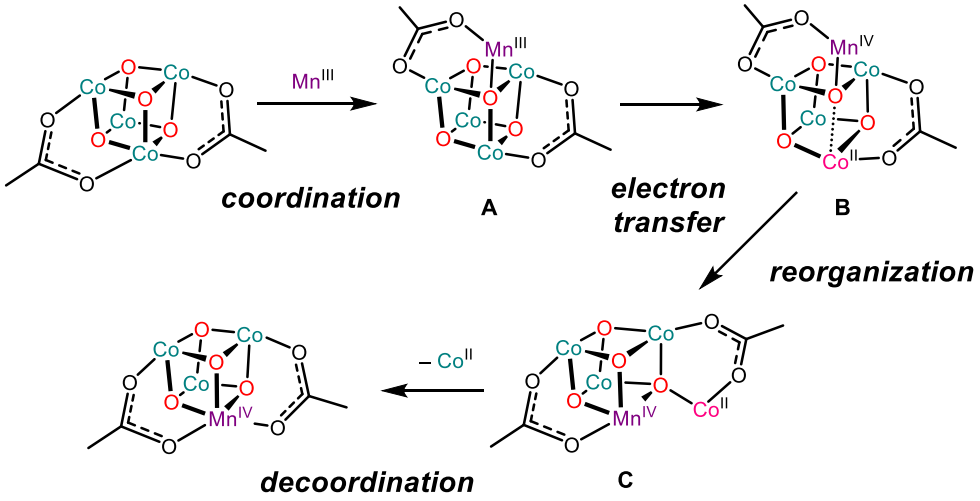
Figure 5. Linear Relationship between $[\mathbf{Mn^{III}(py)^{+}}]_0$ and the initial rate constant for metal-metal exchange between **Co₄(py-H)** and $Mn^{III}(py)^{+}$. (a) $[\mathbf{Mn^{III}(py)^{+}}]_0$ vs the rate of metal-metal exchange; k_{init} varies linearly with $[\mathbf{Mn^{III}(py)^{+}}]_0$. (b) Double logarithm plot of $[\mathbf{Mn^{III}(py)^{+}}]_0$ vs. k_{init} indicating a reaction order of 0.8(2) order in $[\mathbf{Mn^{III}(py)^{+}}]_0$.

The above results are consistent with the simplified mechanistic model for metal-metal exchange shown in Scheme . Initially, the $[Co_4O_4]$ cubane binds the incoming Mn center by donation from a μ_3-oxo ligand, which is likely assisted by an acetate migration (**A**). An inner-sphere electron transfer in this intermediate produces a Co^{II} center, which should significantly weaken the resulting μ_4-O–Co^{II} bond (**B**). Note that Co–O bond elongations occur upon binding a Lewis acid, even without a reduction process as observed in dicopper adduct **Cu₂Co₄** (*vide supra*), but Co–O bond elongations are expected to be more pronounced with a reduced Co^{II} center and the resulting population of Co–O antibonding orbitals. The more labile Co^{II} center should then readily participate in a reorganization that exchanges it for the Mn^{IV} ion that is more stable in the octahedral site of the cubane (**C**). Note that this rearrangement may occur without dissociation or change in the binding mode for the acetate ligands, to give a $MnCo_3$ oxo cubane core with a labile Co^{II} species in a "dangler" position, analogous to that of the previously isolated complex $MnCo_4(\mu_4\text{-}O)(\mu_3\text{-}O)_3(OAc)_6(NO_3)(py)_3$.[46] This labile Co^{II} ion is readily lost by ligand exchange reactions in the reaction mixture; however, this step may be relatively slow given isolation of the aforementioned nitrate analogue Evidence for an analogous dangler intermediate during metal-metal exchange comes from ^{1}H NMR monitoring of the formation of **MnCo₃** from the reaction of **Co₄** and $Mn(OAc)_2$, which reveals the build-up of an intermediate, proposed to be $MnCo_4(\mu_4\text{-}O)(\mu_3\text{-}O)_3(OAc)_7(t\text{-}Bupy)_3$, with resonances corresponding to the unique spectroscopic signature of those for $MnCo_4(\mu_4\text{-}O)(\mu_3\text{-}O)_3(OAc)_6(NO_3)(py)_3$ (Figure S98).

In general, the binding of a Lewis acidic metal center to a bridging oxo ligand is expected to raise the reduction potential of the cubane. As described above, this effect is observed in complex **Cu₂Co₄**, and is also observed for the protonated cobalt oxo cubane, which exhibits an irreversible reduction event at approximately –0.6 V vs. Fc/Fc^+ in MeCN.[67] It is noteworthy that Mn^{III} reduces Co^{II} in this scenario because Mn^{III} complexes such as $Mn(acac)_3$ ($Mn^{III/IV}$ $E_{1/2}$ in MeCN = 0.58 V vs. Fc/Fc^+), $\mathbf{Mn^{III}(\textit{t}\text{-}Bupy)^+}$, and basic manganese acetate $Mn_3(OAc)_6(H_2O)_3(\mu_3\text{-}O)$, are generally mild oxidants that would not be expected to reduce **Co₄** (E_{pc} in MeCN = ~–1.3 V vs. Fc/Fc^+) in an outer sphere manner.[68-70] This mismatch in redox potentials between Mn^{III} sources and Co_4O_4 cubanes supports the hypothesis that an outer-sphere electron transfer pathway for metal-metal exchange is unlikely. Thus, the structural data of **Cu₂Co₄** and electrochemical data of **Co₄**, **Cu₂Co₄**,

and **Mn^{III}(py)**, support the hypothesis that the reduction from Co^{III} to Co^{II} occurs in an intermediate pentametallic species such as **A**.

Scheme 3. Proposed Mechanism for M-M Exchange Between a [Co_4O_4] Cubane and Mn^{III}.



The reduction of a substitutionally inert, low spin, d^6 Co^{III} by a d^4 Mn^{III} ion is reminiscent of the classic studies on inner-sphere electron transfer between $Co^{III}Cl$ and a d^4 Cr^{II} ion, to give Co^{II} and $Cr^{III}Cl$.[71, 72] However, in the Co-Mn exchanges discussed here, ligand exchange is likely a consequence of the binding event (**A**) and the dynamic behavior of the acetate ligands, rather than electron transfer through an acetate bridge.[73] In this inner-sphere process, the bridging ligand critical to electron-transfer is probably the μ_4–oxo ligand.[74-76] Nonetheless, the carboxylate ligands are assumed to play an important, secondary role in influencing the electron-transfer driving force by modulating redox potentials, and by contributing to the rate of initial adduct formation.

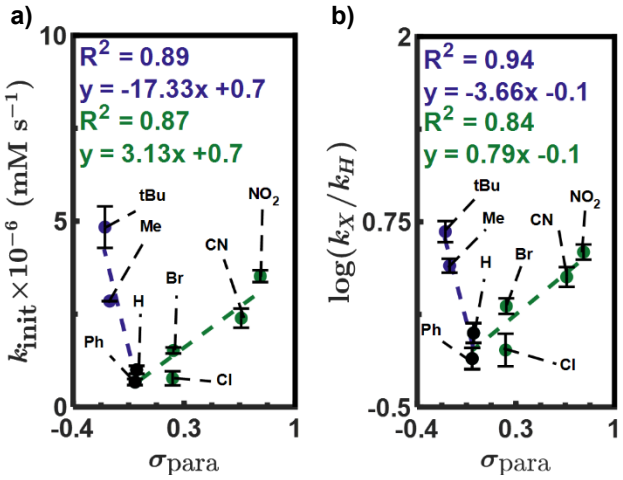


Figure 6. Influence of the *para*-benzoate ligand substituent of **Co_4(OBz-X)** on the initial rate constant for metal-metal exchange. (a) *para*-Hammett parameter vs. initial rate constant of metal-metal exchange for **Co_4(OBz -^{t}Bu**, **-Me**, **-Ph**, **-H**, **-Cl**, **-Br**, **-CN**, and **-NO_2**). Rates increase with both more donating (^{t}Bu, Me, H) and withdrawing (NO_2, CN, Cl, Br, H) substituents, with an inflection point at Co_4(OBz-H). (B) Hammett plot relating the *para*-benzoate substituent and $\log(k_X/k_H)$ with ρ values determined from the slope of the linear fits. The ρ value for electron donating substituents (–3.7(6)) compared to ρ for the electron withdrawing substituents (0.8(2)) indicates that benzoate plays a more substantial role in the electron donating regime than it does in the electron withdrawing regime.

To investigate these electronic effects on the reaction rates, Hammett plots were constructed with data from reactions of cubanes possessing substituted pyridine and benzoate ligands. Due to solubility constraints, the data were collected on reactions in CH_2Cl_2, with 10 equiv of **Mn^{III}(py)** or **Mn^{III}(*t*-Bupy)** to give pseudo first-order conditions. Interestingly, a plot of k_{init} vs. σ_{para} parameters shows that for benzoate ligands, the rate may be accelerated by both electron-donating and electron-withdrawing substituents (Figure 6), suggesting the operation of opposing electronic effects. More donating benzoate ligands (X = ^{t}Bu, Me) are expected to promote the basicity of the μ_3-oxo ligands, thereby favoring formation of adduct species **A**. On the other hand, electron-withdrawing substituents (X = NO_2, CN, Br, Cl) decrease the basicity of the oxo ligands, but increase the reduction potential of the cubane, rendering Co^{III} more susceptible to the reduction step to produce **C**. An inflection point associated with the balance between these two effects corresponds to X = H/Ph. The influence of the more basic benzoate ligands, determined by the ratio of the rate constants k_X/k_H (ρ = –3.7(6)), is greater than that of the more acidic benzoate ligands (ρ = 0.8(2)), which indicates that the ability of the cubane to coordinate Mn^{III} is critical to metal-metal exchange reactivity. This would suggest that for the Co_4O_4 cubane system, the Lewis acidity of the incoming metal ion is more important than its reducing potential in influencing the rate of metal-metal exchange. Interestingly, the most electron-rich oxo cubane in this series, **$Co_4(O_2CC_6H_4$-OMe)**, reacts with **Mn^{III}(*t*-Bupy)$^+$** but does not undergo metal-metal exchange (by ^{1}H NMR spectroscopy). This is perhaps due to stabilization of the oxidized cubane, **$Co_4(O_2CC_6H_4$-OMe)$^+$** in this case.

In the case of the substituted pyridine ligands, stronger donors result in faster metal-metal exchange, and the small, negative slope (ρ = –0.4(1) from the Hammett plot indicates that pyridine substituents are less effective than benzoates in modulating k_{init}. This is consistent with previous observations that the pyridine ligands impact the redox properties less than the chelating, anionic ligands (Figure 7).[65]

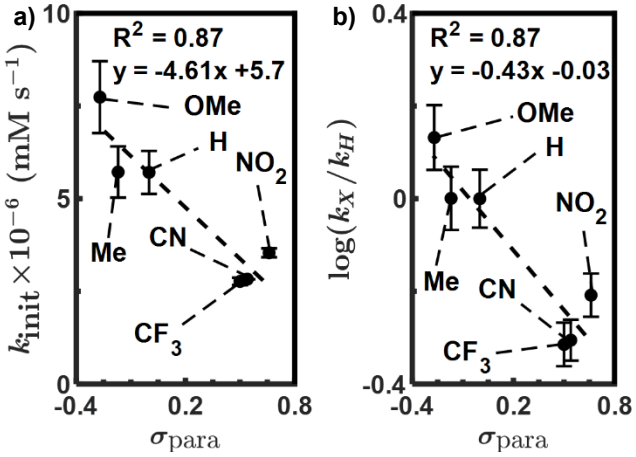


Figure 7. The influence of the *para*-pyridyl substituents of **Co_4(py-X)** on the rate constant for metal-metal exchange. (a) *para*-Hammett parameter vs. initial rate of metal-metal exchange for **Co_4(py -OMe**, **-Me**, **-H**, **-CF_3**, **-CN**, **-NO_2**) The rate inversely correlates with the Hammett parameter (σ_{para}) of the substituent, with stronger donors leading to more rapid exchange. (b) Hammett plot relating the *para*-pyridyl substituent and log(k_X/k_H) with ρ determined from the slope of the linear fit. The low ρ value (–0.4(1)) determined from the Hammett plot is consistent with prior observations that the pyridine ligands influence the cubane redox potentials less than the chelating ligands (S140), and with the pyridine ligands mostly tuning the basicity of the oxo ligands.

Role of Acetate and Pyridine Ligand Transfers in Co-Mn Exchange. To further investigate the role of ligand transfer during metal-metal exchange, deuterium-labeling studies were conducted

on acetate complexes. When an MeCN solution of **Co4** was treated with the Mn^{II} reagent Mn(OAc-d_3)$_2$ (corresponding to a 4-fold excess of OAc-d_3) for 48 h at only 23 °C, HR-ESI-MS analysis did not detect **MnCo3**$^+$ as a product, while complete scrambling of the OAc-d_3 label into **Co4** gave a binomial distribution of isotopologues (Figure S197). This indicates that the initial adduct formation step in the metal-metal exchange process to give **A** may be reversible. Heating an identical reaction mixture at 70 °C for 2 h, and analysis by HR-ESI-MS, revealed that acetate ligand scrambling was incomplete as judged by the degree of OAc-d_3 incorporation into **Co4** (33%) and **MnCo3**$^+$ (51%). Thus, acetate ligand exchange appears to be somewhat faster than metal-metal exchange such that the latter is accompanied by some degree of acetate ligand transfer. In another set of experiments, an acetonitrile solution of oxidized cubane **Co4**$^+$[PF_6] was treated with 2 equiv of Mn(OAc-d_3)$_2$ at 40 °C for 2 h. In this case, HR-ESI-MS analysis revealed 39% incorporation of the acetate label compared to 30% incorporation of the label in "unreacted" **Co4**$^+$. These experiments indicate that the cubane acetate ligands can exchange with the Mn acetate ligands before and during the metal-metal exchange reaction and suggests that a pentametallic complex may form during the metal-metal exchange process. In both cases, a binomial distribution of labeled acetates was also observed for the Co(OAc)$_n$(OAc-d_3)$_{2-n}$ (n = 0-2) and [Co$_2$(μ_2-OH)$_2$(OAc)$_n$(OAc-d_3)$_{3-n}$(^{t}Bupy)$_4$]$^+$ (n = 0-3) byproducts.

For comparison, acetate ligand incorporation into cubane **Co4** from acetic acid and acetate was examined. A MeCN solution of **Co4** was stirred with four equiv of acetic acid-d_4, or triethylammonium acetate-d_4 (generated in situ by treatment of triethylamine with acetic acid-d_4) at 23 °C, and the reaction mixtures were subjected to HR-ESI-MS analysis. In both experiments, the deuterium label was incorporated rapidly (ca. 10 min), resulting in a binomial distribution of all five possible cubane isotopologues Co$_4$(μ_3-O)$_4$(OAc)$_n$(OAc-d_3)$_{4-n}$ (n = 0-4). In a control experiment, equimolar MeCN solutions of Co$_4$(μ_3-O)$_4$(OAc)$_4$(py)$_4$ and Co$_4$(μ_3-O)$_4$(OAc-d_3)$_4$(py-d_5)$_4$ (the fully deuterated isotopologue) were combined and after 24 h at 40 °C, no acetate or pyridine isotope crossover was observed by HR-ESI-MS, which is consistent with slow ligand dissociation from a low spin Co^{III} center (Figure S192). In the presence of 2 equivs of Mn(OAc)$_2$, and heating at 70 °C for 0.5 h, these isotopologues undergo exchange of pyridine ligands. Analysis by HR-ESI-MS revealed a binomial distribution of all possible product isotopologues of the starting cubane Co$_4$(μ_3-O)$_4$(OAc)$_4$(py)$_n$(py-d_5)$_{4-n}$ (n = 1-4) before any of the corresponding Mn cubane was detected. This experiment indicates that the pyridine ligands redistribute before the metal-metal exchange reaction. It should be noted that a redistribution of pyridine ligands was also observed when HOAc was added in place of Mn(OAc)$_2$ under otherwise identical conditions. A pyridine-exchange process involving related dinuclear cobalt species has been reported.[56]

In summary, the acetate ligands of a [Co$_4$O$_4$] cubane exchange with the acetate ligands of Mn(OAc-d_3)$_2$, and this process is competitive with metal-metal exchange. The [Co$_4$O$_4$] cubane pyridine ligands exchange under the experimental conditions at a rate significantly faster than metal-metal exchange, which indicates a pyridine-dissociative mechanism, but the measured order in pyridine indicates that this does not influence the metal-metal exchange reactivity. The observed isotopologues of **MnCo3**$^+$ produced in these labeling experiments suggest the formation of an intermediate pendent metal complex in which ligand exchange is facile.

CONCLUDING REMARKS

The study described here significantly enhances the small but growing knowledge base associated with the synthesis and properties of transition metal oxo cubanes that possess an associated

"dangler" metal ion. Such clusters may serve as models for the Mn[$CaMn_3O_4$] oxygen evolving complex, especially if the dangler ion is redox active and bound to the cubane through carboxylate bridges. The very few known structures of this type include the Co[$MnCo_3O_4$] complex in Scheme 1c, L$CaMn_3O_4$Ag, L'$CaMn_4O_4$ (L,L' are 1,3,5-triarylbenzene-substituted ligand scaffolds) and [$Mn_4CaO_4(Bu^tCO_2)_8(Bu^tCO_2H)_2$(py)] (and related lanthanide derivatives).[19,20,45] Formation of the dicopper dangler **Cu_2Co_4** from well-defined precursors, by use of additional acetate ligands to tether the copper ions to the cubane, provides a unique example whereby dangler ions are bound to a [Co_4O_4] cubane. Notably, the acetate ligands in this complex, like the carboxylate groups of the OEC, support a dangler ion-μ_4-oxo interaction that may play an important role in chemical transformations of the assembly. In the OEC, the comparable dangler interaction is thought to enable the structural changes required for water activation.[37] Indeed, attempts to extend the synthesis of **Cu_2Co_4** to manganese provides evidence for formation of a carboxylate-supported Mn[Co_4O_4] intermediate complex possessing a Mn(μ_4-O)Co_3 arrangement. The latter transitory structure appears to be key to electron-transfer processes that ultimately lead to a redox-driven exchange of metals that introduces manganese via a structural rearrangement of the oxo cubane core.

These studies on the chemical behavior of metal clusters in solution provide design principles for the development of new metal-metal exchange reactions.[25] The observed exchange reaction is a rare example of a well-defined metal-metal redox exchange reaction for a tetrametallic cubane cluster. Importantly, the efficiency of this process suggests its broader utility for the controlled synthesis of predetermined oxo metal clusters with intricate structures.[77] Furthermore, the conveyance of a manganese ion to a cubane cluster is perhaps relevant to the biochemical mechanism for assembly of the OEC, which is believed to occur by photochemically driven redox processes whereby Mn^{II} is incorporated by a stepwise process into the cluster.[31,78] Additionally, the details of metal additions and exchanges of this sort may help in the development of synthetic schemes for assembly of mixed-metal nanoclusters and bulk materials. Indeed, related galvanic exchange reactions have been employed to modify an oxide or sulfide structure to incorporate a heterometal.[51-53,77,79]

Further investigations into the role of redox active dangler ions should help shed light on the possible role of these species in controlling chemical transformations of the oxo cluster core. The concepts developed in this study will be used in syntheses of new heterometallic oxo cubanes.

ACKNOWLEDGMENT

This work was funded by the U.S. Department of Energy, Office of Science, Office of Basic Energy Sciences, Chemical Sciences, Geosciences, and Biosciences Division, under Contract DE-AC02-05CH11231. The LBNL Catalysis Laboratory provided HR-ESI-MS, FTIR, and UV-vis instrumentation. This research used the resources of the Advanced Light Sources, which is a DOE Office of Sciences User Facility under contract no. DE-AC02-05CH11231. NMR spectra were collected at the College of Chemistry NMR facility, at the University of California, Berkeley, which is supported in part by the National Institutes of Health under grant no. S10Od024998. The authors thank Dr. Hasan Celik for assistance with NMR spectroscopy, Dr. Simon Teat for assistance with crystallography, and Dr. Cooper Citek, Dr. Chithra Asokan, and Dr. Miao Zhang for assistance with LBNL Catalysis Laboratory instrumentation. Dr. Rex Handford, Dr. Benjamin Suslick, Dr Jaruwan Amtawong, Dr. Stefan Künzi, and Matt See are thanked for their thoughtful discussion.

REFERENCES

(1) Huang, H. L.; Brudvig, G. W. Oxygen Evolution of Photosystem II. In *Comprehensive Coordination Chemistry III*; Elsevier, 2021; Chapter 22, pp 569-588.

(2) Yano, J.; Yachandra, V., Mn_4Ca Cluster in Photosynthesis: Where and How Water is Oxidized to Dioxygen. *Chem. Rev.* **2014,** *114*, 4175-4205.

(3) Beinert, H., Iron-Sulfur Proteins: Ancient Structures, Still Full of Surprises. *JBIC Journal of Biological Inorganic Chemistry* **2000,** *5*, 2-15.

(4) Bigness, A.; Vaddypally, S.; Zdilla, M. J.; Mendoza-Cortes, J. L., Ubiquity of Cubanes in Bioinorganic Relevant Compounds. *Coord. Chem. Rev.* **2022,** *450*.

(5) Brown, A. C.; Suess, D. L. M. Synthetic Iron-Sulfur Clusters. In *Comprehensive Coordination Chemistry III*, Elsevier, 2021; Chapter 8 pp 134-156.

(6) Johnson, D. C.; Dean, D. R.; Smith, A. D.; Johnson, M. K., Structure, Function, and Formation of Biological Iron-Sulfur Clusters. *Annu. Rev. Biochem* **2005,** *74*, 247-81.

(7) Liu, J.; Chakraborty, S.; Hosseinzadeh, P.; Yu, Y.; Tian, S.; Petrik, I.; Bhagi, A.; Lu, Y., Metalloproteins Containing Cytochrome, Iron–Sulfur, or Copper Redox Centers. *Chem. Rev.* **2014,** *114*, 4366-4469.

(8) Barber, J., A Mechanism for Water plitting and Oxygen Production in Photosynthesis. *Nature Plants* **2017,** *3*, 17041.

(9) Lee, S. C.; Lo, W.; Holm, R. H., Developments in the Biomimetic Chemistry of Cubane-Type and Higher Nuclearity Iron–Sulfur Clusters. *Chem. Rev.* **2014,** *114*, 3579-3600.

(10) Paul, S.; Neese, F.; Pantazis, D. A., Structural Models of the Biological Oxygen-Evolving Complex: Achievements, Insights, and Challenges for Biomimicry. *Green Chemistry* **2017,** *19*, 2309-2325.

(11) Wieghardt, K., The Active Sites in Manganese-Containing Metalloproteins and Inorganic Model Complexes. *Angewandte Chemie International Edition in English* **1989,** *28*, 1153-1172.

(12) Dismukes, G. C.; Brimblecombe, R.; Felton, G. A. N.; Pryadun, R. S.; Sheats, J. E.; Spiccia, L.; Swiegers, G. F., Development of Bioinspired Mn_4O_4−Cubane Water Oxidation Catalysts: Lessons from Photosynthesis. *Acc. Chem. Res.* **2009,** *42*, 1935-1943.

(13) Brudvig, G. W.; Thorp, H. H.; Crabtree, R. H., Probing the Mechanism of Water Oxidation in Photosystem II. *Acc. Chem. Res.* **1991,** *24*, 311-316.

(14) Christou, G., Manganese Carboxylate Chemistry and Its Biological Relevance. *Acc. Chem. Res.* **1989,** *22*, 328-335.

(15) Lee, H. B.; Tsui, E. Y.; Agapie, T., A $CaMn_4O_2$ Model of the Biological Oxygen Evolving Complex: Synthesis via Cluster Expansion on a Low Symmetry Ligand. *Chem. Commun.* **2017,** *53*, 6832-6835.

(16) Lee, H. B.; Marchiori, D. A.; Chatterjee, R.; Oyala, P. H.; Yano, J.; Britt, R. D.; Agapie, T., *S* = 3 Ground State for a Tetranuclear $Mn^{IV}_4O_4$ Complex Mimicking the S_3 State of the Oxygen-Evolving Complex. *J. Am. Chem. Soc.* **2020,** *142*, 3753-3761.

(17) Yachandra, V. K.; Sauer, K.; Klein, M. P., Manganese Cluster in Photosynthesis: Where Plants Oxidize Water to Dioxygen. *Chem. Rev.* **1996,** *96*, 2927-2950.

(18) Lee, H. B.; Shiau, A. A.; Marchiori, D. A.; Oyala, P. H.; Yoo, B.-K.; Kaiser, J. T.; Rees, D. C.; Britt, R. D.; Agapie, T., $CaMn_3^{IV}O_4$ Cubane Models of the Oxygen-Evolving Complex: Spin Ground States $S<9/2$ and the Effect of Oxo Protonation. *Angew. Chem. Int. Ed.* **2021,** *60*, 17671-17679.

(19) Kanady, J. S.; Lin, P.-H.; Carsch, K. M.; Nielsen, R. J.; Takase, M. K.; Goddard, W. A.; Agapie, T., Toward Models for the Full Oxygen-Evolving Complex of Photosystem II by Ligand Coordination To Lower the Symmetry of the Mn_3CaO_4 Cubane: Demonstration That Electronic Effects Facilitate Binding of a Fifth Metal. *J. Am. Chem. Soc.* **2014,** *136*, 14373-14376.

(20) Zhang, C.; Chen, C.; Dong, H.; Shen, J.-R.; Dau, H.; Zhao, J., A Synthetic Mn_4Ca-Cluster Mimicking the Oxygen-Evolving Center of Photosynthesis. *Science* **2015,** *348*, 690-693.

(21) Lee, H. B.; Oyala, P. H.; Agapie, T., Synthesis, Electronic Structure, and Spectroscopy of Multinuclear Mn Complexes Relevant to the Oxygen Evolving Complex of Photosystem II. In *Oxygen Production and Reduction in Artificial and Natural Systems*, Wolrd Scientific: 2018; pp 259-283.

(22) Shiau, A. A.; Lee, H. B.; Oyala, P. H.; Agapie, T., Coordination Number in High-Spin–Low-Spin Equilibrium in Cluster Models of the S_2 State of the Oxygen Evolving Complex. *J. Am. Chem. Soc.* **2023,** *145*, 14592-14598.

(23) Chen, C.; Chen, Y.; Yao, R.; Li, Y.; Zhang, C., Artificial Mn_4Ca Clusters with Exchangeable Solvent Molecules Mimicking the Oxygen-Evolving Center in Photosynthesis. *Angew. Chem. Int. Ed.* **2019,** *58*, 3939-3942.

(24) Chen, Q.-F.; Guo, Y.-H.; Yu, Y.-H.; Zhang, M.-T., Bioinspired Molecular Clusters for Water Oxidation. *Coord. Chem. Rev.* **2021,** *448*, 214164.

(25) Thompson, N. B.; Namkoong, G.; Skeel, B. A.; Suess, D. L. M., Facile and Dynamic Cleavage of Every Iron–Sulfide Bond in Cuboidal Iron–Sulfur Clusters. *Proc. Natl. Acad. Sci. U. S. A.* **2023,** *120*, e2210528120.

(26) Hong, J. S.; Rabinowitz, J. C., Base-catalyzed Exchange of the Iron and Sulfide of Clostridial Ferredoxin. *J. Biol. Chem.* **1970,** *245*, 6582-6587.

(27) Britt, R. D.; Rao, G.; Tao, L., Bioassembly of Complex Iron–Sulfur Enzymes: Hydrogenases and Nitrogenases. *Nat. Rev. Chem.* **2020,** *4*, 542-549.

(28) Badding, E. D.; Srisantitham, S.; Lukoyanov, D. A.; Hoffman, B. M.; Suess, D. L. M., Connecting the Geometric and Electronic Structures of The Nitrogenase Iron–Molybdenum Cofactor through Site-Selective ^{57}Fe Labelling. *Nat. Chem.* **2023,** *15*, 658-665.

(29) Namkoong, G.; Suess, D. L. M., Cluster-selective 57Fe Labeling of a Twitch-Domain-Containing Radical SAM Enzyme. *Chem. Sci.* **2023,** *14*, 7492-7499.

(30) Zabret, J.; Bohn, S.; Schuller, S. K.; Arnolds, O.; Möller, M.; Meier-Credo, J.; Liauw, P.; Chan, A.; Tajkhorshid, E.; Langer, J. D.; Stoll, R.; Krieger-Liszkay, A.; Engel, B. D.; Rudack, T.; Schuller, J. M.; Nowaczyk, M. M., Structural Insights into Photosystem II Assembly. *Nat. Plants.* **2021,** *7*, 524-538.

(31) Sato, A.; Nakano, Y.; Nakamura, S.; Noguchi, T., Rapid-Scan Time-Resolved ATR-FTIR Study on the Photoassembly of the Water-Oxidizing Mn_4CaO_5 Cluster in Photosystem II. *J. Phys. Chem. B* **2021,** *125*, 4031-4045.

(32) Bao, H.; Burnap, R. L., Photoactivation: The Light-Driven Assembly of the Water Oxidation Complex of Photosystem II. *Front. Plant Sci.* **2016,** *7*, 578.

(33) Gulam Rabbani, S. M.; Miró, P., Computational Insights into Iron Heterometal Installation in Polyoxovanadate–Alkoxide Clusters. *Inorg. Chem.* **2023,** *62*, 1797-1803.

(34) Lee, S. C.; Holm, R. H., The Clusters of Nitrogenase: Synthetic Methodology in the Construction of Weak-Field Clusters. *Chem. Rev.* **2004,** *104*, 1135-1158.

(35) Dobbek, H.; Svetlitchnyi, V.; Gremer, L.; Huber, R.; Meyer, O., Crystal Structure of a Carbon Monoxide Dehydrogenase Reveals a [Ni-4Fe-5S] Cluster. *Science* **2001,** *293*, 1281-1285.

(36) Suga, M.; Akita, F.; Hirata, K.; Ueno, G.; Murakami, H.; Nakajima, Y.; Shimizu, T.; Yamashita, K.; Yamamoto, M.; Ago, H.; Shen, J.-R., Native Structure of Photosystem II at 1.95 Å Resolution Viewed by Femtosecond X-ray Pulses. *Nature* **2015,** *517*, 99-103.

(37) Cox, N.; Pantazis, D. A.; Lubitz, W., Current Understanding of the Mechanism of Water Oxidation in Photosystem II and Its Relation to XFEL Data. *Annu. Rev. Biochem* **2020**.

(38) Suga, M.; Akita, F.; Yamashita, K.; Nakajima, Y.; Ueno, G.; Li, H.; Yamane, T.; Hirata, K.; Umena, Y.; Yonekura, S.; Yu, L.-J.; Murakami, H.; Nomura, T.; Kimura, T.; Kubo, M.; Baba, S.; Kumasaka, T.; Tono, K.; Yabashi, M.; Isobe, H.; Yamaguchi, K.; Yamamoto, M.; Ago, H.; Shen, J.-R., An Oxyl/Oxo Mechanism for Oxygen-Oxygen Coupling in PSII Revealed by an X-ray Free-Electron Laser. *Science* **2019,** *366*, 334.

(39) Siegbahn, P. E. M., Structures and Energetics for O_2 Formation in Photosystem II. *Acc. Chem. Res.* **2009,** *42*, 1871-1880.

(40) Ruickoldt, J.; Basak, Y.; Domnik, L.; Jeoung, J.-H.; Dobbek, H., On the Kinetics of CO2 Reduction by Ni, Fe-CO Dehydrogenases. *ACS Catalysis* **2022,** *12*, 13131-13142.

(41) Fesseler, J.; Jeoung, J.-H.; Dobbek, H., How the $[NiFe_4S_4]$ Cluster of CO Dehydrogenase Activates CO_2 and NCO^-. *Angew. Chem. Int. Ed.* **2015,** *54*, 8560-8564.

(42) Bhowmick, A.; Hussein, R.; Bogacz, I.; Simon, P. S.; Ibrahim, M.; Chatterjee, R.; Doyle, M. D.; Cheah, M. H.; Fransson, T.; Chernev, P.; Kim, I.-S.; Makita, H.; Dasgupta, M.; Kaminsky, C. J.; Zhang, M.; Gätcke, J.; Haupt, S.; Nangca, I. I.; Keable, S. M.; Aydin, A. O.; Tono, K.; Owada, S.; Gee, L. B.; Fuller, F. D.; Batyuk, A.; Alonso-Mori, R.; Holton, J. M.; Paley, D. W.; Moriarty, N. W.; Mamedov, F.; Adams, P. D.; Brewster, A. S.; Dobbek, H.; Sauter, N. K.; Bergmann, U.; Zouni, A.; Messinger, J.; Kern, J.; Yano, J.; Yachandra, V. K., Structural Evidence for Intermediates during O_2 Formation in Photosystem II. *Nature* **2023,** *617*, 629-636.

(43) Kern, J.; Chatterjee, R.; Young, I. D.; Fuller, F. D.; Lassalle, L.; Ibrahim, M.; Gul, S.; Fransson, T.; Brewster, A. S.; Alonso-Mori, R.; Hussein, R.; Zhang, M.; Douthit, L.; de Lichtenberg, C.; Cheah, M. H.; Shevela, D.; Wersig, J.; Seuffert, I.; Sokaras, D.; Pastor, E.; Weninger, C.; Kroll, T.; Sierra, R. G.; Aller, P.; Butryn, A.; Orville, A. M.; Liang, M.; Batyuk, A.; Koglin, J. E.; Carbajo, S.; Boutet, S.; Moriarty, N. W.; Holton, J. M.; Dobbek, H.; Adams, P. D.; Bergmann, U.; Sauter, N. K.; Zouni, A.; Messinger, J.; Yano, J.; Yachandra, V. K., Structures of the iIntermediates of Kok's Photosynthetic Water Oxidation Clock. *Nature* **2018,** *563*, 421-425.

(44) Nguyen, A. I.; Suess, D. L. M.; Darago, L. E.; Oyala, P. H.; Levine, D. S.; Ziegler, M. S.; Britt, R. D.; Tilley, T. D., Manganese–Cobalt Oxido Cubanes Relevant to Manganese-Doped Water Oxidation Catalysts. *J. Am. Chem. Soc.* **2017,** *139*, 5579-5587.

(45) Yao, R.; Li, Y.; Chen, Y.; Xu, B.; Chen, C.; Zhang, C., Rare-Earth Elements Can Structurally and Energetically Replace the Calcium in a Synthetic Mn_4CaO_4-Cluster Mimicking the Oxygen-Evolving Center in Photosynthesis. *J. Am. Chem. Soc.* **2021,** *143*, 17360-17365.

(46) Nguyen, A. I.; Darago, L. E.; Balcells, D.; Tilley, T. D., Influence of a "Dangling" Co(II) Ion Bound to a [$MnCo_3O_4$] Oxo Cubane. *J. Am. Chem. Soc.* **2018,** *140*, 9030-9033.

(47) Amtawong, J.; Nguyen, A. I.; Tilley, T. D., Mechanistic Aspects of Cobalt–Oxo Cubane Clusters in Oxidation Chemistry. *J. Am. Chem. Soc.* **2022**.

(48) Dasgupta, J.; Ananyev, G. M.; Dismukes, G. C., Photoassembly of the Water-Oxidizing Complex in Photosystem II. *Coord. Chem. Rev.* **2008,** *252*, 347-360.

(49) Vinyard, D. J.; Badshah, S. L.; Riggio, M. R.; Kaur, D.; Fanguy, A. R.; Gunner, M. R., Photosystem II Oxygen-Evolving Complex Photoassembly Displays an Inverse H/D solvent Isotope Effect under Chloride-Limiting Conditions. *Proceedings of the National Academy of Sciences* **2019,** *116*, 18917.

(50) Xia, X.; Wang, Y.; Ruditskiy, A.; Xia, Y., 25th Anniversary Article: Galvanic Replacement: A Simple and Versatile Route to Hollow Nanostructures with Tunable and Well-Controlled Properties. *Adv. Mater.* **2013,** *25*, 6313-6333.

(51) Oh, M. H.; Yu, T.; Yu, S.-H.; Lim, B.; Ko, K.-T.; Willinger, M.-G.; Seo, D.-H.; Kim, B. H.; Cho, M. G.; Park, J.-H.; Kang, K.; Sung, Y.-E.; Pinna, N.; Hyeon, T., Galvanic Replacement Reactions in Metal Oxide Nanocrystals. *Science* **2013,** *340*, 964-968.

(52) Beberwyck, B. J.; Surendranath, Y.; Alivisatos, A. P., Cation Exchange: A Versatile Tool for Nanomaterials Synthesis. *The Journal of Physical Chemistry C* **2013,** *117*, 19759-19770.

(53) Zhang, D.; Wong, A. B.; Yu, Y.; Brittman, S.; Sun, J.; Fu, A.; Beberwyck, B.; Alivisatos, A. P.; Yang, P., Phase-Selective Cation-Exchange Chemistry in Sulfide Nanowire Systems. *J. Am. Chem. Soc.* **2014,** *136*, 17430-17433.

(54) Zhang, J.; Wu, Z.; Polo-Garzon, F., Recent Developments in Revealing the Impact of Complex Metal Oxide Reconstruction on Catalysis. *ACS Catalysis* **2023**, 15393-15403.

(55) Evans, D. F., 400. The Determination of the Paramagnetic Susceptibility of Substances in Solution by Nuclear Magnetic Resonance. *Journal of the Chemical Society (Resumed)* **1959**, 2003-2005.

(56) DeLucia, A. A.; Kelly, K. A.; Herrera, K. A.; Gray, D. L.; Olshansky, L., Intramolecular Hydrogen-Bond Interactions Tune Reactivity in Biomimetic Bis(μ-hydroxo)dicobalt Complexes. *Inorg. Chem.* **2021,** *60*, 15599-15609.

(57) DeLucia, A. A.; Olshansky, L., Carboxylate Shift Dynamics in Biomimetic $Co_2(\mu–OH)_2$ Complexes. *Inorg. Chem.* **2024,** *63*, 1109-1118.

(58) Beattie, J. K.; Hambley, T. W.; Klepetko, J. A.; Masters, A. F.; Turner, P., The Chemistry of Cobalt Acetate—IV. The Isolation and Crystal Structure of the Symmetric Cubane, Tetrakis[(μ-acetato)(μ_3-oxo) (pyridine)cobalt(III)] · Chloroform Solvate, $[Co_4(\mu_3\text{-}O)_4(\mu\text{-}CH_3CO_2)_4(C_5H_5N)_4]$ · 5CHCl and of the Dicationic Partial Cubane, Trimeric, [(μ-acetato)(acetato)tris(μ-hydroxy(μ3-oxo)hexakispyridinetricobalt(III)]hexafluorophosphate · Water Solvate, $[Co_3(\mu_3\text{-}O)(\mu\text{-}OH)_3(\mu\text{-}CH_3CO_2(CH_3CO_2(C_5H_5N)_6[PF_6]_2 \cdot 2H_2O$. *Polyhedron* **1998,** *17*, 1343-1354.

(59) Beattie, J. K.; Klepetko, J. A.; Masters, A. F.; Turner, P., The Chemistry of Cobalt Acetate. VIII. New Members of the Family of Oxo-Centred Trimers, $[Co_3(\mu_3\text{-}O)(\mu\text{-}O_2CCH_3)_{5-p}(\mu\text{-}OR)_pL_5]^{2+}$ (R=H, alkyl, L=ligand, p=0–4). The Preparation and Characterisation of the Trimeric tetrakis(μ-acetato)-(μ-hydroxo)-μ_3-oxo-pentakis(pyridine)-tri-cobalt(III) hexafluorophosphate, $[Co_3(\mu_3\text{-}O)(\mu\text{-}O_2CCH_3)_4(\mu\text{-}OH)(C_5H_5N)_5][PF_6]_2$, and the Preparation and Crystal Structure of the Trimeric tris(μ-acetato)-(μ-hydroxo)-(μ-methoxo)-μ_3-oxo-pentakis(pyridine)-tri-cobalt(III) Hexafluorophosphate·Methanol·Water Solvate $[Co_3(\mu_3\text{-}O)(\mu\text{-}O_2CCH_3)_3(\mu\text{-}OH)(\mu\text{-}OCH_3)(C_5H_5N)_5][PF_6]_2 \cdot CH_3O_H \cdot 0.25H_2O$. *Polyhedron* **2003,** *22*, 947-965.

(60) Snider, B. B.; Patricia, J. J.; Kates, S. A., Mechanism of Manganese(III)-Based Oxidation of *β*-Keto Esters. *The Journal of Organic Chemistry* **1988,** *53*, 2137-2143.

(61) Tategami, S.-i.; Yamada, T.; Nishino, H.; Korp, J. D.; Kurosawa, K., Formation of 1,2-Dioxacyclohexanes by the Reaction of Alkenes with Tris(2,4-pentanedionato)manganese(III) or with β-Ketocarbonyl Compounds in the Presence of Manganese(III) Acetate. *Tetrahedron Lett.* **1990,** *31*, 6371-6374.

(62) Melikyan, G. G., Carbon–Carbon Bond-Forming Reactions Promoted by Trivalent Manganese. In *Organic Reactions*, 2004; pp 427-675.

(63) Nishino, H., Direct Diacetylmethylation of Aromatic Compounds with Tris(2,4-pentanedionato)manganese(III). *Bull. Chem. Soc. Jpn.* **1986,** *59*, 1733-1739.

(64) Goff, H. M.; Hines, J.; Griesel, J.; Mossman, C., Synthesis, Characterization, and use of a Cobalt(II) Complex as an NMR shift Reagent: An Integrated Laboratory Experiment. *J. Chem. Educ.* **1982,** *59*, 422.

(65) Chakrabarty, R.; Bora, S. J.; Das, B. K., Synthesis, Structure, Spectral and Electrochemical Properties, and Catalytic Use of Cobalt(III)−Oxo Cubane Clusters. *Inorg. Chem.* **2007,** *46*, 9450-9462.

(66) Nguyen, A. I.; Wang, J.; Levine, D. S.; Ziegler, M. S.; Tilley, T. D., Synthetic Control and Empirical Prediction of Redox Potentials for Co_4O_4 Cubanes over a 1.4 V Range: Implications for Catalyst Design and Evaluation of High-valent Intermediates in Water Oxidation. *Chem. Sci.* **2017,** *8*, 4274-4284.

(67) Amtawong, J.; Skjelstad, B. B.; Balcells, D.; Tilley, T. D., Concerted Proton–Electron Transfer Reactivity at a Multimetallic Co_4O_4 Cubane Cluster. *Inorg. Chem.* **2020,** *59*, 15553-15560.

(68) Gritzner, G.; Murauer, H.; Gutmann, V., The Polarographic and Voltammetric Behaviour of Acetylacetonato and Hexafluoroacetylacetonato Complexes in Acetonitrile. *Journal of Electroanalytical Chemistry and Interfacial Electrochemistry* **1979,** *101*, 177-183.

(69) Gritzner, G.; Murauer, H.; Gutmann, V., Solvent and Salt Effects on the Redox Behaviour of Trisacetylacetonato manganese(III). *Journal of Electroanalytical Chemistry and Interfacial Electrochemistry* **1979,** *101*, 185-200.

(70) Carli, S.; Benazzi, E.; Casarin, L.; Bernardi, T.; Bertolasi, V.; Argazzi, R.; Caramori, S.; Bignozzi, C. A., On the stability of manganese tris(β-diketonate) complexes as redox mediators in DSSCs. *PCCP* **2016,** *18*, 5949-5956.

(71) Taube, H.; Myers, H.; Rich, R. L., Observations on the Mechanism of Electron Transfer in Solution. *J. Am. Chem. Soc.* **1953,** *75*, 4118-4119.

(72) Taube, H., Electron Transfer Between Metal Complexes: Retrospective. *Science* **1984,** *226*, 1028-1036.

(73) Burdett, J. K., A Molecular Orbital Approach to Electron-Transfer Reactions between Transition-Metal Ions in Solution. *Inorg. Chem.* **1978,** *17*, 2537-2552.

(74) Haim, A., Role of the Bridging Ligand in Inner-Sphere Electron-Transfer Reactions. *Acc. Chem. Res.* **1975,** *8*, 264-272.

(75) Thompson, G. A. K.; Sykes, A. G., Assignment of Mechanism to Titanium(III) Reductions of Cobalt(III) complexes. Hard and Soft Theory as a Means of Assessing Bridging Ligands for Inner-Sphere Electron Transfer. *Inorg. Chem.* **1976,** *15*, 638-642.

(76) Taube, H.; Gould, E. S., Organic Molecules as Bridging Groups in Electron-Transfer Reactions. *Acc. Chem. Res.* **1969,** *2*, 321-329.

(77) Zhang, D.; Yang, Y.; Bekenstein, Y.; Yu, Y.; Gibson, N. A.; Wong, A. B.; Eaton, S. W.; Kornienko, N.; Kong, Q.; Lai, M.; Alivisatos, A. P.; Leone, S. R.; Yang, P., Synthesis of Composition Tunable and Highly Luminescent Cesium Lead Halide Nanowires through Anion-Exchange Reactions. *J. Am. Chem. Soc.* **2016,** *138*, 7236-7239.

(78) Murray, J. W.; Rutherford, A. W.; Nixon, P. J., Photosystem II in a State of Disassembly. *Joule* **2020,** *4*, 2082-2084.

(79) da Silva, A. G. M.; Rodrigues, T. S.; Haigh, S. J.; Camargo, P. H. C., Galvanic replacement reaction: recent developments for engineering metal nanostructures towards catalytic applications. *Chem. Commun.* **2017,** *53*, 7135-7148.

Supporting Information For

Metal-Metal Redox Exchange to Produce Manganese-Cobalt Oxo Cubanes via a "Dangler" Intermediate

T. Alexander Wheeler, T. Don Tilley

Table of Contents

General Considerations 57

Synthesis and Characterization: 59

Spectroscopic Experiments: 116

Cyclic Voltammetry: 128

Kinetics Details: 144

HR-ESI-MS Data and Isotope Experiments: 170

X-ray Crystallographic Details and Tables: 186

ALL RAW DATA AND PROCESSING AVAILABLE UPON REQUEST

General Considerations

Unless specified otherwise, all reactions were performed in the presence of air and atmospheric water. Ambient or room temperature is defined as 22 °C ± 4 °C and was *not* routinely measured. Yields for reactions involving $Co(OAc)_2(H_2O)_4$ are reported with respect to this cobalt reagent.

Reagents

All reagents were used as purchased without further purification. $Co(OAc)_2(H_2O)_4$ and $Cu(OAc)_2$ were purchased from Alfa-Aesar (Tewksbury, MA), 4-*tert*butylpyridine, H_2O_2 (33-37% in water), NH_4PF_6, $Mn(OAc)_2$, $Mn(OTf)_2$, pyridine (spectrophotometric grade), $AgNO_3$ (analytical grade), and $N(^nBu)_4PF_6$ (analytical grade) were purchased from Millipore-Sigma-Aldrich (Milwaukee, WI), solvent (HPLC grade) was purchased from Fischer Scientific (Hampton, NH), and deuterated solvents were purchased from Cambridge Isotope Labs (Tewksbury, MA). When air-free techniques were applied, solvents were degassed with argon and dried with a JC Meyers SDS, and then stored over activated 3 Å molecular sieves in an N_2 filled glovebox. All thin-layer chromatography (TLC) plates were glass-backed silica. For air-free experiments with acetonitrile-d_3, acetonitrile-d_3 was dried over calcium hydride for at least one week before undergoing three freeze-pump-thaw cycles and being vacuum transferred and stored in a Teflon-tapped Schlenk flask.

NMR Spectroscopy

All ^1H, $^{13}C\{^1H\}$, $^{19}F\{^1H\}$, and $^{31}P\{^1H\}$ experiments were performed using Bruker Avance-300, Avance-400, Avance-400, Avance-500, Neo-500 or Avance III-600 MHz spectrometers at room temperature. ^1H and $^{13}C\{^1H\}$ NMR experiments were calibrated to residual monoprotio-isotopologue relative to tetramethylsilane (δ $CHCl_3$ = 7.26, C_6D_5H = 7.16, $CDHCl_2$ = 5.54, $CD_2H(S{=}O)CD_3$ = 2.50, $CD_2H(C{=}O)CD_3$ = 2.05 ppm, CD_2HCN = 1.94 ppm) (δ $^{13}CDCl_3$ = 77.2, $^{13}C_6D_6$ = 128.1, $^{13}CD_2Cl_2$ = 53.9, $(^{13}CD_3)_2SO$ = 39.5, $(^{13}CD_3)_2CO$ = 29.8 ppm, $^{13}CD_3CN$ = 1.3 ppm). $^{19}F\{^1H\}$ NMR were calibrated externally to 1,4-difluorobenzene, calibrated to trifluoroacetic acid (δ $C_6H_4F_2$ = -120.94 ppm). $^{31}P\{^1H\}$ experiments were calibrated externally to triphenylphosphine (δ PPh_3 = –5.0 ppm). Spectra were analyzed using MestReNova.[1] Magnetic moments were determined by the method of Evans.[2] The NMR facility at the University of California, Berkeley is partially funded by the NIH.

IR Spectroscopy

FTIR spectra were collected on solid samples (unless otherwise noted) with a Bruker Vertex 80 FTIR spectrometer equipped with a Platinum ATR as the average of 100 spectra, which were background corrected prior to measurement.

Analytical Characterization

Electrospray ionization mass spectrometry (HR-ESI-MS) experiments were performed using a PerkinElmer time-of-flight mass spectrometer AxION 2 TOF tuned and calibrated in the positive ion range. Microanalyses were conducted by Dr. Elena Kreimer at the Microanalytical Facility at the University of California, Berkeley using a Perkin Elmer CHNS 2400 Series II Analyzer or ThermoFisher Flash Smart Elemental Analyzer. Cubane samples are most conveniently handled in air under ambient conditions, even though they are hygroscopic and take up ~4 equiv of water upon storage. Kinetic studies were conducted immediately following purification.

X-ray Crystallography

Single crystal X-ray diffraction for was performed at UC Berkeley CheXRay crystallographic facility. Data collection was performed using a Rigaku XtaLAB P200 equipped with a MicroMax 007HF rotating anode and a Pilatus 200k hybrid pixel array detector using Mo Kα radiation (λ = 0.71073 Å) monochromated by a graphite monochromator. All other diffraction studies were collected at the Advanced Light Source beamline 12.2.1 using a Bruker D85 three-circle diffractometer equipped with a PHOTON II CCD area detector using synchrotron radiation (λ = 0.7288 Å) monochromated using a channel-cut Si(111) monochromator. Structure solution, modeling, and refining was performed using both the OLEX2 and Shelxle GUI and SHELX software packages.[3-6]

Electrochemical experiments

Electrochemical experiments were performed at ambient temperature using a BASi EC Epsilon potentiostat/galvanostat and a PWR-3 Power Module. A 3 mm diameter glassy carbon electrode was used as the working electrode, which was polished with 0.30 μm alumina, rinsed with deionized water, followed by 0.05 μm alumina, rinsed with water, then HPLC grade acetone, and dried in air before use. Platinum and silver wires were used as the counter and reference electrodes respectively. Analytical grade tetrabutylammonium hexafluorophosphate (0.2 M) was used as the electrolyte in HPLC grade MeCN or CH_2Cl_2. Ferrocene was added at the end of each experiment as an internal reference against the half-potential of $[Cp_2Fe]^0/[Cp_2Fe]^+$ (Fc/Fc^+). Internal resistance compensation was carried out for each experiment to correct for solution resistance. Analyte concentration was 1.0 mM in the case of cubanes **Co_4(py-X)** and cubanes **Co_4(OBz-X)** and 0.18 mM in the case of **Cu_2Co_4**. The E° values reported are the midpoints of the anodic (E_{pa}) and cathodic (E_{pc}) peak potentials, calculated as $E^\circ = (E_{pa} + E_{pc})/2$. The reversibility of the redox events was determined by the peak-to-peak separations and $\Delta E_p = E_{pa} - E_{pc}$. The peak currents were determined with EC Lab software.

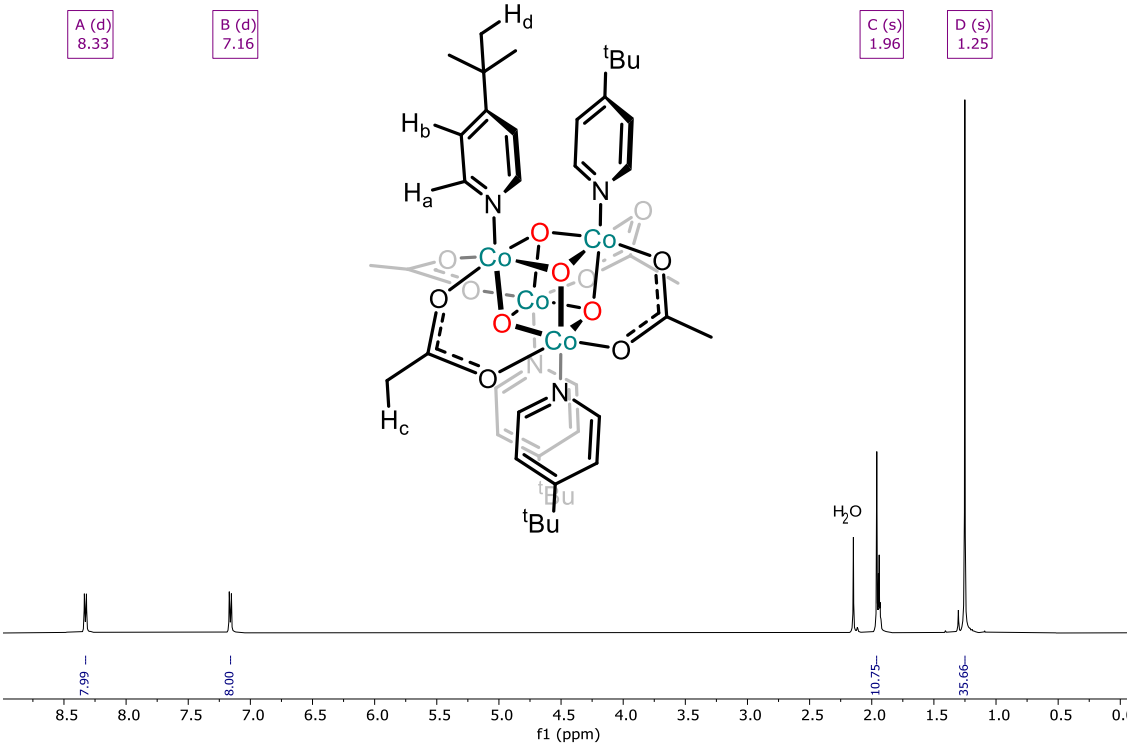
UV-visible Spectroscopy

UV-visible spectra were collected at 24-25 °C using a Shimadzu UV-2600i spectrometer equipped with a CPS multicell. Quartz cuvettes with screw cap tops or Teflon stoppers were used to limit the influence of solvent evaporation. When Teflon stoppers were used, they were always used in tandem with screw cap stoppers to apply pressure to the top of the Teflon stopper. Spectra were baseline corrected and zeroed with the solvent employed in the reaction. Spectra were analyzed using UVProbe software. Epsilon values were determined from the slope of five different concentrations of the compound in MeCN or CH_2Cl_2. All other spectra are given as absorbances ,which by definition is unitless.

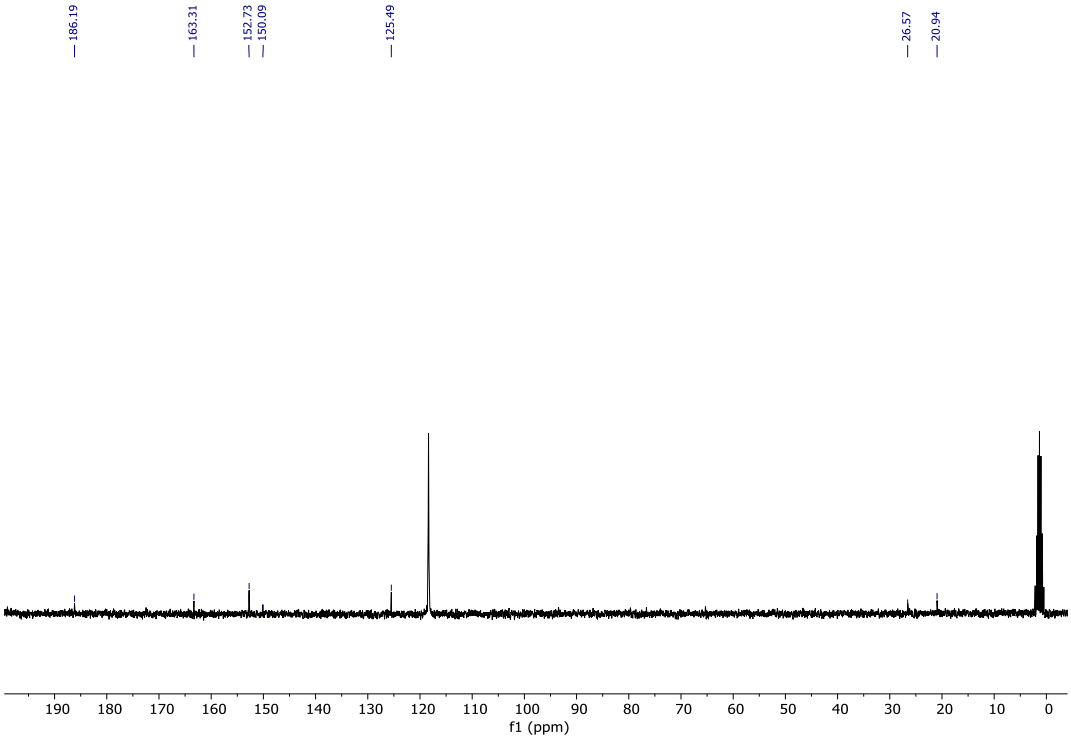
Synthesis and Characterization

$Co_4O_4(OAc)_4$(*t*-Bupy)$_4$ (Co_4)

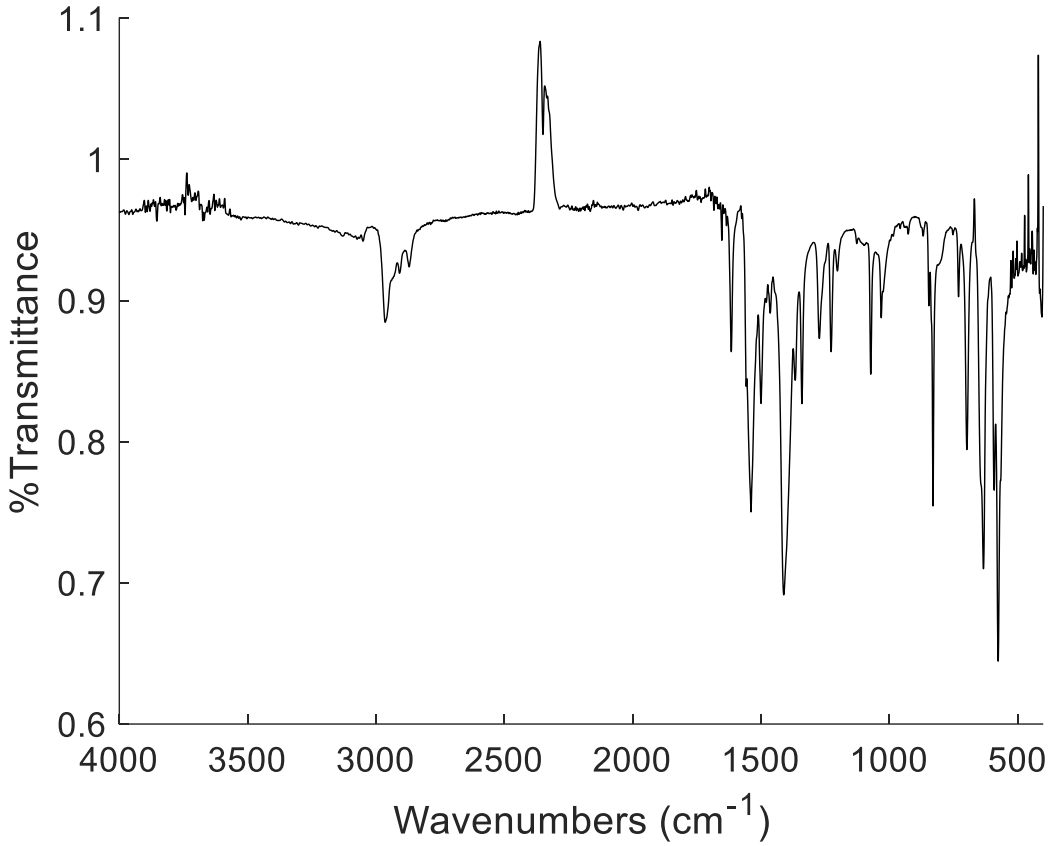
A 100 mL round-bottom flask was charged with a stir bar, $Co(OAc)_2(H_2O)_4$ (5.0 g, 20 mmol, 1 equiv), 4-*tert*-butylpyridine (2.7 g, 20 mmol, 1 equiv), and methanol (25 mL). The solution was stirred until complete dissolution of the $Co(OAc)_2$. To this solution was added aqueous technical grade (33-37%) H_2O_2 (10 mL, 100 mmol, 5 equiv) over 20 min with vigorous stirring. Following complete addition of H_2O_2, the round-bottom flask was transferred to an oil bath and heated to 60 °C for 12 h. The solvent was removed *in vacuo*, and the resulting solids were dissolved in biphasic CH_2Cl_2 (25 mL) and water (15 mL). The CH_2Cl_2 was separated, and the aqueous phase was extracted with CH_2Cl_2 (5 x 25 mL). The combined CH_2Cl_2 extracts were dried over $MgSO_4$ and filtered to remove $MgSO_4$ before removing the solvent *in vacuo*. The dark solids were directly decanted onto a pre-wetted silica plug (150 mL) and washed from the silica plug using pipettes of CH_2Cl_2 (100 x 2 mL) into a Büchner flask under reduced pressure. The solvent was removed *in vacuo* to give **Co_4** contaminated with a small amount of acetic acid that can be removed under vacuum. Single-crystal X-ray diffraction quality crystals were grown by dissolving **Co_4** in minimal CH_2Cl_2, chilling this CH_2Cl_2 solution to –5 °C, layering with chilled pentane, and allowing the layers to diffuse over several days at –5 °C to give black blocks of **Co_4**. Yield: 2.00 grams; 40%. **Characterization data:** ^{1}H NMR (400 MHz, acetonitrile-d_3) δ 8.34 (d, J = 5.8 Hz, 8H, H_a), 7.16 (d, J = 5.8 Hz, 8H, H_b), 1.96 (s, 12H, H_c), 1.25 (s, 36H, H_d). ^{13}C{^{1}H} NMR (101 MHz, acetonitrile-d_3) δ 186.19, 163.31, 152.73, 150.09, 125.49, quaternary carbon was not detected. 26.57, 20.94. ^{1}H NMR (500 MHz, benzene-d_6) δ 9.11 (d, J = 5.8 Hz, 8H), 6.75 (m, 8H), 2.29 (s, 12H), 0.89 (s, 36H). ^{1}H NMR (400 MHz, acetone-d_6) δ 8.48 (d, J = 6.8 Hz, 8H), 7.20 (d, J = 6.8 Hz, 8H), 2.09 (s, 12H), 1.30 (s, 36H). Anal. Calcd. for $C_{45}H_{68}Co_4N_4O_{12}$: C, 49.46; H, 6.27; N, 5.13. Found: C, 49.34; H, 6.29; N, 5.12. IR (cm^{-1}): 3073 (*very* weak), 2962 (w), 2870 (w), 1712 (w), 1616 (w), 1533 (m, *broad*), 1499 (w), 1408 (s), 1366 (w), 1340(w), 1127(w), 1072(w), 1024 (w), 829 (m), 697 (m), 633 (s), 576 (s). HR-ESI-MS Calc'd for **Co_4**-H$^+$: 1077.1922; found: 1077.1930.



S1. ^{1}H NMR spectrum of **Co$_4$** (acetonitrile-d_3, 400 MHz).



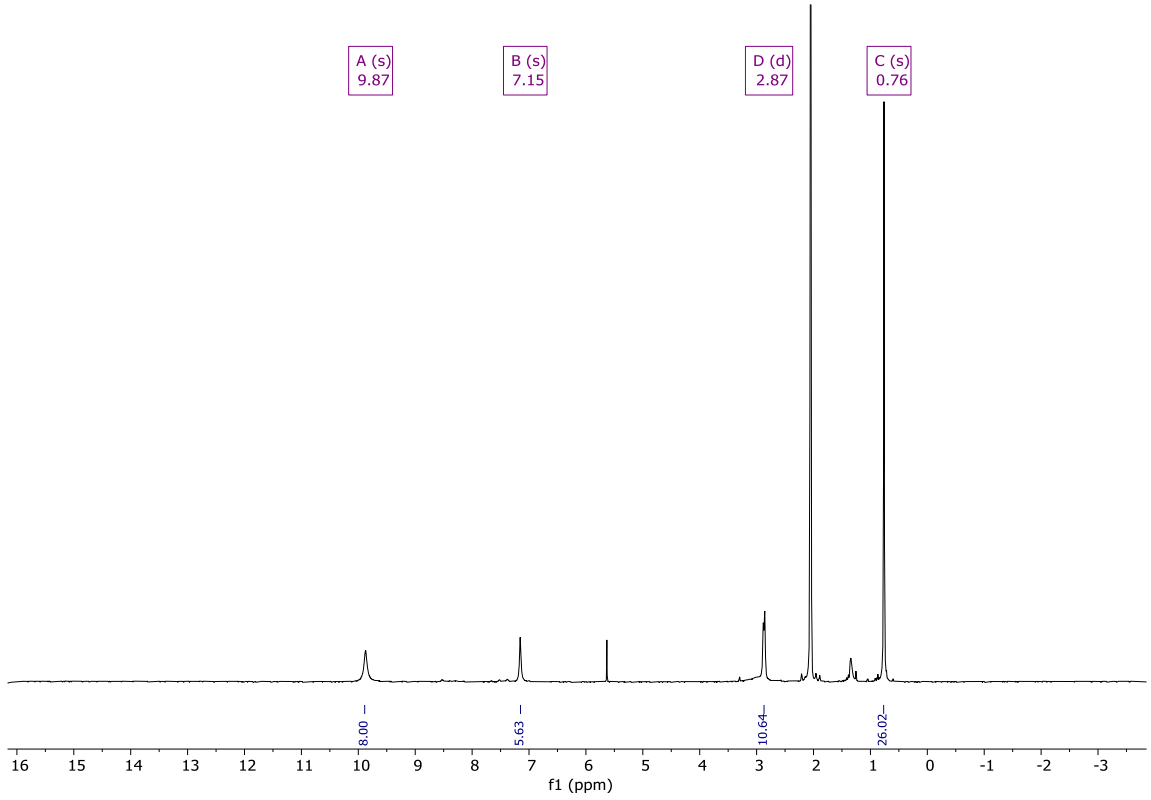
S2. ^{13}C{^{1}H} NMR of **Co$_4$** (acetonitrile-d_3, 101 MHz).



S3. FTIR spectrum of **Co4**. Inverted peak is a result of poor baseline correction for CO_2 and is inconsequential to the spectrum.

[Co_4O_4(OAc)$_4$(*t*-Bupy)$_4$][PF_6] (Co_4^+[PF_6])

A 100 mL round-bottom flask was charged with a stir bar, **Co_4** (Co_4O_4(OAc)$_4$(*t*-Bupy)$_4$) (0.5008 g, 0.4653 mmol, 1.00 equiv.) and water (15 mL). The solution was stirred until **Co_4** was completely dissolved. A solution of $Ce^{IV}(NO_3)_6(NH_4)_2$ (0.2879 g,0.5253 mmol, 1.13 equiv.) in water (5 mL) was added to the solution of **Co_4** over 15 s. The solution was stirred for 3 min at which point solid NH_4PF_6 (0.085 g, 5214 mmol, 1.13 equiv) was added as a solid in one portion, resulting in the immediate precipitation of solids. The solids were separated by vacuum filtration through a fine porosity sintered frit with a Büchner flask, and washed with water (2 x 10 mL). The solution was discarded, and the solids were extracted from the frit with CH_2Cl_2 (10 mL). The solvent was reduced to roughly half volume under a flow of nitrogen in the Büchner flask (*ca*. 5 mL remaining) and layered with chilled pentane. The layers were allowed to diffuse at –5 °C resulting in 0.144 g (24% yield) of small blocks of **Co_4^+**[PF_6]. **Characterization data:** ^{1}H NMR (400 MHz, acetone-d_6) δ 9.87 (s, 8H), 7.15 (s, 8H), 2.87 (d, J = 10.2 Hz, 12H), 0.76 (s, 36H). Note that trace residual **Co_4** in **Co_4^+**[PF_6] is accompanied by an equilibrium between the two species that shows up as signal averaging by ^{1}H NMR spectroscopy. Satisfactory ^{13}C{^{1}H} NMR was not attainable due to paramagnetic broadening. Anal. Calcd for: $C_{44}H_{64}Co_4F_6N_4O_{12}P$: C, 43.26; H, 5.28; N, 4.59. Found: C, 43.20; H, 5.41; N, 4.50.

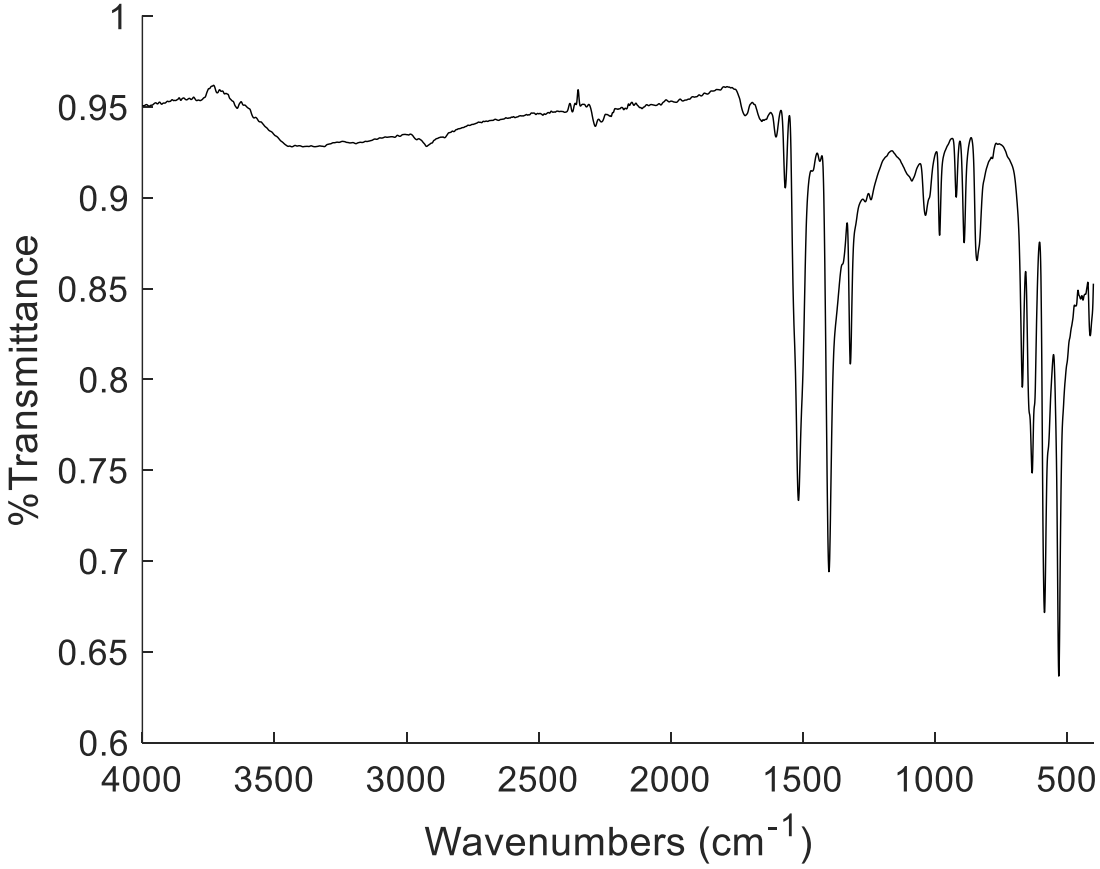


S4. ^{1}H NMR spectrum of **Co_4^+**[PF_6] (acetone-d_6, 400 MHz).

Co_4O_4(OAc)$_4$(py-d_5)$_4$ (d_{20}): Synthesized according to literature procedure except that in place of pyridine, pyridine-d_5 was used (20% yield).[7]

Co_4O_4(OAc-d_3)$_4$(py)$_4$ (d_{12}): Synthesized according to literature procedure except that in place of sodium acetate, sodium acetate-d_3 was used (15% yield).[7]

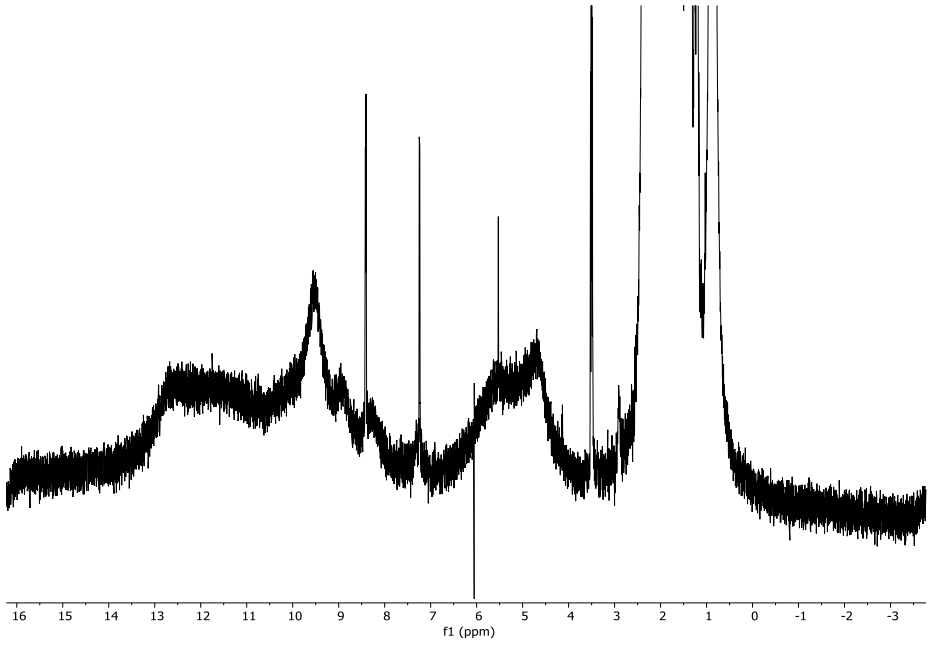
$Co_4O_4(OAc\text{-}d_3)_4(py\text{-}d_5)_4$ (d_{32}): Synthesized according to literature procedure except that in place of pyridine and sodium acetate, pyridine-d_5 and sodium acetate-d_3 were used (12% yield).[7] **Characterization data:** IR (cm^{-1}): 2966 (very weak), 2920 (very weak), 2847 (very weak), 1718 (w), 1653 (w), 1600 (weak), 1567 (w), 1516 (s), 1463 (shoulder, w), 1436 (w), 1401 (s), 1346 (shoulder, w), 1320 (m), 1260 (w), 1242 (w), 1090 (w), 1035 (w), 981 (w/m), 919 (w), 890 (w), 842 (w), 669 (m), 631 (s), 585 (s) 531 (s). HR-ESI-MS calc'd for $C_{28}D_{32}Co_4N_4O_{12}^+$ m/z = 884.1348; found: 884.1630.



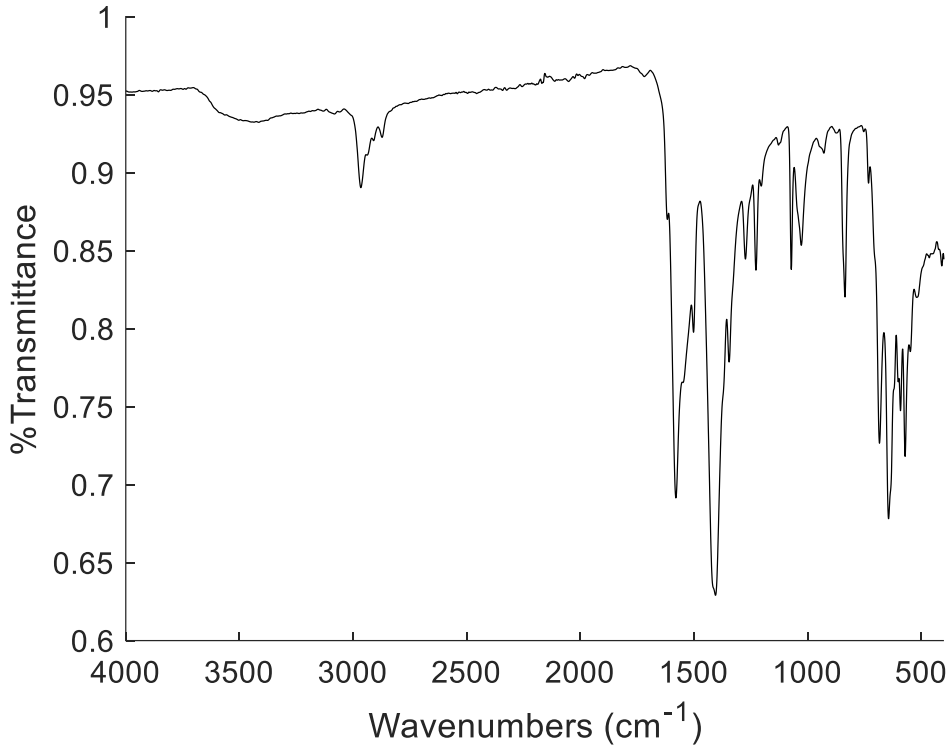
S5. FTIR spectrum of $Co_4O_4OAc_4(py)_4$-d_{32}.

$Cu_2Co_4(\mu_4\text{-}O)_2(\mu_3\text{-}O)_2(OAc)_6(Cl)_2(t\text{-}Bupy)_4$ (Cu_2Co_4)

A 20 mL vial was charged with a stir bar, **Co_4** (CH_2Cl_2 solvate, alternatively, *ca.* 0.1 mL of CH_2Cl_2 was added, 0.1000 mg, 0.0932 mmol (calculated on the basis of the unsolvated complex), 1.00 equiv) and $Cu_2(OAc)_4(H_2O)_2$ (0.0187 mg, 0.0468 mmol, 1.01 equiv.) MeCN (*ca*. 4 mL) was added, the vial was sealed, transferred to an oil bath, stirred, and heated to 70 °C. The reaction was followed by TLC (5% MeOH in CH_2Cl_2), until complete consumption of **Co_4** (R_f *ca*. 0.3) was observed, 72 h. The vial was removed from the oil bath and allowed to cool to ambient temperature. The solvent was removed *in vacuo*, and the resulting solids were dissolved in CH_2Cl_2, filtered through a glass wool plug in a pipette into a 20 mL vial, and the solvent was removed *in vacuo*. The resulting solids were pulverized with a spatula, a stir bar was added, and Et_2O (20 mL) was added, following which the suspension was stirred vigorously for *ca*. 30 min. The suspension was filtered through a glass wool filter in a pipette, and the solids were washed with additional Et_2O until the solution ran clear (*ca*. 10 mL). The solids were extracted from the filter with CH_2Cl_2 (5 mL) into a 20 mL vial, then the solution was chilled to –5 °C and layered with cold pentane. The layers were allowed to diffuse at –5 °C for several days to give microcrystalline $Cu_2Co_4O_4(OAc)_6(Cl)_2(t\text{-}Bupy)_4$ (**Cu_2Co_4**) in 29% yield (39.2 mg). XRD quality crystals were grown from MeCN/Et_2O vapor diffusion at –5 °C over several weeks*. **Characterization data:** HR-ESI-MS calc'd for: $Cu_2Co_4O_4(OAc)_7(t\text{-}Bupy)_4$ m/z = 1379.0830; found: 1379.0591 m/z. calc'd for: $Cu_2Co_4O_4(OAc)_6(Cl)(^t BuPy)_5$, m/z = 1490.1433, found, 1490.1114 m/z. Anal. calcd for $C_{48}H_{70}Cl_2Co_4Cu_2N_4O_{16}$: C, 41.39; H, 5.07; N, 4.02. Found: C, 38.70; H, 5.35; N, 3.48. (Repeated combustion analysis consistently gave low carbon and nitrogen values despite no detectable impurities by HR-ESI-MS or ^{1}H NMR spectroscopy, suggesting incomplete combustion or loss of pyridine upon drying *in vacuo*). IR (cm^{-1}): 2965 (w), 2937 (w), 2909 (w), 2872 (w), 1617 (w/m), 1579 (s), 1536 (s, sh), 1501 (m), 1405 (s), 1345 (m), 1272 (m), 1226 (m), 1203 (w), 1127 (w), 1071 (m), 1027 (m), 928 (w), 835 (m), 683 (s), 643 (s), 601 (s, sh), 590 (s), 570 (s), 547 (s), 518 (m), 464 (m), 408 (m).

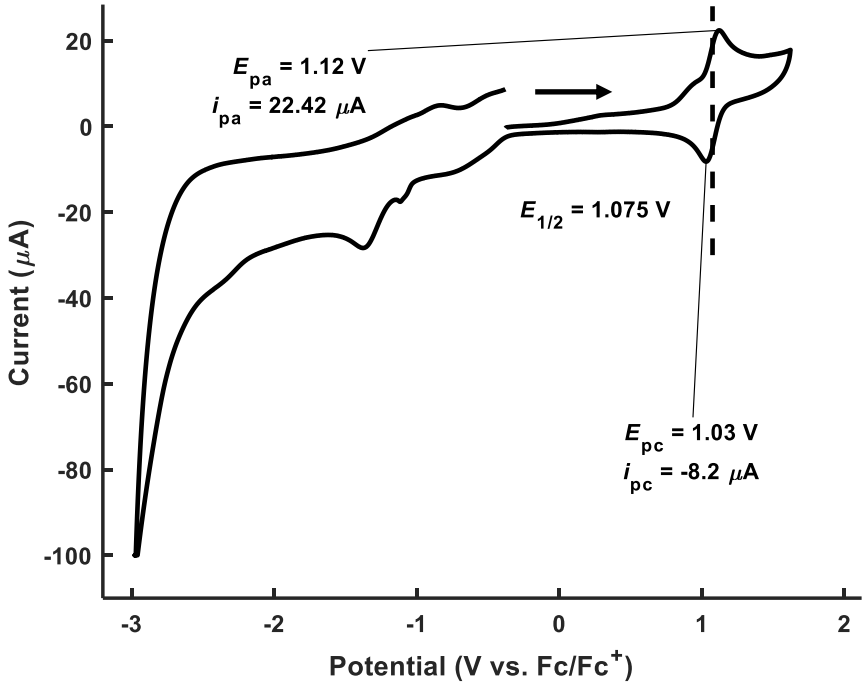


S6. ^{1}H NMR spectrum of **Cu_2Co_4** (acetonitrile-d_3). Note that the diamagnetic peaks correspond to trace residual *t*-Bupy and Et_2O that only appear intense due to the overall spectrum intensity.

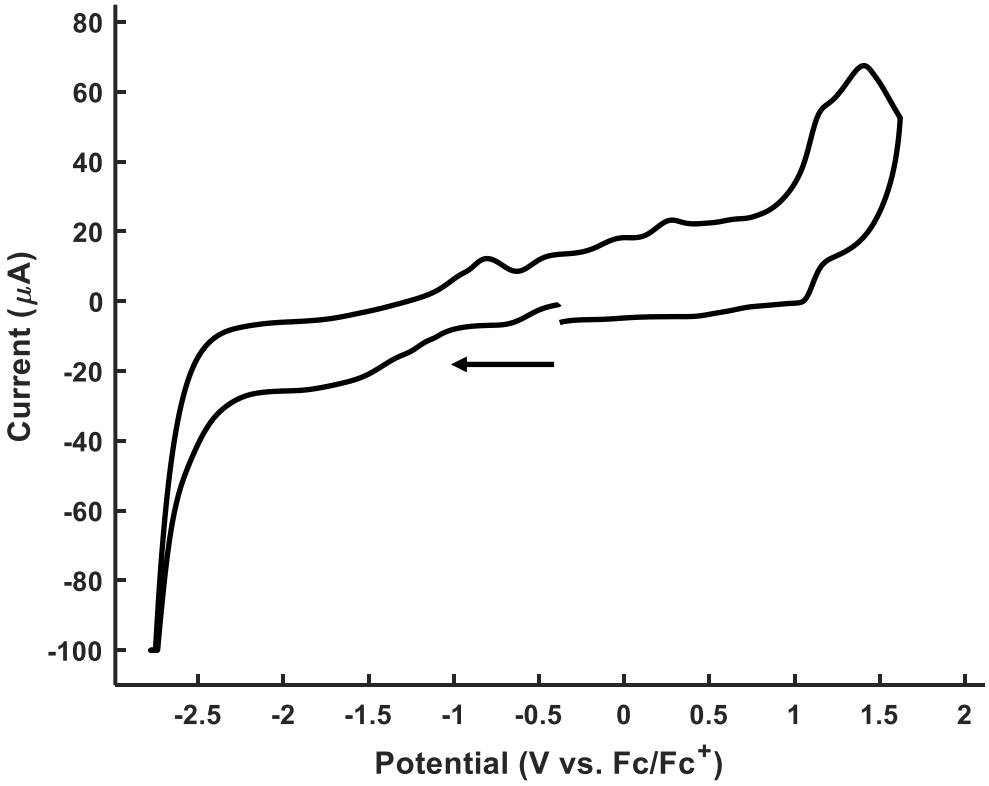


S7. FTIR spectrum of **Cu_2Co_4**.

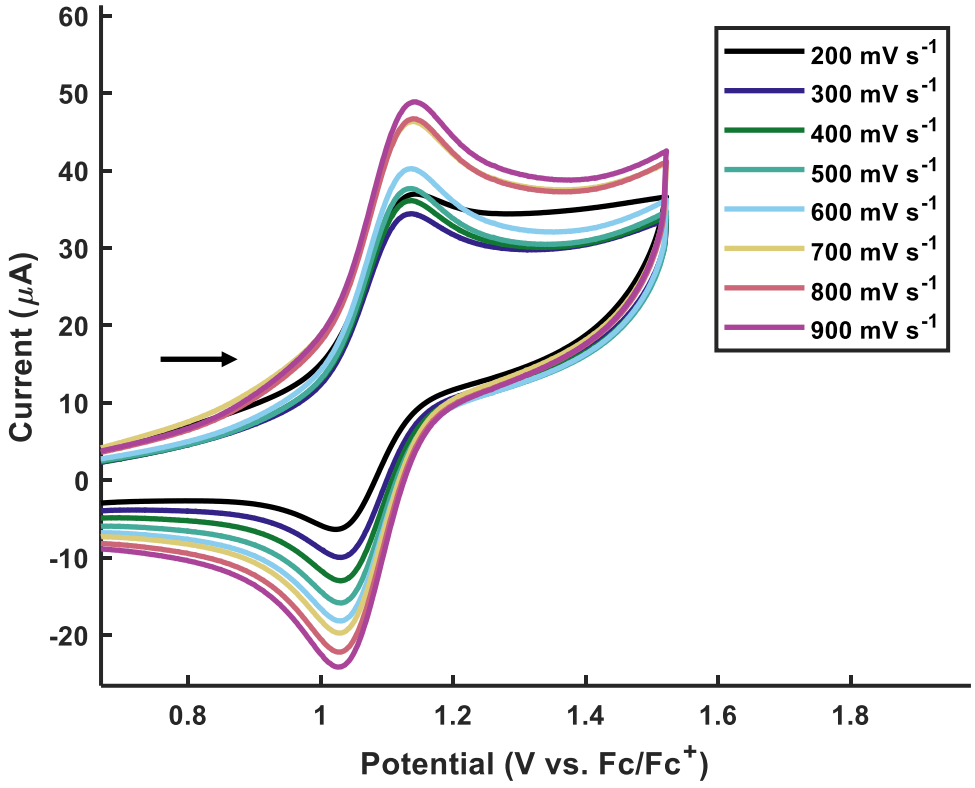
*Note: If an excess of $Cu_2(OAc)_4(H_2O)_2$ is used, blue crystals of $Cu_2(OAc)_4(t\text{-Bupy})_2$ preferentially crystallize under these conditions, sometimes from the crude reaction mixture. Anal. calcd for $C_{26}H_{38}Cu_2N_2O_8$: C, 49.28; H, 6.04; N, 4.42. Found: C, 49.46; H 6.28; N, 4.75. IR (cm^{-1}): 2962 (w), 2903 (w), 2868 (w), 1622 (s), 1551 (w), 1504 (w), 1473 (w), 1420 (s), 1365 (w), 1344 (w), 1276 (w), 1230 (w), 1201 (w), 1072 (w), 1047 (w), 1021 (w/m), 936 (w), 878 (w), 836 (m), 723 (w), 679 (m/s), 625 (m), 571 (m/s), 539 (w), 464 (w).



S8. Cyclic voltammogram of **Cu_2Co_4**, at a scan rate of 100 mV s^{-1}.



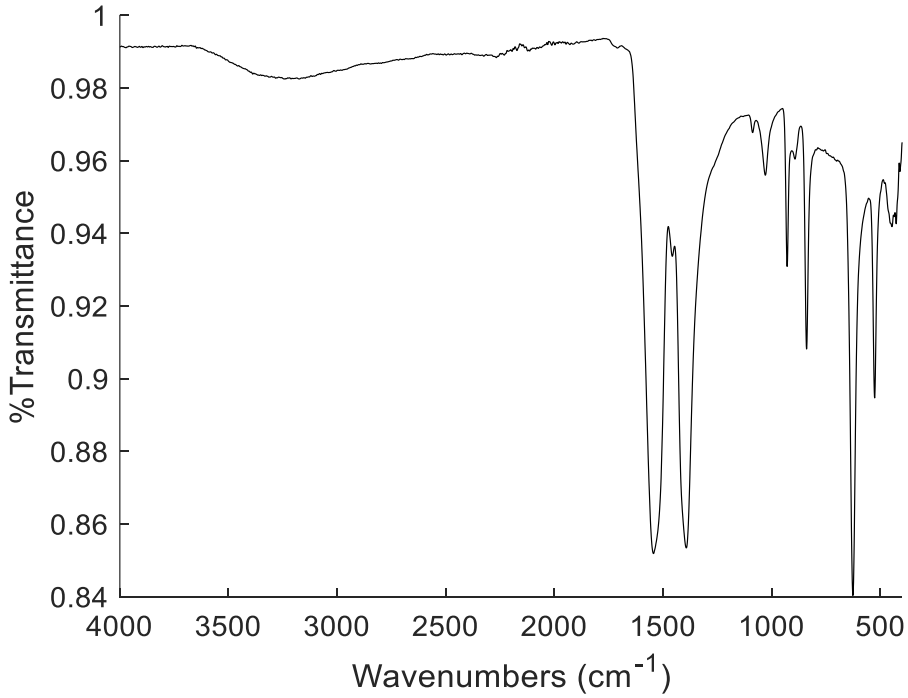
S9. Cyclic voltammogram of **Cu_2Co_4**, at a scan rate of 100 mV s^{-1}.



S10. Scan rate study of **Cu_2Co_4**.

$Mn(OAc)_2$-d_6

A 25 mL round-bottom flask was charged with a stir bar, a freshly opened ampule of D_2O (1 mL), and $Mn(CO_3)_2$ (0.5075 g, 4.415 mmol). The mixture was stirred until the slurry was uniformly suspended. At room temperature, the flask was sealed with a rubber septum and acetic acid-d_4 (1 mL, 17 mmol) was added dropwise over one minute. Occasional effervescence was observed, and the stirring rate was increased, which was accompanied by vigorous gas evolution. The pressure was periodically vented as the reaction stirred for 15 min, at which point the flask was transferred to an oil bath heated to 65 °C. The solution was magnetically stirred at 65 °C, periodically venting to relieve pressure. After 3 h, the mixture was cooled to room temperature, and filtered through a Celite® filter supported on a glass wool plug in a pipette, resulting in a fine suspension. The resulting fine suspension was transferred to a centrifuge tube and centrifuged at 2400 RPM for 2 min, after which the supernatant was carefully collected with a pipette and filtered through a glass wool plug in a pipette; the solvent was then removed in vacuo. The resultant pink solid was contaminated with small amounts of a brown solid (likely $Mn(CO_3)_2$), and the solids were therefore dissolved in minimal water (*ca*. 3 mL) and allowed to sit for 16 h. A brown precipitate resulted, which was separated by gravity filtration through a glass wool plug supported Celite® filter in a pipette to give a clear pink solution. The solvent of the pale pink filtrate was removed *in vacuo* at 80 °C, resulting in 113.6 mg (0.634 mmol, 14.5% yield) of $Mn(OAc)_2$-d_6. **Characterization data:** IR (cm^{-1}): 1545 (s, broad), 1458, (m) 1394 (s, broad), 1085 (w), 1031 (w), 928 (m), 894 (w), 839(m), 625 (very strong), 525 (m), 449 (w), 427, (w). Anal. calcd for: C, 26.83; D, 6.75. Found: C, 26.42; H, 3.41. –Comment on elemental analysis: Elemental analysis that uses the Pregl-Dumas technique does not automatically account for the mass of deuterium in the final mass percentage. The found hydrogen content can be converted to the found deuterium content by multiplying by 1.9985, i.e., Found: C, 26.42; D, 6.81.[8]



S11. FTIR spectrum of $Mn(OAc)_2$-d_6.

p-Pyridine Substituted Benzoate Cubanes

General Comments

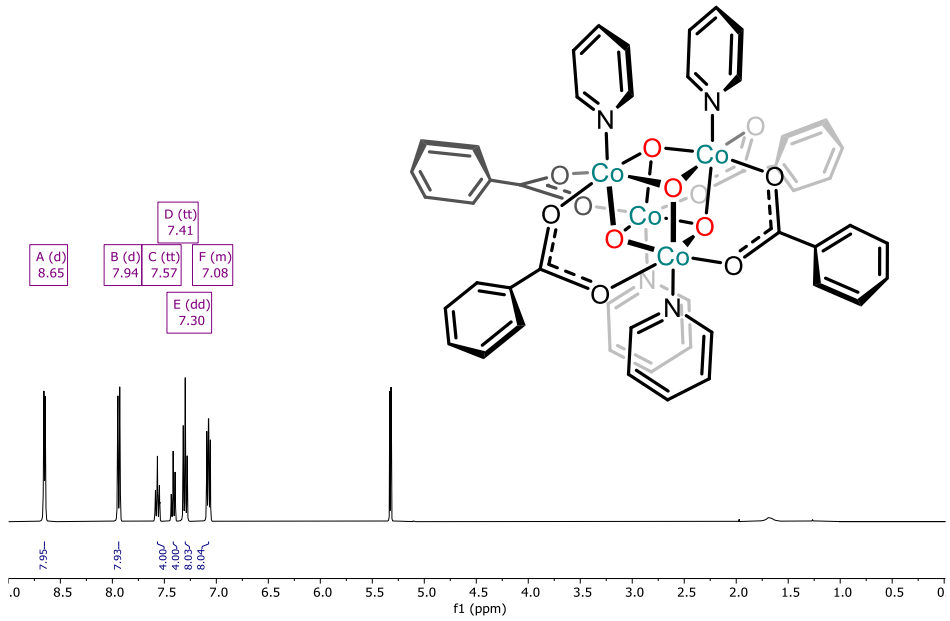
All *p*-R-pyridine complexes were synthesized by way of self-assembly reactions between $Co(NO_3)_2•(H_2O)_6$, sodium benzoate, and the respective substituted pyridine, with no difference in workup except in the case of *p*-cyanopyridine. The *t*-Bupy derivative can also be synthesized according to the synthetic procedure described in the substituted benzoates section. HR-ESI-MS data is presented where possible, note that some cubanes did not ionize under the experimental conditions.

Synthetic Procedure

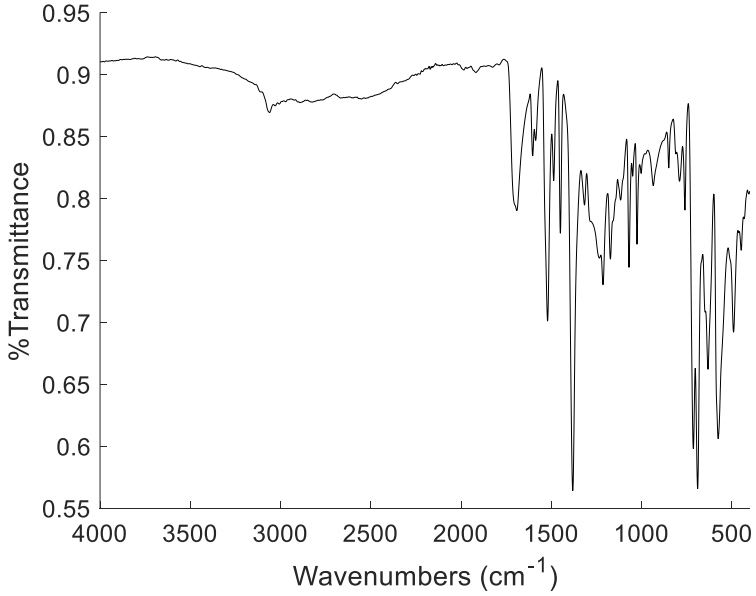
A 25 mL round-bottom flask was charged with a stir bar, solid $Co(NO_3)_2•(H_2O)_6$ (1.000 g, 3.4 mmol) and sodium benzoate (1.015 g, 7.0 mmol, 2 equiv). Methanol (8 mL) was added and then the flask was charged with the substituted pyridine (3.2 mmol, 0.95 equiv). The flask was placed in a 50 °C oil bath, and the solution was magnetically stirred for 15 min to fully dissolve all reagents, at which point hydrogen peroxide (technical grade 33-37%, 2.2 mL, 22.6 mmol, 6.6 equiv.) was added carefully in *ca*. 0.2 mL portions over 1 h. After complete addition, the solution was stirred for between 8-18 h at 50 °C; the reaction is likely complete after 2-3 h. The flask was then removed from the oil bath and allowed to cool to room temperature. Then, the solvent was removed under reduced pressure with a rotary evaporator. The resulting solids were then dissolved in CH_2Cl_2 (25 mL) and transferred to a separatory funnel*. The solution was washed with a Na_4EDTA solution (15 mL, 0.11 M in water), the CH_2Cl_2 layer separated, and the aqueous layer was discarded. The CH_2Cl_2 layer was then washed with brine (10 mL), separated, and the aqueous layer was discarded. The CH_2Cl_2 was evacuated under reduced pressure with a rotary evaporator. The resulting solids were then dissolved in minimal CH_2Cl_2 or 2.5% MeOH:DCM and loaded onto a short (2 cm × 7.5 cm, 15 mL, *ca*. 2/3 full) silica plug. The silica plug was washed with 2.5% MeOH:DCM (typically *ca*. 200 mL) until the dark band fully eluted. The solvent was removed under reduced pressure with a rotary evaporator to yield the substituted cubane product in low (but scalable) yield: **Co_4(py** 33% (–**OMe**), 20% (–**Me**), 12% (–**CF_3**), 25% (–**CN**), 35% (–**Ac**), 15% (–***t*Bu**), 69% (–**H**).

*The *p*-cyanopyridine substituted cubane was gravity filtered through filter paper at this point due to the formation/precipitation of solids.

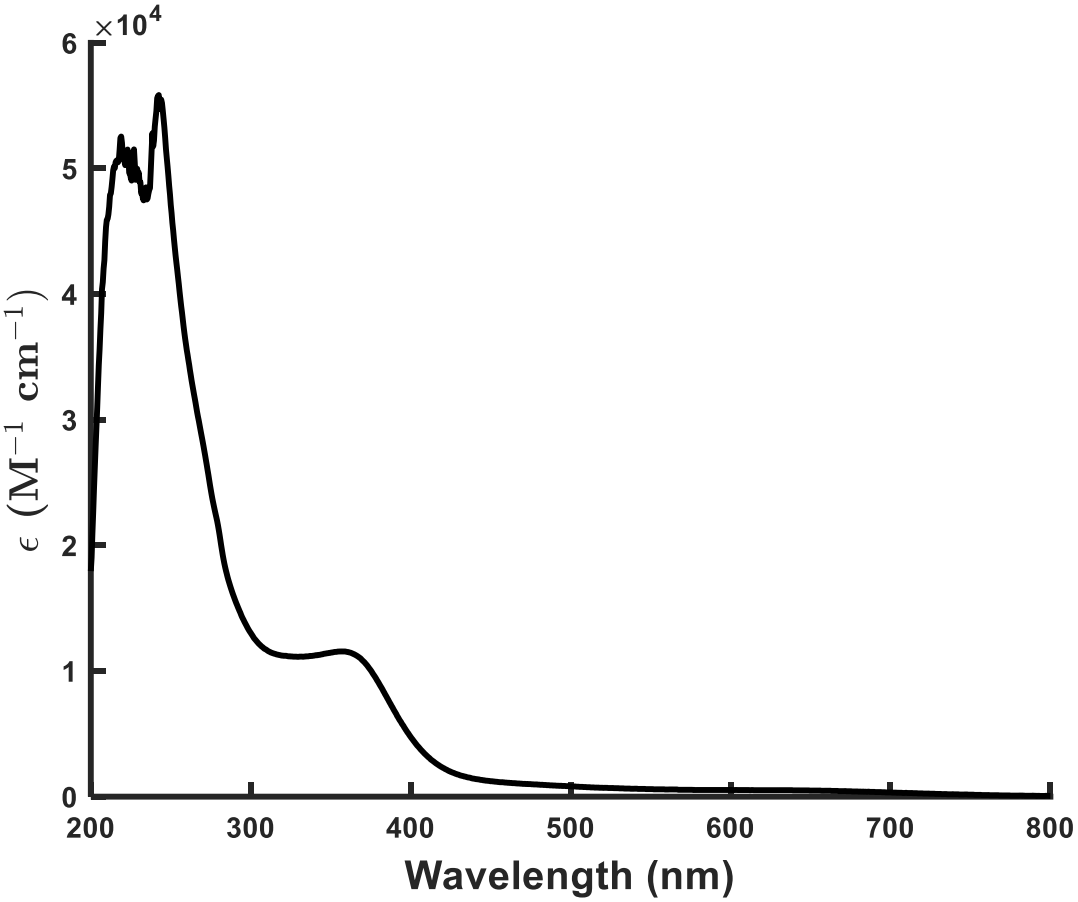
$Co_4O_4(OBz)_4(pyridine)_4$ (Co_4(py-H)): ^{1}H NMR (400 MHz, methylene chloride-d_2) δ 8.65 (dt, J = 5.0, 1.6 Hz, 8H), 7.94 (d, 8H), 7.57 (tt, J = 7.6, 1.6 Hz, 4H), 7.41 (tt, 4H), 7.30 (dd, J = 8.3, 7.0 Hz, 8H), 7.08 (m, 8H). IR (cm^{-1}): 3062 (w), 1692 (m), 1603 (m), 1586 (w/m), 1520 (s), 1487 (m), 1449 (w), 1381 (s), 1316 (m), 1213 (s), 1172 (m), 1114 (w), 1070 (m), 1025 (m), 935 (w), 849 (w), 789 (w), 759 (w), 713 (s), 689 (s), 633 (s), 574 (s), 490 (s), 448 (m/s) HR-ESI-MS calc'd for: $C_{48}H_{41}Co_4N_4O_{12}^+$ m/z = 1101.0039; found: 1100.9792 m/z. Anal. Calcd for $C_{48}H_{44}Co_4N_4O_{16}$ (• $2H_2O$): C, 50.72; H, 3.90; N, 4.93. Found: C, 50.55; H, 3.77; N, 4.86.



S12. ^{1}H NMR spectrum of $Co_4O_4(OBz)_4(py)_4$ (**Co_4(py-H)**). (methylene chloride-d_2, 400 MHz).

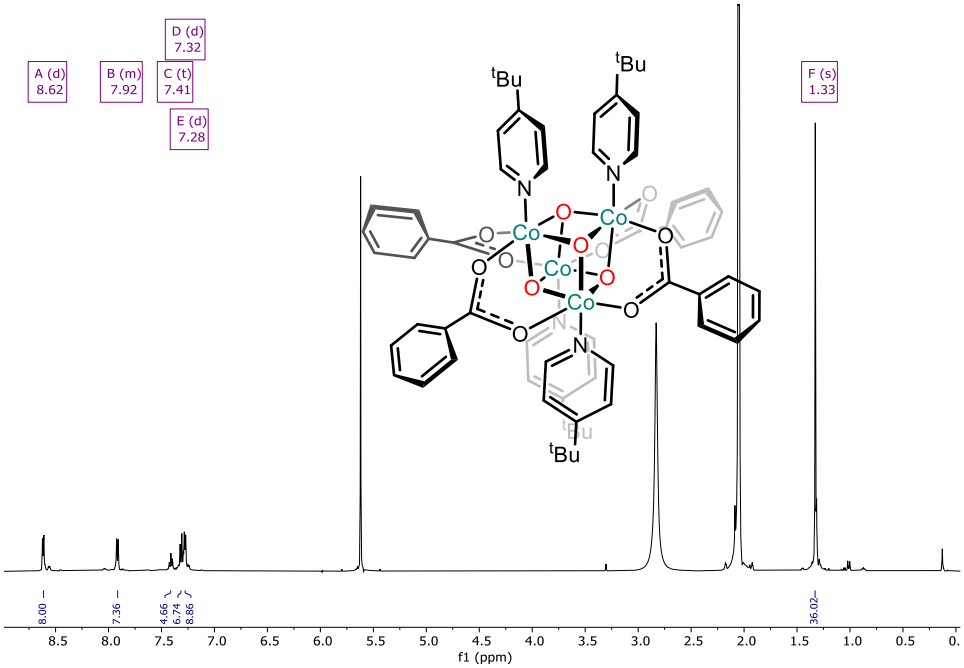


S13. FTIR spectrum of $Co_4O_4(OBz)_4(py)_4$ (**Co_4(py-H)**).

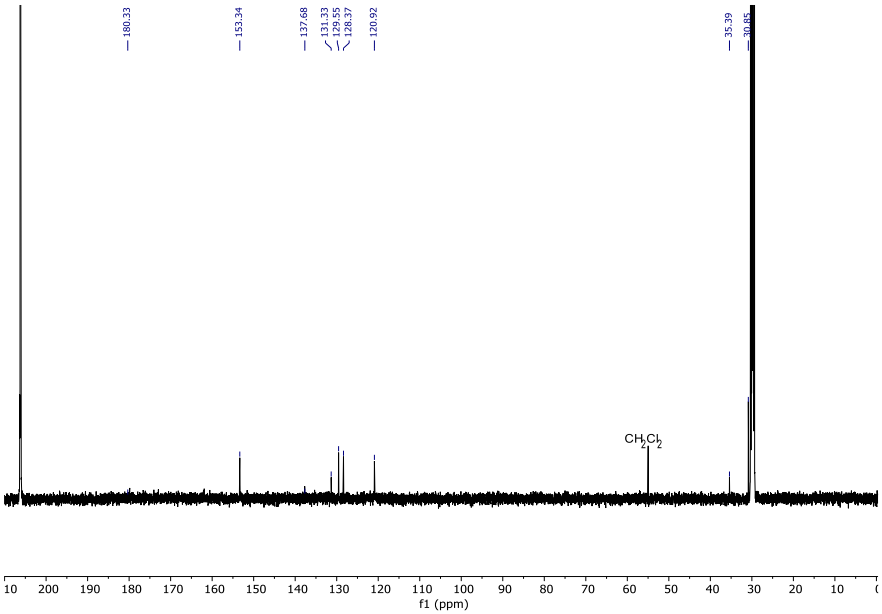


S14. Molar absorptivity values for $Co_4O_4(OBz)_4(py)_4$ (**Co_4(py-H)**) in MeCN.

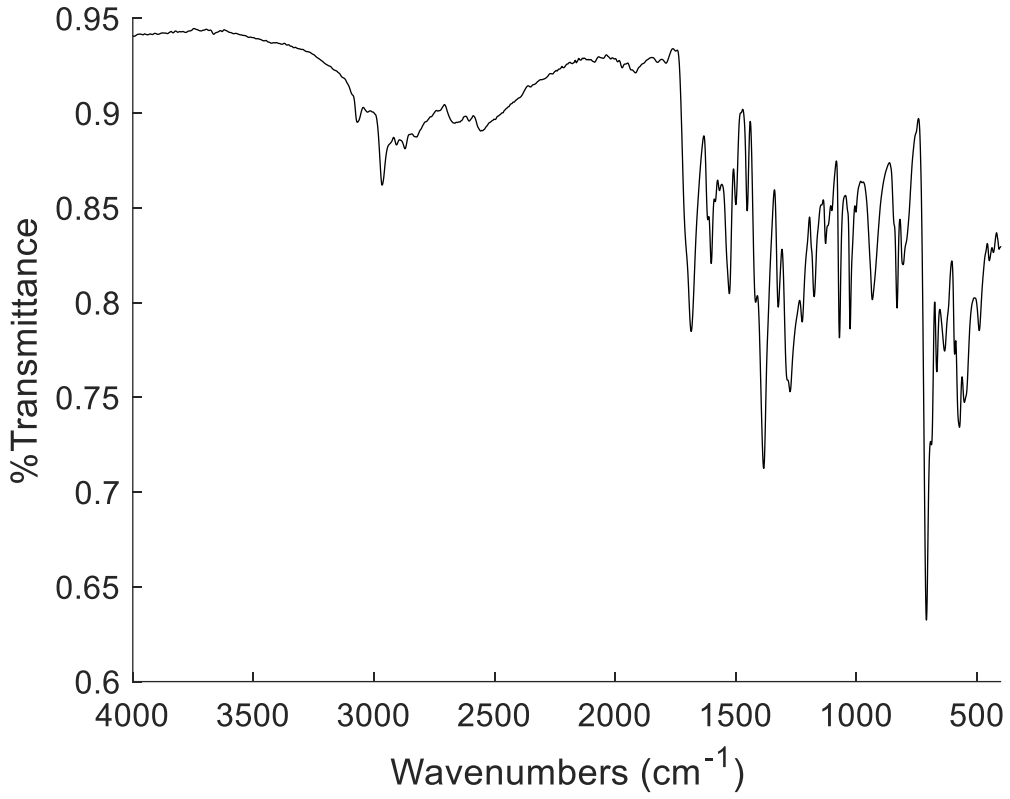
$Co_4O_4(OBz)_4$(4-*tert*-butylpyridine)$_4$ (Co_4(py-*t*Bu)): ^{1}H NMR (500 MHz, acetone-d_6) δ 8.62 (d, J = 6.8 Hz, 8H), 7.92 (m, 8H), 7.41 (t, J = 7.5 Hz, 4H), 7.32 (d, J = 7.7 Hz, 8H), 7.28 (d, J = 6.8 Hz, 8H), 1.33 (s, 36H). ^{13}C{^{1}H} NMR (126 MHz, acetone-d_6) δ 180.3, 153.3, 131.3, 129.5, 128.3, 120.9, 35.39, 30.8. IR (cm^{-1}): 3071 (w), 2969 (w), 2907 (w), 2871 (w), 1685 (m, br), 1601 (m), 1585 (w), 1526 (m), 1499 (w), 1452 (w), 1385 (s), 1324 (m/s), 1274 (s), 1225 (m/s), 1174 (w/m), 1128 (w), 1070 (s), 1026 (s), 934 (m), 832 (m), 807 (m), 709 (very strong), 667 (s), 634 (s), 572 (s), 552 (s), 491 (s/m), 450 (w/m), 431 (w/m). Anal. Calcd for $C_{64}H_{72}Co_4N_4O_{12}$: C, 58.01; H, 5.48; N, 4.23. Found: C, 58.26; H, 5.54; N, 4.23.



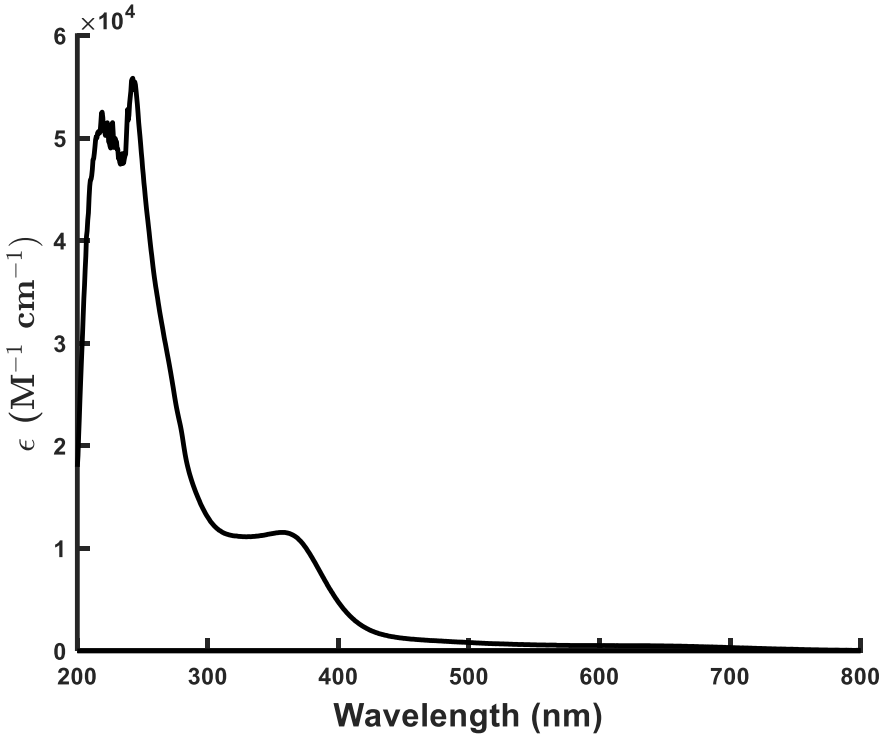
S15. ^{1}H NMR spectrum of $Co_4O_4(OBz)_4$(4-*tert*-butylpyridine)$_4$ (**Co_4(py-*t*Bu)**). (acetone-d_6, 400 MHz).



S16. ^{13}C{^{1}H} NMR spectrum of $Co_4O_4(OBz)_4$(4-*tert*-butylpyridine)$_4$ (**Co_4(py-*t*Bu)**) (acetone-d_6, 126 MHz).

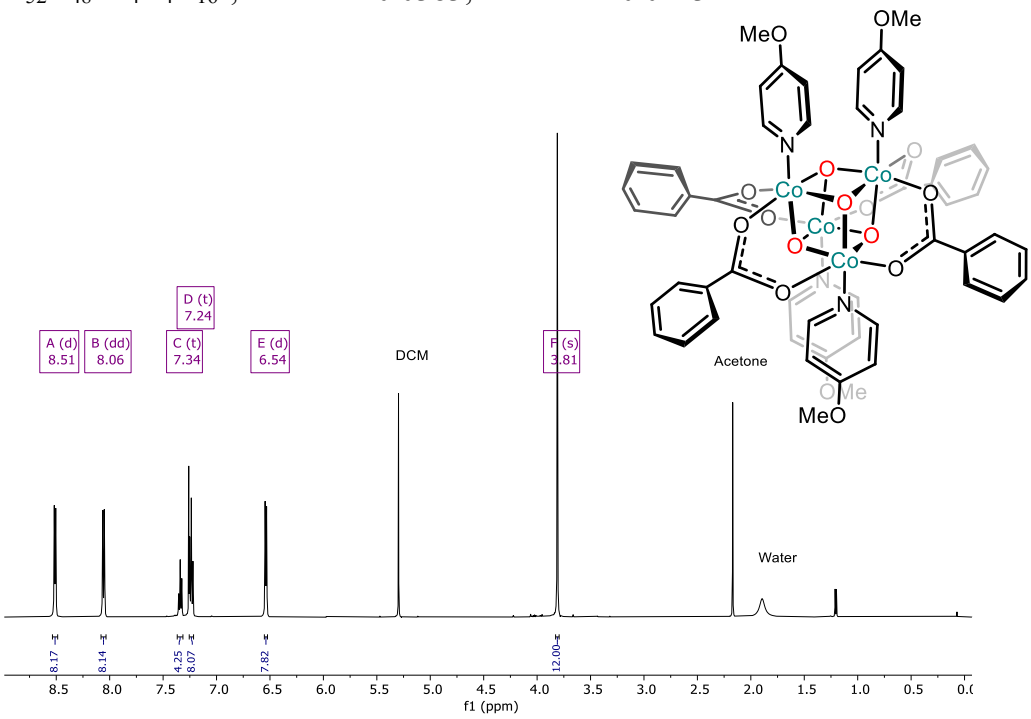


S17. FTIR spectrum of $Co_4O_4(OBz)_4$(4-*tert*-butylpyridine)$_4$ (**Co_4(py-*t*Bu)**).

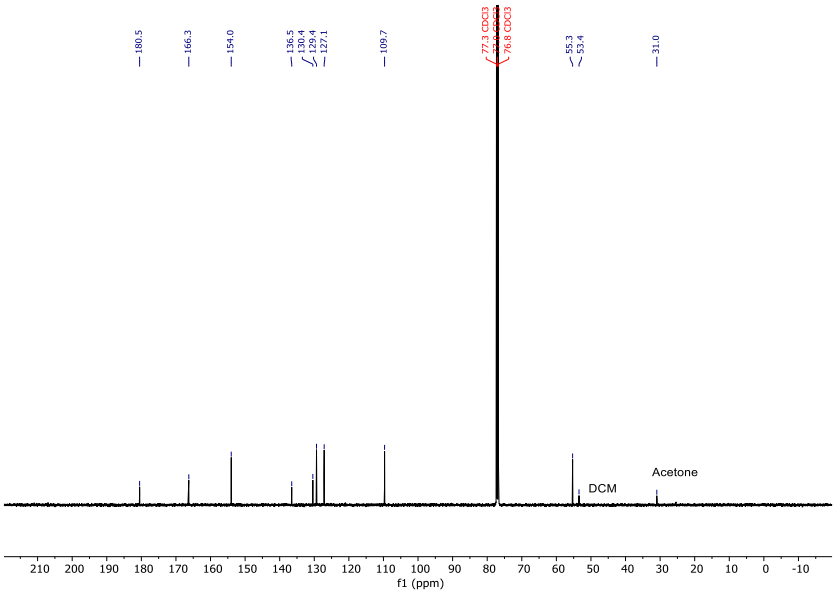


S18. Molar absorptivity values for $Co_4O_4(OBz)_4$(*t*-Bupy)$_4$ in MeCN (**Co_4(py-*t*Bu)**).

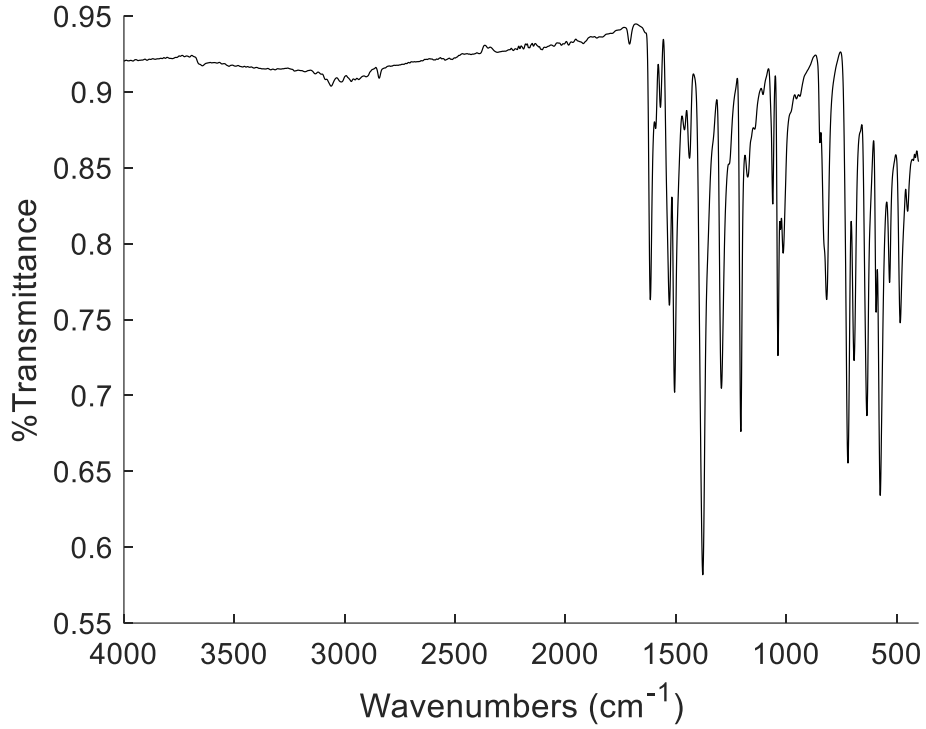
$Co_4O_4(OBz)_4$(4-methoxypyridine)$_4$ (Co_4(py-OMe)): ^{1}H NMR (500 MHz, chloroform-*d*) δ 8.51 (d, *J* = 6.8 Hz, 8H), 8.06 (dd, *J* = 7.0, 1.1 Hz, 8H), 7.34 (t, *J* = 7.3 Hz, 4H), 7.24 (t, *J* = 7.6 Hz, 8H), 6.54 (d, *J* = 6.6 Hz, 8H), 3.81 (s, 12H). ^{13}C{^{1}H} NMR (126 MHz, chloroform-*d*) δ 180.5, 166.3, 154.0, 136.5, 130.4, 129.4, 127.1, 109.7, 55.3. IR (cm^{-1}): 3063 (very weak), 3013 (vw), 2845 (vw), 1709 (w), 1615 (s), 1570 (w), 1529 (s), 1505 (s), 1461 (w), 1436 (m), 1378 (very strong), 1293 (s), 1205 (s), 1174 (w), 1104 (w), 1060 (m), 1037 (s), 1013 (m), 937 (w), 847 (w), 816 (m/s), 721 (s), 692 (s), 634 (s), 592 (m/s), 574 (s), 532 (m), 483 (m), 452 (m). HR-ESI-MS cacl'd for: $C_{52}H_{48}Co_4N_4O_{16}^+$, m/z = 1220.0383; found: 1220.0123 m/z.



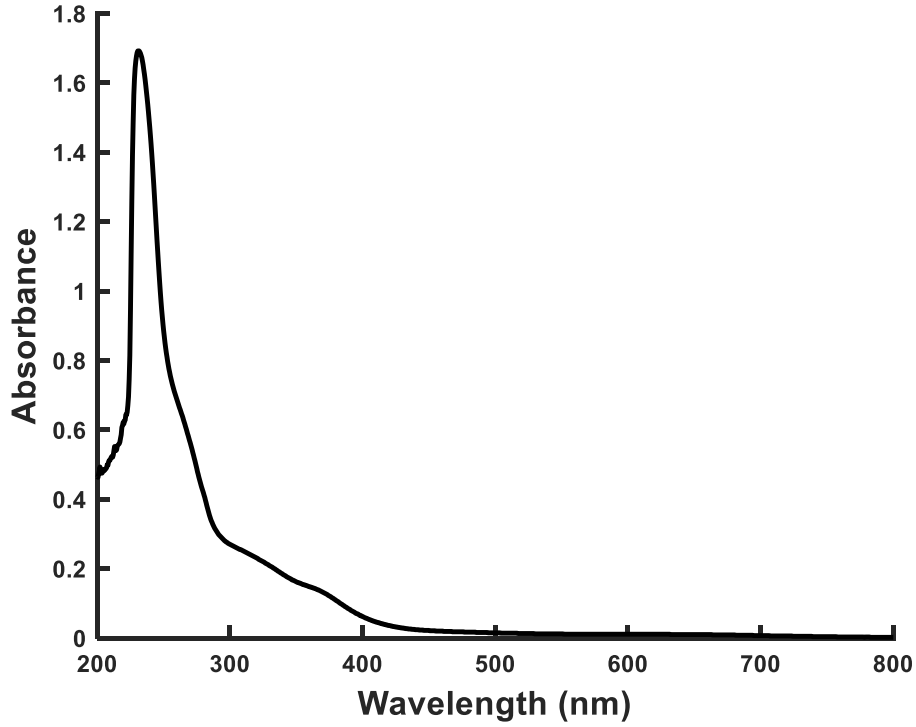
S19. ^{1}H NMR spectrum of $Co_4O_4(OBz)_4$(4-methoxypyridine)$_4$ (**Co_4(py-OMe)**) (chloroform-*d*, 500 MHz).



S20. ^{13}C{^{1}H} NMR spectrum of $Co_4O_4(OBz)_4$(4-methoxypyridine)$_4$ (**Co_4(py-OMe)**). (chloroform-*d*, 126 MHz).

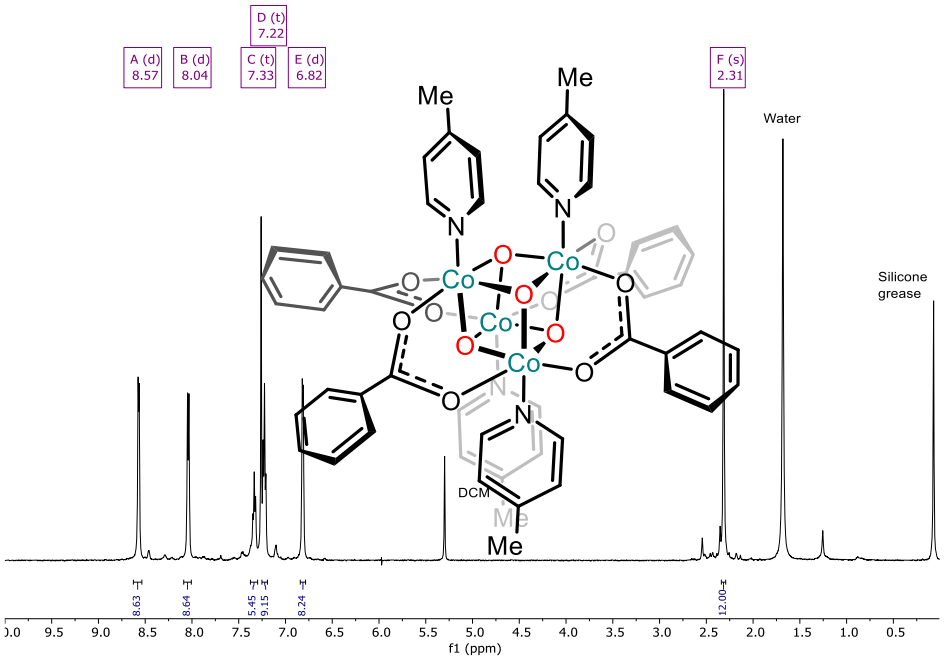


S21. FTIR spectrum of $Co_4O_4(OBz)_4$(4-methoxypyridine)$_4$ (**Co_4(py-OMe)**).

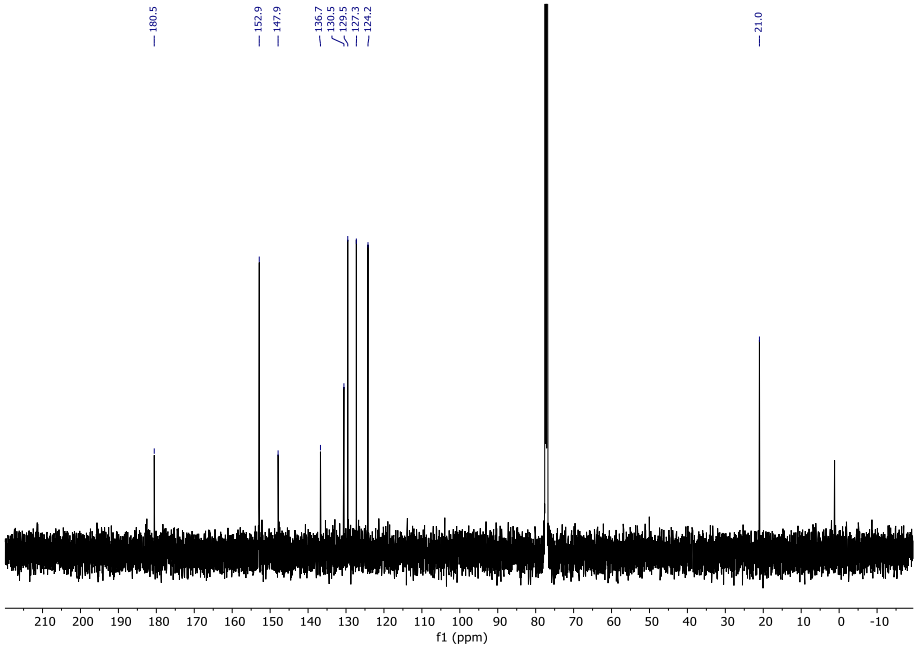


S22. UV-vis spectrum of $Co_4O_4(OBz)_4$(4-methoxypyridine)$_4$ in CH_2Cl_2 from which a molar absorptivity value was approximated.

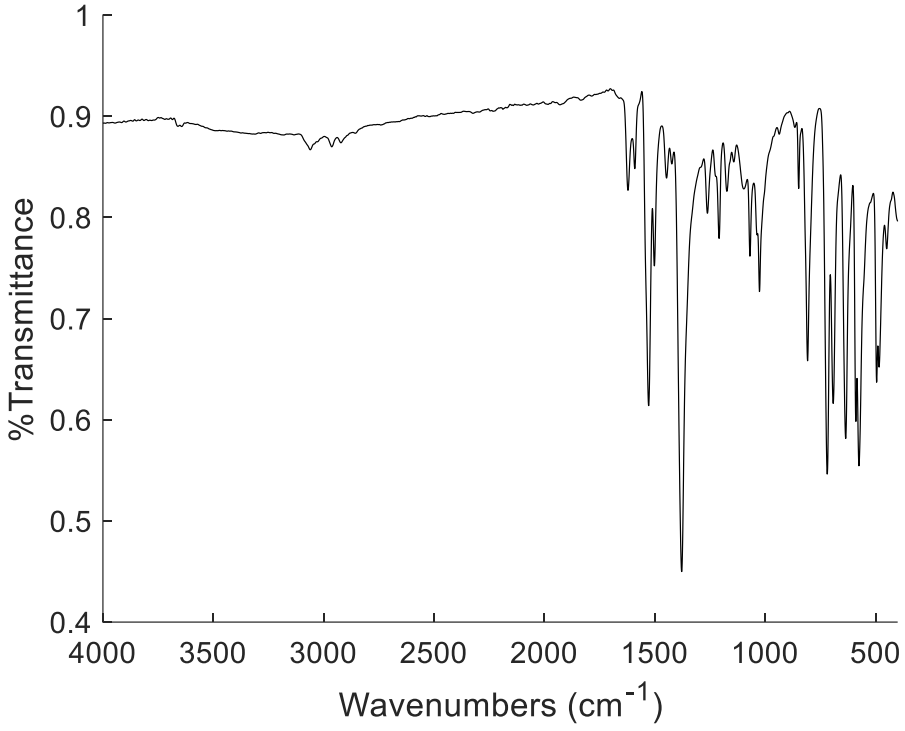
$Co_4O_4(OBz)_4$(4-methylpyridine)$_4$ (Co_4(py-Me)): ^{1}H NMR (500 MHz, chloroform-*d*) δ 8.57 (d, *J* = 5.6 Hz, 8H), 8.04 (d, *J* = 7.6 Hz, 8H), 7.33 (t, *J* = 7.4 Hz, 4H), 7.22 (t, *J* = 7.6 Hz, 8H), 6.82 (d, *J* = 5.6 Hz, 8H), 2.31 (s, 12H). ^{13}C{^{1}H} NMR (126 MHz, chloroform-*d*) δ 180.5, 152.9, 147.9, 136.7, 130.5, 129.5, 127.3, 124.2, 21.0. IR (cm^{-1}): 3059 (w), 2963 (w), 2923 (w), 1621 (w), 1590 (w), 1526 (s), 1502 (m), 1446 (w), 1423 (w), 1378 (very strong), 1261 (m), 1208 (m), 1173 (w), 1608 (m), 1026 (m), 848 (w), 808 (m), 719 (s), 692 (s), 635 (s), 589 (s), 575 (s), 495 (s), 483 (s), 450 (m). HR-ESI-MS calc'd for: $C_{52}H_{48}Co_4N_4O_{12}^+$, m/z = 1156.0586; found: 1156.0413 m/z.



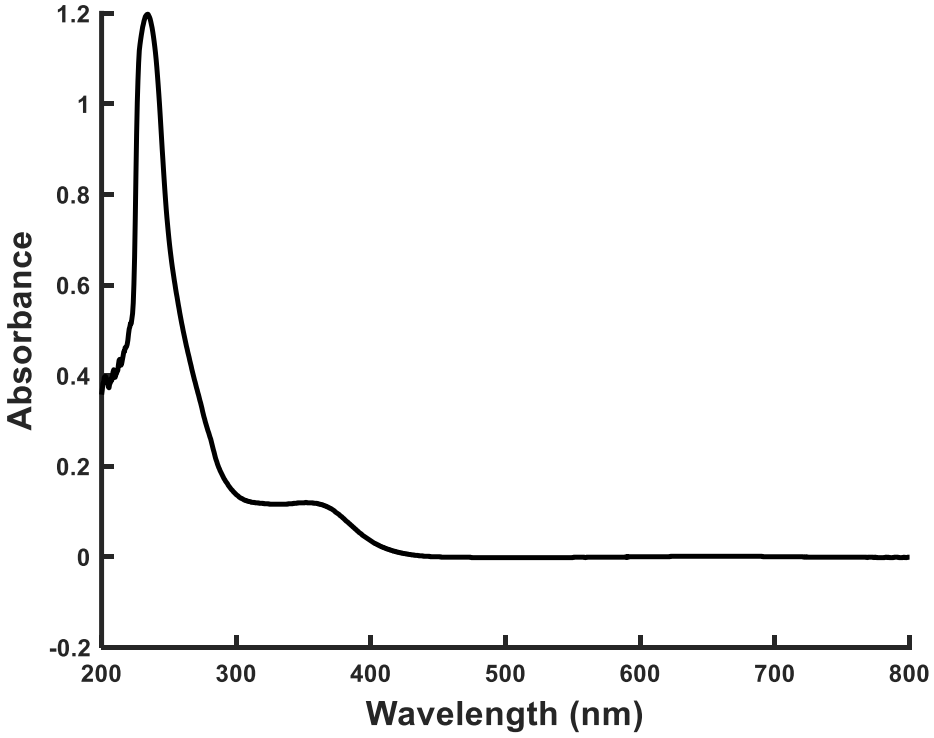
S23. ^{1}H NMR spectrum of $Co_4O_4(OBz)_4$(4-methylpyridine)$_4$ (chloroform-*d*, 500 MHz) (**Co_4(py-Me)**).



S24. ^{13}C{^{1}H} NMR of $Co_4O_4(OBz)_4$(4-methylpyridine)$_4$ (chloroform-*d*, 126 MHz) (**Co_4(py-Me)**).

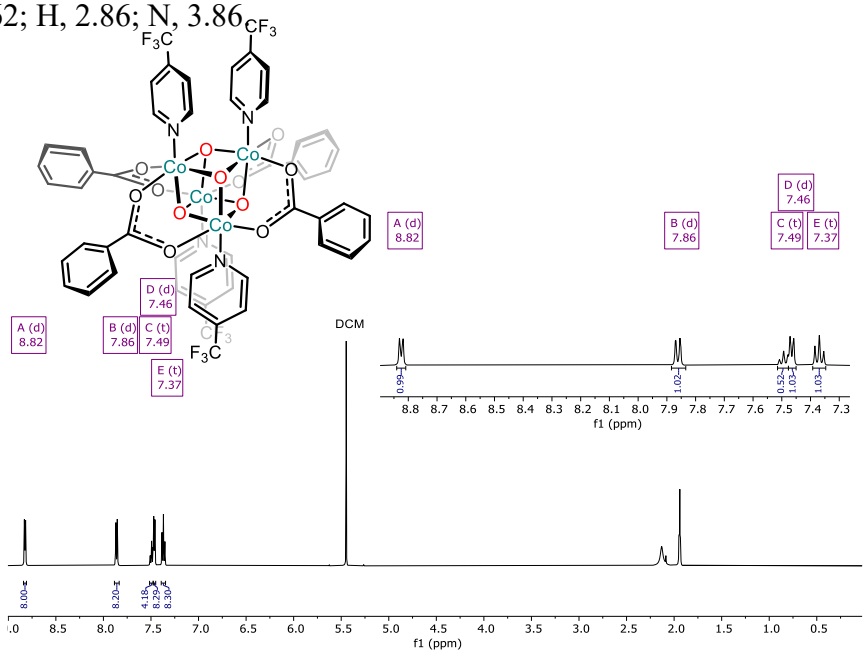


S25. FTIR spectrum of $Co_4O_4(OBz)_4$(4-methylpyridine)$_4$ (**Co_4(py-Me)**).

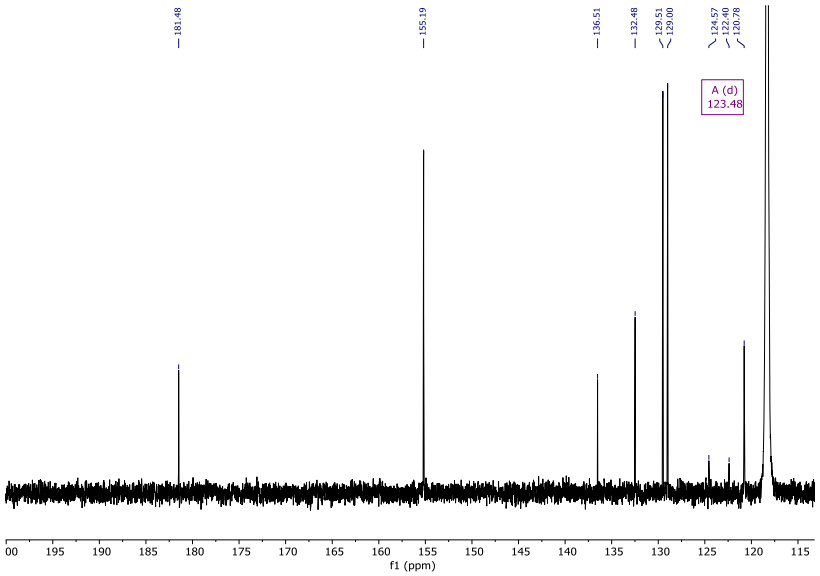


S26. UV-vis spectrum of $Co_4O_4(OBz)_4$(4-methylpyridine)$_4$ in CH_2Cl_2 from which a molar absorptivity value was approximated.

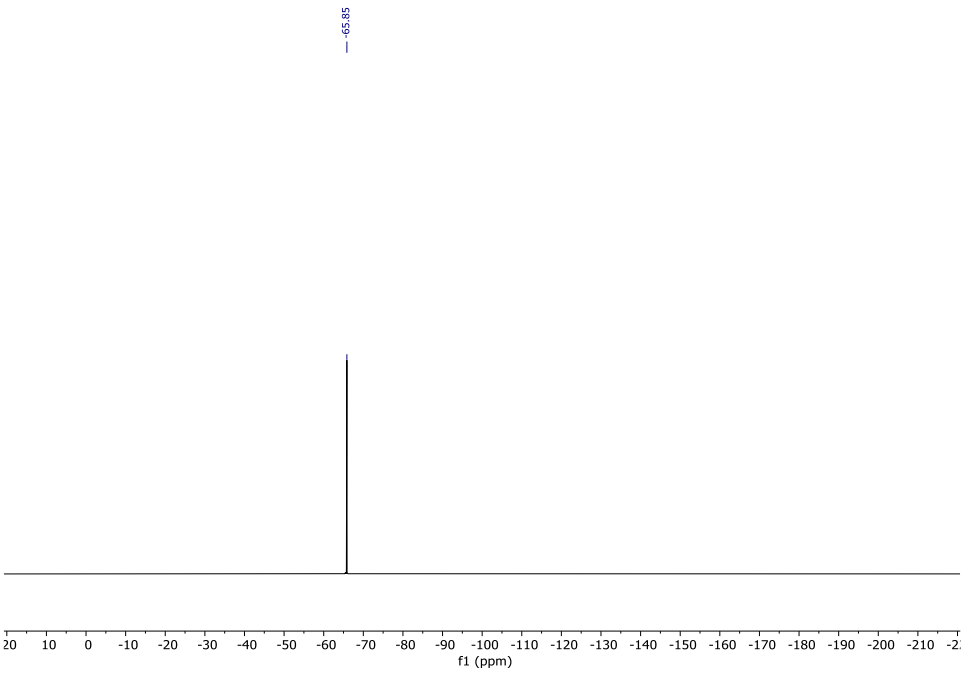
$Co_4O_4(OBz)_4$(4-trifluoromethylpyridine)$_4$ (Co_4(py-CF_3)).: ^{1}H NMR (500 MHz, acetonitrile-d_3) δ 8.82 (d, J = 6.4 Hz, 8H), 7.86 (d, J = 7.5 Hz, 8H), 7.49 (t, J = 7.4 Hz, 4H), 7.46 (d, J = 6.4 Hz, 8H), 7.37 (t, J = 7.8 Hz, 8H). ^{13}C{^{1}H} NMR (126 MHz, acetonitrile-d_3) δ 181.5, 155.2, 136.5, 132.5, 129.5, 129.0, 124.6, 123.4 ($J_{C\text{-}F}$ = 272 Hz), 120.8. ^{19}F{^{1}H} NMR (470 MHz, acetonitrile-d_3) δ –65.85. IR (cm^{-1}): 3064 (w), 3028 (w), 1695 (w), 1623 (very weak), 1601 (w), 1589 (w), 1519 (m), 1451(w), 1421 (m), 1381 (s), 1322 (very strong), 1242 (m), 1175 (s), 1135(s), 1086 (s), 1062 (s), 1026 (m), 937 (m), 836 (s), 812 (m), 788 (m), 714 (s), 696 (s), 679 (s), 634 (s), 606 (s), 573 (s), 492 (s), 450 (m), 402 (m). HR-ESI-MS Calcd for: $C_{52}H_{37}Co_4F_{12}N_4O_{12}$ m/z = 1372.9534; found: 1372.9485 m/z. Anal. Calcd for $C_{52}H_{38}Co_4F_{12}N_4O_{13}$ (• 1 H_2O): C, 44.91; H, 2.75; N, 4.03. Found: C, 44.62; H, 2.86; N, 3.86



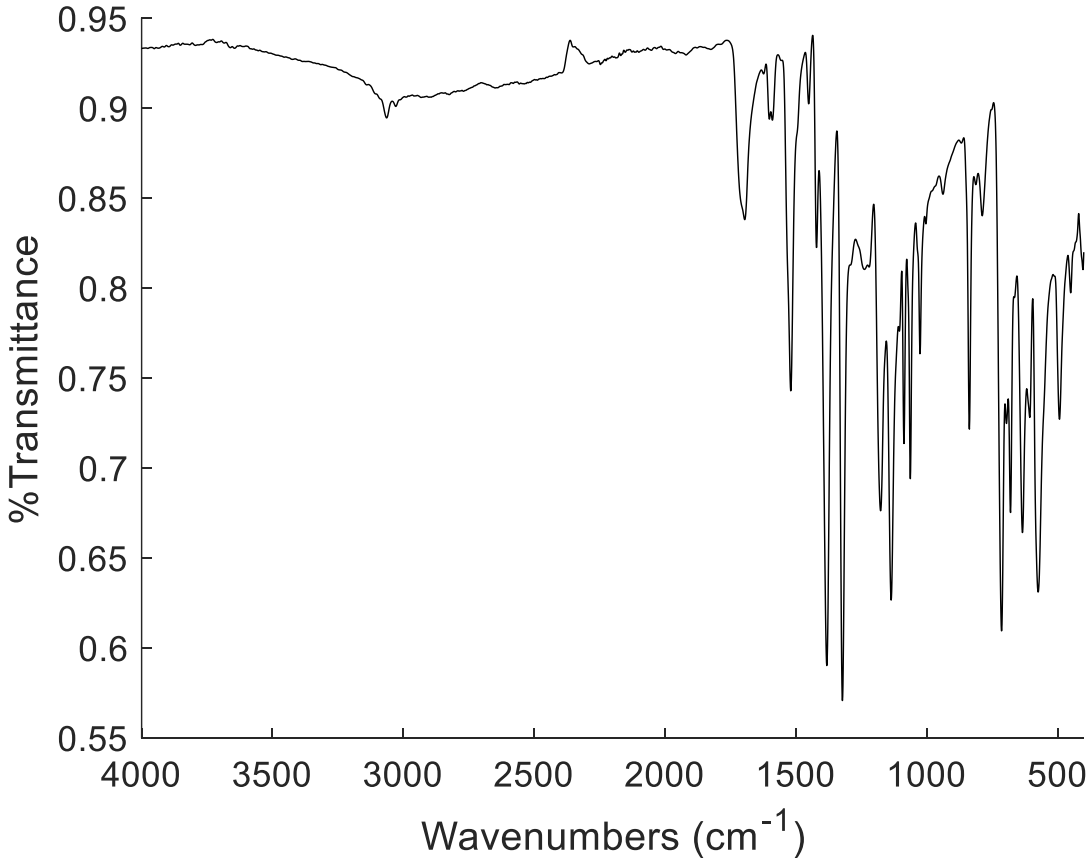
S27. ^{1}H NMR spectrum of $Co_4O_4(OBz)_4$(4-trifluoromethylpyridine)$_4$ (**Co_4(py-CF_3)**). (acetonitrile-d_3, 500 MHz). Inset displays aromatic region with relative integral set to 1.



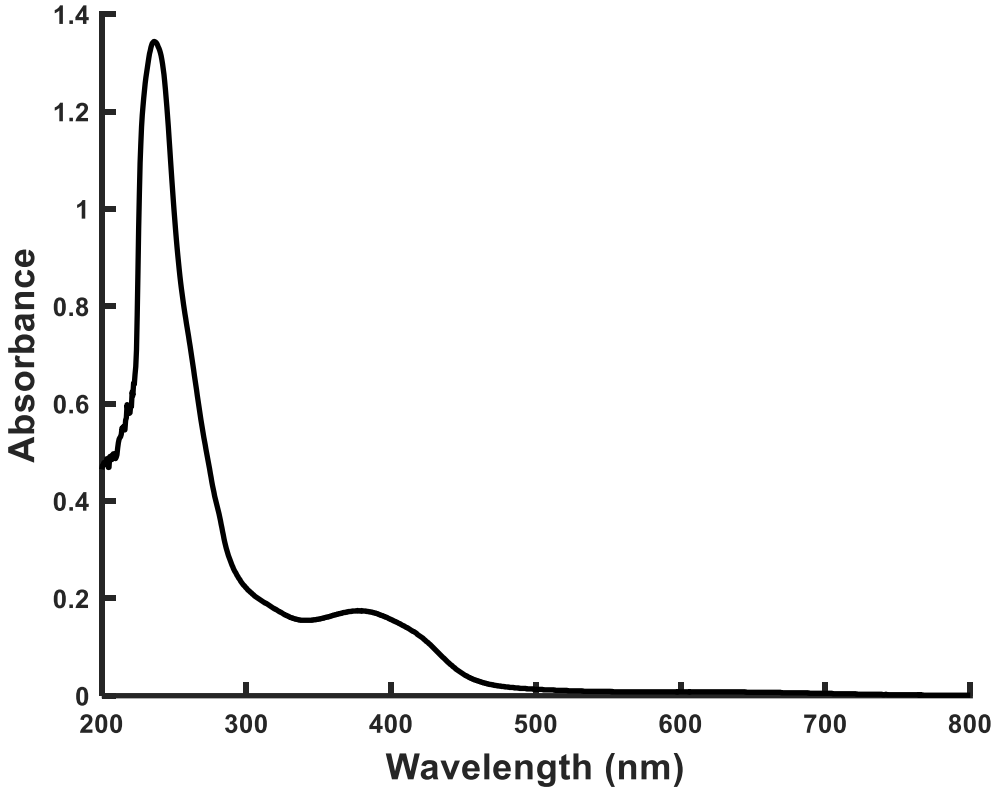
S28. ^{13}C{^{1}H} NMR spectrum of $Co_4O_4(OBz)_4$(4-trifluoromethylpyridine)$_4$ (**Co_4(py-CF_3)**). (acetonitrile-d_3, 126 MHz).



S29. $^{19}F\{^{1}H\}$ NMR spectrum of $Co_4O_4(OBz)_4$(4-trifluoromethylpyridine)$_4$ (**Co_4(py-CF_3)**). (acetonitrile-d_3, 470 MHz).

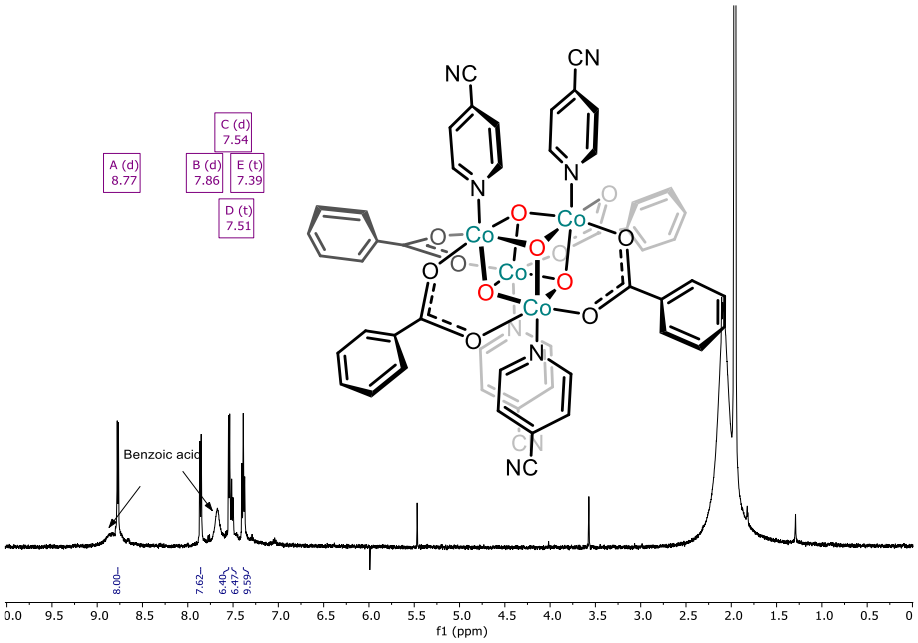


S30. FTIR spectrum of $Co_4O_4(OBz)_4$(4-trifluoromethylpyridine)$_4$ (**Co_4(py-CF_3)**).

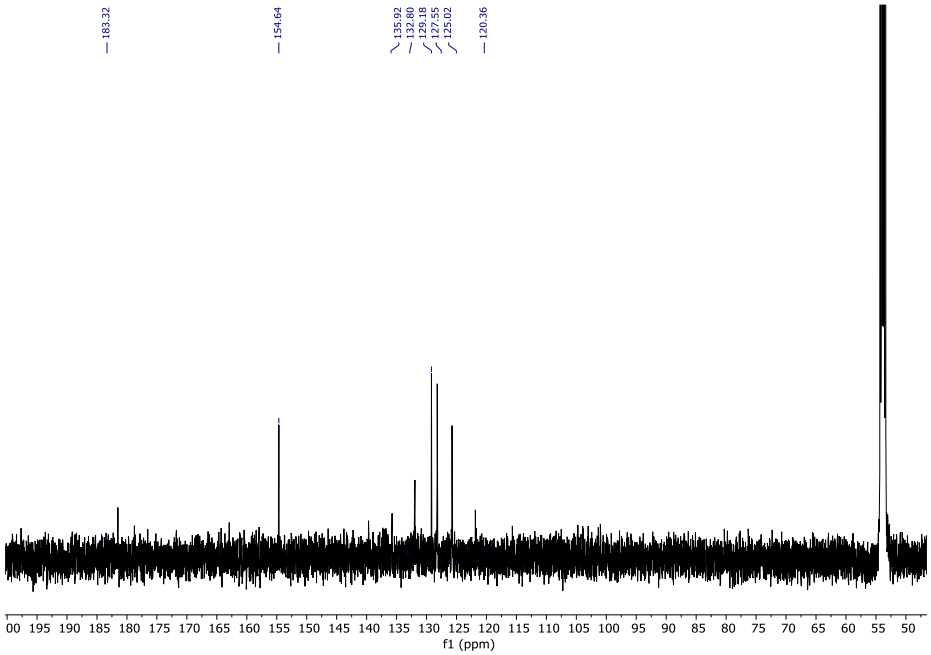


S31. UV-vis spectrum of $Co_4O_4(OBz)_4$(4-trifluoromethylpyridine)$_4$ (**Co_4(py-CF_3)**). in CH_2Cl_2 from which a molar absorptivity value was estimated.

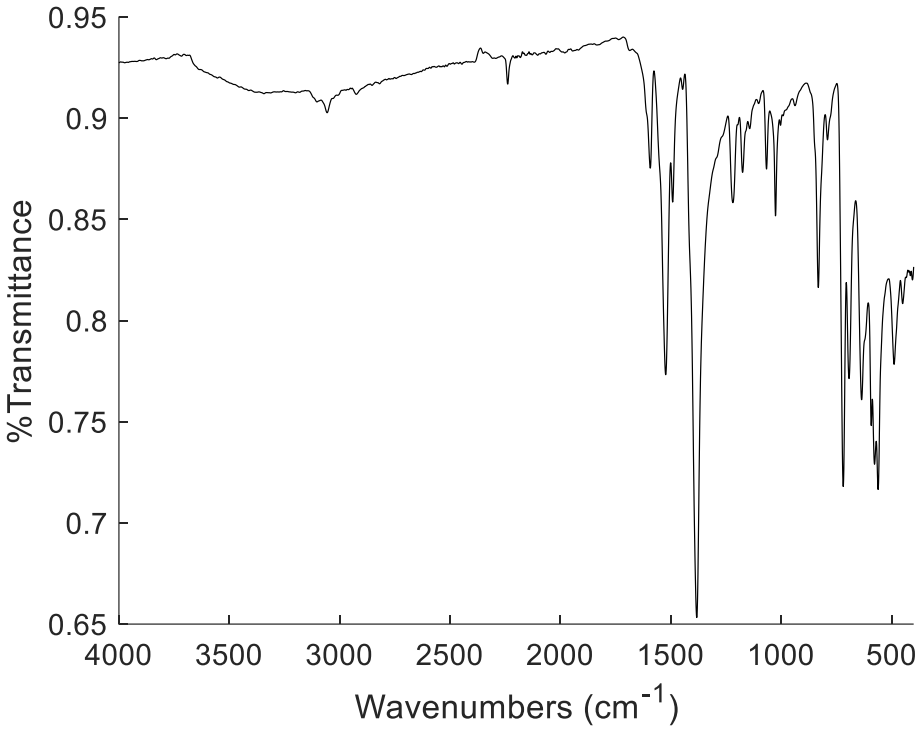
$Co_4O_4(OBz)_4$(4-cyanopyridine)$_4$ (Co_4(py-CN)): ^{1}H NMR (500 MHz, acetonitrile-d_3) δ 8.77 (d, J = 6.6 Hz, 8H), 7.86 (d, J = 7.2 Hz, 8H), 7.54 (d, J = 6.6 Hz, 8H), 7.51 (t, J = 7.5 Hz, 4H), 7.39 (t, J = 7.7 Hz, 8H). ^{13}C{^{1}H} NMR (126 MHz, methylene chloride-d_2) δ 183.3, 154.6, 135.9, 132.8, 129.1, 127.5, 125.0, 120.3. (The cyanide-carbon resonance was not detected). IR (cm^{-1}): 3101 (w), 3055 (w), 2922 (w), 2238 (w), 1593 (m), 1523 (s), 1491 (m), 1446 (w),1381 (s), 1218 (m), 1174 (s), 1142 (w), 1065 (w/m), 1026 (m), 937 (w), 832 (w), 790 (m), 719 (s), 693 (s), 635 (s), 591 (s), 577 (s), 561 (s), 488 (s), 450 (m), 415 (w), 405 (w).



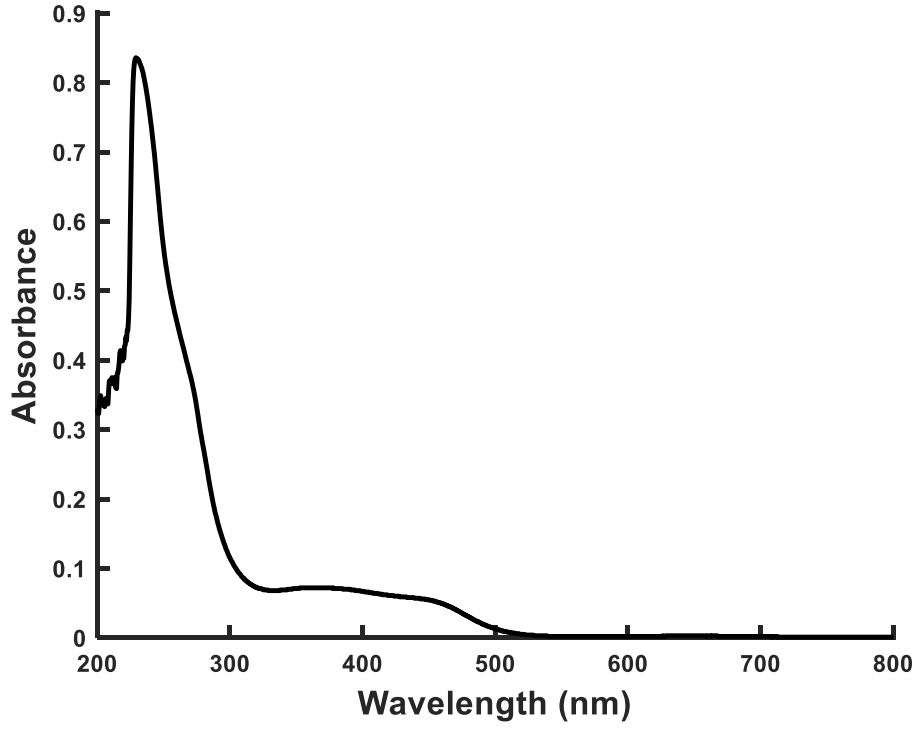
S32. ^{1}H NMR spectrum of $Co_4O_4(OBz)_4$(4-cyanopyridine)$_4$ (**Co_4(py-CN)**) (acetonitrile-d_3, 500 MHz).



S33 ^{13}C{^{1}H} NMR spectrum of $Co_4O_4(OBz)_4$(4-cyanopyridine)$_4$ (**Co_4(py-CN)**) (acetonitrile-d_3, 126 MHz).

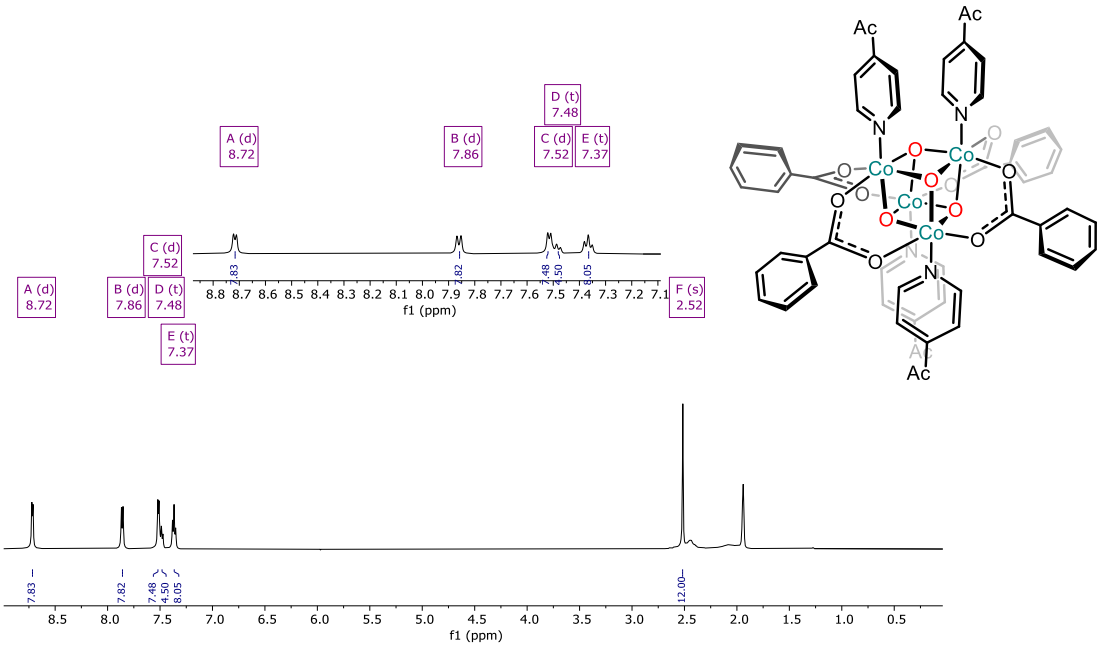


S34. FTIR spectrum of $Co_4O_4(OBz)_4$(4-cyanopyridine)$_4$ (**Co_4(py-CN)**).

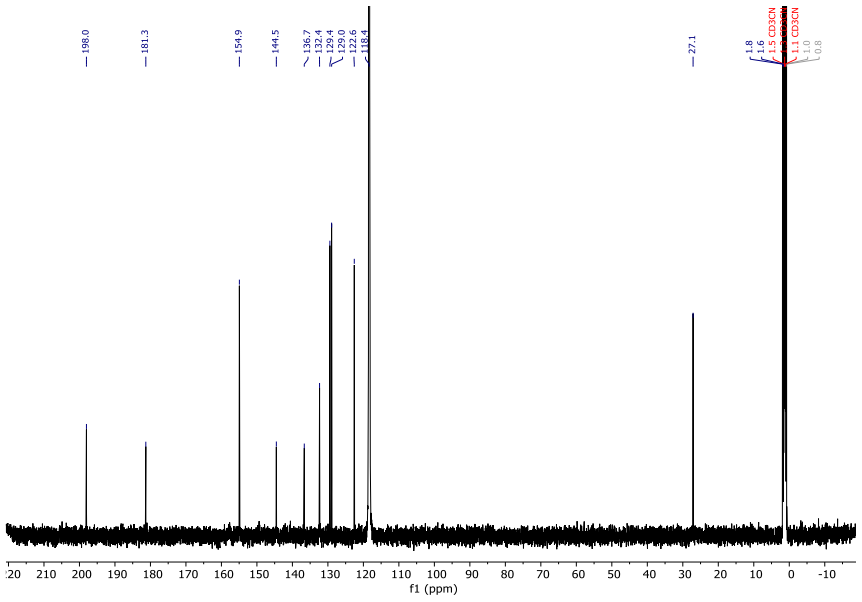


S35. UV-vis spectrum of $Co_4O_4(OBz)_4$(4-cyanopyridine)$_4$ (**Co_4(py-CN)**). in CH_2Cl_2 from which a molar absorptivity value was estimated.

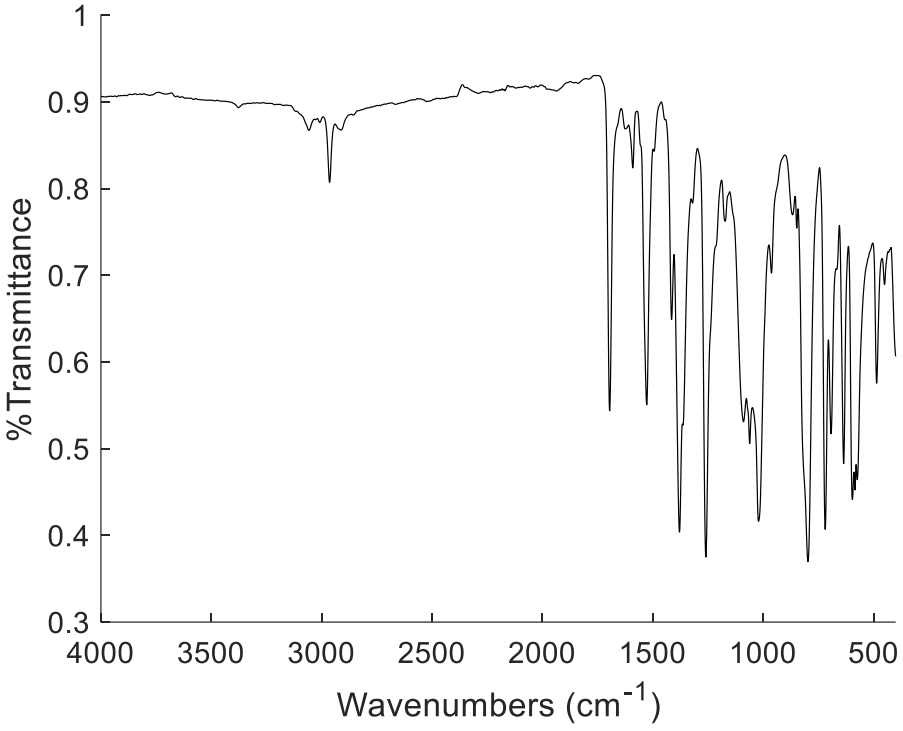
$Co_4O_4(OBz)_4$(4-acetylpyridine)$_4$ (Co_4(py-Ac)): ^{1}H NMR (500 MHz, acetonitrile-d_3) δ 8.72 (d, J = 5.7 Hz, 8H), 7.86 (d, J = 7.7 Hz, 8H), 7.52 (d, J = 5.8 Hz, 8H), 7.48 (t, J = 7.4 Hz, 4H), 7.37 (t, J = 7.6 Hz, 8H), 2.52 (s, 12H). ^{13}C{^{1}H} NMR (126 MHz, acetonitrile-d_3) δ 198.0, 181.3, 154.9, 144.5, 136.7, 132.4, 129.4, 129.0, 122.6, 27.1. IR (cm^{-1}): 3059 (w), 30009 (w), 2963 (w), 1695 (s), 1624 (w), 1590 (m), 1527 (s), 1415 (s), 1379 (vs), 1320 (m), (1259 (vs), 1173 (m), 1089 (s), 1061 (s), 1021 (vs), 962 (m), 867 (w/m), 847 (w/m), 797 (vs), 719 (vs), 692 (vs), 635 (s), 595 (vs), 585 (vs), 573 (vs). HR-ESI-MS Calcd for: $C_{56}H_{48}Co_4N_4O_{16}$ m/z = 1268.0383; found: 1268.0263 m/z. Anal. Calcd for $C_{56}H_{48}Co_4N_4O_{16}$ (• 4-Acpy): C, 54.44; H, 3.99; N,5.04. Found: C, 54.93; H, 4.17; N, 5.07 (consistent with ^{1}H NMR spectrum following prolonged storage).



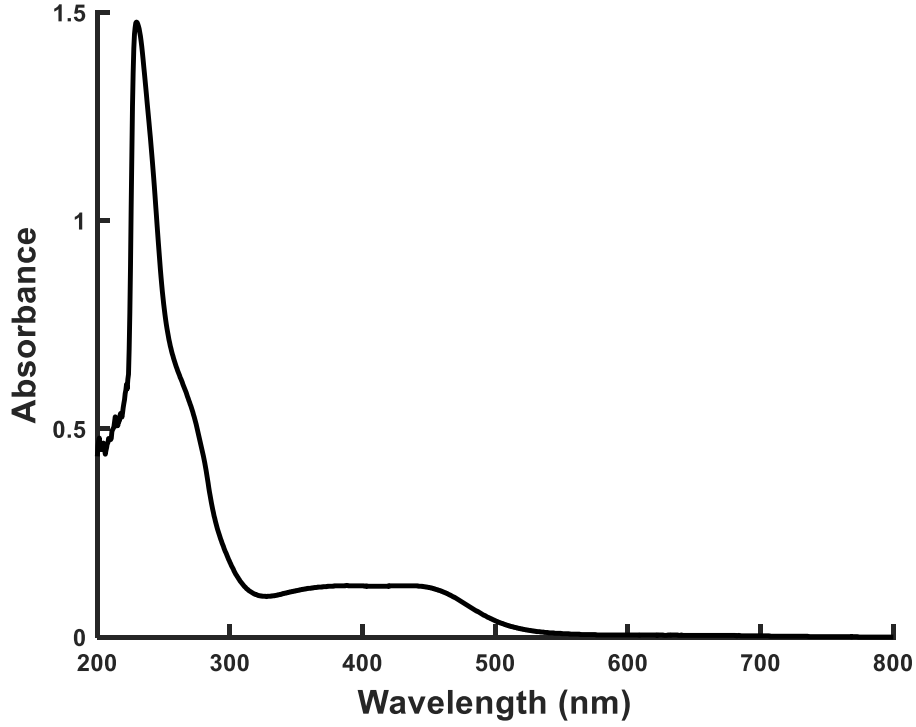
S36. ^{1}H NMR spectrum of $Co_4O_4(OBz)_4$(4-acetylpyridine)$_4$ (**Co_4(py-Ac)**). (500 MHz, acetonitrile-d_3).



S37. ^{13}C{^{1}H} NMR spectrum of $Co_4O_4(OBz)_4$(4-acetylpyridine)$_4$ (**Co_4(py-Ac)**) (acetonitrile-d_3, 126 MHz).



S38. FTIR spectrum of $Co_4O_4(OBz)_4$(4-acetylpyridine)$_4$ (**Co_4(py-Ac)**).



S39. UV-vis spectrum of $Co_4O_4(OBz)_4$(4-acetylpyridine)$_4$ in CH_2Cl_2 from which a molar absorptivity value was estimated.

p-Benzoate Substituted *p-tert*butylpyridine Cubanes

General Comments

All *para*-R-benzoate (R = NO_2, CN, Cl, Br, Ph, Me, *t*Bu, OMe) complexes were synthesized by way of ligand exchange reactions between the $Co_4O_4(OAc)_4$(*t*-Bupy)$_4$ cubane and the respective benzoic acid under forcing conditions. In brief, acetic acid is distilled from the cubane solution in the presence of an excess of ligand (10-40 equiv. depending on the pK_a of the substituted benzoic acid) at elevated temperatures and with short reaction times. Under these conditions, cubane decomposition and the retro ligand substitution reaction are minimized. For the substituted benzoic acids with pK_a values within 0.5 units of acetic acid, a larger excess was required. HR-ESI-MS data was not collected for most of the products.

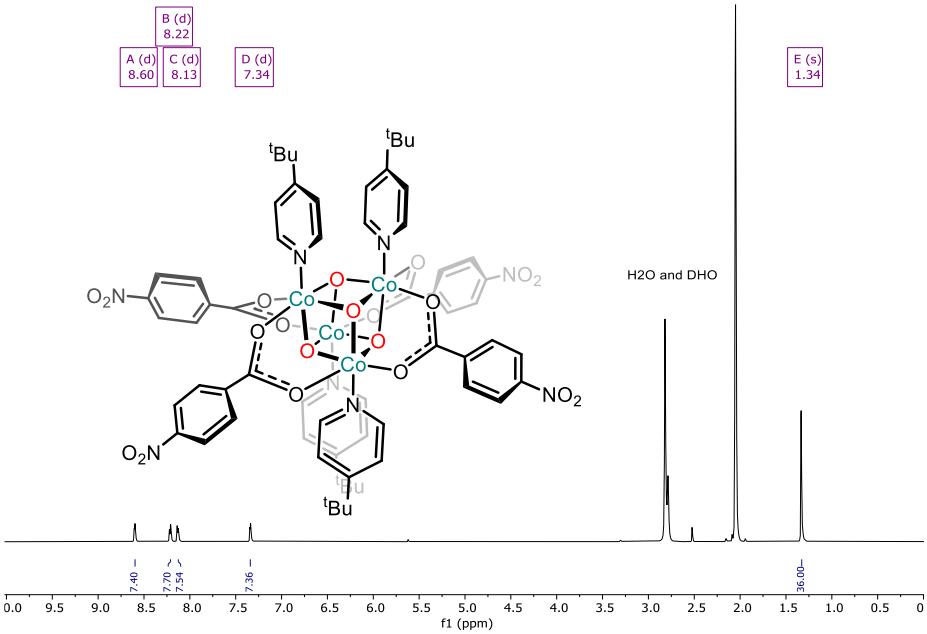
General Synthetic Procedure

$Co_4(O_4)(OAc)_4$(*t*-Bupy)$_4$ (0.500 g, 0.465 mmol, 1.00 equiv.) was dissolved in a 5 mL dram vial using DMSO (8 mL) and transferred to a 50 mL round-bottom flask containing a stir bar in an oil bath. While stirring, the substituted benzoic acid [(*ca*. 1.5 g (depending on substituent), 9.0 mmol, 19 equiv.) {for weaker acids (R = Me, *t*Bu, OMe; 18.4 mmol, 40 equiv)}] was added as a solid in one portion and rinsed into the flask with DMSO (5 mL). A short path vacuum distillation head with a 25 mL receiving flask was attached, the vacuum side-arm was connected to a Schlenk line, and the receiving flask was cooled in an ice water bath. While stirring, the solution was heated to 90 °C. After 5 min, vacuum was **carefully** applied until the solution began to boil, then the stopcock was left partially open to slowly distill DMSO and acetic acid into the receiving flask. Once the receiving flask condensed *ca*. 6 mL of DMSO (15-30 min), atmospheric pressure was reestablished, and the short path distillation head was removed so that DMSO (6 mL) could be added to the reaction mixture. The reactions were monitored by TLC (5% MeOH:DCM), and at this point an aliquot was taken for analysis. The distillation head was reattached, and vacuum was carefully reapplied. This process was repeated until a single new spot was observed by TLC, 1-2 h. The flask was removed from the oil bath, atmospheric pressure was reestablished, and the short path distillation head was removed. When the solution cooled to ambient temperature, the solution was transferred to an Erlenmeyer flask (250 mL), and saturated aqueous sodium bicarbonate (30 mL) was added. The residual material from the reaction flask was rinsed from the round-bottom flask with CH_2Cl_2 (50 mL) into the same Erlenmeyer flask. The Erlenmeyer flask was then swirled vigorously until the resulting effervescence dissipated. The solution was then transferred to a separatory funnel. The organic phase was separated, washed with brine (30 mL), separated, and then washed with saturated sodium bicarbonate (20 mL) ***caution: release of CO_2 may cause pressure buildup in the separatory funnel!**** The organic phase was separated, dried over $MgSO_4$, and gravity filtered through filter paper into a 200 mL round-bottom flask. The solvent was removed with a rotary evaporator resulting in the respective substituted cubane. To further purify the 4-*tert*butylbenzoate cubane, it was dissolved in pentane and filtered through a fine frit or a glass wool plug, and the solvent was removed with a rotary evaporator.

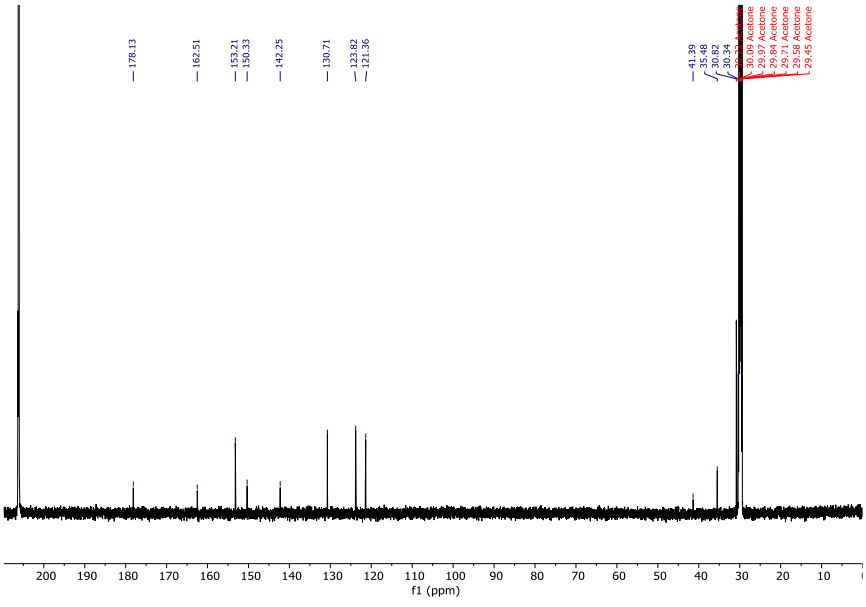
Co_4(OBz –NO_2 = 325 mg, 46%; –**CN** = 395 mg, 60%; –**Cl** =380 mg, 56%; –**Br** =297, 39%; –**Ph** =283 mg, 40%, –**Me** =80 mg, 12%*; –***t*Bu** =356 mg, 49%; –**OMe** = 322 mg, 48%**)**.

*XRD quality crystals of most of these cubanes can be grown from CH_2Cl_2 layered with pentane. 4-Me-Benzoate was crystallized from CH_2Cl_2 layered with pentane as a part of the purification (in low yield).

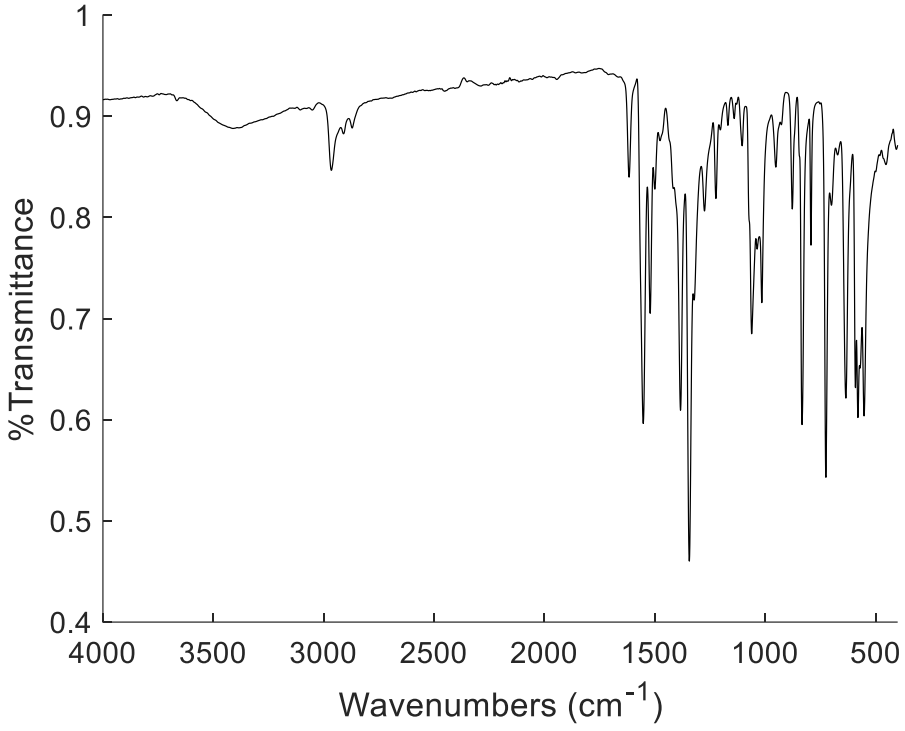
Co_4O_4(4-nitrobenzoate)$_4$(*t*-Bupy)$_4$ (Co_4(OBz-NO_2)): ^{1}H NMR (600 MHz, acetone-d_6) δ 8.60 (d, J = 5.5 Hz, 8H), 8.22 (d, J = 8.1 Hz, 8H), 8.13 (d, J = 7.9 Hz, 8H), 7.34 (d, J = 5.2 Hz, 8H), 1.34 (s, 36H). ^{13}C{^{1}H} NMR (151 MHz, acetone-d_6) δ 178.1, 162.5, 153.2, 150.3, 142.2, 130.7, 123.8, 121.4, 35.5, 30.8. IR (cm^{-1}): 2965 (m), 2909 (w), 2871 (w), 1616 (m), 1552 (s), 1520 (s), 1499 (m), 1477 (w), 1383 (s), 1343 (very strong), 1322 (s), 1274 (m), 1222 (m), 1168 (w), 1139 (w), 1104 (w/m), 1060 (s), 1036 (m/s), 1015 (s), 951 (m), 927 (s), 877 (m), 833 (s), 792 (m), 725 (s), 700 (m), 671 (w), 634 (s), 590 (s), 580 (s), 570 (s), 552 (s), 454 (w/m), 404 (w). Anal. Calcd for $C_{56}H_{56}Co_4N_4O_{20}$ (• 4 H_2O): C, 48.74; H, 4.86; N, 7.11. Found: C, 48.37; H, 4.73; N, 6.85.



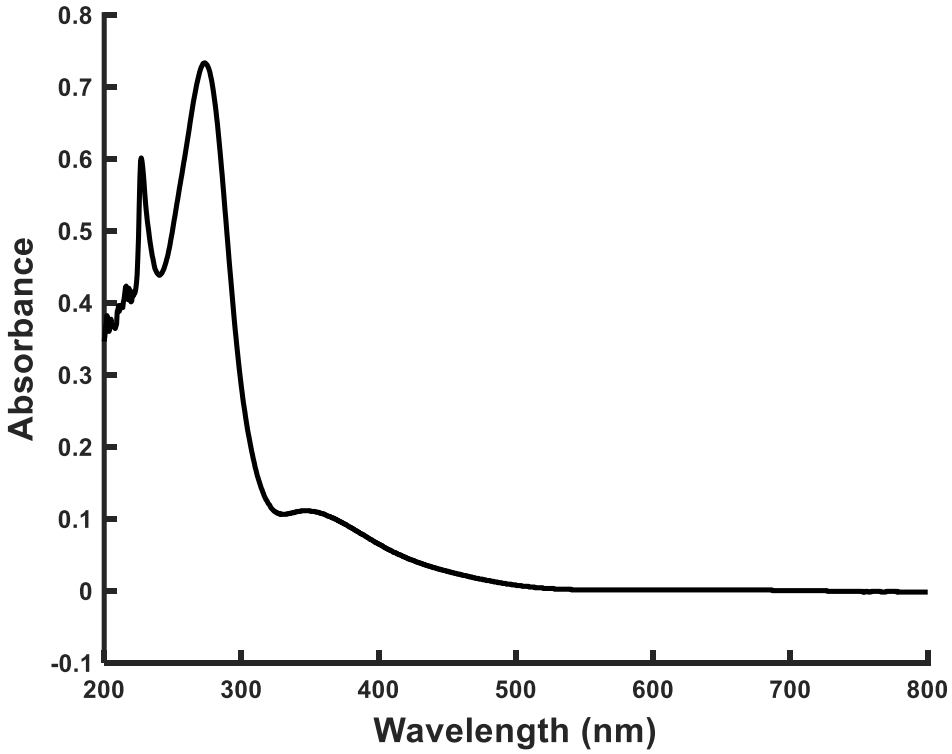
S40. ^{1}H NMR spectrum of Co_4O_4(4-nitrobenzoate)$_4$(*t*-Bupy)$_4$ (**Co_4(OBz-NO_2)**) (acetone-d_6, 600 MHz).



S41. ^{13}C{^{1}H} NMR spectrum of Co_4O_4(4-nitrobenzoate)$_4$(*t*-Bupy)$_4$ (**Co_4(OBz-NO_2)**) (acetone-d_6, 151 MHz).

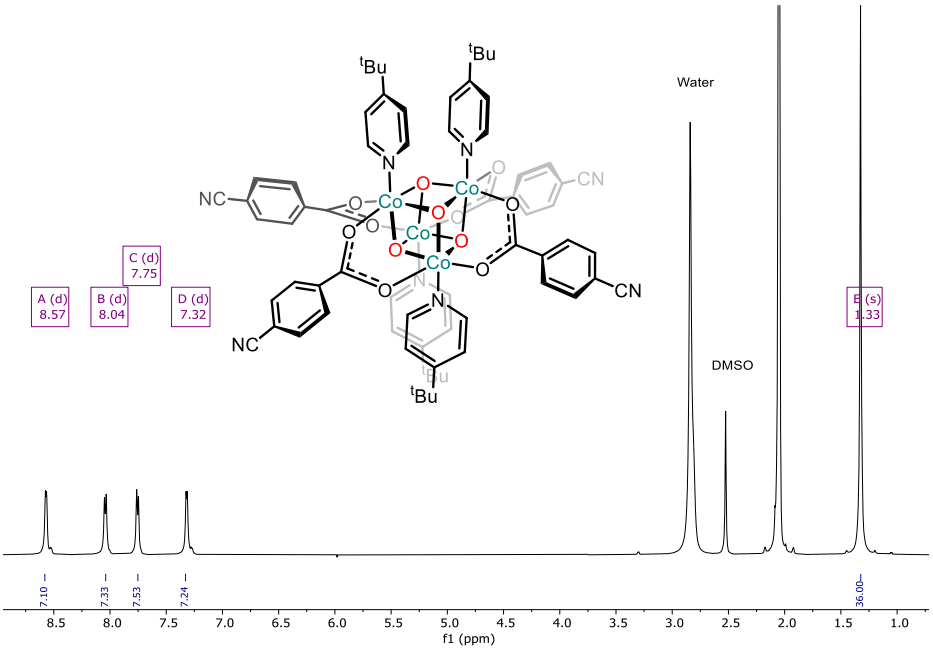


S42. FTIR spectrum of Co_4O_4(4-nitrobenzoate)$_4$(*t*-Bupy)$_4$ (**Co_4(OBz-NO_2)**)

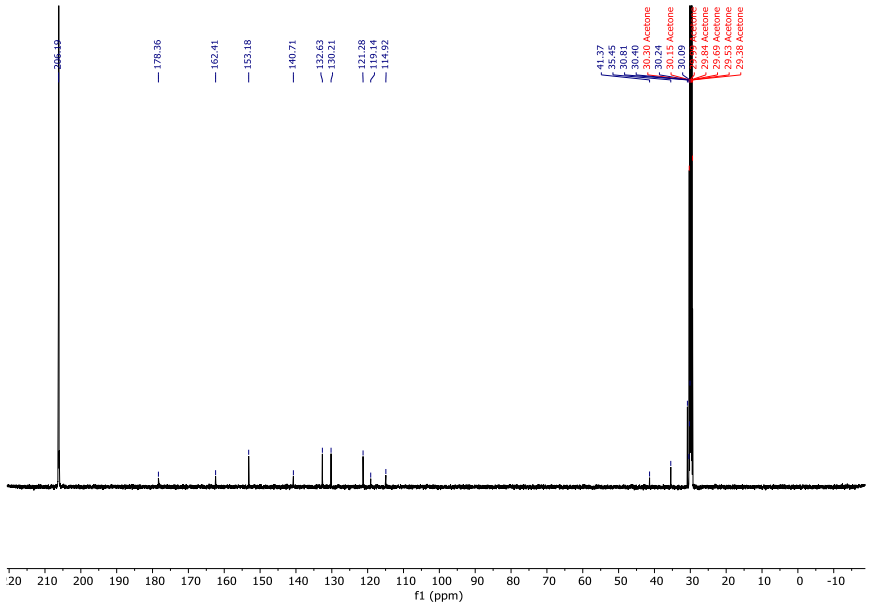


S43. UV-vis spectrum of Co_4O_4(4-nitrobenzoate)$_4$(*t*-Bupy)$_4$ in CH_2Cl_2 from which a molar absorptivity value was estimated.

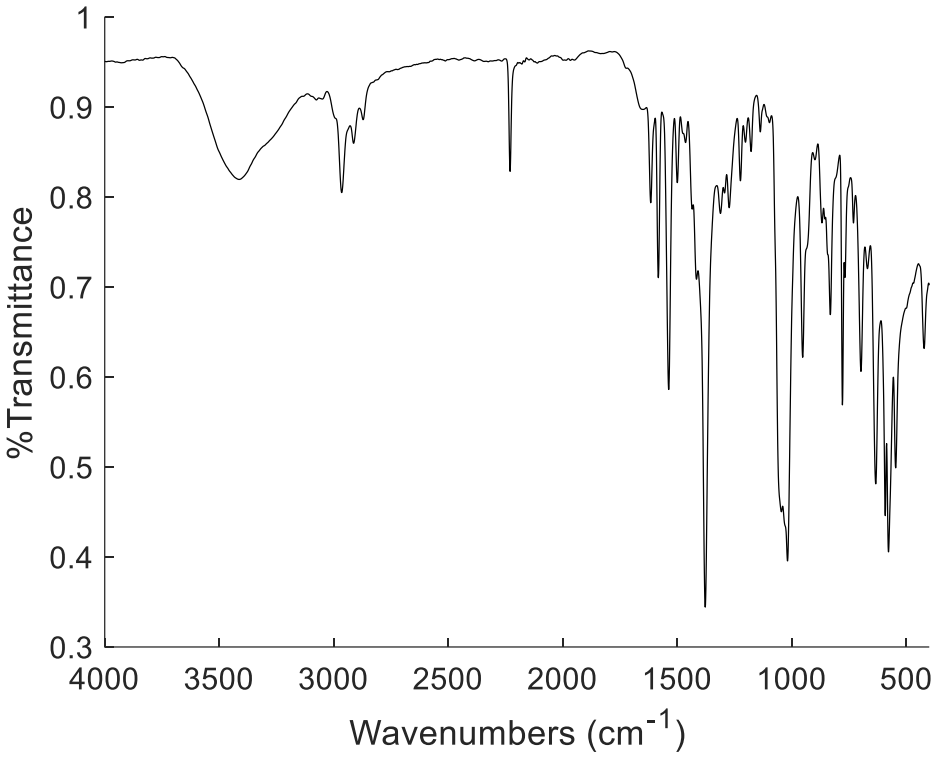
Co_4O_4(4-cyanobenzoate)$_4$(*t*-Bupy)$_4$ (Co_4(OBz-CN)): ^{1}H NMR (500 MHz, acetone-d_6) δ 8.57 (d, J = 5.8 Hz, 8H), 8.04 (d, J = 8.0 Hz, 8H), 7.75 (d, J = 8.1 Hz, 8H), 7.32 (d, J = 6.0 Hz, 8H), 1.33 (s, 36H). ^{13}C{^{1}H} NMR (126 MHz, acetone-d_6) δ 178.4, 162.4, 153.2, 140.7, 132.6, 130.2, 121.3, 119.1, 114.9, 35.5, 30.8. IR (cm^{-1}): [trace water at 3410 (hygroscopic sample)]; 2964 (w/m), 2912 (w), 2873 (w), 2229 (w/m), 1614 (w/m), 1582 (m), 1537(s), 1499 (w), 1462 (w), 1346 (w, sh), 1415 (m, sh), 1378 (s), 1311 (m), 1273 (m), 1224 (w), 1201 (w), 1177 (w), 1137 (w), 1097 (w), 1046 (s, sh), 1018 (s), 952 (m), 898 (w), 868 (w/m), 832 (m), 779 (s), 767 (m), 730 (w), 698 (m/s), 670 (m), 633 (s), 591 (s), 577 (s), 545 (s), 423 (m). Anal. Calcd for $C_{68}H_{76}Co_4N_8O_{16}$ (• 4 H_2O): C, 54.55; H, 5.12; N, 7.48. Found: C, 52.63; H, 5.06; N 7.01.



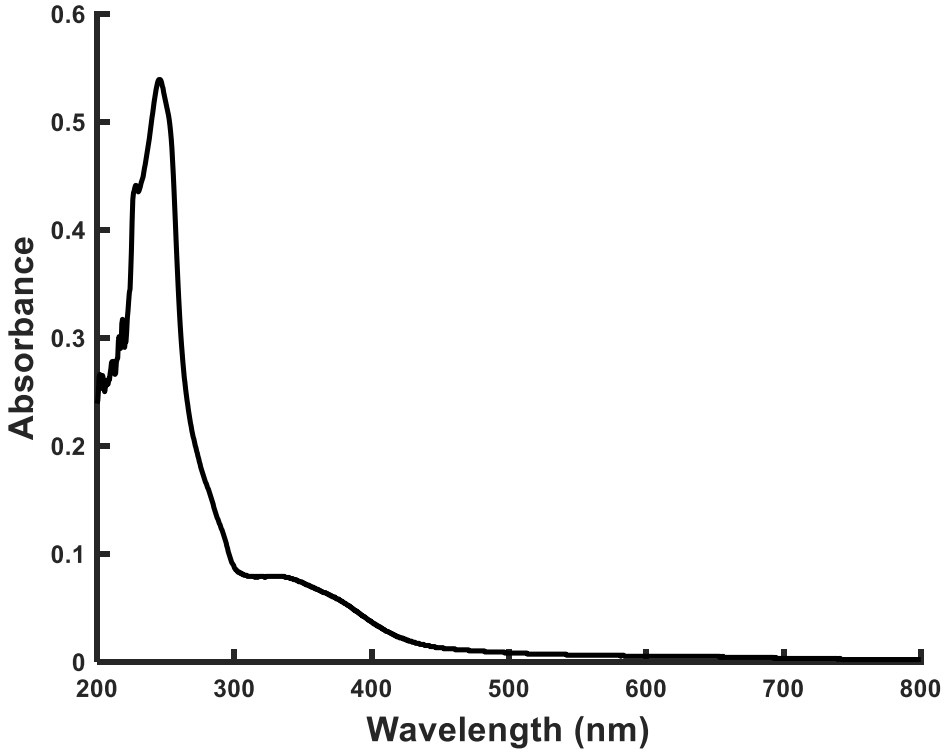
S44. ^{1}H NMR spectrum of Co_4O_4(4-cyanobenzoate)$_4$(*t*-Bupy)$_4$ (**Co_4(OBz-CN)**) (acetone-d_6, 500 MHz).



S45. ^{13}C{^{1}H} NMR spectrum of Co_4O_4(4-cyanobenzoate)$_4$(*t*-Bupy)$_4$ (acetone-d_6, 126 MHz).

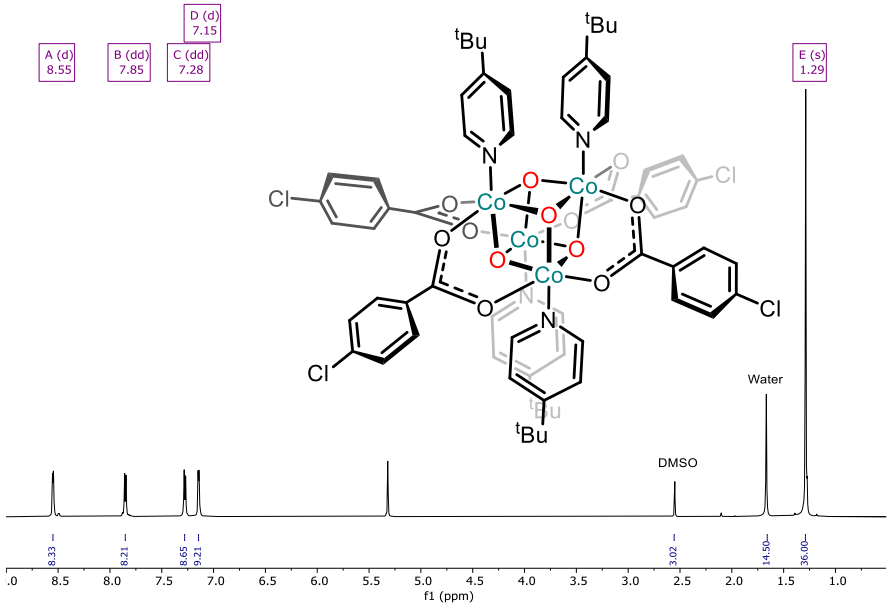


S46. FTIR spectrum of Co_4O_4(4-cyanobenzoate)$_4$(*t*-Bupy)$_4$ (**Co_4(OBz-CN)**).

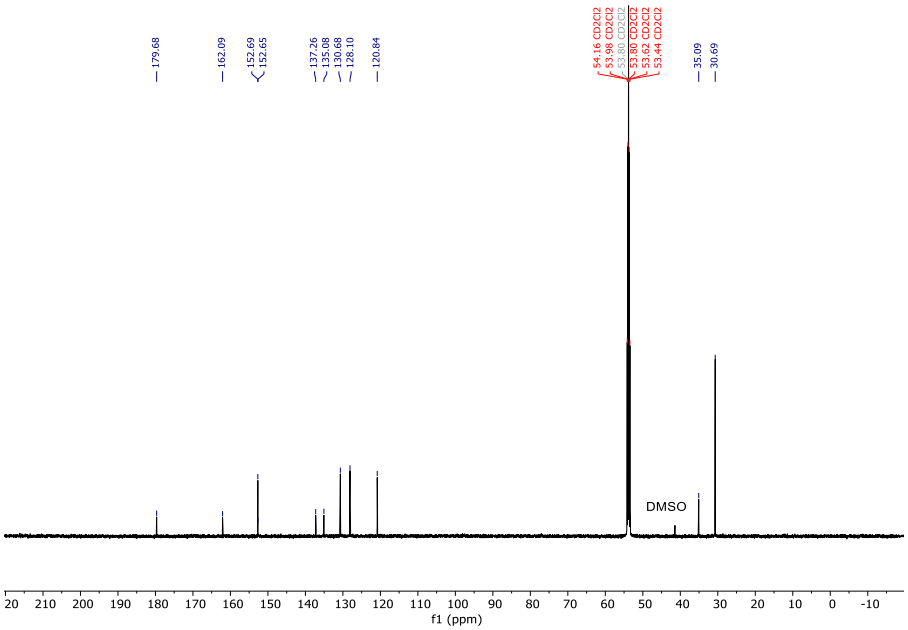


S47. UV-vis spectrum of Co_4O_4(4-cyanobenzoate)$_4$(*t*-Bupy)$_4$ in CH_2Cl_2 from which a molar absorptivity value was estimated.

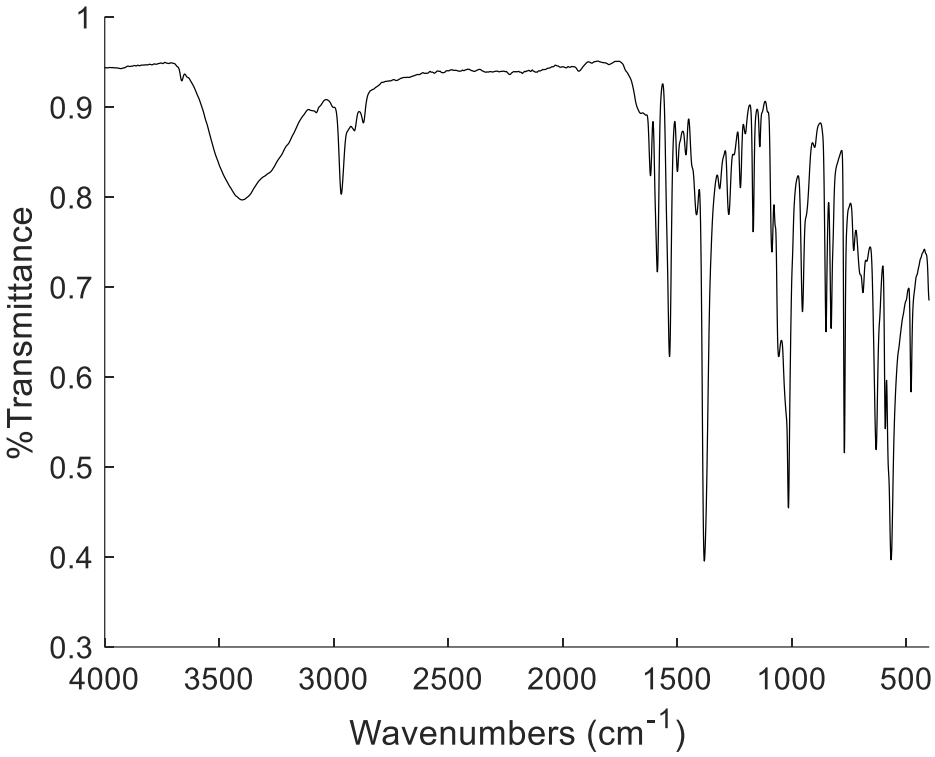
Co_4O_4(4-chlorobenzoate)$_4$(*t*-Bupy)$_4$ (Co_4(OBz-Cl)): ^{1}H NMR (600 MHz, methylene chloride-d_2) δ 8.55 (d, J = 4.6 Hz, 8H), 7.85 (dd, J = 8.6, 2.3 Hz, 8H), 7.28 (dd, J = 8.6, 2.3 Hz, 8H), 7.15 (d, J = 4.7 Hz, 8H), 1.29 (s, 36H). ^{13}C{^{1}H} NMR (151 MHz, methylene chloride-d_2) δ 179.7, 162.1, 152.7 (d, J = 5.3 Hz), 137.3, 135.1, 130.7, 128.1, 120.8, 35.1, 30.7. IR (cm^{-1}): [trace water at 3400 (hygroscopic sample)]; 2966 (w/m), 2919 (w), 2871 (w), 1617 (w/m), 1587 (m), 1533 (s), 1499 (w/m), 1462 (w), 1417 (m), 1381 (very strong), 1315 (m), 1274 (m), 1224 (m), 1203 (w), 1168 (m), 1139 (w), 1086 (m), 1056 (s), 1014 (s), 953 (m), 898 (w), 850 (s), 828 (s), 770 (s), 729 (m), 689 (m), 632 (s), 591 (s), 566 (s), 479 (s). Anal. Calcd for $C_{64}H_{76}Cl_4Co_4N_4O_{16}$ (• 4 H_2O): C, 50.08; H, 4.99; N, 3.65. Found: C, 49.77; H, 5.18; N, 3.54.



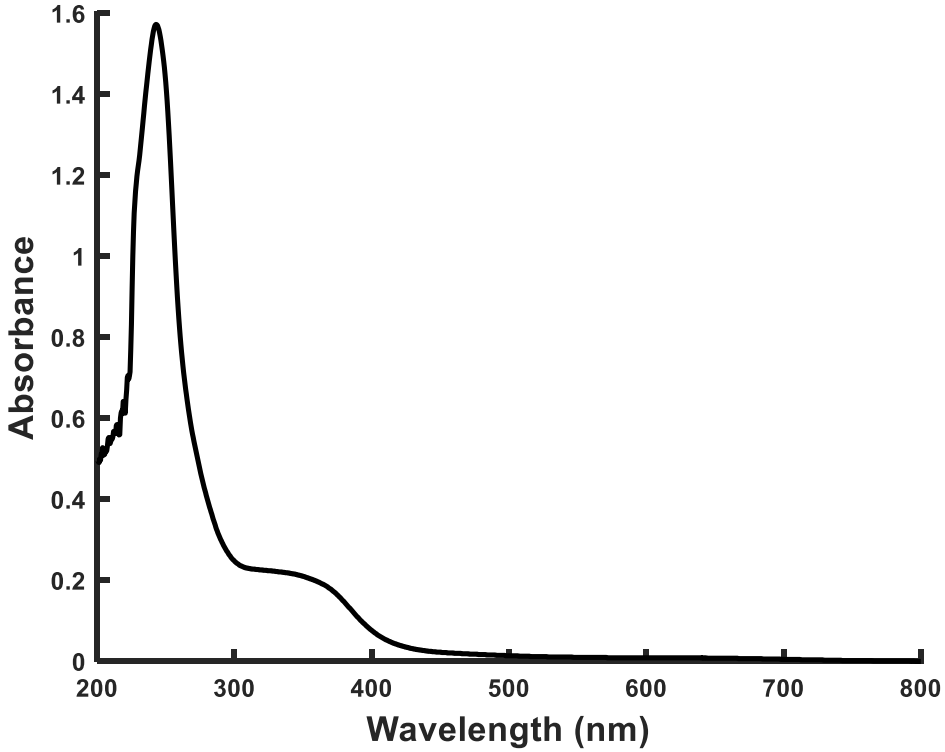
S48. ^{1}H NMR spectrum of Co_4O_4(4-chlorobenzoate)$_4$(*t*-Bupy)$_4$ (**Co_4(OBz-Cl)**) (methylene chloride-d_2, 600 MHz).



S49. ^{13}C{^{1}H} NMR spectrum of Co_4O_4(4-chlorobenzoate)$_4$(*t*-Bupy)$_4$ (**Co_4(OBz-Cl)**) (methylene chloride-d_2, 151 MHz).

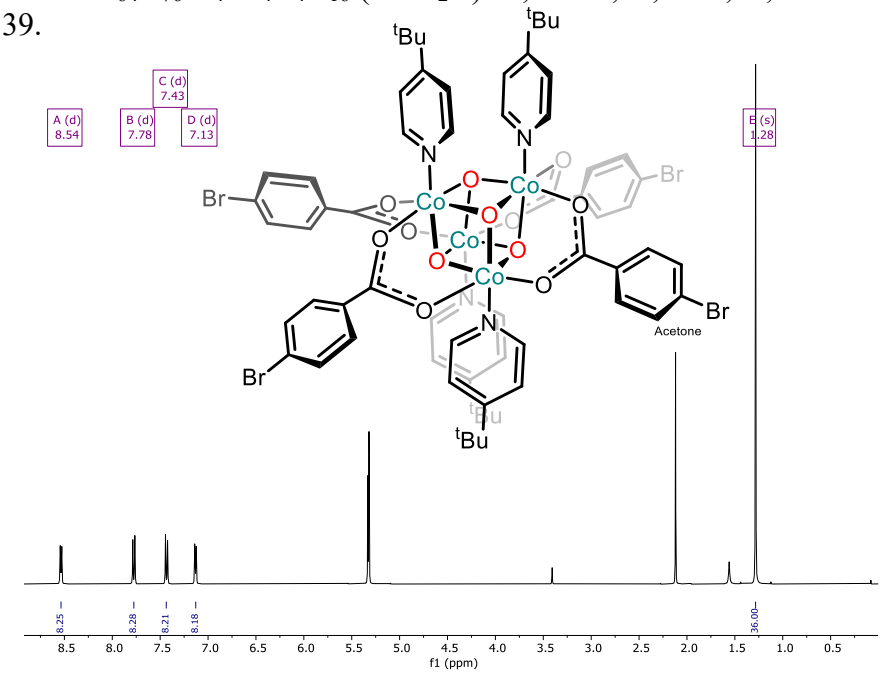


S50. FTIR spectrum Co_4O_4(4-chlorobenzoate)$_4$(*t*-Bupy)$_4$ (**Co_4(OBz-Cl)**).

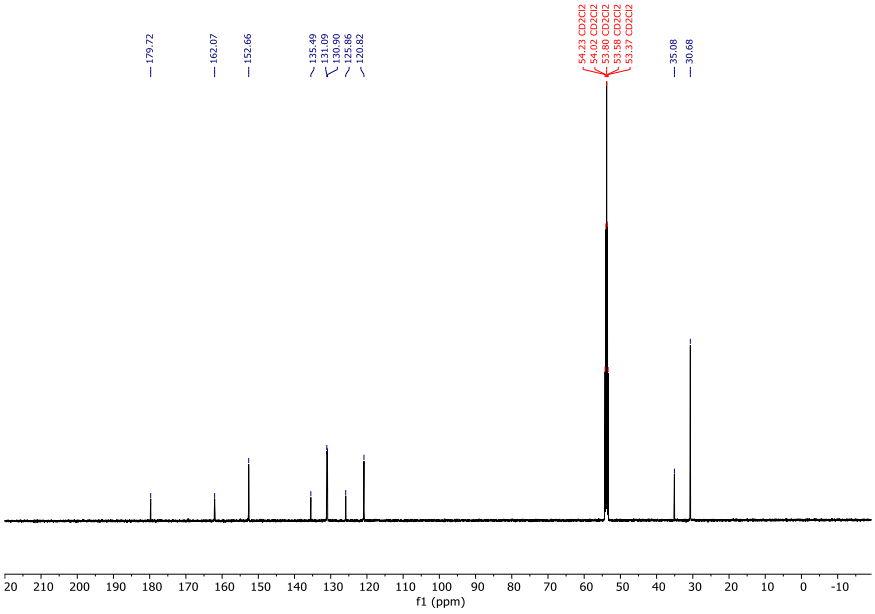


S51. UV-vis spectrum of Co_4O_4(4-chlorobenzoate)$_4$(*t*-Bupy)$_4$ in CH_2Cl_2 from which a molar absorptivity value was estimated.

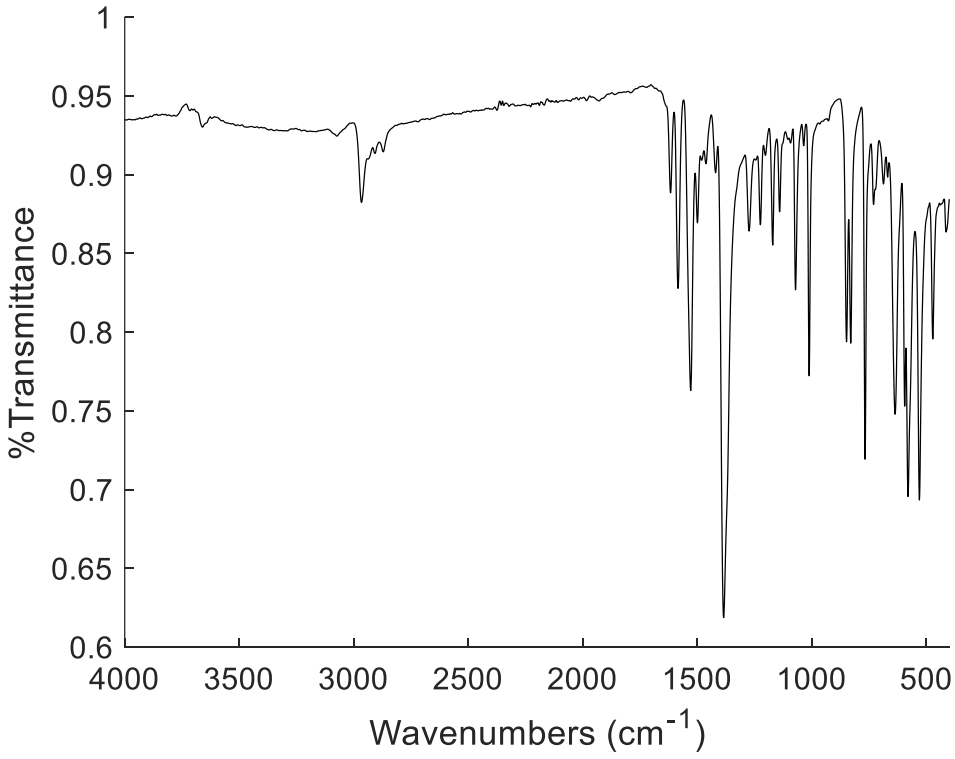
Co_4O_4(4-bromobenzoate)$_4$(*t*-Bupy)$_4$ (Co_4(OBz-Br)): ^{1}H NMR (400 MHz, methylene chloride-d_2) δ 8.54 (d, J = 6.8 Hz, 8H), 7.78 (d, J = 8.5 Hz, 8H), 7.43 (d, J = 8.5 Hz, 8H), 7.13 (d, J = 6.7 Hz, 8H), 1.28 (s, 36H). ^{13}C{^{1}H} NMR (126 MHz, methylene chloride-d_2) δ 179.72, 162.07, 152.66, 135.49, 131.09, 130.90, 125.86, 120.82, 54.23, 54.02, 53.80, 53.58, 53.37, 35.08, 30.68. IR (cm^{-1}): 2965 (w/m), 2908 (w), 2872 (w), 1617 (m), 1583 (m), 1528 (s), 1499 (m), 1481 (w), 1463 (w), 1420 (w), 1384 (s), 1273 (w/m), 1223 (w/m), 1170 (m), 1140 (s), 1071 (m), 1011 (s), 848 (s), 830 (s), 767 (s), 729 (w), 687 (w), 669 (w), 636 (s), 594 (s), 580 (s), 530 (s), 471 (m), 413 (w). Anal. Calcd for $C_{64}H_{76}Cl_4Co_4N_4O_{16}$ (• 4 H_2O): C, 44.88; H, 4.47; N, 3.27. Found: C, 44.58; H, 4.24; N, 3.39.



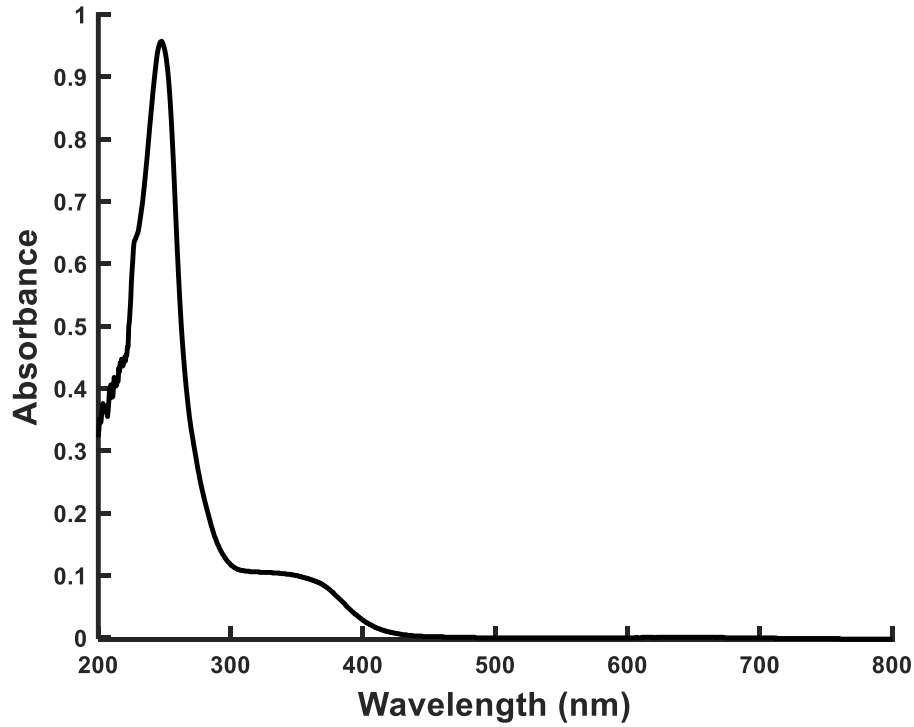
S52. ^{1}H NMR spectrum of Co_4O_4(4-bromobenzoate)$_4$(*t*-Bupy)$_4$ (**Co_4(OBz-Br)**) (methylene chloride-d_2, 400 MHz).



S53. ^{13}C{^{1}H} NMR spectrum of Co_4O_4(4-bromobenzoate)$_4$(*t*-Bupy)$_4$ (**Co_4(OBz-Br)**) (methylene chloride-d_2, 126 MHz).

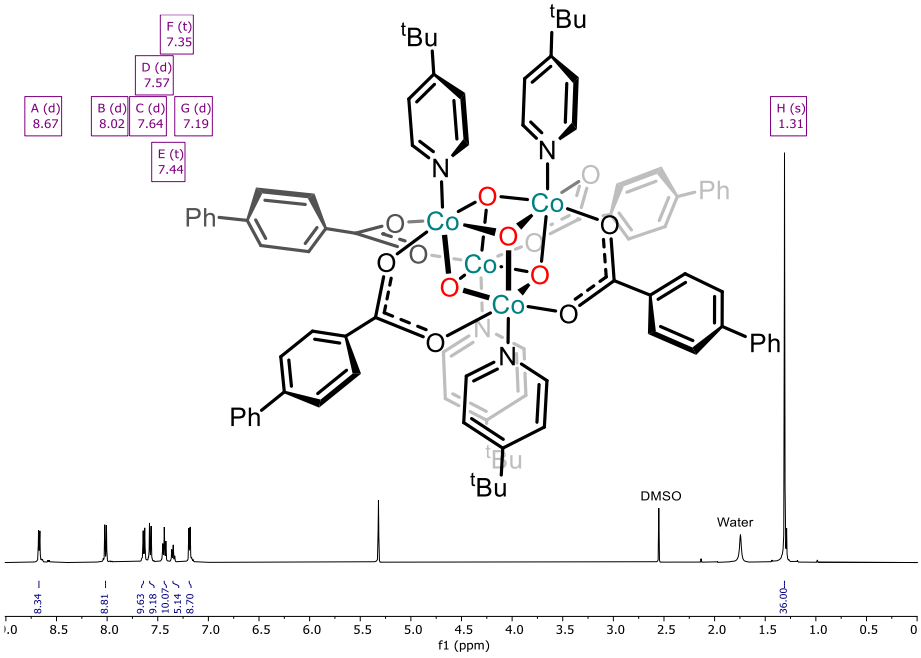


S54. FTIR spectrum of Co_4O_4(4-bromobenzoate)$_4$(*t*-Bupy)$_4$ (**Co_4(OBz-Br)**).

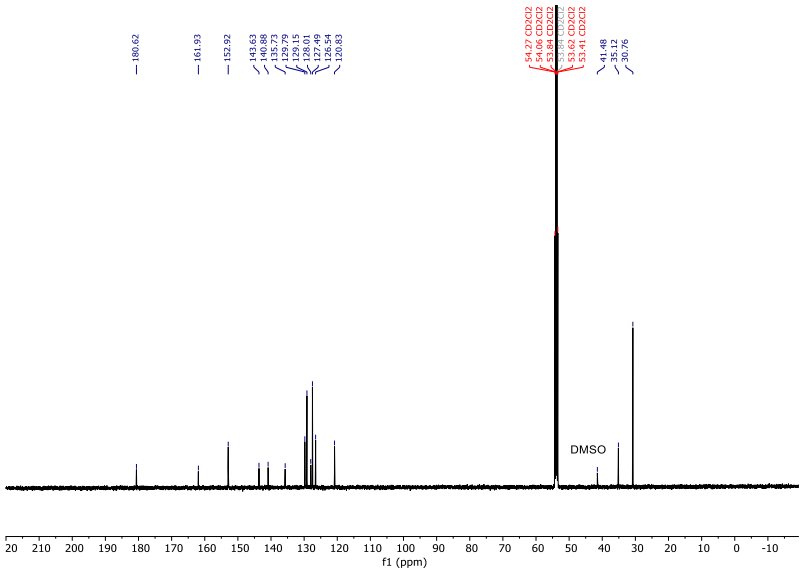


S55. UV-vis spectrum of Co_4O_4(4-bromobenzoate)$_4$(*t*-Bupy)$_4$ from which a molar absorptivity value was estimated.

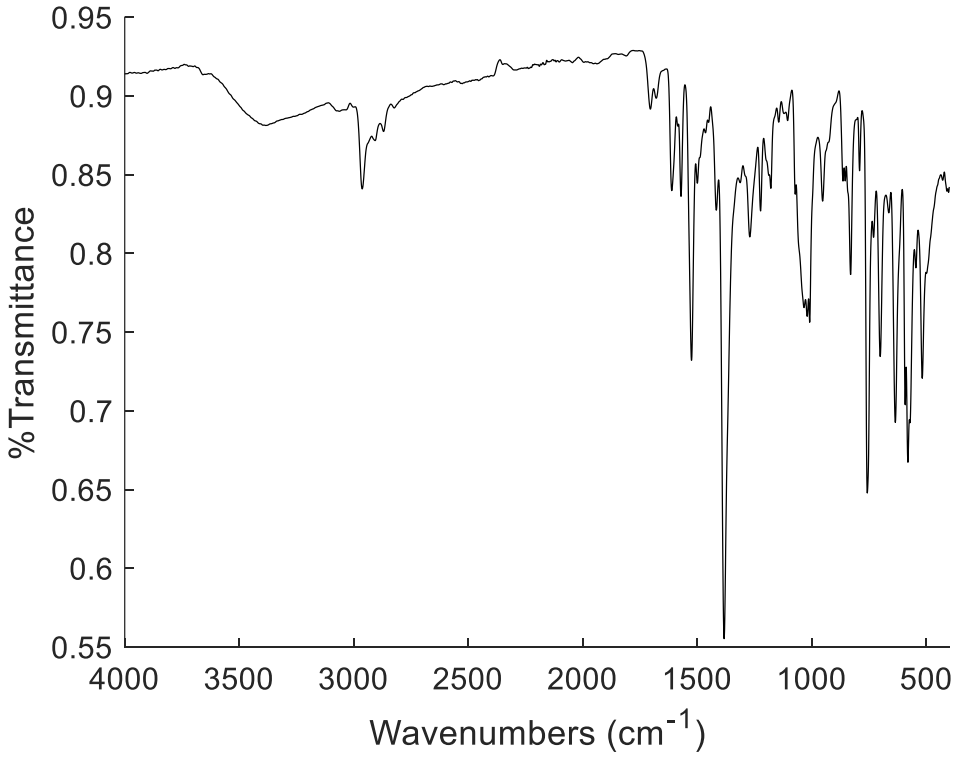
Co_4O_4(4-phenylbenzoate)$_4$(*t*-Bupy)$_4$ (Co_4(OBz-Ph)): ^{1}H NMR (500 MHz, methylene chloride-d_2) δ 8.67 (d, J = 6.8 Hz, 8H), 8.02 (d, J = 8.3 Hz, 8H), 7.64 (d, J = 7.0 Hz, 8H), 7.57 (d, J = 8.4 Hz, 8H), 7.44 (t, J = 7.7 Hz, 8H), 7.35 (t, J = 7.3 Hz, 4H), 7.19 (d, J = 6.8 Hz, 8H), 1.31 (s, 36H). ^{13}C{^{1}H} NMR (126 MHz, methylene chloride-d_2) δ 180.6, 161.9, 152.9, 143.6, 140.9, 135.7, 129.8, 129.2, 128.0, 127.5, 126.5, 120.8, 35.1, 30.8. IR (cm^{-1}): 2963 (w/m), 2909 (w), 2868 (w), 1704 (w), 1697 (w), 1611 (w/m), 1571 (w/m), 1524 (s), 1499 (m), 1418 (m), 1382 (s), 1312 (w/m), 1271 (m), 1233 (m), 1178 (w/m), 1144 (w), 1105 (w), 1072 (m, sh), 1034 (s), 1020 (s), 1009 (s), 952 (m), 863 (m), 854 (m), 831 (s), 791 (m), 757 (s), 730 (m), 701 (s), 665 (m), 635 (s), 591 (s), 580 (s), 571 (s, sh), 545 (m), 517 (s), 429 (w), 410 (w), 401 (w). Anal. Calcd for $C_{88}H_{96}Co_4N_4O_{16}$ (• 4 H_2O): C, 62.12; H, 5.69; N, 3.29. Found: C, 61.94; H, 5.50; N, 3.19.



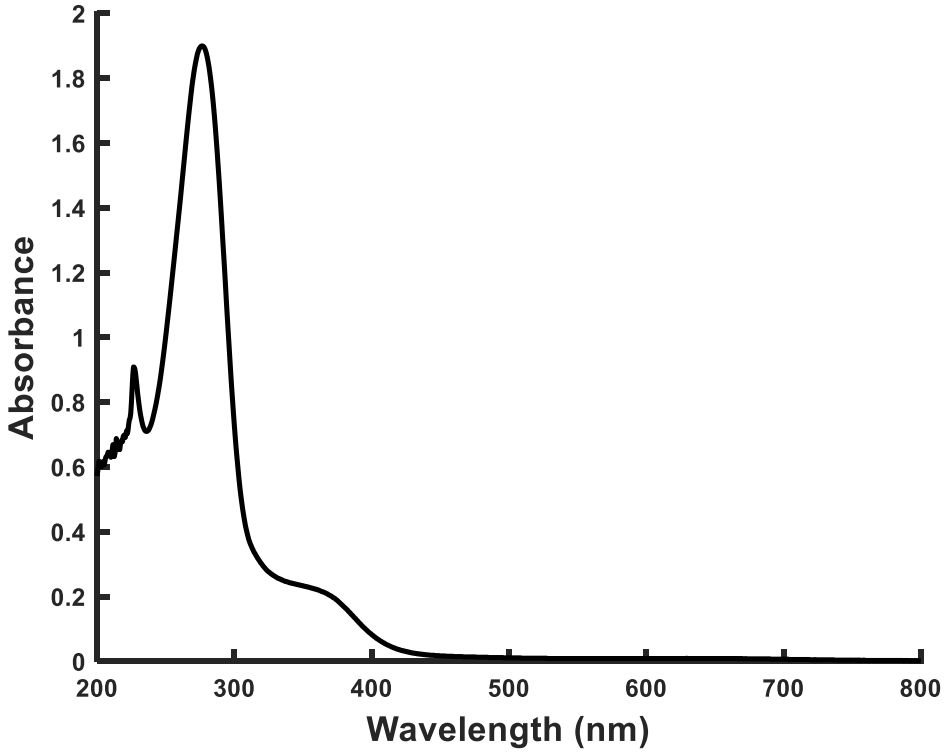
S56. ^{1}H NMR spectrum of Co_4O_4(4-phenylbenzoate)$_4$(*t*-Bupy)$_4$ (**Co_4(OBz-Ph)**) (methylene chloride-d_2, 500 MHz).



S57. ^{13}C{^{1}H} NMR spectrum of Co_4O_4(4-phenylbenzoate)$_4$(*t*-Bupy)$_4$ (**Co_4(OBz-Ph)**) (methylene chloride-d_2, 126 MHz).

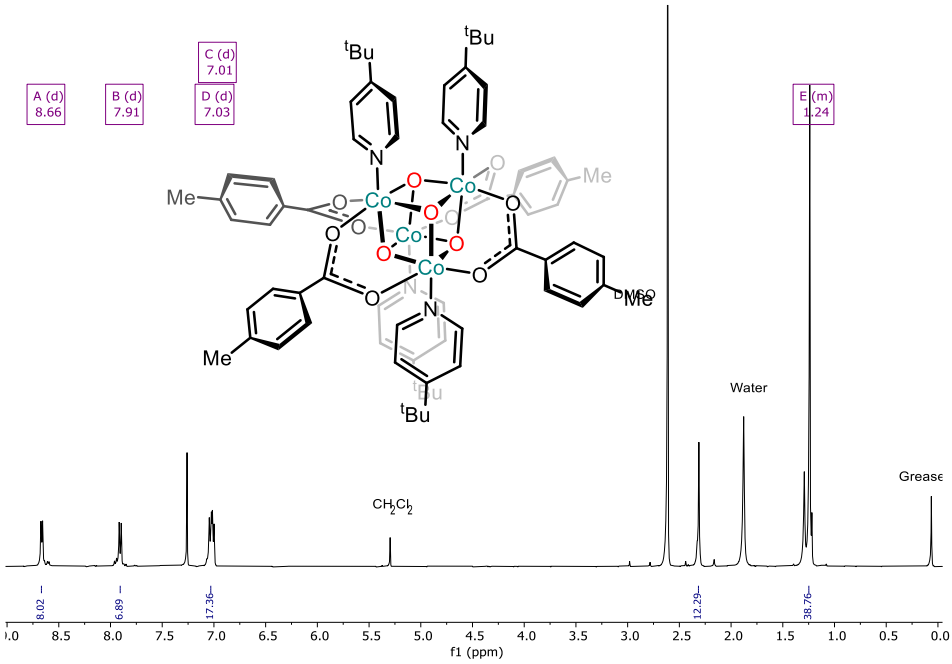


S58. FTIR spectrum of Co_4O_4(4-phenylbenzoate)$_4$(*t*-Bupy)$_4$ (**Co_4(OBz-Ph)**).

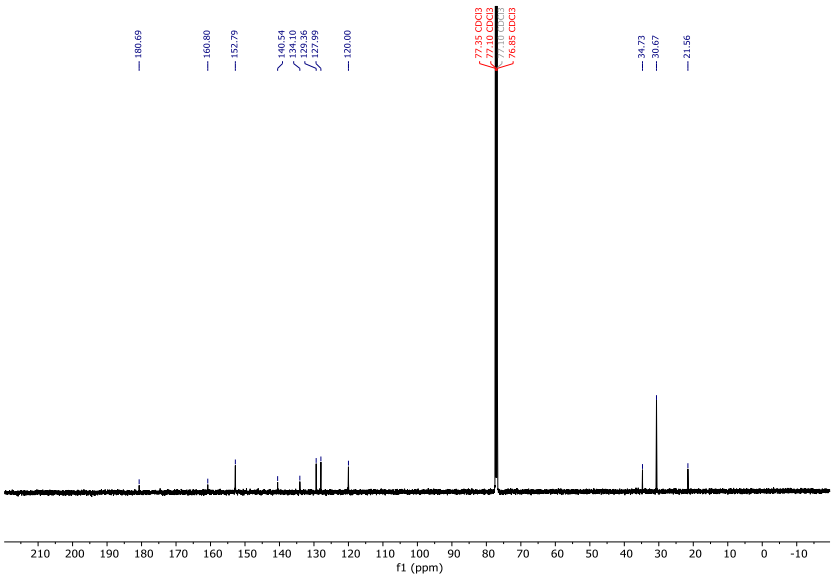


S59. UV-vis spectrum of Co_4O_4(4-phenylbenzoate)$_4$(*t*-Bupy)$_4$ in CH_2Cl_2 from which a molar absorptivity value was estimated.

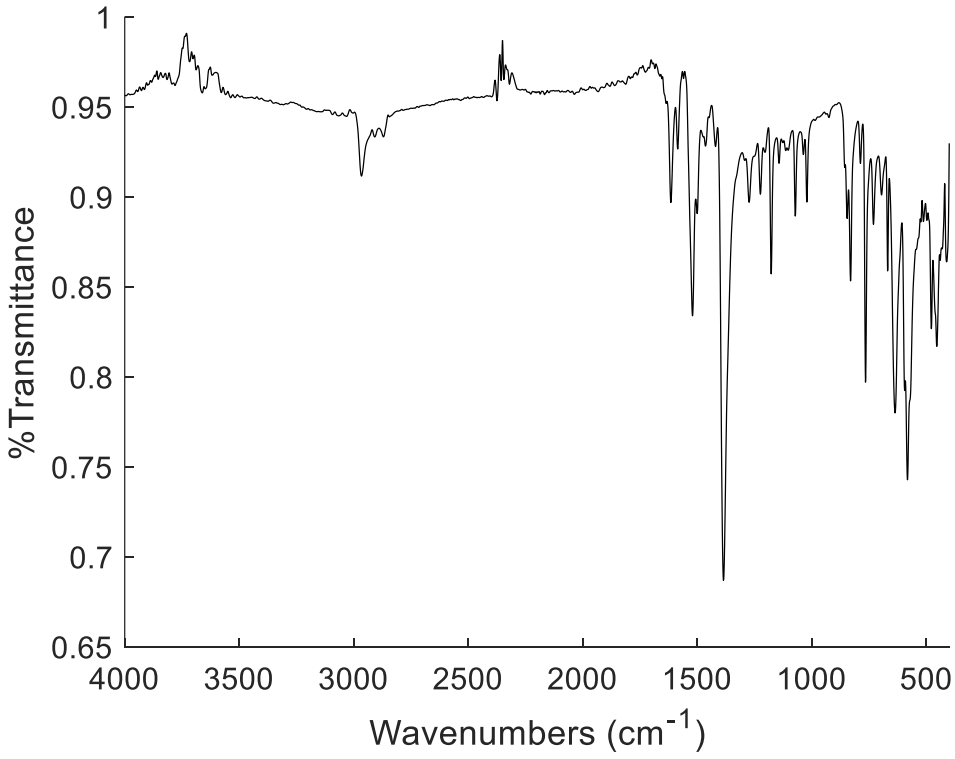
Co_4O_4(4-methylbenzoate)$_4$(*t*-Bupy)$_4$ (Co_4(OBz-Me)): ^{1}H NMR (500 MHz, chloroform-*d*) δ 8.66 (d, *J* = 5.9 Hz, 8H), 7.90 (d, *J* = 7.9 Hz, 8H), 7.03 (m, 16H), 2.32 (s, 12 H), 1.25 (s, 36 H). ^{13}C{^{1}H} NMR (126 MHz, chloroform-*d*) δ 180.7, 160.8, 152.8, 140.5, 134.1, 129.4, 128.0, 120.0, 34.7, 30.7, 21.6. IR (cm^{-1}): 2965 (w), 2908 (w), 2869 (w), 1615 (m), 1583 (w), 1520 (m/s), 1499 (m), 1563 (w), 1421 (w), 1385 (s), 1273 (m), 1224 (w), 1177 (m), 1142 (w), 1072 (m), 1036 (w), 1021 (m), 845 (m), 831 (m/s), 787 (w), 765 (s), 730 (m), 695 (m/w), 669 (w/m), 634 (s), 594 (s, sh), 582 (s), 511 (w), 478 (m), 454 (s), 440 (m), 411 (m). HR-ESI-MS Calcd for $C_{68}H_{81}Co_4N_4O_{12}^+$ m/z = 1381.3169; found: 1381.2970 m/z. Anal. Calcd for $C_{68}H_{80}Co_4N_4O_{12}$ (• 4 H_2O): C, 56.20; H, 6.10; N, 3.86. Found: C, 52.26; H, 4.44; N, 4.67.



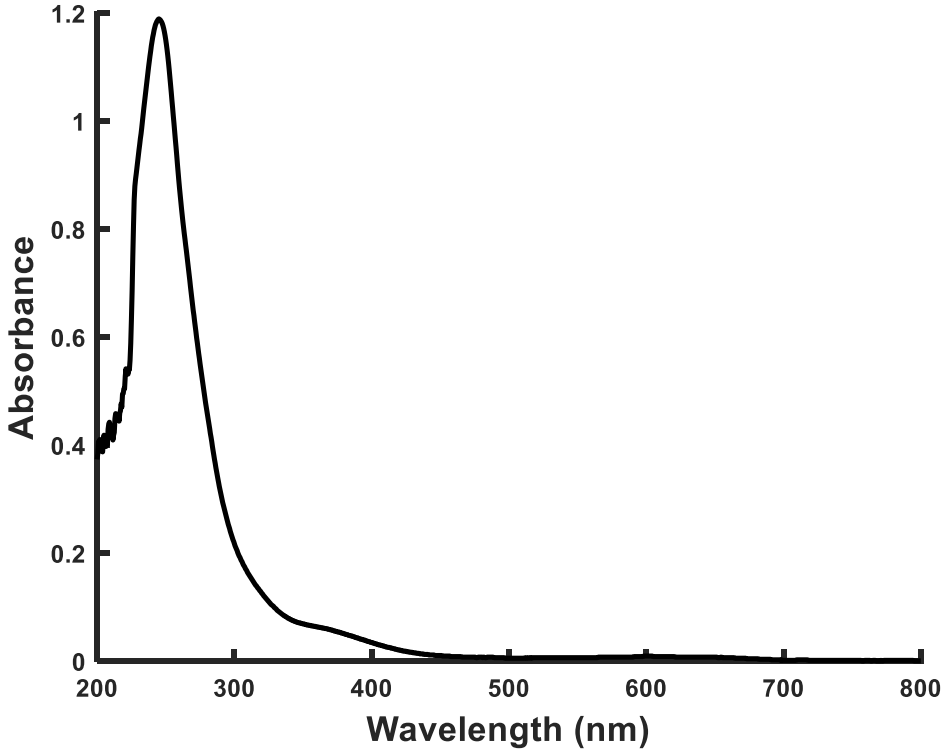
S60. ^{1}H NMR spectrum of Co_4O_4(4-methylbenzoate)$_4$(*t*-Bupy)$_4$ (**Co_4(OBz-Me)**) (chloroform-*d*, 500 MHz).



S61. ^{13}C{^{1}H} NMR spectrum of Co_4O_4(4-methylbenzoate)$_4$(*t*-Bupy)$_4$ (**Co_4(OBz-Me)**) (chloroform-*d*, 126 MHz).

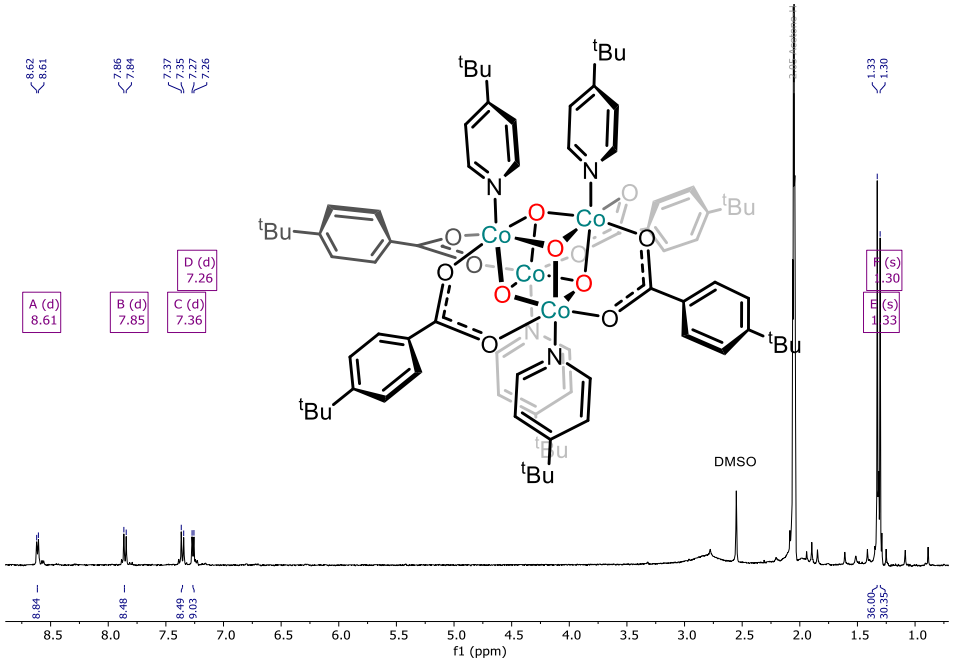


S62. FTIR spectrum of Co_4O_4(4-methylbenzoate)$_4$(*t*-Bupy)$_4$ (**Co_4(OBz-Me)**).

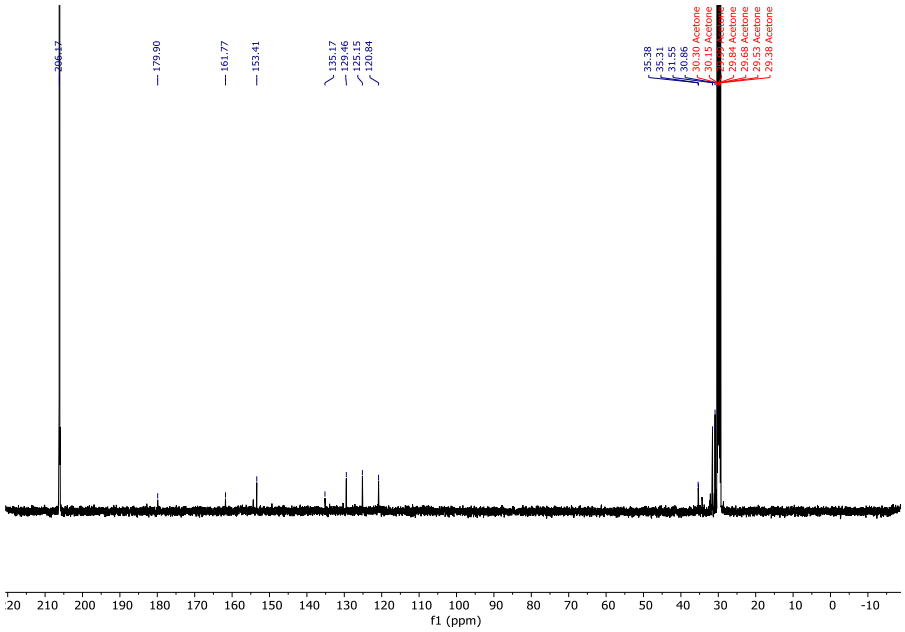


S63. UV-vis spectrum of Co_4O_4(4-methylbenzoate)$_4$(*t*-Bupy)$_4$ in CH_2Cl_2 from which a molar absorptivity value was estimated.

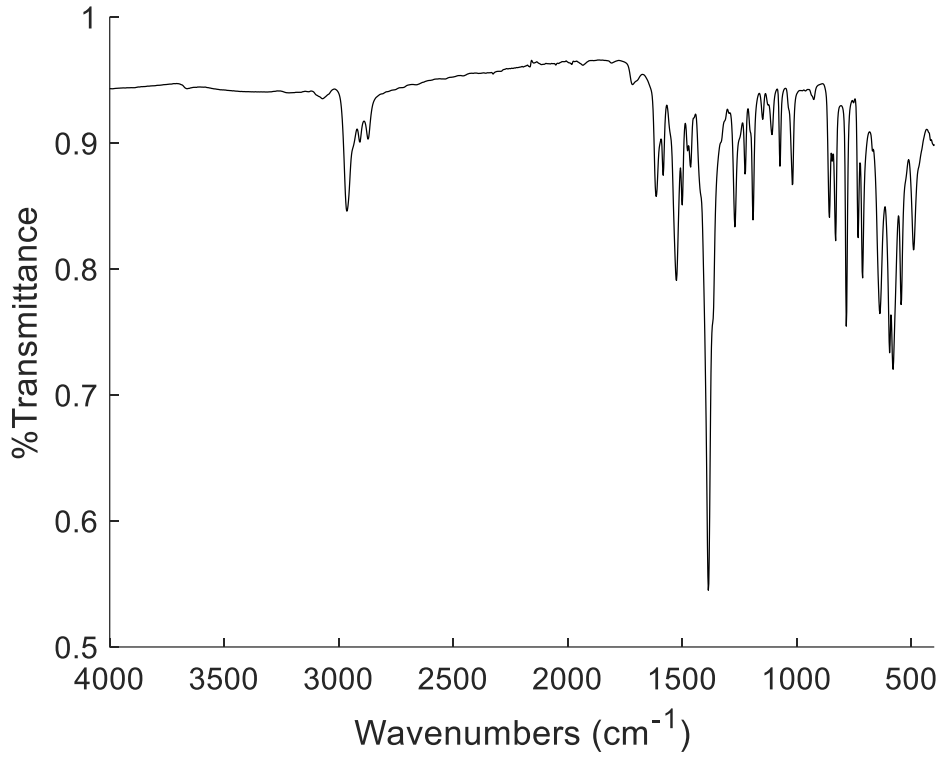
Co_4O_4(4-*tert*butylbenzoate)$_4$(*t*-Bupy)$_4$ (Co_4(OBz-*t*Bu)): ^{1}H NMR (400 MHz, acetone-d_6) δ 8.61 (d, J = 5.9 Hz, 8H), 7.85 (d, J = 8.2 Hz, 8H), 7.36 (d, J = 8.4 Hz, 8H), 7.26 (d, J = 6.5 Hz, 8H), 1.33 (s, 36H), 1.30 (s, 36H). $^{13}C\{^1H\}$ NMR (126 MHz, acetone-d_6) δ 206.17, 179.90, 161.77, 153.41, 135.17, 129.46, 125.15, 120.84, 35.38, 35.31, 31.55, 30.86 IR (cm^{-1}): 2965 (m), 2907 (w), 2872 (w), 1614 (m), 1583 (w/m), 1525 (m), 1500 (w/m), 1463 (w), 1386 (s), 1270 (m), 1226 (w), 1191 (m), 1148 (w), 1108 (w), 1071 (w), 1019 (m), 857 (m), 848 (w), 830 (m), 784 (m/s), 732 (m), 712 (m/s), 637 (m/s), 594 (s), 579 (s), 544 (m), 488 (m). Anal. Calcd for $C_{80}H_{112}Co_4N_4O_{16}$ (• 4 H_2O): C, 59.26; H, 6.95; N, 3.46. Found: C, 53.59; H, 6.24; N, 2.88.



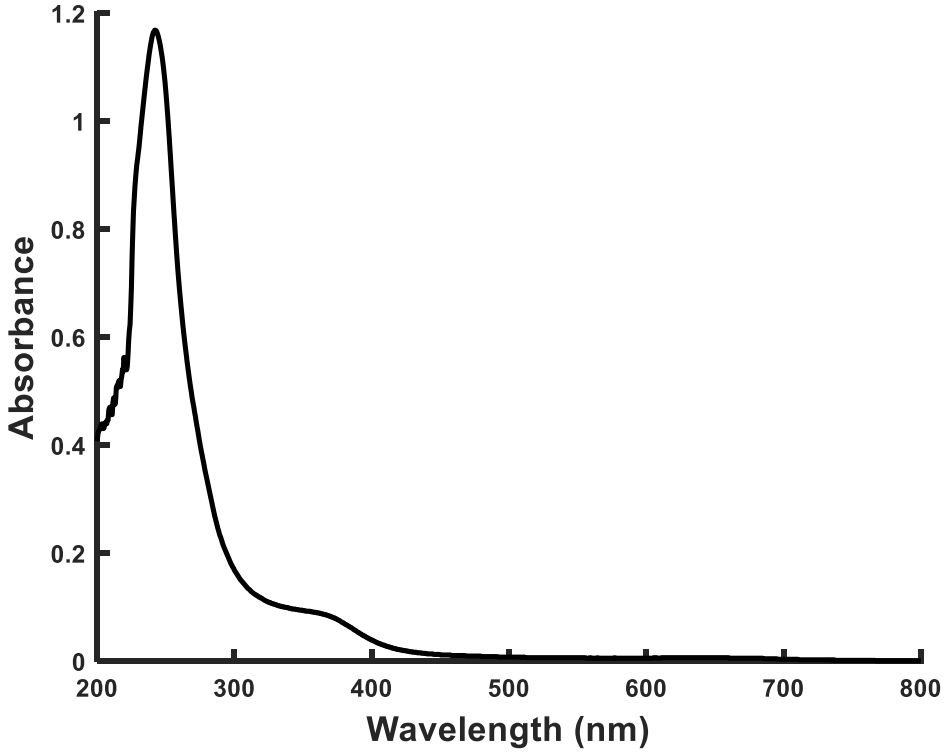
S64. ^{1}H NMR spectrum of Co_4O_4(4-*tert*butylbenzoate)$_4$(*t*-Bupy)$_4$ (**Co_4(OBz-*t*Bu)**) (acetone-d_6, 400 MHz).



S65. $^{13}C\{^1H\}$ NMR spectrum of Co_4O_4(4-*tert*butylbenzoate)$_4$(*t*-Bupy)$_4$ (**Co_4(OBz-*t*Bu)**) (acetone-d_6, 400 MHz).

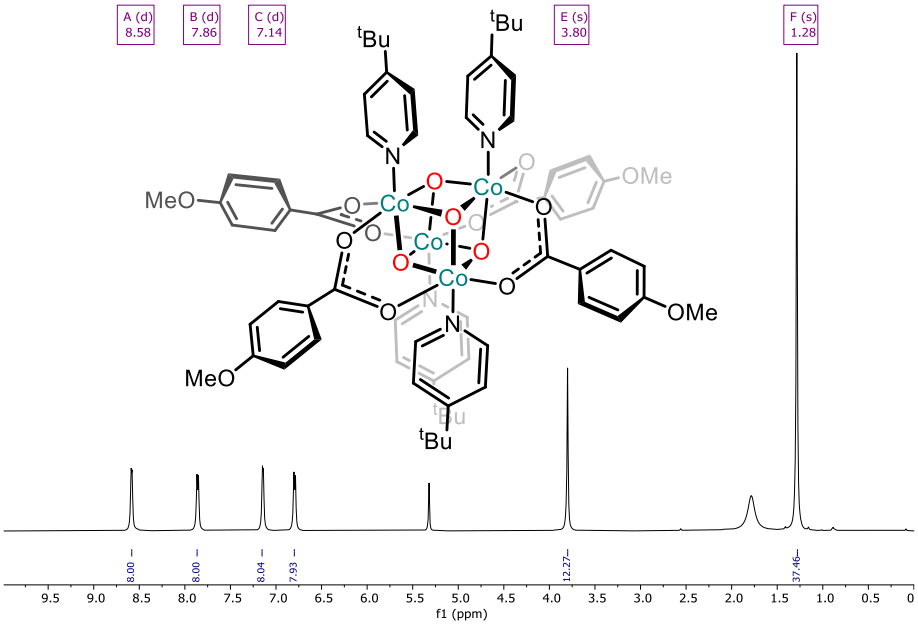


S66. FTIR spectrum of Co_4O_4(4-*tert*butylbenzoate)$_4$(*t*-Bupy)$_4$ (**Co_4(OBz-*t*Bu)**).

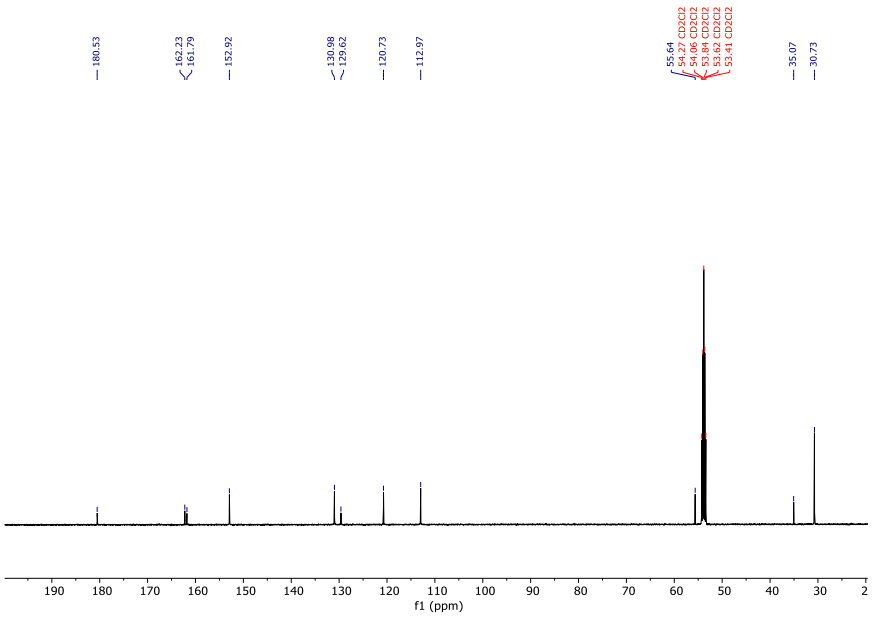


S67. UV-vis spectrum of Co_4O_4(4-*tert*butylbenzoate)$_4$(*t*-Bupy)$_4$ in CH_2Cl_2 from which a molar absorptivity value was estimated.

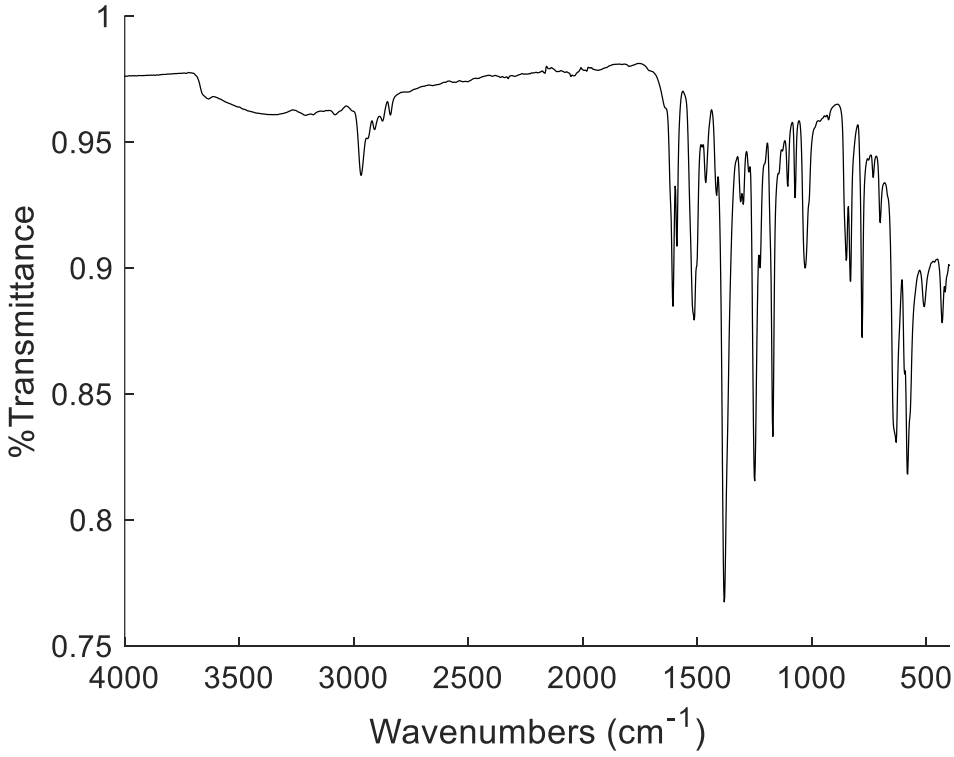
Co_4O_4(4-methoxybenzoate)$_4$(*t*-Bupy)$_4$ (Co_4(OBz-OMe)): ^{1}H NMR (500 MHz, methylene chloride-d_2) δ 8.58 (d, J = 5.8 Hz, 1H), 7.86 (d, J = 8.3 Hz, 1H), 7.14 (d, J = 5.8 Hz, 1H), 6.79 (d, J = 8.3 Hz, 1H), 3.80 (s, 2H), 1.28 (s, 5H). ^{13}C{^{1}H} NMR (126 MHz, methylene chloride-d_2) δ 180.53, 162.23, 161.79, 152.92, 130.98, 129.62, 120.73, 112.97, 55.64, 35.07, 30.73. IR (cm^{-1}): 2967 (w/m), 2907 (w) 2874 (w), 2839 (w), 1606 (m), 1589 (m), 1513 (m), 1463 (m), 1415 (m), 1382 (s), 1311 (w), 1299 (w), 1249 (s), 1226 (m, sh), 1170 (s), 1104 (w), 1037 (w), 1029 (m), 849 (m), 830 (m), 780 (m/s), 730 (w), 701 (w), 631 (s), 581 (s), 508 (m), 430 (m/s), 418 (m). HR-ESI-MS Calcd for $C_{68}H_{81}Co_4N_4O_{16}^+$ m/z = 1445.2965; found: 1445.3973. Anal. Calcd for $C_{68}H_{88}Co_4N_4O_{16}$ (• 4 H_2O): C, 53.83; H, 5.85; N, 3.69. Found: C, 53.59; H, 5.84; N, 3.50.



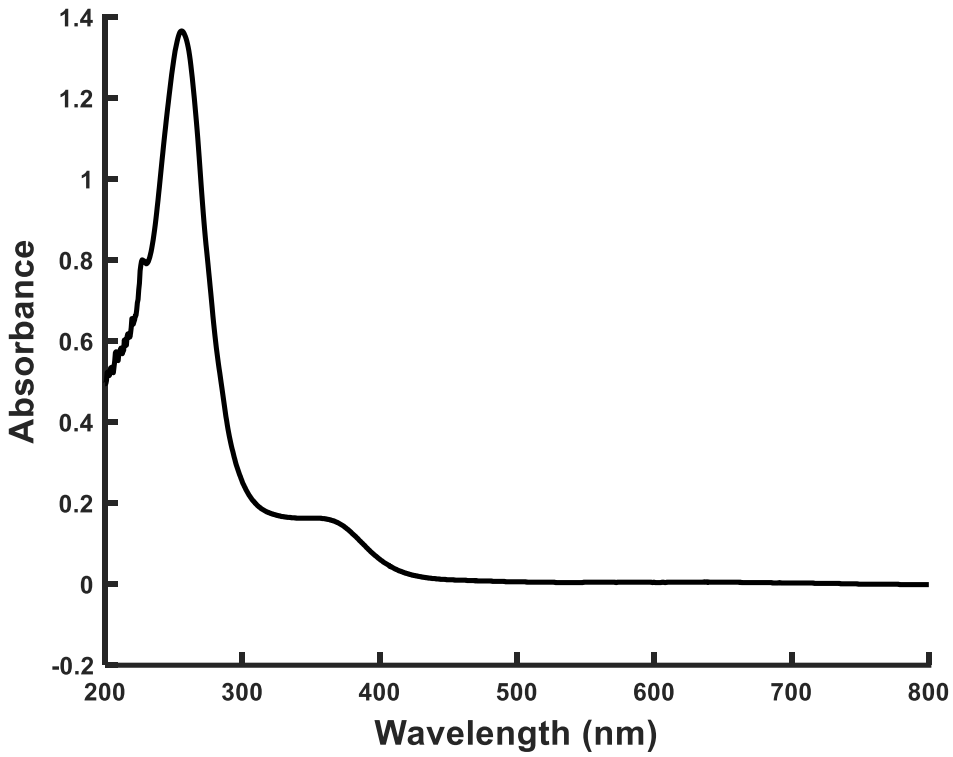
S68. ^{1}H NMR spectrum of Co_4O_4(4-methoxybenzoate)$_4$(*t*-Bupy)$_4$ (**Co_4(OBz-OMe)**) (methylene chloride-d_2, 400 MHz)



S69. $^{13}C\{^{1}H\}$ NMR spectrum of Co_4O_4(4-methoxybenzoate)$_4$(*t*-Bupy)$_4$ (**Co_4(OBz-OMe)**) (methylene chloride-d_2, 121 MHz)



S70. FTIR spectrum of Co_4O_4(4-methoxybenzoate)$_4$(*t*-Bupy)$_4$ (**Co_4(OBz-OMe)**).



S71. UV-vis spectrum of Co_4O_4(4-methoxybenzoate)$_4$(*t*-Bupy)$_4$ in CH_2Cl_2 from which a molar absorptivity value was estimated.

Mn(acetylacetonate)$_3$ related derivatives and [Mn(acac)$_2$(L)$_2$][PF$_6$] Salts:

The syntheses outlined in this section were all roughly based on literature procedures.[9, 10]

Mn(*bis*-benzoylacetylacetonate)$_3$:

A 100 mL round-bottom flask was charged with a stir bar, $Mn(OAc)_2$ (0.5002 g, 2.908 mmol, 1.000 equiv), dibenzoylmethane (2.7246 g, 12.16 mmol, 12 equiv) and toluene (50 mL). The flask was transferred to an oil bath heated to 75 °C and stirred magnetically for 16 h. After 16 h, the flask was removed from the oil bath and allowed to cool to room temperature. The solvent was removed with a rotary evaporator. The solids were taken in Et_2O (50 mL) and MeOH was added (6 mL). The solution and solids were stirred for 15 minutes to fully dissolve. The resulting solution was then filtered through a glass wool plug in a pipette into a 150 mL Erlenmeyer flask. The resulting solution was allowed to stand uncovered for several hours, during which time crystals began to precipitate. The Erlenmeyer flask was then covered with parafilm that was pierced to allow slow evaporation. After standing for 14 h, the solids were collected on a medium sintered fritted funnel and washed with cold (–5 °C) pentane to give 0.8230 g of the title compound (39% yield). **Characterization data:** Anal. Calcd for $C_{45}H_{33}MnO_6$: C, 74.58; H, 4.59. Found: C, 74.54; H, 5.01.

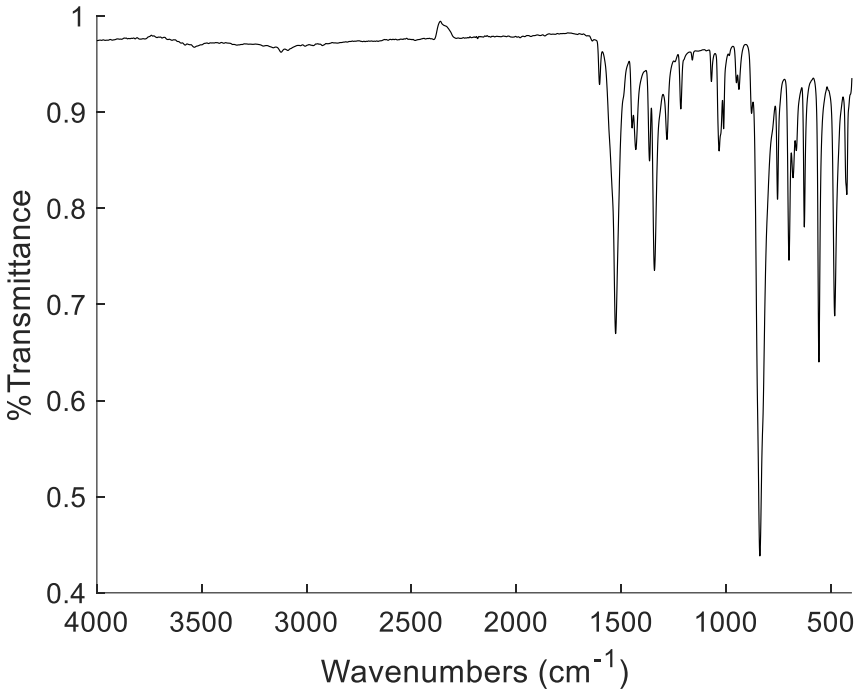
Mn(*bis*-*tert*-butylacetylacetonate)$_3$:

A 500 mL round-bottom flask was charged with a large stir bar, $MnSO_4$ hydrate (1.0001 g, 5.917 mmol, 1.0 equiv), MeOH (4 mL), water (20 mL); then, dipivaloylmethane (2,2,6,6-tetramethyl-2,5-heptanedione) (3.4071 g, 18.51 mmol) was added in one portion. Aw saturated ammonium hydroxide solution (8 mL) was added dropwise to this solution, producing an oily green precipitate. The solution was allowed to stir for 30 minutes, following which the solids were collected on filter paper. The solids were washed with 1:9 MeOH:H_2O (100 mL) and dried in air for 5 minutes. The solids were transferred to an Erlenmeyer and dissolved in 100 mL of hot ^{i}PrOH and filtered hot through filter paper. The solvent was then removed by way of rotary evaporation, and the resulting solids were dissolved hexanes. The solution was then filtered through a glass wool plug, and the solvent removed with a rotary evaporator, resulting in 1.9345 g of analytically pure green solids (56% yield) of the title complex. **Characterization data:** Anal. Calcd for $C_{33}H_{57}MnO_6$: C, 65.54; H, 9.50. Found: C, 65.49; H, 9.41.

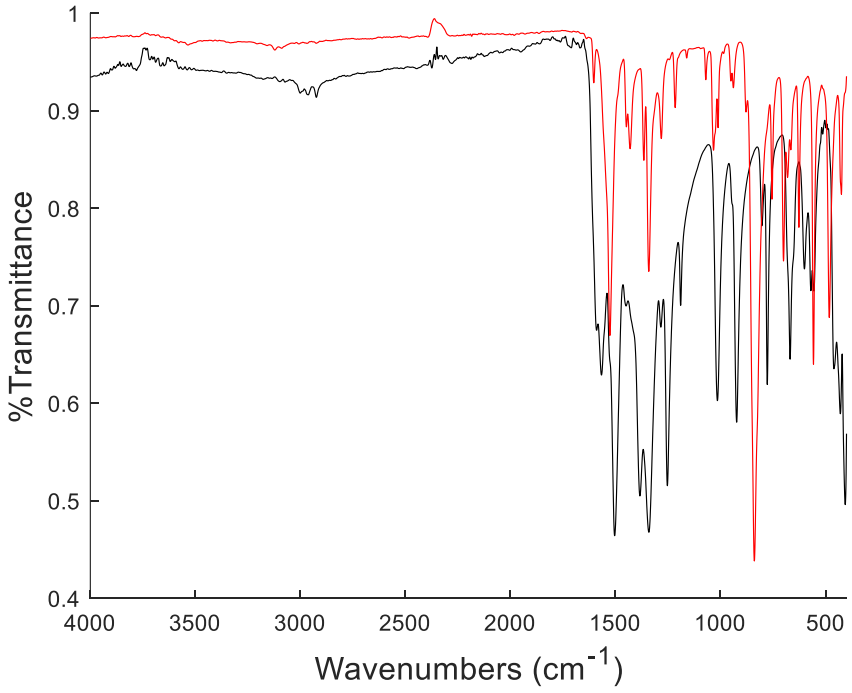
[Mn(acac)$_2$(py)$_2$][PF$_6$] (Mn(py)[PF$_6$]):

A 20 mL vial was charged with a stir bar, $Mn(acac)_3$ (0.500 g, 1.42 mmol, 1.0 equiv.), MeCN (*ca*. 8 mL), and pyridine (0.30 mL, 3.72 mmol, 2.6 equiv). The vial was placed in a 55 °C oil bath and stirred for 1 h. Then, NH_4PF_6 (0.288 g, 1.76 mmol, 1.25 equiv.) was added as a solid in one portion. The solution was stirred for an additional 5 min, at which point the vial was removed from the oil bath and allowed to cool to room temperature. The solvent was removed by way of rotary evaporator, and the resulting solids were then extracted into minimal CH_2Cl_2, placed into a 20 mL vial, chilled to –5 °C, then layered with *ca*. 1.1 times the volume of chilled pentane. The layers were allowed to diffuse at –5 °C for 48 h, during which time a powder precipitated. This powder was then collected on a medium sintered frit washed with water (10 mL) and pentane (10 mL), then dried in vacuo to give 0.700 g (89% yield) of the title complex. **Characterization Data**: IR (cm^{-1}): 3122 (w), 3090 (w), 1603 (w), 1526 (s), 1447 (w), 1430 (w), 1364 (m), 1341 (s), 1282 (w), 1216 (w), 1160 (w), 1069 (w), 1032 (m), 1011(w/m), 949(w), 938 (w), 878 (w), 838 (very strong),

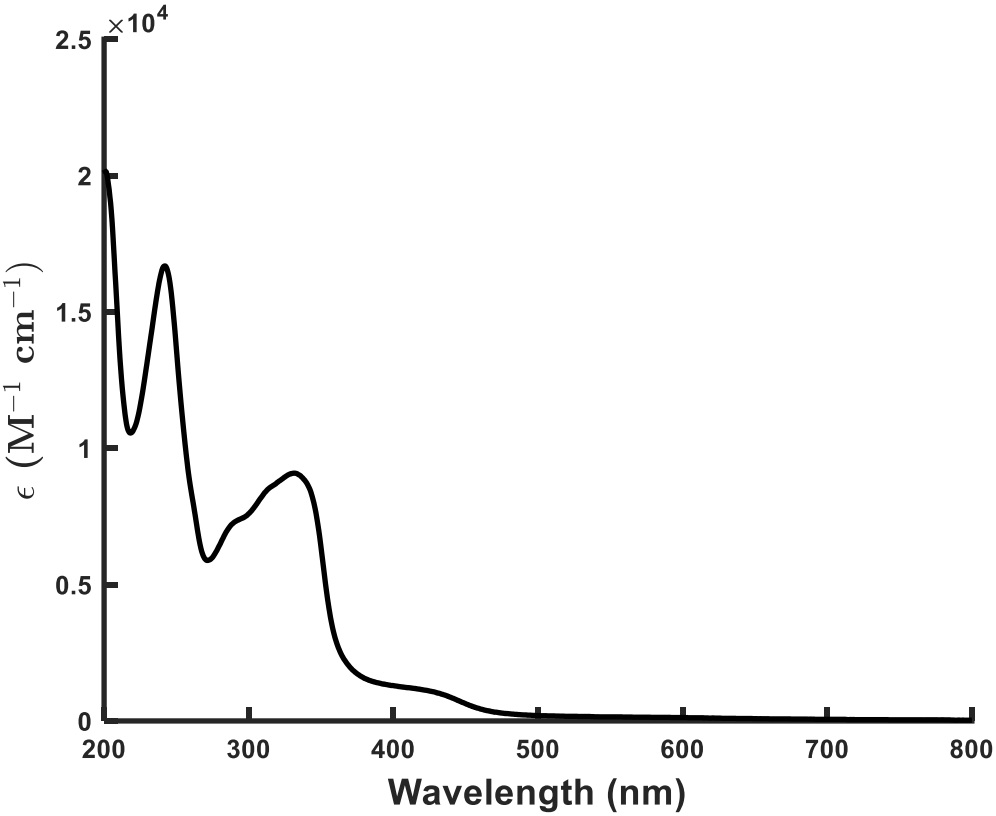
754 (s), 700 (s), 680 (s), 665 (m), 626 (s), 557 (s), 481 (s), 424 (m). Anal. Calcd for: $C_{20}H_{24}F_6MnN_2O_4P$: C, 43.18; H, 4.35; N, 5.04. Found: C, 42.10; H, 4.25; N, 4.90.



S72. FTIR spectrum of $[Mn(acac)_2(py)_2][PF_6]$ (**Mn^{III}(py)**$[PF_6]$).



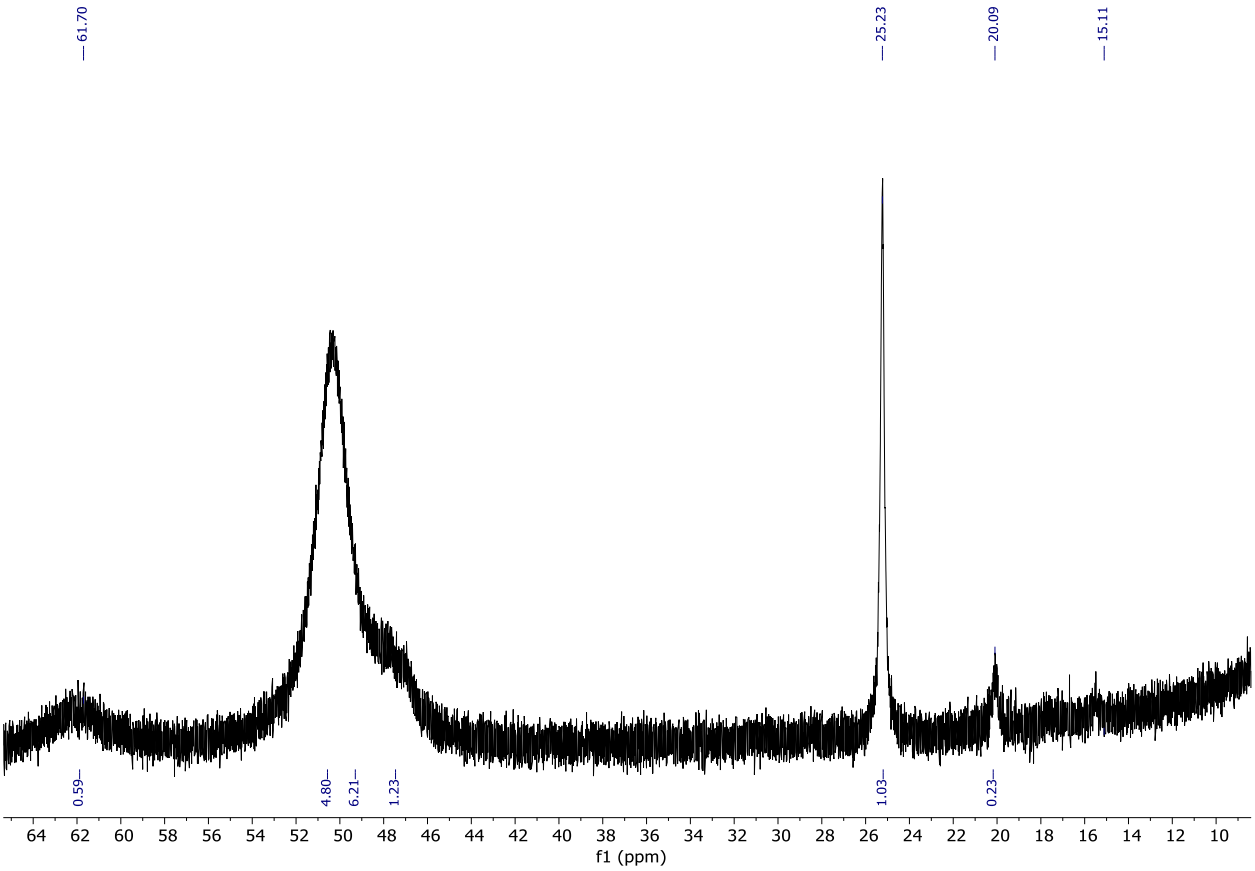
S73. FTIR spectrum of $[Mn(acac)_2(Py)_2][PF_6]$ (red) overlayed with the FTIR spectrum of $Mn(acac)_3$ (black).



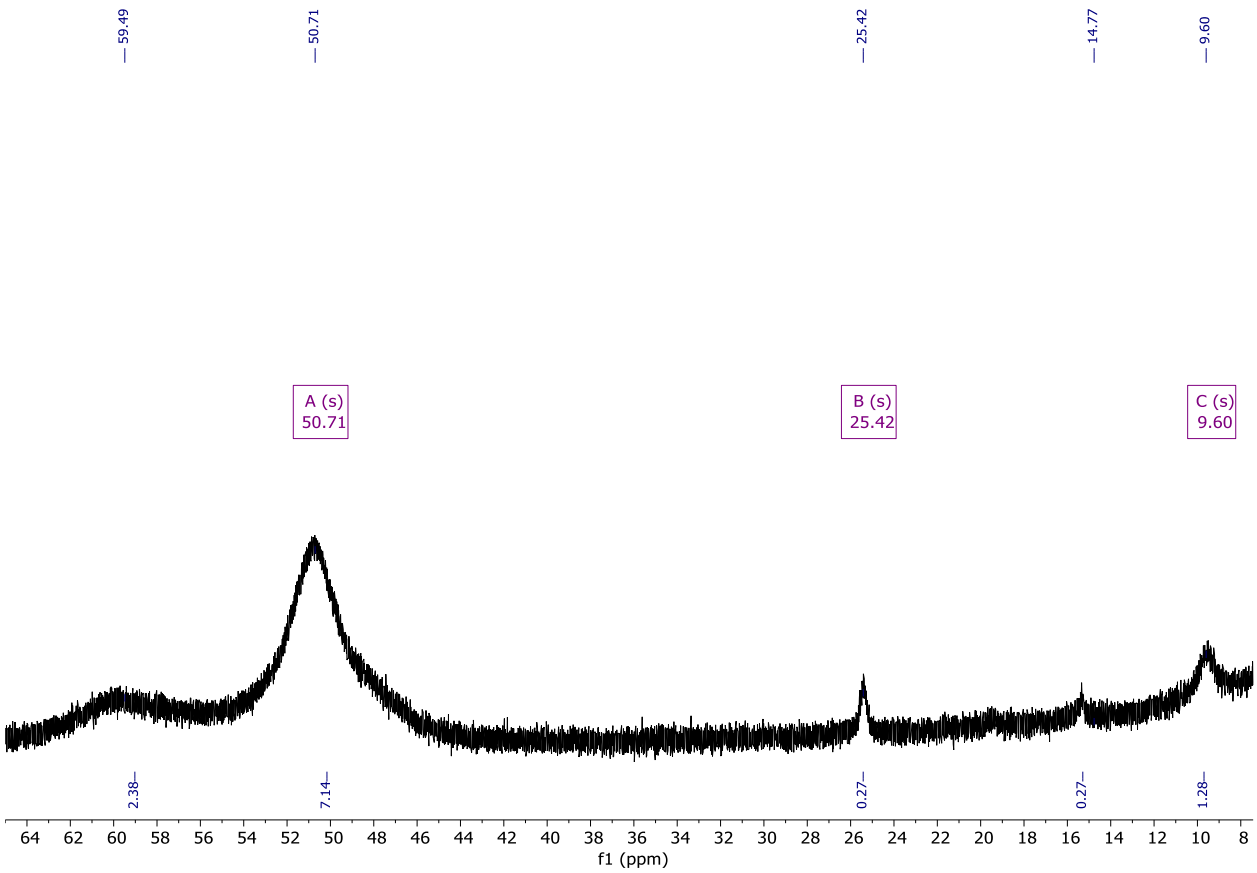
S74. Molar extinction coefficients for $[Mn(acac)_2(py)_2][PF_6]$ (**Mn^{III}(py)**$[PF_6]$) in MeCN.

[Mn(acac)$_2$(4-*tert*butylpyridine)$_2$][PF$_6$] (Mn^{III}(*t*-Bupy)[PF$_6$]):

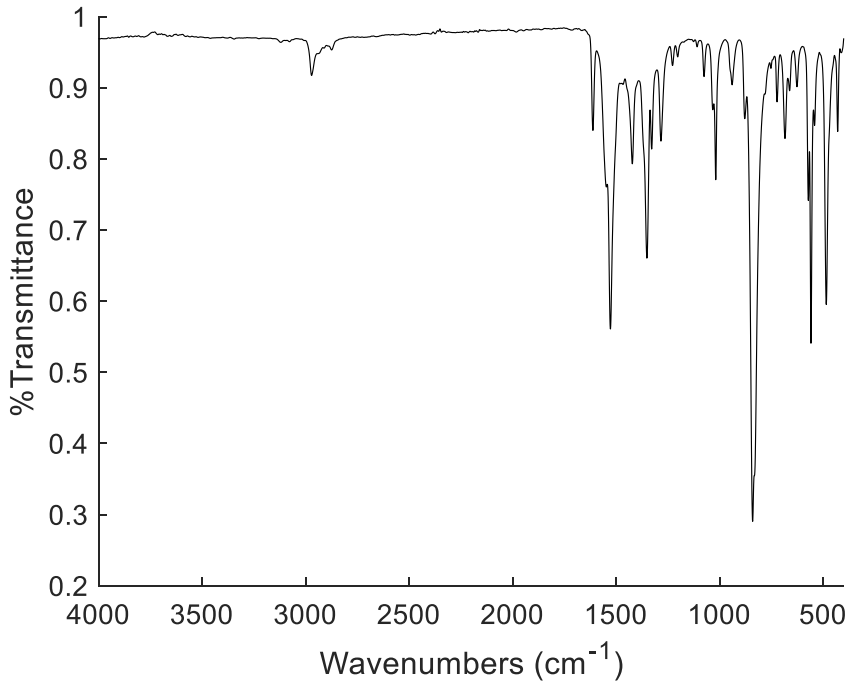
A round-bottom flask was charged with a stir bar, Mn(acac)$_3$ (1.05 g, 3 mmol, 1.0 equiv), MeCN (3 mL) and 4-*tert*butylpyridine (1 mL, 7.18 mmol, 2.4 equiv). After complete dissolution, the flask was transferred to a 50 °C oil bath and the solution was stirred. After 5 min of stirring, NH_4PF_6 (0.58 g, 3.5 mmol, 1.2 equiv) was added in one portion as a solid. The solution was stirred for an additional hour, then the flask was removed from the oil bath, sealed with a rubber septum, and transferred to a –5 °C freezer. After 16 h, the solution was vacuum filtered through a medium porosity sintered fritted funnel and a red solid was collected. The red material was washed with H_2O (80 mL) and crushed to ensure even mixing. The red solid was then washed with cold pentane (20 mL), and air was then pulled through the frit to dry the solids, which turned progressively more yellow upon drying. The solids were collected from the frit and dried *in vacuo* (1.30 g, 1.94 mmol, 65% yield). ^{1}H NMR (400 MHz, acetonitrile-d_3) δ 50.38 (broad s), 25.23 (broad s), 20.09 (broad s) ^{1}H NMR (400 MHz, methylene chloride-d_2) δ 59.49 (broad s), 50.71 (broad s), 25.42 (broad s), 14.77 (broad s), 9.60 (broad s). **Characterization data**: Anal. Calcd for $C_{28}H_{40}F_6MnN_2O_4P$: C, 50.30; H, 6.03; N, 4.19. Found: C, 50.01; H, 6.09; N, 4.53. IR (cm^{-1}): 2970 (w), 2867 (w), 1611 (w), 1546 (m), 1526 (s), 1421 (w), 1350 (m), 1327 (w), 1282 (w), 1227 (vw), 1201 (vw), 1109 (vw), 1075 (w), 1033 (w), 1018 (m), 939 (w), 878 (w/m), 839 (very strong), 722 (w), 684 (w), 661 (w), 626 (w), 571 (m), 558 (s), 540 (w), 484 (s), 428 (w). HR-ESI-MS calc'd for $C_{28}H_{40}MnN_2O_4^+$ m/z = 523.2364; found: 523.2018 m/z.



S75. ^{1}H NMR spectrum of [Mn(acac)$_2$(4-*tert*butylpyridine)$_2$][PF$_6$] (**Mn^{III}(*t*-Bupy)**[PF$_6$]) (acetonitrile-d_3, 400 MHz)



S76. ^{1}H NMR spectrum of [Mn(acac)$_2$(4-*tert*butylpyridine)$_2$][PF$_6$] (methylene chloride-d_2, 400 MHz)



S77. FTIR spectrum of [Mn(acac)$_2$(4-*tert*butylpyridine)$_2$][PF$_6$].

Manganese Containing Cubanes:

[$MnCo_3O_4(OAc)_4$(*t*-Bupy)$_4$][X]:

Method A (Moderate Scale): Reaction of $Mn(OAc)_2$ + $Co^{III}_4O_4(OAc)_4$(*t*-Bupy)$_4$

A 20 mL vial was charged with a stir bar, **Co$_4$** ($Co^{III}_4O_4(OAc)_4$(*t*-Bupy)$_4$) (0.4000 g, 0.36 mmol), NH_4PF_6 (0.060 g, 0.36 mmol) and MeCN (5 mL). The solution was stirred vigorously as $Mn(OAc)_2$ (0.062 g, 0.36 mmol) was added in one portion. The vial was capped, transferred to an oil bath, the solution was stirred, and heated to 70 °C for 16 h, resulting in a rusty red solution. The vial was removed from the oil bath and allowed to cool to ambient temperature. The solvent was removed *in vacuo*, and the resulting solids were taken up in CH_2Cl_2 (5 mL) and filtered into a 20 mL vial through Celite® supported on a glass wool plug in a pipette. The resulting solution was allowed to evaporate slowly at ambient conditions over 48 h by covering the vial with an inverted rubber septum punctured with a wide gauge needle, and the resulting microcrystalline solids were collected on a fine porosity fritted funnel. The solids were dissolved in minimal CH_2Cl_2, chilled to –5 °C, and layered with –5 °C hexanes. The layers were allowed to diffuse at –5 °C over 40 h to form blocks of **MnCo$_3$**[PF_6] ([$MnCo_3O_4(OAc)_4$(*t*-Bupy)$_4$][PF_6]) suitable for X-ray diffraction analysis. Yield: 0.141 g (33%). **Characterization data:** ^{1}H NMR (400 MHz, acetonitrile-d_3) δ 9.74 (s, 4H), 7.99 (s, 1H), 3.66 (s, 7H), 2.43 (s, 9H), 2.15 (s, 15H), 1.33 (s, 36H), due to the paramagnetic broadening, some resonances were unobserved, and the integrals are not internally consistent. ^{19}F{^{1}H} NMR (376 MHz, acetonitrile-d_3) δ –72.35 (d, $J_{F\text{-}P}$ = 705.7 Hz). ^{31}P{^{1}H} NMR (162 MHz, acetonitrile-d_3) δ –143.19 (d, $J_{P\text{-}F}$ = 706.2 Hz). IR (cm^{-1}): 2966 (w), 2873 (w), 1618 (m), 1529 (m, broad), 1499 (m), 1402 (s, broad), 1346 (w), 1273 (w), 1071 (m), 1063 (w), 830 (s), 734 (m), 694 (s), 626 (s), 577 (s). Anal. Calcd for $C_{44}H_{64}Co_3F_6MnN_4O_{12}P$: C, 43.40; H, 5.30; N, 4.60. Found: C, 43.02; H, 5.50; N, 4.45. HRMS (ESI): m/z: Calcd. for $[C_{44}H_{64}Co_3MnN_4O_{12}]^+$: 1072.1892 Found: 1072.2026.

Method A (Small Scale): Reaction of $Mn(OAc)_2$ + $Co^{III}_4O_4(OAc)_4$(*t*-Bupy)$_4$

A 20 mL vial was charged with a stir bar, **Co$_4$** ($Co^{III}_4O_4(OAc)_4$(^{t}Bupy)$_4$) (20.0 mg, 0.019 mmol) NH_4PF_6 (3.0 mg, 0.018 mmol) and $Mn(OAc)_2$ (3.2 mg, 0.018 mmol). MeCN (5 mL) was added, the vial was capped, transferred to an oil bath, and the solution was stirred vigorously at 55 °C for 16 h. The vial was then removed from the oil bath and allowed to cool to ambient temperature, then solvent was removed *in vacuo*. The resulting solids were dissolved in CH_2Cl_2 (*ca*. 3 mL) and filtered into a 20 mL vial through a glass wool plug filter in a pipette. The solution was cooled to –5 °C, layered with chilled pentane (*ca*. 1 mL), and placed in a –5 °C freezer and the layers were allowed to diffuse for 16 h, resulting in dark red crystals of **MnCo$_3$**[PF_6] ([$MnCo_3O_4(OAc)_4$(^{t}Bupy)$_4$][PF_6]) (Isolated yields from three separate experiments: 12.0 mg, 7.5 mg, 9.6 mg; 52%, 33%, 42%).*

**Note:* The yield of small-scale experiments was highly dependent on the efficiency of the recrystallization. Addition of excess antisolvent results in some co-crystallization of some of the cobalt oligomers described in the text, while too little anti-solvent resulted in lower yields. HR-ESI-MS and ^{1}H NMR spectroscopic analysis confirmed the product to be highly pure with only trace oligomeric cobalt species present.

Method B: Reaction of $Mn(OAc)_2$ + $[Co^{IV}Co^{III}_3O_4(OAc)_4(t\text{-Bupy})_4][PF_6]$

A 20 mL vial was charged with a stir bar, **$Co_4^+[PF_6]$** ($[Co^{IV}Co^{III}_3O_4(OAc)_4(t\text{-Bupy})_4][PF_6]$) (20.0 mg, 0.01638 mmol, 1.00 equiv) and $Mn(OAc)_2$ (2.8 mg, 0.01627 mmol, 1.00 equiv). MeCN (*ca.* 4 mL) was added, the vial was capped, transferred to an oil bath, heated to 40 °C and stirred vigorously for 16 h. Following this, the solvent was removed *in vacuo*, and the resulting solids were taken up in CH_2Cl_2 (*ca*. 3 mL) and filtered through a glass wool plug in a pipette into a 20 mL vial. The solution was cooled to –5 °C, layered with chilled pentane (*ca*. 1 mL), and placed in a –5 °C freezer in which the layers were allowed to diffuse for 16-40 h, resulting in dark red crystals of **$MnCo_3[PF_6]$** ($[MnCo_3(O)_4(OAc)_4(t\text{-Bupy})_4][PF_6]$) (11.1 mg, 11.0 mg, 12.6 mg; 56%, 55%, 63%). The mother liquors were separated from the crystalline material and the solvent removed *in vacuo*. The solids were then dissolved in minimal CH_2Cl_2 and the solution transferred to a 4 mL vial. The solution was chilled to –5 °C, then layered with an equal volume of cold pentane to exhaustively crystallize **$MnCo_3[PF_6]$**. Combined yield: (Isolated yields from three separate experiments: 16.5 mg, 15.4 mg,15.9 mg; 83%, 76%, 80%).* Exhaustive crystallization of the mother liquors yields $[Co_2(OH)_2(OAc)_3(t\text{-Bupy})_4][PF_6]$ in very low (>1% yield).

**Note*: This reaction is less sensitive to crystallization conditions than Method A.

Method C: Reaction of $Mn(OTf)_2$ + $Co^{III}_4O_4(OAc)_4(t\text{-Bupy})_4$

A 20 mL vial was charged with a stir bar, **Co_4** ($Co^{III}O_4(OAc)_4(t\text{-Bupy})_4$) (20.0 mg, 0.019 mmol), and $Mn(OTf)_2$ (8.2 mg, 0.023 mmol). MeCN (5 mL) was added, the vial was capped, then transferred to an oil bath, and heated to 55 °C for 16 h while the reaction mixture was stirred. The vial was then removed from the oil bath and allowed to cool to ambient temperature, then the solvent was removed *in vacuo*. The resulting solids were dissolved in CH_2Cl_2 (*ca*. 3 mL) and filtered through a glass wool plug in a pipette into a 20 mL vial. The solution was chilled to –5 °C and layered with cold pentane (*ca*. 1.5 mL). The layers were allowed to diffuse at –5 °C for 48 h, resulting in red crystals of $[MnCo_3O_4(OAc)_4(t\text{-Bupy})_4][OTf]$ (9.8 mg, 7.6 mg, 10.1 mg; 43%, 33%, 45%)

Note*:* The yield of these small scale $Co^{III}_4O_4$ reactions was highly dependent on the efficiency of the crystallization. HR-ESI-MS and ^1H NMR confirmed the product to be mostly pure with only trace oligomeric cobalt species see S and S.

Note: Monitoring by ^1H NMR spectroscopy, the reaction between $Mn(OTf)_2$ and $Co^{III}O_4(OAc)_4(^t\text{Bupy})_4$ first results in a desymmetrized Co_4O_4 product, presumably $Co^{III}O_4(OAc)_3(OTf)(t\text{-Bupy})_4$. See S

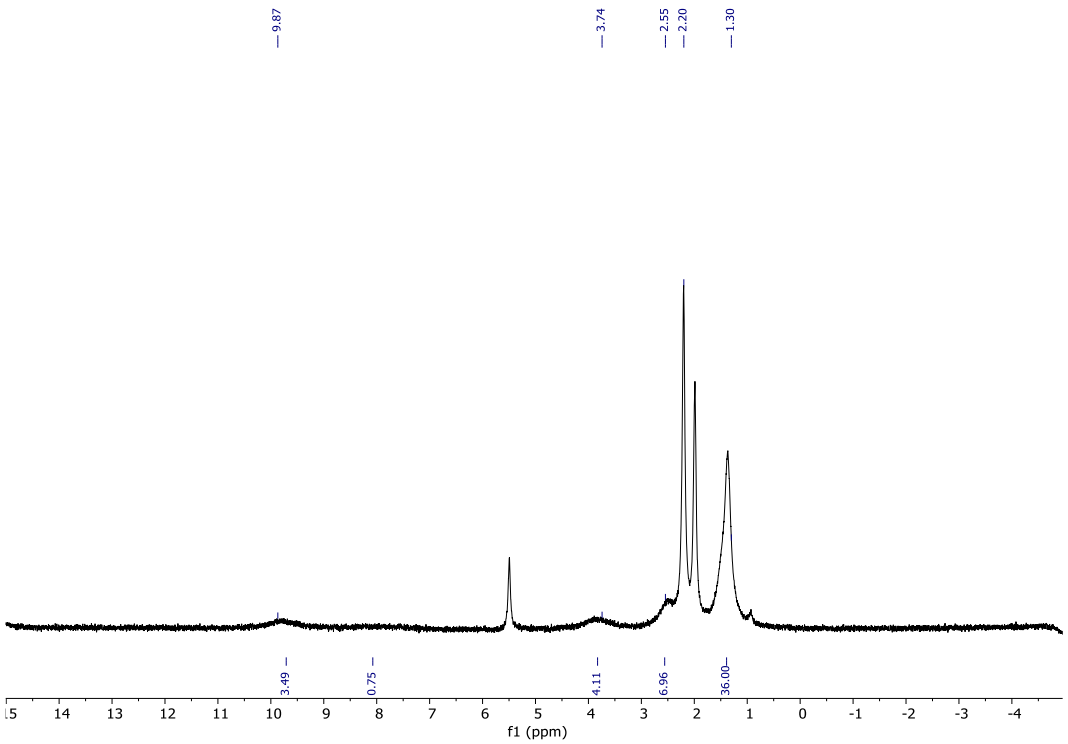
Method D: Reaction of $Mn(OTf)_2$ + $[Co^{IV}Co^{III}_3O_4(OAc)_4(t\text{-Bupy})_4][PF_6]$:

A 20 mL vial was charged with a stir bar, $[Co^{IV}Co^{III}_3O_4(OAc)_4(^t\text{Bupy})_4][PF_6]$ (20.0 mg, 0.016 mmol), $Mn(OTf)_2$ (2.8 mg, 0.016 mmol) and MeCN (5 mL). The vial was capped, transferred to an oil bath, and heated to 30 °C for 16 h. The vial was then removed from the oil bath, and the solvent removed *in vacuo*. The resulting solids were dissolved in CH_2Cl_2 (*ca*. 3 mL) and filtered through a glass wool plug in a pipette into a 20 mL vial. The solution was chilled to –5 °C and layered with cold pentane (*ca*. 1.5 mL). The layers were allowed to diffuse at –5 °C for 48 h, resulting in small crystals of **$MnCo_3[PF_6]$** $[MnCo_3O_4(OAc)_4(t\text{-Bupy})_4][PF_6]$. (Isolated yields from three separate experiments:6.0 mg, 9.0 mg, 7.2 mg, 60%, 90%, 72%)

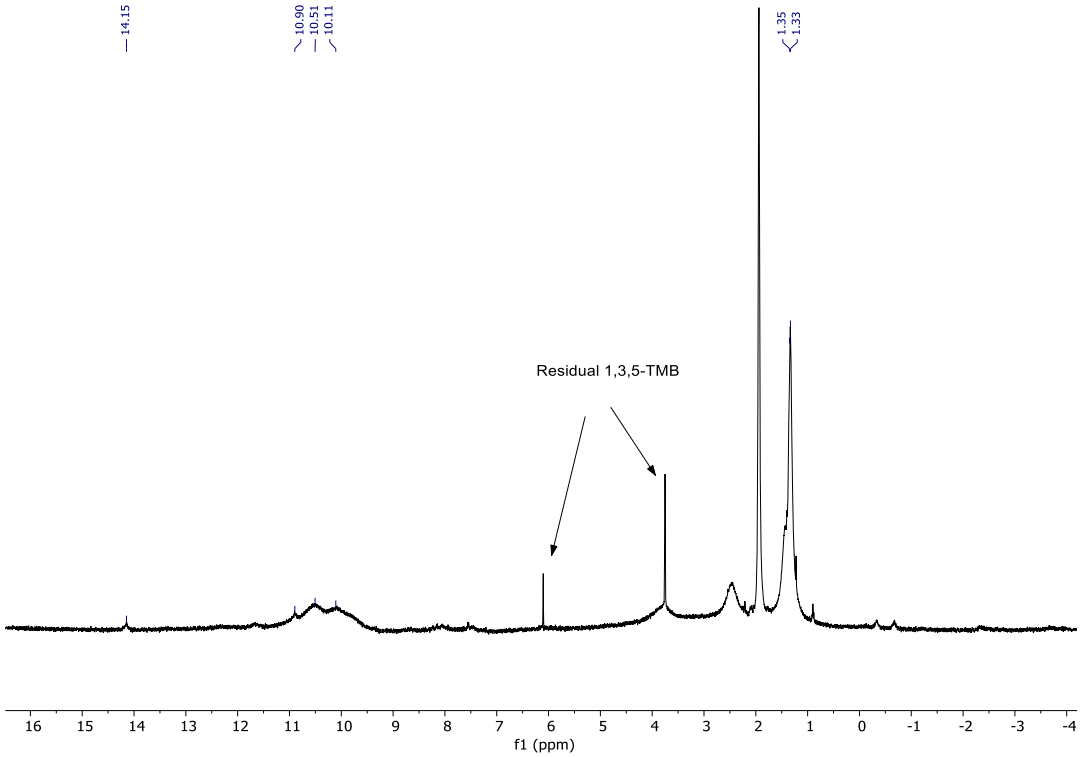
Method E: Reaction of $Mn(acac)_3$ + $Co^{III}_4O_4(OAc)_4$(*t*-Bupy)$_4$:

A 20 mL vial was charged with a stir bar, $Co^{III}_4O_4(OAc)_4$(*t*-Bupy)$_4$ (0.200 g, 0.18 mmol), NH_4PF_6 (0.030 g, 0.18 mmol), $Mn(acac)_3$ (0.064 g, 0.18 mmol), and MeCN (3 mL). The vial was capped, transferred to an oil bath, the solution was stirred, and heated to 40 °C for 16. The volatile components were removed in vacuo to give brown solids. The solids were extracted into minimal CH_2Cl_2 and transferred to a 2.5 cm in diameter by 35 cm column loaded with 27 cm of silica gel that was wet-loaded in 5% MeOH in CH_2Cl_2. The column was washed with 5% MeOH:CH_2Cl_2 to elute a red/pink band ([Co(acac)$_2$(*t*-Bupy)$_2$][PF_6] by ^{1}H NMR spectroscopy) with a moderate R_f (0.38) and a dark brown band with R_f = 0.06 ([$MnCo_3O_4(OAc)_4$(*t*-Bupy)$_4$][PF_6])/[$MnCo_3O_4(OAc)_3$(acac)(*t*-Bupy)$_4$][PF_6]).* The dark brown solution from the second band was collected and the volatiles removed in vacuo to give dark brown solids. These solids are slightly contaminated (by ^{1}H NMR spectroscopic analysis) with residual **Co$_4$** and [Co(acac)$_2$(*t*-Bupy)$_2$][PF_6]. Material free from these impurities (by HR-ESI-MS analysis and ^{1}H NMR spectroscopy) was obtained following crystallization from a chilled CH_2Cl_2 solution of the product layered with chilled pentane that was allowed to diffuse at –5 °C for several days (0.077 g, 33%). For material obtained directly following chromatography. Anal. Calcd for $C_{47}H_{68}Co_3F_6MnN_4O_{12}P$: C, 44.88; H, 5.45; N, 4.45. Found: C, 47.75; H, 5.75; N, 5.08. Note that this analysis was calculated for the acac ligand substituted cubane, and is consistent with one equiv of residual 4-*tert*-butylpyridine present in the sample.

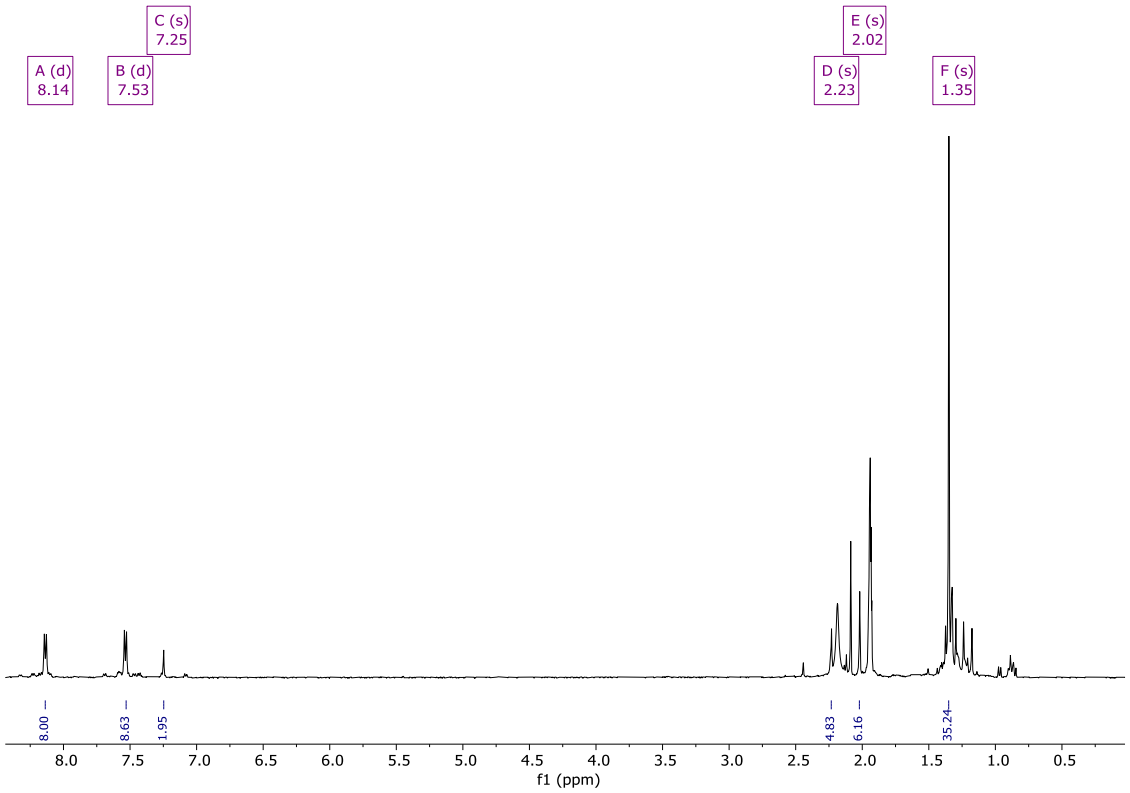
**Note:* The R_f values of [$MnCo_3O_4(OAc)_4$(*t*-Bupy)$_4$][PF_6] and [$MnCo_3O_4(OAc)_3$(acac)(*t*-Bupy)$_4$][PF_6] are only slightly different, which makes their separation by column chromatography difficult. In 10% MeOH:CH_2Cl_2, the still smeared spots are the most distinct, with R_f values of 0.85, and 0.80.



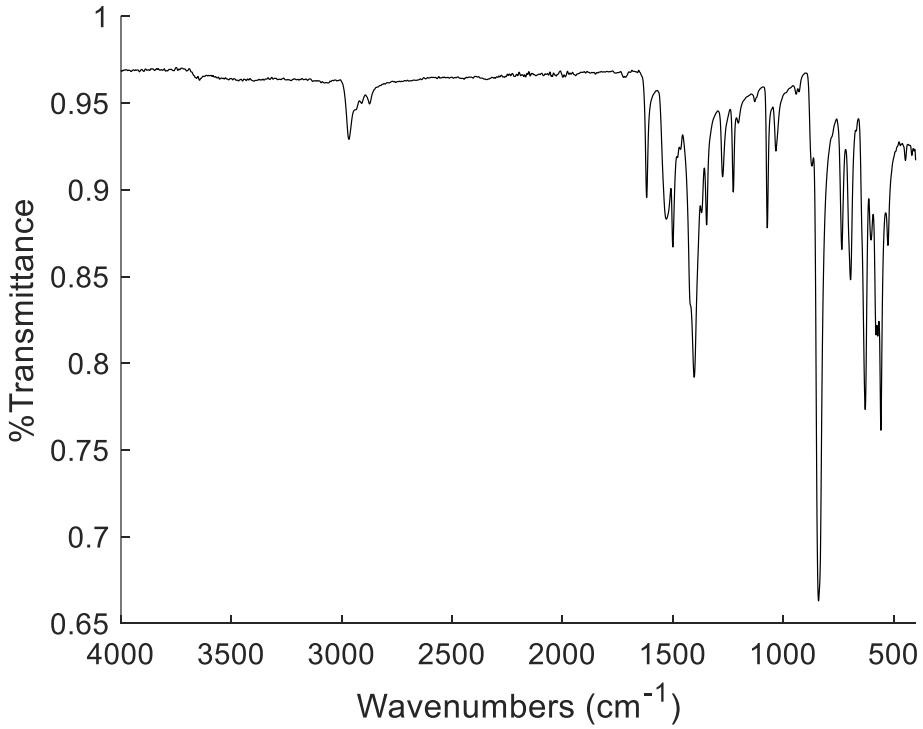
S78. ^{1}H NMR spectrum of **MnCo$_3$**[PF$_6$] [MnCo$_3$O$_4$(OAc)$_4$(*t*-Bupy)$_4$][PF$_6$] (acetonitrile-d_3, 400 MHz). Peak at 5.49 ppm is residual CH_2Cl_2.



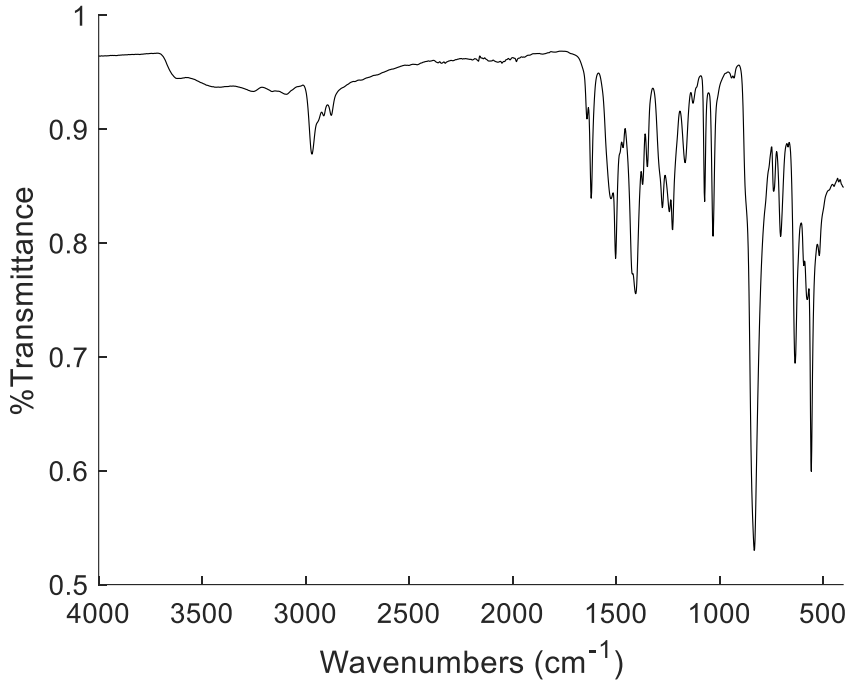
S79. ^{1}H NMR spectrum of **MnCo$_3$**[OTf] [MnCo$_3$O$_4$(OAc)$_4$(*t*-Bupy)$_4$][OTf] (acetonitrile-d_3, 400 MHz), some residual 1,3,5-trimethylbenzene (1,3,5-TMB) present (used as internal standard).



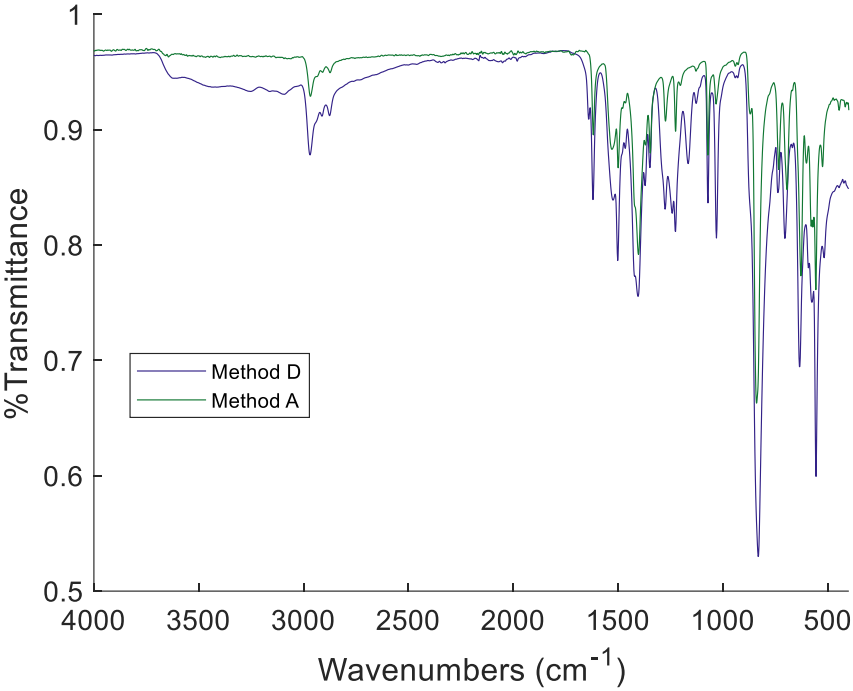
S80. ^{1}H NMR spectrum of $[Co_2(OH)_2(OAc)_3(t\text{-Bupy})_4][PF_6]$ (acetonitrile-d_3, 400 MHz). The values match those reported in the literature.[11]



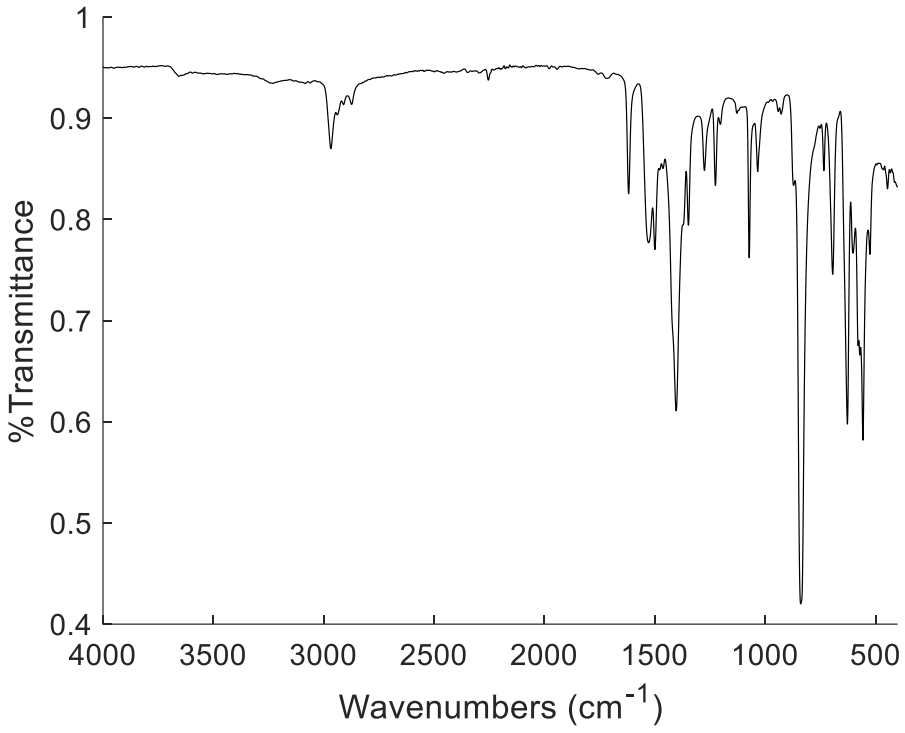
S81. FTIR spectrum of $[MnCo_3O_4(OAc)_4(t\text{-Bupy})_4][PF_6]$ (**MnCo$_3$**[PF_6]) produced by Method A.



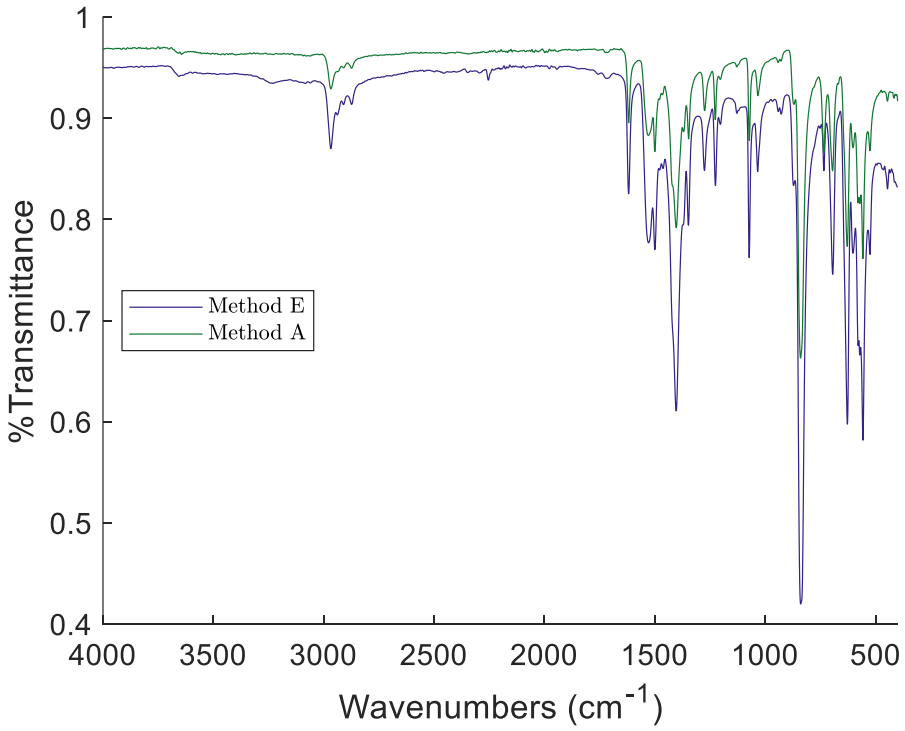
S82. FTIR spectrum of $[MnCo_3O_4(OAc)_4(t\text{-Bupy})_4][PF_6]$ (**MnCo$_3$**$[PF_6]$) produced by method D. The low intensity of the sulfonate stretch suggests that the material is primarily the PF_6 salt. Note that the $^{-}$OTf and $^{-}PF_6$ anions have very similar molecular weights (149.06 and 144.96) respectively and thus any $^{-}$OTf anion present does not significantly change the % yield of the manganese cobalt oxo cubane product.



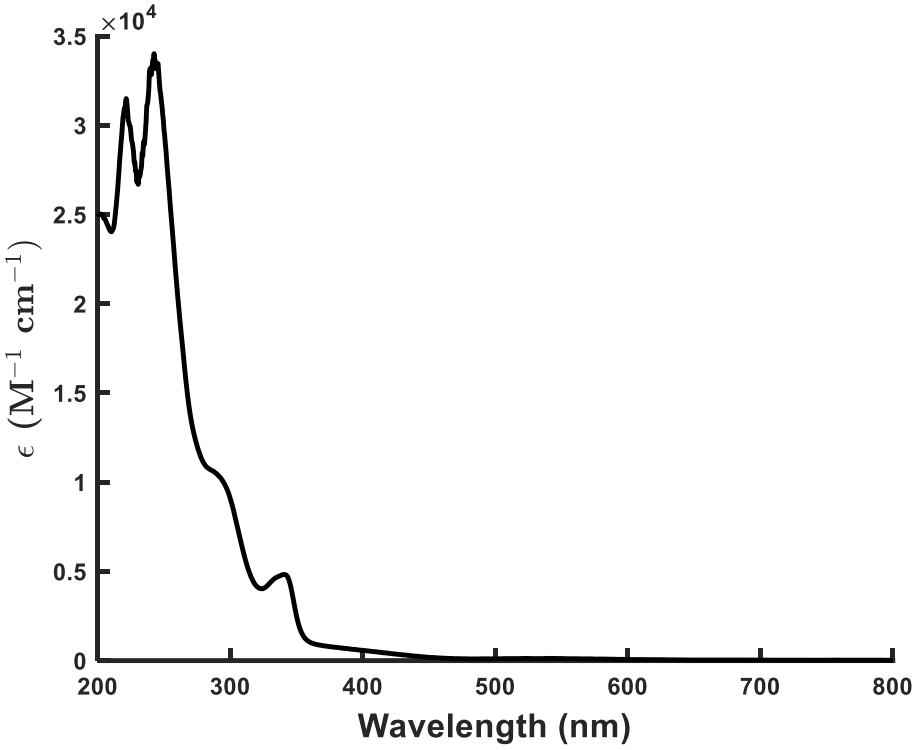
S83. Stacked spectra from figure **S81** and **S82** demonstrating (by comparison of the PF_6 stretch at 830 cm^{-1} and sulfate stretch at *ca*. 1020 cm^{-1}) that triflate substitution for hexafluorophosphate is minimal in this product.



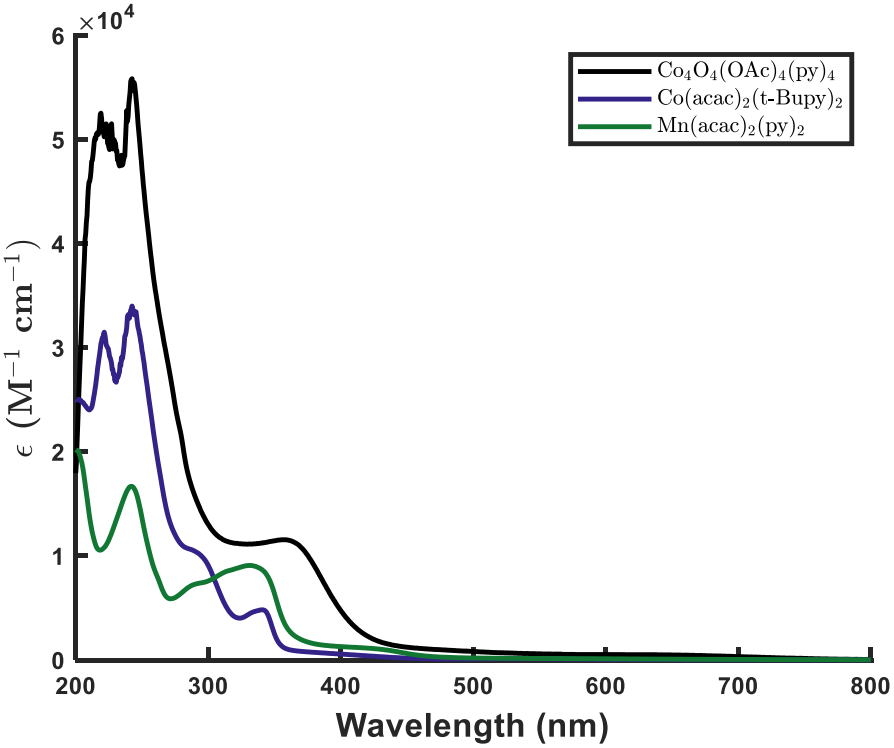
S84. FTIR spectrum of $[MnCo_3O_4(OAc)_4(t\text{-Bupy})_4][PF_6]$/$[MnCo_3O_4(OAc)_3(acac)(t\text{-Bupy})_4][PF_6]$ **$MnCo_3$/$MnCo_3$(acac)**$[PF_6]$ produced by method E.



S85. Stacked spectra from figure **S81** and **S84** demonstrating that despite some amount of (acac) ligand substitution the overall composition of the $[MnCo_3O_4]$ cubane present is similar.

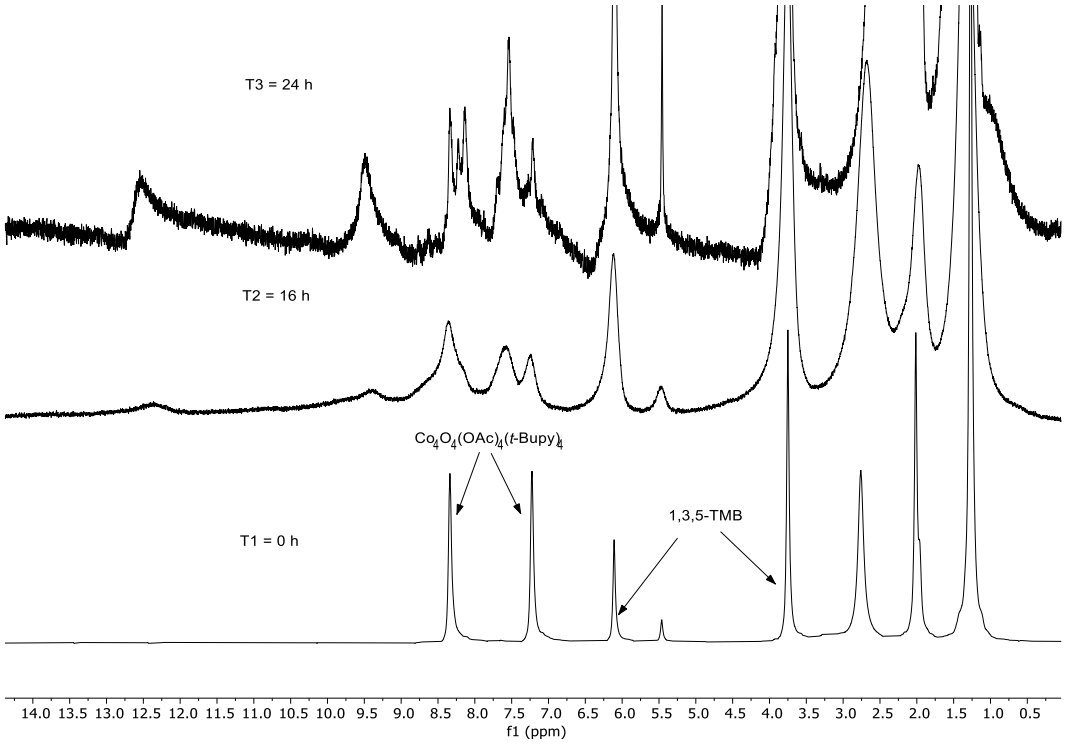


S86. Molar extinction coefficients for $[Co(acac)_2(t\text{-Bupy})_2][PF_6]$ in MeCN.

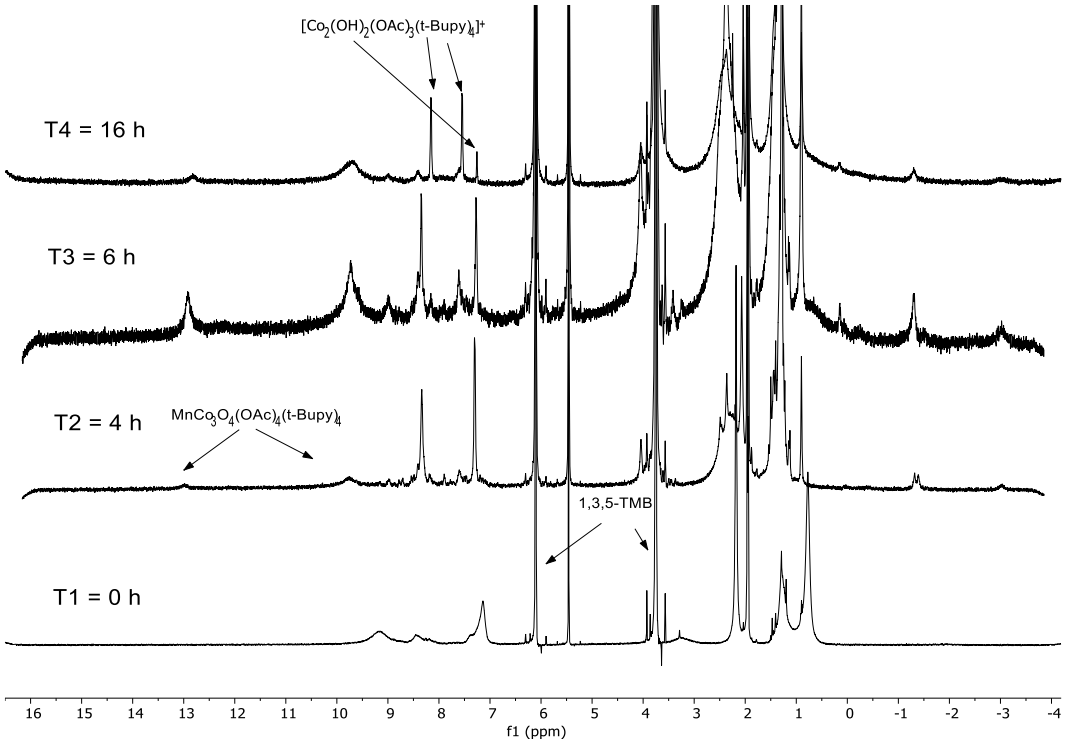


S87. Comparison of molar extinction coefficients for the key metal complexes used in this study.

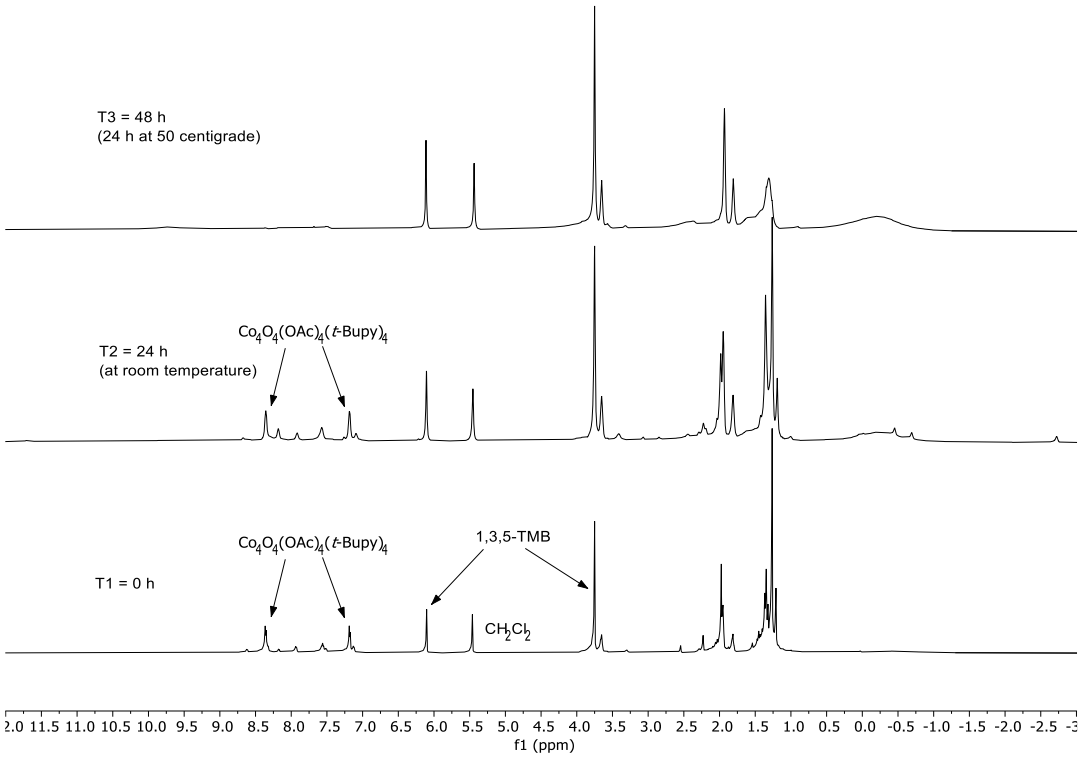
NMR SPECTRA OF REACTION MIXTURES



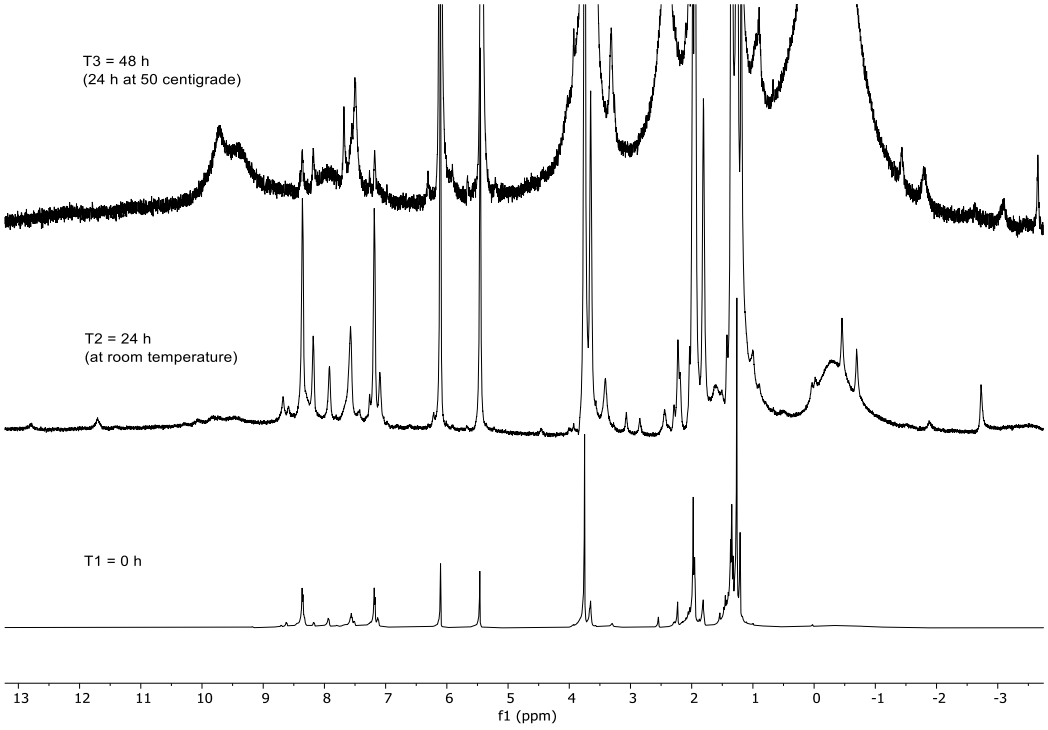
S88. Representative ^{1}H NMR spectra from data collected in triplicate of the reaction between equimolar $Mn(OAc)_2$ and **Co$_4$** at T = 0 h, after 24 h at room temperature, and after 24 h at 50 °C (acetonitrile-d_3, 400 MHz). 1,3,5-TMB = 1,3,5-trimethoxybenzene.



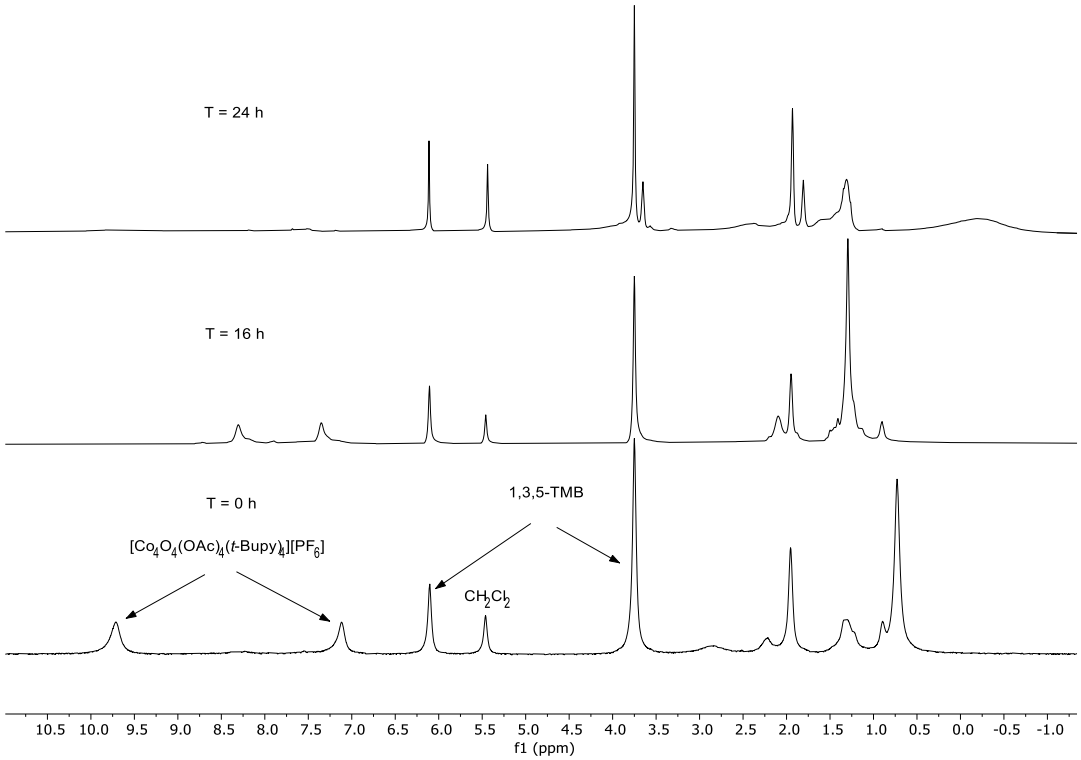
S89. Representative ^{1}H NMR spectra from data collected in triplicate of the reaction between equimolar $Mn(OAc)_2$ and **Co$_4$**$^+$[PF_6] at T = 0h, after 24 h at room temperature, and after 24 h at 50 °C (acetonitrile-d_3, 400 MHz). 1,3,5-TMB = 1,3,5-trimethoxybenzene.



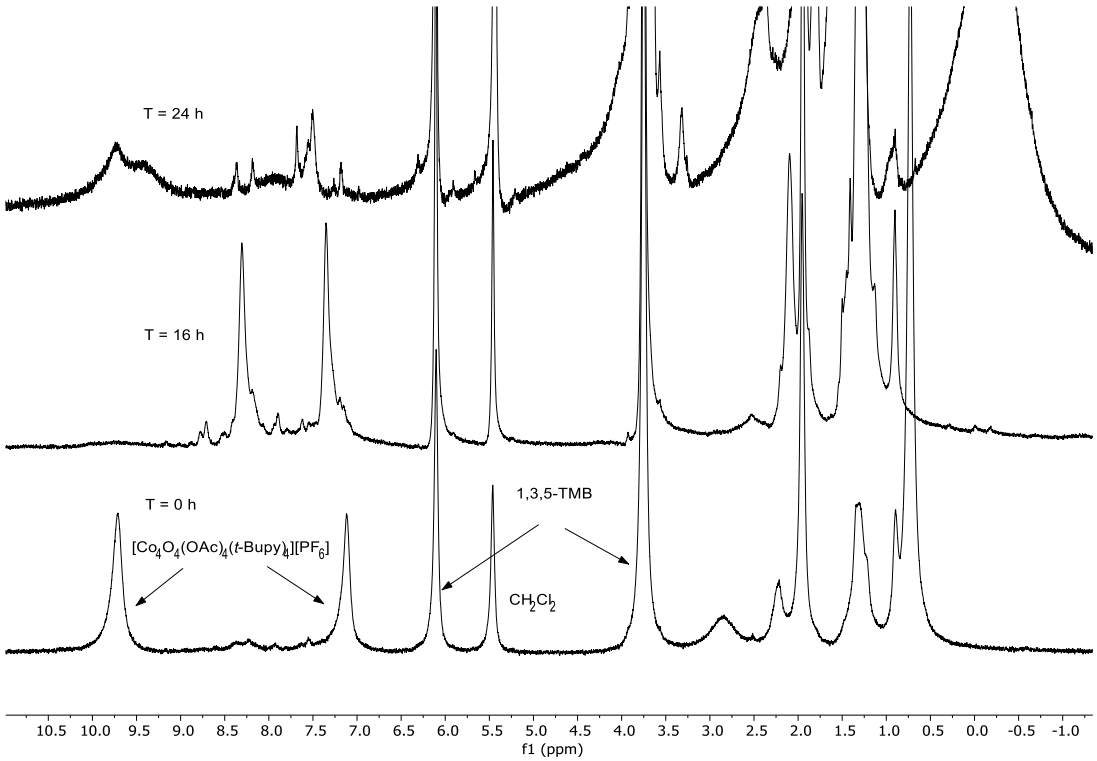
S90. Representative ^{1}H NMR spectra from data collected in triplicate of the reaction between equimolar $Mn(OAc)_2$ and **Co$_4$** under an N_2 atmosphere with dried acetonitrile-d_3 at T = 0 h, after 24 h at room temperature, and after 24 h at 50 °C (acetonitrile-d_3, 400 MHz). 1,3,5-TMB = 1,3,5-trimethoxybenzene.



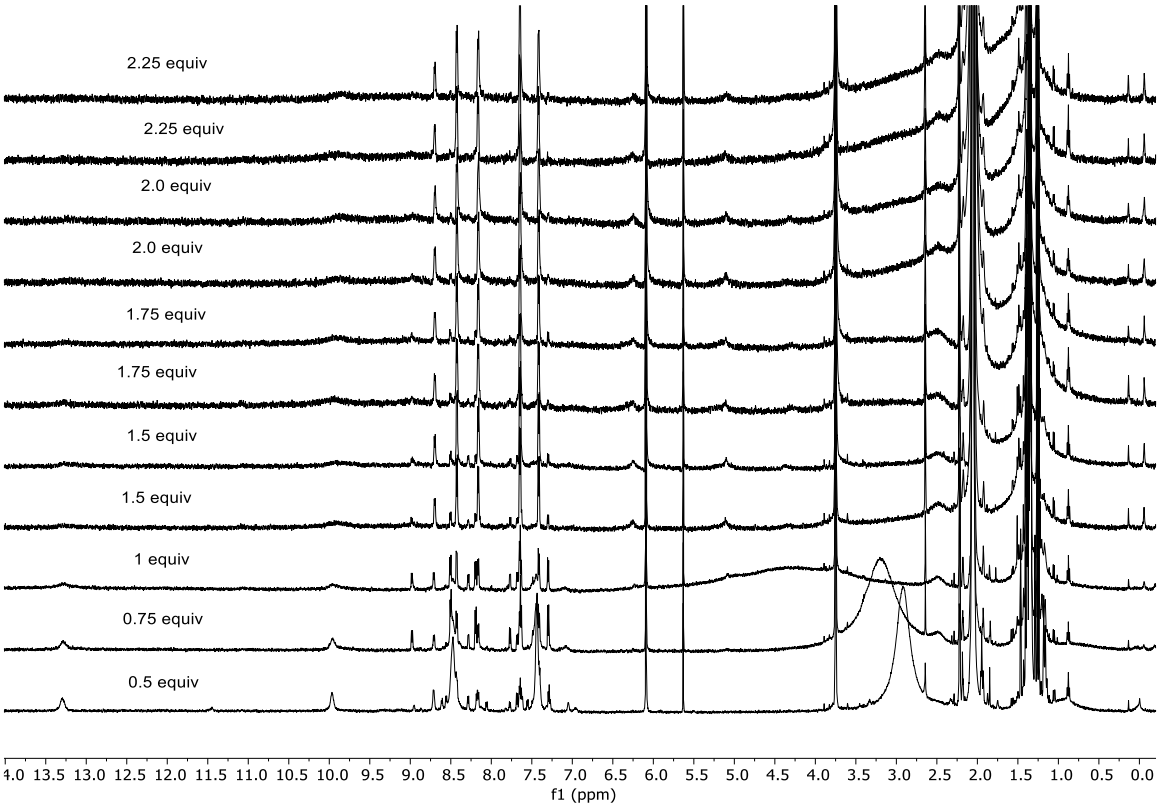
S91. Enhancement of the signal intensity of figure **S90** to show formation of paramagnetic product **MnCo$_3$**[PF_6]. 1,3,5-TMB = 1,3,5-trimethoxybenzene.



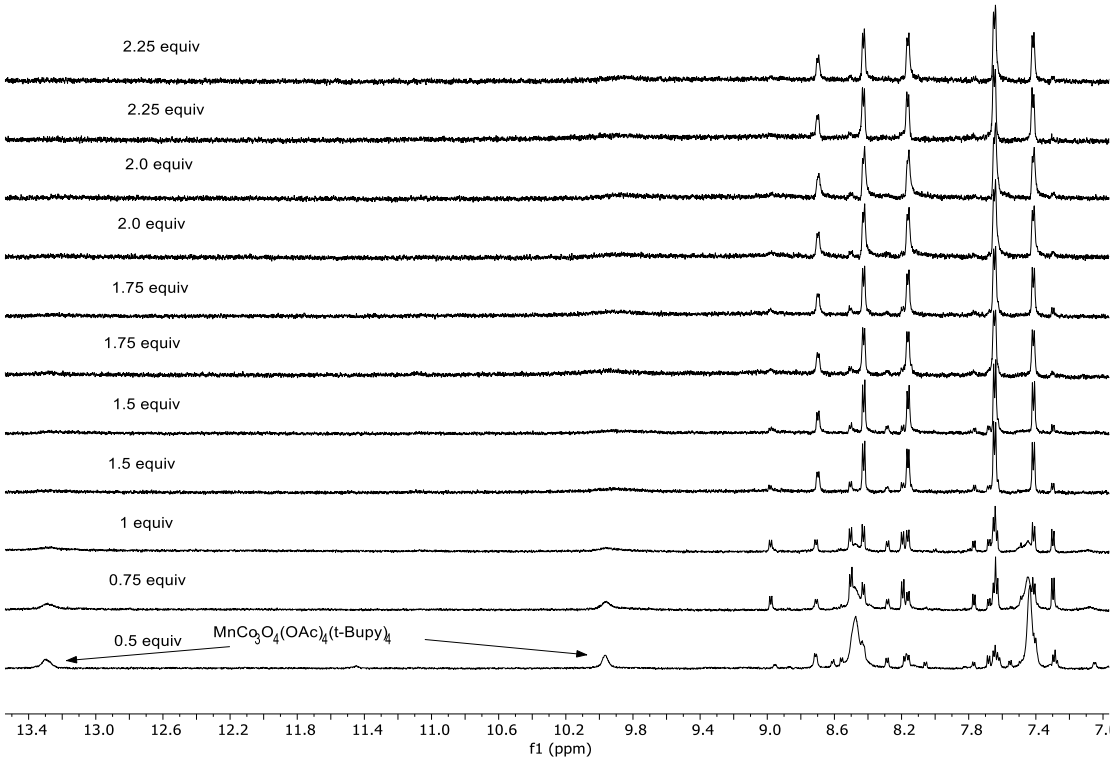
S92. Representative ^{1}H NMR spectra from data collected in triplicate of the reaction between equimolar $Mn(OAc)_2$ and $\mathbf{Co_4}^{+}[PF_6]$ under an N_2 atmosphere with dried acetonitrile-d_3 after 24 h at room temperature, and after 24 h at 50 °C (acetonitrile-d_3, 400 MHz). 1,3,5-TMB = 1,3,5-trimethoxybenzene.



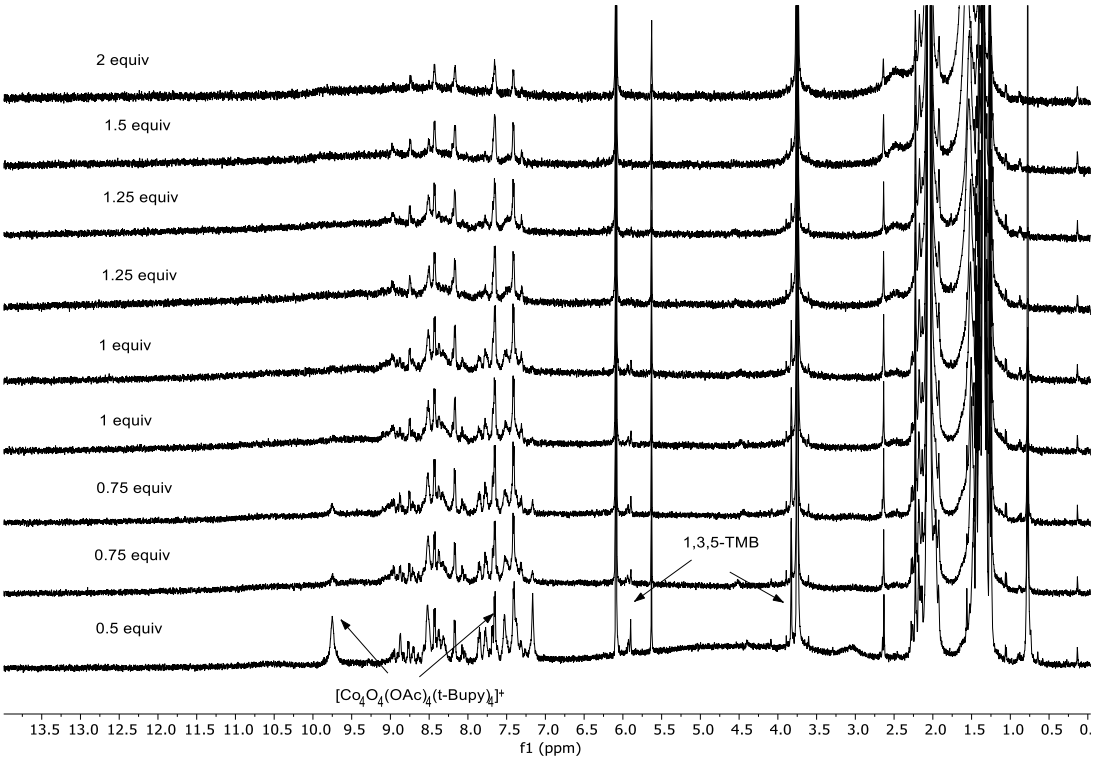
S93. Enhancement of the signal intensity of figure **S92** to show formation of paramagnetic product $\mathbf{MnCo_3}[PF_6]$. 1,3,5-TMB = 1,3,5-trimethoxybenzene.



S94. ^{1}H NMR spectra of various ratios of **Co4**:Mn(OTf)$_2$ heated for 16 h at 60 °C (acetonitrile-d_3, 400 MHz).

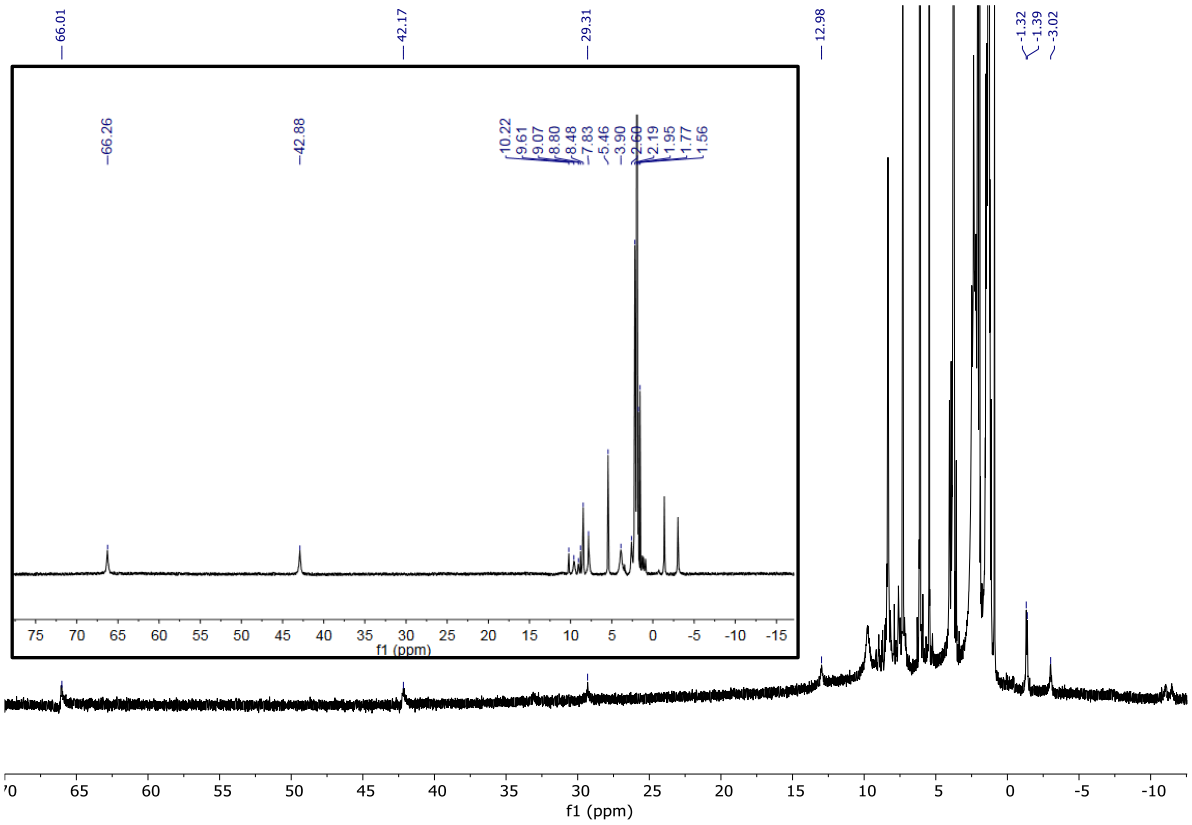


S95. Contraction of the spectral window ^{1}H NMR spectra of various ratios of **Co4**:Mn(OTf)$_2$ displayed in Figure **S94**, (acetonitrile-d_3, 400 MHz).

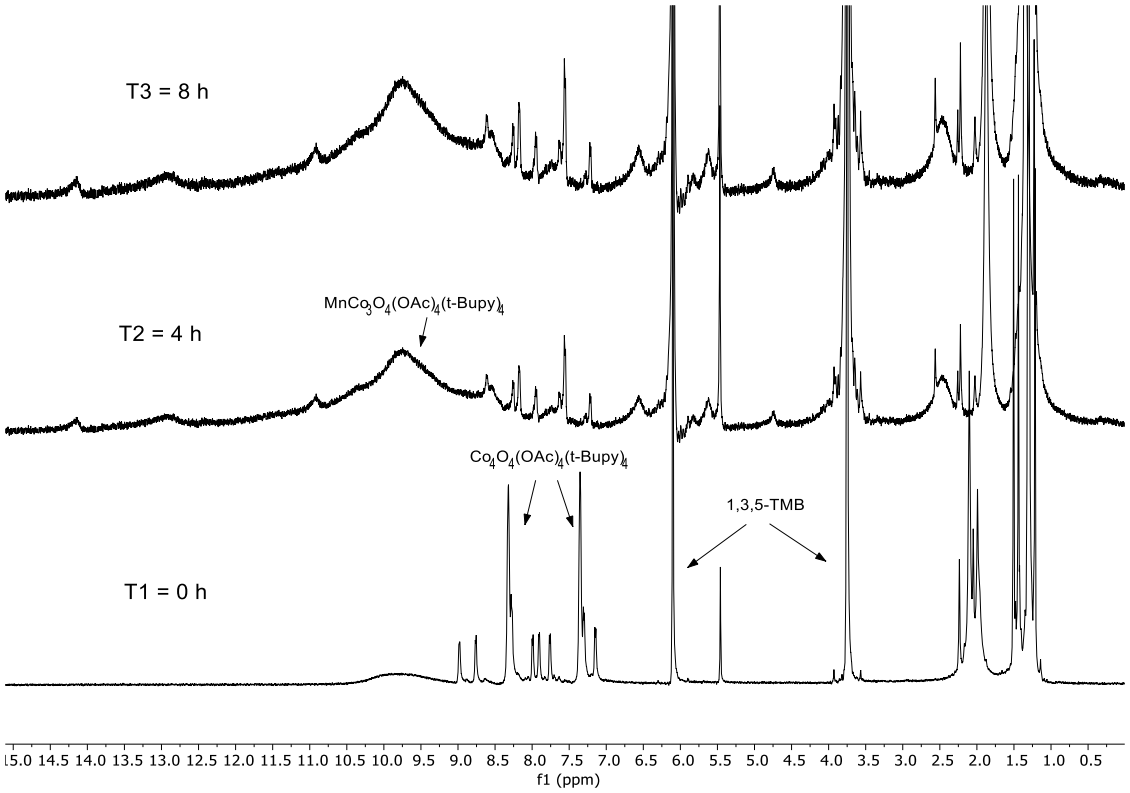


S96. ^{1}H NMR spectra of various ratios of **Co$_4$$^+$[PF$_6$]**:Mn(OTf)$_2$ heated for 16 h at 30°C (acetonitrile-d_3, 400 MHz).

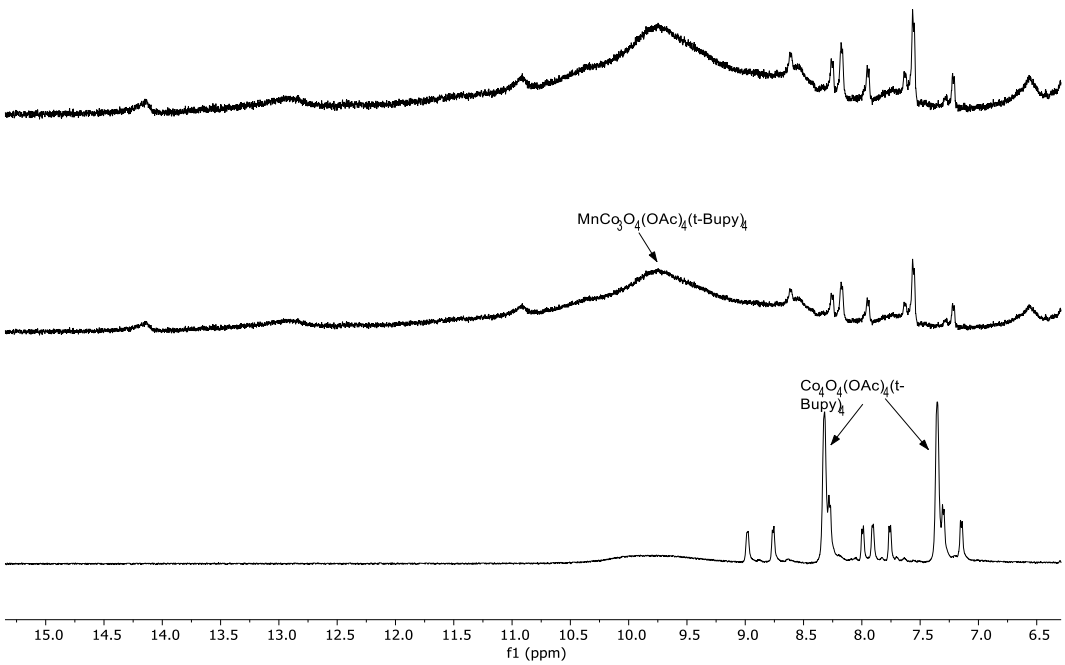
S97. ^{19}F{^{1}H} NMR taken after the reaction of **Co$_4$$^+$**[PF$_6$] with 1 equiv of Mn(OTf)$_2$ (acetonitrile-d_3, 376 MHz). The broad resonance at –74.4 ppm is consistent with the ^{19}F NMR spectrum reported for a tetradentate ligand containing Co^{II}(OTf)$_2$ complex, and though far from definitive, supports the notion that Co(OTf)$_2$ forms in solution.[12]



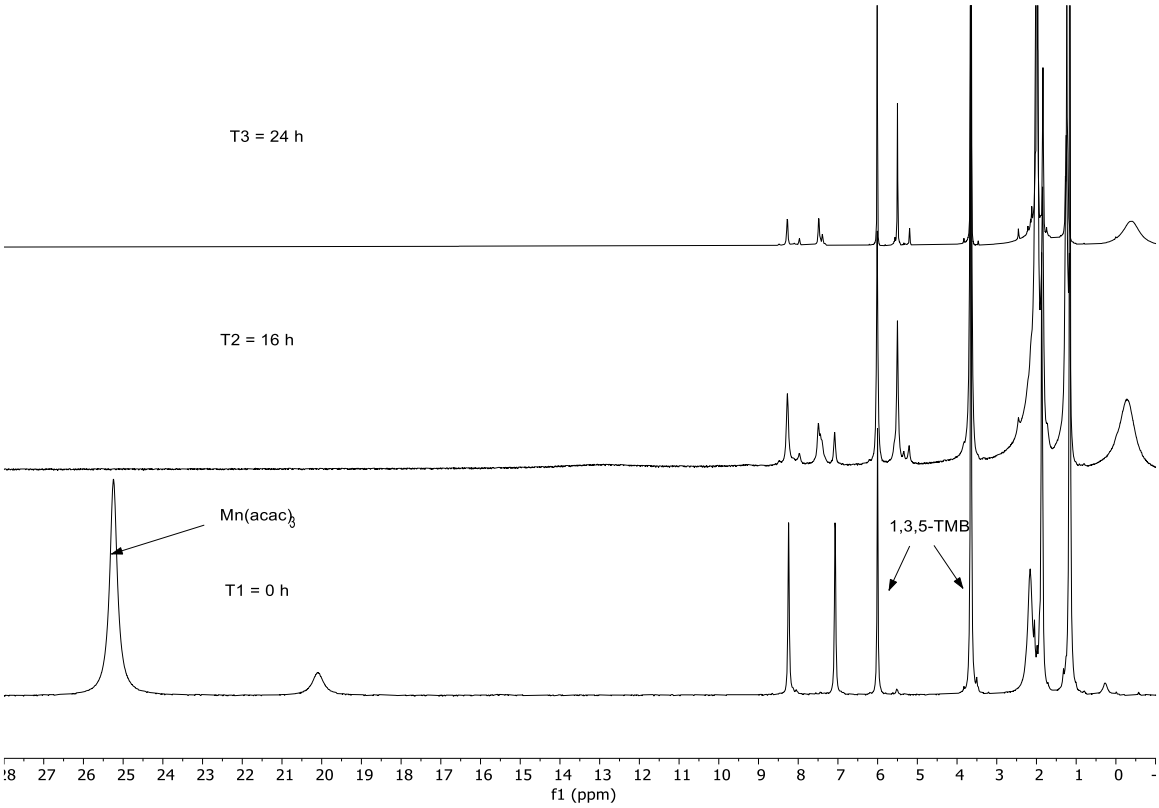
S98. ^{1}H NMR spectroscopic evidence for the formation of a $MnCo_4O_4(OAc)_7(t\text{-Bupy})_3$ cubane in the reaction between **Co4** and $Mn(OAc)_2$ at T2 = 4 h. The peaks at 66.01 ppm, 42.17 ppm, and 12.98 ppm are diagnostic of the previously reported nitrate dangler complex (Inset figure reproduced from Nguyen *et. al* 2018).[13]



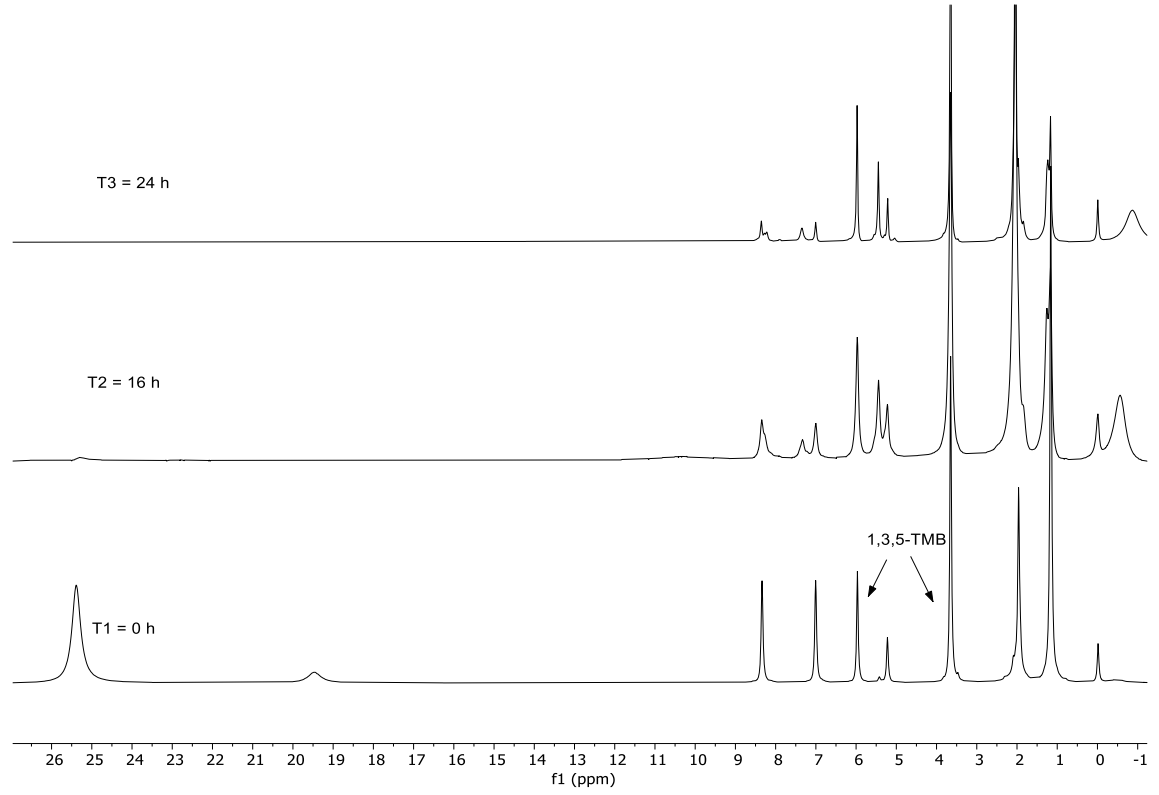
S99. Reaction of equimolar quantities of **Co4** and $Mn(OTf)_2$ as monitored by ^1H NMR spectroscopy (acetonitrile-d_3, 400 MHz). The observation of a low-symmetry species in the T1 = 0 h spectrum is consistent with exchange of acetate for triflate ligands. 1,3,5-TMB = 1,3,5-trimethoxybenzene.



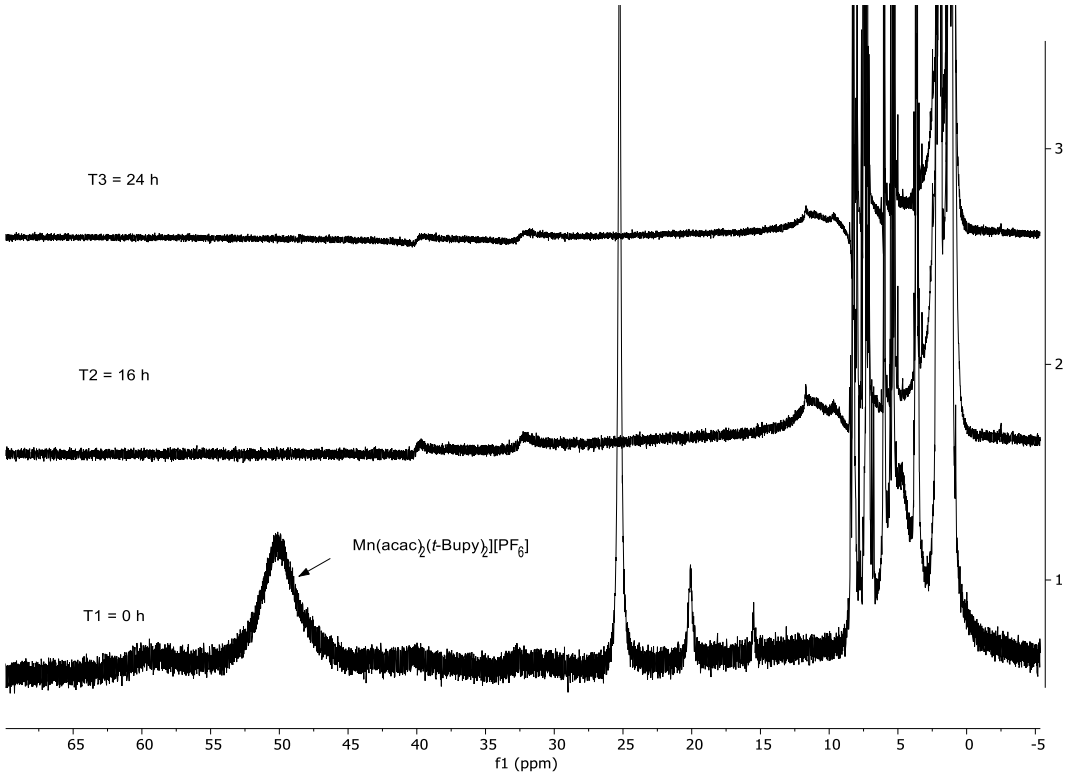
S100. Contraction of the spectral window of the ^1H NMR spectra displayed in **S99** (acetonitrile-d_3, 400 MHz).



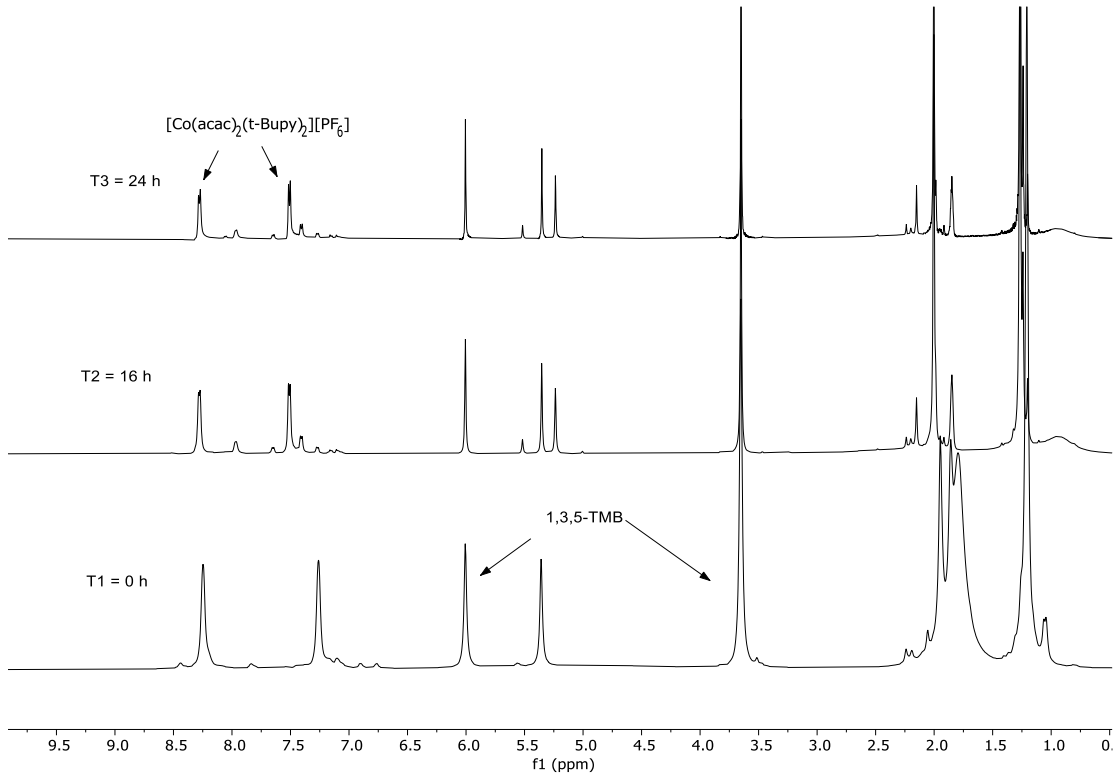
S101. The reaction of 2 equiv of $Mn(acac)_3$ with **Co4** as monitored by ^1H NMR spectroscopy (acetonitrile-d_3, 400 MHz).



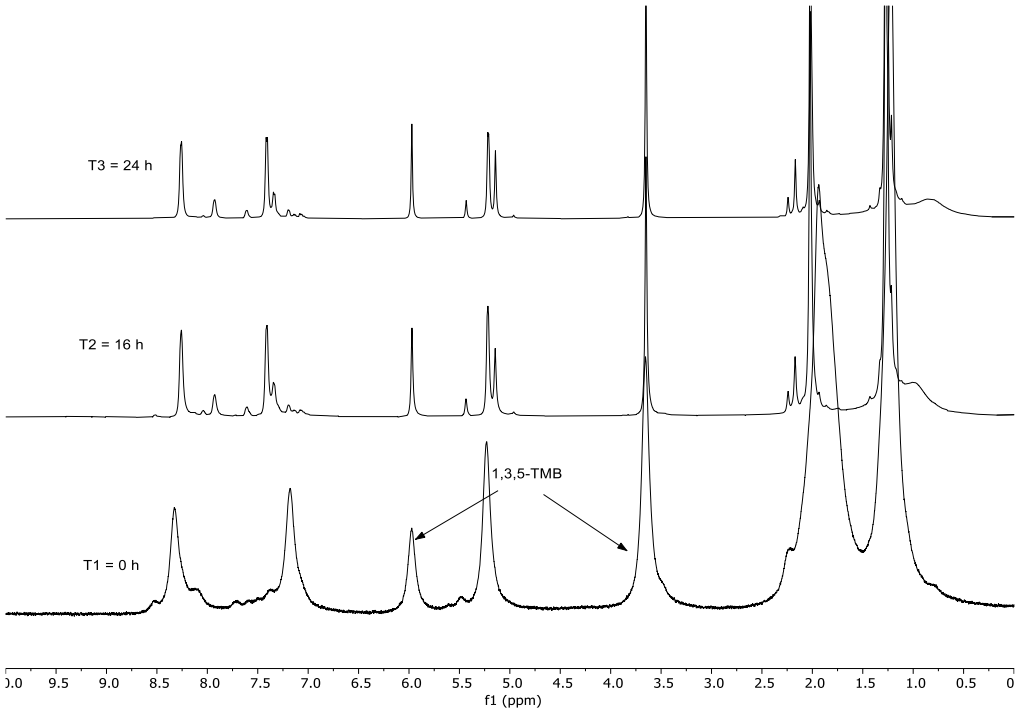
S102. The reaction of 2 equiv of $Mn(acac)_3$ with **Co4** as monitored by ^1H NMR spectroscopy (methylene cloride-d_2, 400 MHz).



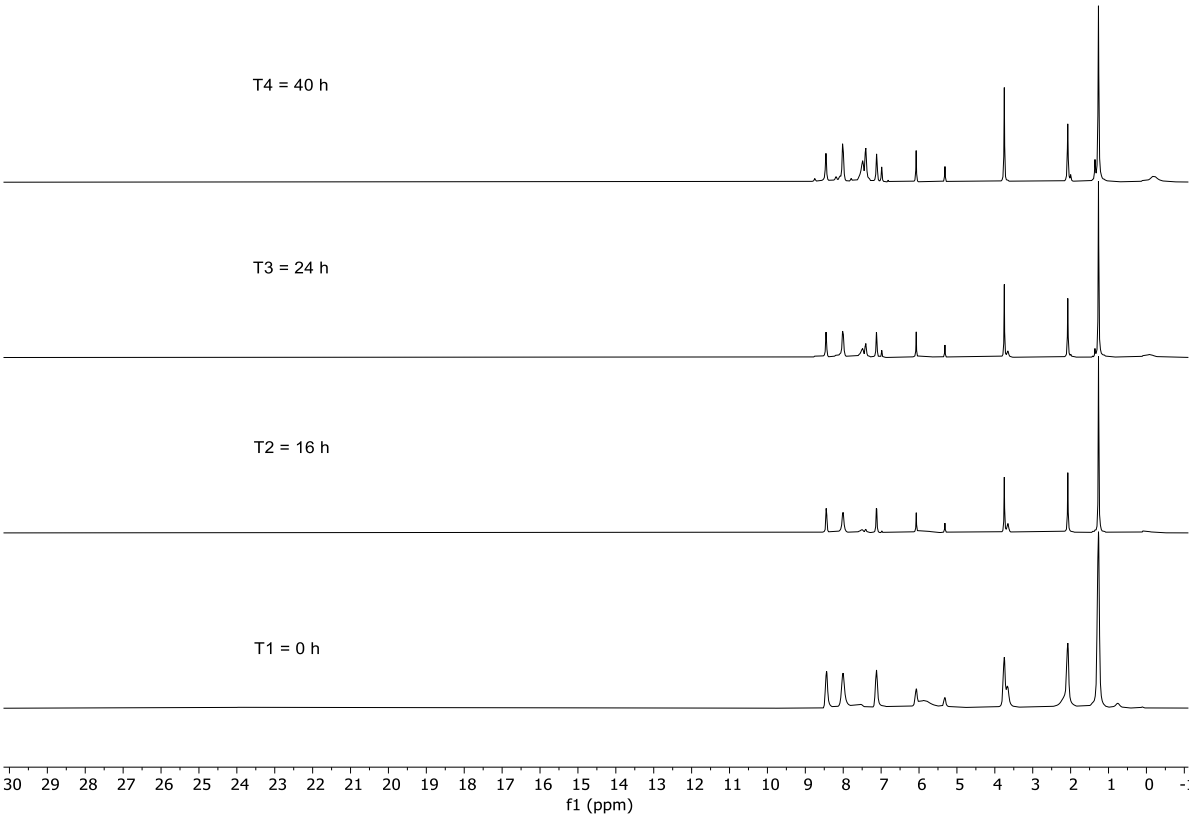
S103. Reaction of 2 equiv of [Mn(acac)$_2$(*t*-Bupy)$_2$][PF$_6$] (**Mn^{III}(*t*-Bupy)**[PF$_6$]) and **Co$_4$** as monitored by ^{1}H NMR spectroscopy (acetonitrile-d_3, 400 MHz).



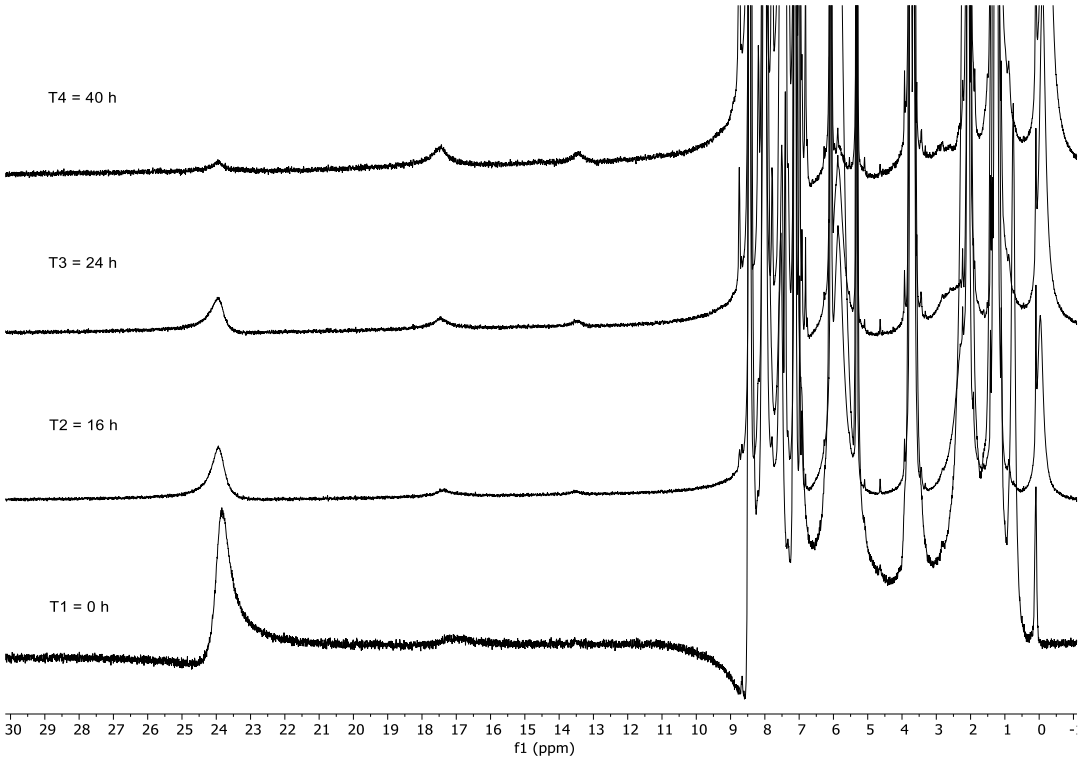
S104. Contraction of the spectral window of the ^{1}H NMR spectra displayed in Figure **S103** (acetonitrile-d_3, 400 MHz). 1,3,5-TMB = 1,3,5-trimethoxybenzene.



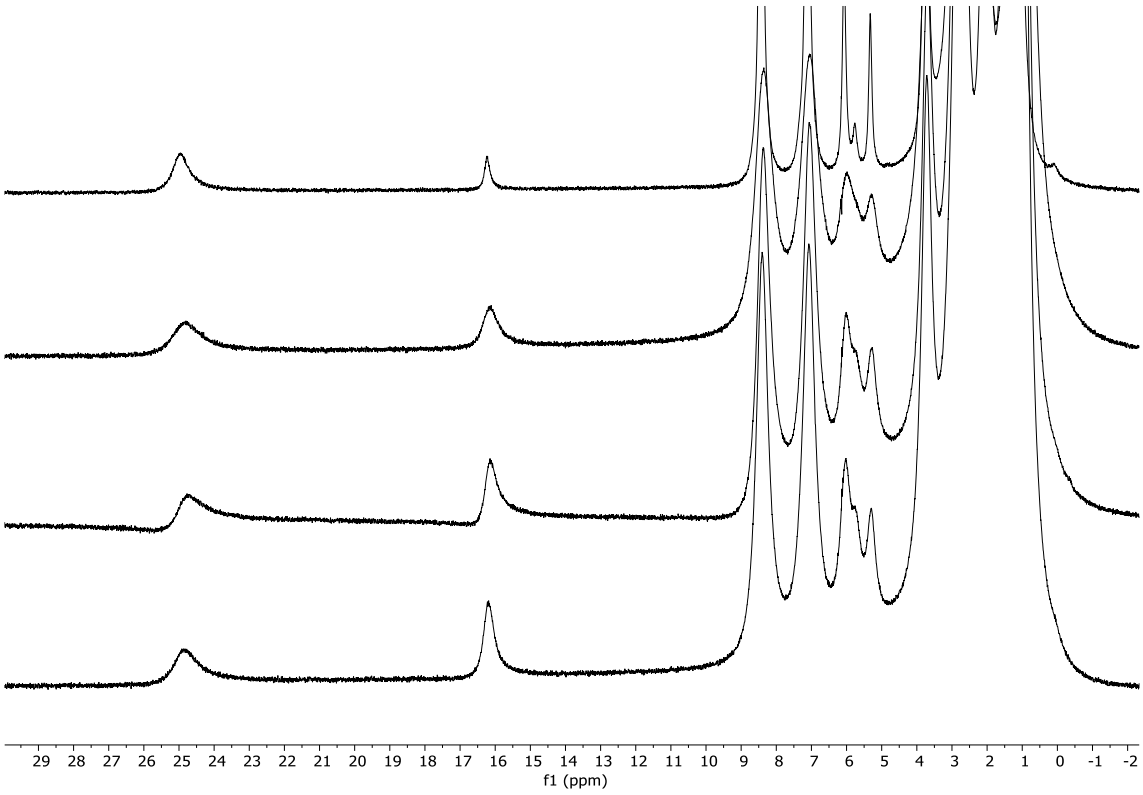
S105. Reaction of 2 equiv of [Mn(acac)$_2$(*t*-Bupy)$_2$][PF$_6$] (**Mn^{III}(*t*-Bupy)**[PF$_6$]) and **Co$_4$** as monitored by ^{1}H NMR spectroscopy (methylene chloride-d_2, 400 MHz). 1,3,5-TMB = 1,3,5-trimethoxybenzene.



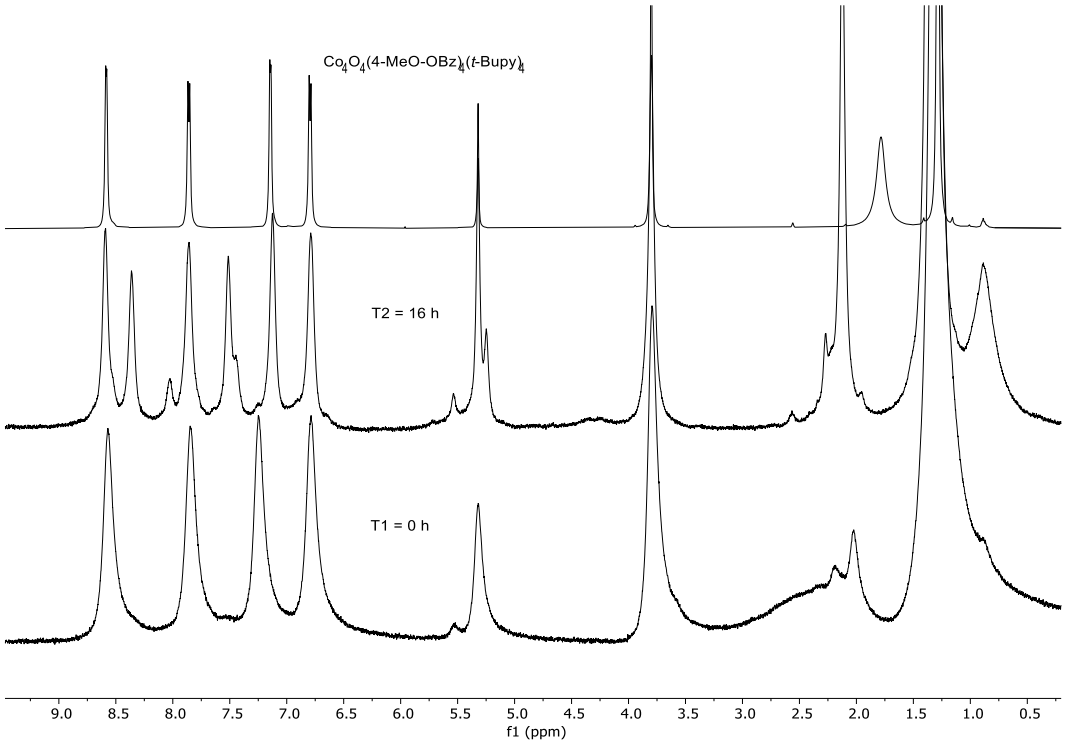
S106. Reaction of 2 equiv of Mn(*bis*-benzoylacetylacetonate)$_3$ and **Co$_4$** as monitored by ^{1}H NMR spectroscopy (methylene chloride-d_2, 400 MHz) with 1,3,5-trimethoxybenzene as an internal standard.



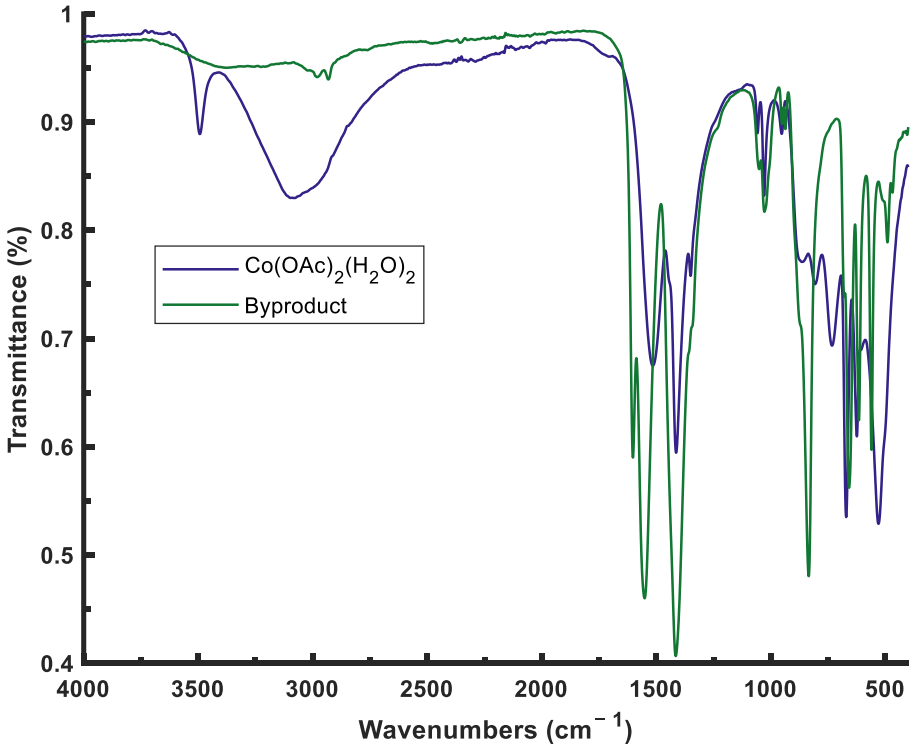
S107. Enhancement of the signal intensity of figure **S106** to show the consumption of Mn(*bis*-benzoylacetylacetonate)$_3$.



S108. Reaction of 2 equiv of Mn(*bis*-*tert*-butylacetylacetonate)$_3$ and **Co4** as monitored by ^{1}H NMR spectroscopy (methylene chloride-d_2, 400 MHz) with 1,3,5-trimethoxybenzene as an internal standard. Neither **Co4** nor the Mn^{III} reagent are consumed.



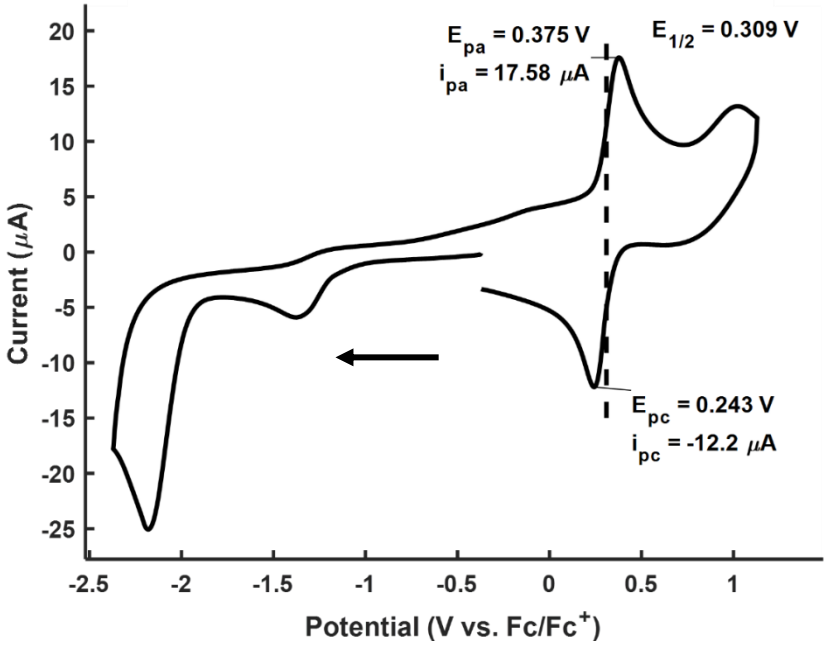
S109. Reaction of 2 equiv of $[Mn(acac)_2(t\text{-Bupy})_2][PF_6]$ with $Co_4O_4(4\text{-OMe-OBz})_4(t\text{-Bupy})_4$ at 35 °C as monitored by ^1H NMR spectroscopy (methylene chloride-d_2, 400 MHz).



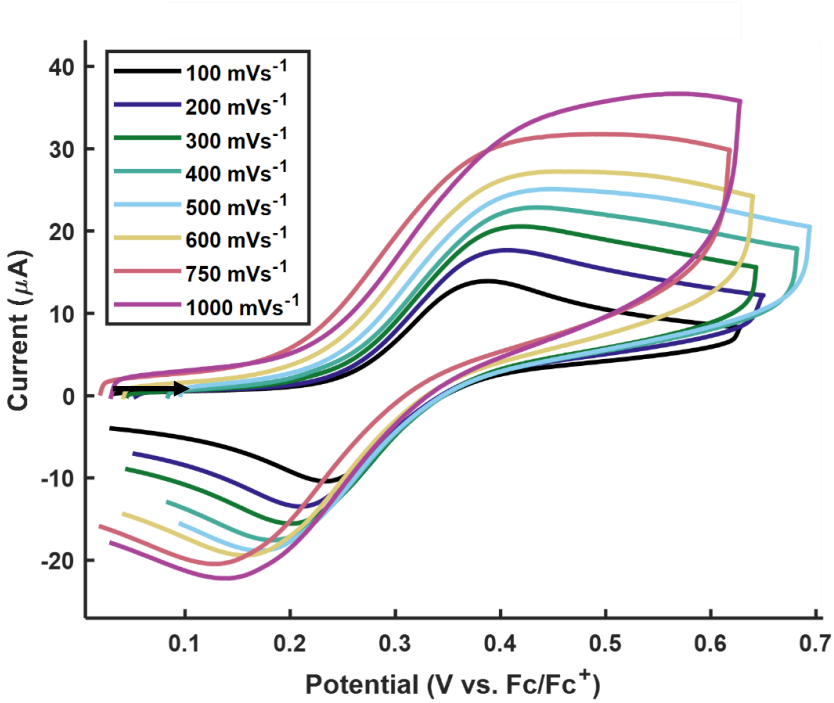
S110. FTIR spectrum of $Co(OAc)_2(H_2O)_4$ and the pink filtrate byproduct from reaction of $Mn(OAc)_2$ with **Co4**. The additional peaks present in the byproduct likely correspond to ligands.

Electrochemistry:

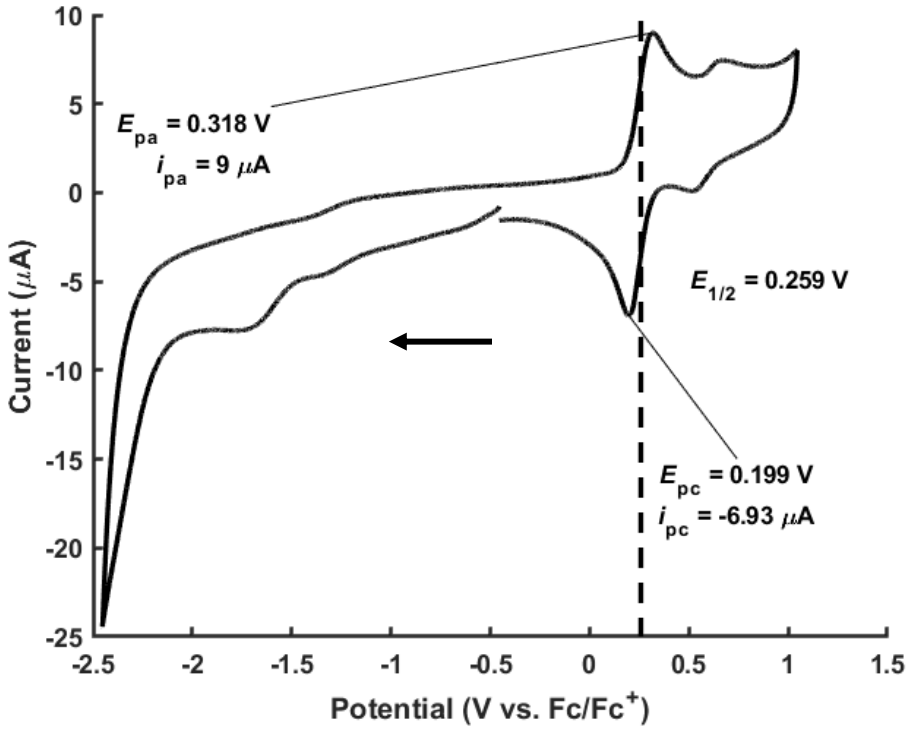
Cyclic Voltammograms of Substituted-Pyridine Cubanes:



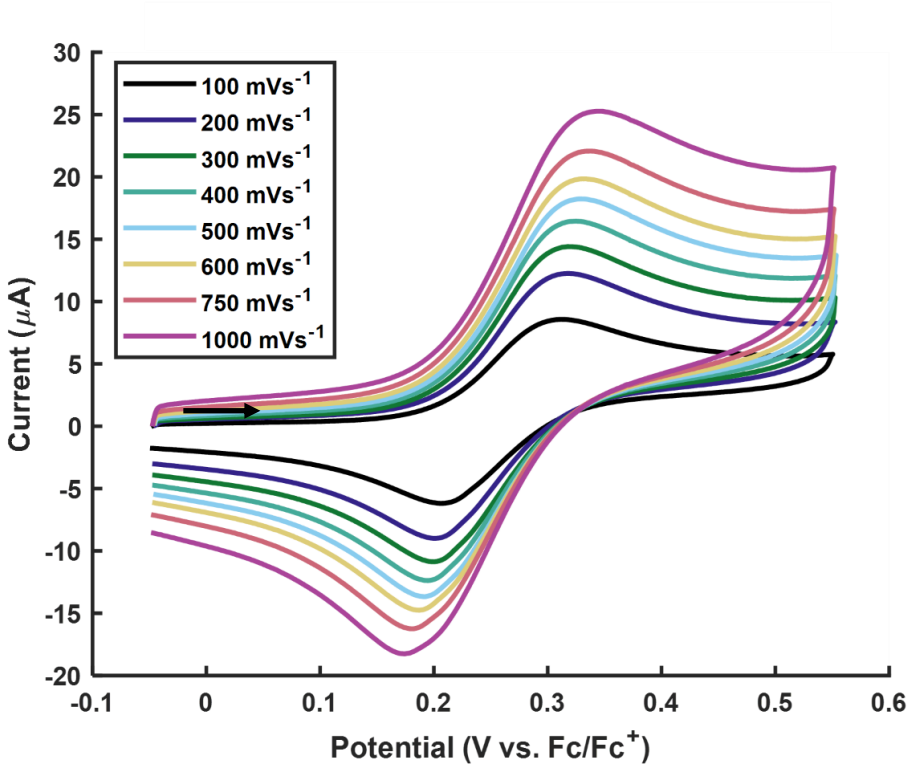
S111. Cyclic voltammogram of $Co_4O_4(OBz)_4(py)_4$ (**Co_4(py-H)**).



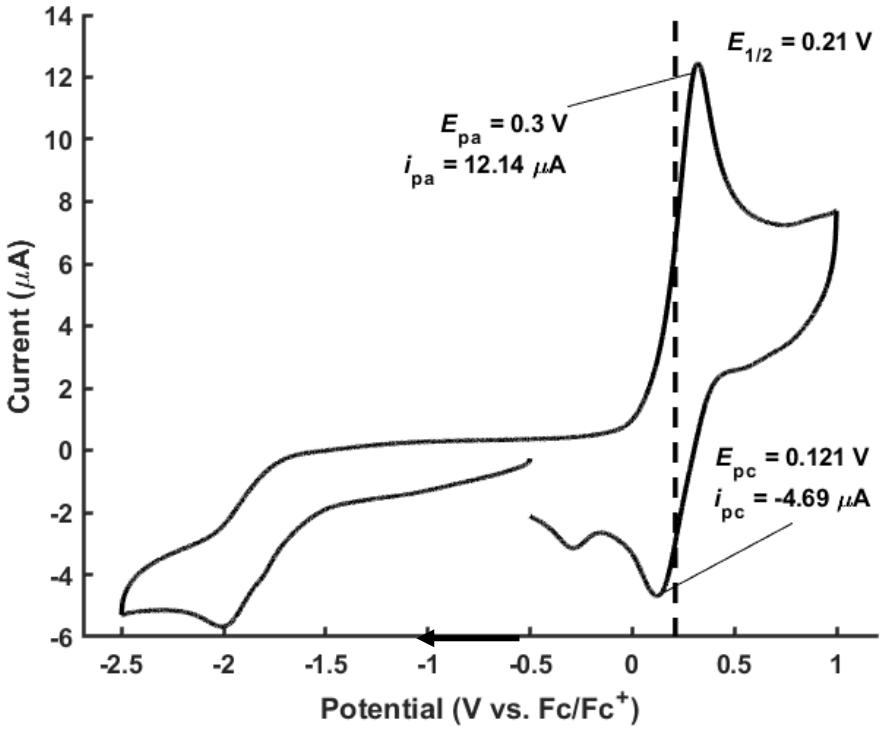
S112. Scan rate study of $Co_4O_4(OBz)_4(py)_4$ (**Co_4(py-H)**).



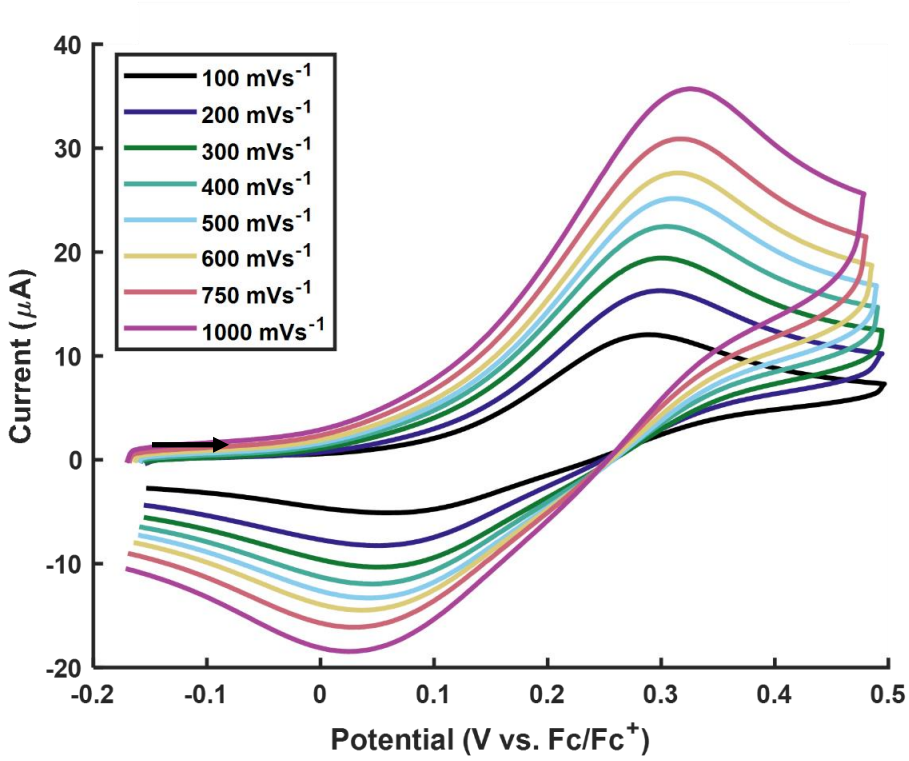
S113. Cyclic voltammogram of $Co_4O_4(OBz)_4(t\text{-Bupy})_4$ (**Co_4(OBz-*t*Bu)**).



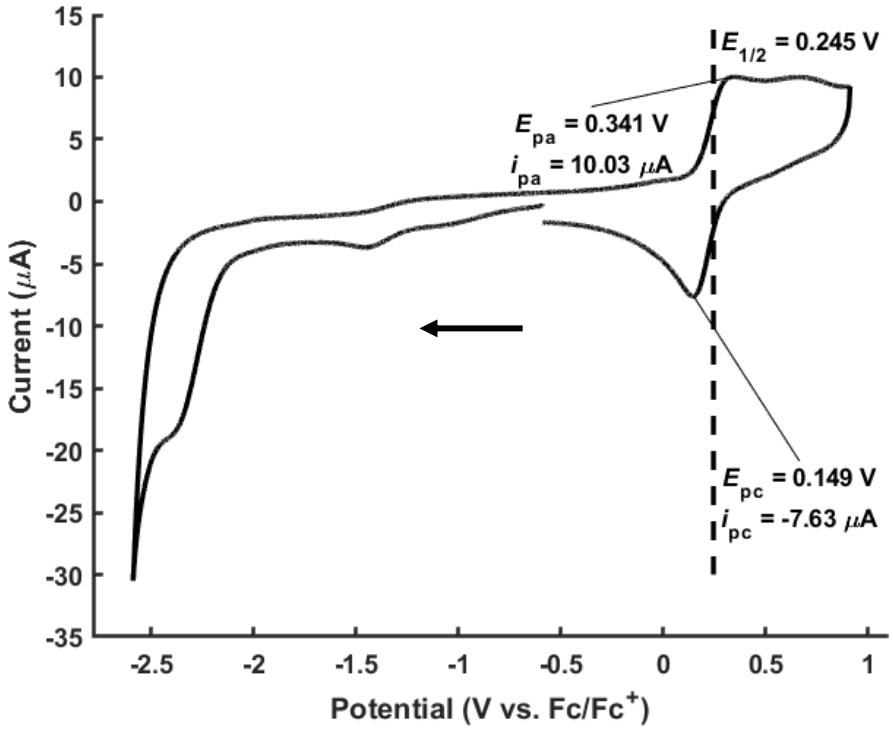
S114. Scan rate study of $Co_4O_4(OBz)_4(t\text{-Bupy})_4$ (**Co_4(OBz-*t*-Bu)**).



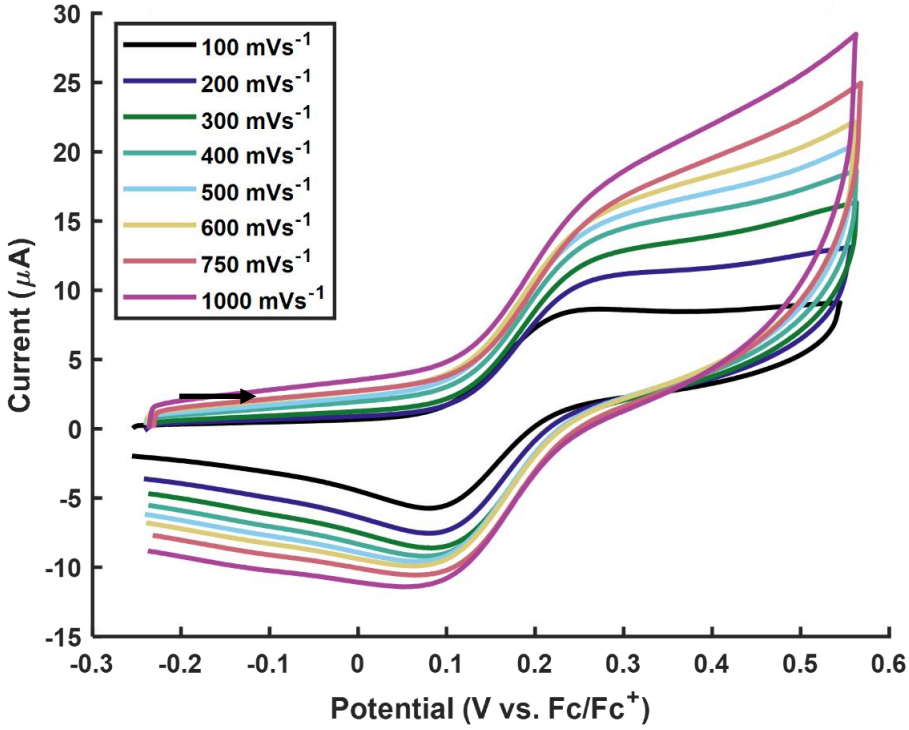
S115. Cyclic voltammogram of $Co_4O_4(OBz)_4(MeOpy)_4$ (**Co_4(py-OMe)**).



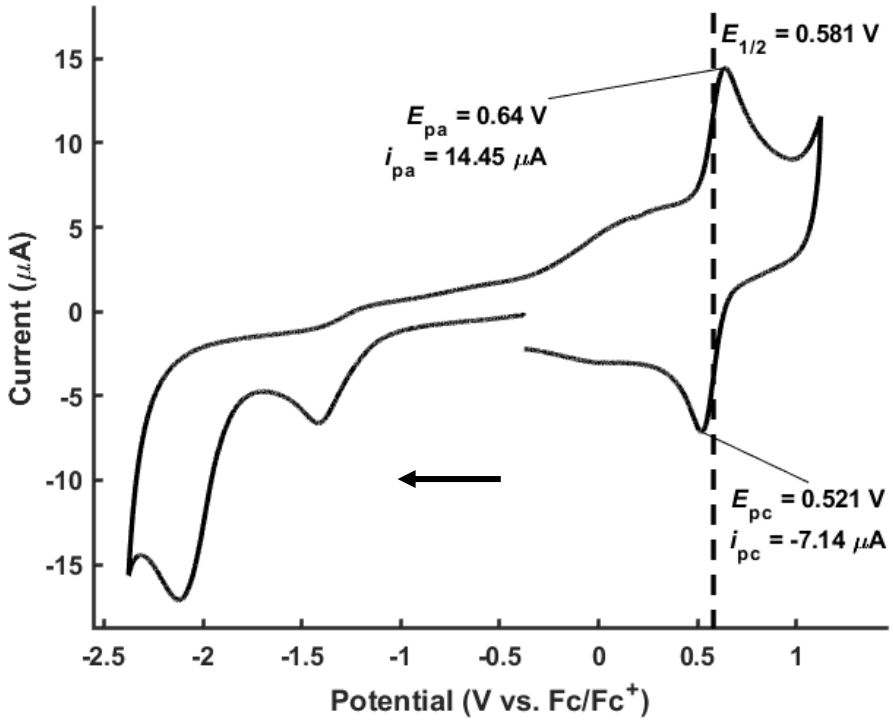
S116. Scan rate study of $Co_4O_4(OBz)_4(MeOpy)_4$ (**Co_4(py-OMe)**).



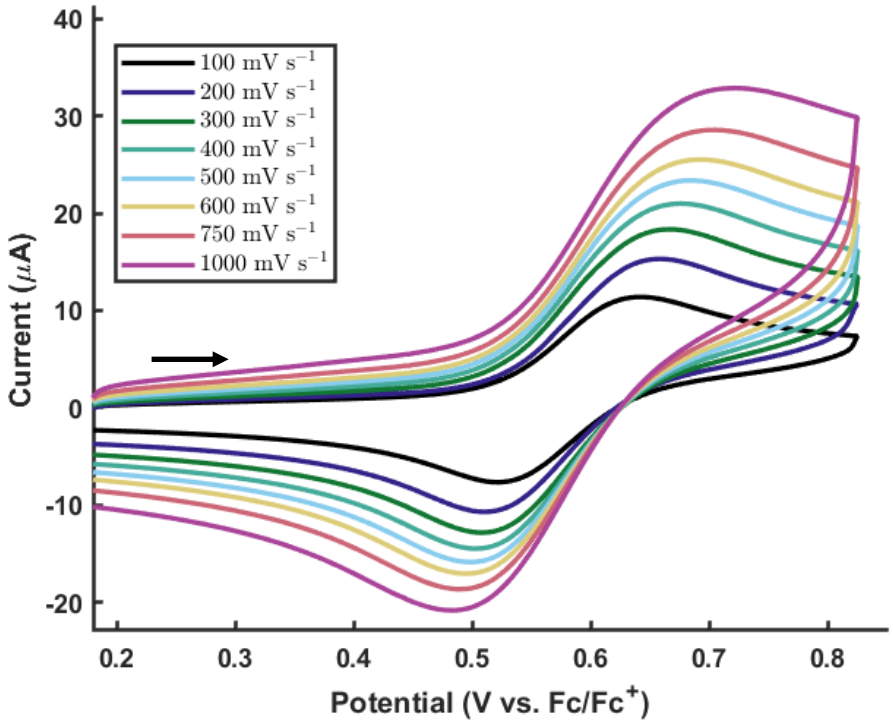
S117. Cyclic voltammogram of $Co_4O_4(OBz)_4(Mepy)_4$ (**Co_4(py-Me)**).



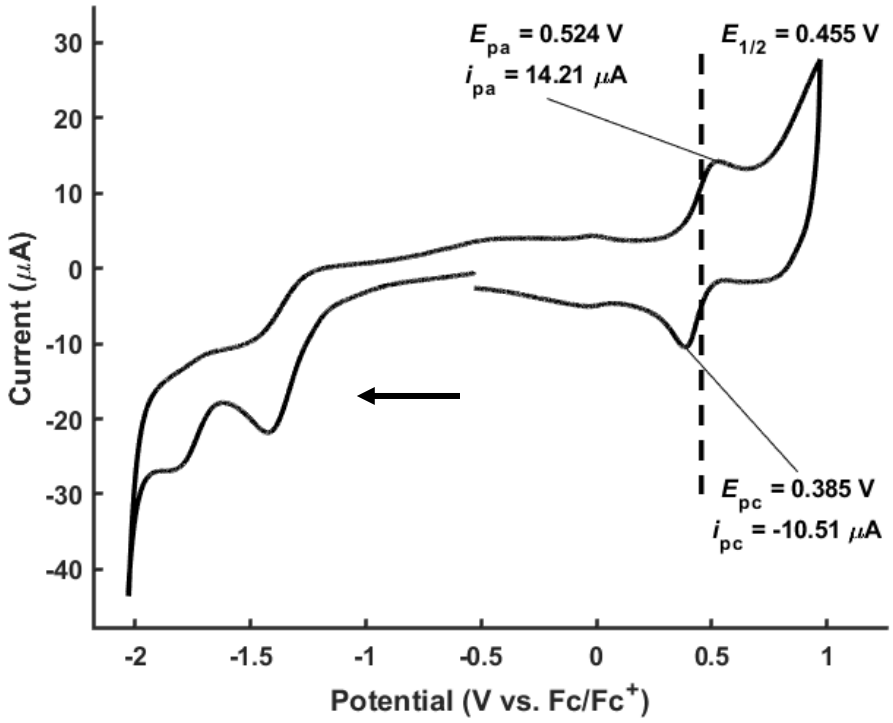
S118. Scan rate study of $Co_4O_4(OBz)_4(Mepy)_4$ (**Co_4(py-Me)**).



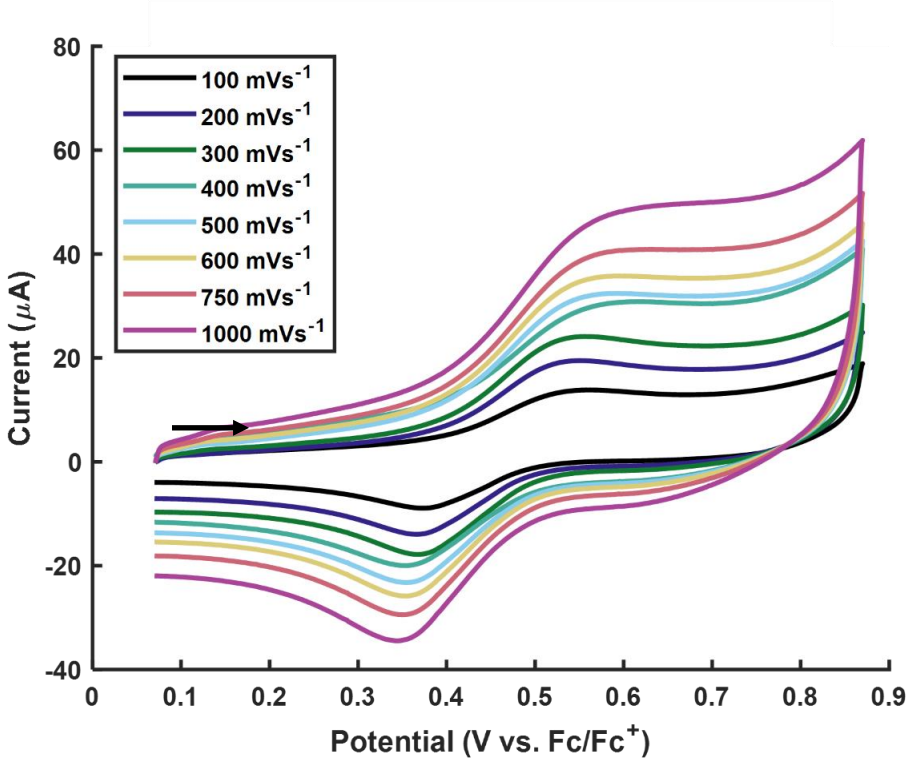
S119. Cyclic voltammogram of $Co_4O_4(OBz)_4(CF_3py)_4$ (**Co_4(py-CF_3)**).



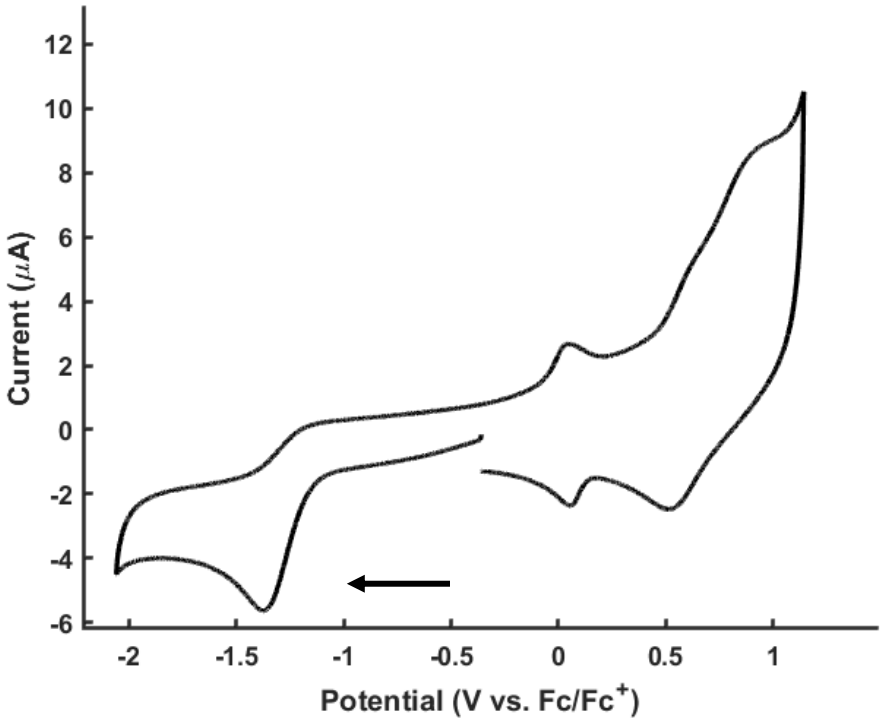
S120. Scan rate study of $Co_4O_4(OBz)_4(CF_3py)_4$ (**Co_4(py-CF_3)**).



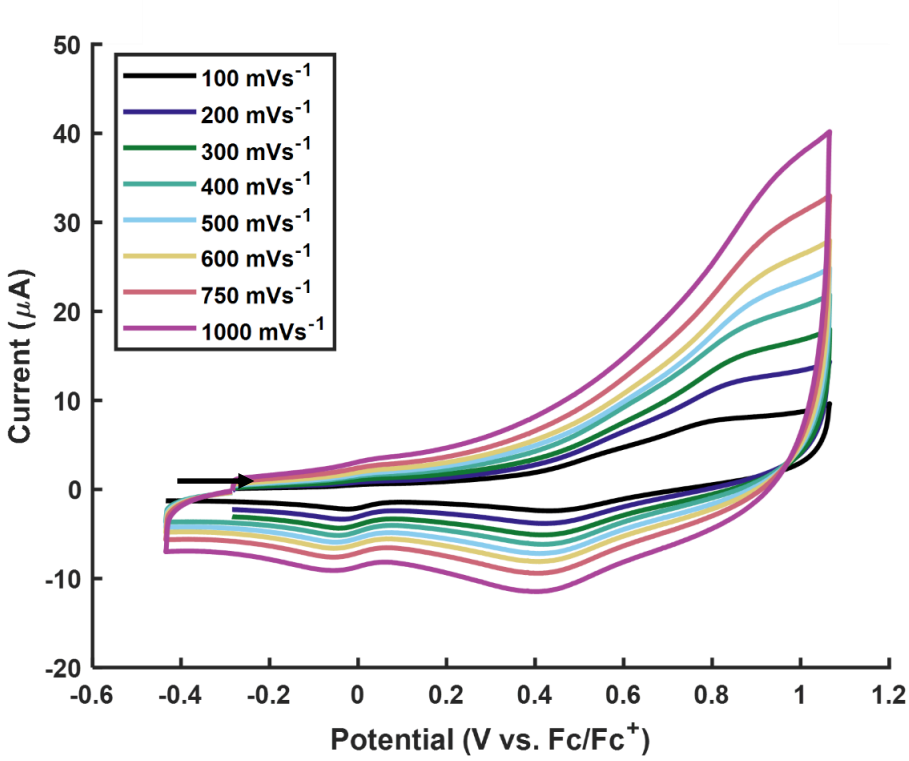
S121. Cyclic voltammogram of $Co_4O_4(OBz)_4$(*p*-Acpy)$_4$ (**Co_4(py-Ac)**).



S122. Scan rate study of $Co_4O_4(OBz)_4$(Acpy)$_4$ (**Co_4(py-Ac)**).

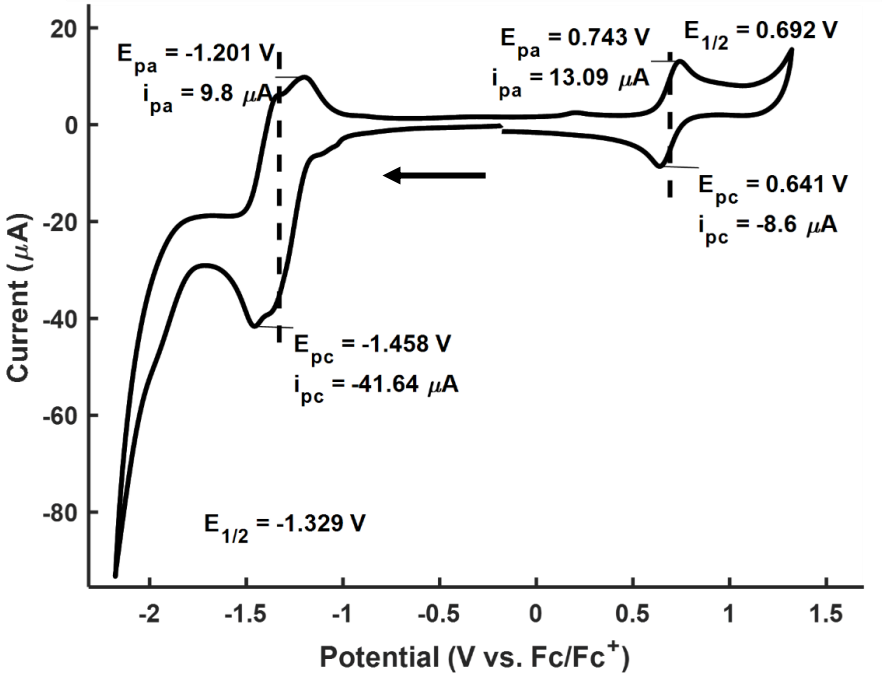


S123. Cyclic voltammogram of $Co_4O_4(OBz)_4(CNpy)_4$ (**Co_4(py-CN)**). Peak centered at 0 is Fc/Fc^+. The oxidation was fully reversible in MeCN.

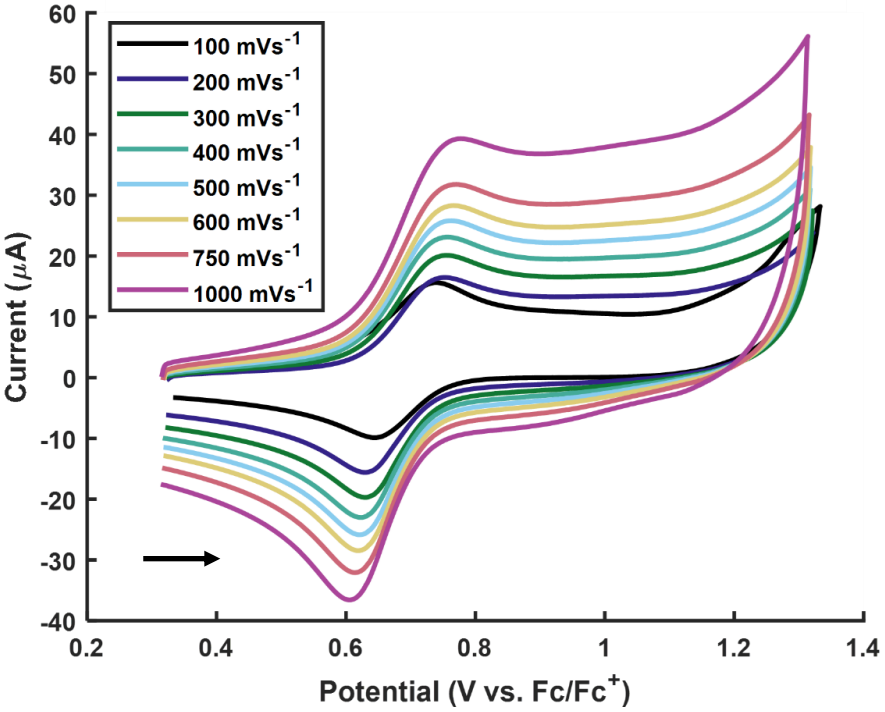


S124. Scan rate study of $Co_4O_4(OBz)_4(CNpy)_4$. (**Co_4(py-CN)**).

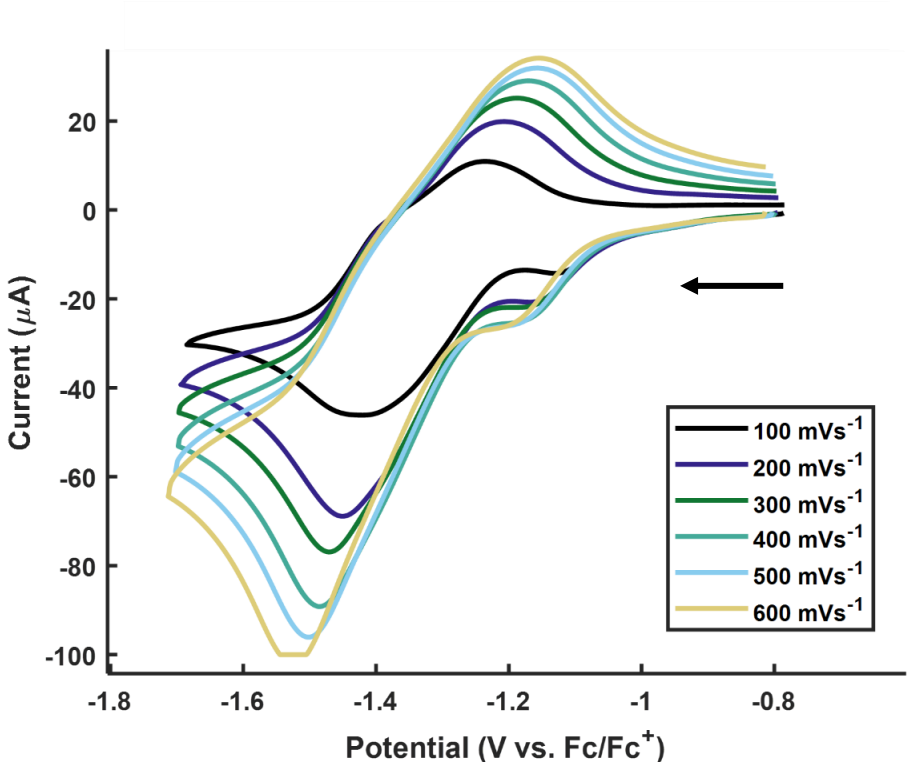
Substituted Benzoates:



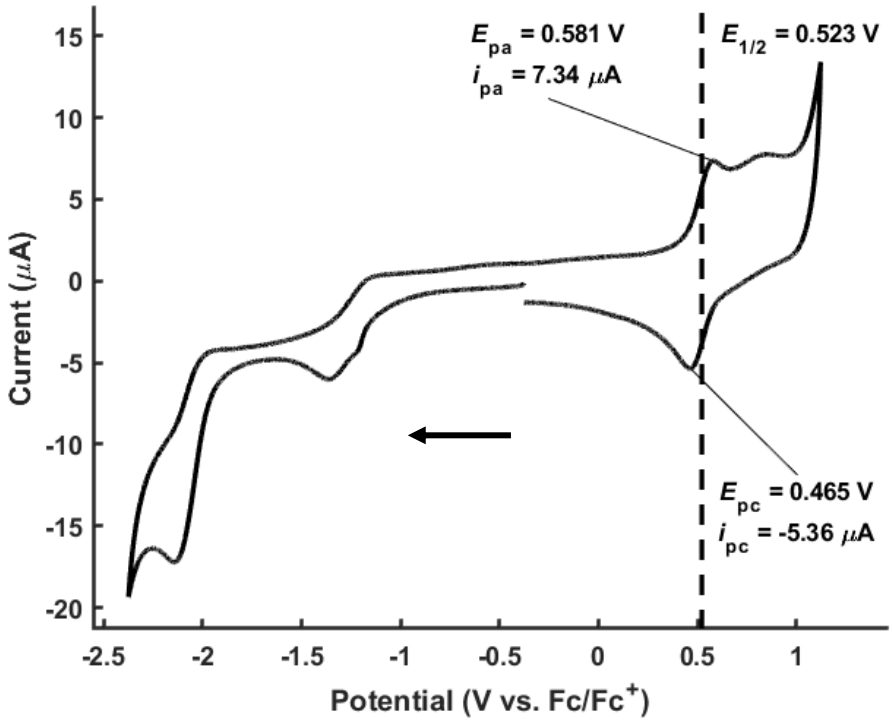
S125. Cyclic voltammogram of $Co_4O_4(4\text{-}NO_2\text{-}OBz)_4(t\text{-}Bupy)_4$ (**Co_4(OBz-NO_2)**).



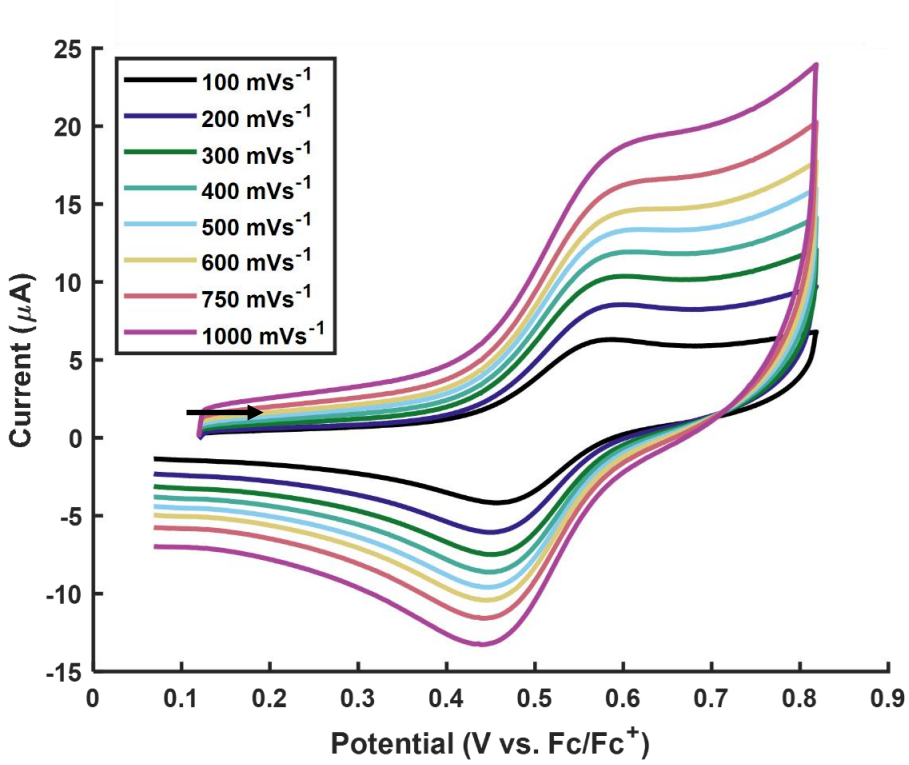
S126. Scan rate study of the oxidation of $Co_4O_4(4\text{-}NO_2\text{-}OBz)_4(t\text{-}Bupy)_4$ (**Co_4(OBz-NO_2)**).



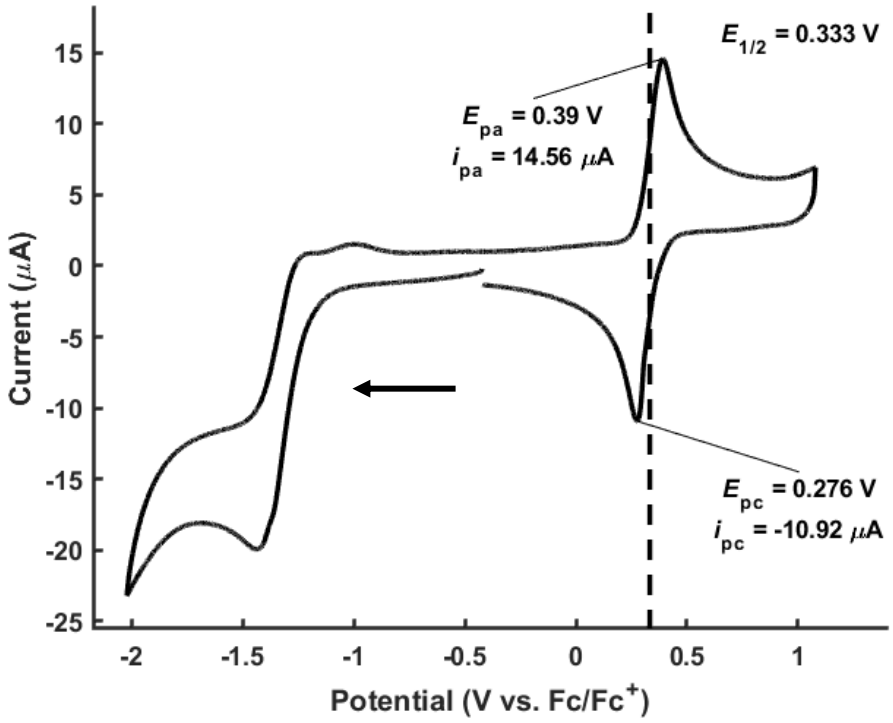
S127. Scan rate study of the reduction event of $Co_4O_4(4\text{-}NO_2\text{-}OBz)_4(t\text{-}Bupy)_4$ (**Co_4(OBz-NO_2)**).



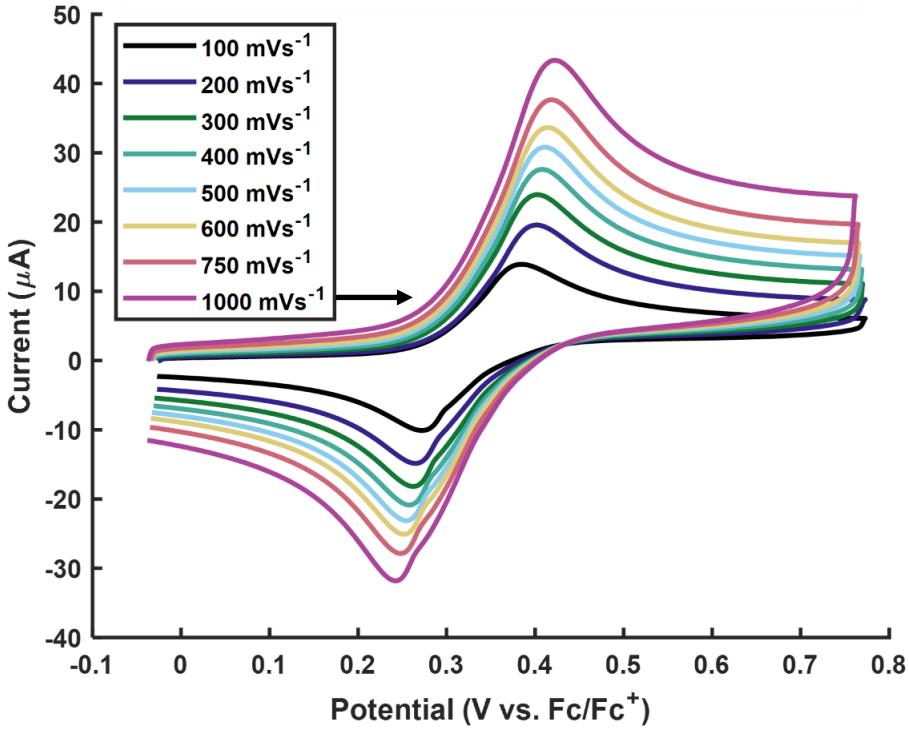
S128. Cyclic voltammogram of Co_4O_4(4-CN-OBz)$_4$(*t*-Bupy)$_4$. (**Co_4(OBz-CN)**).



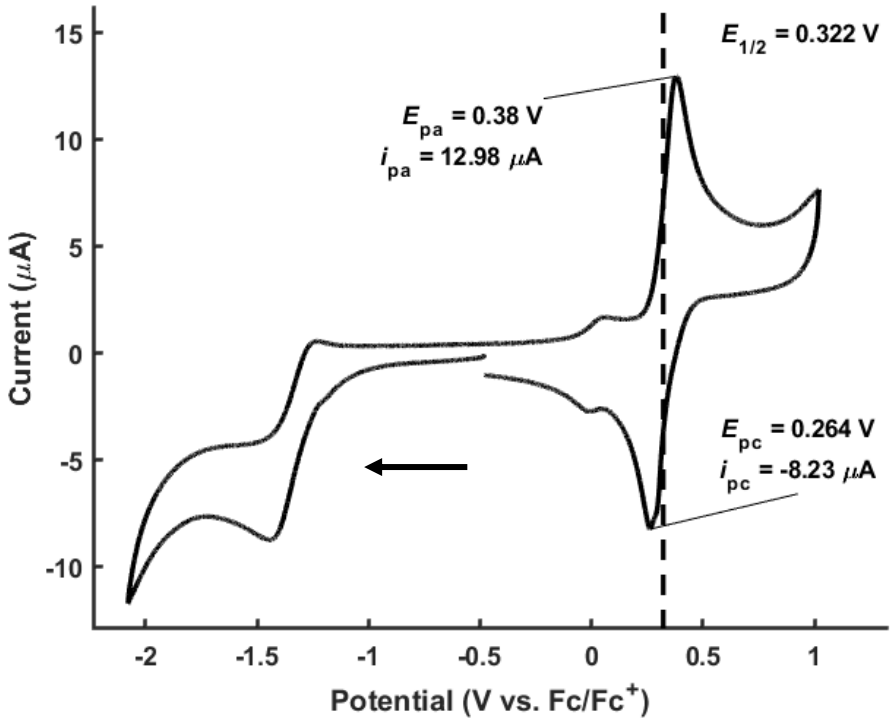
S129. Scan rate study of Co_4O_4(4-CN-OBz)$_4$(*t*-Bupy)$_4$ (**Co_4(OBz-CN)**).



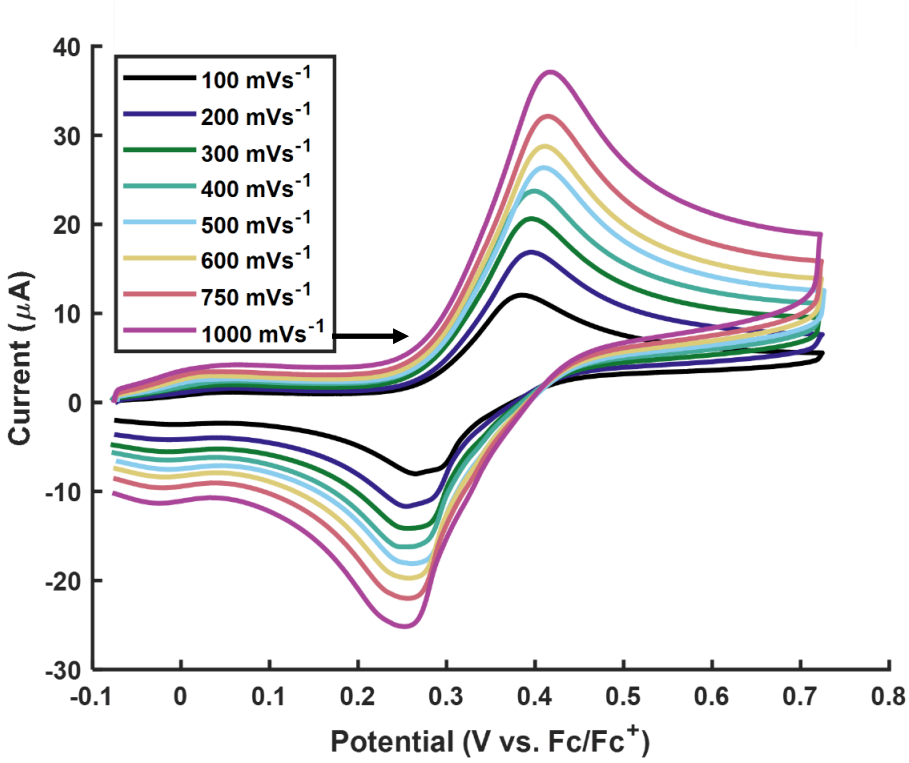
S130. Cyclic voltammogram of Co_4O_4(4-Br-OBz)$_4$(*t*-Bupy)$_4$ (**Co_4(OBz-Br)**).



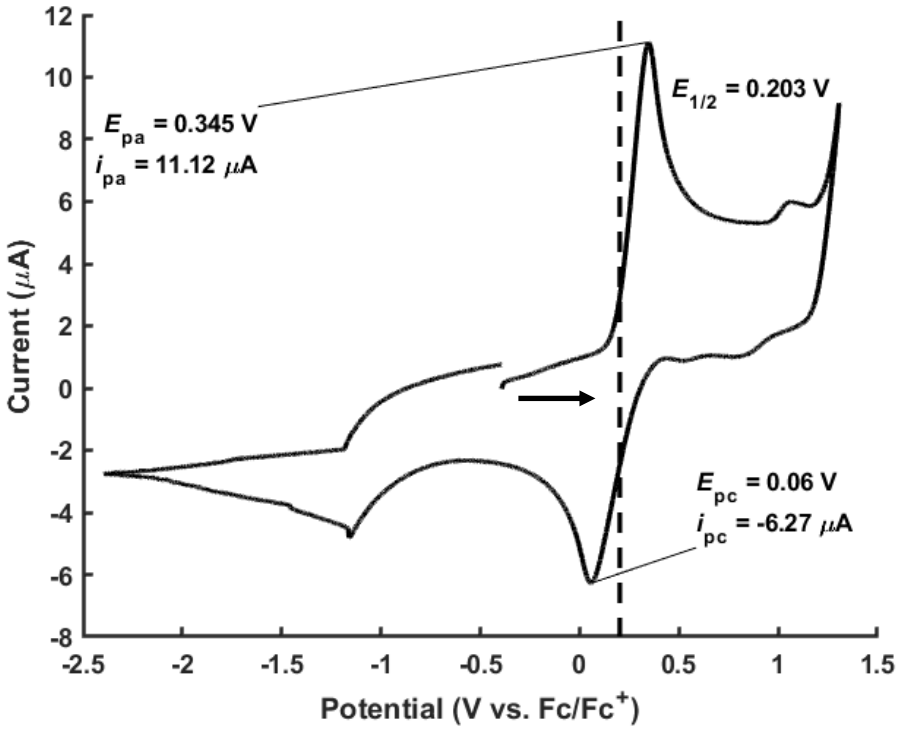
S131. Scan rate study of Co_4O_4(4-Br-OBz)$_4$(*t*-Bupy)$_4$ (**Co_4(OBz-Br)**).



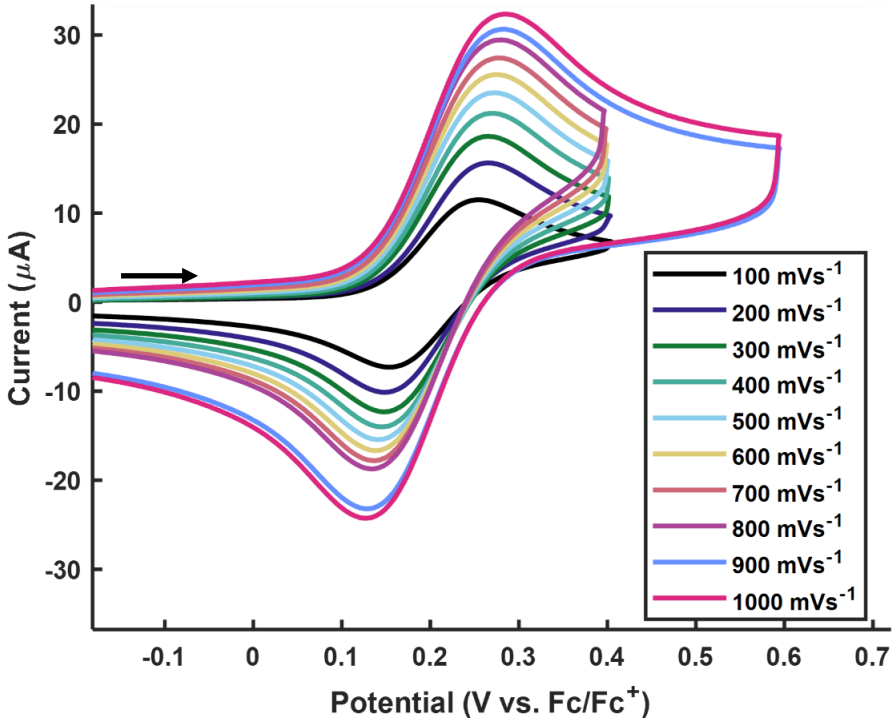
S132. Cyclic voltammogram of Co_4O_4(4-Cl-OBz)$_4$(*t*-Bupy)$_4$ (**Co_4(OBz-Cl)**).



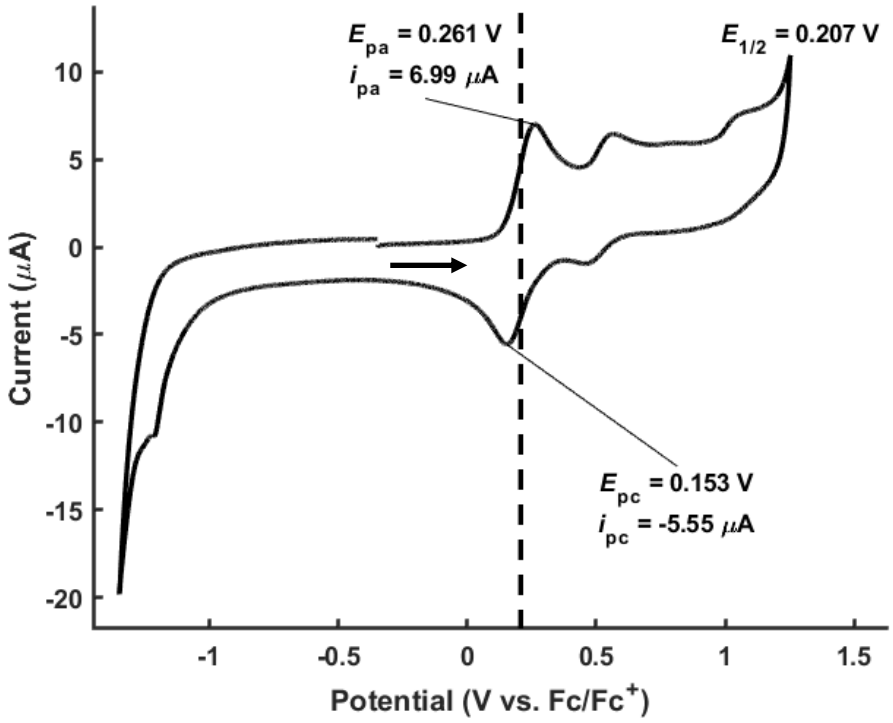
S133. Scan rate study of Co_4O_4(4-Cl-OBz)$_4$(*t*-Bupy)$_4$ (**Co_4(OBz-Cl)**).



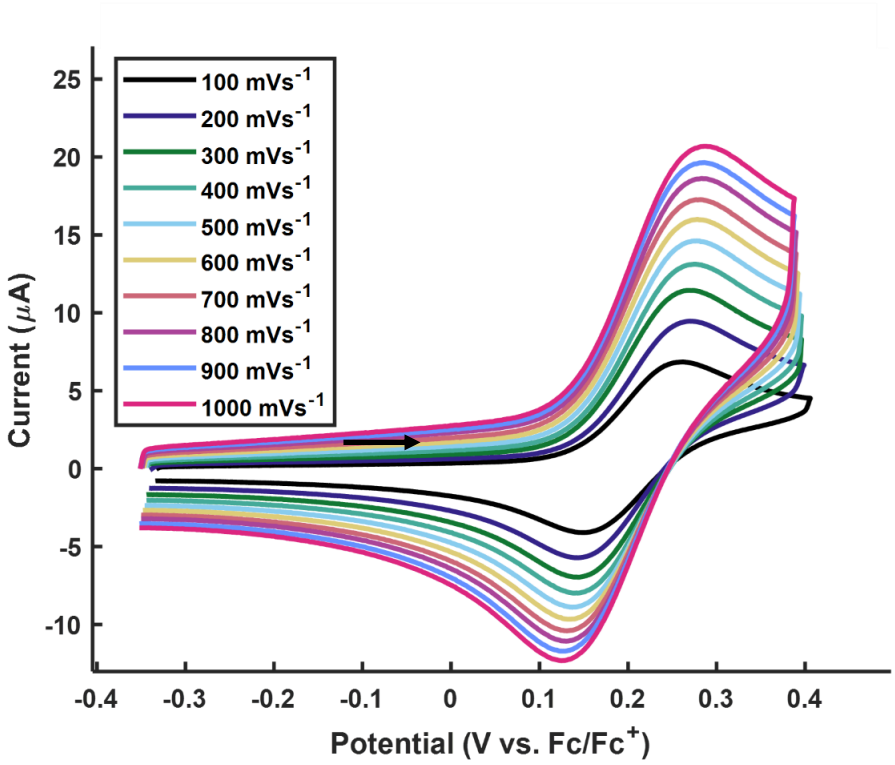
S134. Cyclic voltammogram of Co_4O_4(4-Me-OBz)$_4$(*t*-Bupy)$_4$ (**Co_4(OBz-Me)**).



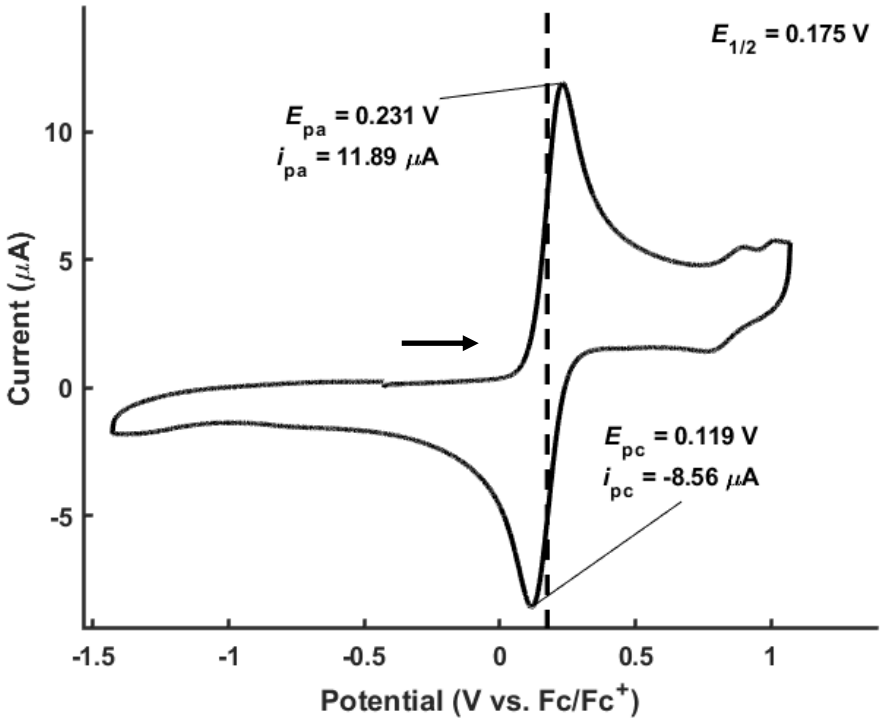
S135. Scan rate study of Co_4O_4(4-Me-OBz)$_4$(*t*-Bupy)$_4$ (**Co_4(OBz-Me)**).



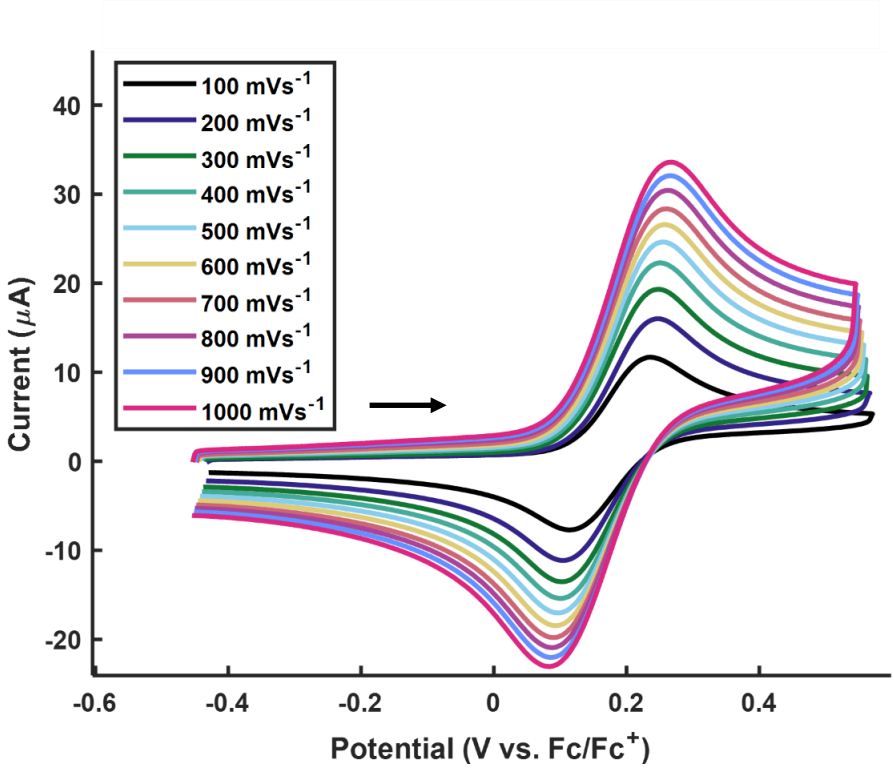
S136. Cyclic voltammogram of Co_4O_4(4-*t*Bu-OBz)$_4$(*t*-Bupy)$_4$ (**Co_4(OBz-*t*Bu)**).



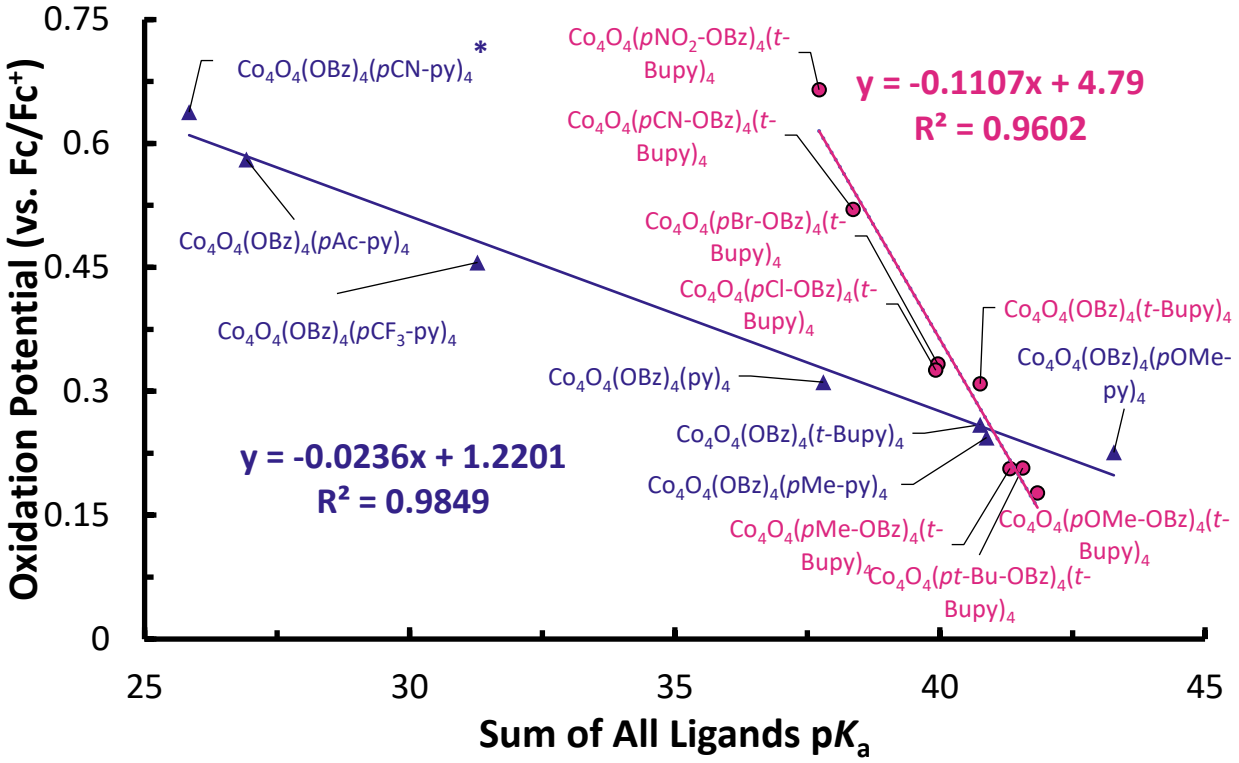
S137. Scan rate study of Co_4O_4(4-*t*Bu-OBz)$_4$(*t*-Bupy)$_4$ (**Co_4(OBz-*t*Bu)**).



S138. Cyclic voltammogram of Co_4O_4(4-MeO-OBz)$_4$(*t*-Bupy)$_4$ (**Co_4(OBz-OMe)**).



S139. Scan rate study of Co_4O_4(4-MeO-OBz)$_4$(*t*-Bupy)$_4$ (**Co_4(OBz-OMe)**).



S140. Plot of the $E_{1/2}$ of the cubanes prepared in this study vs. the sum of the pK_a of all of the benzoate and pyridine ligands on the cubane. *Estimated $E_{1/2}$.

Table S1. Tabulation of the pK_a Values Used to Predict the $E_{1/2}$ Values for the Cubanes Presented in this Study.

Compound	Ligand – Substituent	E_{pc}	E_{pa}	$E_{1/2}$	X-Ligand pK_a	L-Ligand pK_a
X-NO_2	OBz-NO_2	0.64	0.74	0.69	3.44[a]	5.99[c]
X-CN	OBz-CN	0.47	0.52	0.52	3.6[a]	5.99[c]
X-Br	OBz-Br	0.28	0.39	0.33	3.96[a]	5.99[c]
X-Cl	OBz-Cl	0.26	0.38	0.32	4.00[a]	5.99[c]
X-H	OBz-H	0.20	0.32	0.26	4.2[a]	5.99[c]
X-Ph	OBz-Ph	~	~	~	4.115[b]	5.99[c]
X-Me	OBz-Me	0.16	0.26	0.21	4.34[a]	5.99[c]
X-^{t}Bu	OBz-^{t}Bu	0.15	0.26	0.21	4.4[a]	5.99[c]
X-OMe	OBz-OMe	0.12	0.23	0.18	4.47[a]	5.99[c]
Y-CN	py-CN			~0.64	4.2[a]	2.26[c]
Y-CF_3	py-CF_3	0.52	0.64	0.58	4.2[a]	2.53[c]
Y-Ac	py-C(O)Me	0.39	0.52	0.46	4.2[a]	3.62[c]
Y-H	py-H	0.24	0.38	0.31	4.2[a]	5.23[a]
Y-Me	py-Me	0.15	0.34	0.25	4.2[a]	5.99[a]
Y-OMe	py-OMe	0.12	0.32	0.22	4.2[a]	6.58[a]

a[14], *b*[15], *c*[16]. Value for *para*-phenylbenzoic acid estimated using equation in reference *b*.

Kinetic Details:

General Considerations: All UV-vis spectroscopy was conducted with a Shimadzu UV-2600i spectrometer, which was baseline corrected on the same solvent used in the reaction and zeroed. A six-cell CPS, temperature controlled multicell allowed the collection of multiple datasets simultaneously. The accuracy of the thermostat was not examined, but according to the manufacturer, the accuracy is to within ± 1 °C. Experiments were performed with either three or six (10 mm x 10 mm x 30/35 mm) cuvettes. When Teflon stoppered cuvettes were used, the stoppered cuvettes were placed between the capped cuvettes, which was sufficient to prevent solvent from escaping (see S below). Solutions of $[Mn(acac)_2(py)_2][PF_6]$ and the appropriate $[Co_4O_4]$ cubane were prepared as separate stock solutions, and a separate vial of solvent or a solution of either the additive (e.g., $[^nBu_4N][OBz]$ or py) was used in each experiment. All reagent solutions were allowed to rest for at least one day prior to kinetic measurements. By UV-vis spectroscopy significant changes were not observed for reagents other than $[Mn(acac)_2(py)_2][PF_6]$; a UV-Vis spectrum of a day-old MeCN solution of the reagent is slightly different from that of a freshly prepared MeCN solution, but the measured rates were unaffected by this change in speciation, which likely reflects the presence of oligomers (as is known for $Co(acac)_2$) or some displacement of py ligands by MeCN.

Procedure for monitoring by UV-vis: After baseline correction at the reaction temperature, cuvettes were placed in the pre-heated sample holder for at least five min. A calibrated autopipette was then used to deliver an equal volume of each solution in the order: $[Co_4O_4]$ → Additional Solvent or Additive → $[Mn(acac)_2(py)_2][PF_6]$. No signs of insufficient initial mixing were observed over the course of the kinetic studies, and the deadtime before initial measurement as timed by a stopwatch was between 30 s and 45 s. In all reactions with MeCN as the solvent, the temperature was 40 °C, and in all reactions with CH_2Cl_2 as the solvent the temperature was 35 °C. Note that the use of a multicell that performs measurements in series introduces systematic error due to serial measurements; this effect was not accounted for. Initial rates were approximated according to:

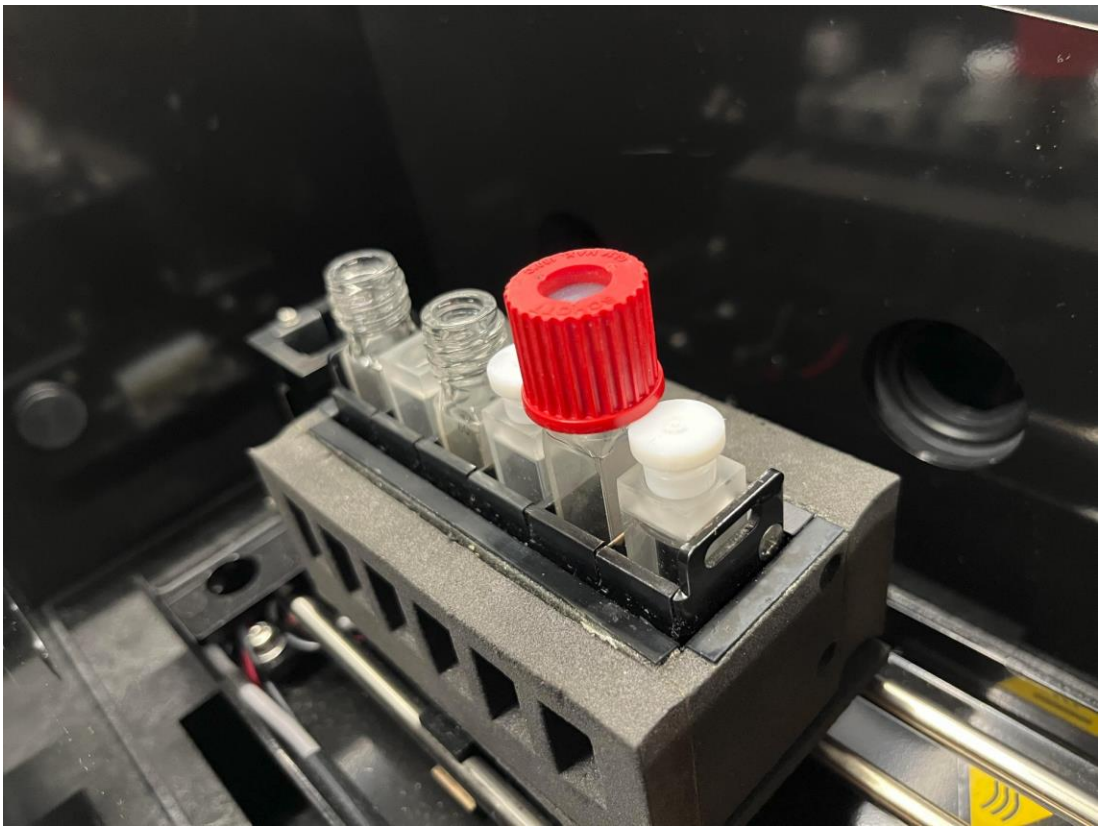
$$k_{initial} = \frac{\frac{A_{\lambda,t_0} - A_{\lambda,t_1}}{\Delta t}}{\varepsilon_{\lambda,M}} \quad (1)$$

Where A is the absorbance at wavelength λ at time t, and $\Delta t = t_0 – t_1$. A MATLAB script was used to simultaneously process and plot all of the data (*vide infra*). The kinetic traces were also fitted to a polynomial (of various orders, dependent on the number of spectra collected to avoid overfitting) in order to obtain the instantaneous derivative at t_0, and the values for $k_{initial}$ obtained this way were similar to the values obtained from the crude approximation of equation 1 above.

Key assumptions:

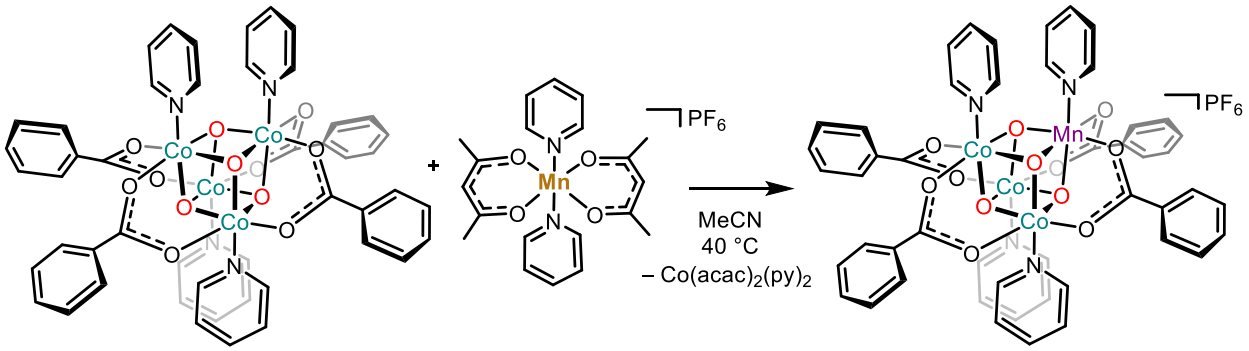
1) The change in absorbance early in the reaction at λ is exclusively proportional to the concentration of the reagent being measured at that wavelength.
2) The first measurement is collected before any reaction has occurred (A_λ at $t_1 = A_\lambda$ at t_0).
3) The background radical and $Co(acac)_2$ oxidation reactivity discussed in the manuscript does not affect $k_{initial}$
4) There are no physical effects such as mixing, changes in the absorption due to differences in the solvent density at different temperatures, or due to solvent evaporation.

Note that attempts were made to study the kinetics of the substitution with $Mn(OTf)_2$ despite the initial ligand substitution reaction observed by ^1H NMR spectroscopy, but the UV-vis traces were not nearly as well-defined as the traces obtained when using Mn^{III} reagents. Kinetic experiments with $Mn(acac)_3$ and $Mn(pvacac)_3$ were also examined and were similar to the kinetic experiments with $[Mn(acac)_2(py)_2][PF_6]$.





S141. Pictures of the alternating stoppered and screw-capped cuvettes, which was used to stop solvent from evaporating out of the stoppered cuvettes over the course of the kinetic experiment.



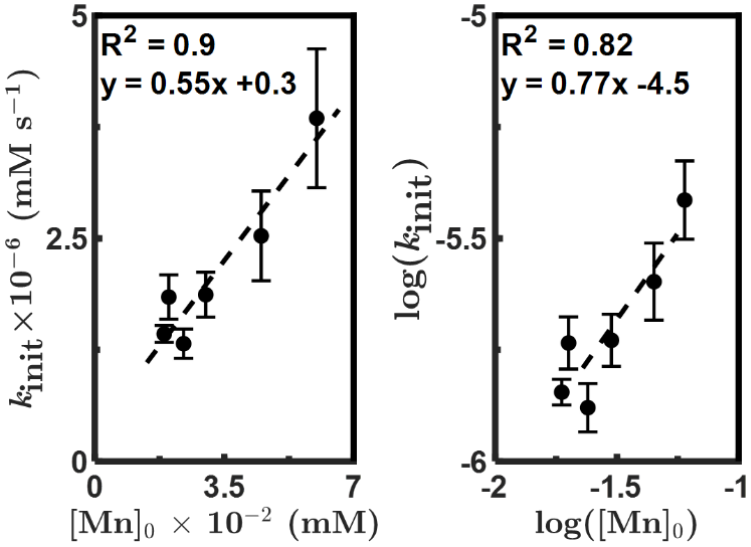
Co_4(py-H)
0.015 mM

Mn^{III}(py)[PF_6]
0.001875 mM
0.002 mM
0.0024 mM
0.003 mM
0.006 mM

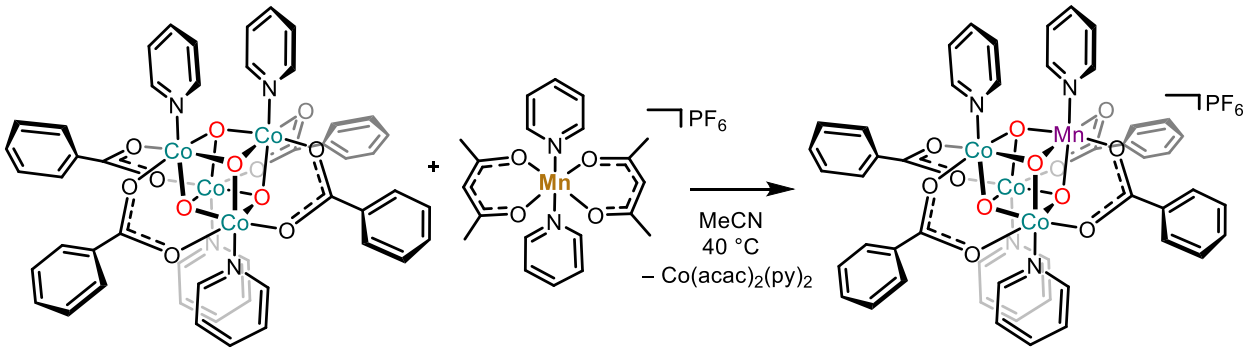
$MnCo_3$(py-H)[PF_6]

Table S2. Relationship Between Rate of Metal-Metal Exchange and [[Mn(acac)$_2$(py)$_2$][PF_6]]$_0$

[Compound]$_0$ × 10^{-2} (mM)	$k_{initial}$ × 10^{-6} (mM s^{-1})
1.8750	1.4(1)
2	1.3(16)
2.4	1.8(25)
4.5	2.5(5)
6	3.8(7)



S142. (A) [Mn(acac)$_2$(py)$_2$][PF_6]$_0$ vs. k_{init} of metal-metal exchange with linear fit represented by the dashed line. The slope of the fit k_{obs} = 5.5(8) × 10^{-5} with error determined as the standard error of the linear regression. (B) log-log plot of depiction of the 0.77 order dependence of the initial rate on [[Mn(acac)$_2$(py)$_2$][PF_6]$_0$ with linear fit represented by the dashed line. The slope of the fit = 0.8(2) with error determined as the standard error of the linear regression.



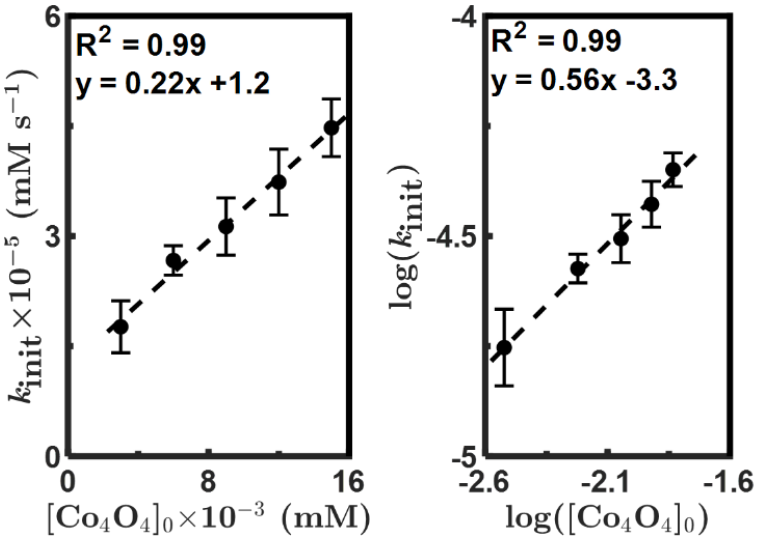
Co_4(py-H)
0.0003 mM
0.0006 mM
0.0009 mM
0.0012 mM
0.0015 mM

Mn^{III}(py)[PF_6]
0.03 mM

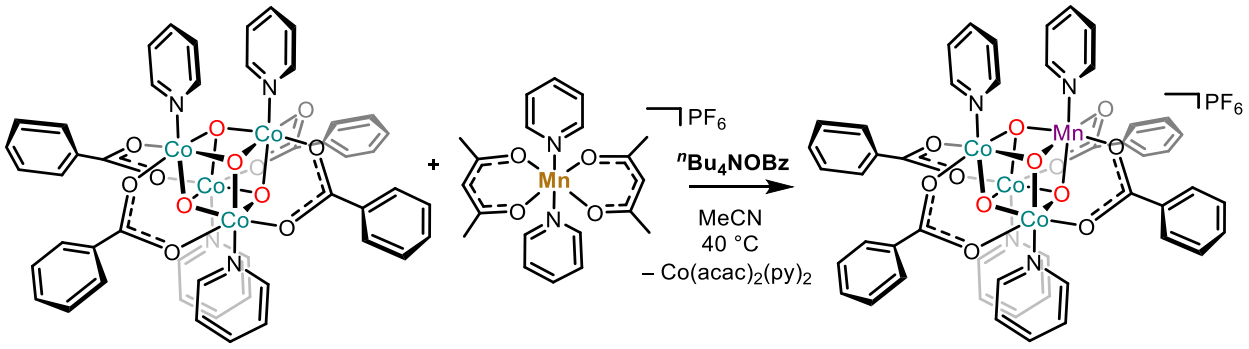
$MnCo_3$(py-H)[PF_6]

Table S3. Relationship Between the Rate of Metal-Metal Exchange and $[Co_4O_4(OBz)_4(py)_4]_0$

$[Co_4O_4(OBz)_4(py)_4]_0 \times 10^{-3}$ (mM)	$k_{initial} \times 10^{-5}$ (mM s^{-1})
3	1.7(3)
6	2.7(2)
9	3.1(4)
12	3.7(4)
15	4.5(4)



S143. (A) $[Co_4O_4(OBz)_4(py)_4]_0$ vs. k_{init} of metal-metal exchange with linear fit represented by the dashed line. The slope of the fit $k_{obs} = 2.2(1) \times 10^{-4}$ s^{-1} with error determined as the standard error of the linear regression. (B) log-log plot of depiction of the 0.56 order dependence of the initial rate on $[Co_4O_4(OBz)_4(py)_4]_0$ with linear fit represented by the dashed line. The slope of the fit = 0.56(3) with error determined as the standard error of linear regression.



Co_4(py-H)
0.005 mM

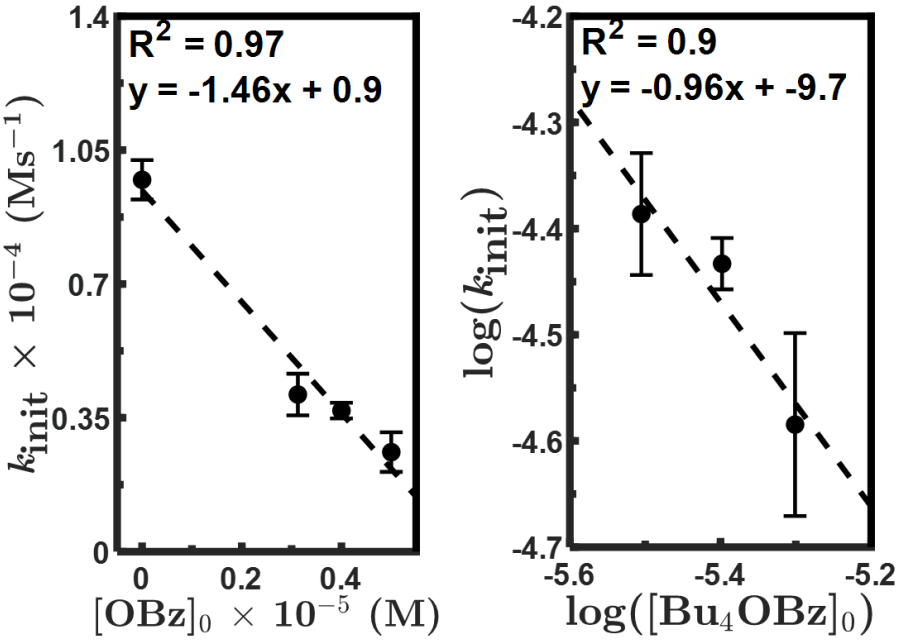
Mn^{III}(py)[PF_6]
0.005 mM

[^{n}NBu$_4$OBz]
0 mM
0.0003125mM
0.0004 mM
0.0005 mM

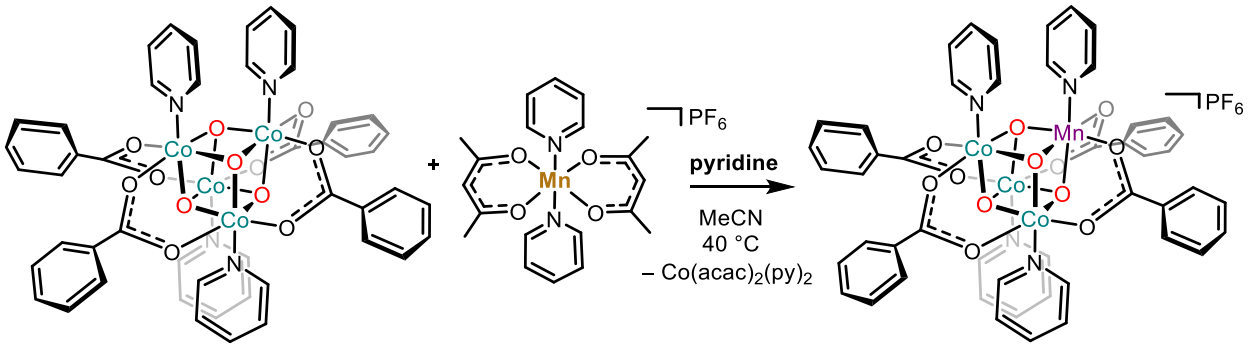
$MnCo_3$(py-H)[PF_6]

Table S4. Relationship Between Rate of Metal-Metal Exchange and [[^{n}Bu$_4$N][OBz]]$_0$

[[^{n}Bu$_4$N][OBz]]$_0$ × 10^{-6} (mM)	$k_{initial}$ × 10^{-5} (mM s^{-1})
0	15.6(8)
3.125	6.6(8)
4	5.9(3)
5	4.1(8)



S144. (A) [[^{n}Bu$_4$N][OBz]]$_0$ vs. k_{init} of metal-metal exchange with linear fit represented by the dashed line. The slope of the fit k_{obs} = 1.46(2) × 10^{-4} s^{-1} with error determined as the standard error of the linear regression. (B) log-log plot of depiction of the –0.9 order dependence of the initial rate on [[^{n}Bu$_4$N][OBz]]$_0$ with linear fit represented by the dashed line. The slope of the fit = –0.9(3) with error determined as the standard error of linear regression.



Co_4(py-H)
0.005 mM

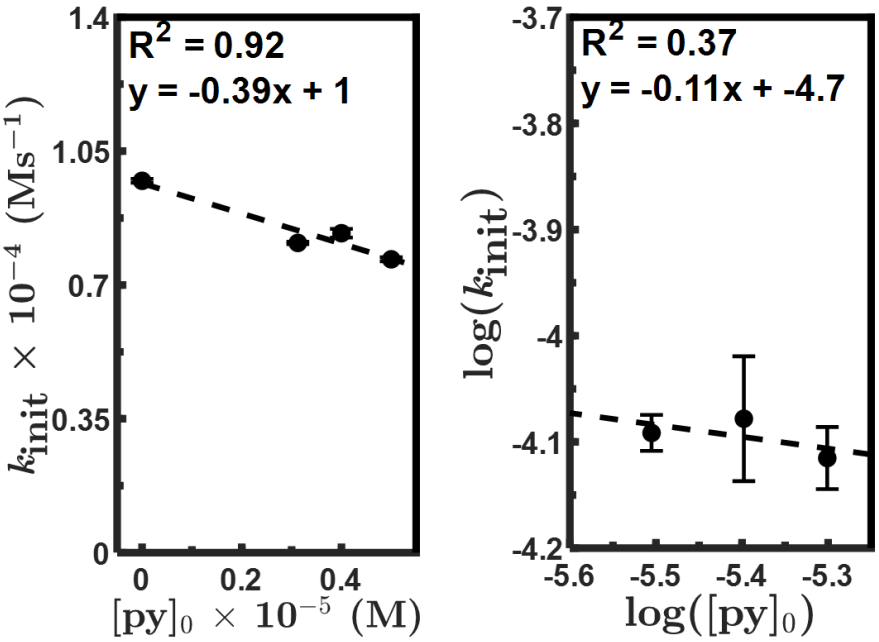
Mn^{III}(py)[PF_6]
0.005 mM

[py]
0 mM
0.0003125 mM
0.0004 mM
0.0005 mM

$MnCo_3$(py-H)[PF_6]

Table S5. Relationship Between Rate of Metal-Metal Exchange and $[py]_0$

$[py]_0 \times 10^{-6}$ (mM)	$k_{initial} \times 10^{-4}$ (mM s^{-1})
0	1.56(8)
3.125	1.50(18)
4	1.34(18)
5	1.23(8)



S145. (A) $[py]_0$ vs. k_{init} of metal-metal exchange with linear fit represented by the dashed line. The slope of the fit $k_{obs} = –3.9(4) \times 10^{-3}$ s^{-1} with error determined as the standard error of the linear regression. (B) log-log plot of depiction of the –0.11 order dependence of the initial rate on $[py]_0$ with linear fit represented by the dashed line. Note that the Pearson correlation coefficient in the log-log plot is extremely low, and the error in the measurement is such that the rates are indistinguishable. Thus, it is probably not useful to ascribe to the $[py]_0$ any inhibitory role.

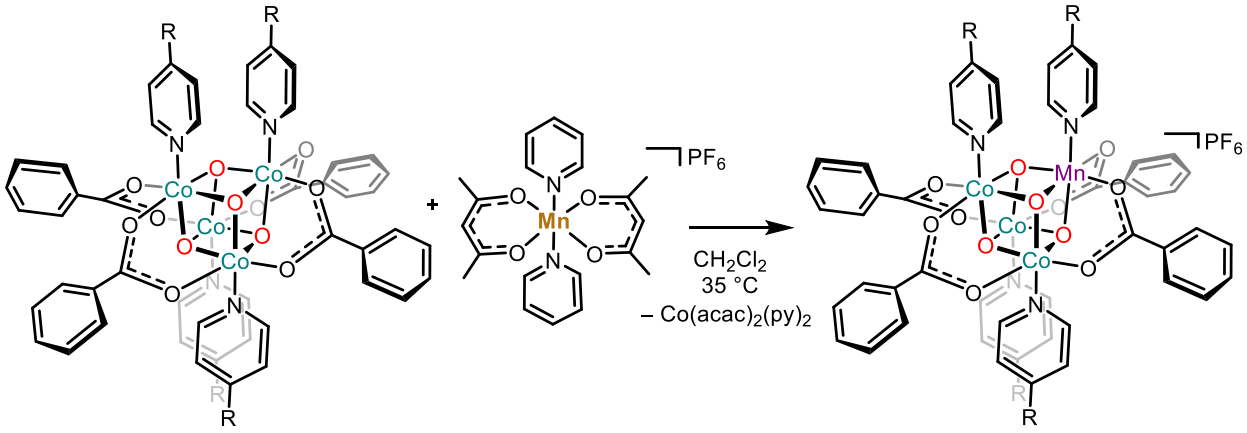
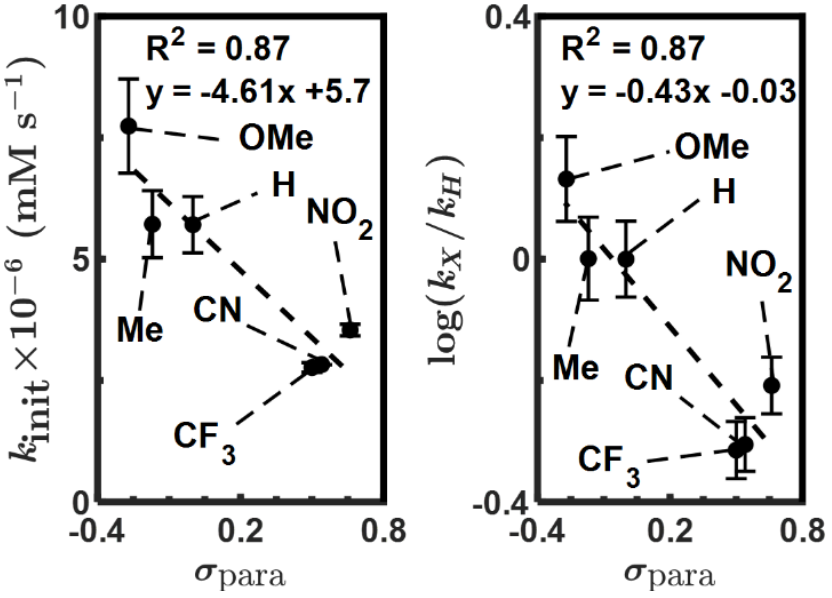


Table S6. Relationship Between Rate of Metal-Metal Exchange and pyridine ligand *para*-Position Substituent.

para-substituent	Compound Number	σ_{para}	$k_{initial} \times 10^{-6}$ (mM s^{-1})	$\log(k_X/k_H)$
OMe		–0.27	7.7(9)	0.13(7)
Me		–0.17	5.7(7)	$8.6(6) \times 10^{-4}$
H		0.00	5.7(6)	0(6)
Ac		0.5	2.8(1)	–0.31(5)
CF_3		0.54	2.8(0)	–0.30(4)
CN		0.66	3.54(1)	–0.20(4)



S146. (A) Substituted-pyridine ligand σ_{para} vs. k_{init} of metal-metal exchange with linear fit represented by the dashed line. The slope of the fit $k_{obs} = –4.6(8) \times 10^{-6}$ with error determined as the standard error of the linear regression. (B) Hammett plot depicting the weak influence of the *para*-substituent on the rate of metal-metal exchange, and that stronger donors induce faster exchange with linear fit represented by the dashed line $\rho = –0.43(8)$.

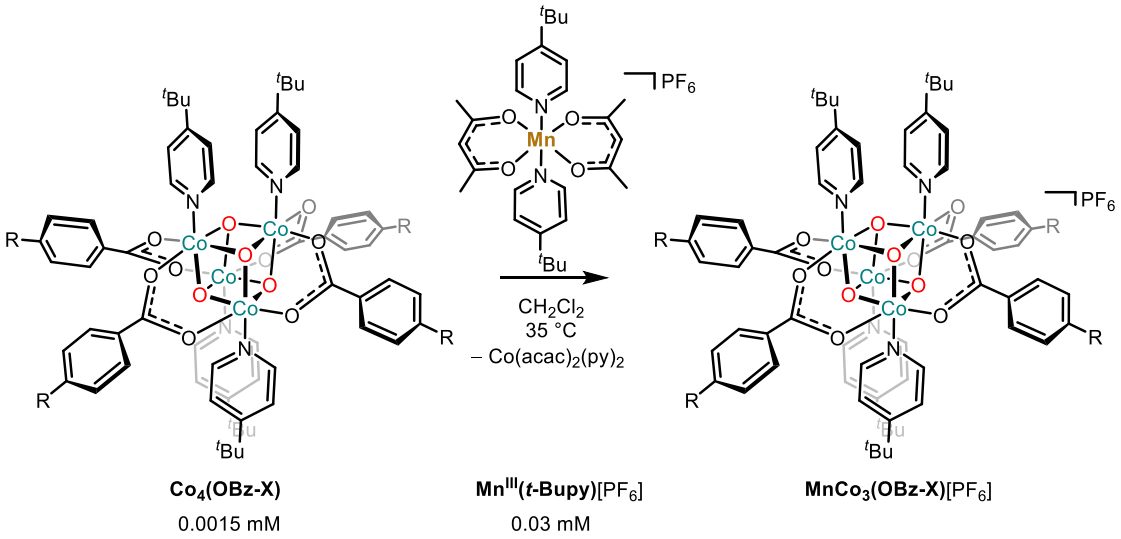
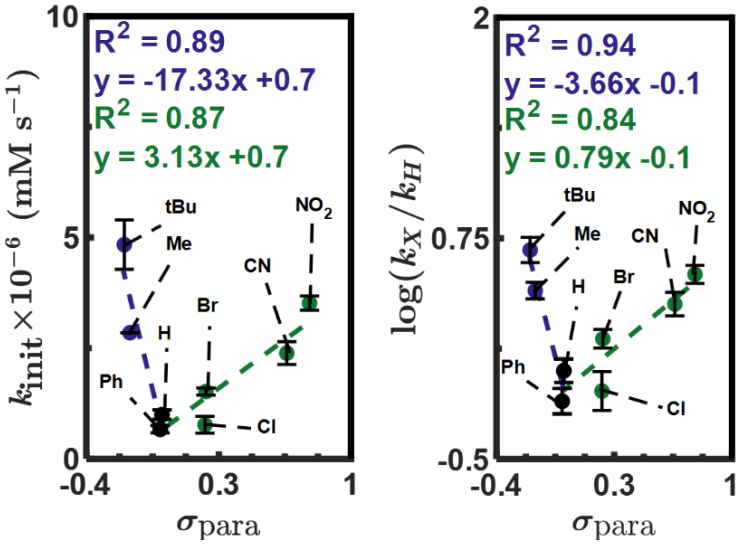


Table S7. Relationship Between the Rate of Metal-Metal Exchange and Benzoate Ligand *para*-Position Substituent

***para*-substituent**	**Compound Number**	**σ_{para}**	**$k_{initial} \times 10^{-6}$ (mM s^{-1})**	**$\log(k_X/k_H)$**
OMe		–0.27		
^{t}Bu		–0.20	4.8(6)	0.68(7)
Me		–0.17	2.9(0)	0.45(5)
Ph		–0.01	0.7(08)	–0.17(7)
H		0.00	1.0(1)	0(0.06)
Cl		0.227	0.8(2)	–0.1(1)
Br		0.232	1.5(08)	0.18(5)
CN		0.66	2.4(25)	0.38(6)
NO_2		0.78	3.5(16)	0.55(5)

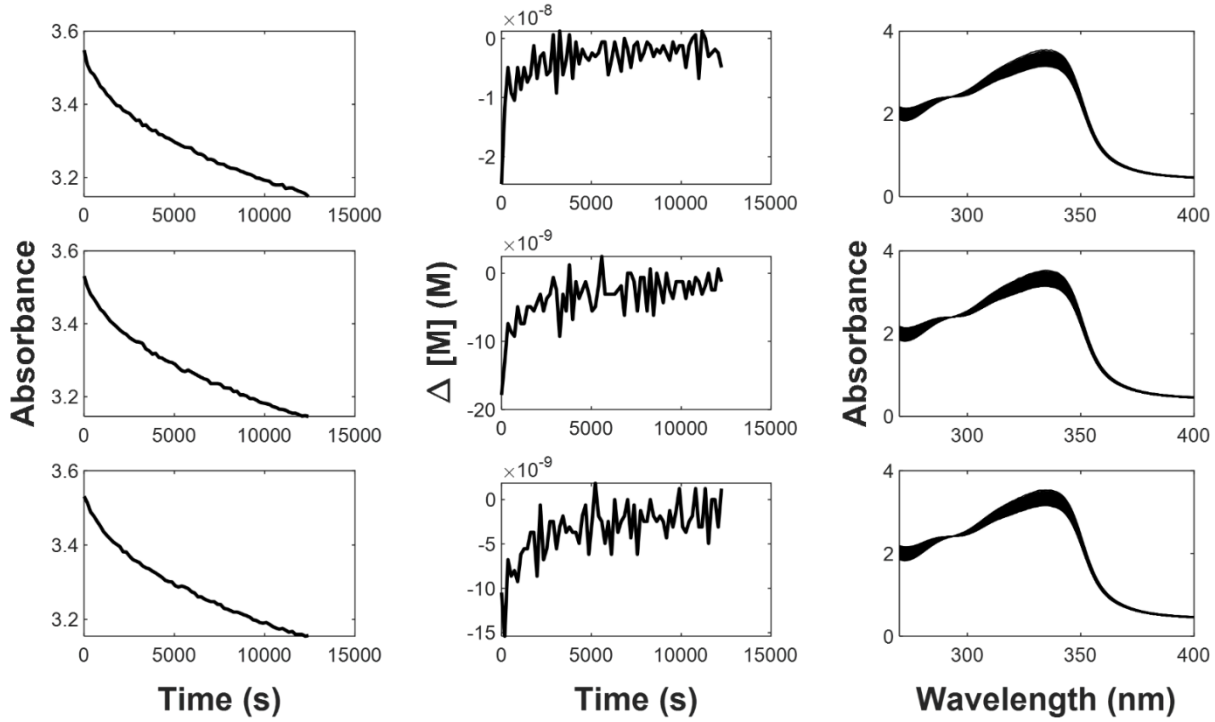


S147. (A) Benzoate ligand σ_{para} vs. k_{init} of metal-metal exchange with error determined as the standard error of the linear regression. The slope of the fit for the donating substituents = $-1.7(4) \times 10^{-5}$ and for the withdrawing substituents = $3.1(6) \times 10^{-6}$.(B) Hammett plot depicts the strong, acceleratory influence of electron-donating substituents on the rate of metal-metal exchange until R = H, at which point electron-withdrawing substituents begin to increase the rate of metal-metal exchange. The slope of the fit for Hammett plot of the donating substituents = –3.6(6), and for the withdrawing substituents the slope = 0.8(2).

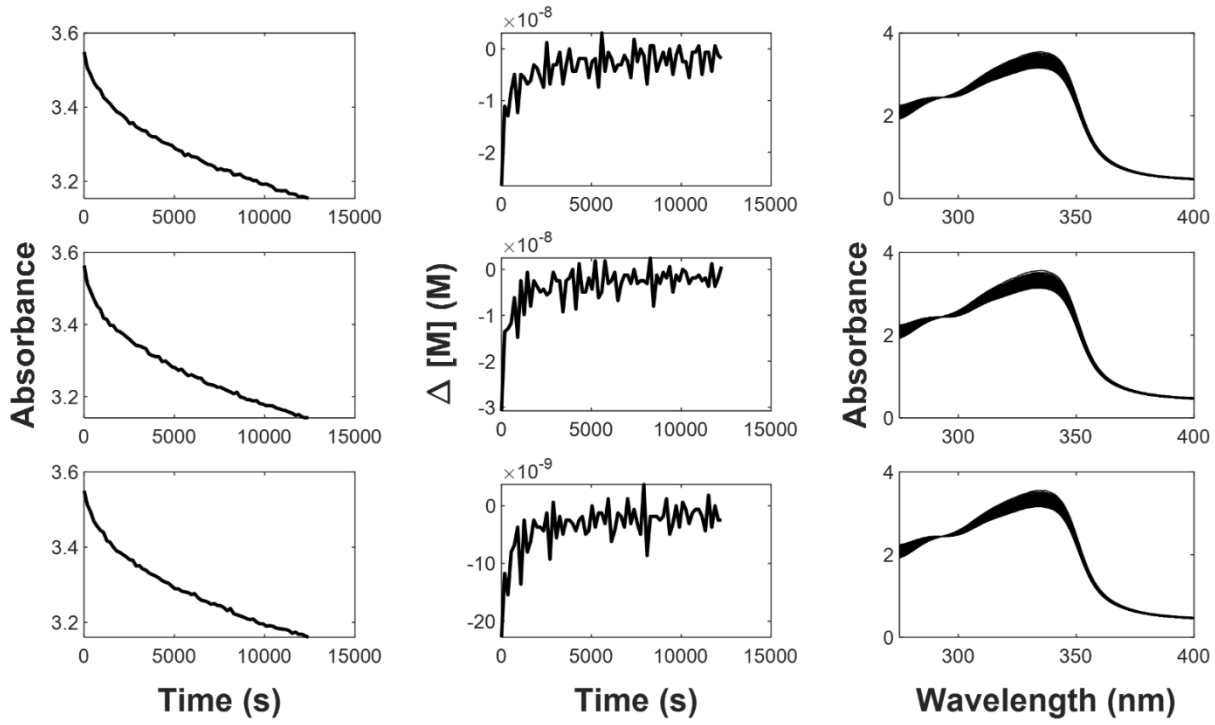
Kinetic Traces:

Guide to interpretation of kinetic traces: Each set of graphs represents one condition collected in triplicate. The three graphs on the left-hand column show the absorbance vs. time of at the specified wavelength. The three graphs in the center column show the change in concentration of [M] vs. time, where [M] is the reagent specified in the caption –this is the approximate derivative of the graph on the left. The graphs on the right-hand column plot the entire spectrum collected at each timepoint.

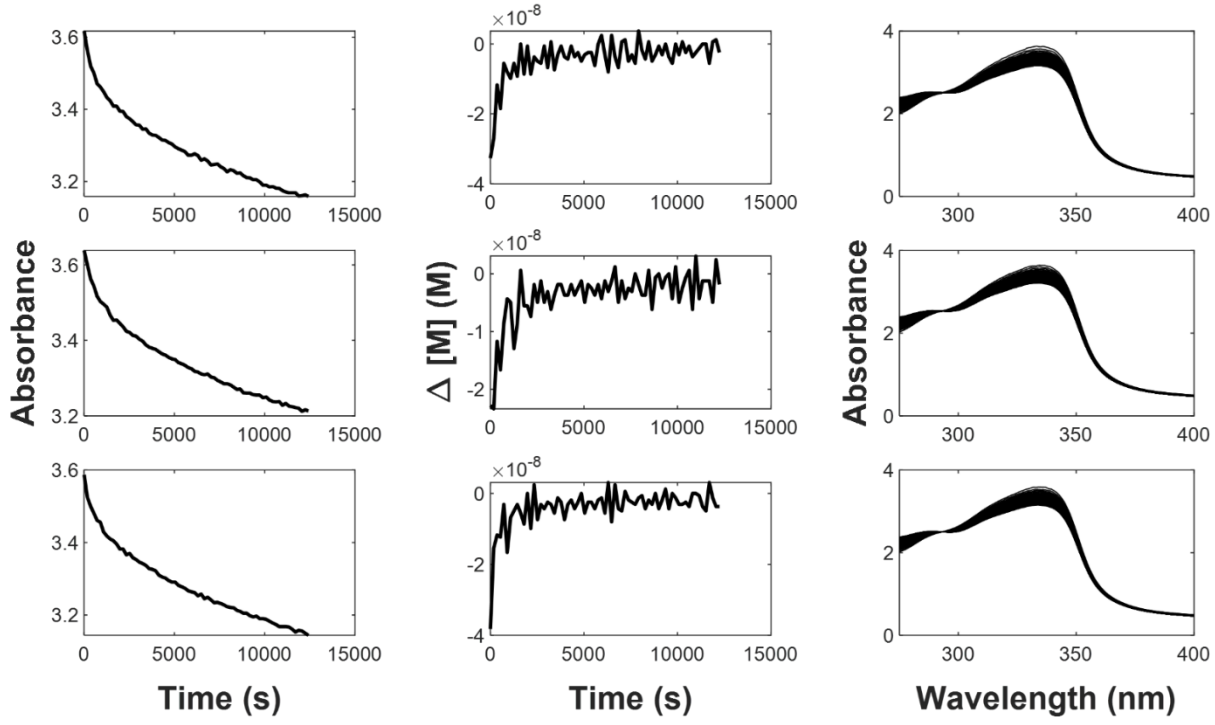
These figures demonstrate the key features observed for each kinetic experiment: for example, in the experiments containing an excess of $[Mn(acac)_2(py)_2][PF_6]$, the absorbance vs. time graphs initially decay with evidently non-exponential behavior, suggestive of the background oxidation chemistry described in the manuscript.



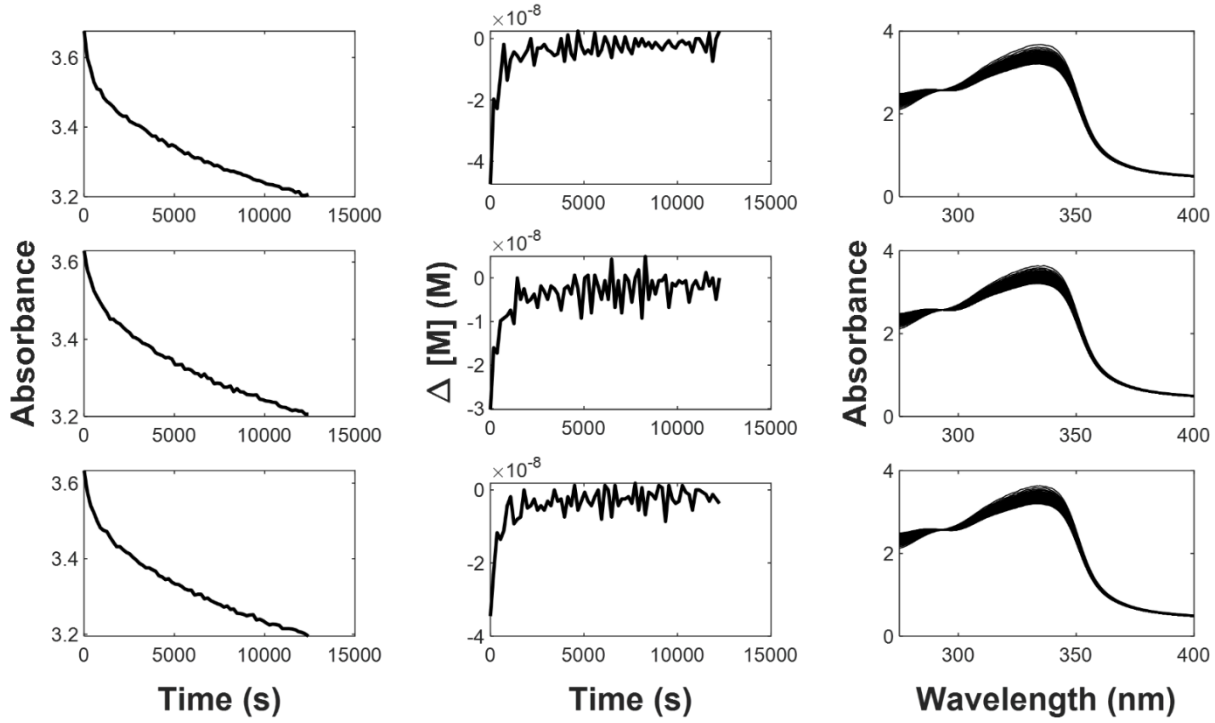
S148. Kinetic traces for the order of **Co_4(py-H)** (entry = 3.0×10^{-6} M) see **Table** for full experimental details. Spectra were collected every 180 s. Wavelength monitored: 335 nm. **Mn^{III}(py)**$[PF_6]$ $\boldsymbol{\varepsilon_{335}}$ = 9018.34 M^{-1} cm^{-1}.



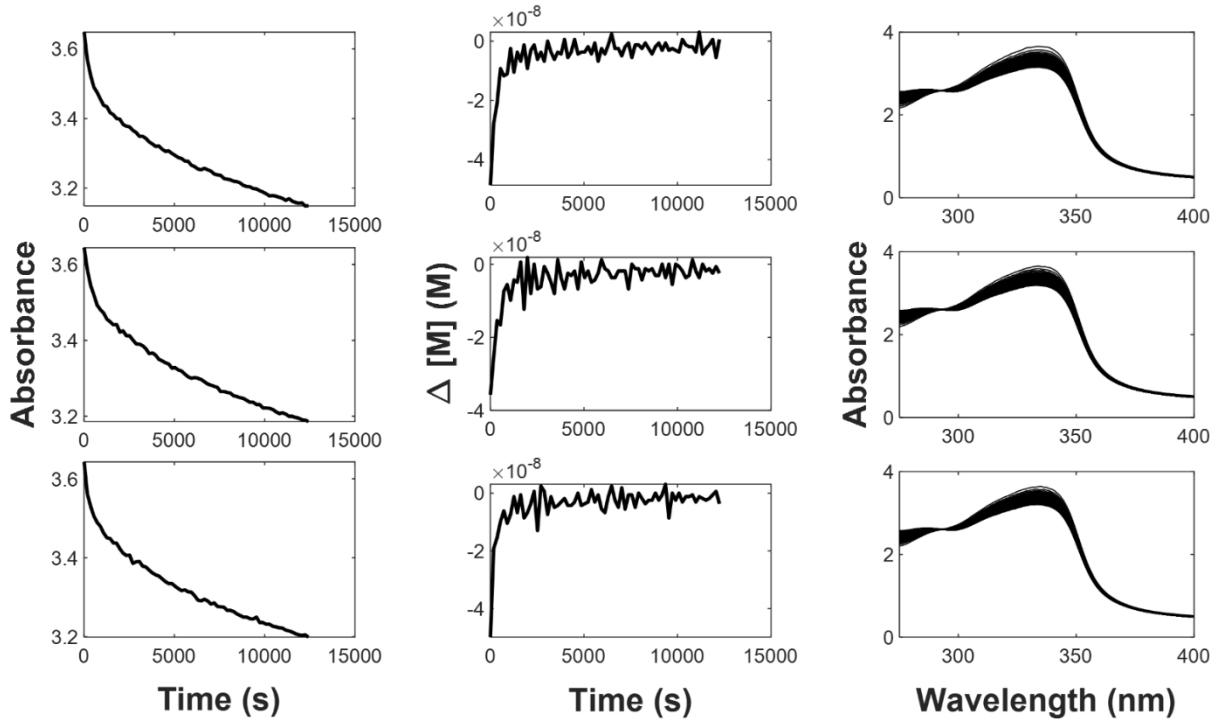
S149. Kinetic traces for the order of **Co_4(py-H)** (entry = 6.0 × 10^{-6} M) see **Table** for full experimental details. Spectra were collected every 180 s. Wavelength monitored: 335 nm. **Mn^{III}(py)**[PF_6] $\boldsymbol{\varepsilon_{335}}$ = 9018.34 M^{-1} cm^{-1}.



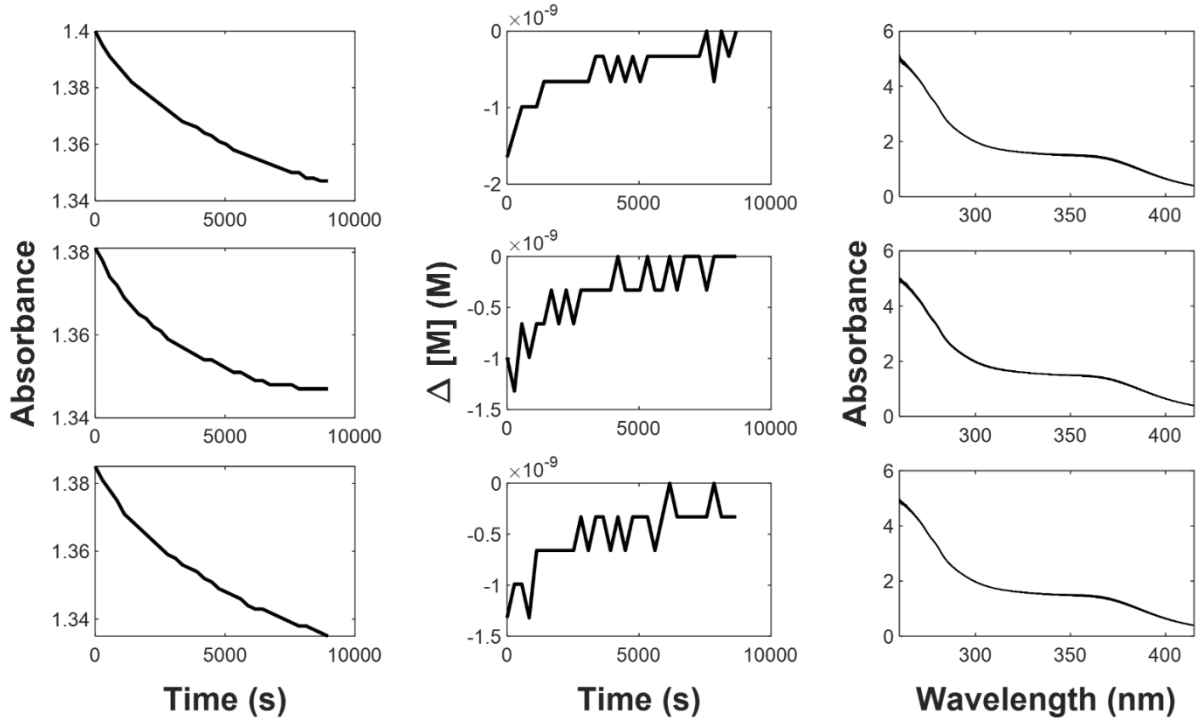
S150. Kinetic traces for the order of **Co_4(py-H)** (entry = 9.0 × 10^{-6} M) see **Table** for full experimental details. Spectra were collected every 180 s. Wavelength monitored: 335 nm. **Mn^{III}(py)**[PF_6] $\boldsymbol{\varepsilon_{335}}$ = 9018.34 M^{-1} cm^{-1}.



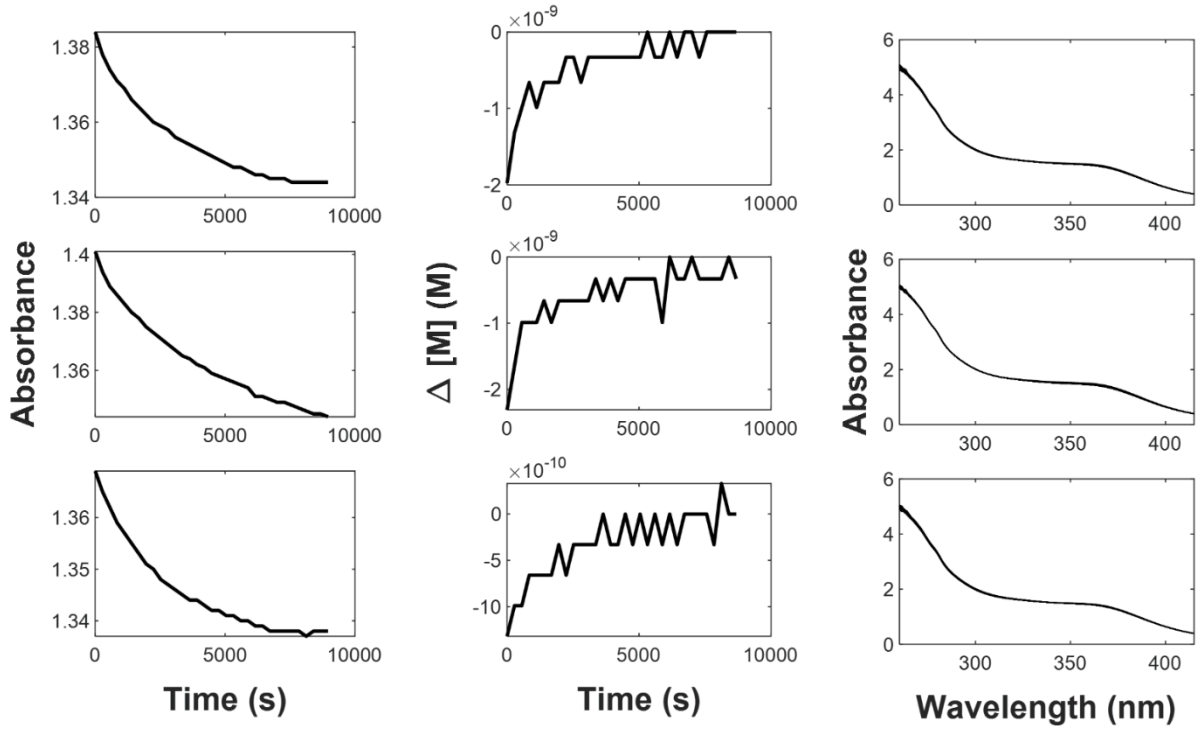
S151. Kinetic traces for the order of **Co_4(py-H)** (entry = 12.0 × 10^{-6} M) see **Table** for full experimental details. Spectra were collected every 180 s. Wavelength monitored: 335 nm. **Mn^{III}(py)**[PF_6] $\boldsymbol{\varepsilon_{335}}$ = 9018.34 M^{-1} cm^{-1}.



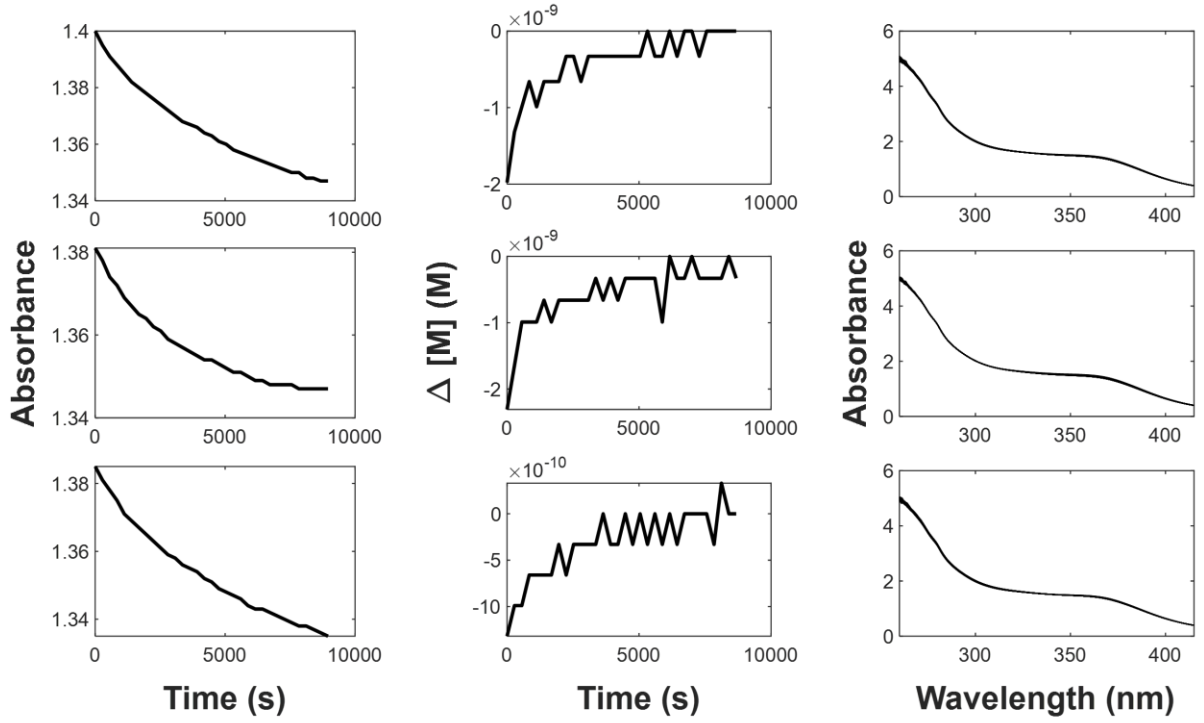
S152. Kinetic traces for the order of **Co_4(py-H)** (entry = 15.0 × 10^{-6} M) see **Table** for full experimental details. Spectra were collected every 180 s. Wavelength monitored: 335 nm. **Mn^{III}(py)**[PF_6] $\boldsymbol{\varepsilon_{335}}$ = 9018.34 M^{-1} cm^{-1}.



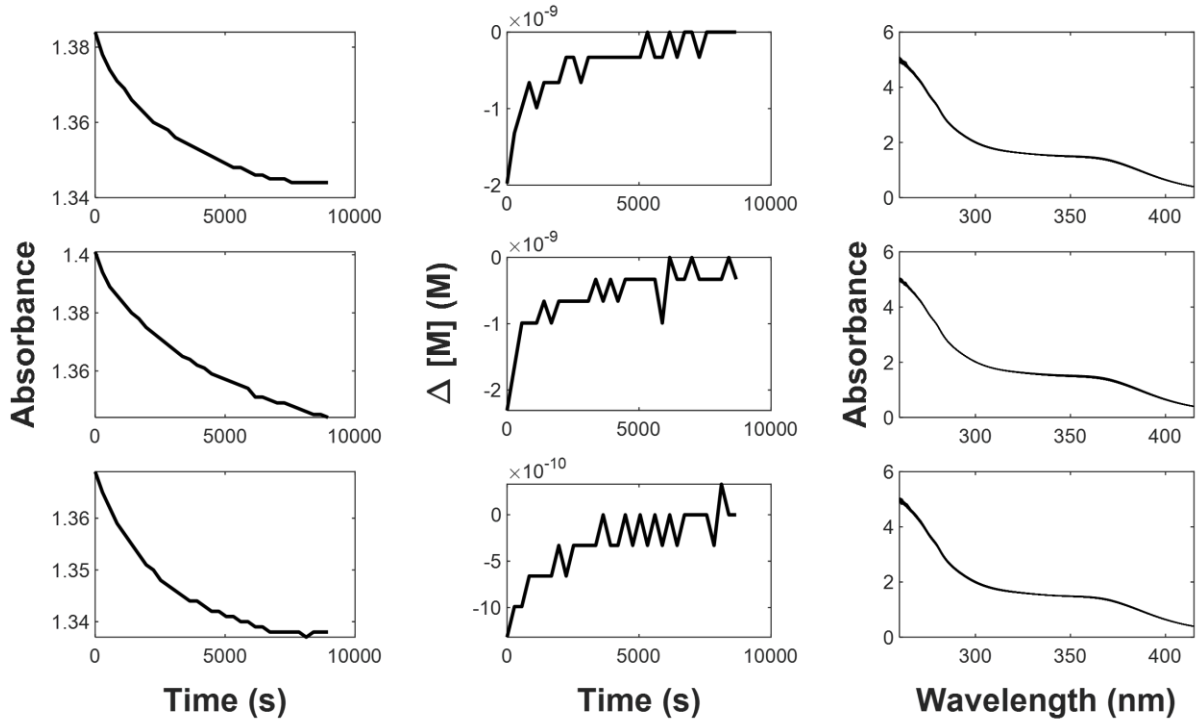
S153. Kinetic traces for the order of **Mn^{III}(py)**[PF_6] (entry = 1.875 × 10^{-5} M) see **Table** for full experimental details. Spectra were collected every 280 s. Wavelength monitored: 370 nm. **Co_4(py-H) ε_{370}** = 10827.69 M^{-1} cm^{-1}.



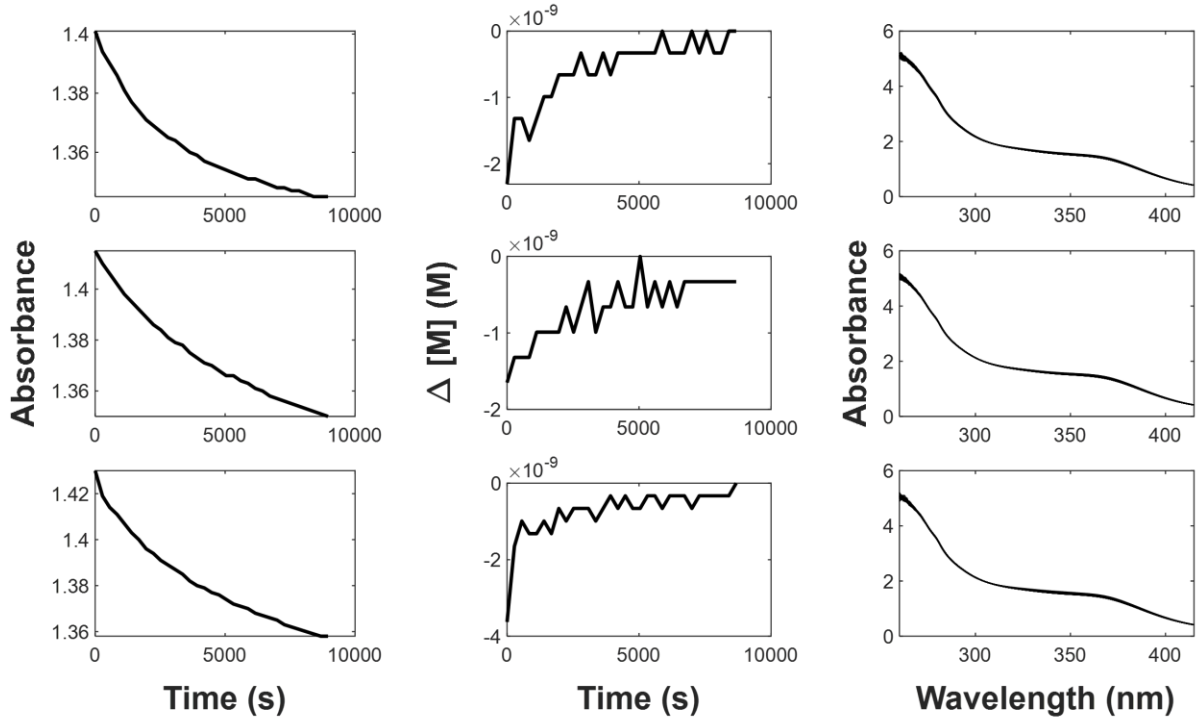
S154. Kinetic traces for the order of **Mn^{III}(py)**[PF_6] (entry = 2 × 10^{-5} M) see **Table** for full experimental details. Spectra were collected every 280 s. Wavelength monitored: 370 nm. **Co_4(py-H) ε_{370}** = 10827.69 M^{-1} cm^{-1}.



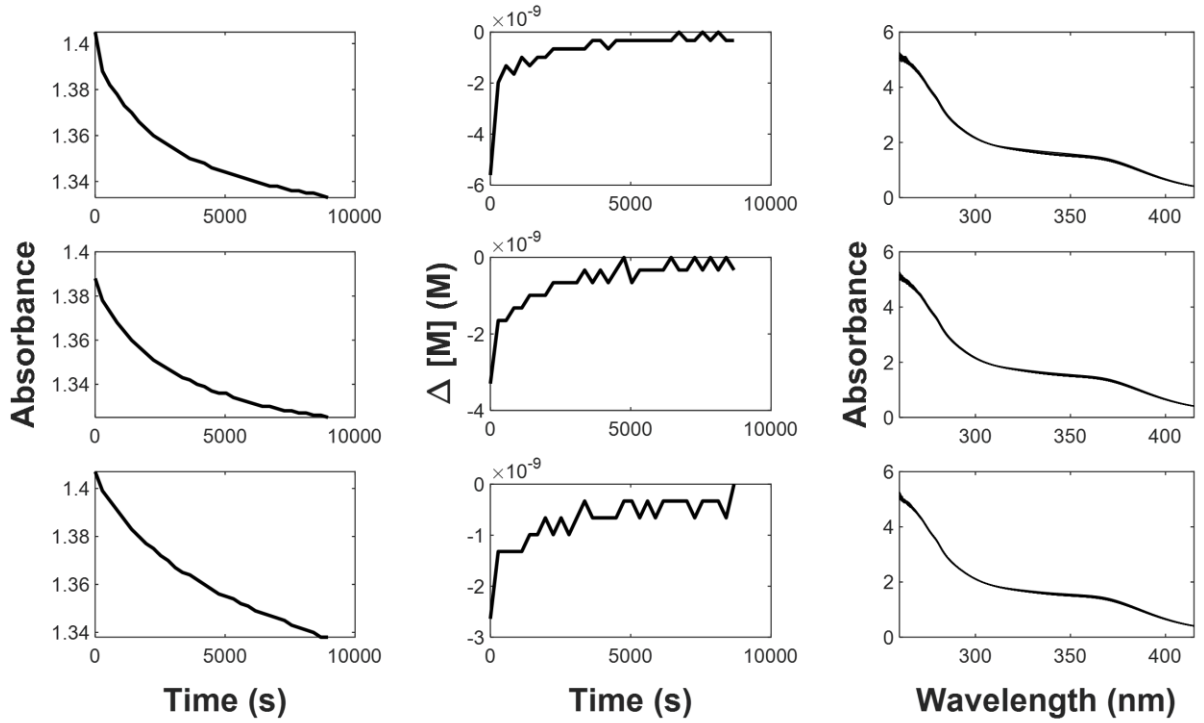
S155. Kinetic traces for the order of **Mn^{III}(py)**[PF_6] (entry = 2.4× 10^{-5} M) see **Table** for full experimental details. Spectra were collected every 280 s. Wavelength monitored: 370 nm. **Co4(py-H) ε_{370}** = 10827.69 M^{-1} cm^{-1}.



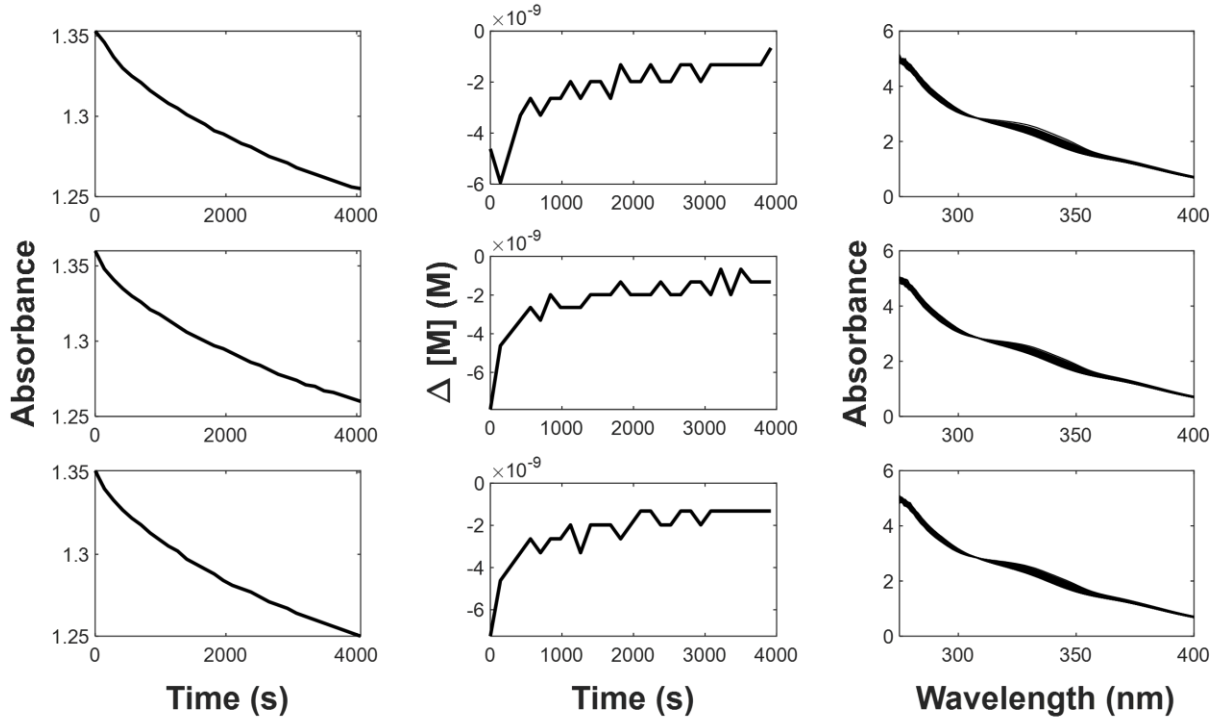
S156. Kinetic traces for the order of **Mn^{III}(py)**[PF_6] (entry = 3 × 10^{-5} M) see **Table** for full experimental details. Spectra were collected every 280 s. Wavelength monitored: 370 nm. **Co4(py-H) ε_{370}** = 10827.69 M^{-1} cm^{-1}.



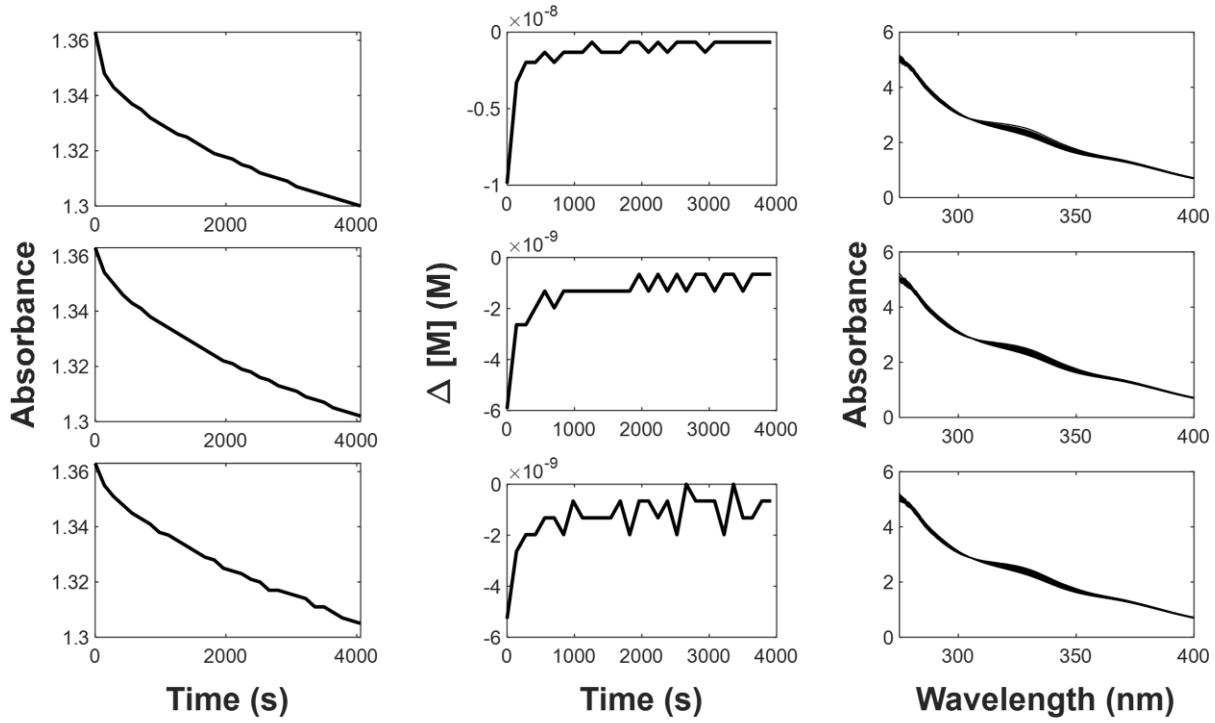
S157. Kinetic traces for the order of **Mn^{III}(py)**[PF_6] (entry = 4.5 × 10^{-5} M) see **Table** for full experimental details. Spectra were collected every 280 s. Wavelength monitored: 370 nm. **Co4(py-H) ε_{370}** = 10827.69 M^{-1} cm^{-1}.



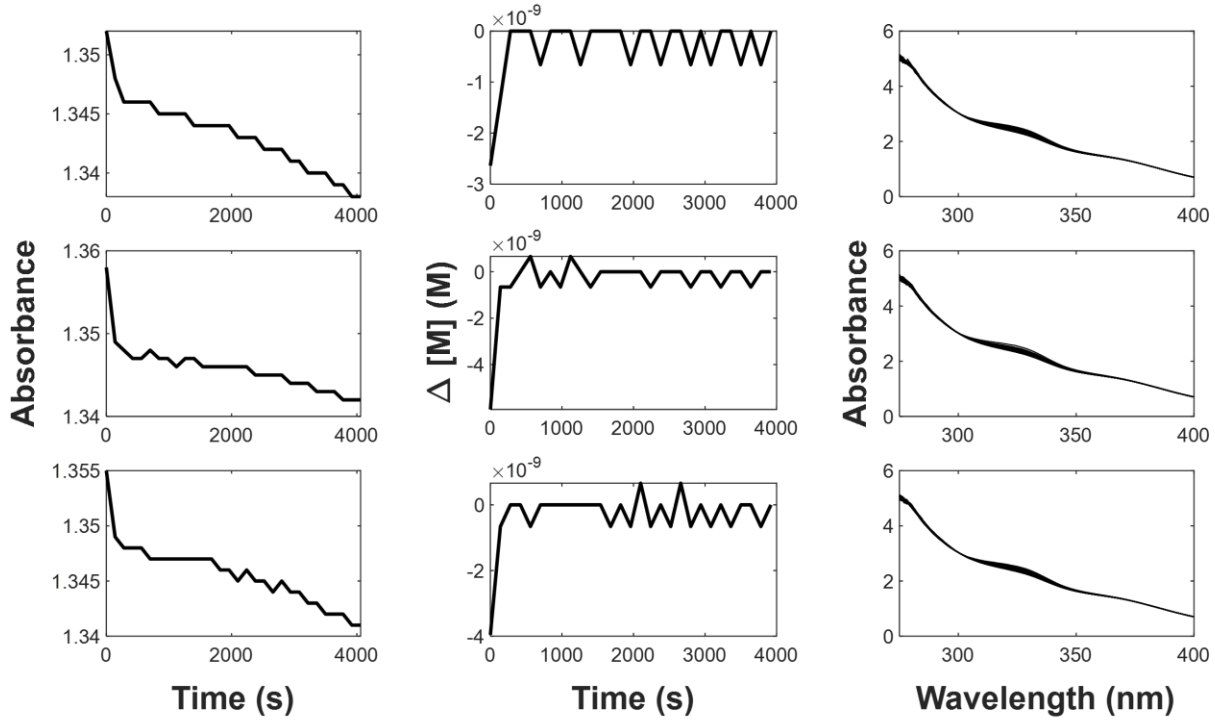
S158. Kinetic traces for the order of **Mn^{III}(py)**[PF_6] (entry = 6 × 10^{-5} M) see **Table** for full experimental details. Spectra were collected every 280 s. Wavelength monitored: 370 nm. **Co4(py-H) ε_{370}** = 10827.69 M^{-1} cm^{-1}.



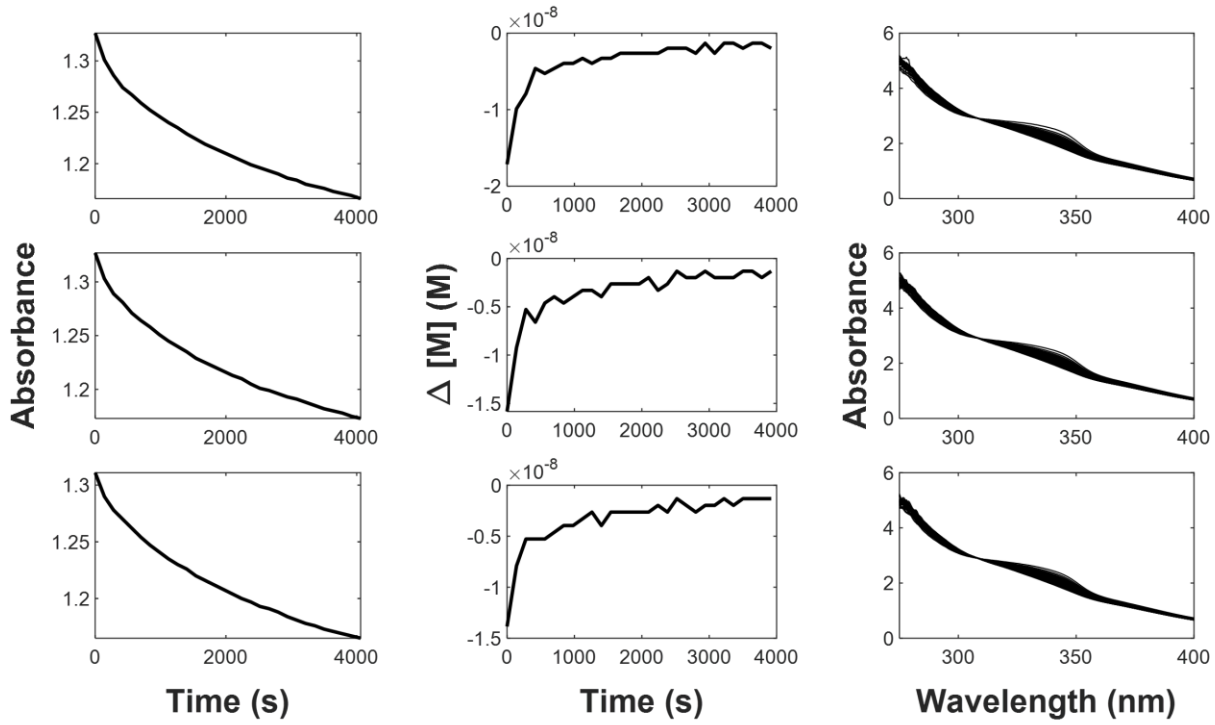
S159. Kinetic traces for the order in benzoate. [[^{n}Bu$_4$N][OBz]] (entry = 3.125 × 10^{-6}) see **Table** for full experimental details. Traces were collected every 140 s. Wavelength monitored: 370 nm. **Co$_4$(py-H) ε_{370}** = 10827.69 M^{-1} cm^{-1}.



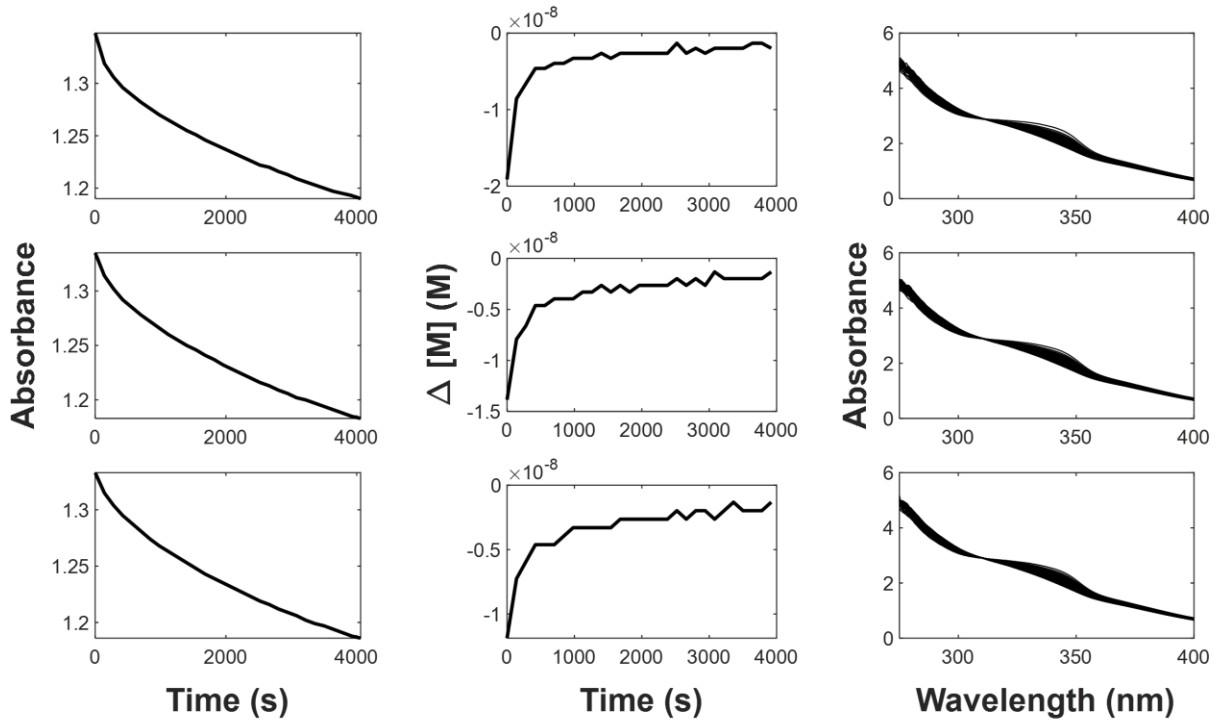
S160. Kinetic traces for the order in benzoate. [[^{n}Bu$_4$N][OBz]] (entry = 4 × 10^{-6}) see **Table** for full experimental details. Traces were collected every 140 s. Wavelength monitored: 370 nm. **Co$_4$(py-H) ε_{370}** = 10827.69 M^{-1} cm^{-1}.



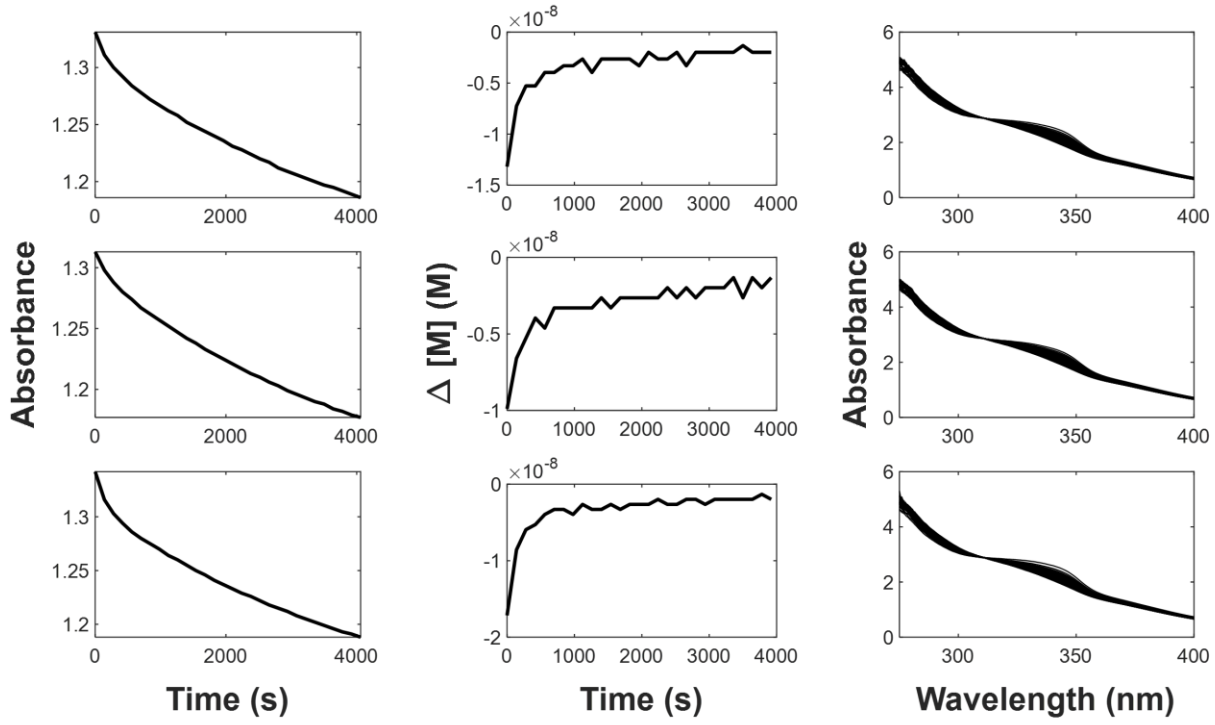
S161. Kinetic traces for the order in benzoate. [[^{n}Bu$_4$N][OBz]] (entry = 5 × 10^{-6}) see **Table** for full experimental details. Traces were collected every 140 s. Wavelength monitored: 370 nm. **Co$_4$(py-H) ε_{370}** = 10827.69 M^{-1} cm^{-1}.



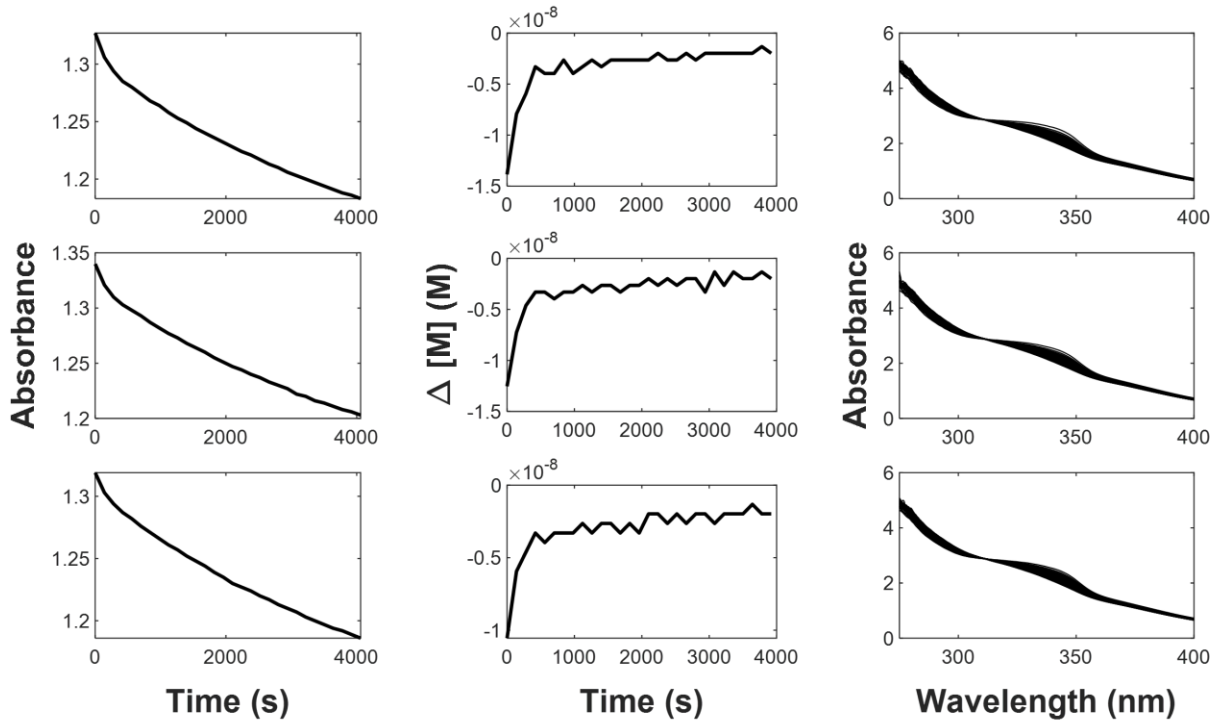
S162. Kinetic traces for the order in benzoate and pyridine. [[^{n}Bu$_4$N][OBz]]$_0$ = [py]$_0$ (0) see **Table** and **Table** for experimental details. Traces collected every 140 s. Wavelength monitored: 370 nm. **Co$_4$(py-H) ε_{370}** = 10827.69 M^{-1} cm^{-1}.



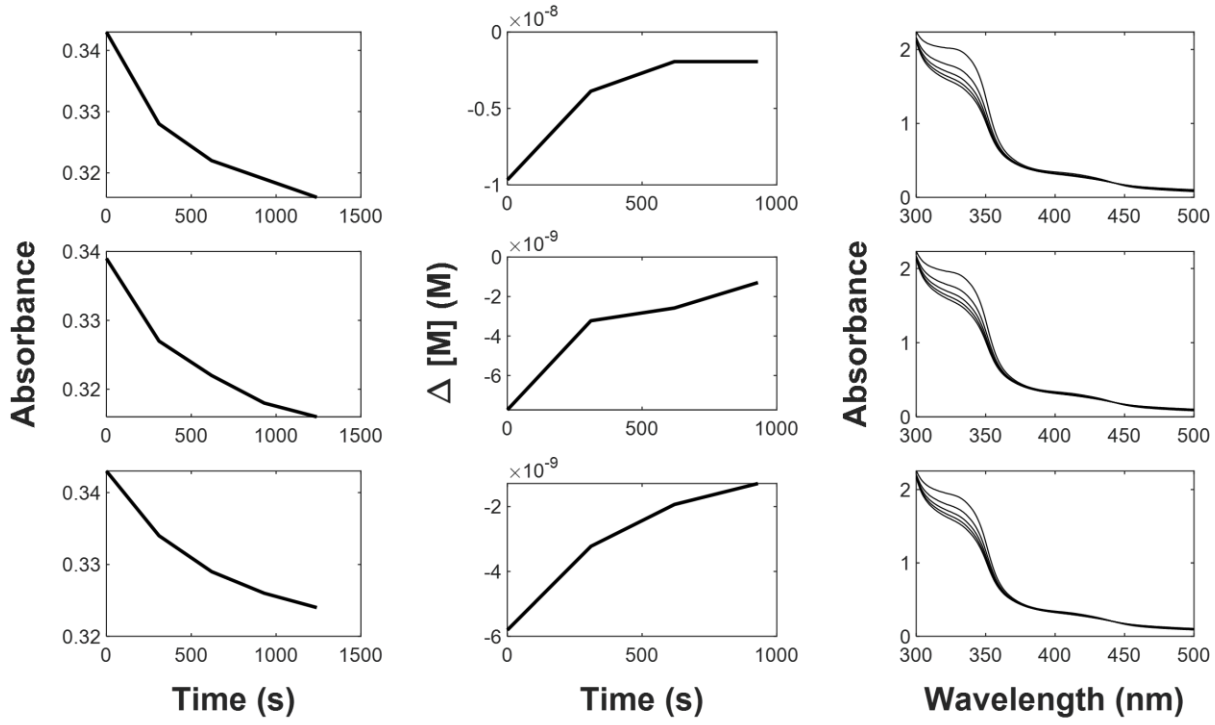
S163. Kinetic traces for the order in pyridine. [py] (entry = 3.125 × 10^{-6}) see **Table** for experimental details. Traces collected every 140 s. Wavelength monitored: 370 nm. **Co_4(py-H) ε_{370}** = 10827.69 M^{-1} cm^{-1}.



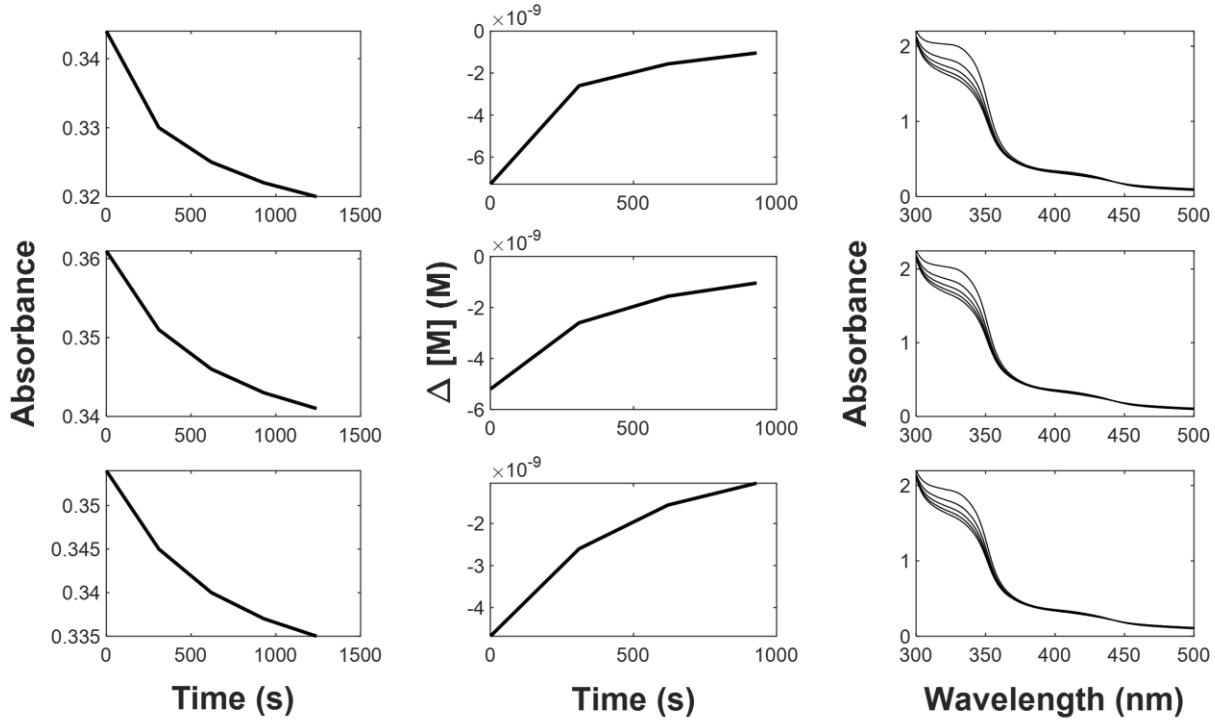
S164. Kinetic traces for the order in pyridine. [py] (entry = 4 × 10^{-6}) see **Table** for experimental details. Traces collected every 140 s. Wavelength monitored: 370 nm. **Co_4(py-H) ε_{370}** = 10827.69 M^{-1} cm^{-1}.



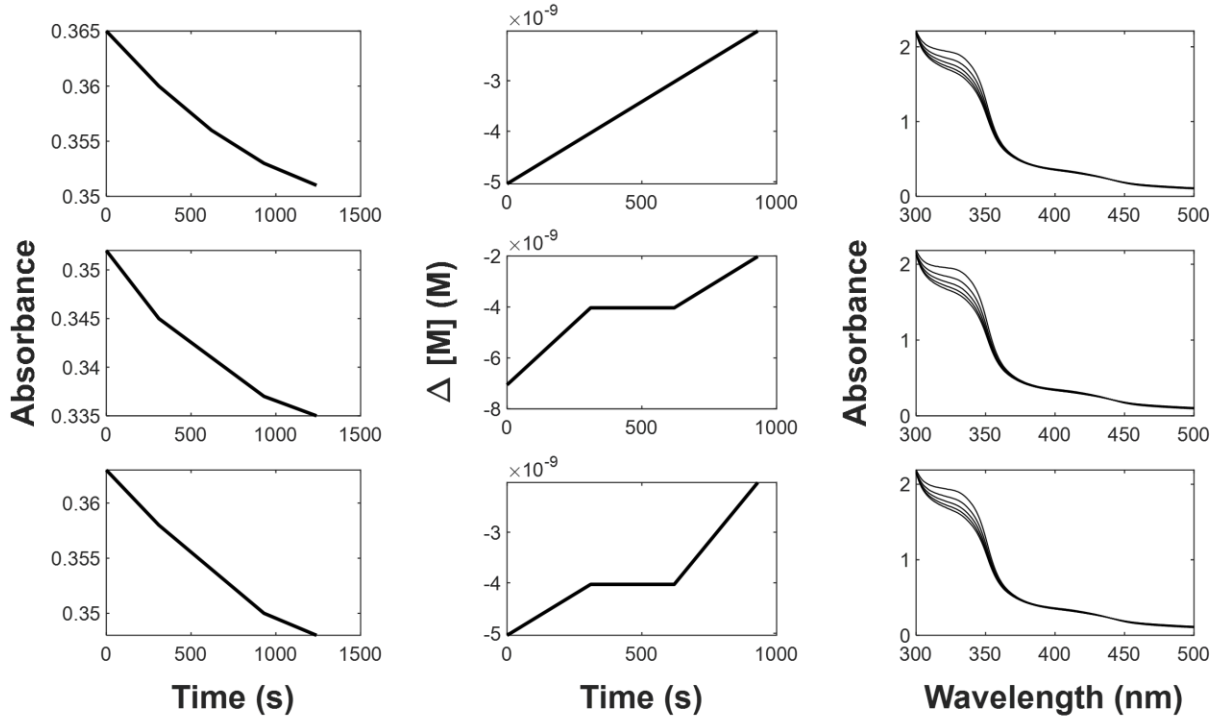
S165. Kinetic traces for the order in pyridine. [py] (entry = 5 × 10^{-6}) see **Table** for experimental details. Traces collected every 140 s. Wavelength monitored: 370 nm. **Co_4(py-H) ε_{370}** = 10827.69 M^{-1} cm^{-1}.



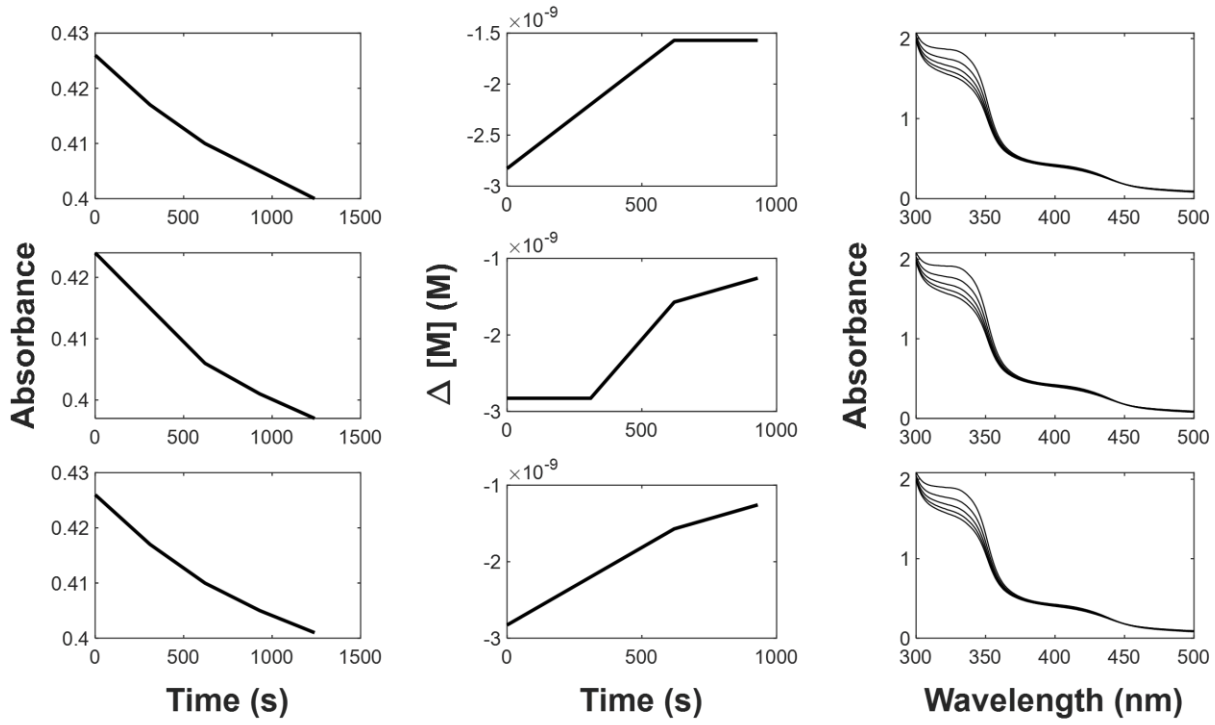
S166. Kinetic traces for the Hammett data for **Co_4(py-OMe)** see **Table** for experimental details. Traces collected every 310 s. Wavelength monitored: 400 nm. **Co_4(py-OMe) ε_{400}** = 5000 M^{-1} cm^{-1}.



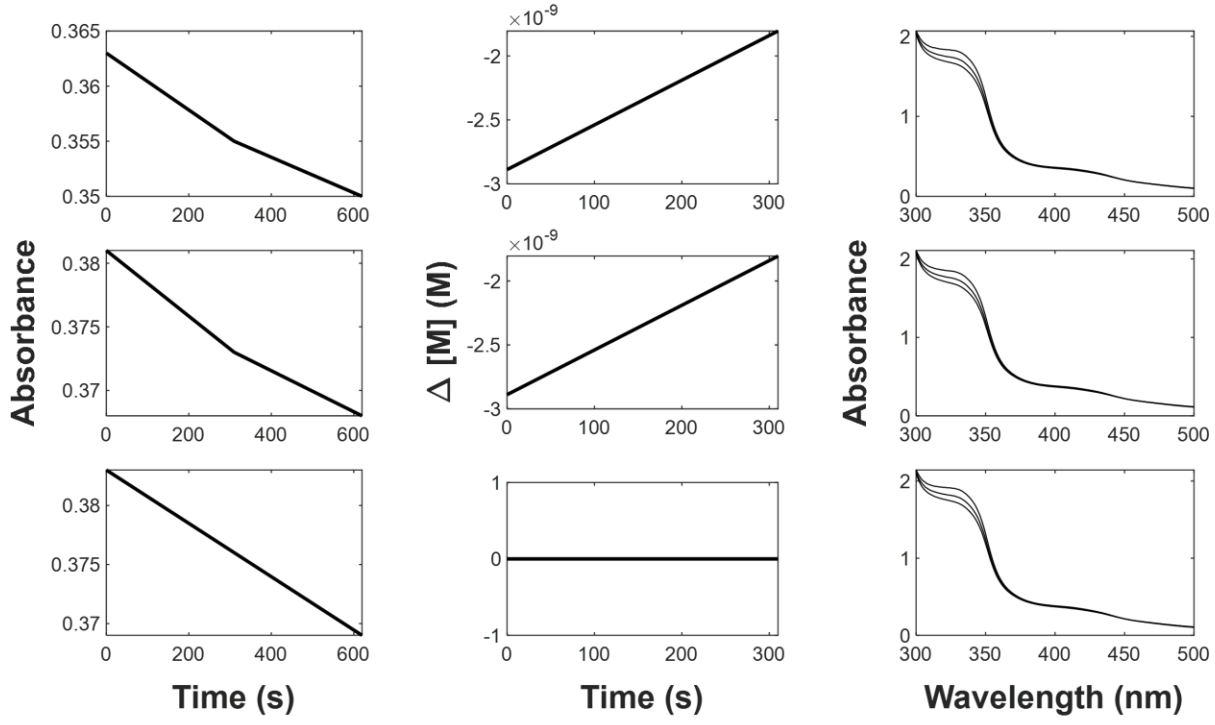
S167. Kinetic traces for the Hammett data for **Co₄(py-Me)** see **Table** for experimental details. Traces collected every 310 s. Wavelength monitored: 400 nm. **Co₄(py-Me)** $\boldsymbol{\varepsilon_{400}}$ = 6200 M^{-1} cm^{-1}.



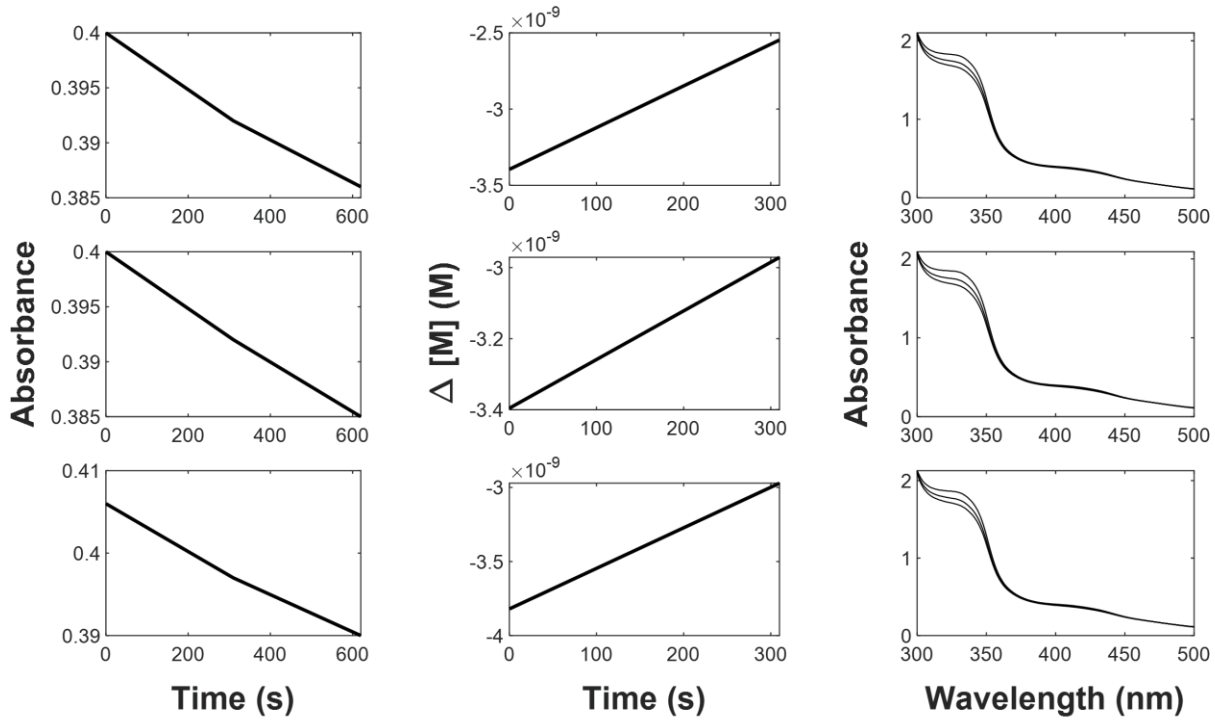
S168. Kinetic traces for the Hammett data for **Co₄(py-H)** see **Table** for experimental details. Traces collected every 310 s. Wavelength monitored: 400 nm. **Co₄(py-H)** $\boldsymbol{\varepsilon_{400}}$ = 3200 M^{-1} cm^{-1}.



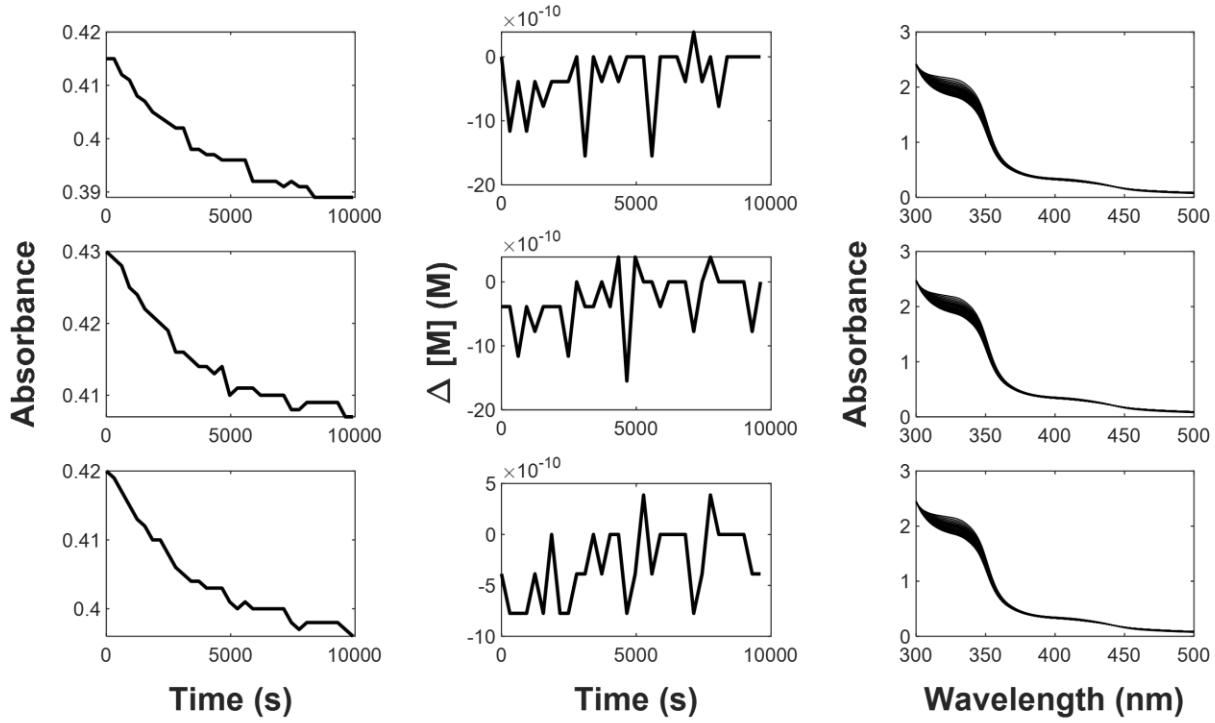
S169. Kinetic traces for the Hammett data for **Co_4(py-CF_3)** see **Table** for experimental details. Traces collected every 310 s. Wavelength monitored: 400 nm. **Co_4(py-CF_3) ε_{400}** = 10266.67 M^{-1} cm^{-1}.



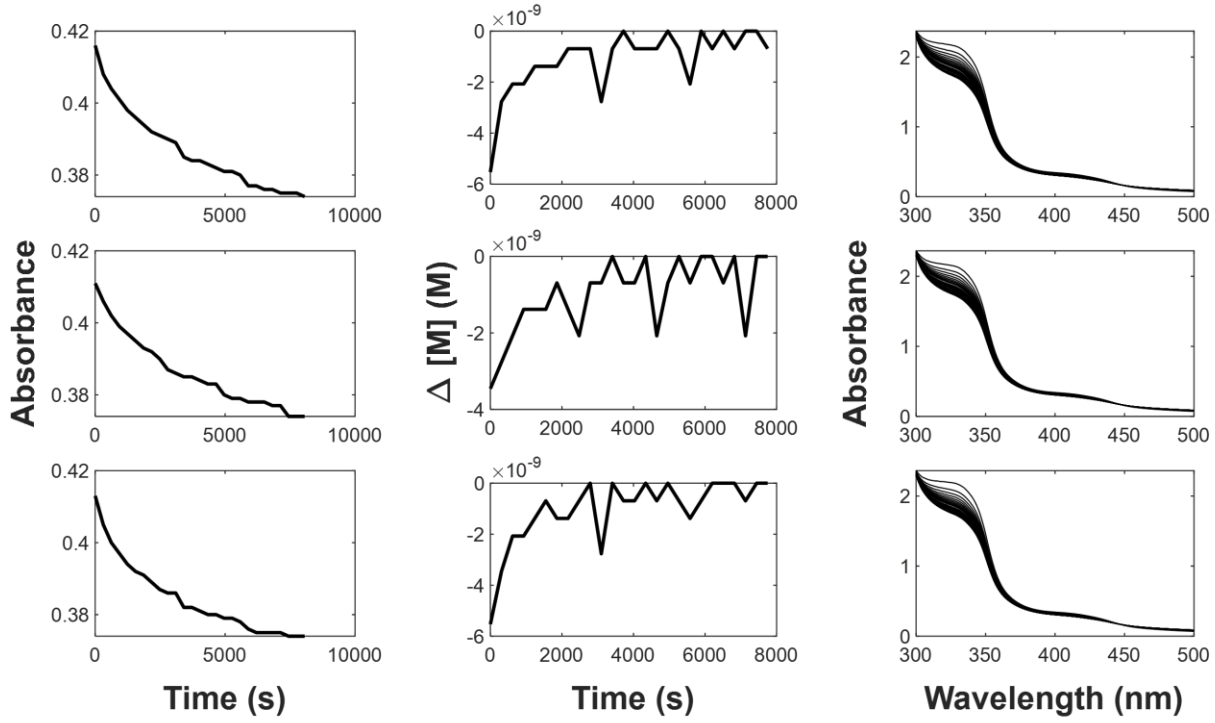
S170. Kinetic traces for the Hammett data for **Co_4(py-Ac)** see **Table** for experimental details. Traces collected every 310 s. Wavelength monitored: 400 nm. **Co_4(py-Ac) ε_{400}** = 8933.33 M^{-1} cm^{-1}.



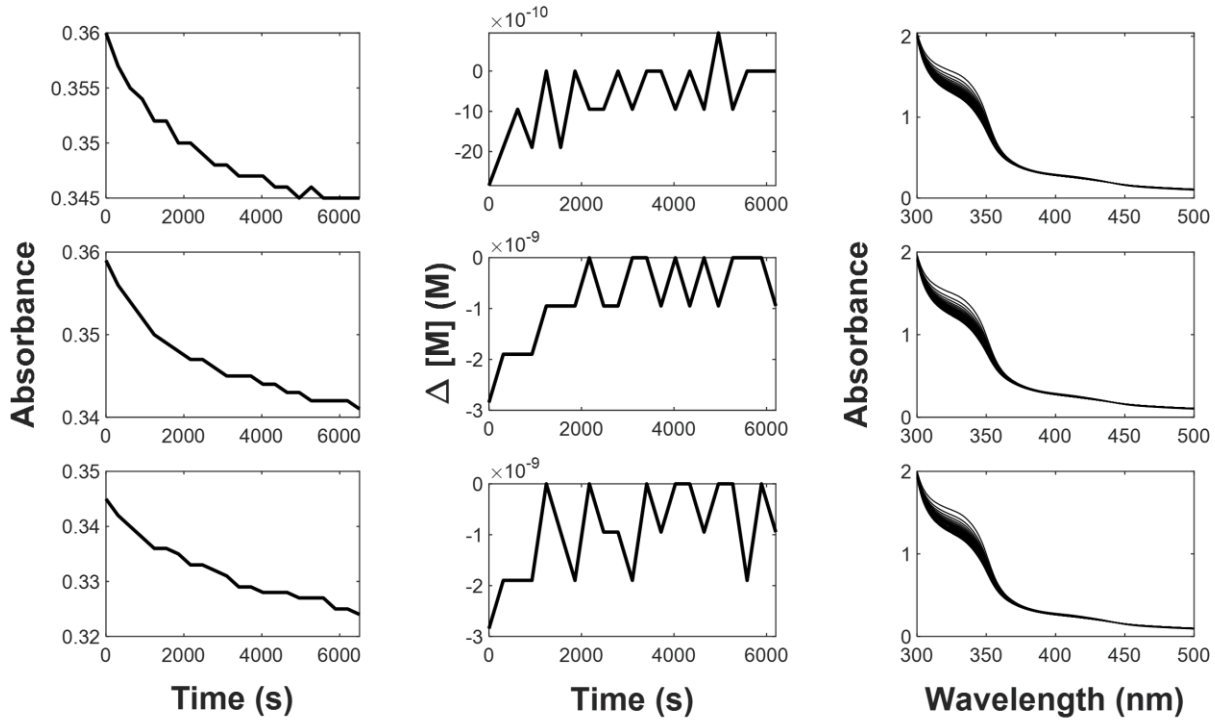
S171. Kinetic traces for the Hammett data for **Co₄(py-CN)** see **Table** for experimental details. Traces collected every 310 s. Wavelength monitored: 400 nm. **Co₄(py-CN)** $\boldsymbol{\varepsilon_{400}}$ = 7600 M^{-1} cm^{-1}.



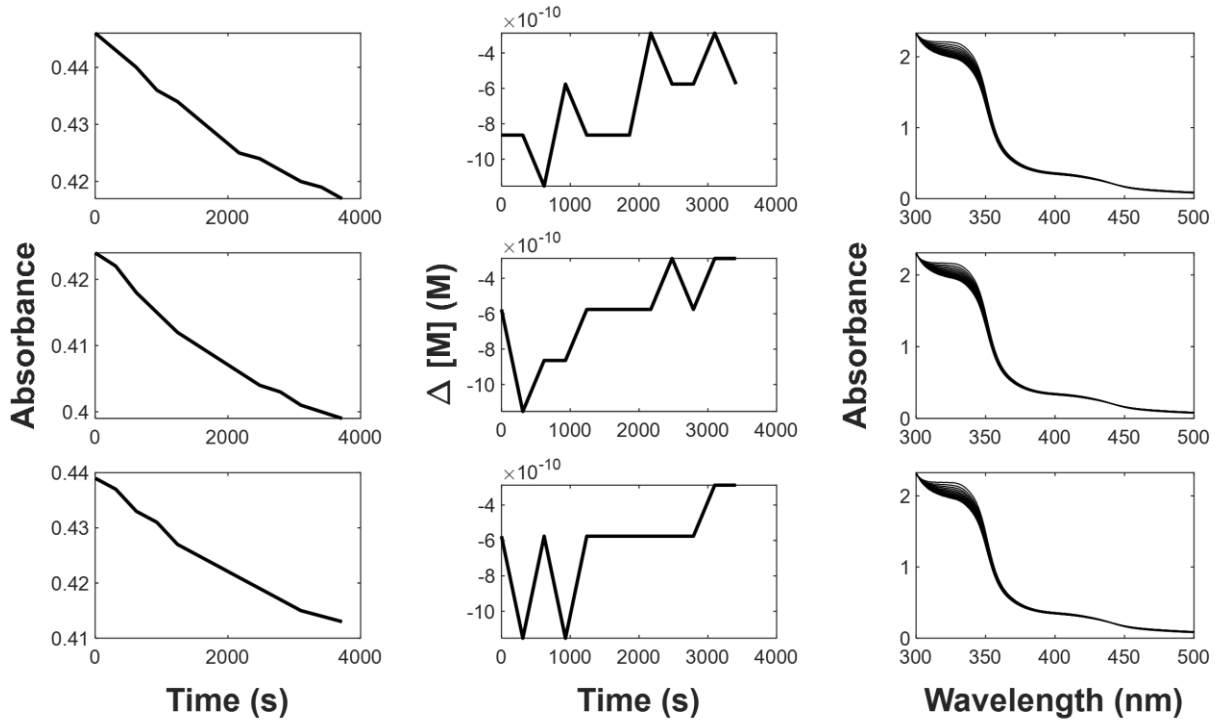
S172. Kinetic traces for the Hammett data for **Co₄(OBz-OMe)** see **Table** for experimental details. Traces collected every 310 s. Wavelength monitored: 380 nm. **Co₄(OBz-Ac)** $\boldsymbol{\varepsilon_{380}}$ = 8333.33 M^{-1} cm^{-1}.



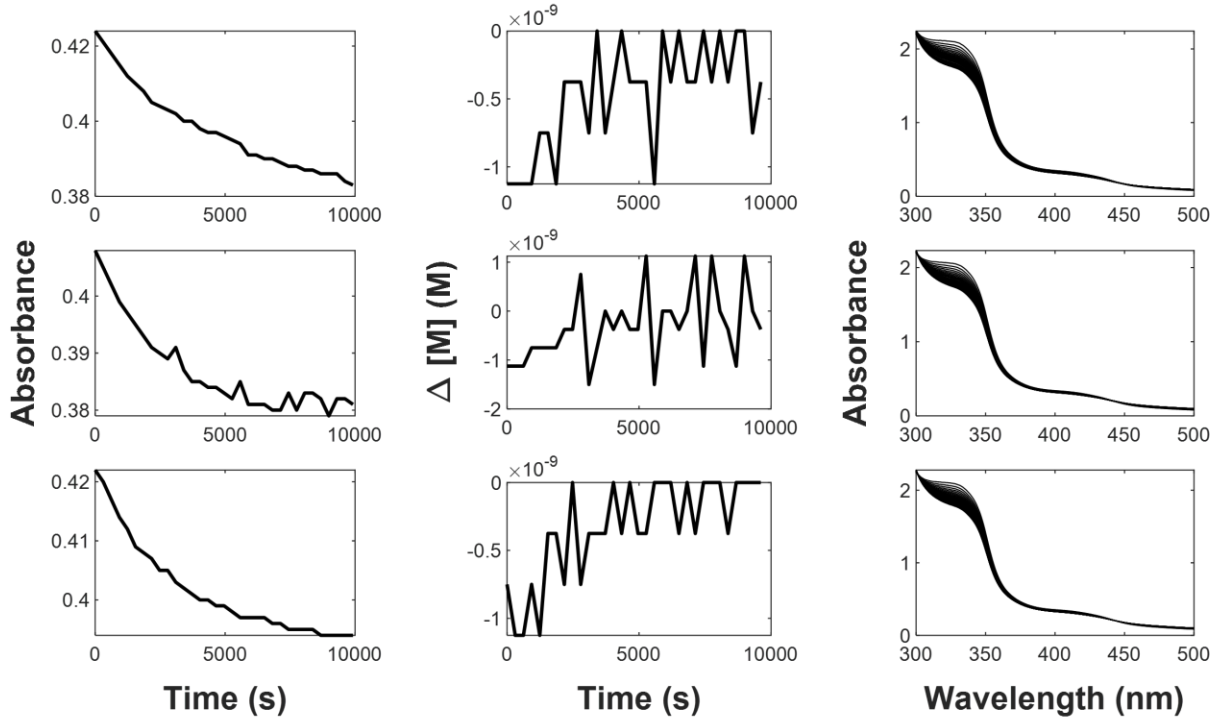
S173. Kinetic traces for the Hammett data for **Co4(OBz-*t*Bu)** see **Table** for experimental details. Traces collected every 310 s. Wavelength monitored: 380 nm. **Co4(OBz-Ac)** $\boldsymbol{\varepsilon_{380}}$ = 8600 M^{-1} cm^{-1}.



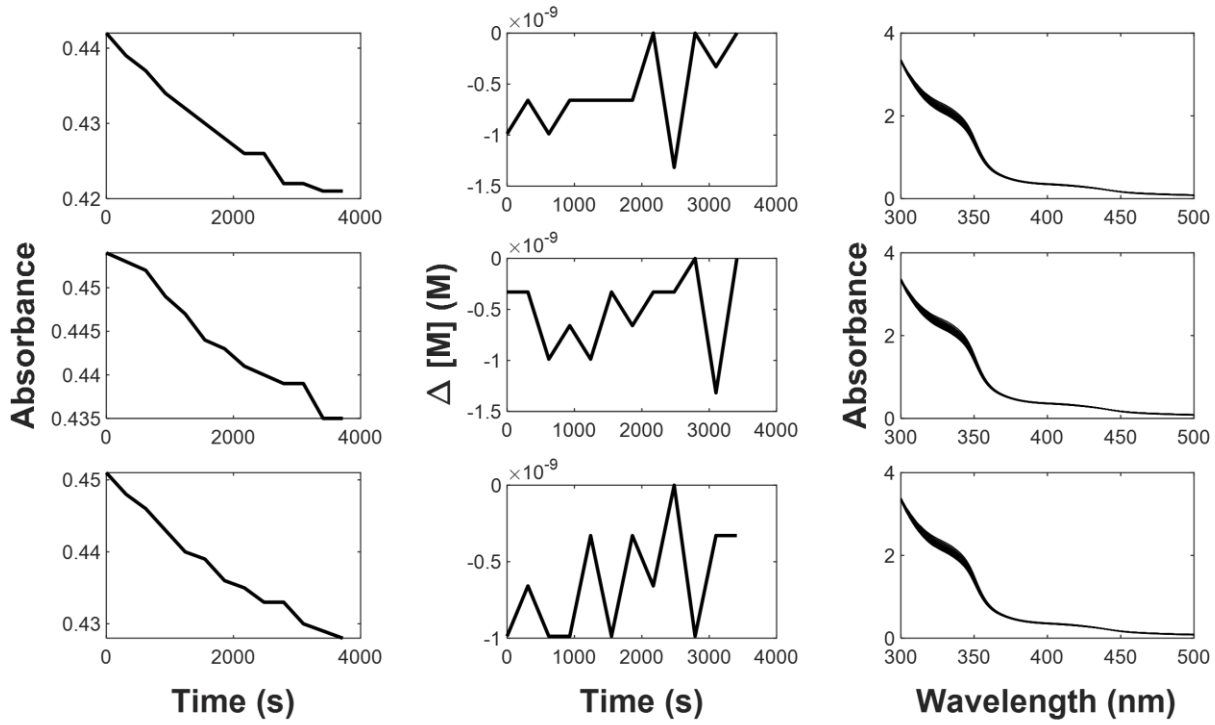
S174. Kinetic traces for the Hammett data for **Co4(OBz-Me)** see **Table** for experimental details. Traces collected every 310 s. Wavelength monitored: 380 nm. **Co4(OBz-Me)** $\boldsymbol{\varepsilon_{380}}$ = 3400 M^{-1} cm^{-1}.



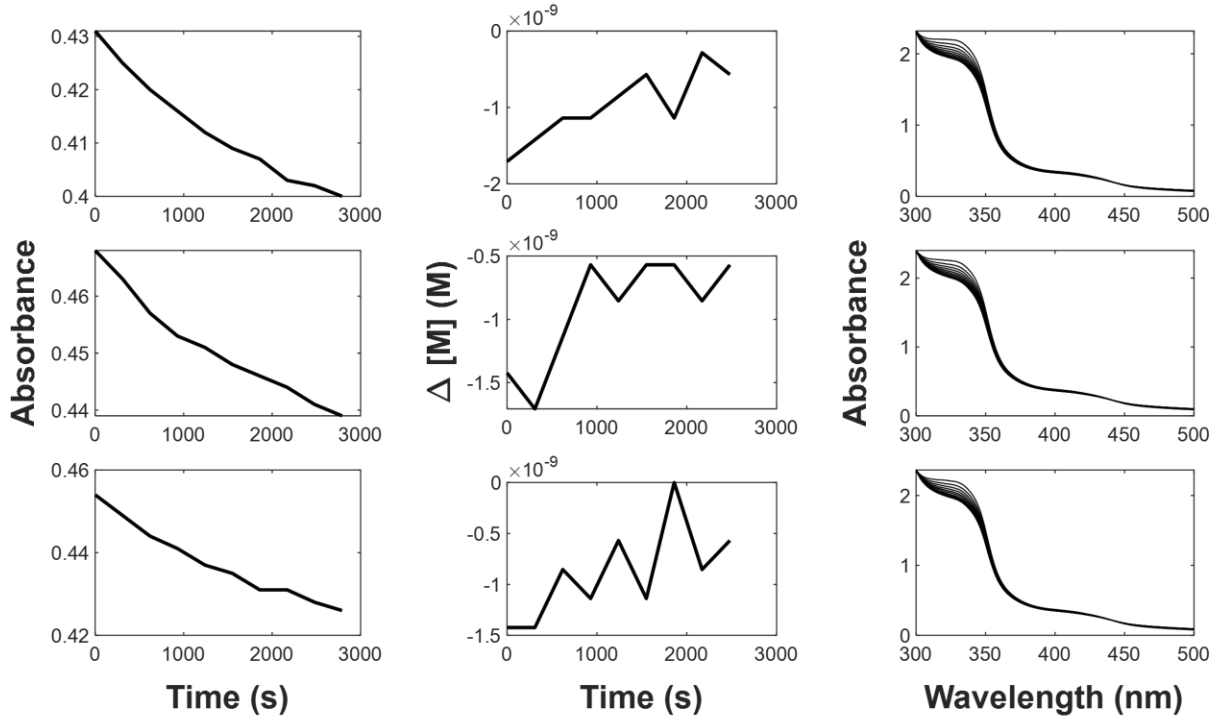
S175. Kinetic traces for the Hammett data for **Co_4(OBz-Ph)** see **Table** for experimental details. Traces collected every 310 s. Wavelength monitored: 380 nm. **Co_4(OBz-Ph) ε_{380}** = 11333.33 M^{-1} cm^{-1}.



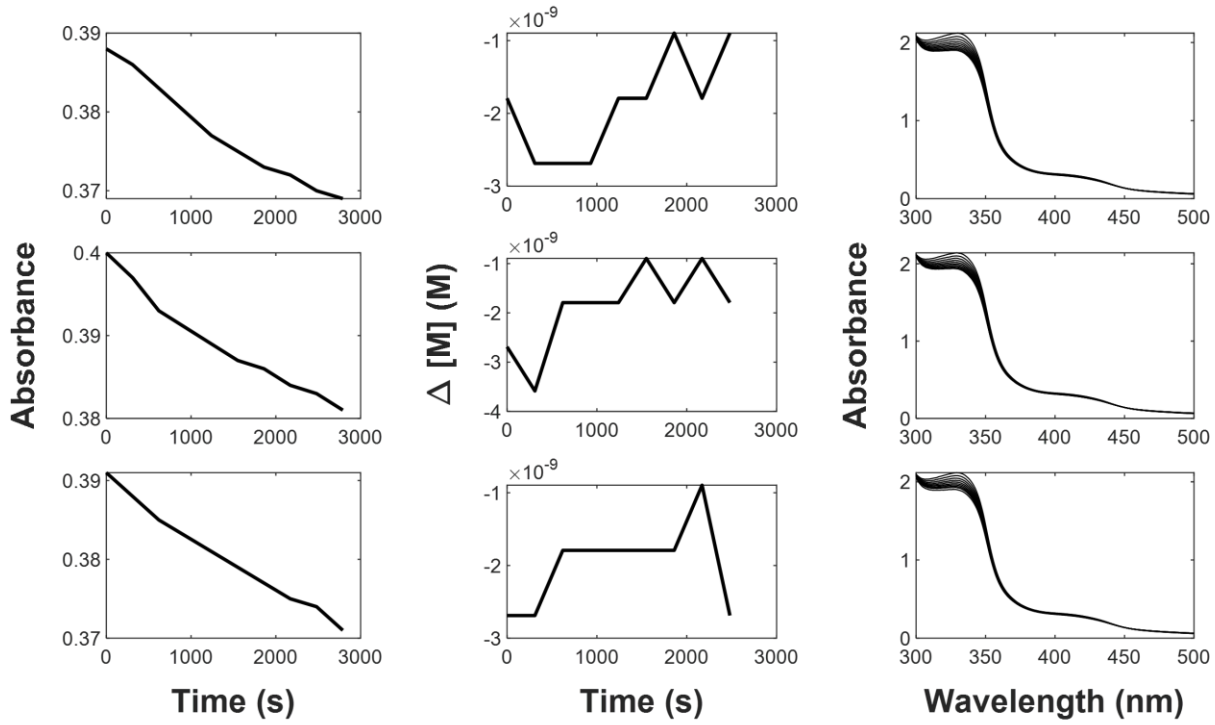
S176. Kinetic traces for the Hammett data for **Co_4(OBz-H)** see **Table** for experimental details. Traces collected every 310 s. Wavelength monitored: 380 nm. **Co_4(OBz-H) ε_{380}** = 8600 M^{-1} cm^{-1}.



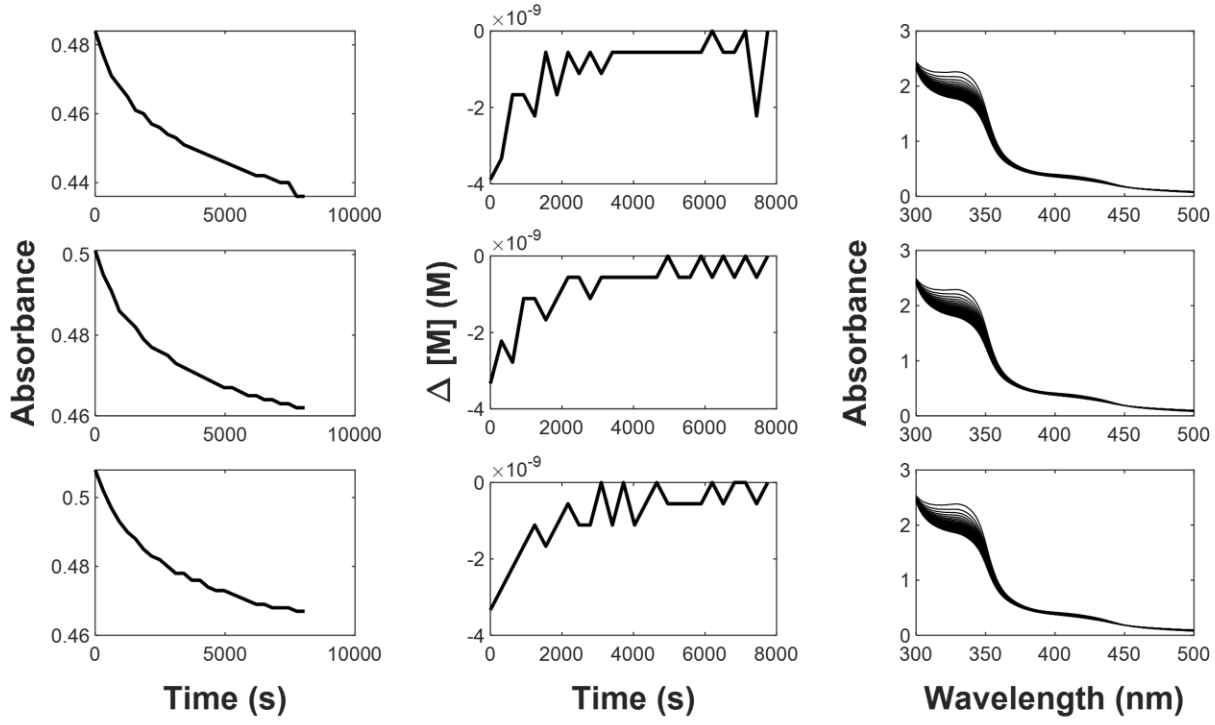
S177. Kinetic traces for the Hammett data for **Co_4(OBz-Cl)** see **Table** for experimental details. Traces collected every 310 s. Wavelength monitored: 380 nm. **Co_4(OBz-Cl) ε_{380}** = 9800 M^{-1} cm^{-1}.



S178. Kinetic traces for the Hammett data for **Co_4(OBz-Br)** see **Table** for experimental details. Traces collected every 310 s. Wavelength monitored: 380 nm. **Co_4(OBz-Br) ε_{380}** = 11333.33 M^{-1} cm^{-1}.

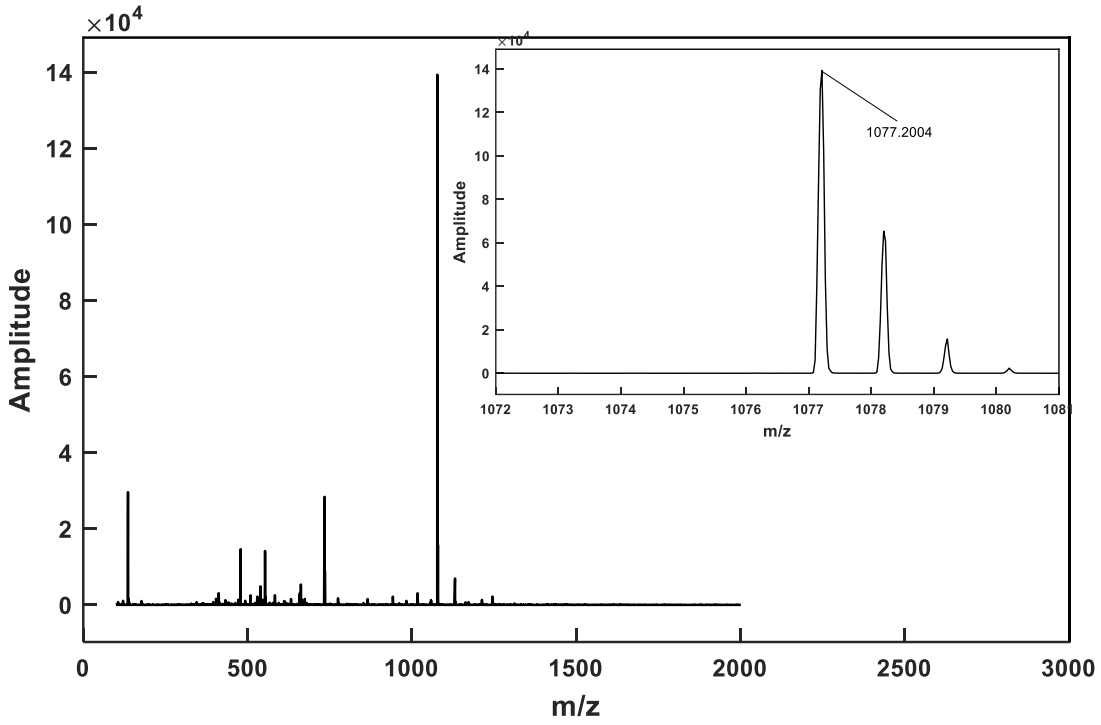


S179. Kinetic traces for the Hammett data for **Co_4(OBz-CN)** see **Table** for experimental details. Traces collected every 310 s. Wavelength monitored: 380 nm. **Co_4(OBz-CN) ε_{380}** = 3600 M^{-1} cm^{-1}.

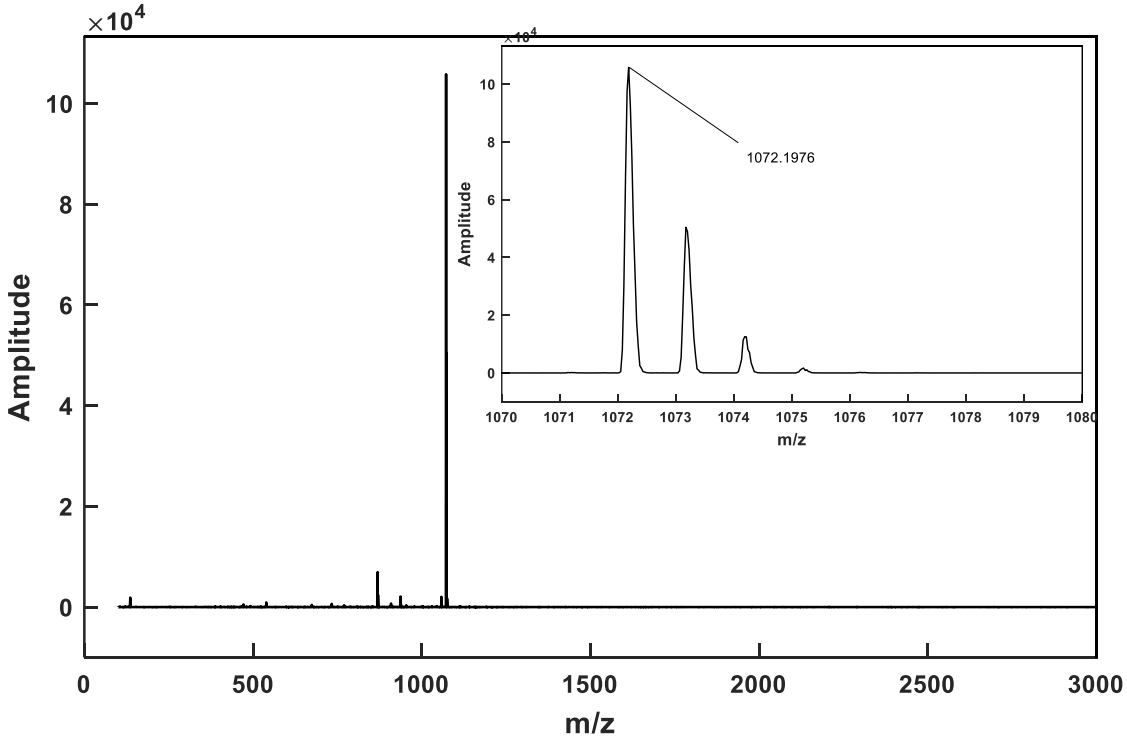


S180. Kinetic traces for the Hammett data for **Co_4(OBz-NO_2)** see **Table** for experimental details. Traces collected every 310 s. Wavelength monitored: 380 nm. **Co_4(OBz-NO_2) ε_{380}** = 5800 M^{-1} cm^{-1}.

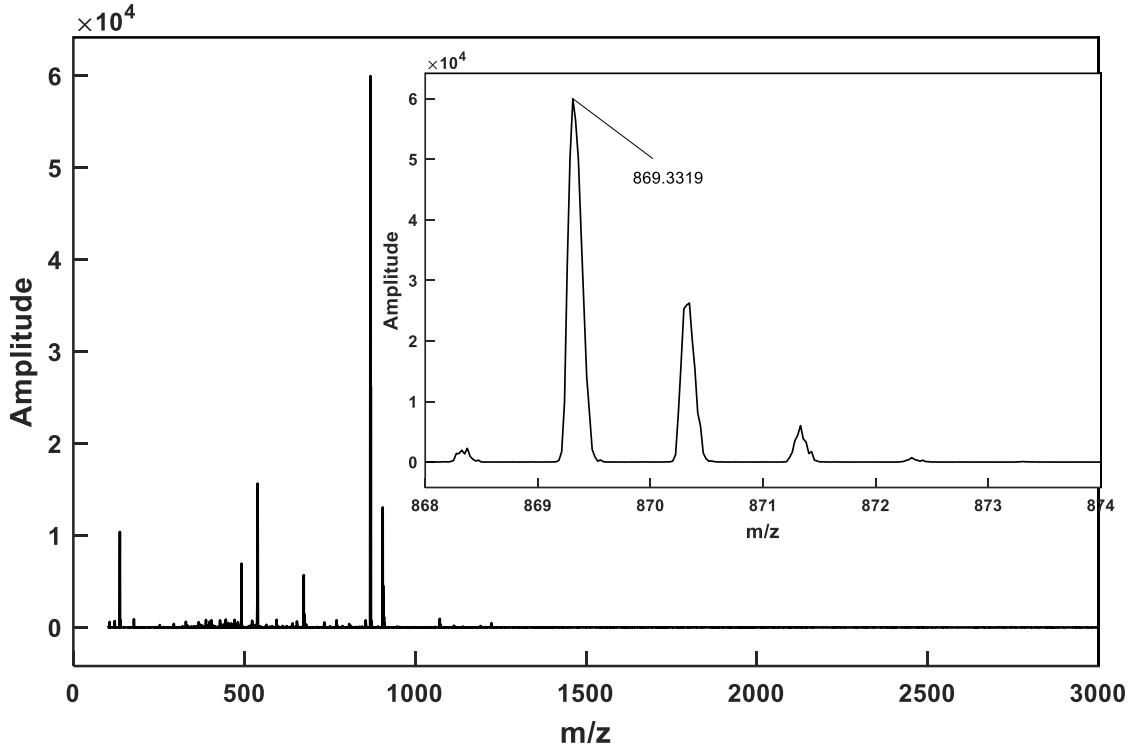
HR-ESI-MS Data and Isotope Experiments:



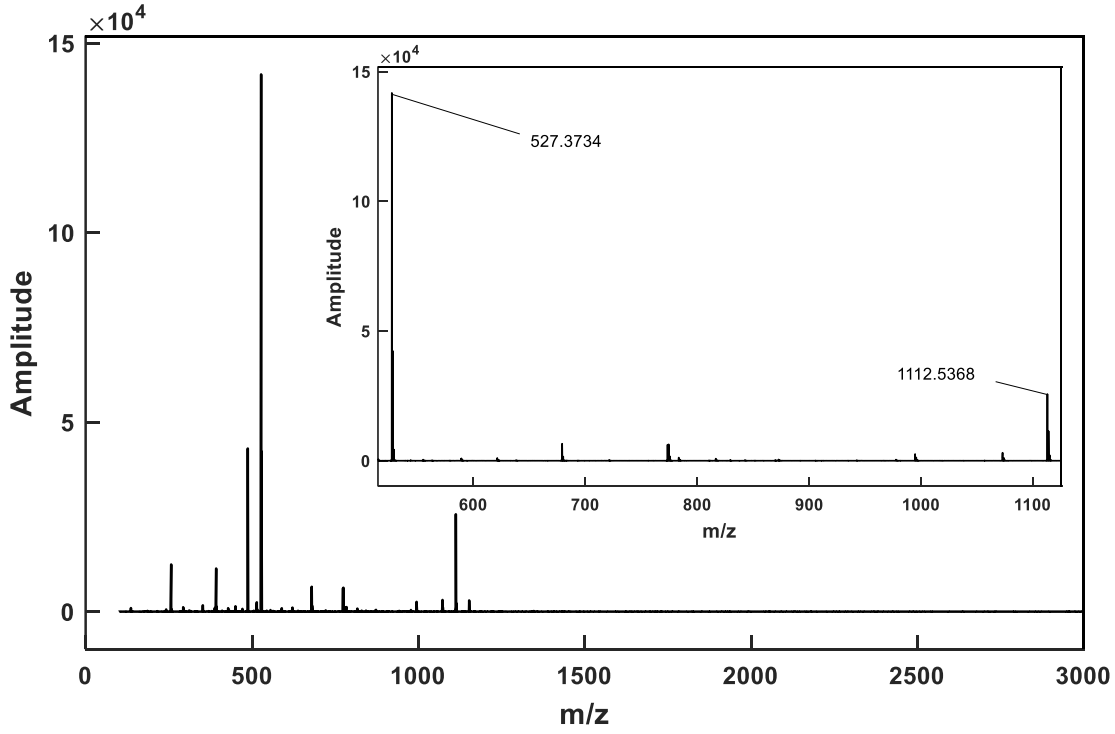
S181. HR-ESI-MS spectrum of **Co4**. Peak shown in inset corresponds to $[Co_4O_4(OAc)_4(t\text{-Bupy})_4H]^+$.



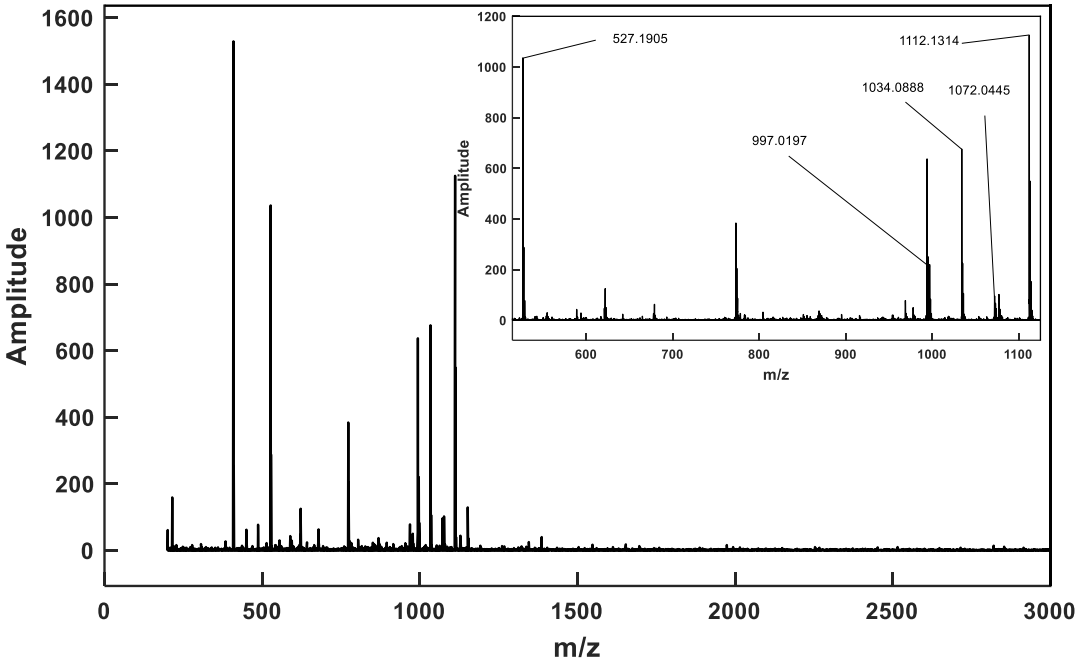
S182. HR-ESI-MS spectrum of **MnCo3**$[PF_6]$. Peak shown in inset corresponds to $[MnCo_3O_4(OAc)_4(t\text{-Bupy})_4]^+$.



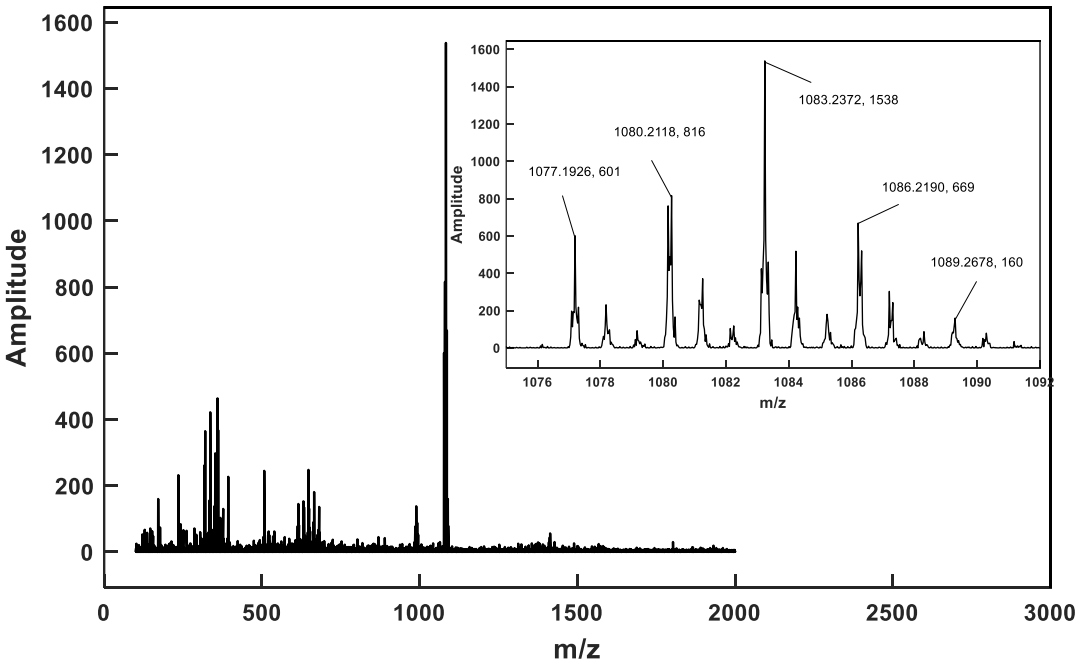
S183. HR-ESI-MS spectrum of cobalt dimer byproduct. Peak shown in inset corresponds to $[Co_2(OH)_2(OAc)_3(t\text{-Bupy})_4]^+$.



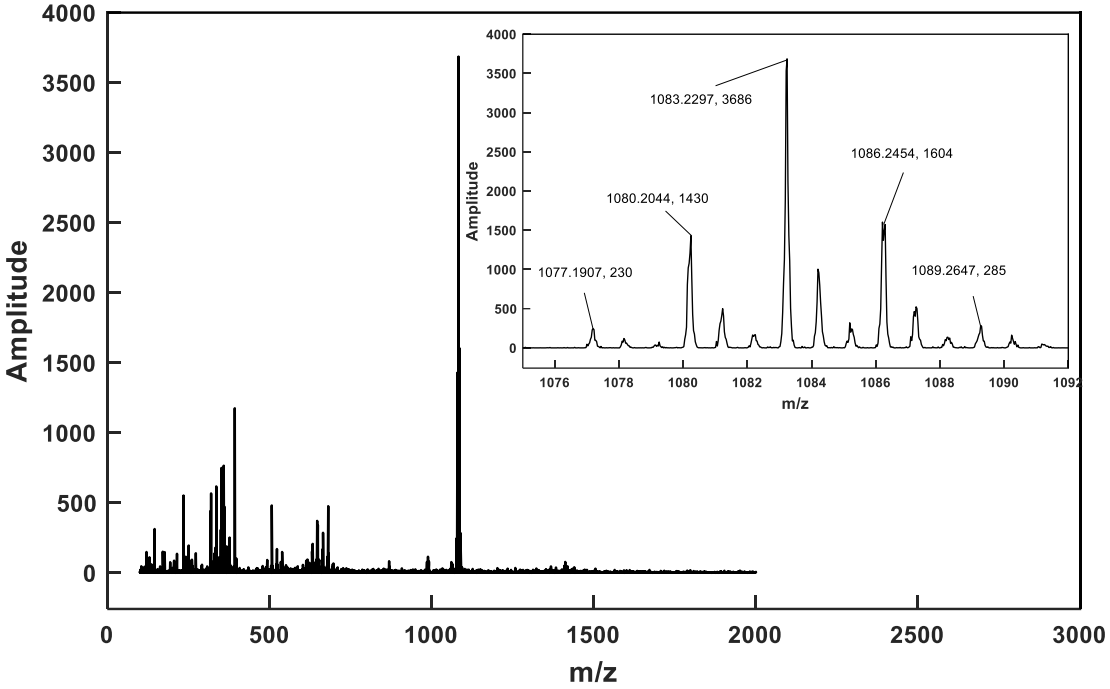
S184. HR-ESI-MS spectrum of **$MnCo_3$**$[PF_6]$ prepared and isolated according to method E prior to recrystallization. The peak at 527.3734 corresponds to $[Co(acac)_2(t\text{-Bupy})_2]^+$ and the peak at 1112.5368 corresponds to $[MnCo_3O_4(OAc)_2(acac)(t\text{-Bupy})_4]^+$. Note that under these ionization conditions the observed peak corresponding to $[Co(acac)_2(t\text{-Bupy})_2]^+$ was always extremely intense.



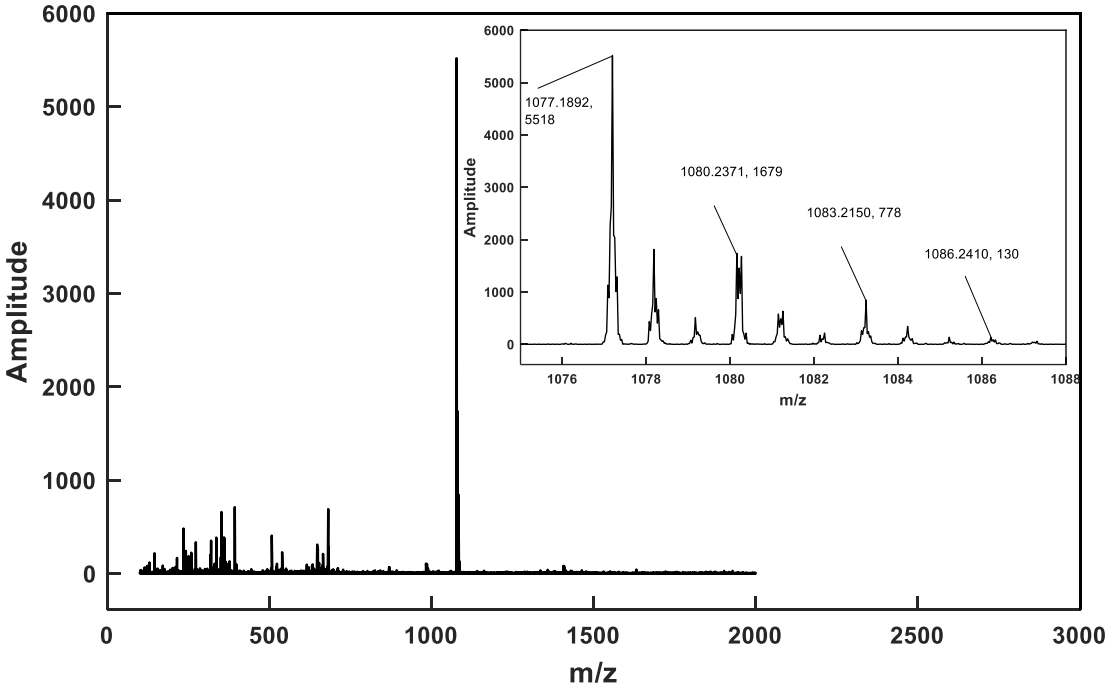
S185. HR-ESI-MS spectrum from a separate experiment to prepare **MnCo$_3$**[PF_6] by method E, prior to recrystallization. The peak at 527.1905 corresponds to $[Co(acac)_2(t\text{-Bupy})_2]^+$, the peak at 997.0197 corresponds to $[MnCo_3O_4(OAc)_5(t\text{-Bupy})_3H]^+$, the peak at 1072.0445 corresponds to $[MnCo_3O_4(OAc)_4(t\text{-Bupy})_4]^+$, and the peak at 1112.1314 corresponds to $[MnCo_3O_4(OAc)_3(acac)(t\text{-Bupy})_4]^+$. In combination with the ^{1}H NMR spectrum of the same material, this spectrum demonstrates that the observed product distributions following isolation according to method E are difficult to determine. HR-ESI-MS analysis of the crystallized material suggests that $[MnCo_3O_4(OAc)_4(t\text{-Bupy})_4]^+$ is the exclusive isolate. See **S** for representative spectrum.



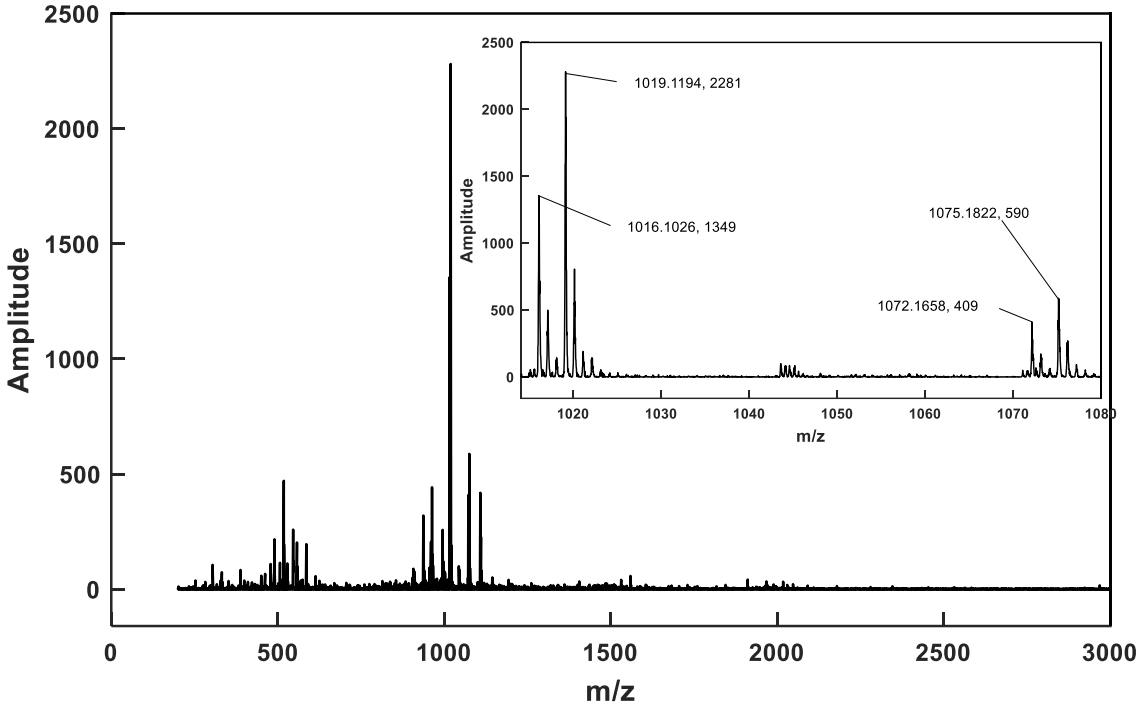
S186. Representative HR-ESI-MS spectrum collected in triplicate of isotopic labeling control experiment between **Co$_4$** and DOAc-d_3. Peaks shown in inset correspond to $[Co_4O_4(OAc)_n(OAc\text{-}d_3)_{4-n}(t\text{-Bupy})_4H]^+$ (n = 4-0), followed by the peak intensity.



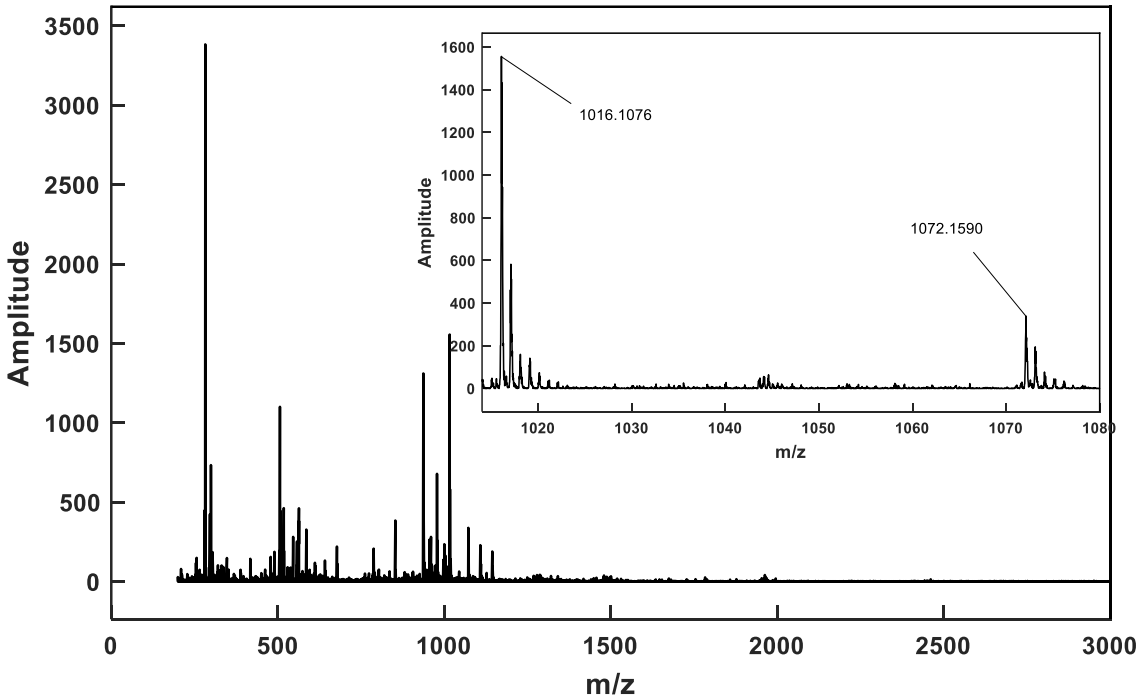
S187. Representative HR-ESI-MS spectrum collected in triplicate of isotopic labeling control experiment between **Co4** and [DNEt$_3$]OAc-d_3. Peaks shown in inset correspond to $[Co_4O_4(OAc)_n(OAc\text{-}d_3)_{4-n}(t\text{-Bupy})_4H]^+$ (n = 4-0), followed by the peak intensity.



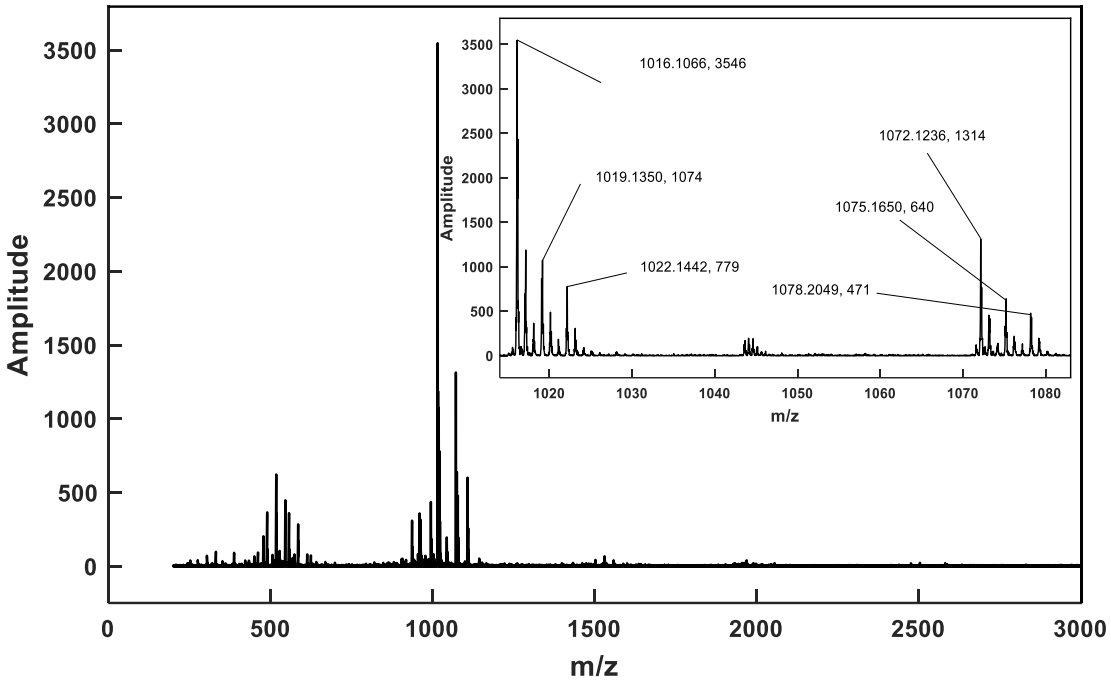
S188. Representative HR-ESI-MS spectrum collected in triplicate of isotopic labeling control experiment between **Co4** and NaOAc-d_3. Peaks shown in inset correspond to $[Co_4O_4(OAc)_n(OAc\text{-}d_3)_{4-n}(t\text{-Bupy})_4H]^+$ (n = 4-1), followed by the peak intensity. The slow rate of OAc ligand exchange is likely due to the limited solubility of NaOAc-d_3 in MeCN.



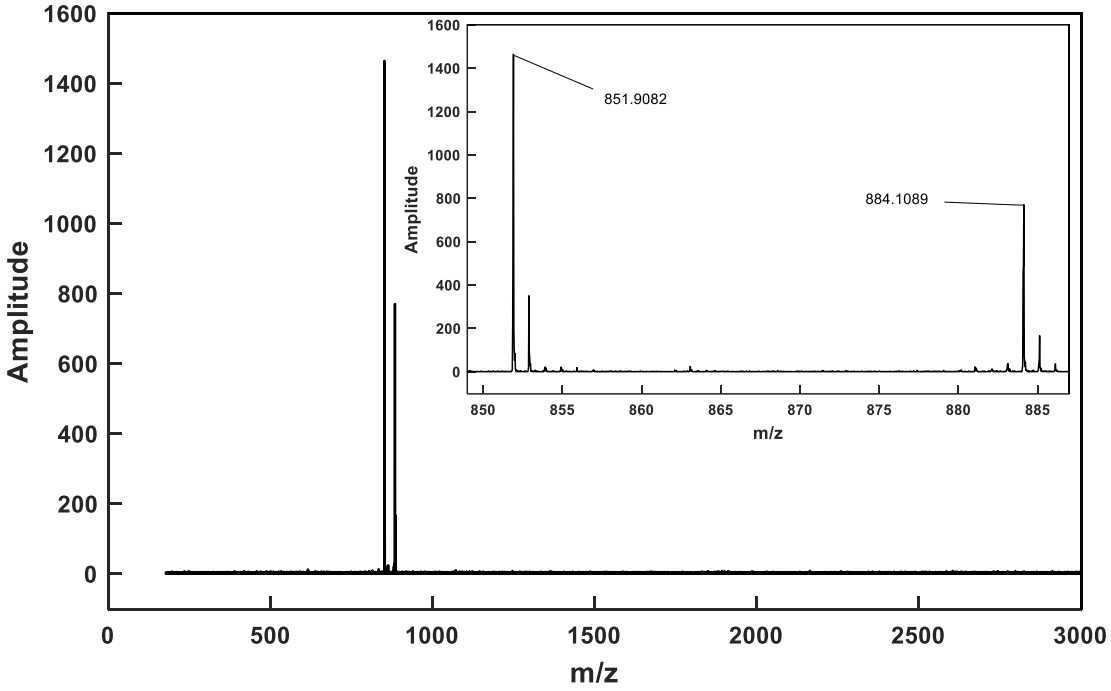
S189. Representative HR-ESI-MS spectrum collected in triplicate of isotopic labeling control experiment between $OAcMnCo_3O_4(OAc)_4$(*t*-Bupy)$_3$ (**$MnCo_3(OAc)$**) and DOAc-d_3. Peaks shown in inset correspond to $[MnCo_3O_4(OAc)_n(OAc\text{-}d_3)_{4-n}(t\text{-Bupy})_4H]^+$ (n = 4,3), followed by the peak intensity.



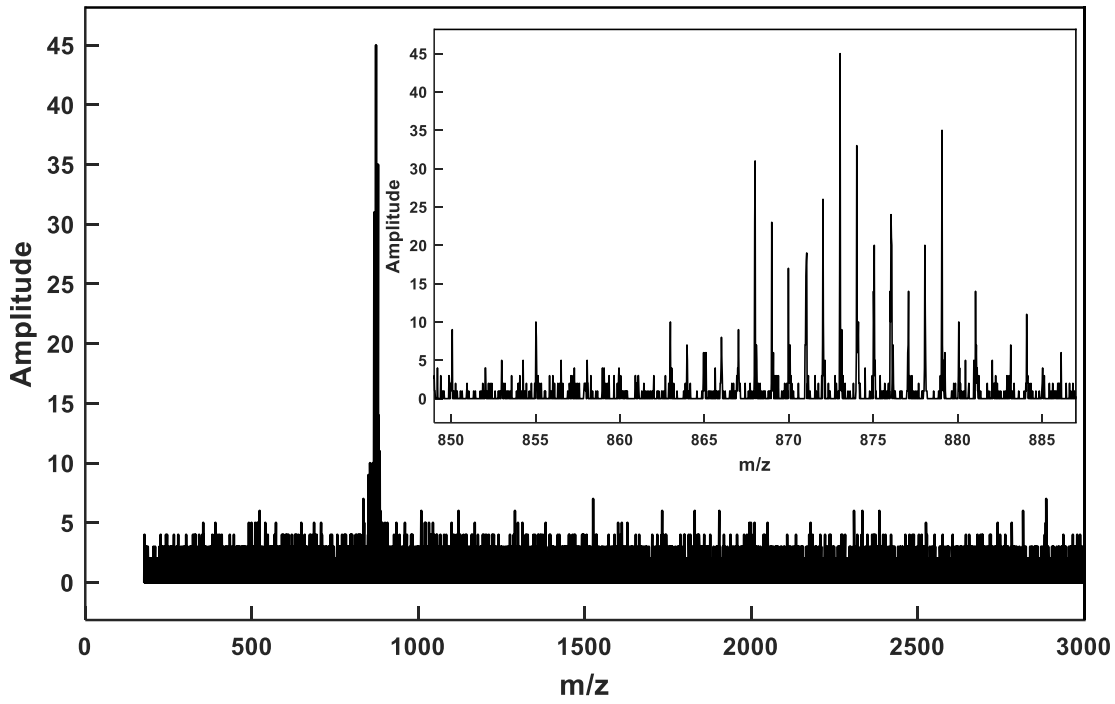
S190. Representative HR-ESI-MS spectrum collected in triplicate of isotope control experiment between $OAcMnCo_3O_4(OAc)_4$(*t*-Bupy)$_3$ (**$MnCo_3(OAc)$**) and NaOAc-d_3. Peaks shown in inset correspond to $[MnCo_3O_4(OAc)_n(OAc\text{-}d_3)_{4-n}(t\text{-Bupy})_4H]^+$ (n = 4).



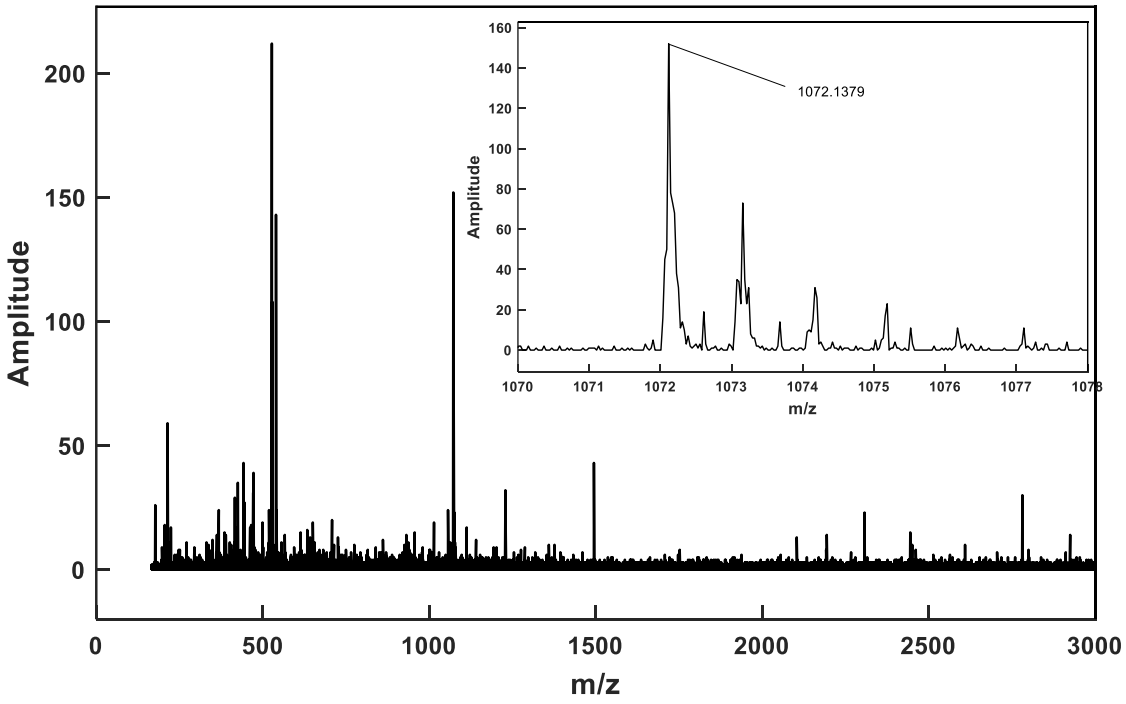
S191. Representative HR-ESI-MS spectrum from data collected in triplicate of isotope control experiment between $OAcMnCo_3O_4(OAc)_4(t\text{-Bupy})_3$ (**$MnCo_3(OAc)$**) and $Mn(OAc\text{-}d_3)_2$. Peaks shown in inset correspond to $[MnCo_3O_4(OAc)_n(OAc\text{-}d_3)_{4-n}(t\text{-Bupy})_4H]^+$ (n = 4-2), followed by the peak intensity.



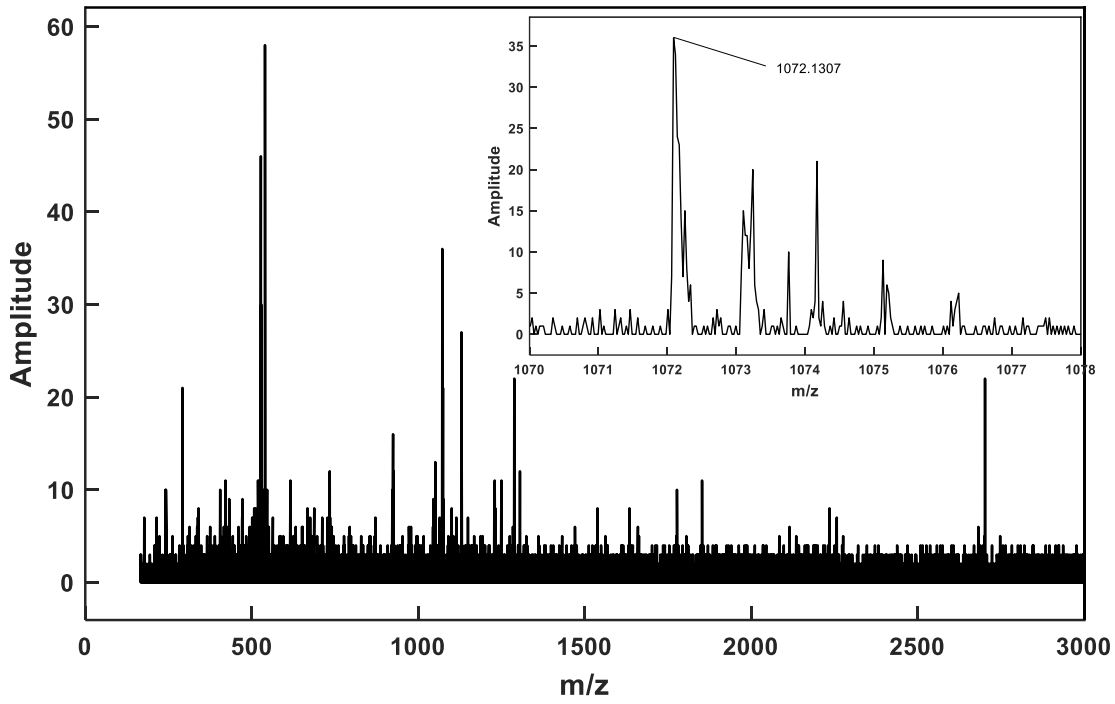
S192. Representative HR-ESI-MS spectrum from data collected in triplicate of isotope crossover control experiment between $Co_4O_4(OAc)_4(py)_4$ and $Co_4O_4(OAc\text{-}d_3)_4(py\text{-}d_5)_4$. Peaks shown in inset correspond to $Co_4O_4(OAc)_n(OAc\text{-}d_3)_{4-n}(py)_m(py\text{-}d_5)_{4-m}$ (n, m = 0 ; n, m = 4). (no crossover).



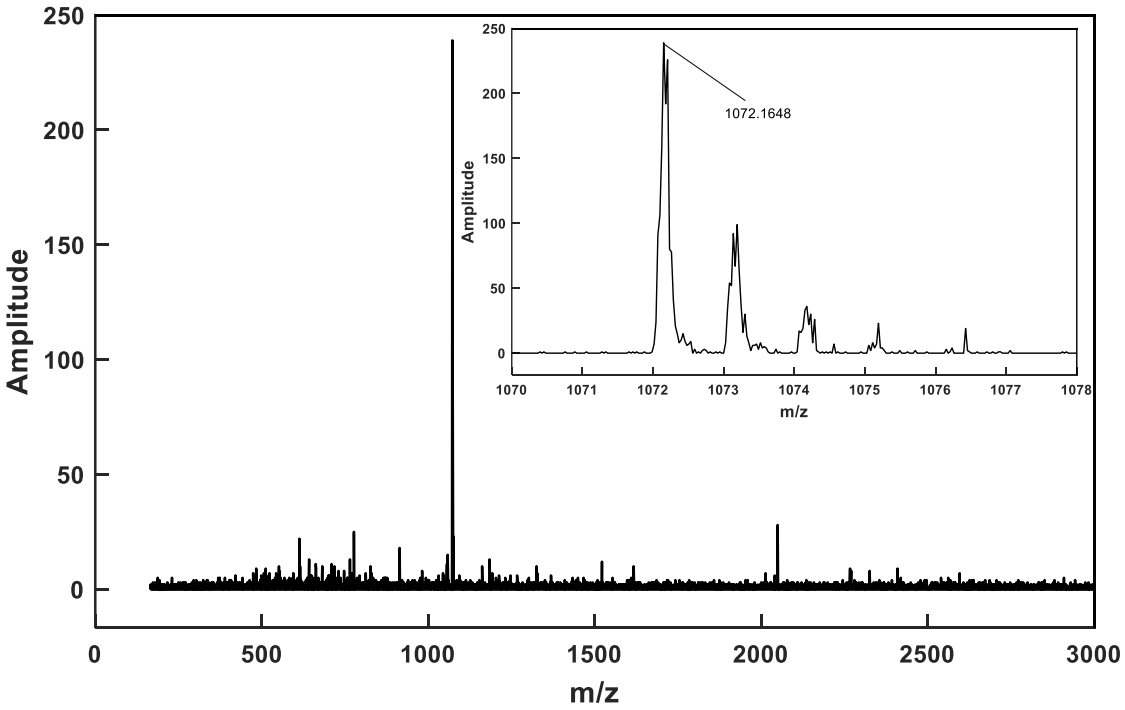
S193. Representative HR-ESI-MS spectrum from data collected in triplicate of isotope crossover control experiment between $Co_4O_4(OAc)_4(py)_4$ and $Co_4O_4(OAc\text{-}d_3)_4(py\text{-}d_5)_4$ after being heated to 40 °C for 24 h. Peaks shown in inset correspond to $Co_4O_4(OAc)_n(OAc\text{-}d_3)_{4-n}(py)_m(py\text{-}d_5)_{4-m}$ (n,m = 1-4). (complete scrambling).



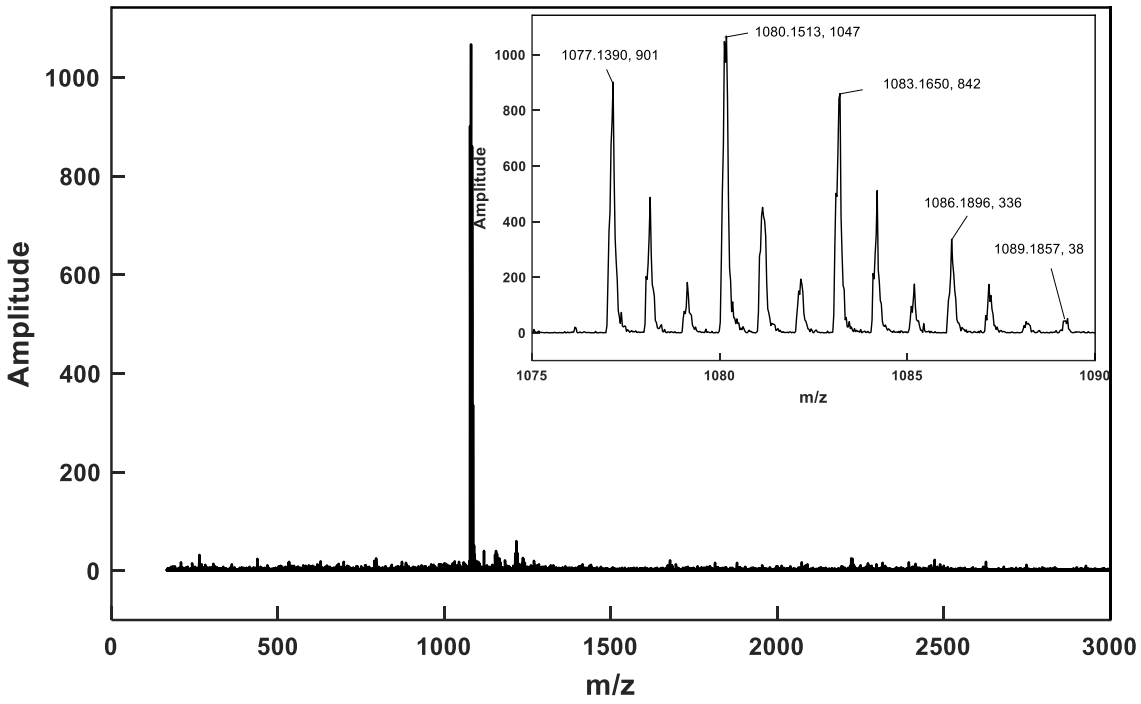
S194. HR-ESI-MS spectrum of the **crude** NMR scale reaction solution (**S95**, **S96**, 2.5 equiv) of $Mn(OTf)_2$ and $\mathbf{Co_4}^+[PF_6]$ following heating. Peak shown in inset corresponds to $\mathbf{MnCo_3}[PF_6]$, $MnCo_3O_4(OAc)_4(t\text{-Bupy})_4^+$.



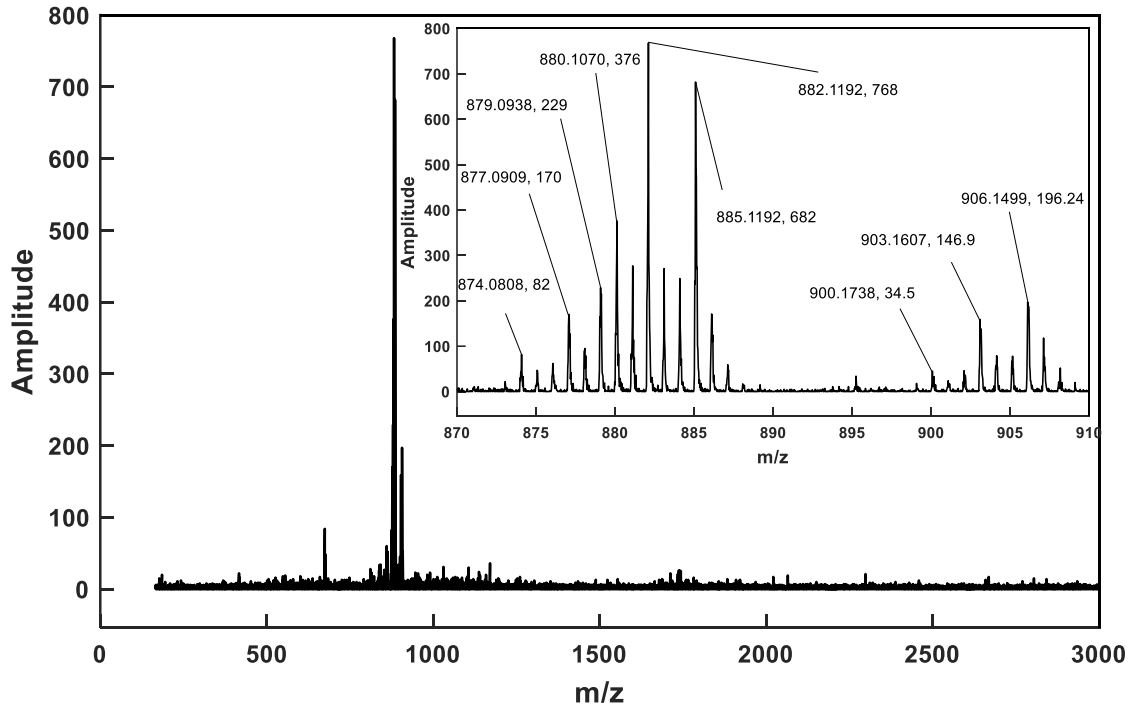
S195. HR-ESI-MS spectrum of the crude NMR scale reaction solution (**Figure 96**, 2 equiv) of $Mn(OTf)_2$ and $\mathbf{Co_4}^+[PF_6]$ following heating. Peak shown in inset corresponds to $\mathbf{MnCo_3}^+$, $MnCo_3O_4(OAc)_4(t\text{-Bupy})_4^+$.



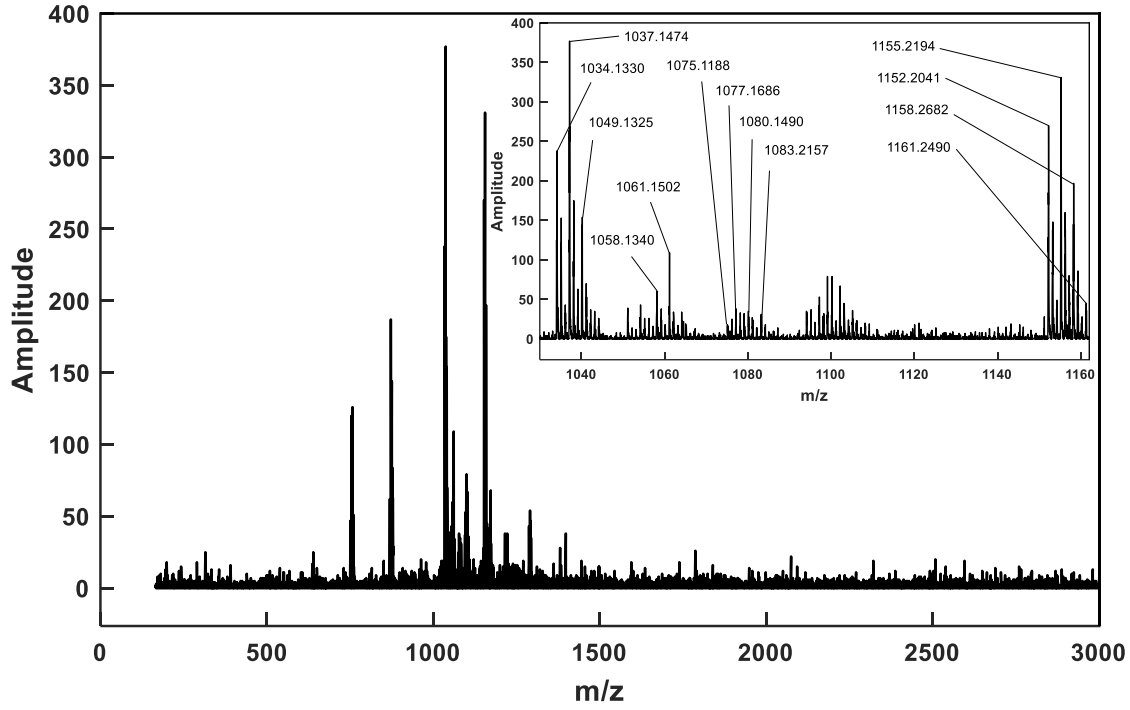
S196. Representative HR-ESI-MS spectrum of $\mathbf{MnCo_3}[PF_6]$ crystallized on small scale to determine isolated yields that provides support for the relative purity of $\mathbf{MnCo_3}[PF_6]$ isolated on <20 mg scale. Common impurities such as $\mathbf{Co_4}H^+$ and $[Co(OH)_2(OAc)_3(t\text{-Bupy})_4]^+$ were typically much more intense under the experimental ionization conditions.



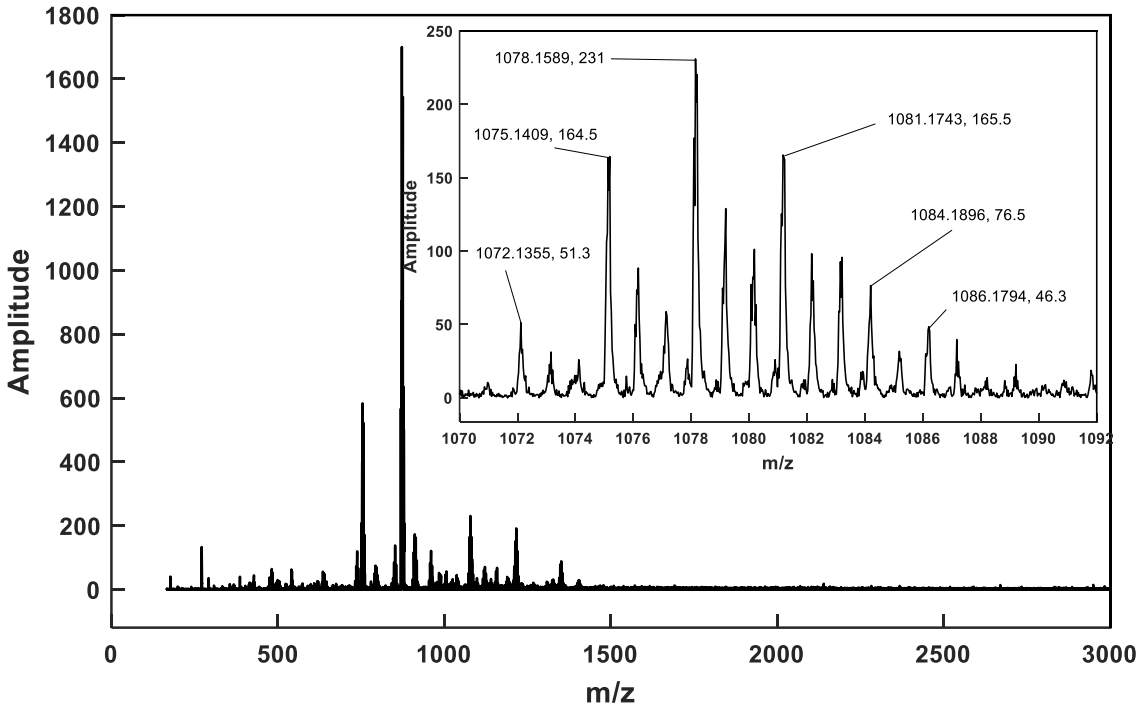
S197. Representative HR-ESI-MS spectrum from data collected in triplicate of isotope experiment between $Mn(OAc\text{-}d_3)_2$ and **Co_4O_4** after 48 h at 23 °C. Peaks shown in inset correspond to $[Co_4O_4(OAc)_n(OAc\text{-}d_3)_{4-n}(t\text{-}Bupy)_4H]^+$ (n = 0-4).



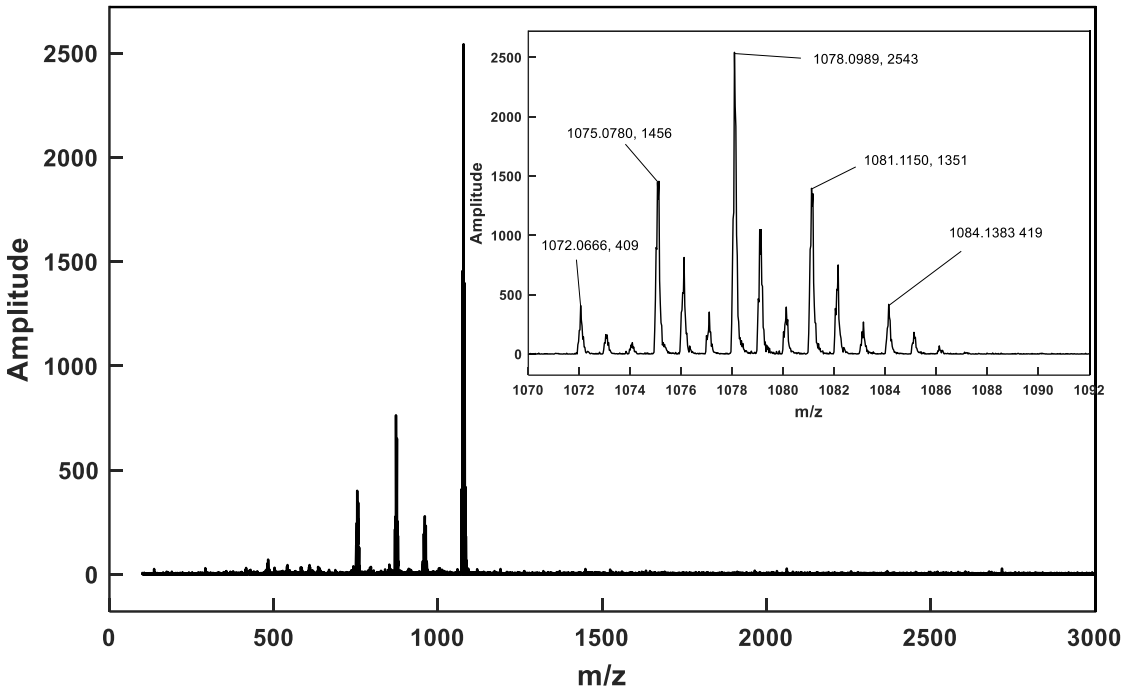
S198. Representative HR-ESI-MS spectrum from data collected in triplicate of isotope experiment between $Mn(OAc)_2$ and $Co_4O_4(OAc\text{-}d_3)_4(py\text{-}d_5)_4$. Peaks shown in inset correspond to $[Co_4O_4(OAc)_n(OAc\text{-}d_3)_{4-n}(py\text{-}d_5)_4Na]^+$ (n = 0,1,2) and $[MnCo_3O_4(OAc)_n(OAc\text{-}d_3)_{4-n}(py\text{-}d_5)_4]^+$ (n = 0, 1, 2, 3)



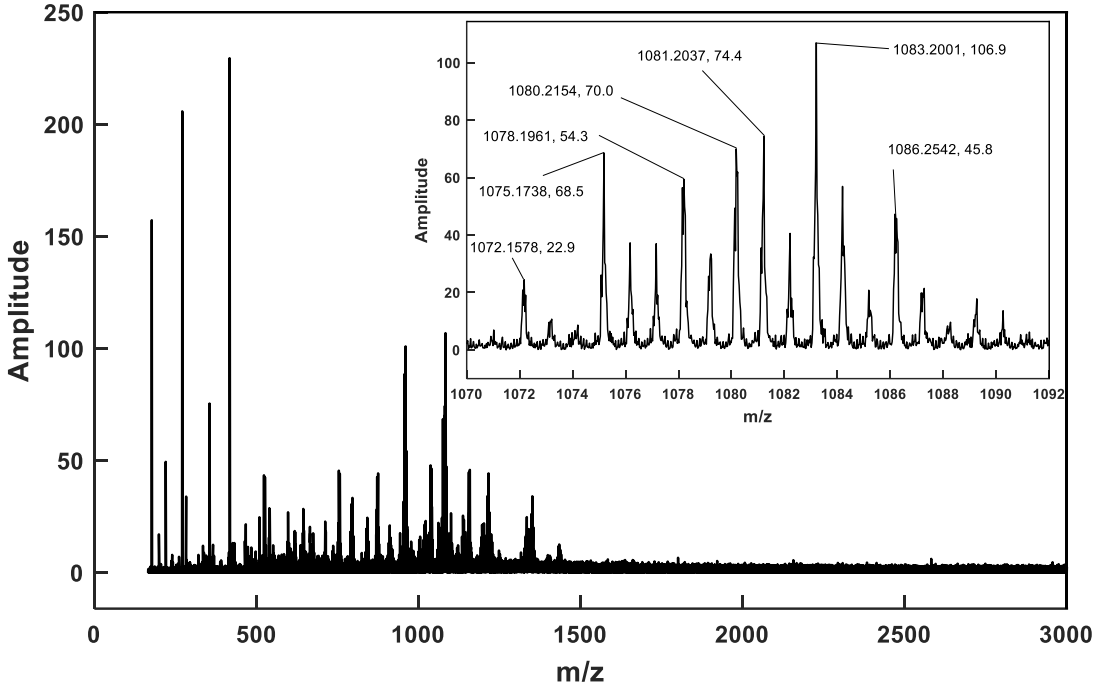
S199. Representative HR-ESI-MS spectrum from data collected in duplicate of isotope experiment between Mn(OAc-d_3)$_2$ and **Co$_4$** after 1 h of heating at 70 °C. This demonstrates that the extent of isotopic enrichment can be tracked by HR-ESI-MS.



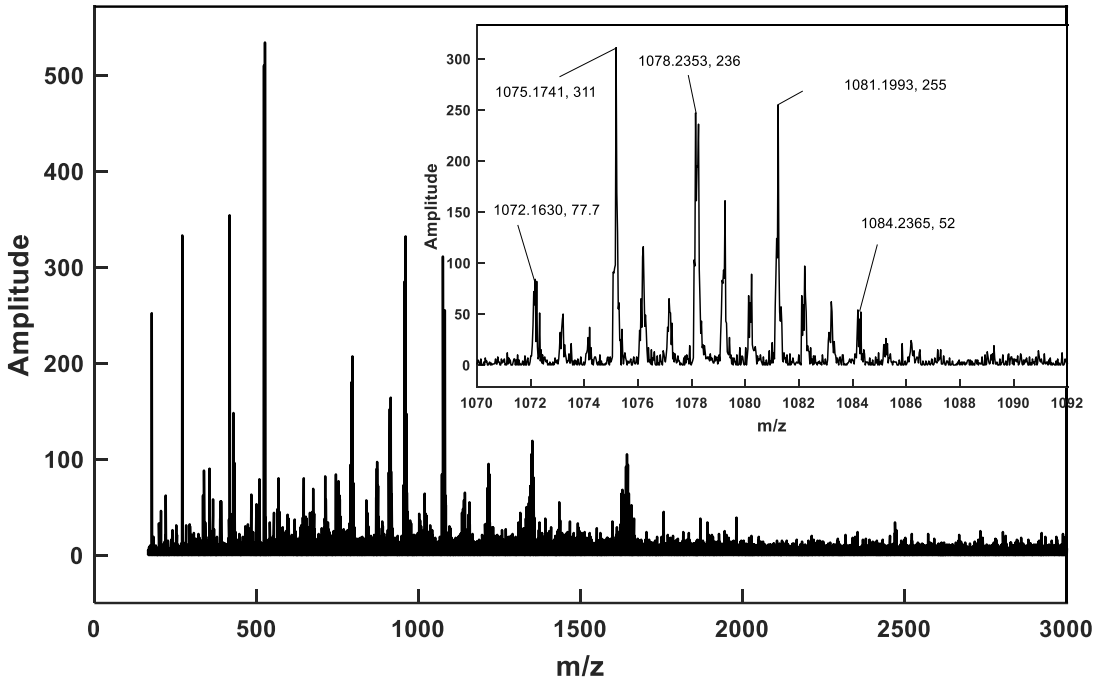
S200. Representative HR-ESI-MS spectrum from data collected in duplicate of isotope experiment between Mn(OAc-d_3)$_2$ and **Co$_4$** after 2 h of heating at 70 °C. Peaks in inset correspond to $MnCo_3O_4(OAc)_4(OAc\text{-}d_3)_{4\text{-}n}(t\text{-Bupy})_4$ (n = 0-4)and $Co_4O_4(OAc)_4(OAc\text{-}d_3)_{4\text{-}n}(t\text{-Bupy})_4$ (n = 0-3), followed by peak intensity.



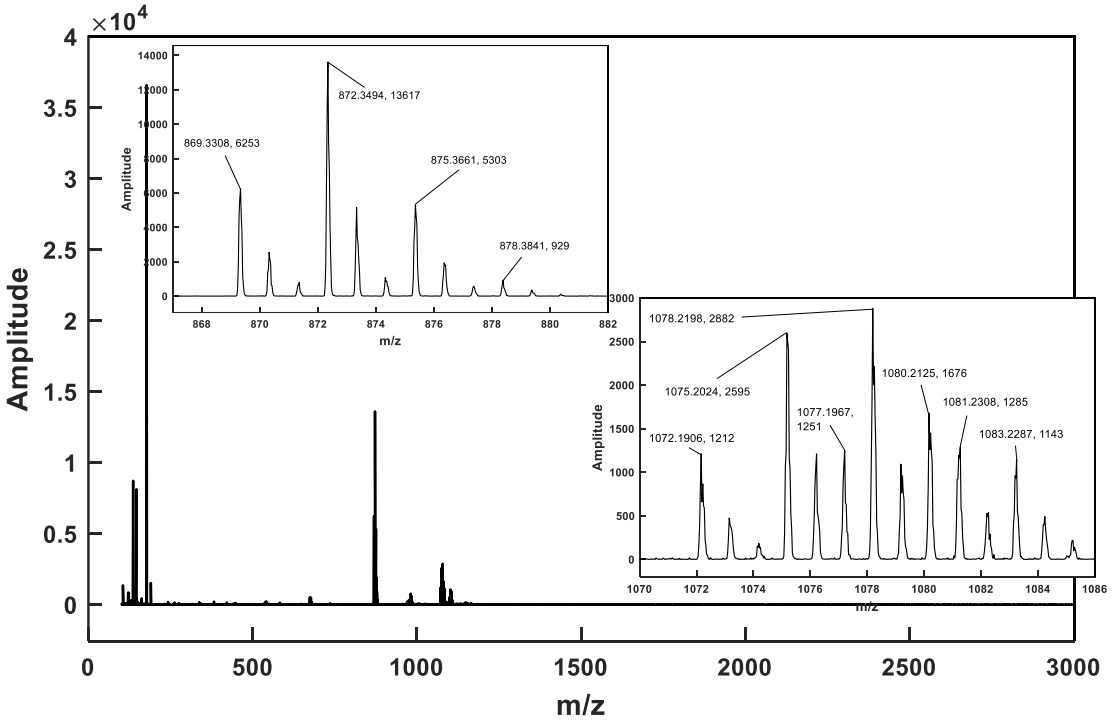
S201. Representative HR-ESI-MS spectrum from data collected in duplicate from the isotope experiment between Mn(OAc-d_3)$_2$ and **Co$_4$** after 16 h of heating at 70 °C. Peaks in inset correspond to $MnCo_3O_4(OAc)_4(OAc\text{-}d_3)_{4\text{-}n}(t\text{-Bupy})_4$ (n = 0-4) followed by peak intensity.



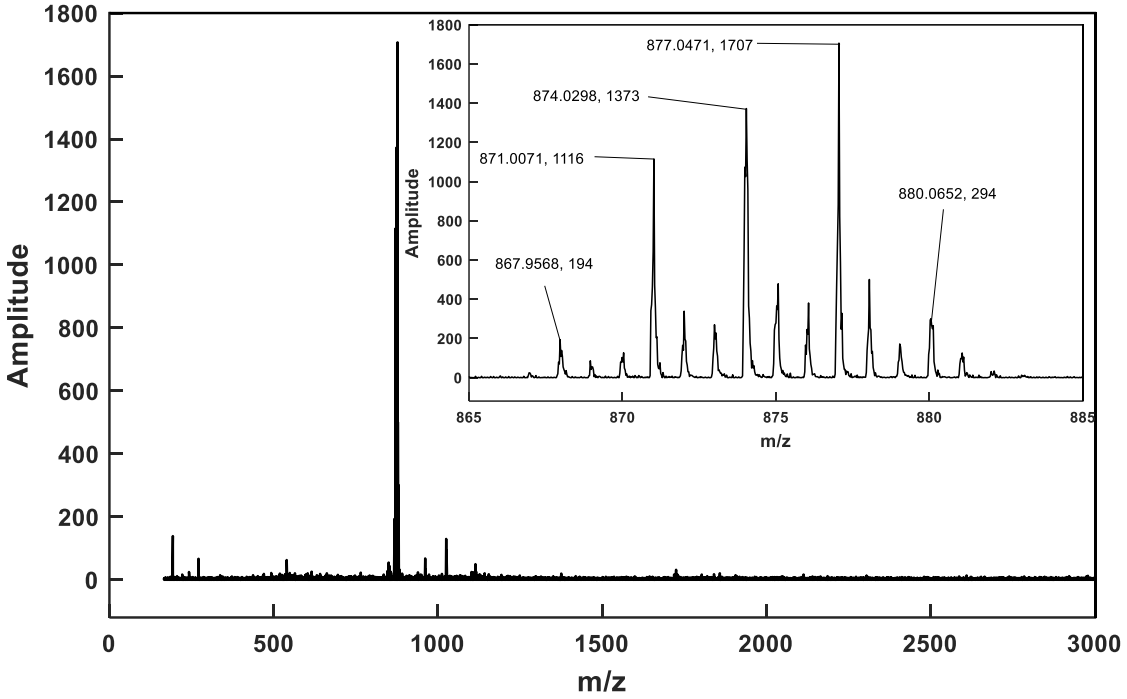
S202. Representative HR-ESI-MS from data collected in duplicate from the isotope experiment between Mn(OAc-d_3)$_2$ and **Co$_4$** with added NH_4PF_6 after 2 h of heating at 70 °C. Peaks in inset correspond to $MnCo_3O_4(OAc)_4(OAc\text{-}d_3)_{4\text{-}n}(t\text{-Bupy})_4$ (n = 0-4) and $Co_4O_4(OAc)_4(OAc\text{-}d_3)_{4\text{-}n}(t\text{-Bupy})_4$ (n = 0-4), followed by peak intensity.



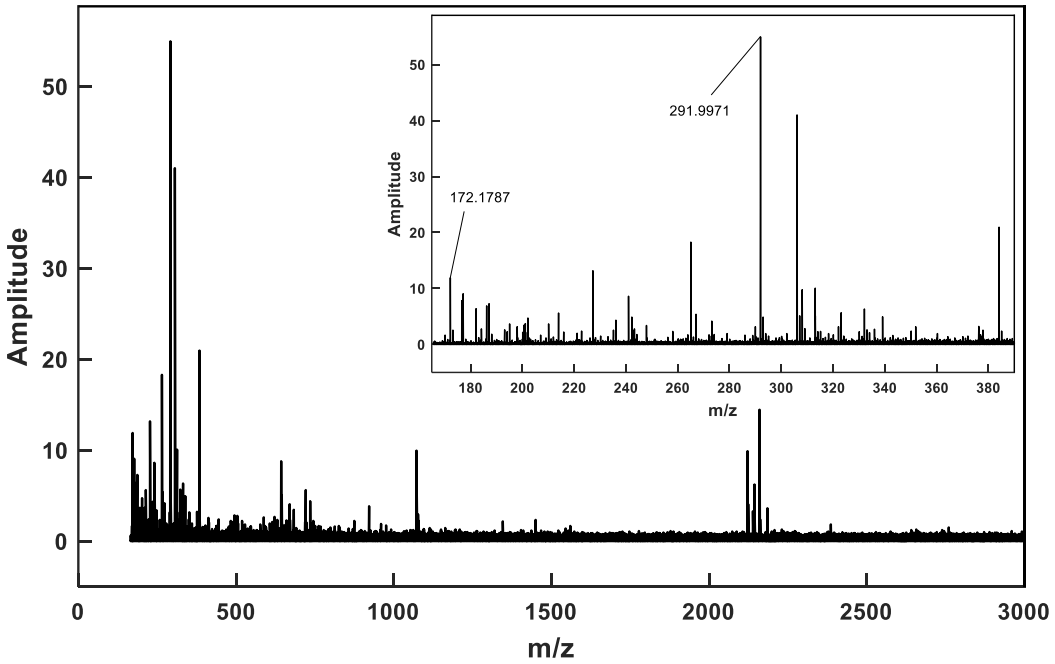
S203. Representative HR-ESI-MS spectrum from data collected in duplicate from the isotope experiment between Mn(OAc-d_3)$_2$ and **Co$_4$** (with added NH_4PF_6) after 16 h of heating at 70 °C. Peaks in inset correspond to $MnCo_3O_4(OAc)_4(OAc\text{-}d_3)_{4\text{-}n}(t\text{-Bupy})_4$ (n = 0-4), followed by peak intensity.



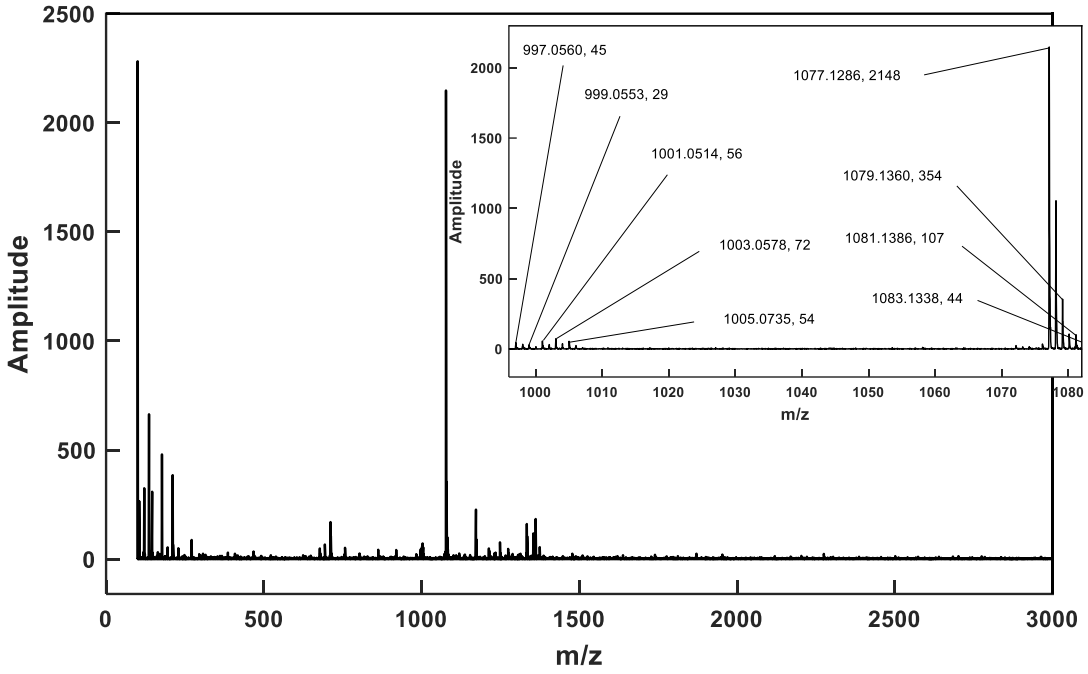
S204. Representative HR-ESI-MS spectrum from data collected in duplicate from the isotope experiment between Mn(OAc-d_3)$_2$ and **Co$_4$**$^+$[PF_6] after 2 h of heating at 40 °C. Peaks in inset correspond to $MnCo_3O_4(OAc)_4(OAc\text{-}d_3)_{4\text{-}n}(t\text{-Bupy})_4$ (n = 0-4), and $Co_4O_4(OAc)_4(OAc\text{-}d_3)_{4\text{-}n}(t\text{-Bupy})_4$ (n = 0-4) followed by peak intensity.



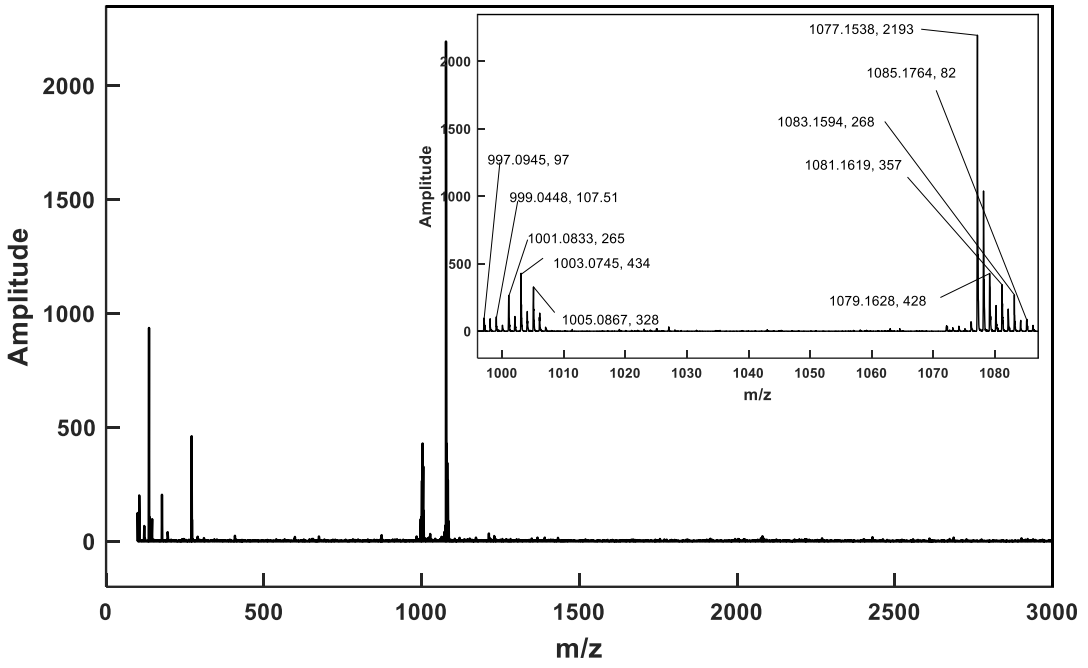
S205. Representative HR-ESI-MS spectrum from data collected in triplicate from the isotope experiment between $Mn(OAc)_2$ and $Co_4O_4(OAc\text{-}d_3)_4(py\text{-}d_5)_4$ after heating at 70 °C for 16 h. Peaks shown in inset correspond to $MnCo_3O_4(OAc)_n(OAc\text{-}d_3)_{4-n}(py)_m(py\text{-}d_5)_4$ (n = 1-4), followed by peak intensity.



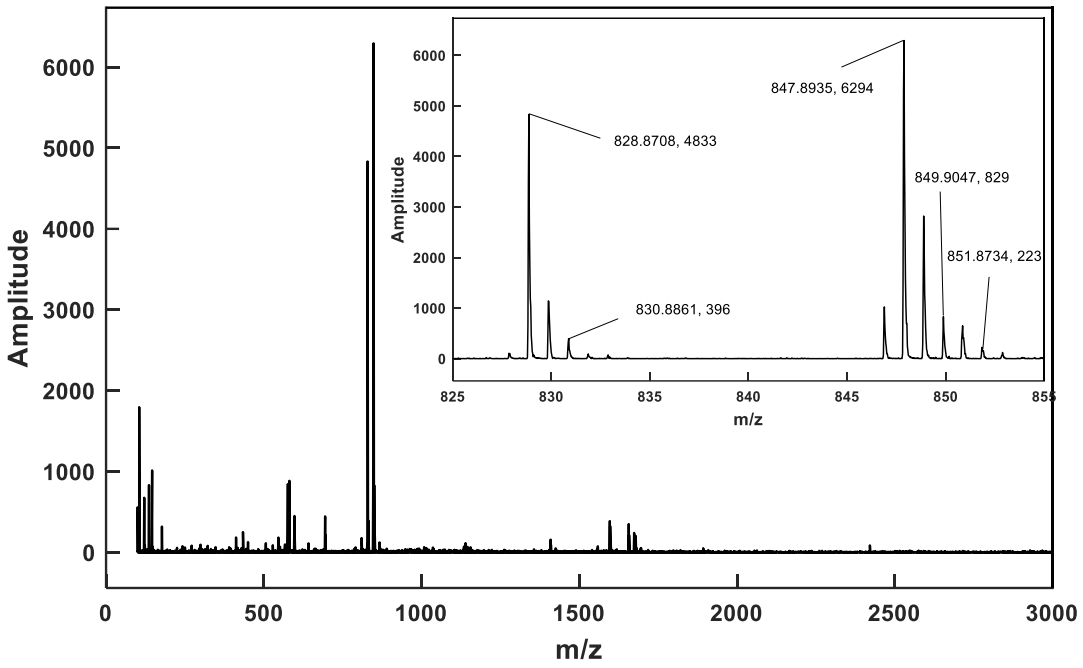
S206. HR-ESI-MS spectrum of the pink $Co(OAc)_2L_2$ byproduct collected as described in the Method A for the synthesis of **MnCo3**[PF_6]. Spectrum collected on material dissolved in MeOH/MeCN Peaks shown in inset correspond to $Co(OAc)_2$ products: $Co(MeCN)_2(MeO)$ $Co(OAc)_2(MeCN)_2(MeOH)$.



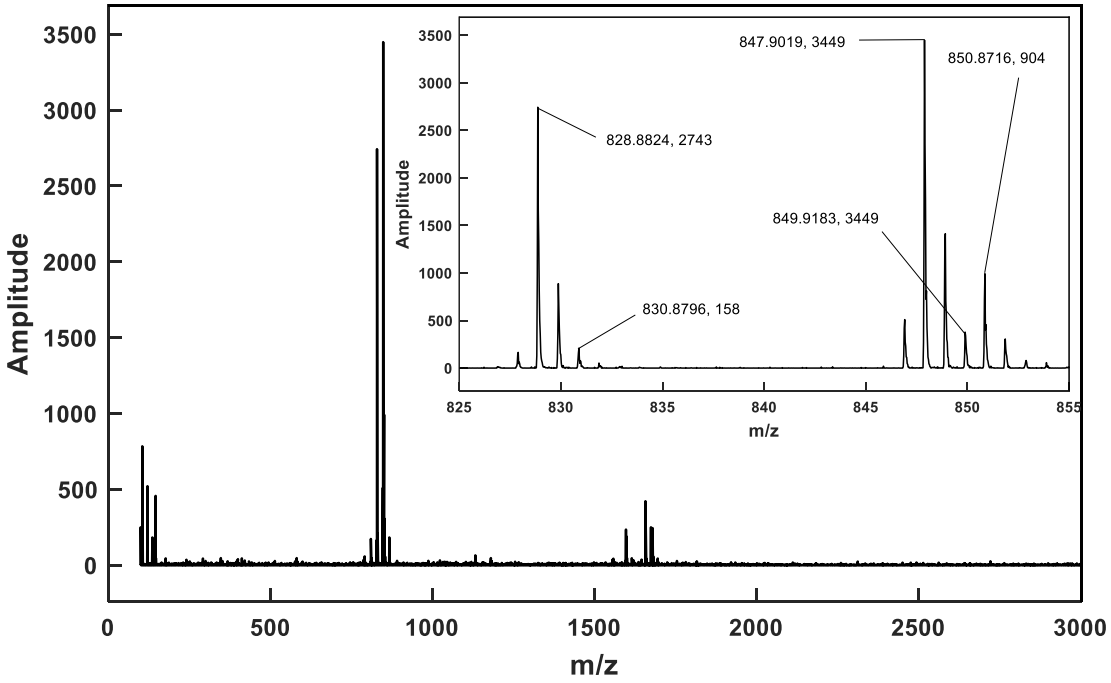
S207. HR-ESI-MS spectrum of an aliquot from the reaction between **Co4** and $Mn(OAc)_2$ in the presence of 2 equiv of $H_2{}^{18}O$ after 1 h at 70 °C. Peaks shown in inset correspond to $[MnCo_3(^{18}O)_4(OAc)_5(t\text{-Bupy})_3H]^+$ and $Co_4(^{18}O)_4(OAc)_4(t\text{-Bupy})_4$ (n = 0-4), followed by peak intensity.



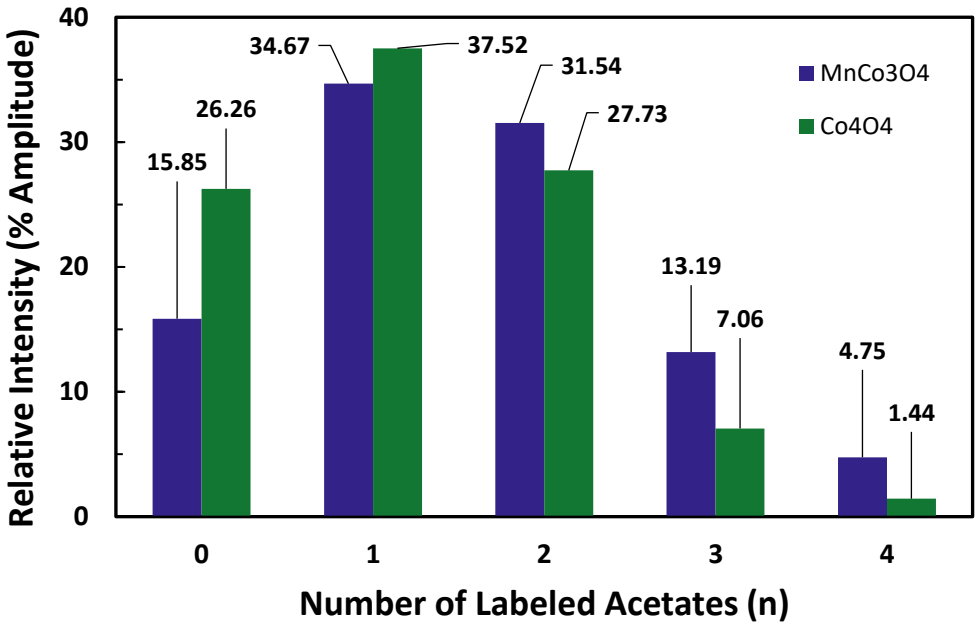
S208. HR-ESI-MS spectrum of an aliquot from the reaction between **Co4** and $Mn(OAc)_2$ in the presence of 2 equiv of $H_2{}^{18}O$ after 2.5 h at 70 °C. Peaks shown in inset correspond to $[MnCo_3(^{18}O)_4(OAc)_5(t\text{-Bupy})_3H]^+$ and $Co_4(^{18}O)_4(OAc)_4(t\text{-Bupy})_4$ (n = 0-4), followed by peak intensity. The significant enrichment of **MnCo3** with ^{18}O oxo ligands suggests that the oxo ligands are more labile during M-M exchange.



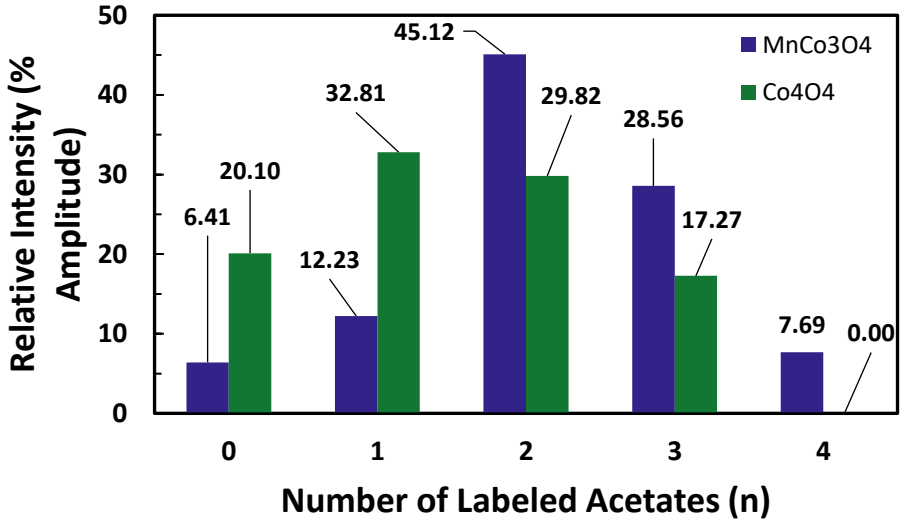
S209. HR-ESI-MS spectrum of an aliquot from the reaction between 4 equiv of $H_2{}^{18}O$ and $MnCo_3O_4(OAc)_5(py)_3$ after 24 h at 70 °C. Peaks shown in inset correspond to $[MnCo_3O_n(^{18}O)_{4-n}(OAc)_5(py)_3H]^+$ (n = 0-1) and $[MnCo_3O_n(^{18}O)_{4-n}(OAc)_4(py)_4]^+$, followed by peak intensity. As predicted for a $Mn^{IV}(Co^{III})_3$ cubane, the oxo ligands exchange very slowly with $H_2{}^{18}O$.



S210. HR-ESI-MS spectrum of an aliquot from the reaction between 4 equiv of $H_2{}^{18}O$ and $MnCo_3O_4(OAc)_5(py)_3$ in the presence of 2 equiv of $Mn(OTf)_2$ after 24 h at 70 °C. Peaks shown in inset correspond to $[MnCo_3O_n(^{18}O)_{4-n}(OAc)_5(py)_3H]^+$, $[MnCo_3O_n(^{18}O)_{4-n}(OAc)_4(py)_4]^+$, and $[MnCo_3O_n(^{18}O)_{4-n}(OAc)_5(py)_3Na]^+$ (n = 0-1), followed by peak intensity. Even in the presence of $Mn(OTf)_2$, the oxo ligands do not exchange appreciably with $H_2{}^{18}O$. This suggests that a degenerate exchange reaction does not occur.



S211. Incorporation of acetate-d_3 into $\mathbf{Co_4}^+$(/$\mathbf{Co_4}H^+$) and $\mathbf{MnCo_3}^+$ from the data shown in **S**. The % acetate-d_3 incorporation, as determined by equation # below, for the $\mathbf{MnCo_3}^+$ is 39% and the acetate incorporation for $\mathbf{Co_4}$ is 30%



S212. Incorporation of acetate-d_3 intro $\mathbf{Co_4}H^+$ and $\mathbf{MnCo_3}^+$ from the data shown in **S**. The % acetate-d_3 incorporation, as determined by equation # below, for the $\mathbf{MnCo_3}^+$ is 54% and the acetate incorporation for $\mathbf{Co_4}$ is 36%.

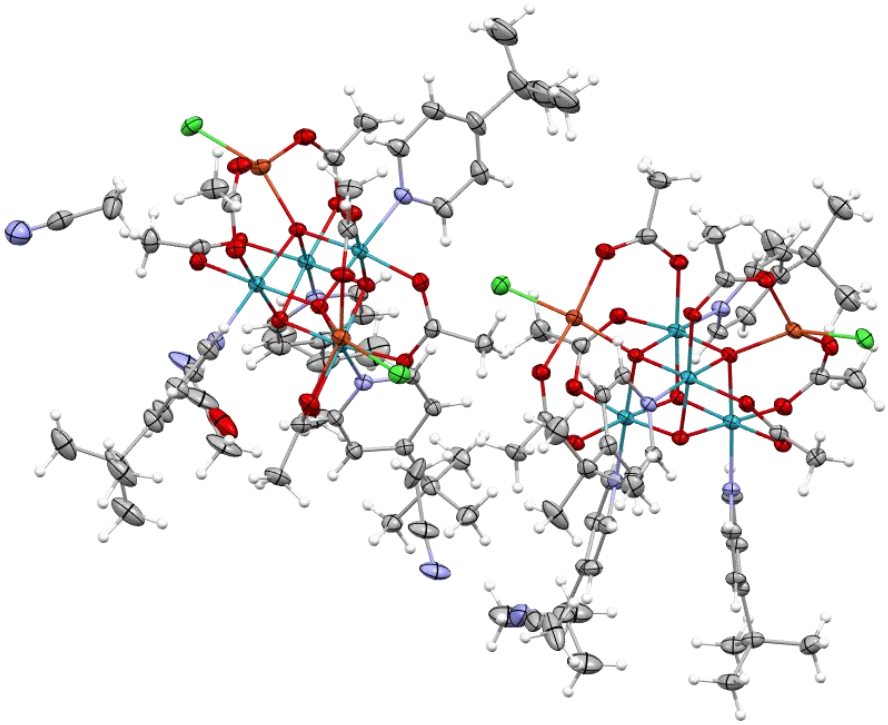
$$\%_{labeled} = \frac{1 \times \mathrm{I}_{n=1} + 2 \times I_{n=2} + 3 \times I_{n=3} + 4 \times I_{n=4}}{4 \times \sum I_{n=1-4}} \quad (\#)$$

Where I_n is the signal intensity for either $\mathbf{Co_4}(\mathrm{OAc}\text{-}d_3)_n$/$\mathbf{MnCo_3}(\mathrm{OAc}\text{-}d_3)_n$.

X-Ray Crystallographic Tables and Refinement Details:

Table S8. Crystal data and structure refinement for **Cu_2Co_4**.

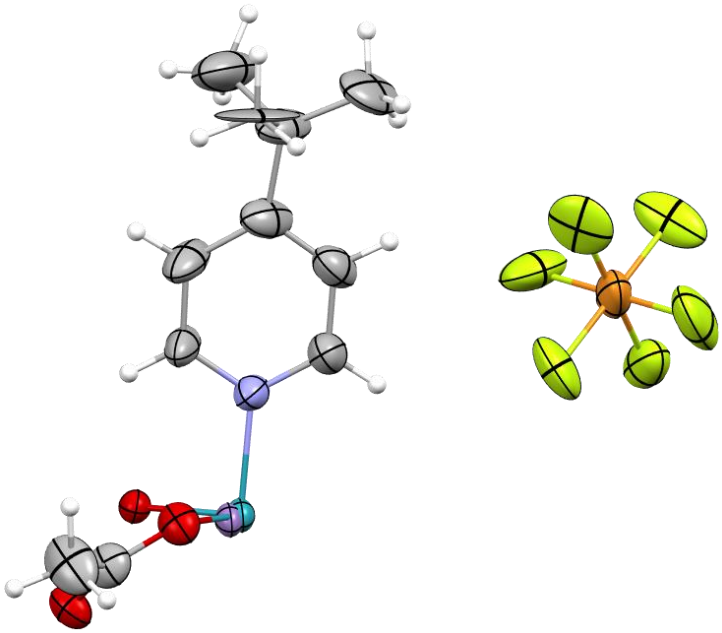
Identification code	
Empirical formula	$C_{50.09}H_{73.5}Cl_2Co_4Cu_2N_{4.96}O_{16.25}$
Formula weight	1438.84
Temperature/K	100.0
Crystal system	monoclinic
Space group	$P2_1$
a/Å	15.1031(15)
b/Å	15.1818(15)
c/Å	28.148(3)
α/°	90
β/°	91.651(3)
γ/°	90
Volume/Å^3	6451.4(11)
Z	4
ρ_{calc}g/cm^3	1.481
μ/mm^{-1}	1.798
F(000)	2955.0
Crystal size/mm^3	0.04 × 0.02 × 0.01
Radiation	Synchrotron (λ = 0.7288)
2Θ range for data collection/°	2.698 to 61.15
Index ranges	$-21 \leq h \leq 21$, $-21 \leq k \leq 21$, $-40 \leq l \leq 40$
Reflections collected	111899
Independent reflections	38613 [R_{int} = 0.0490, R_{sigma} = 0.0654]
Data/restraints/parameters	38613/16/1486
Goodness-of-fit on F^2	1.046
Final R indexes [I>=2σ (I)]	R_1 = 0.0472, wR_2 = 0.1209
Final R indexes [all data]	R_1 = 0.0595, wR_2 = 0.1263
Largest diff. peak/hole / e Å^{-3}	1.17/-0.92
Flack parameter	0.049(3)



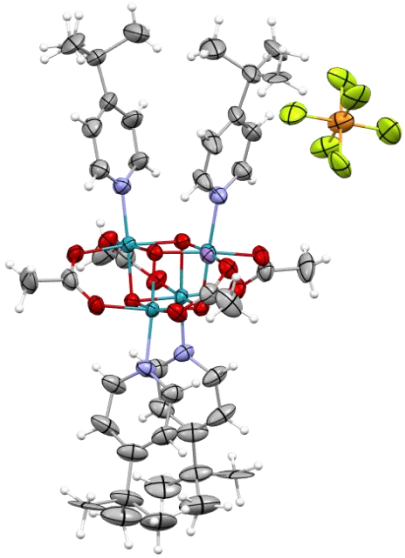
S213. Solid-state molecular structure of **Cu_2Co_4** depicting the two cubanes in the asymmetric unit**.** White: H, light-grey: C, pale-blue: N, red: O, teal: Co, orange: Cu, green: Cl.

Table S9. Crystal data and structure refinement for **$MnCo_3$**[PF_6]

Empirical formula	$C_{3.83}H_{5.57}Co_{0.35}F_{0.52}N_{0.35}O_{1.04}P_{0.09}$
Formula weight	106.24
Temperature/K	100
Crystal system	tetragonal
Space group	P-4*n*2
a/Å	13.195(3)
b/Å	13.195(3)
c/Å	19.182(6)
α/°	90
β/°	90
γ/°	90
Volume/Å^3	3339.6(18)
Z	23
ρ_{calc}g/cm^3	1.215
μ/mm^{-1}	1.132
F(000)	1258.0
Crystal size/mm^3	0.02 × 0.02 × 0.02
Radiation	Synchrotron (λ = 0.7288)
2Θ range for data collection/°	4.354 to 58.1
Index ranges	-17 ≤ h ≤ 17, -17 ≤ k ≤ 17, -25 ≤ l ≤ 25
Reflections collected	52649
Independent reflections	4149 [R_{int} = 0.0534, R_{sigma} = 0.0200]
Data/restraints/parameters	4149/226/198
Goodness-of-fit on F^2	1.112
Final R indexes [I>=2σ (I)]	R_1 = 0.0512, wR_2 = 0.1562
Final R indexes [all data]	R_1 = 0.0540, wR_2 = 0.1589
Largest diff. peak/hole / e Å^{-3}	0.48/-0.46
Flack parameter	0.42(3)



S214. Asymmetric unit from the solid-state molecular structure of **MnCo$_3$**[PF_6]**.** White: H, light-grey: C, pale-blue: N, red: O, neon-green: F, purple: Mn, teal: Co orange: P. Due to the high-symmetry of the cell, the structural model required the extensive use of constraints and an equivalent of solvent was removed using SQUEEZE. The 4-*tert*-butylpyridine ligands *tert*-butyl group was modeled across two positions that were linked by a free variable. The PF_6^- counterion P–F 1-2 and 1-3 distances were restrained with SADI; in addition, SIMU and RIGU restraints were applied to the ADPs. The Mn site occupancy was set at 0.25 and the Co site occupancy was set at 0.75; attempts to freely refine this parameter resulted in only a slight improvement to the model fit, and roughly equal occupancy of the Mn and Co sites. Without a secondary Mn site, and a Co site of occupancy 1.0, R_1 = 5.01. With the partially occupied Mn site, R_1 = 4.89. The two orientations of the 4-*tert*-butylpyridine ligand is also consistent with the partial occupancy Mn site, which would have a different orientation of the 4-*tert*-butylpyridine ligand.



S7. Solid-state structure of **MnCo$_3$**[PF_6]. White: H, light-grey: C, pale-blue: N, red: O, neon-green: F, purple: Mn, teal: Co orange: P.

Citations:

1. Research, M., MestReNova.
2. Evans, D. F., 400. The determination of the paramagnetic susceptibility of substances in solution by nuclear magnetic resonance. *J Chem. Soc. (Resumed)* **1959**, 2003-2005.
3. Sheldrick, G., Crystal structure refinement with SHELXL. *Acta Crys. C* **2015,** *71*, 3-8.
4. Sheldrick, G., SHELXT - Integrated space-group and crystal-structure determination. *Acta Cryst. A* **2015,** *71*, 3-8.
5. Dolomanov, O. V.; Bourhis, L. J.; Gildea, R. J.; Howard, J. A. K.; Puschmann, H., OLEX2: a complete structure solution, refinement and analysis program. *J. Appl. Crystallogr.* **2009,** *42*, 339-341.
6. Hubschle, C. B.; Sheldrick, G. M.; Dittrich, B., ShelXle: a Qt Graphical User Interface for SHELXL. *Journal of Applied Crystallography* **2011,** *44*, 1281-1284.
7. Nguyen, A. I.; Ziegler, M. S.; Oña-Burgos, P.; Sturzbecher-Hohne, M.; Kim, W.; Bellone, D. E.; Tilley, T. D., Mechanistic Investigations of Water Oxidation by a Molecular Cobalt Oxide Analogue: Evidence for a Highly Oxidized Intermediate and Exclusive Terminal Oxo Participation. *J. Am. Chem. Soc.* **2015,** *137*, 12865-12872.
8. IonicVIPEr Forum. https://www.ionicviper.org/forum-topic/deuterium-labeling-chn-analysis (accessed 03-21).
9. Carli, S.; Benazzi, E.; Casarin, L.; Bernardi, T.; Bertolasi, V.; Argazzi, R.; Caramori, S.; Bignozzi, C. A., On the stability of Manganese tris(β-diketonate) Complexes as Redox Mediators in DSSCs. *PCCP* **2016,** *18*, 5949-5956.
10. Green, S. A.; Huffman, T. R.; McCourt, R. O.; van der Puyl, V.; Shenvi, R. A., Hydroalkylation of Olefins To Form Quaternary Carbons. *J. Am. Chem. Soc.* **2019,** *141*, 7709-7714.
11. DeLucia, A. A.; Kelly, K. A.; Herrera, K. A.; Gray, D. L.; Olshansky, L., Intramolecular Hydrogen-Bond Interactions Tune Reactivity in Biomimetic Bis(μ-hydroxo)dicobalt Complexes. *Inorganic Chemistry* **2021,** *60*, 15599-15609.
12. Britovsek, G. J. P.; England, J.; White, A. J. P., Iron(ii), Manganese(ii) and Cobalt(ii) Complexes Containing Tetradentate Biphenyl-bridged Ligands and their Application in Alkane Oxidation Catalysis. *Dalton Trans.* **2006,** *11*, 1399-1408.
13. Nguyen, A. I.; Darago, L. E.; Balcells, D.; Tilley, T. D., Influence of a "Dangling" Co(II) Ion Bound to a $[MnCo_3O_4]$ Oxo Cubane. *J. Am. Chem. Soc.* **2018,** *140*, 9030-9033.
14. table, p., **https://organicchemistrydata.org/hansreich/resources/pka/pka_data/pka-compilation-williams.pdf**.
15. McDaniel, D. H.; Brown, H. C., An Extended Table of Hammett Substitutent Constants Based on the Ionization of Substituted Benzoic Acids. *J. Org. Chem.* **1958,** *23*, 420-427.
16. Chakrabarty, M. R.; Handloser, C. S.; Mosher, M. W., Thermodynamics of protonation of substituted pyridines in aqeous solutions. *J. Chem. Soc. Perkin Transactions* **1973,** (7), 938-942.

Chapter 4

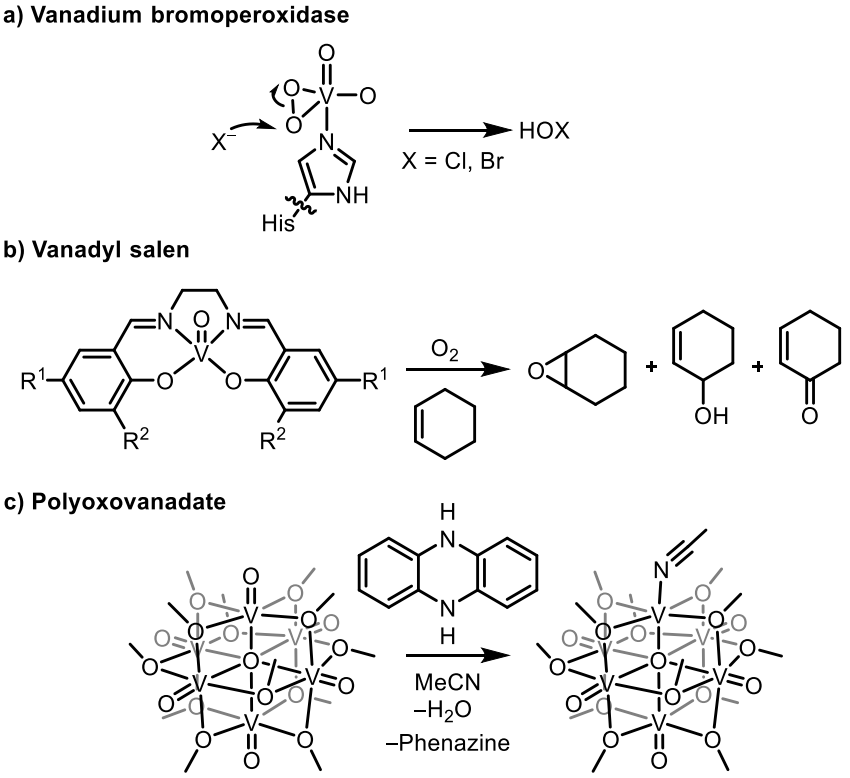
Vanadium—Cobalt Oxo Cubanes Synthesized by way of Metal-Metal Exchange.

Introduction:

Vanadium oxo species play an important role in a wide range of oxidative transformations.[1-3] In industry, V_2O_5 is a catalyst for the large-scale production of sulfuric acid, adipic acid, and phthalic anhydride,[4] while homogeneous vanadium oxo complexes are widely used in chemical synthesis, to catalyze olefin epoxidation, C–H bond hydroxylation, and peroxidative halogenation.[5-13] The latter type of transformation is inspired by vanadium haloperoxidases, which utilize a vanadium oxo active site to generate a hypohalous acid (XOH) from hydrogen peroxide and a halide, which then halogenates electron-rich substrates.[14-17] In these reactions, the vanadium oxo moiety plays a variety of roles. At the active site of vanadium bromoperoxidase, hydrogen peroxide adds to a vanadium center by displacing an oxo ligand to form a peroxide complex that subsequently oxidizes Br^-. Additionally, oxo vanadium catalysts have been proposed to oxidize alcohols by a formal V^{III}-V^{V} redox process, and to cleave C–O bonds operating by a V^{IV}-V^{V} pathway.[18-20] The development of well-defined vanadium oxo complexes has provided insight into structural features that influence this diverse reactivity, and the mechanisms by which vanadium complexes mediate oxidative transformations (Scheme 1).

An important class of well-established vanadium oxo complexes that affect a number of oxidative transformations are polyoxovanadates.[21-24] These clusters exhibit a variety of structures but of particular interest are those that adopt a Lindqvist structure, such as $V_6(\mu_6\text{-}O)O_6(\mu_6\text{-}O)(\mu_2\text{-}OMe)_{12}$, which are well-defined, functional models for catalytically active heterogeneous vanadium oxides and vanadium-based electrolytes for redox flow batteries.[25-27] These polyoxovanadates serve as platforms for demonstrating fundamental chemical transformations, such as the generation of O-atom vacancies and the introduction of heterometals (Scheme 1c). More complex polyoxometalates containing heterometals have advanced an understanding of the interactions between heterometals and metal oxide supports.[28-33] Notably, studies of well-defined transition metal oxo clusters containing vanadium as a heterometal are quite limited, but are expected to provide insights into the possible role of synergistic metal-metal interactions in promoting activity and/or selectivity.

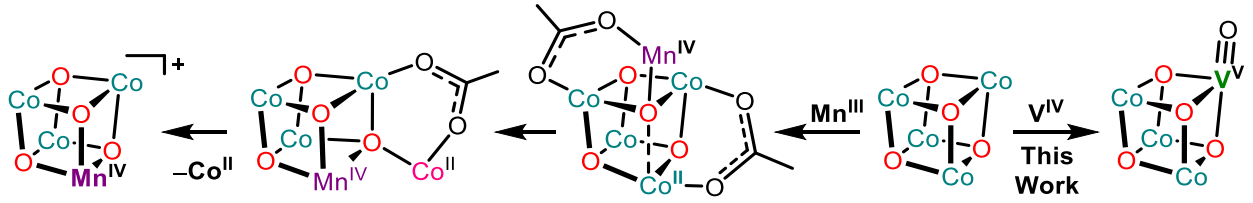
Scheme 1. Noteworthy Oxidative Transformations Catalyzed by Vanadium Oxo Moieties and Well-Studied Vanadium Polyoxometallates.



a) The mechanism for halogenation by vanadium haloperoxidases is believed to involve generation of hypohalous acid by a vanadium active site. b) Oxidations catalyzed by vanadium oxo complexes may proceed through one- or two- electron mechanisms depending on the supporting ligands. c) Linqvist clusters with demonstrated control over heterometal content.

Promising heterometallic oxides include those containing cobalt and vanadium, since both metals are associated with useful oxidation catalysis. For example, incorporation of vanadium into cobalt oxide/hydroxide materials results in catalysts for the oxygen evolution reaction (OER) that exhibit enhanced activity and stability under catalytic conditions.[34-38] Indeed, heterometallic V-Co oxide materials feature overpotentials for OER that are lower than those of either homometallic oxide, with V^{III}-β-$Co(OH)_2$ reported to have one of the lowest overpotentials of any Co-based electrocatalyst. This enhanced electrocatalytic performance was attributed to metal-metal cooperativity between Co and V, but the origin of this effect is not well understood.[39] Critically, the heterogeneity of these materials present a challenge for mechanistic studies that probe the origin of such synergistic effects. Thus, model vanadium-cobalt oxide clusters are of interest for probing the behavior of vanadium in a cobalt oxide environment. To the best of our knowledge, a well-defined vanadium-cobalt oxo cubane has not been reported.[40-42] In this context, the cobalt oxo cubane $Co_4(\mu_3\text{-}O)_4(OAc)_4(py)_4$ with a $[Co_4O_4]$ core is a potentially useful starting point, given its ability to model certain properties of cobalt oxide.[43-50] In addition, the Co_4O_4 cubane possesses tunable redox potentials[51] and versatile oxidation activity[52] that mimics CoO_x materials.

Scheme 2. Routes to Heteroatomic Cubanes.



The synthesis of mixed-metal cobalt oxo cubane clusters has proven to be challenging. Previous success is limited to use of permanganate or perruthenate as metal-based oxidants in modifications to the procedure for synthesis of $[Co_4O_4]$ cubanes, to obtain heterometallic oxo cubanes ($[MCo_3O_4]$, M = Ru, Mn).[53-55] However, a recent discovery in this laboratory (Chapter 3) suggests the possibility of more general access to mixed-metal oxo cubanes by way of a redox-mediated metal-metal exchange. This exchange was observed in the reaction of $Co_4(\mu_3\text{-}O)_4(OAc)_4(t\text{-}Bupy)_4$ with $Mn(OAc)_2$ (and NH_4PF_6) to produce the cubane $[MnCo_3(\mu_3\text{-}O)_4(OAc)_4(t\text{-}Bupy)_4][PF_6]$, by the formal redox process 2 Co^{III} + Mn^{II} → 2 Co^{II} + Mn^{IV}. In this reaction, it is believed that $Mn^{II}(OAc)_2$ is initially oxidized to a Mn^{III} complex, which is the active transmetalating species. The metal-metal exchange is initiated by coordination of the incoming Mn^{III} ion to a μ_3-oxo ligand, and subsequent electron transfer to produce Mn^{IV} and a labile Co^{II} species leads to an exchange mediated by bridging acetates, which incorporates the more stable Mn^{IV} ion into the octahedral coordination site (Scheme 2). This redox driven mechanism suggests that other reducing metal ions could participate in a related metal-metal exchange, and this contribution describes application of such a strategy through the use of V^{IV} in the production of a VCo_3O_4 cubane possessing a terminal $O{\equiv}V^{V}$ bond.

Results and Discussion

Synthesis and characterization of a vanadium-cobalt oxo cubane. The synthesis of a vanadium-containing oxo cubane utilizing the reductive metal-metal exchange described in Scheme 2 was investigated with the reaction of $VCl_4(THF)_2$ and the cobalt oxo cubane $Co_4(\mu_3\text{-}O)_4(OAc)_4(t\text{-}Bupy)_4$ (**Co4**). Under air-free conditions, dropwise addition of a dark red THF solution of $VCl_4(THF)_2$ to a THF solution of **Co4** resulted in rapid color changes from olive green to orange, and finally to dark blue green over ca. 10 minutes. The ^{1}H NMR spectrum of an aliquot of the reaction mixture in benzene-d_6 reveals numerous broad resonances that are difficult to assign, but analysis by high-resolution electrospray ionization mass spectrometry (HR-ESI-MS) revealed the presence of a cluster containing a $[VCo_3O_4]$ core. Indeed, blue crystals of $[O{\equiv}VCo_3(\mu_3\text{-}OH)(\mu_3\text{-}O)_3(OAc)_4(t\text{-}Bupy)_3][CoCl_3(t\text{-}Bupy)]$ (**[HVCo3][Co]**) were isolated in 3% yield by slow evaporation of a toluene solution, permitting structural characterization by single-crystal X-ray diffraction (SC-XRD, Figure 1). The origin of the additional oxo ligand, and the role of adventitious water in producing higher yields of **[HVCo3][Co]**), is discussed below. The ^{1}H NMR spectrum (benzene-d_6 solution) is consistent with a diamagnetic species, displaying two inequivalent acetate resonances in a 1:1 ratio, and two sets of pyridine resonances in a 1:2 ratio, consistent with the C_s symmetry observed in the solid-state (*vide infra*). Notably, the inequivalent

pyridine ligand resonances display well-resolved splitting, while the equivalent pyridine ligands appear as broad resonances with apparent lower than anticipated intensity, likely resulting from interaction with the paramagnetic $[CoCl_3(t\text{-Bupy})]^-$ counterion which is associated with the cubane core via a μ_3-O–H–Cl hydrogen bond. The ^{51}V NMR spectrum of [**HVCo$_3$**][**Co**] in acetonitrile-d_3 (105 MHz, δ relative to $VOCl_3$) exhibits a single resonance at –304 ppm, consistent with a relatively electron poor vanadium center,[50,51] although by this metric [**HVCo$_3$**][**Co**] is likely more electron rich than mixed polyoxoalkoxovanadates such as $[V_6O_{12}(OCH_3)_7]^-$ ($\delta(^{51}V)$ = –453.2, –465.0, –472.3, –478.3 ppm)[52] or polyoxovanadates such as V_2O_5 ($\delta_{iso}(^{51}V)$ = –612 ppm) or VO_4^{3-} ($\delta(^{51}V)$ = –541ppm). Note that ^{51}V NMR spectra of d^0 vanadium complexes are affected by electronic shielding at the vanadium center, with more electronegative substituents resulting in higher-field resonances, an effect that has been referred to as the "inverse electronegativity dependence of shielding."[56-59]

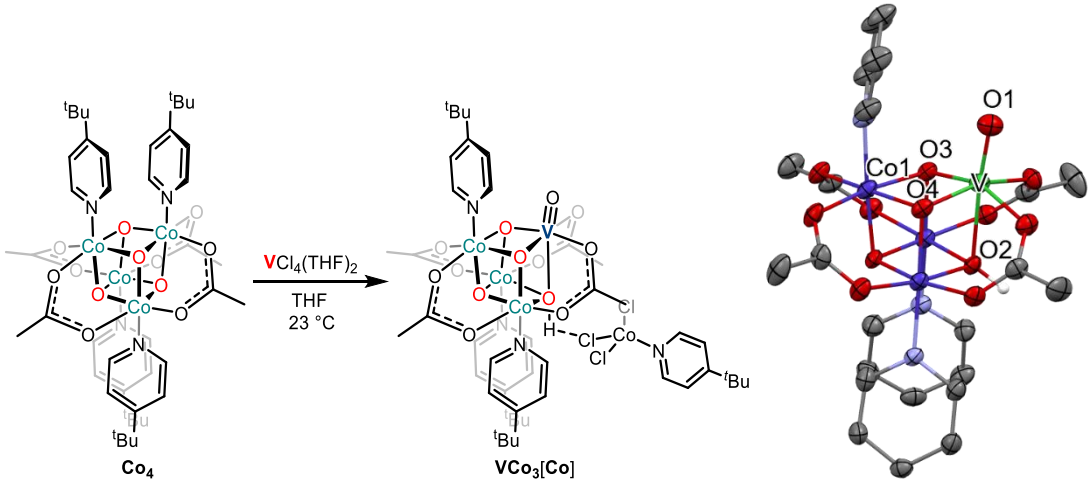


Figure 1. Synthesis of [**HVCo$_3$**][**Co**] and solid-state molecular structure of the cationic fragment Most hydrogen atoms, tert-butyl groups, solvent of crystallization, and counterion removed for clarity. 50% thermal ellipsoids are displayed.

The solid-state molecular structure determined by SC-XRD confirms retention of the cubane geometry with significant distortions at the vanadium vertex (Figure 1). The geometric distortion manifests as a protrusion of the vanadium atom out of the plane defined by the O4—Co1—O3 atoms by 0.21 Å. This distortion is significant when compared to other previously synthesized heterometal cobalt oxo cubanes; for comparison, the displacement of the heterometal above the O—Co—O plane for the $O{=}RuCo_3(\mu_3\text{-}O)_4(OAc)_4(py)_3$ ([$O{=}RuCo_3O_4$]) and $Mn(OAc)Co_3(\mu_3\text{-}O)_4(OAc)_4(py)_3$ ([$MnCo_3O_4$]) cubanes is 0.02 and –0.10 Å respectively.[53, 55] This distortion is likely the result of the long V–O2 bond (2.224(5) Å) *trans* to the terminal oxo. The hydrogen atom of the μ_3-OH group was located in the Fourier difference map and refined isotropically; notably, no residual electron density or evidence of hydrogen bonding could be found near the O1 (terminal oxo) atom or any other bridging oxo ligand.

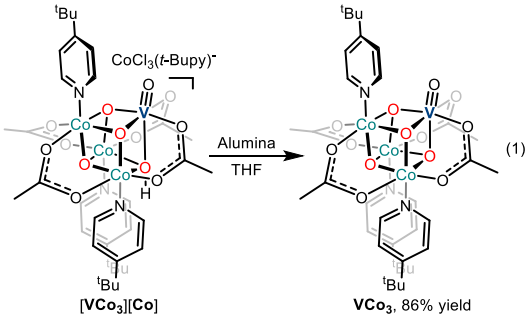
The terminal vanadium oxo bond distance (V–O1, 1.594(5) Å) is similar to that of known V^V-oxo bonds in octahedral environments, such as $[V^V_6O_{13}(TRIOL\text{-}NO_2)_2]^{2-}$ ($TRIOL\text{-}NO_2 = (OCH_2)_3C\text{-}NO_2$) and $[V_6O_{12}(OCH_3)_7]^-$ (1.599(2)-1.607(3) and 1.591(7) Å, respectively) (Table 1).[25, 60] The

vanadium *cis* cubane-oxo bond lengths (V–O_3 and V–O_4; av 1.847(5) Å) are slightly longer than those in the vanadium *cis* polyoxometalate-oxo $[V_6O_{12}(OCH_3)_7]^-$ (V–O_b) 1.826(7) Å). The IR spectrum of [**HVCo$_3$**][**Co**] exhibits a ν_{O-H} stretching mode at 3200 cm^{-1} and a $\nu_{V\equiv O}$ stretching mode at 987 cm^{-1}, indicating a marginally stronger V≡O bond in comparison to $[V_6O_{12}(OCH_3)_7]^-$ ($\nu_{V\equiv O}$ 965 cm^{-1}).[61]

Table 1. Selected bond distances for 2 and relevant M-cobalt oxo cubanes and polyalkoxovanadates.

Bond	O≡$VCo_3O_4H^+$	O=$RuCo_3O_4$	OAc-$MnCo_3O_4$	$[V_6O_{12}(OCH_3)_7]^-$	O≡VCo_3O_4
M–$O^{avg.}_{terminal}$	1.594(5) Å	1.721(6) Å		1.591(7) Å	1.612(6) Å
M–$O^{avg.}_{cis}$	1.847(5) Å	1.935(5) Å	1.856(4) Å	1.826(7) Å	1.846(4) Å
M–$O^{avg.}_{trans}$	2.224(5) Å	2.015(6) Å	1.864(5) Å	2.212(6) Å	2.041(5) Å

Passage of a THF solution of [**VCo$_3$H**][**Co**] through anhydrous basic alumina, followed by removal of the solvent *in vacuo,* provided the neutral vanadium cubane cluster O≡$VCo_3(\mu_3\text{-}O)_4(OAc)_4$(*t*-Bupy)$_3$ (**VCo$_3$**) in 86% yield as an analytically pure jade-green solid (eq 1). In contrast to [**HVCo$_3$**][**Co**], the splitting of the pyridyl resonances in the ^{1}H NMR spectrum of **VCo$_3$** in acetonitrile-d_3 are all well-resolved.



The ^{51}V NMR resonance of **VCo$_3$** in acetonitrile-d_3 appears further downfield at –264 ppm ($\Delta\delta(^{51}V)$ = –40 ppm), indicating a more electron rich vanadium center, and broadens (give peak width at half-max), consistent with the effects of reduced local symmetry on the quadrupolar ^{51}V nucleus.[57] The IR spectrum of **VCo$_3$** confirms the absence of a ν_{O-H} stretch and supports a bathochromic shift of the O≡V stretch ($\nu_{O\equiv V}$ = 931 cm^{-1}, $\Delta\nu_{O\equiv V}$ = –56 cm^{-1}), indicating a weaker bond due to the stronger *trans* influence of the μ_3-oxo vs. μ_3-hydroxo group.

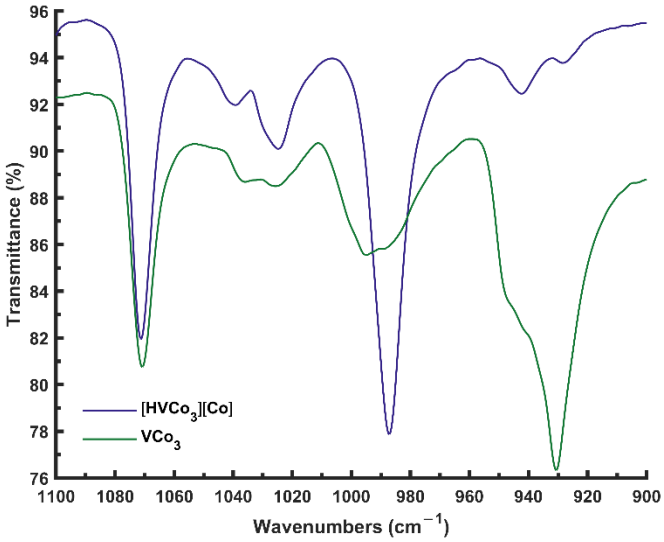


Figure 2. ATR-FTIR spectra of [**VCo$_3$**][**Co**] (purple) and **VCo$_3$** (green). The O–H stretch is unobserved and the O≡V stretch shifts.

The solid-state molecular structure of **VCo$_3$** (Figure 3) reveals retention of the VCo_3O_4 cubane core, and dramatic contraction of the V–O_{trans} (O2) distance (Δ = –0.183(5) Å) with a concomitant minor increase in the V–$O_{terminal}$ (O1) distance (Δ = 0.018(6) Å). The vanadium oxo V–O_{trans} bond distance is longer than the corresponding Ru–O_{trans} distance of the [O=$RuCoO_4$] cubane (Table 1), which highlights the difference between the metal-terminal oxo bond orders in these cases. The product **VCo$_3$** was also isolated directly from the reaction mixture involving **Co$_4$** and $VCl_4(THF)_2$ following workup with basic alumina (supporting information), which enabled optimization of the synthetic procedure.

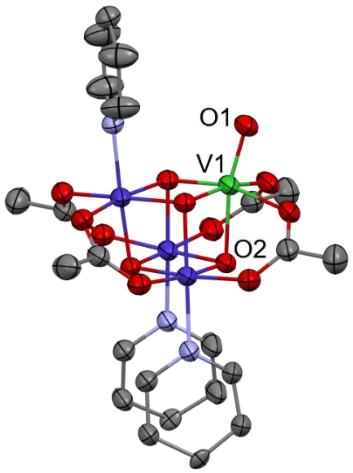
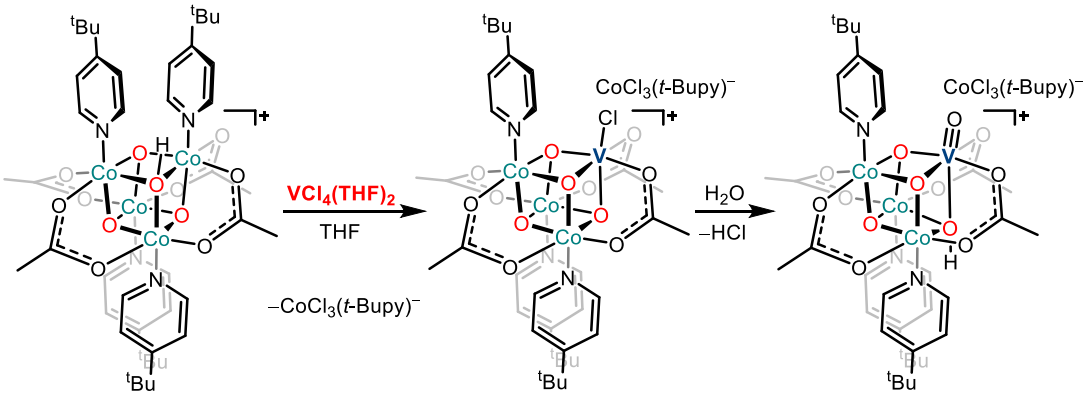


Figure 3. Solid-state molecular structure of VCo_3. Hydrogen atoms, tert-butyl groups, solvent of recrystallization and lesser occupancy disordered components removed for clarity. Thermal ellipsoids are shown at the 50% probability level.

The direct access to **VCo$_3$** allowed more thorough investigations of reaction conditions, and mechanistic experiments involving both [**HVCo$_3$**][**Co**] and **VCo$_3$**. With thoroughly dried reagents,

cubane **Co4** in THF reacted with rigorously purified $VCl_4(THF)_2$ to give the expected deep blue solution after ca. 10 minutes. However, HR-ESI-MS analysis of the reaction solution did not provide evidence for the presence of either [**HVCo3**][**Co**] or **VCo3**, and standard workup did not yield either complex. Interestingly, addition of one equiv of water under these same conditions (to a solution of **Co4** in THF with $VCl_4(THF)_2$) gave **HVCo3**$^+$ by HR-ESI-MS analysis, which was isolated from the reaction mixture in 10% yield. This experiment suggested that the terminal oxo may have originated from adventitious water. An experiment with one equiv of $H_2{}^{18}O$ under these conditions resulted in partial ^{18}O enrichment of the O≡V moiety ($\nu_{O\equiv V}$ = 892 cm^{-1}) to give a single additional isotopologue of **VCo3** by HR-ESI-MS and IR spectroscopic analyses, with no evidence for ^{18}O incorporation into the **VCo3** cubane core. A separate experiment involving **VCo3** and 5 equiv of $H_2{}^{18}O$ provided evidence for one ^{18}O isotopologue of **VCo3** exclusively. Additionally, the incorporation of ^{18}O into **Co4** is significantly slower than the **VCo3** synthesis timescale. The results of these experiments are difficult to interpret but suggest that H_2O may be generated in situ by decomposition of **Co4** under acidic conditions. An experiment with a statistical mixture of dry $^{32}O_2/^{34}O_2/^{36}O_2$ resulted in no isotopic enrichment, indicating that adventitious O_2 is also not the source of the terminal oxo ligand. Addition of one equiv of water, MeOH, 3,5,-di-*tert*-butylphenol, or pentafluorophenylaniline, results in dramatically improved yields of **VCo3**, while the presence of bases prohibits the metal-metal exchange. The best yield was obtained from reaction of 1.4 equiv of water, **Co4** and $VCl_4(THF)_2$ at –77 °C for 1 h. Thus, the terminal oxo ligand of [**HVCo3**][**Co**] likely originates from water, which may be generated by decomposition of **Co4**. (Scheme 3). The results of further investigation are summarized in the supporting information (Table S1).

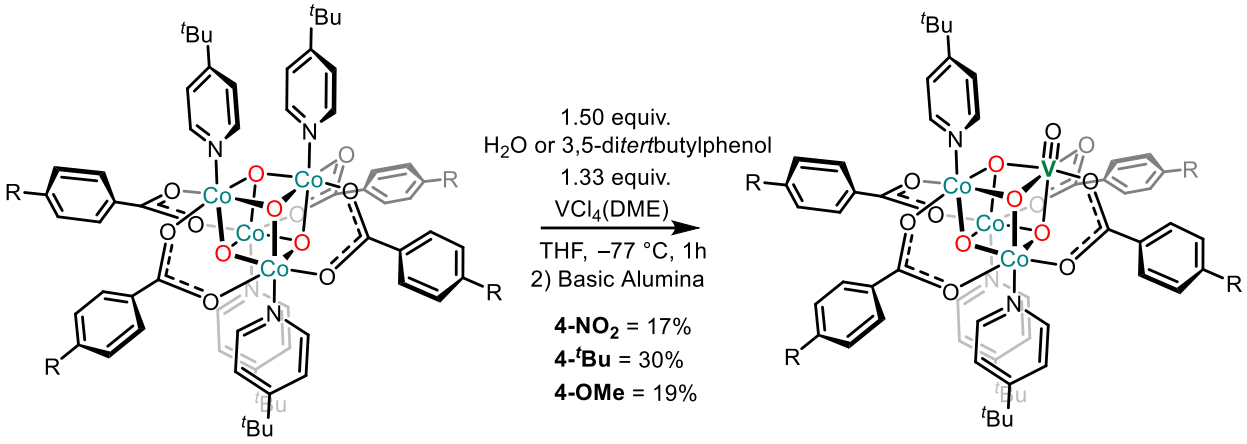
Scheme 3. Possible path to [**VCo3**][**Co**] demonstrating the dual role of **Co4** and $VCl_4(THF)_2$.



With an optimized synthesis of **VCo3** in hand, the metal-metal exchange conditions were applied to substituted $Co_4(\mu_3\text{-}O)_4(O_2CC_6H_4\text{-}R)_4(t\text{-Bupy})_4$ (*para*-substituted benzoate, R = NO_2, ^{t}Bu, OMe) cubanes to give the corresponding $O{\equiv}VCo_3(\mu_3\text{-}O)_4(O_2CC_6H_4\text{-}R)_4(t\text{-Bupy})_3$ cubane (**$VCo_3(O_2CC_6H_4)$-NO_2,^{t}Bu,OMe**) in 17%, 19% and 30% yields, respectively (Scheme 4). The ^{1}H NMR spectra of cubanes **$VCo_3(O_2CC_6H_4$-R)** are consistent with two inequivalent benzoate ligands and a 2:1 ratio of inequivalent *t*-Bupy ligands. Interestingly, while the nitrobenzoate

derivatized [Co_4O_4] cubane is a deep red color, **$VCo_3(O_2CC_6H_4$-R)** are all jade-green in color, as is **VCo_3**.

Scheme 4. Synthesis of Substituted $O{\equiv}VCo_3O_4$ Cubanes.



The $\nu_{V\equiv O}$ stretching frequencies of **VCo_3** and **$VCo_3(O_2CC_6H_4$-NO_2/^{t}Bu/OMe)** are all within 930-934 cm^{-1}, with no clear relationship between the benzoate ligand substituent and the stretching frequency. A similar range and absence of correlation was observed with the [$O{=}RuCo_3O_4$] cubane system.[53] The substituted [$O{\equiv}VCo_3O_4$] cubane ^{51}V NMR chemical shifts in acetonitrile-d_3 were also effectively invariant with respect to the substituent (**$VCo_3(O_2CC_6H_4)$-OMe**: –263 ppm, **-NO_2**: –262 ppm, **-^{t}Bu**: –286 ppm), suggesting minimal electronic communication between the vanadium center and the rest of the cubane core.

Electrochemical studies. Cyclic voltammetry of **VCo_3** and **$VCo_3(O_2CC_6H_4)$-NO_2/^{t}Bu/OMe** in MeCN reveals quasireversible, formally $Co^{III/IV}$ oxidations at 0.85, 0.92, 0.91, 0.86 V vs. Fc/Fc^+; respectively, and two irreversible reduction events (E_{pc}) at –0.82 and –1.33 V vs. Fc/Fc^+ for **VCo_3**. For comparison, the respective parent [Co_4O_4] cubanes are reversibly oxidized at 0.28, 0.67, 0.20, and 0.18 V, and irreversibly reduced between –1.5 and –2.0 V. Thus, the oxidation potential of the [$O{\equiv}VCo_3O_4$] cubanes are anodically shifted by ~0.55 V, and the reduction event at –0.82 is likely vanadium centered (corroborated by theory, *vide infra*). The correlation between the vanadium cubane oxidation potentials and the pK_a of the ligands is weaker (Figure 4) than that of the analogously substituted [Co_4O_4] cubane system,[45] (–0.11 V/pK_a) and almost comparable to that of the ruthenium cubane system[47] (–0.04 V/pK_a) despite the pyridine ligands having less influence than the acetate ligands on the oxidation potential.[51, 53] These results are consistent with a decrease in metal-metal electronic communication in the [$O{\equiv}VCo_3O_4$] cubane compared to the [$O{=}RuCo_3O_4$], [$MnCo_3O_4$] and [Co_4O_4] cubane systems. Attempts to measure the oxidation potential in other solvents (CH_2Cl_2, THF, *ortho*-difluorobenzene, (*o*DFB)) resulted in completely irreversible oxidation events and occasional deposition of a solids layer onto the electrode.

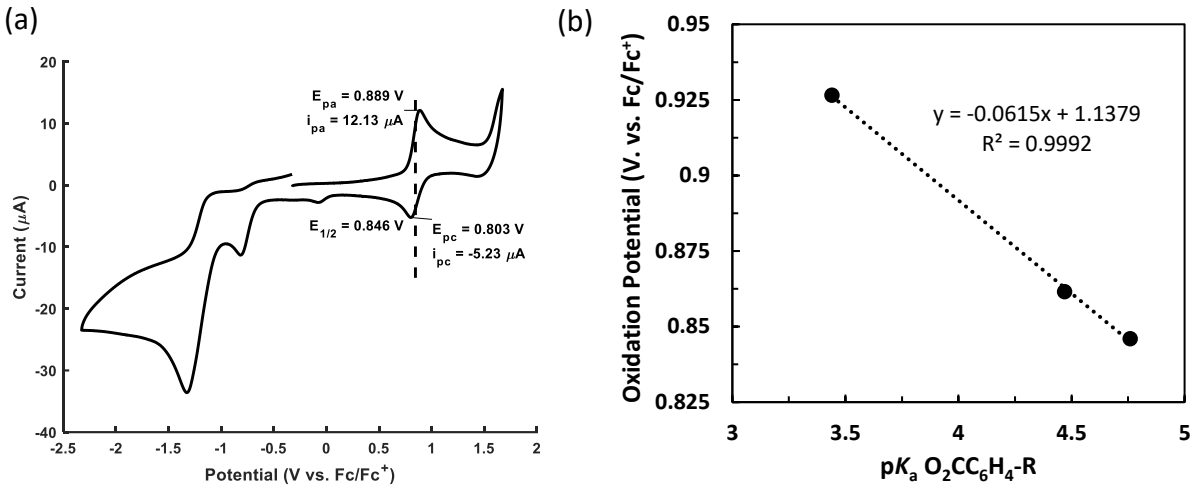
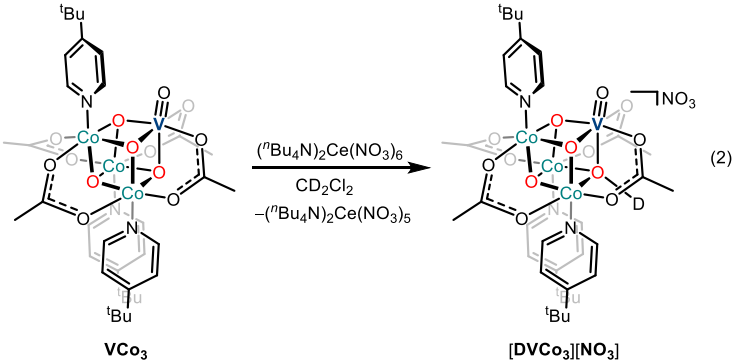


Figure 4. (a) Electrochemistry of **VCo$_3$**. Conditions: 0.2 M [^{n}Bu$_4$N][PF$_6$] MeCN solution, glassy carbon working electrode, Pt wire counterelectrode, Ag wire floating pseudoreference, 100 mV s^{-1}. (b) Plot of the oxidation potential of the *para*-substituted benzoate ligand **VCo$_3$** cubanes, **VCo$_3$(O$_2$CC$_6$H$_4$)-NO$_2$/^{t}Bu/OMe** respectively.

Despite the high oxidation potential, it appeared that oxidized **VCo$_3$** might be accessible through use of strong chemical oxidants. Treatment of *o*DFB solutions of **VCo$_3$** with oxidants such as thianthrenium tetrafluoroborate or "Magic Blue" yielded an intractable mixture of products by ^{1}H and ^{51}V NMR spectroscopy that was inconsistent with clean oxidation of **VCo$_3$**. The reaction of an acetonitrile-d_3 solution of **VCo$_3$** with Ce^{IV}(NO$_3$)$_6$(NH$_4$)$_2$ (CAN) immediately resulted in a red solution of the protonated vanadium cubane [**HVCo$_3$**][**NO$_3$**] in quantitative yield by ^{1}H NMR spectroscopy (vs an internal standard) and 90% isolated yield. The ^{51}V resonance at –304 ppm and the $\nu_{V\equiv O}$ IR stretch at 987 cm^{-1} confirms the identity of [**HVCo$_3$**][**NO$_3$**]. FTIR spectroscopic analysis of the material obtained from reaction of **VCo$_3$** with (^{n}Bu$_4$N)$_2$Ce^{IV}(NO$_3$)$_6$ (CTAN) in dichloromethane-d_2 revealed the absence of a ν_{O-H} stretch and a broad new frequency assigned to a ν_{O-D}stretch at 2732 cm^{-1} (eq 2); attempts to observe the deuterated product by HR-ESI-MS were inconclusive due to rapid exchange of the deuteron with atmospheric water. Thus, the product of [**HVCo$_3$**][**NO$_3$**] is likely the result of a solvent C–H bond activation. This C–H bond activation event is consistent with the inaccessibility of the quasireversible oxidation event of **VCo$_3$** in organic solvents other than acetonitrile, which is typically more stable to oxidative conditions.



(2)

The C–H bond activation reactivity prompted an examination into the thermodynamics of H-atom abstraction by oxidized **VCo3**. The pK_a of **HVCo3**$^+$ was estimated to be within the region of 6-7 by combining [**HVCo3**][**NO3**] and a variety of organic bases; unfortunately, due to complicated equilibria a more precise pK_a measurement was not achievable by this method. To determine the BDFE$_{O–H}$, a thermodynamic square scheme was constructed using eq 3, where C_G is $E°(H^+/H^•)$ equal to 52.6 kcal/mol.[62, 63]

$$BDFE_{O-H} = 1.37pK_a + 23.06E° + C_G \quad (3)$$

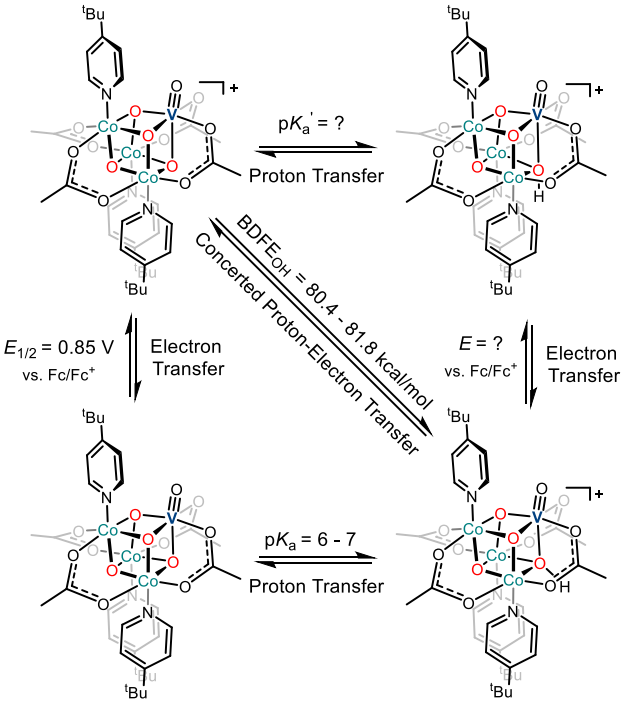


Figure 5. Thermodynamic square scheme describing the relationship between **VCo3**, **VCo3**$^+$, and **HVCo3**$^+$.

Compared to the BDFE$_{O–H}$ of 74 kcal/mol for $Co_4O_4(OAc)_4(py)_4$,[52] and 65.5 kcal/mol for $O{=}RuCo_3O_4(OAc)_4(4\text{-MeO-py})_3$,[54] the **HVCo3**$^+$ O–H bond is markedly stronger, and is much stronger than the BDFE$_{O–H}$ of 60-62 kcal/mol of the polyoxovanadate $V_6(\mu_6\text{-}O)O_6(\mu_6\text{-}O)(\mu_2\text{-}OMe)_{12}$. Despite the significantly lower pK_a of **HVCo3**$^+$ compared to the [Co_4O_4] cubane, the significantly higher oxidation potential of **VCo3** leads to a much higher BDFE$_{O–H}$.

To gauge the H-atom abstraction capabilities of **VCo3**$^+$, reactivity with weak C–H bonds such as those of 9,10-dihydroanthracene (DHA) was examined. Generation of **VCo3**$^+$ in *o*DFB with CAN in the presence of DHA results in full conversion to [**HVCo3**][**NO3**], and formation of anthracene, however the latter product forms in low (<1%) yield. The low yield of anthracene indicates that the lifetime of **VCo3**$^+$ in solution may be too short to engender meaningful H-atom abstraction reactivity, as **VCo3**$^+$ is capable of activating the relatively stronger bonds of CD_2Cl_2 (*vide supra*). Attempts to activate DHA using the more soluble CTAN under these conditions invariably resulted in quantitative yield of [**HVCo3**][**NO3**], but no conversion of DHA. Additionally, endeavors to

render this reaction catalytic using Ag_2O, as was done with the $[Co_4O_4]$ cubane system, resulted in low conversion of (<1%) of DHA after 48 h. These unsuccessful C–H bond activation attempts suggested that understanding the persistence of $\mathbf{VCo_3}^+$ could hold the key to developing the $\mathbf{VCo_3}^+$ platform for challenging bond activations. This reactivity is examined computationally further on.

The stability of $\mathbf{VCo_3}^+$ at low temperature was investigated by UV-vis spectroscopy by tracking the reaction between equimolar CTAN and $\mathbf{VCo_3}$ in CH_2Cl_2 at –93 °C. Under these conditions, the Ce^{IV} signal is 90% consumed in 22 min, indicating that the oxidation of $\mathbf{VCo_3}$ is relatively sluggish. The overlapping signal for a putative $\mathbf{VCo_3}^+$ decays simultaneously over this period, and after 90% consumption of Ce^{IV} the resulting absorption features continue to dissipate for the next 28 min. The slow oxidation of $\mathbf{VCo_3}$ by CTAN in CH_2Cl_2 at –93 °C suggested that it may be possible to observe a more reversible oxidation feature for $\mathbf{VCo_3}$ in CH_2Cl_2 at low temperature. Unfortunately, cyclic voltammetry of $\mathbf{VCo_3}$ in 0.1 M $[^nBu_4N][PF_6]$ CH_2Cl_2 in at –95 °C did not provide evidence for a reduction feature. With some preliminary successes, efforts are underway to observe and characterize the $\mathbf{VCo_3}^+$ by EPR spectroscopy.

Reactivity studies. The chemistry of V^V is characterized by hydrolytic instability, depending on the nature of the ligands, and for the $O{\equiv}V^V$ moiety specifically, oxidative reactivity such as epoxidation, hydroxylation, or oxo transfer.[3] To gauge the ability of the $[Co_3O_4]$ framework to influence chemical transformations at the V≡O group, reactions of $\mathbf{VCo_3}$ toward organic and inorganic substrates were examined. Treatment of *o*DFB solutions of $\mathbf{VCo_3}$ with 9,10-dihydroanthracene, *cis*-stilbene, tricyclohexylphosphine, *p*-toluenesulfonylamide or adamantylisocyanate resulted in no reaction after 24 h at 23 °C, or 55 °C. Heating these solutions at 85 °C resulted in complete consumption of $\mathbf{VCo_3}$ with no appreciable consumption of the organic substrates. Furthermore, attempts to heat solutions of $\mathbf{VCo_3}$ above 85 °C also resulted in intractable mixtures after 16 h, indicating that $\mathbf{VCo_3}$ is thermally unstable and relatively unreactive toward organic substrates. For this reason, Lewis acidic substrates were examined.

Lewis acids are sometimes associated with enhanced oxidation reactivity for metal oxos, and indeed this effect has been suggested for the essential calcium ion in the oxygen evolving complex. Addition of $B(C_6F_5)_3$ to a benzene-d_6 solution of $\mathbf{VCo_3}$ resulted in an immediate color change to deep red. By ^1H NMR analysis, quantitative conversion to a single new product, $[(F_5C_6)_3B]O{\equiv}VCo_3(\mu_3\text{-}O)_4(OAc)_4(t\text{-}Bupy)_3$ (**VCo_3(BCF)**) occurred, and further NMR experiments ($^{19}F\{^1H\}$, $^{11}B\{^1H\}$, and ^{51}V) indicated formation of a borane adduct of the terminal oxo atom (Figure 6). Surprisingly, the ^{51}V resonance shifts downfield by approximately 200 ppm, as is expected for a more electron-rich vanadium center, but this counterintuitive shift has been observed in another V^V oxo adduct, $[(C_6F_5)_3B]OV(NEt_2)_3$, which was attributed to a change in the π-donor ability of the terminal oxo ligand.[64]

The solid-state molecular structure clearly indicates that the borane has added to the terminal oxo ligand, rather than to the *trans* μ_3-oxo ligand as is the case for protonated cubane $\mathbf{HVCo_3}^+$. As a confirmation of the basicity of the of the *trans* μ_3-oxo ligand, addition of one equiv of *para*-

toluenesulfonic acid to an acetonitrile-d_3 solution of **VCo$_3$** results in quantitative conversion to **HVCo$_3^+$** as evidenced by ^{1}H and ^{51}V NMR spectroscopy. As expected, the O≡V bond of **VCo$_3$(BCF)** elongates (to 1.716(2) Å), while the O_{trans}–V bond contracts to 1.916(2) Å. Upon addition of the borane, the infrared $\nu_{V\equiv O}$ stretch shifts relative to that of **VCo$_3$,** but unfortunately is obfuscated by the aryl C–F stretching frequencies of the tris(pentafluorophenyl)borane group. Density functional theory (DFT) calculations predict a bathochromic shift of 18 cm^{-1} (*vide infra*). Thus, similar to vanadium oxo alkoxides, **VCo$_3$** is generally unreactive toward aprotic organic substrates, but capable of binding strong Lewis acids.[3, 64, 65]

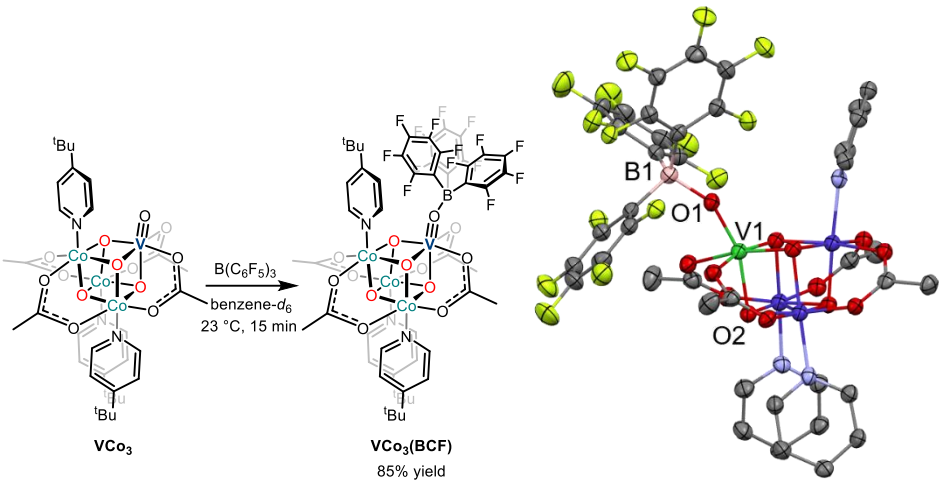
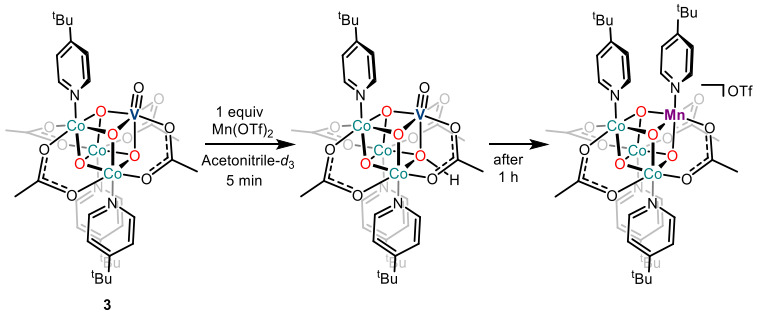


Figure 6. Solid-state molecular structure of VCo$_3$(BCF) with hydrogen atoms, tert-butyl groups, and solvent of crystallization removed for clarity. Thermal ellipsoids are shown at the 50% probability level.

The ability of **VCo$_3$** to bind a Lewis acid suggests that it may also coordinate metal ions in solution and undergo further metal-metal exchange, to provide access to heterotrimetallic oxo cubanes. Thus, the reaction of **VCo$_3$** with Mn(OTf)$_2$, a Mn source known to induce metal-metal exchange, was investigated. As monitored by ^{1}H and ^{51}V NMR spectroscopy, an acetonitrile-d_3 solution of **VCo$_3$** treated with equimolar Mn(OTf)$_2$ gave near quantitative conversion to the protonated cluster, [O≡VCo$_3$(μ$_4$-OH)(μ$_3$-O)$_4$(OAc)$_4$(*t*-Bupy)$_3$][OTf] ([**HVCo$_3$**][OTf]) (Scheme 5), likely the result of protonation by $Mn(H_2O)_6^{2+}$ from reaction of water present in the solvent with Mn(OTf)$_2$. In the presence of manganese, the ^{1}H NMR resonances associated with [**HVCo$_3$**][**OTf**] decay over 1 h to give broad resonances consistent with the [MnCo$_3$O$_4$] cubane, MnCo$_3$(μ$_3$-O)$_4$(OAc)$_4$(*t*-Bupy)$_4$][OTf], which was confirmed spectroscopically following isolation of this product in 40% yield. A HR-ESI-MS analysis provided no evidence for a [Co$_2$VMnO$_4$] oxo cubane, but this is consistent with the hypothesized mechanism for metal-metal exchange, as the LUMO of **VCo$_3$** is predominantly V^V centered (*vide supra*) and this should lead to exclusive substitution at this site. Note that the observed metal-metal exchange of **VCo$_3$** and Mn(OTf)$_2$ is faster than the metal-metal exchange of **Co$_4$** and Mn(OTf)$_2$, which requires either extended reaction times or heating to achieve comparable conversions. Thus, metal-metal exchange appears to be reactivity characteristic of both **Co$_4$** and **VCo$_3$** complexes, and cubane **VCo$_3$** may be a useful starting point to examine further M-M exchange reactivity.

Scheme 5. Reaction of VCo_3 with $Mn(OTf)_2$.



Density functional theory calculations. While the connectivity and formal oxidation states of the $[O{\equiv}VCo_3O_4]$ and $[O{=}RuCo_3O_4]$ cubanes are identical, the electronic structure and reactivity appear to be distinct, i.e., in the $[O{\equiv}VCo_3O_4]$ cubane system, a μ_3-oxo ligand observed while in the $[O{=}RuCo_3O_4]$ cubane system, a terminal oxyl ligand is the reactive site. To elucidate the origin of these effects, truncated $\mathbf{HVCo_3}^+$ and $\mathbf{VCo_3}$ were examined with density-functional theory. All calculations were done at the TPSSh level of theory with a def2-SVP(H, N, O_{OAc})//def2-TZVP(O_{oxo}, V, Co) basis for geometry optimizations and def2-TZVP basis for single-point calculations in addition to the RIJCOSX auxiliary basis in ORCA;[66] these parameters were previously optimized for the Ru and Mn cubane systems.[40,49,55] Whereas the SOMO of the $[O{=}RuCo_3O_4]$ cubane is localized on the Ru and $O_{terminal}$ atoms, the HOMO of $\mathbf{VCo_3}$ is substantially localized on the $[O{\equiv}VCo_3O_4]$ cubane core oxo ligand *trans* to the terminal oxo moiety. (Figure 7a).

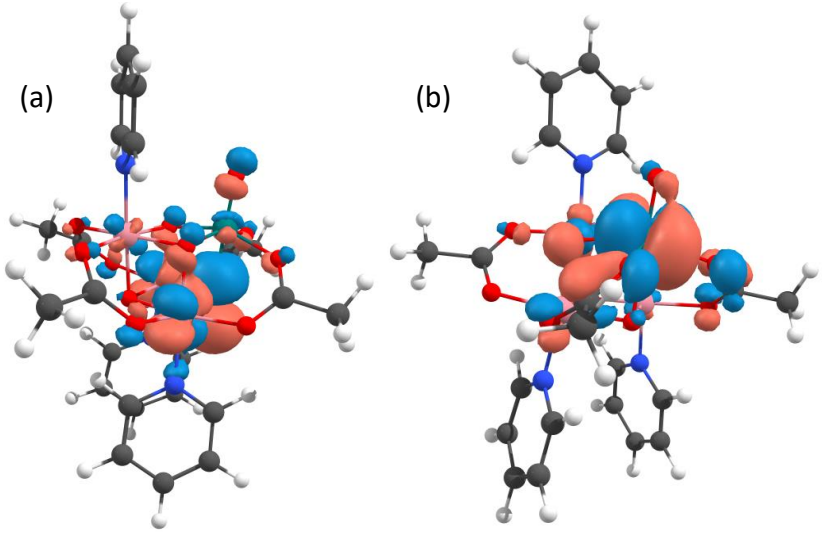


Figure 7. Canonical HOMO (a) and LUMO (b) for VCo_3 with a contour value of 0.03.

This is also in stark contrast to the all-cobalt system, wherein the HOMO has been calculated to be delocalized over the entire cubane.[43, 67] The localized HOMO of $\mathbf{VCo_3}$ is consistent with the site of protonation observed in $\mathbf{HVCo_3}^+$. The LUMO of $\mathbf{VCo_3}$ is of the b_2, non-bonding V d_{xy} orbital , with minor contributions from the cis and terminal oxo ligands (Figure 7b). This indicates

that the reduction event observed by cyclic voltammetry is V-centered, consistent with the additional reduction event anodically shifted from the typically observed $Co^{II/III}$ reduction. The O≡V bonding orbitals are much lower in energy (e.g., HOMO –29) than the frontier orbitals, consistent with a vanadium oxo moiety that is mostly a spectator ligand. These results indicate that the coordination of $B(C_6F_5)_3$ is driven by the steric inaccessibility of the core cubane oxo ligands. To quantify this steric effect, the stability of the cubane oxo vs the terminal oxo adduct of $B(C_6F_5)_3$ and the boron trifluoride were examined. Indeed, while the smaller boron trifluoride is more stable as the O_{cubane} adduct (ΔG = –25 $kcal^{-1}$ mol^{-1}), the $B(C_6F_5)_3$ adduct is significantly more stable when bound to as the $O_{terminal}$ adduct (ΔG = –54 $kcal^{-1}$ mol^{-1}).

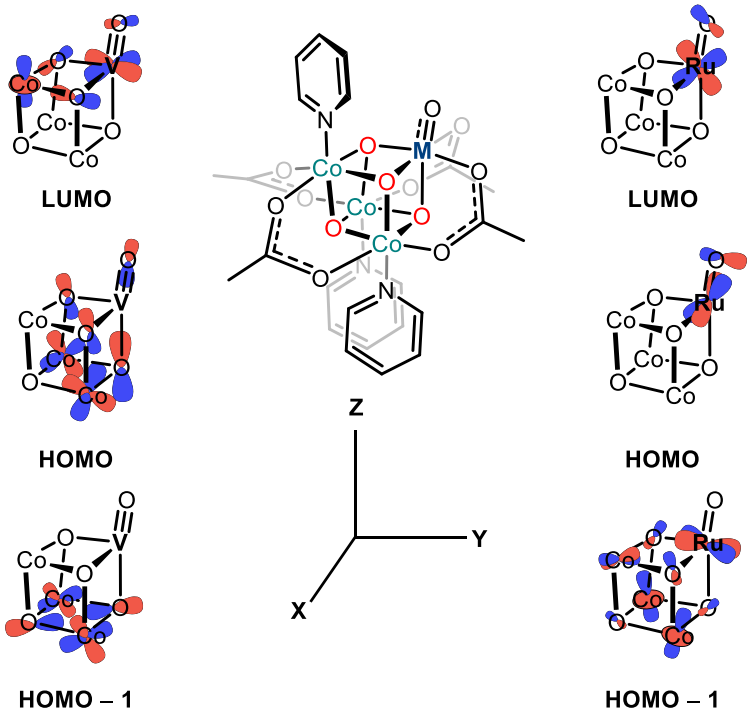


Figure 7. Molecular orbital depiction of the two isolated O–MCo_3O_4 cubanes.

Analysis of the Wiberg bond indices (WBIs) of **$HVCo_3^+$**, **VCo_3**, and **VCo_3(BCF)** substantiated the observed bonding metrics.[68] The calculated V≡O WBIs of **$HVCo_3^+$** and **VCo_3** are similar (2.59, 2.62), consistent with triple bond character, and the dominant role of the terminal oxo ligand in the bonding at the vanadium center. The WBIs determined for the V–O_{trans} moiety of **$HVCo_3^+$** (0.27) and **VCo_3** (0.73) reflect that a moderate increase in bond order occurs upon deprotonation, but that this interaction is still weaker than the V–O_{cis} interaction (1.11, 1.15).

The structures of the oxidized cubane **VCo_3^+** with multiplicities of 2, 4, and 6 were optimized and the doublet state found to be modestly lower in energy (<10 kcal/mol) than the other spin states. In the calculated structure of **VCo_3^+**, the V–O_{trans} bond distance was calculated to elongate to 2.45 Å, with concomitant contraction of the V≡O bond. Interestingly, the WBI for V–O_{trans} in this system (0.24) is even lower than that of **$HVCo_3^+$**, and a significant portion of the spin density of this system is localized on this same oxo (ρ = 0.45). The barrier to H-atom abstraction of 1,4-

cyclohexadiene by $\mathbf{VCo_3}^+$ was calculated to be 4.2 kcal/mol, 15.8 kcal/mol lower than the previously calculated barrier for H-atom abstraction by the $[Co_4O_4]$ cubane (Figure 8).[52] Similar to the $[Co_4O_4]$ system, dispersion effect play an important role in lowering that activation barrier, with exclusion of a dispersion correction resulting in a barrier that was 15.3 kcal/mol higher in energy.

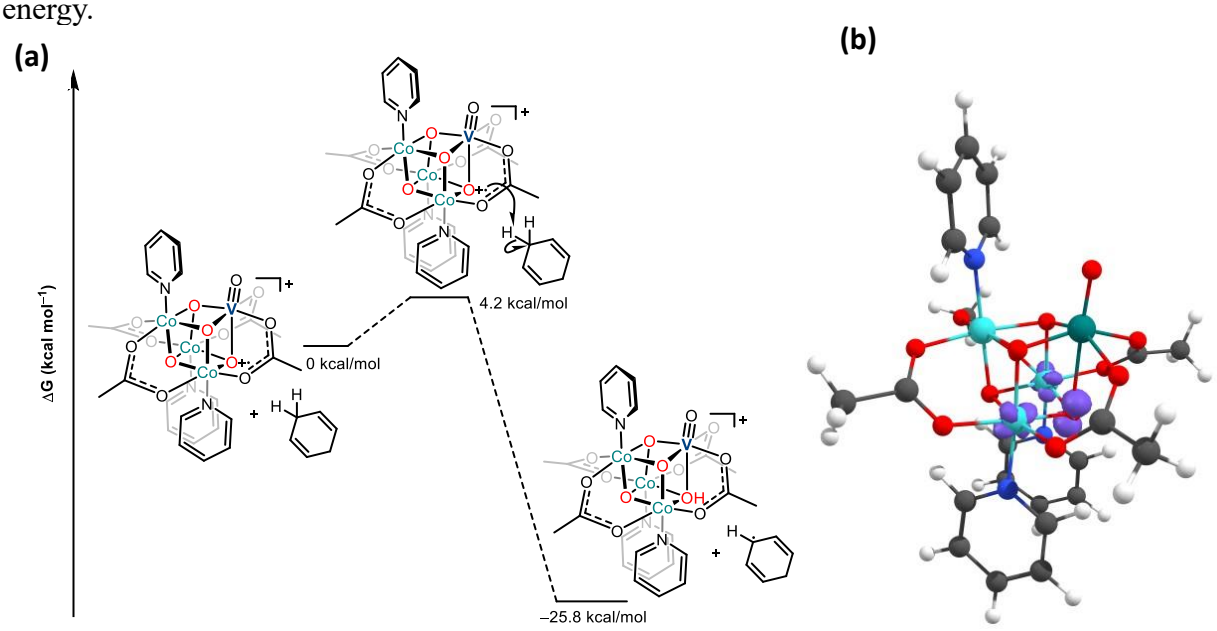


Figure 8. (a) Calculated energy profile for the reaction between 1,4-cyclohexadiene and $\mathbf{VCo_3}^+$. (b) Calculated spin-density of $\mathbf{VCo_3}^+$ shown at an isovalue of 0.033.

The barrier to H-atom abstraction by $\mathbf{VCo_3}^+$ is consistent with the observed oxidation reactivity. The low yield of anthracene in the reaction of DHA with $\mathbf{VCo_3}^+$ generated in situ is likely due to the high reactivity of this oxidized species. The DFT calculations suggest a synchronous CPET transition state.

Conclusion

The first example of a heteroatomic metal oxo cubane synthesized by way of a metal-metal exchange reaction has been reported. The vanadium-cobalt oxo cubane recenters the reactivity of heterometal-cobalt cubanes onto the cubane oxos, which is distinct from the previously observed reactivity for manganese or ruthenium heterometal-cobalt oxo cubanes.[53, 55] Electrochemical experiments indicate that incorporating an acidic, redox-inactive metal center into the $[Co_3O_4]$ core anodically shifts the oxidation potential by 0.55 V compared to the all cobalt cubane system. DFT analysis has shown that in comparison to the $[O{=}RuCo_3O_4]$ cubane system that stabilizes an oxyl radical by competitive π-bonding into the Ru SOMO, the $[O{\equiv}VCo_3O_4]$ cubane system may best be thought of as an $O{\equiv}V(OR)_4$ system that is destabilized by the dative interaction of a cubane oxo *trans* to the terminal oxo.

The synthesis of a previously inaccessible heterometal-cobalt oxo cubane demonstrates the utility of a redox metal-metal exchange route to the development of metal-heteroatom clusters. It is plausibly relevant to iron-sulfur clusters such as the $[VFe_7S_8C]$ cofactor of vanadium dependent

nitrogenases, as iron-sulfur clusters have been established to engage in rapid metal-metal exchange reactivity.[69, 70] Additionally, the observed influence of a redox-inactive V ion on the electronic structure of a metal oxo cubane has implications for the role of the Ca^{II} ion in the OEC, which is believed to precisely tune the electrophilicity of a μ_3-oxo ligand.[71-74] These effects may also be related to the oxidation reactivity of vanadium-cobalt oxide materials, which may manifest in future studies on the oxidation reactivity of the $[VCo_3O_4]$ cubane.

References:

1. Nomura, K., Vanadium. In *Comprehensive Coordination Chemistry III*, Constable, E. C.; Parkin, G.; Que Jr, L., Eds. Elsevier: Oxford, 2021; pp 237-298.
2. Hirao, T., Vanadium in Modern Organic Synthesis. *Chem. Rev.* **1997,** *97*, 2707-2724.
3. Langeslay, R. R.; Kaphan, D. M.; Marshall, C. L.; Stair, P. C.; Sattelberger, A. P.; Delferro, M., Catalytic Applications of Vanadium: A Mechanistic Perspective. *Chem. Rev.* **2019,** *119*, 2128-2191.
4. Bauer, G.; Güther, V.; Hess, H.; Otto, A.; Roidl, O.; Roller, H.; Sattelberger, S., Vanadium and Vanadium Compounds. In *Ullmann's Encyclopedia of Industrial Chemistry*, 2000.
5. Chang, C. J.; Labinger, J. A.; Gray, H. B., Aerobic Epoxidation of Olefins Catalyzed by Electronegative Vanadyl Salen Complexes. *Inorg. Chem.* **1997,** *36*, 5927-5930.
6. Adão, P.; Costa Pessoa, J.; Henriques, R. T.; Kuznetsov, M. L.; Avecilla, F.; Maurya, M. R.; Kumar, U.; Correia, I., Synthesis, Characterization, and Application of Vanadium−Salan Complexes in Oxygen Transfer Reactions. *Inorg. Chem.* **2009,** *48*, 3542-3561.
7. Ferraz-Caetano, J.; Teixeira, F.; Cordeiro, M. N. Systematic Development of Vanadium Catalysts for Sustainable Epoxidation of Small Alkenes and Allylic Alcohols *International Journal of Molecular Sciences* [Online], 2023.
8. Adam, M. S. S.; Shaaban, S.; El-Metwaly, N. M., Two Ionic Oxo-vanadate and Dioxo-Molybdate Complexes of Dinitro-Aroylhydrazone Derivative: Effective Catalysts for Epoxidation Reactions, Biological Activity, ctDNA binding, Density Functional Theory, and in Silico Investigations. *Appl. Organomet. Chem.* **2022,** *36*, e6763.
9. Ligtenbarg, A. G. J.; Hage, R.; Feringa, B. L., Catalytic oxidations by Vanadium Complexes. *Coord. Chem. Rev.* **2003,** *237*, 89-101.
10. Butler, A.; Clague, M. J.; Meister, G. E., Vanadium Peroxide Complexes. *Chem. Rev.* **1994,** *94*, 625-638.
11. Colpas, G. J.; Hamstra, B. J.; Kampf, J. W.; Pecoraro, V. L., A Functional Model for Vanadium Haloperoxidase. *J. Am. Chem. Soc.* **1994,** *116*, 3627-3628.
12. Colpas, G. J.; Hamstra, B. J.; Kampf, J. W.; Pecoraro, V. L., Functional Models for Vanadium Haloperoxidase: Reactivity and Mechanism of Halide Oxidation. *J. Am. Chem. Soc.* **1996,** *118*, 3469-3478.
13. King, A. E.; Nippe, M.; Atanasov, M.; Chantarojsiri, T.; Wray, C. A.; Bill, E.; Neese, F.; Long, J. R.; Chang, C. J., A Well-Defined Terminal Vanadium(III) Oxo Complex. *Inorg. Chem.* **2014,** *53*, 11388-11395.
14. Carter-Franklin, J. N.; Butler, A., Vanadium Bromoperoxidase-Catalyzed Biosynthesis of Halogenated Marine Natural Products. *J. Am. Chem. Soc.* **2004,** *126*, 15060-15066.
15. Clague, M. J.; Keder, N. L.; Butler, A., Biomimics of Vanadium Bromoperoxidase: Vanadium(V)-Schiff Base Catalyzed Oxidation of Bromide by Hydrogen Peroxide. *Inorg. Chem.* **1993,** *32*, 4754-4761.
16. Gribble, G. W., *Naturally Occurring Organohalogen Compounds-a Comprehensive Update*. Springer Science & Business Media: 2009; Vol. 91.
17. Wever, R.; Krenn, B., V. Vanadium Haloperoxidases. *Vanadium in Biological Systems: Physiology and Biochemistry* **2012**, pp 81-98.
18. Radosevich, A. T.; Musich, C.; Toste, F. D., Vanadium-Catalyzed Asymmetric Oxidation of α-Hydroxy Esters Using Molecular Oxygen as Stoichiometric Oxidant. *J. Am. Chem. Soc.* **2005,** *127*, 1090-1091.

19. Hanson, S. K.; Baker, R. T.; Gordon, J. C.; Scott, B. L.; Sutton, A. D.; Thorn, D. L., Aerobic Oxidation of Pinacol by Vanadium(V) Dipicolinate Complexes: Evidence for Reduction to Vanadium(III). *J. Am. Chem. Soc.* **2009,** *131*, 428-429.
20. Son, S.; Toste, F. D., Non-Oxidative Vanadium-Catalyzed C–O Bond Cleavage: Application to Degradation of Lignin Model Compounds. *Angew. Chem. Int. Ed.* **2010,** *49*, 3791-3794.
21. Pope, M. T.; Müller, A., Polyoxometalate Chemistry: An Old Field with New Dimensions in Several Disciplines. *Angew. Chem. Int. Ed.* **1991,** *30*, 34-48.
22. Mizuno, N.; Kamata, K., Catalytic Oxidation of Hydrocarbons with Hydrogen Peroxide by Vanadium-Based Polyoxometalates. *Coord. Chem. Rev.* **2011,** *255*, 2358-2370.
23. Lv, H.; Geletii, Y. V.; Zhao, C.; Vickers, J. W.; Zhu, G.; Luo, Z.; Song, J.; Lian, T.; Musaev, D. G.; Hill, C. L., Polyoxometalate Water Oxidation Catalysts and the Production of Green Fuel. *Chem. Soc. Rev.* **2012,** *41*, 7572-7589.
24. Wang, S.-S.; Yang, G.-Y., Recent Advances in Polyoxometalate-Catalyzed Reactions. *Chem. Rev.* **2015,** *115*, 4893-4962.
25. Fertig, A. A.; Brennessel, W. W.; McKone, J. R.; Matson, E. M., Concerted Multiproton–Multielectron Transfer for the Reduction of O_2 to H_2O with a Polyoxovanadate Cluster. *J. Am. Chem. Soc.* **2021,** *143*, 15756-15768.
26. Fertig, A. A.; Rabbani, S. M. G.; Koch, M. D.; Brennessel, W. W.; Miró, P.; Matson, E. M., Physicochemical Implications of Surface Alkylation of High-valent, Lindqvist-type Polyoxovanadate-Alkoxide Clusters. *Nanoscale* **2021,** *13*, 6162-6173.
27. Proe, K. R.; Schreiber, E.; Matson, E. M., Proton-Coupled Electron Transfer at the Surface of Polyoxovanadate-Alkoxide Clusters. *Acc. Chem. Res.* **2023,** *56*, 1602-1612.
28. Schreiber, E.; Fertig, A. A.; Brennessel, W. W.; Matson, E. M., Oxygen-Atom Defect Formation in Polyoxovanadate Clusters via Proton-Coupled Electron Transfer. *J. Am. Chem. Soc.* **2022,** *144*, 5029-5041.
29. VanGelder, L. E.; Forrestel, P. L.; Brennessel, W. W.; Matson, E. M., Site-selectivity in the halogenation of titanium-functionalized polyoxovanadate–alkoxide clusters. *Chem. Commun.* **2018,** *54*, 6839-6842.
30. VanGelder, L. E.; Brennessel, W. W.; Matson, E. M., Tuning the Redox Profiles of Polyoxovanadate-alkoxide Clusters via Heterometal Installation: toward Designer Redox Reagents. *Dalton Transactions* **2018,** *47*, 3698-3704.
31. Petel, B. E.; Fertig, A. A.; Maiola, M. L.; Brennessel, W. W.; Matson, E. M., Controlling Metal-to-Oxygen Ratios via M═O Bond Cleavage in Polyoxovanadate Alkoxide Clusters. *Inorg. Chem.* **2019,** *58*, 10462-10471.
32. Petel, B. E.; Meyer, R. L.; Brennessel, W. W.; Matson, E. M., Oxygen Atom Transfer with Organofunctionalized Polyoxovanadium Clusters: O-atom Vacancy Formation with Tertiary Phosphanes and Deoxygenation of Styrene Oxide. *Chem. Sci.* **2019,** *10*, 8035-8045.
33. Li, F.; VanGelder, L. E.; Brennessel, W. W.; Matson, E. M., Self-Assembled, Iron-Functionalized Polyoxovanadate Alkoxide Clusters. *Inorg. Chem.* **2016,** *55*, 7332-7334.
34. Liardet, L.; Hu, X., Amorphous Cobalt Vanadium Oxide as a Highly Active Electrocatalyst for Oxygen Evolution. *ACS Catalysis* **2018,** *8*, 644-650.
35. Jiang, C.; Yang, J.; Zhao, T.; Xiong, L.; Guo, Z.-X.; Ren, Y.; Qi, H.; Wang, A.; Tang, J., Co^{3+}-O-V^{4+} Cluster in $CoVO_x$ Nanorods for Efficient and Stable Electrochemical Oxygen Evolution. *Appl. Catal. B: Environmental* **2021,** *282*, 119571.

36. Cui, Y.; Xue, Y.; Zhang, R.; Zhang, J.; Li, X. a.; Zhu, X., Vanadium–Cobalt Oxyhydroxide Shows Ultralow Overpotential for the Oxygen Evolution Reaction. *J. Mater. Chem. A* **2019,** *7*, 21911-21917.
37. Xing, M.; Kong, L.-B.; Liu, M.-C.; Liu, L.-Y.; Kang, L.; Luo, Y.-C., Cobalt Vanadate as Highly Active, Stable, Noble Metal-free Oxygen Evolution Electrocatalyst. *J. Mater. Chem. A* **2014,** *2*, 18435-18443.
38. Huang, H.; Li, Y.; Li, W.; Chen, S.; Wang, C.; Cui, M.; Ma, T., Enhancing Oxygen Evolution Reaction Electrocatalytic Performance with Vanadium-doped Co/CoO Encapsulated in Carbon Nanorod. *Inorg. Chem. Commun.* **2019,** *103*, 1-5.
39. Anantharaj, S.; Karthick, K.; Murugan, P.; Kundu, S., V^{3+} Incorporated β-$Co(OH)_2$: A Robust and Efficient Electrocatalyst for Water Oxidation. *Inorg. Chem.* **2020,** *59*, 730-740.
40. Sullivan, K. P.; Wieliczko, M.; Kim, M.; Yin, Q.; Collins-Wildman, D. L.; Mehta, A. K.; Bacsa, J.; Lu, X.; Geletii, Y. V.; Hill, C. L., Speciation and Dynamics in the $[Co_4V_2W_{18}O_{68}]^{10-}$/Co(II)aq/$CoO_x$ Catalytic Water Oxidation System. *ACS Catalysis* **2018,** *8*, 11952-11959.
41. Soriano-López, J.; Musaev, D. G.; Hill, C. L.; Galán-Mascarós, J. R.; Carbó, J. J.; Poblet, J. M., Tetracobalt-polyoxometalate catalysts for water oxidation: Key Mechanistic Details. *J. Catal.* **2017,** *350*, 56-63.
42. Glass, E. N.; Fielden, J.; Huang, Z.; Xiang, X.; Musaev, D. G.; Lian, T.; Hill, C. L., Transition Metal Substitution Effects on Metal-to-Polyoxometalate Charge Transfer. *Inorg. Chem.* **2016,** *55*, 4308-4319.
43. McAlpin, J. G.; Stich, T. A.; Ohlin, C. A.; Surendranath, Y.; Nocera, D. G.; Casey, W. H.; Britt, R. D., Electronic Structure Description of a $[Co(III)_3Co(IV)O_4]$ Cluster: A Model for the Paramagnetic Intermediate in Cobalt-Catalyzed Water Oxidation. *J. Am. Chem. Soc.* **2011,** *133*, 15444-15452.
44. Brodsky, C. N.; Hadt, R. G.; Hayes, D.; Reinhart, B. J.; Li, N.; Chen, L. X.; Nocera, D. G., In situ characterization of cofacial Co(IV) centers in Co_4O_4 cubane: Modeling the High-Valent Active Site in Oxygen-Evolving Catalysts. *Proc. Natl. Acad. Sci. U.S.A.* **2017,** *114*, 3855-3860.
45. Nguyen, A. I.; Ziegler, M. S.; Oña-Burgos, P.; Sturzbecher-Hohne, M.; Kim, W.; Bellone, D. E.; Tilley, T. D., Mechanistic Investigations of Water Oxidation by a Molecular Cobalt Oxide Analogue: Evidence for a Highly Oxidized Intermediate and Exclusive Terminal Oxo Participation. *J. Am. Chem. Soc.* **2015,** *137*, 12865-12872.
46. Amtawong, J.; Nguyen, A. I.; Tilley, T. D., Mechanistic Aspects of Cobalt–Oxo Cubane Clusters in Oxidation Chemistry. *J. Am. Chem. Soc.* **2022**.
47. McCool, N. S.; Robinson, D. M.; Sheats, J. E.; Dismukes, G. C., A Co4O4 "Cubane" Water Oxidation Catalyst Inspired by Photosynthesis. *J. Am. Chem. Soc.* **2011,** *133*, 11446-11449.
48. Smith, P. F.; Hunt, L.; Laursen, A. B.; Sagar, V.; Kaushik, S.; Calvinho, K. U. D.; Marotta, G.; Mosconi, E.; De Angelis, F.; Dismukes, G. C., Water Oxidation by the $[Co_4O_4(OAc)_4(py)_4]^+$ Cubium is Initiated by OH^- Addition. *J. Am. Chem. Soc.* **2015,** *137*, 15460-15468.
49. McAlpin, J. G.; Surendranath, Y.; Dincă, M.; Stich, T. A.; Stoian, S. A.; Casey, W. H.; Nocera, D. G.; Britt, R. D., EPR Evidence for Co(IV) Species Produced During Water Oxidation at Neutral pH. *J. Am. Chem. Soc.* **2010,** *132*, 6882-6883.
50. Ullman, A. M.; Nocera, D. G., Mechanism of Cobalt Self-Exchange Electron Transfer. *J. Am. Chem. Soc.* **2013,** *135*, 15053-15061.
51. Nguyen, A. I.; Wang, J.; Levine, D. S.; Ziegler, M. S.; Tilley, T. D., Synthetic Control and Empirical Prediction of Redox Potentials for Co_4O_4 Cubanes over a 1.4 V Range: Implications

for Catalyst Design and Evaluation of High-Valent Intermediates in Water Oxidation. *Chem. Sci.* **2017,** *8*, 4274-4284.
52. Amtawong, J.; Skjelstad, B. B.; Balcells, D.; Tilley, T. D., Concerted Proton–Electron Transfer Reactivity at a Multimetallic Co_4O_4 Cubane Cluster. *Inorg. Chem.* **2020,** *59*, 15553-15560.
53. Amtawong, J.; Balcells, D.; Wilcoxen, J.; Handford, R. C.; Biggins, N.; Nguyen, A. I.; Britt, R. D.; Tilley, T. D., Isolation and Study of Ruthenium–Cobalt Oxo Cubanes Bearing a High-Valent, Terminal RuV–Oxo with Significant Oxyl Radical Character. *J. Am. Chem. Soc.* **2019,** *141*, 19859-19869.
54. Amtawong, J.; Skjelstad, B. B.; Handford, R. C.; Suslick, B. A.; Balcells, D.; Tilley, T. D., C–H Activation by $RuCo_3O_4$ Oxo Cubanes: Effects of Oxyl Radical Character and Metal–Metal Cooperativity. *J. Am. Chem. Soc.* **2021,** *143*, 12108-12119.
55. Nguyen, A. I.; Suess, D. L. M.; Darago, L. E.; Oyala, P. H.; Levine, D. S.; Ziegler, M. S.; Britt, R. D.; Tilley, T. D., Manganese–Cobalt Oxido Cubanes Relevant to Manganese-Doped Water Oxidation Catalysts. *J. Am. Chem. Soc.* **2017,** *139*, 5579-5587.
56. Rehder, D.; Weidemann, C.; Duch, A.; Priebsch, W., Vanadium-51 Shielding in Vanadium(V) Complexes: a Reference Scale for Vanadium Binding Sites in Biomolecules. *Inorg. Chem.* **1988,** *27*, 584-587.
57. Rehder, D., Metal NMR of Organometallic (d-block) Systems. *Coord. Chem. Rev.* **1991,** *110*, 161-210.
58. Rehder, D.; Polenova, T.; Bühl, M., Vanadium-51 NMR. In *Annual Reports on NMR Spectroscopy*, Webb, G. A., Ed. Academic Press: 2007; Vol. 62, pp 49-114.
59. Rehder, D., Vanadium NMR of Organovanadium Complexes. *Coord. Chem. Rev.* **2008,** *252*, 2209-2223.
60. Hou, D.; Kim, G.-S.; Hagen, K. S.; Hill, C. L., Synthesis and Characterization of a Polyvanadate Polyester Involving a Monodentate Alcohol, $[(n\text{-}C_4H_9)_4N][V_6O_{12}(OCH_3)_7]$. *Inorg. Chim. Acta* **1993,** *211*, 127-130.
61. Daniel, C.; Hartl, H., A Mixed-Valence V^{IV}/V^{V} Alkoxo-polyoxovanadium Cluster Series $[V_6O_8(OCH_3)_{11}]^{n+/-}$: Exploring the Influence of a μ-Oxo Ligand in a Spin Frustrated Structure. *J. Am. Chem. Soc.* **2009,** *131*, 5101-5114.
62. Agarwal, R. G.; Coste, S. C.; Groff, B. D.; Heuer, A. M.; Noh, H.; Parada, G. A.; Wise, C. F.; Nichols, E. M.; Warren, J. J.; Mayer, J. M., Free Energies of Proton-Coupled Electron Transfer Reagents and Their Applications. *Chem. Rev.* **2022,** *122*, 1-49.
63. Wise, C. F.; Agarwal, R. G.; Mayer, J. M., Determining Proton-Coupled Standard Potentials and X–H Bond Dissociation Free Energies in Nonaqueous Solvents Using Open-Circuit Potential Measurements. *J. Am. Chem. Soc.* **2020,** *142*, 10681-10691.
64. Wolff, F.; Choukroun, R.; Lorber, C.; Donnadieu, B., Reactivity of $B(C_6F_5)_3$ with Oxovanadium(V) Complexes VOL_3 (L = OCH_2CF_3, NEt_2): Formation of the Organometallic Vanadium(V) Complex $[VO(\mu\text{-}OCH_2CF_3)(OCH_2CF_3)(C_6F_5)]_2$ and the Lewis Acid Adduct $[(Et_2N)_3VOB(C_6F_5)_3]$. *Eur. J. Inorg. Chem.* **2003,** *2003*, 628-632.
65. Priebsch, W.; Rehder, D., Oxovanadium alkoxides: structure, reactivity and vanadium-51 NMR characteristics. Crystal and Molecular Structures of Tris(2-chloroethoxo)oxovanadium and Aquadichlorooxobis(tetrahydrofuran)vanadium. *Inorg. Chem.* **1990,** *29*, 3013-3019.
66. Neese, F.; Wennmohs, F.; Becker, U.; Riplinger, C., The ORCA quantum chemistry program package. *The Journal of Chemical Physics* **2020,** *152*, 224108.

67. Hadt, R. G.; Hayes, D.; Brodsky, C. N.; Ullman, A. M.; Casa, D. M.; Upton, M. H.; Nocera, D. G.; Chen, L. X., X-ray Spectroscopic Characterization of Co(IV) and Metal–Metal Interactions in Co_4O_4: Electronic Structure Contributions to the Formation of High-Valent States Relevant to the Oxygen Evolution Reaction. *J. Am. Chem. Soc.* **2016,** *138*, 11017-11030.
68. Wiberg, K. B., Application of the Pople-Santry-Segal CNDO Method to the Cyclopropylcarbinyl and Cyclobutyl Cation and to Bicyclobutane. *Tetrahedron* **1968,** *24*, 1083-1096.
69. Thompson, N. B.; Namkoong, G.; Skeel, B. A.; Suess, D. L. M., Facile and Dynamic Cleavage of Every Iron–Sulfide Bond in Cuboidal Iron–Sulfur Clusters. *Proc. Natl. Acad. Sci. U.S.A.* **2023,** *120*, e2210528120.
70. Namkoong, G.; Suess, D. L. M., Cluster-selective ^{57}Fe Labeling of a Twitch-Domain-Containing Radical SAM Enzyme. *Chem. Sci.* **2023,** *14*, 7492-7499.
71. Kanady, J. S.; Tsui, E. Y.; Day, M. W.; Agapie, T., A Synthetic Model of the Mn_3Ca Subsite of the Oxygen-Evolving Complex in Photosystem II. *Science* **2011,** *333*, 733-736.
72. Tsui, E. Y.; Tran, R.; Yano, J.; Agapie, T., Redox-Inactive Metals Modulate the Reduction Potential in Heterometallic Manganese–Oxido Clusters. *Nat. Chem.* **2013,** *5*, 293-299.
73. Lionetti, D.; Suseno, S.; Shiau, A. A.; de Ruiter, G.; Agapie, T., Redox Processes Involving Oxygen: The Surprising Influence of Redox-Inactive Lewis Acids. *JACS Au* **2024**, *4*, 344-368
74. Yano, J.; Yachandra, V., Mn_4Ca Cluster in Photosynthesis: Where and How Water is Oxidized to Dioxygen. *Chem. Rev.* **2014,** *114*, 4175-4205.

Supporting Information For

Vanadium—Cobalt Oxo Cubanes Synthesized by way of Metal-Metal Exchange.

T. Alexander Wheeler and T. Don Tilley

Table of Contents

General Considerations	**213**
Synthesis and Characterization	**215**
Reaction NMR Spectra	**240**
HR-ESI-MS	**245**
Electrochemistry:	**251**
Computational Details:	**257**
X-ray Crystallographic Details and Tables:	**265**

ALL RAW DATA AVAILABLE UPON REQUEST

General Considerations:

Unless specified otherwise, all reactions were performed in the presence of air and atmospheric water. Ambient/Room temperature is defined as 22 °C ± 4 °C and was *not* routinely measured. Yields for self-assembled reactions are reported with respect to the cobalt reagent regardless of the stoichiometry required to produce the final cluster.

Reagents:

All reagents were used as purchased without further purification. $Co(OAc)_2 \cdot 4H_2O$ was purchased from Alfa-Aesar (Tewksbury, MA), 4-*tert*butylpyridine, H_2O_2 (33-37% in water), NH_4PF_6, $Mn(OTf)_2$, pyridine (spectrophotometric grade), $AgNO_3$ (analytical grade), and $N(^nBu)_4PF_6$ (analytical grade) were purchased from Millipore-Sigma-Aldrich (Milwaukee, WI), solvent (HPLC grade) was purchased from Fischer Scientific (Hampton, NH), deuterated solvents and $H_2{}^{18}O$ were purchased from Cambridge Isotope Labs (Tewksbury, MA). When air-free techniques were applied, solvents were degassed with argon, dried and collected with a JC Meyers SDS, and stored over activated 3 Å molecular sieves in an N_2 filled glovebox. All thin-layer chromatography (TLC) plates were glass backed silica. Benzene-d_6 was dried over calcium hydride for at least one week before undergoing three freeze-pump-thaw cycles and being vacuum transferred and stored in a Teflon-capped 20 mL vial over 3 Å molecular sieves. **Co4** (and substituted derivatives; chapter 3) $(^nBu_4N)_2Ce(NO_3)_6$,[1] $VCl_4(THF)_2$[2] were synthesized according to literature procedure.

NMR Spectroscopy:

All ^1H, $^{13}C\{^1H\}$, $^{19}F\{^1H\}$, and $^{31}P\{^1H\}$ experiments were performed using Bruker Avance-300, Avance-400, Avance-400, Avance-500, Neo-500 or Avance III-600 MHz spectrometers at room temperature. ^1H and $^{13}C\{^1H\}$ NMR experiments were calibrated to residual monoprotio-isotopologue relative to tetramethylsilane (δ $CHCl_3$ = 7.26, C_6D_5H = 7.16, $CDHCl_2$ = 5.54, $CD_2H(S{=}O)CD_3$ = 2.50, $CD_2H(C{=}O)CD_3$ = 2.05 ppm, CD_2HCN = 1.94 ppm) (δ $^{13}CDCl_3$ = 77.2, $^{13}C_6D_6$ = 128.1, $^{13}CD_2Cl_2$ = 53.9, $(^{13}CD_3)_2SO$ = 39.5, $(^{13}CD_3)_2CO$ = 29.8 ppm, $^{13}CD_3CN$ = 1.3 ppm). $^{19}F\{^1H\}$ NMR were calibrated externally to 1,4-difluorobenzene, calibrated to trifluoroacetic acid (δ $C_6H_4F_2$ = -120.94 ppm). $^{31}P\{^1H\}$ experiments were calibrated externally to triphenylphosphine (δ PPh_3 = –5.0 ppm). Spectra were analyzed using MestReNova.[3] Magnetic moments were determined by the method of Evans.[4] The NMR facility at the University of California, Berkeley is partially funded by the NIH

IR Spectroscopy:

FTIR spectra were collected on solid samples (unless otherwise noted) with a Bruker Vertex 80 FTIR spectrometer equipped with a Platinum ATR as the average of 100 spectra, which were background corrected prior to measurement.

Analytical Characterization:

Electrospray ionization mass spectrometry (HR-ESI-MS) experiments were performed using a PerkinElmer time-of-flight mass spectrometer AxION 2 TOF tuned and calibrated in the positive ion range. **Note that the specific TOF spectrometer used in these studies is no longer**

operational as a high-resolution spectrometer due to the age/wear of the instrument, however the data are presented as supporting evidence where possible. Microanalyses were conducted by Dr. Elena Kreimer at the Microanalytical Facility at the University of California, Berkeley using a Perkin Elmer CHNS 2400 Series II Analyzer or ThermoFisher Flash Smart Elemental Analyzer.

X-ray Crystallography:

Single crystal X-ray diffraction data was collected at the Advanced Light Source beamline 12.2.1 using a Bruker D85 three-circle diffractometer equipped with a PHOTON II CCD area detector using synchrotron radiation (λ = 0.7288 Å) monochromated using a channel-cut Si(111) monochromator. Structure solution, modeling, and refining was performed using both the OLEX2 and Shelxle GUI and SHELX software packages. [5-8]

Electrochemical Experiments:

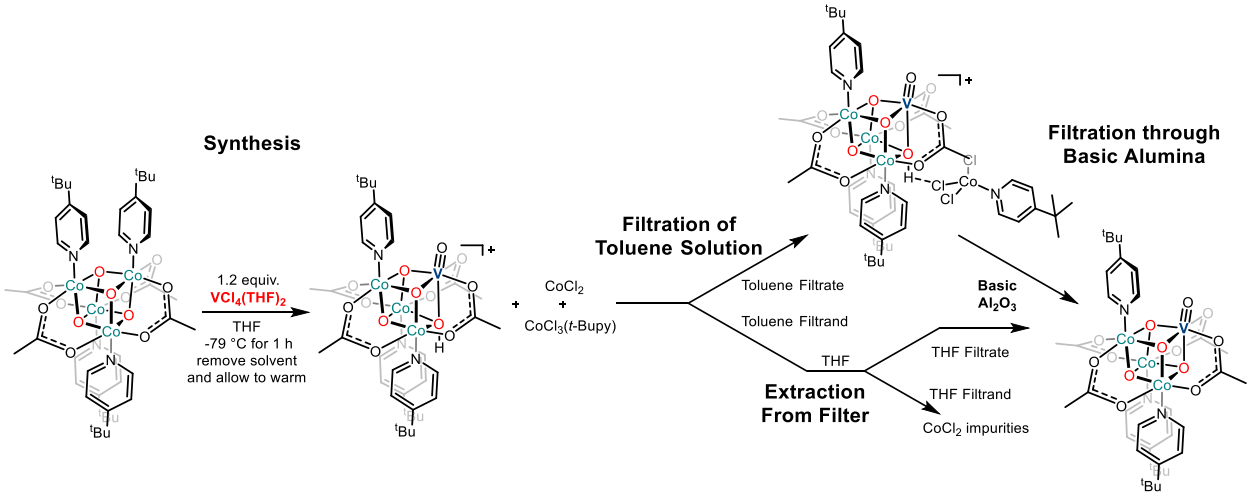
Electrochemical experiments were performed at ambient temperature using a BASi EC Epsilon potentiostat/galvanostat and a PWR-3 Power Module. A 3 mm diameter glassy carbon electrode was used as the working electrode, which was polished with 0.30 μm alumina, rinsed with deionized water, followed by 0.05 μm alumina, rinsed with water, then HPLC grade acetone, and dried in air before use. Platinum and silver wires were used as the counter and reference electrodes respectively. Analytical grade tetrabutylammonium hexafluorophosphate (0.2 M) was used as the electrolyte in HPLC grade MeCN or CH_2Cl_2. Ferrocene was added at the end of each experiment as an internal reference against the half-potential of $[Cp_2Fe]^0/[Cp_2Fe]^+$ (Fc/Fc^+). Internal resistance compensation was carried out for each experiment to correct for solution resistance. Analyte concentration was 1.0 mM in all cases. The E° values reported are the midpoints of the anodic (E_{pa}) and cathodic (E_{pc}) peak potentials, calculated as $E^\circ = (E_{pa} + E_{pc})/2$. The reversibility of the redox events was determined by the peak-to-peak separations and $\Delta E_p = E_{pa} - E_{pc}$. The peak currents were determined with EC Lab software.

UV-visible Spectroscopy:

UV-visible spectra were collected at 24-25 °C unless otherwise specified using a Shimadzu UV-2600i spectrometer equipped with a CPS multicell. Quartz cuvettes with screw cap tops or Teflon stoppers were used to limit the influence of solvent evaporation. Spectra were baseline corrected and zeroed with the solvent employed in the reaction. Spectra were analyzed using UVProbe software. Molar absorptivity values were determined from the slope of five different concentrations of the compound in MeCN or CH_2Cl_2. All other spectra are reported as absorbances ,which by definition is unitless.

Experimental:

Notes on the Synthesis of [HVCo$_3$][Co] and VCo$_3$. To directly obtain the highest yield of **VCo$_3$** requires the isolation of **[HVCo$_3$][Co]**, and the synthetic procedure to isolate these species is sequential. The procedure presented below is therefore broken up into two sections, one of which isolates **[HVCo$_3$][Co]**, and the other isolates **VCo$_3$**. When **VCo$_3$** was the desired product, the **[HVCo$_3$][Co]** produced in this way was converted to **VCo$_3$** immediately following isolation by passage of a THF solution of **[HVCo$_3$][Co]** through a pipette of basic alumina (typically 4-5 cm). A diagram showing the synthesis and products is shown below.



Synthesis of VCo$_3$[Co]: A video recording of portions of this synthesis is available. In an N_2 filled glovebox, a 200 mL Schlenk tube was charged with a stir bar, **Co$_4$**, (2.7252 g, 2.532 mmol), and THF (10 mL), then the solution was stirred vigorously. A separate 100 mL Schenk tube was charged with a stir bar, $VCl_4(THF)_2$ (1.0348 g, 3.0800 mmol) and THF (20 mL), and then the solution was stirred vigorously. Both Schlenk tubes were transferred from the glovebox and cycled onto a Schlenk line, where THF (20 mL) was added to both Schlenk tubes. The solution of $VCl_4(THF)_2$ was then submerged in a dry ice acetone bath and stirred vigorously. Water (60.0 µL, 0.06 mg, 3.798 mmol) was added to the Schlenk tube containing **Co$_4$**. The solution of **Co$_4$** was cannula transferred dropwise over 15 min into the solution of $VCl_4(THF)_2$, over which time a color change from olive-green to dull orange red was observed. After 1 h, the atmosphere was opened to vacuum. After bumping due to solvent removal slowed, the dry ice acetone bath was removed. The volatiles were removed *in vacuo* as the solution warmed slowly, over which time the solution turned a vibrant green-blue. Dark green solids result after *ca.* 2 h. Toluene (25 mL) was added, and the solution was vigorously agitated to dislodge the solids, resulting in a suspension of dark-blue/green solids in a dark green solution. The solution was then filtered through a glass wool plug on a cannula into a 100 mL Schlenk tube. The washing process was repeated two more times, resulting in *ca*. 75 mL of toluene solution, which was concentrated to roughly 2/3 the initial volume *in vacuo*, and then both Schlenk tubes were transferred into a glovebox. The toluene solution was transferred into three 20 mL vials that were capped ajar to allow the vapors to slowly diffuse. After 12-36 h, blue crystals of **VCo$_3$H$^+$**[Co] (suitable for single-crystal X-ray diffraction) resulted, which were collected by decanting the toluene solution, washing with –35 °C toluene (*ca*. 6 mL), and drying *in vacuo* to give 0.4552 g of **VCo$_3$H$^+$** (15% yield).

Characterization data: ^{1}H NMR (400 MHz, acetonitrile-d_3) δ 8.81 (d, J = 6.6 Hz, 2H), 8.06 (d, J = 5.5 Hz, 4H), 7.81 (d, J = 6.9 Hz, 2H), 7.27 (s, 4H), 2.24 (s, 6H), 2.13 (s, 6H), 1.42 (s, 6H), 1.26 (s, 18H). ^{51}V NMR (105 MHz, acetonitrile-d_3) – 303 ppm. IR (cm^{-1}): 3168 (w), 2964 (w), 2934 (w), 2907 (w), 2872 (w), 1616 (m), 1538 (s), 1533 (s, sh), 1520 (s), 115(s), 1505 (s), 1500 (s), 1464 (s), 1406 (vs), 1369 (s), 1342 (s), 1273 (m), 1226 (m), 1202 (w), 1122 (w), 1101 (w), 1071 (s), 1039 (w), 1024 (w/m), 987 (s), 942 (w), 834 (s), 760 (w), 733 (w), 708 (w),680 (s), 668 (s), 625 (s), 614 (s), 570 (s), 533 (s). HR-ESI-MS: calc'd for, 950.0930; found, 950.1562. Anal. Calcd for $C_{44}H_{65}Cl_3Co_4N_4O_{13}V$: C, 43.49; H, 3.22; N, 2.58. Found: C, 41.51; H, 3.68; N, 2.26.

The toluene-insoluble material was dissolved in THF (20 mL) and loaded onto 20 mL of basic alumina in a 30 mL filter frit on a Büchner flask. The alumina was washed with THF (*ca*. 30 mL), and vacuum was periodically applied to extract the THF from the alumina plug, resulting in a jade-green solution. Caution should be taken to avoid overextraction, which results in a dark blue (presumably) $CoCl_2$ solvate. The solvent was removed *in vacuo* resulting in a jade-green solid. The solids were transferred to a 20 mL vial, which was charged with Et_2O (20 mL) and a stir bar, which was stirred vigorously for 16 h. The solution was vacuum filtered through a fritted glass funnel, the solids were washed with ether (10 mL), and the Et_2O solution was discarded. The solids were transferred to a 20 mL vial and dried *in vacuo* to give 0.3753 g of **VCo$_3$** (15.6% yield). Crystals suitable for single-crystal X-ray diffraction were grown by vapor diffusion of pentane into a saturated THF solution of **VCo$_3$** containing one equiv of phenylisocyanate at –35 °C over 24 h (after allowing the vapor to diffuse at room temperature for 2 h). Multiple attempts to grow crystals under the same conditions without phenyl isocyanate resulted in samples that diffracted to 0.95 Å. The isocyanate may seed crystals of **VCo$_3$** or react with the products of a small amounts of **VCo$_3$** decomposition, which encourages the growth of microcrystals. Note that the material prepared in this way was less pure than the material prepared from crystallized **VCo$_3$**[Co], as determined by the ratio of the equivalent and inequivalent pyridine ligand protons (see figures S & S), which is attributed to trace **VCo$_3$H**$^+$[X] (X = $CoCl_3$(*t*-Bupy)$^-$ or Cl^- or $CoCl_4^{2-}$) as an impurity.

Characterization data: ^{1}H NMR (400 MHz, acetonitrile-d_3) δ 8.97 (d, J = 6.8 Hz, 2H), 8.21 (d, J = 6.9 Hz, 4H), 7.80 (d, J = 6.8 Hz, 2H), 7.18 (d, J = 6.9 Hz, 4H), 2.17 (s, 6H), 1.99 (s, 6H), 1.46 (s, 9H), 1.25 (s, 18H). ^{13}C{^{1}H} NMR (126 MHz, acetonitrile-d_3) δ 187.7, 182.8, 164.6, 163.6, 153.7, 152.3, 123.1, 121.7, 35.8, 35.4, 30.7, 30.6, 26.2, 25.1. ^{51}V NMR (105 MHz, acetonitrile-d_3) δ –263. IR (cm^{-1}): 2962 (w), 2905 (w), 2870 (w), 1616 (w), 1533 (m), 1498 (m), 1416 (s), 1367 (m), 1343 (m), 1272 (w), 1223 (m), 1121 (w), 1070 (m), 1028 (w), 995 (w), 930 (s), 863 (w), 828 (s), 731 (w/m), 690 (s), 673 (s), 628 (s), 572 (s), 533 (s). UV-vis (MeCN) λ_{max}, nm (ε, M^{-1} cm^{-1}): 216 (6348), 306 (1331), 381 (351). HR-ESI-MS: calc'd for, 950.0930; found, . Anal. Calcd for $C_{35}H_{51}Co_3N_3O_{13}V$: C, 44.29; H, 5.41; N, 4.43. Found: C, 44.29; H, 5.35; N, 4.41. Anal. Calcd **for less pure material**: $C_{35}H_{51}Co_3N_3O_{13}V$: C, 44.29; H, 5.41; N, 4.43. Found: C, 43.98; H, 5.65; N, 4.29.

Synthesis of O≡VCo$_3$O$_4$(4-methoxybenzoate)$_4$(*t*-Bupy)$_3$:

In a N_2 filled glovebox, a 20 mL vial was charged with a stir bar, Co_4O_4(OBz-OMe)$_4$(*t*-Bupy)$_4$ (0.0500 g, 0.0346 mmol), 3,5-di*tert*-butylphenol (0.0107 g, 0.0519 mmol), and THF (5 mL). The solution was stirred vigorously until the reagents were completely dissolved. A solution of VCl_4(DME) (0.0137 g, 0.0484 mmol) in THF (4 mL) was prepared in a separate 20 mL vial, and both vials were placed in an N_2 chilled cold well. After cooling for 2 min, half of the THF solution of VCl_4(DME) was added dropwise over 1 min to the solution of [Co_4O_4] cubane, which was

swirled over the course of the addition. The orange reaction solution was removed from the cold well, placed on a stir plate, and magnetically stirred for 2 min. The vial was returned to the cold well, and chilled for 2 min; the rest of the THF solution of VCl_4(DME) was added dropwise over 1 min to the reaction solution. The vial containing the reaction solution was returned to the stir plate and stirred vigorously for 5 minutes. For the next 1.5 h, the reaction solution was alternated between stirring for 5 min, and being placed in the freezer at –35 °C for 10 min. Over this time, the reaction solution turned bright blue-green. The volatiles were removed *in vacuo* to give dark blue solids. The solids were partially dissolved in toluene (5 mL) and the suspension was filtered through a Celite® plug (1 cm) supported by glass wool in a pipette into a 20 mL vial. The toluene solution was capped ajar, and the vapors were allowed to slowly evaporate. The solids were washed from the filter with THF (2 × 2.5 mL), and the THF solution was filtered through a pipette filled with basic alumina (4 cm) supported by glass wool. The alumina was washed with THF until the eluant was pale green, at which point the plug was discarded. The volatiles were removed *in vacuo* to give 0.0036 g of **VCo_3(OBz-OMe)** (8% yield). After 24 h, blue crystals had precipitated from the toluene solution; the solvent was decanted from the vial, and the crystalline material was washed with –35 °C toluene (1 mL). The blue crystals were dissolved in THF (2 mL) and filtered through a pipette filled with basic alumina (3 cm) supported by glass wool, which was washed with THF until the eluant was pale green. The volatiles were removed *in vacuo* to give 0.0053 g of **VCo_3(OBz-OMe)** as a jade green solid (12% yield; 20% combined yield).

Characterization data: ^{1}H NMR (400 MHz, acetonitrile-d_3) δ 9.08 (d, J = 6.1 Hz, 2H), 8.29 (d, J = 6.1 Hz, 4H), 7.88 (d, J = 8.6 Hz, 4H), 7.85 (d, J = 8.6 Hz, 4H), 7.80 (d, J = 6.2 Hz, 2H), 7.16 (d, J = 6.3 Hz, 4H), 6.91 (d, J = 8.9 Hz, 4H), 6.90 (d, J = 8.8 Hz, 4H), 3.81 (s, 12H), 1.43 (s, 9H), 1.23 (s, 18H). ^{51}V NMR (105 MHz, acetonitrile-d_3) δ –259. IR (cm^{-1}): 2965 (w), 2909 (w), 2872 (w), 1618 (m), 1600 (m), 1558 (m), 1529 (m), 1504 (m), 1448 (w), 1390 (s), 1274 (w), 1226 (w), 1177 (w), 1071 (w), 1027 (w), 988 (w shoulder), 959 (sh), 936 (s), 830 (s), 797 (s), 718 (s), 676 (s), 633 (s), 569 (s), 484 (m), 465 (m), 438 (m), 403 (w). HR-ESI-MS: calc'd for: $C_{59}H_{68}Co_3N_3O_{17}V^+$, 1318.1979; found, 1318.1763.

Synthesis of O≡VCo_3O_4(4-nitrobenzoate)$_4$(*t*-Bupy)$_3$:

This procedure is very similar to the procedure for the synthesis of **VCo_3(OBz-OMe)** above, with key differences in the purification; for consistency, the synthetic procedure for **VCo_3(OBz-OMe)** is repeated below. In a N_2 filled glovebox, a 20 mL vial was charged with a stir bar, Co_4O_4(OBz-NO_2)$_4$(*t*-Bupy)$_4$ (0.1000 g, 0.0664 mmol), 3,5-di*tert*-butylphenol (0.0137 g, 0.0664 mmol), and THF (5 mL). The solution was stirred vigorously until the reagents were completely dissolved. A solution of VCl_4(DME) (0.0263 g, 0.0929 mmol) in THF (4 mL) was prepared in a separate 20 mL vial, and both vials were placed in an N_2 chilled cold well. After cooling for 2 min, half of the THF solution of VCl_4(DME) was added dropwise over 1 min to the solution of [Co_4O_4] cubane, which was swirled over the course of the addition. The orange reaction solution was removed from the cold well, placed on a stir plate, and magnetically stirred for 2 min. The vial was returned to the cold well, and chilled for 2 min; the rest of the THF solution of VCl_4(DME) was added dropwise over 1 min to the reaction solution. The vial containing the reaction solution was returned to the stir plate and stirred vigorously for 5 minutes. For the next 1.5 h, the reaction solution was alternated between stirring for 5 min, and being placed in the freezer at –35 °C for 10 min. Over this time, the reaction solution became dark brown. The volatiles were removed *in vacuo* to give dark brown-blue solids. The solids were partially dissolved in toluene (5 mL) and the suspension was filtered through a Celite® plug (1 cm) supported by glass wool in a pipette into a 20 mL vial,

and the filter was discarded. The toluene solution was capped ajar, and the vapors were allowed to slowly evaporate. After 24 h, blue crystals had precipitated from the toluene solution; the solvent was decanted from the vial, and the crystalline material was washed with –35 °C toluene (1 mL). The blue crystals were dissolved in THF (2 mL) and filtered through a pipette filled with basic alumina (5 cm) supported by glass wool, which was washed with THF until the eluant was pale green. The volatiles were removed *in vacuo* to give 0.0156 g of **VCo_3(OBz-NO_2)** as a jade green solid (17% yield).

Characterization data: ^{1}H NMR (400 MHz, acetonitrile-d_3) δ 9.08 (d, J = 6.8 Hz, 2H), 8.31 (d, J = 6.8 Hz, 4H), 7.93 (d, J = 7.0 Hz, 4H), 7.90 (d, J = 7.4 Hz, 4H), 7.82 (d, J = 6.8 Hz, 2H), 7.43 (d, J = 7.8 Hz, 4H), 7.41 (d, J = 7.4 Hz, 4H), 7.21 (m, 4H), 1.44 (s, 9H), 1.24 (s, 18H). ^{51}V NMR (105 MHz, acetonitrile-d_3) δ –__. IR (cm^{-1}): 2965 (w), 2940 (w), 2911 (w), 2874 (w), 2841 (w), 1606 (m), 1548 (m), 1511 (m), 1461 (w), 1417 (m), 1386 (s), 1313 (w), 1253 (s), 1172 (m), 1147 (w), 1106 (w), 1071 (w), 1027 (m), 986 (w), 936 (shoulder), 848 (s), 830 (s), 778 (s), 730 (s), 701 (s), 637 (s), 620 (s), 571 (s), 511 (s).

Synthesis of O≡VCo_3O_4(4-*tert*-butylbenzoate)$_4$(*t*-Bupy)$_3$:

This procedure is very similar to the procedure for the synthesis of **VCo_3(OBz-NO_2)** above, with key differences in the purification; for consistency, the synthetic procedure for **VCo_3(OBz-NO_2)** is repeated below. In a N_2 filled glovebox, a 20 mL vial was charged with a stir bar, Co_4O_4(OBz-*t*Bu)$_4$(*t*-Bupy)$_4$ (0.0460 g, 0.0292 mmol), 3,5-di*tert*-butylphenol (0.0107 g, 0.0519 mmol), and THF (5 mL). The solution was stirred vigorously until the reagents were completely dissolved. A solution of VCl_4(DME) (0.0137 g, 0.0485 mmol) in THF (4 mL) was prepared in a separate 20 mL vial, and both vials were placed in an N_2 chilled cold well. After cooling for 2 min, half of the THF solution of VCl_4(DME) was added dropwise over 1 min to the solution of [Co_4O_4] cubane, which was swirled over the course of the addition. The orange reaction solution was removed from the cold well, placed on a stir plate, and magnetically stirred for 2 min. The vial was returned to the cold well, and chilled for 2 min; the rest of the THF solution of VCl_4(DME) was added dropwise over 1 min to the reaction solution. The vial containing the reaction solution was returned to the stir plate and stirred vigorously for 5 minutes. For the next 1.5 h, the reaction solution was alternated between stirring for 5 min, and being placed in the freezer at –35 °C for 10 min. Over this time, the reaction solution became dark blue-green. The volatiles were removed *in vacuo* to give dark blue solids. The solids were dissolved in toluene (5 mL) and the suspension was filtered through a Celite® plug (1 cm) supported by glass wool in a pipette into a 20 mL vial. The toluene solution was capped ajar, and the vapors were allowed to slowly evaporate. The solids were washed from the filter with THF (2 × 1 mL), and the THF solution was filtered through a pipette filled with basic alumina (4 cm) supported by glass wool. The alumina was washed with THF until the eluant was pale green, at which point the plug was discarded. The volatiles were removed *in vacuo* to give a dark green solid. The green material was washed with pentane (2 × 4 mL), and the volatiles removed *in vacuo* to give 0.0039 g of **VCo_3(OBz-*t*Bu)** as a jade green solid (9% yield). After 48 h, blue crystals had precipitated from the toluene solution; the solvent was decanted from the vial, and the crystalline material was washed with –35 °C toluene (1 mL). The blue crystals were dissolved in THF (2 mL) and filtered through a pipette filled with basic alumina (5 cm) supported by glass wool, which was washed with THF until the eluant was pale green. The volatiles were removed *in vacuo* to give 0.0073 g of **VCo_3(OBz-*t*Bu)** as a jade green solid (18% yield, 27% combined yield).

Characterization data: ^{1}H NMR (400 MHz, acetonitrile-d_3) δ 9.07 (d, J = 6.4 Hz, 2H), 8.31 (d, J = 6.8 Hz, 4H), 7.86 (d, J = 8.5 Hz, 4H), 7.83 (t, J = 8.4, 6.8 Hz, 4H), 7.80 (s, 2H), 7.47 (d, J = 3.2 Hz, 4H), 7.45 (d, J = 3.2 Hz, 4H), 7.17 (m, 4H), 1.43 (s, 9H), 1.31 (s, 36H), 1.23 (s, 18H). ^{51}V NMR (105 MHz, acetonitrile-d_3) δ –__. IR (cm^{-1}): 2967 (w), 2907 (w), 2870 (w), 1618 (w), 1590 (w), 1527 (m), 1500 (m), 1463 (w), 1382 (s), 1274 (w), 1224 (w), 1174 (w), 1071 (w), 1027 (m), 936 (w), 830 (w), 718 (s), 693 (s), 635 (s), 573 (s), 484 (m), 448 (m), 407 (w). HR-ESI-MS: calc'd for: $C_{64}H_{84}Co_3N_5O_{11}V$, 1326.3603; found, 1325.2364.

Synthesis of (B(C$_6$F$_5$)$_3$)O≡VCo$_3$O$_4$(OAc)$_4$(*t*-Bupy)$_3$:

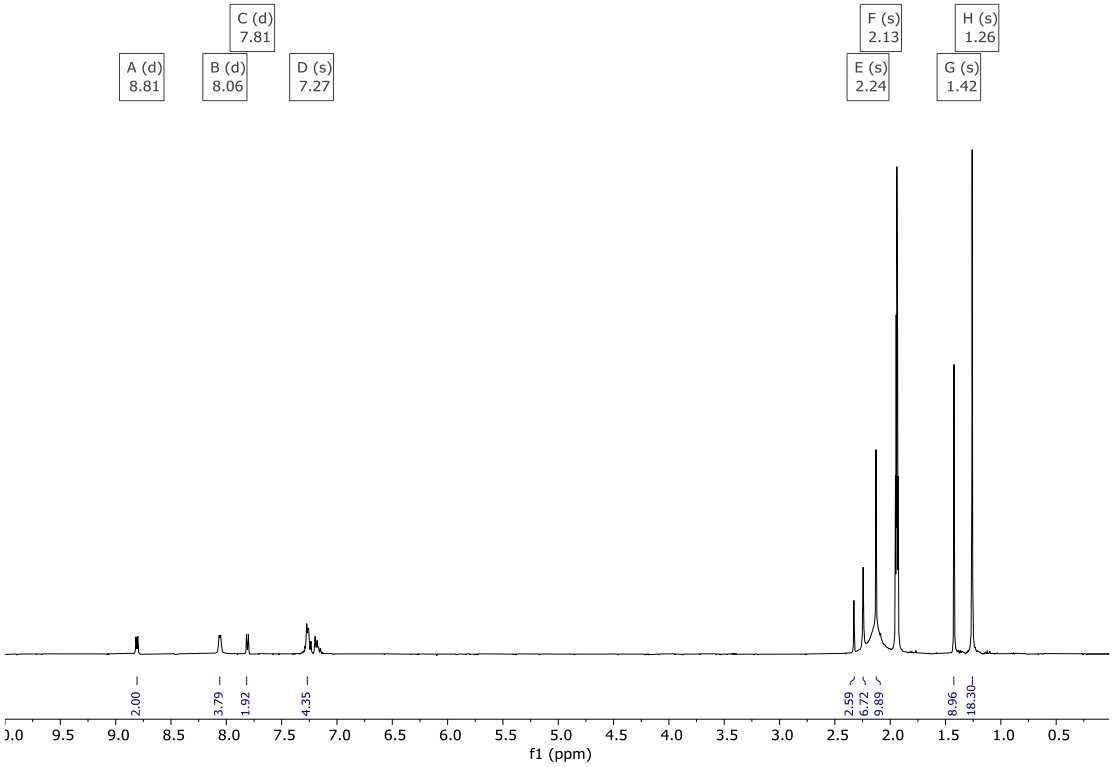
A 20 mL vial was charged with a stir bar, **VCo$_3$** (0.0250 g, 0.0263 mmol), tris(pentafluorophenyl)borane (0.0139, 0.0271 mmol, and *ortho*-difluorobenzene (*o*DFB). The solution was stirred vigorously for 1 min, after which the volatiles were removed *in vacuo* giving an oily, dark red solid. The solids were washed with pentane (5 mL), and the volatiles removed *in vacuo*. The solids were scraped from the sides of the vial, pentane was added (8 mL) and the suspension was stirred vigorously for 5 min. The suspension was filtered through a Celite® plug (1 cm) supported by glass wool in a pipette, the solids were washed with pentane (2 mL), and the extracts were discarded. The solids were washed from the filter with *o*DFB (2 × 1.5 mL) into a 20 mL vial, and the filter was discarded. The volatiles were removed *in vacuo*, resulting in 0.0369 g of **(BCF)VCo$_3$** (95% yield). Crystals suitable for single-crystal x-ray diffraction studies were grown by pentane vapor diffusion into a saturated toluene solution of **(BCF)VCo$_3$** at room temperature over several days, resulting in red plates of **(BCF)VCo$_3$**.

Characterization data: ^{1}H NMR (400 MHz, benzene-d_6) δ 9.30 (d, J = 6.8 Hz, 2H), 8.32 (d, J = 6.8 Hz, 4H), 7.35 (d, J = 6.8 Hz, 2H), 6.55 (d, J = 6.9 Hz, 4H), 1.95 (s, 6H), 1.69 (s, 6H), 1.07 (s, 9H), 0.79 (s, 18H). ^{11}B{^{1}H} NMR (128 MHz) δ 1.5. ^{19}F{^{1}H} NMR (376 MHz, benzene-d_6) δ –130.44 (d, J = 17.2 Hz, 2F), –160.21 (t, J = 20.4 Hz, 1F), –165.50 (t, J = 19.3 Hz,2F). ^{51}V NMR (105 MHz, acetonitrile-d_3) δ –52. IR (cm^{-1}): 2971 (w), 2940 (w), 2913 (w), 2876 (w), 1645 (m), 1619 (m), 1535 (m), 1513 (s), 1465 (s), 1423 (s), 1372 (m), 1349 (m), 1276 (m), 1224 (m), 1204 (w), 1089 (s), 1073 (s), 1029 (w), 979 (s), 898 (s), 847 (m), 832 (s), 791 (m), 772 (m), 762 (m), 749 (m) 732 (s), 695 (s), 677 (s), 654 (s), 633 (s), 598 (s), 571 (s), 525 (s), 484 (m), 467 (m), 413 (w).HR-ESI-MS: calc'd for: $C_{55}H_{54}BCo_3F_{15}N_5O_{11}V$, 1484.1109; found, 1483.9903. Elemental analysis: calc'd for $C_{53}H_{51}BCo_3F_{15}N_3O_{13}V$: C, 43.56; H, 3.52; N, 2.88. Found: C, 44.71; H, 3.87; N, 2.66.

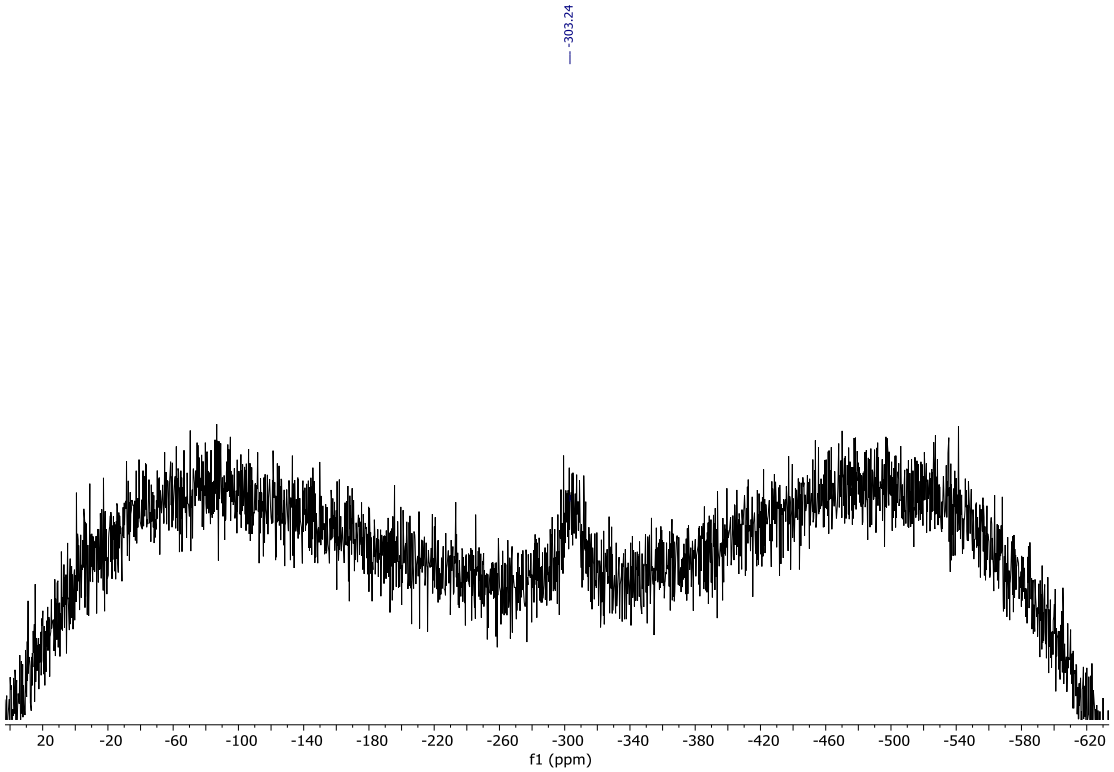
Synthesis of O≡VCo$_3$O$_4$(OAc)$_4$(*t*-Bupy)$_3$[NO$_3$]:

A 20 mL vial was charged with a stir bar, **VCo$_3$** (0.0500 g, 0.0526 mmol), and THF (1.5 mL). The rapidly stirred solution was treated with a THF (2 mL) solution of (^{n}Bu$_4$N)$_2$Ce(NO$_3$)$_6$ (0.0525 g, 0.0526 mmol). A color change from jade-green to brown-red was observed. After 5 min, the volatiles were removed *in vacuo* to give an oily brown solid. The solid was washed with pentane, and the volatiles removed *in vacuo*. The solids were scraped from the vial, toluene (5 mL) was added, and the oily suspension was stirred vigorously for 30 min. The suspension was filtered through a Celite® plug (1 cm) supported by glass wool in a pipette. The residual oils in the vial were washed with toluene (2 x 5 mL), filtered through the plug and the extracts were discarded. The oils were washed from the vial and the filter with *o*DFB (2 × 1.5 mL) into a 20 mL vial, and the filter was discarded. The volatiles were removed *in vacuo*, resulting in 0.0460 g of **VCo$_3$**[NO$_3$] (86% yield).

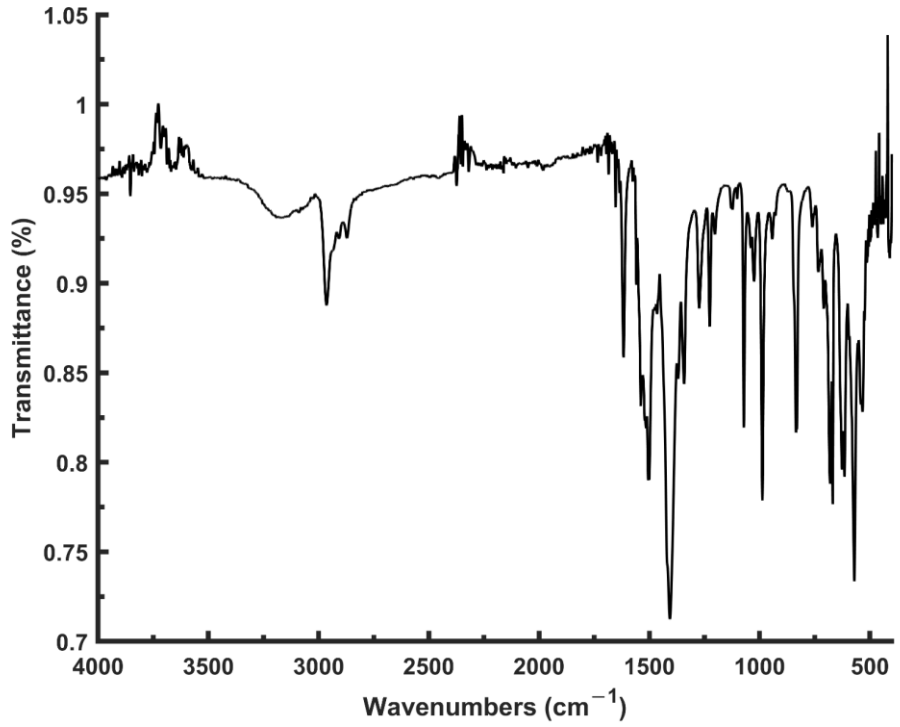
Characterization data: ^{1}H NMR (400 MHz, acetonitrile-d_3) δ 8.82 (d, J = 6.8 Hz, 2H), 8.28 (d, J = 6.8 Hz, 4H), 7.82 (d, J = 6.8 Hz, 2H), 7.35 (d, J = 6.9 Hz, 4H), 2.19 (s, 6H), 2.13 (s, 6H), 1.43 (s, 9H), 1.26 (s, 18H). ^{51}V NMR (105 MHz, acetonitrile-d_3) δ –310. IR (cm^{-1}): 2966 (m), 2937 (w), 2909 (w), 2876 (w), 1619 (m), 1500 (s), 1464 (s), 1409 (s), 1370 (s), 1343 (s), 1291 (s), 1226 (m), 1204 (m), 1128 (w), 1071 (m), 1031 (m), 989 (s), 834 (s), 817 (s), 736 (s), 708 (s), 681 (s), 627 (s), 596 (s), 573 (s), 539 (s). UV-vis (MeCN) λ_{max}, nm (ε, M^{-1} cm^{-1}): 217 (5248), 304 (1099), 381 (351).



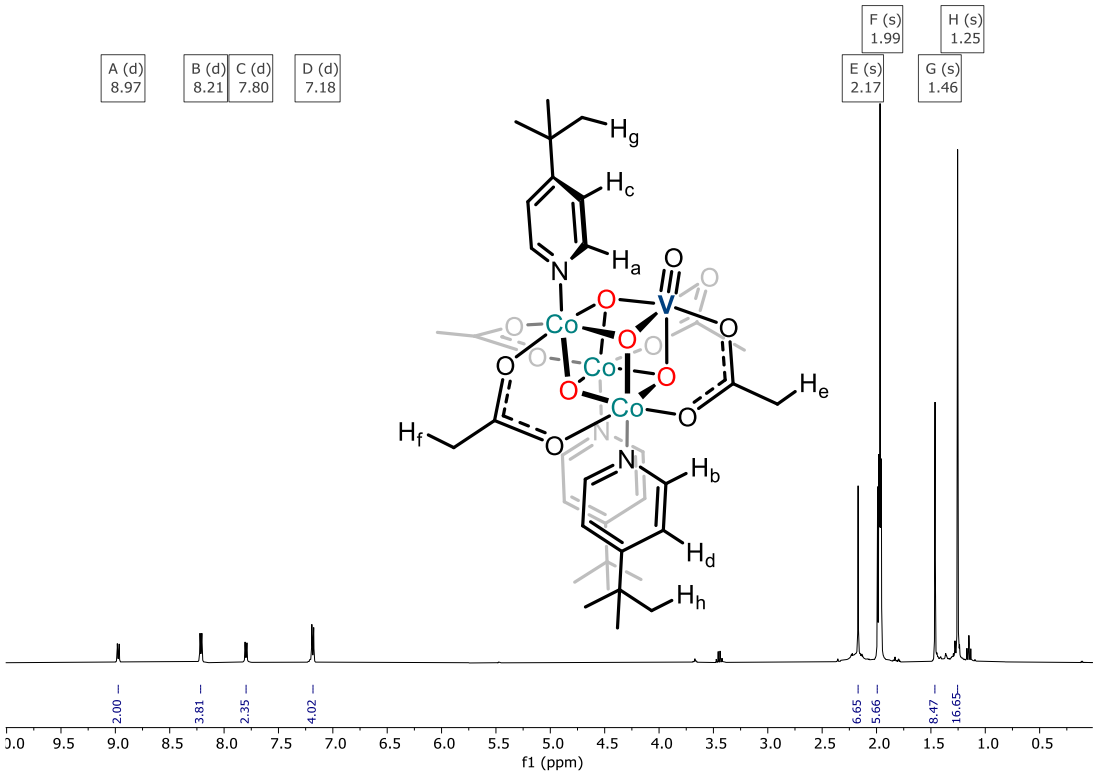
S1. ^{1}H NMR of [OVCo$_3$(OH)(O)$_3$(OAc)$_4$(*t*-Bupy)$_3$][CoCl$_3$(*t*-Bupy)] (400 MHz, acetonitrile-d_3), with residual toluene (*ca*. 0.9 equiv) of crystallization present in sample.



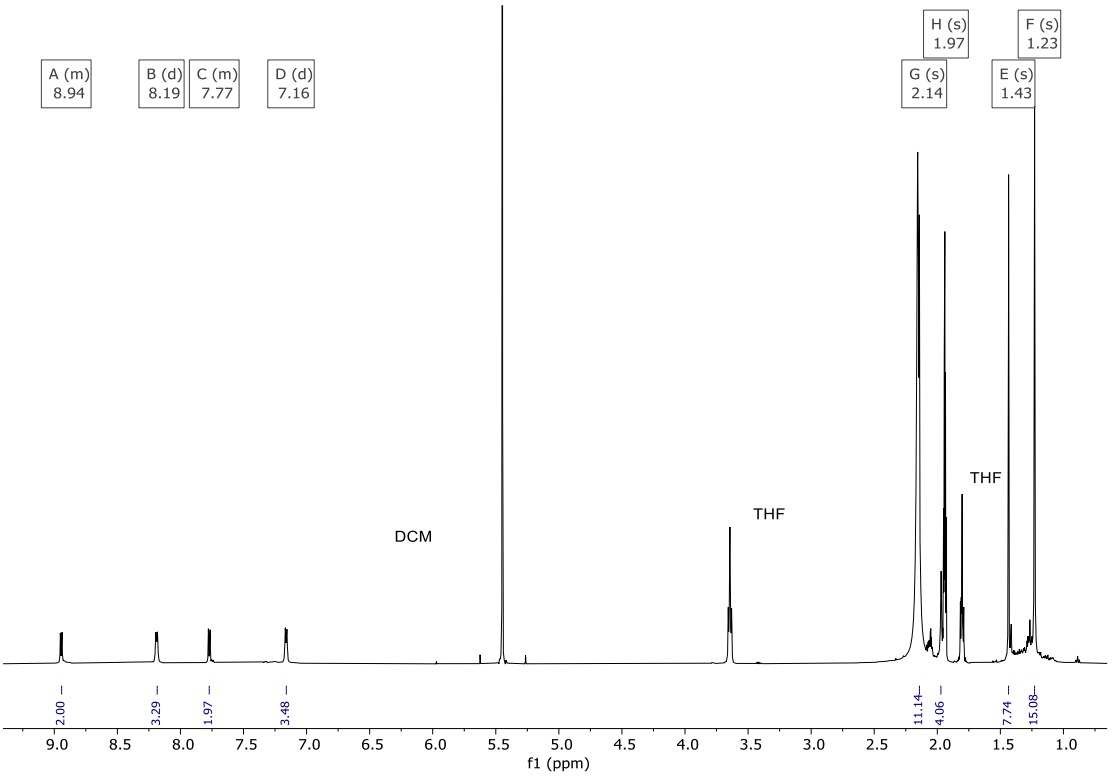
S2. ^{51}V NMR spectrum of [OVCo$_3$(OH)(O)$_3$(OAc)$_4$(*t*-Bupy)$_3$][CoCl$_3$(*t*-Bupy)] **VCo$_3$**[Co] (105.2 MHz, acetonitrile-d_3).



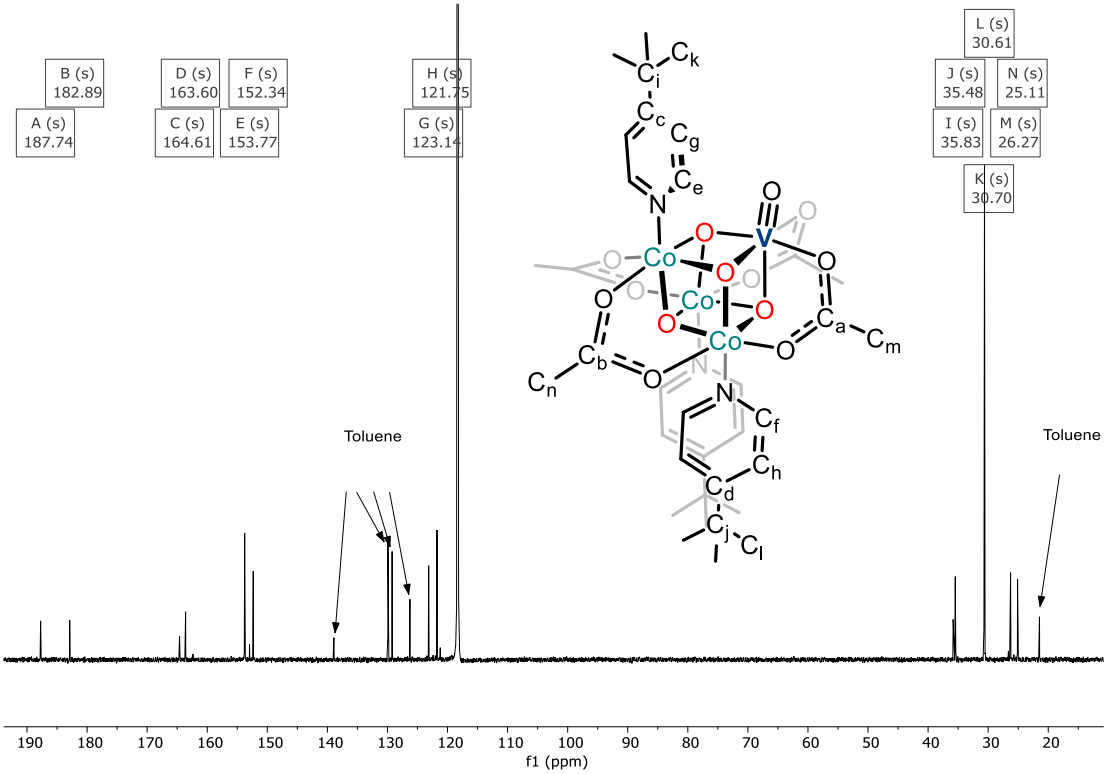
S3. FTIR spectrum of **VCo$_3$**[Co]



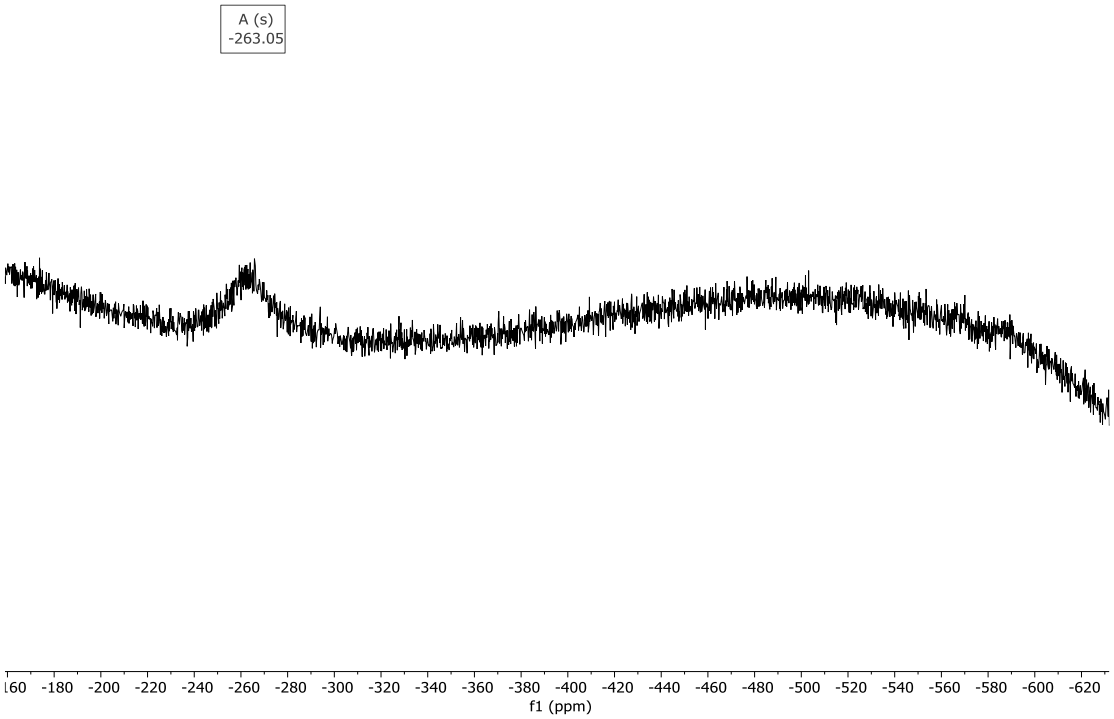
S4. ^{1}H NMR spectrum of OVCo$_3$O$_4$(OAc)$_4$(*t*-Bupy)$_3$ (**VCo$_3$**) (400 MHz, acetonitrile-*d*$_3$).



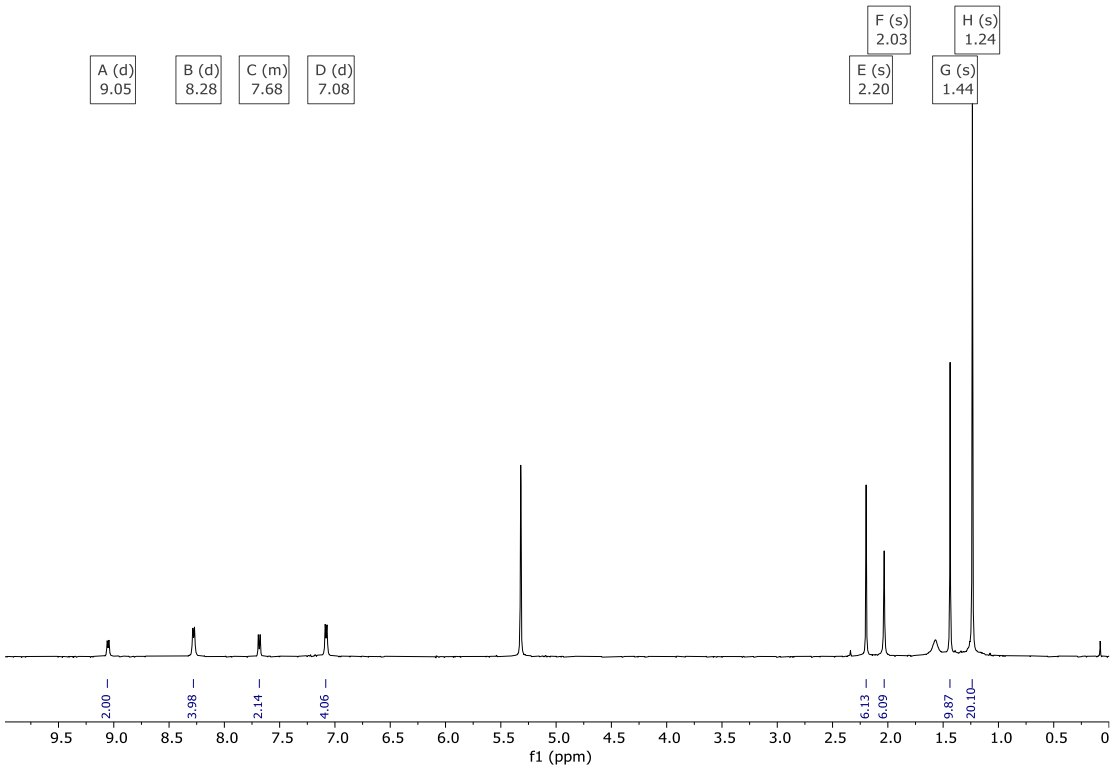
S5. ^{1}H NMR spectrum of $OVCo_3O_4(OAc)_4$(*t*-Bupy)$_3$ (**VCo$_3$**) isolated directly from the metal-metal exchange reaction (400 MHz, acetonitrile-d_3). Note that the ratio of $H_{a/c}$:$H_{b/d}$ is significantly different from that of material prepared from **VCo$_3$**[Co] (**S**).



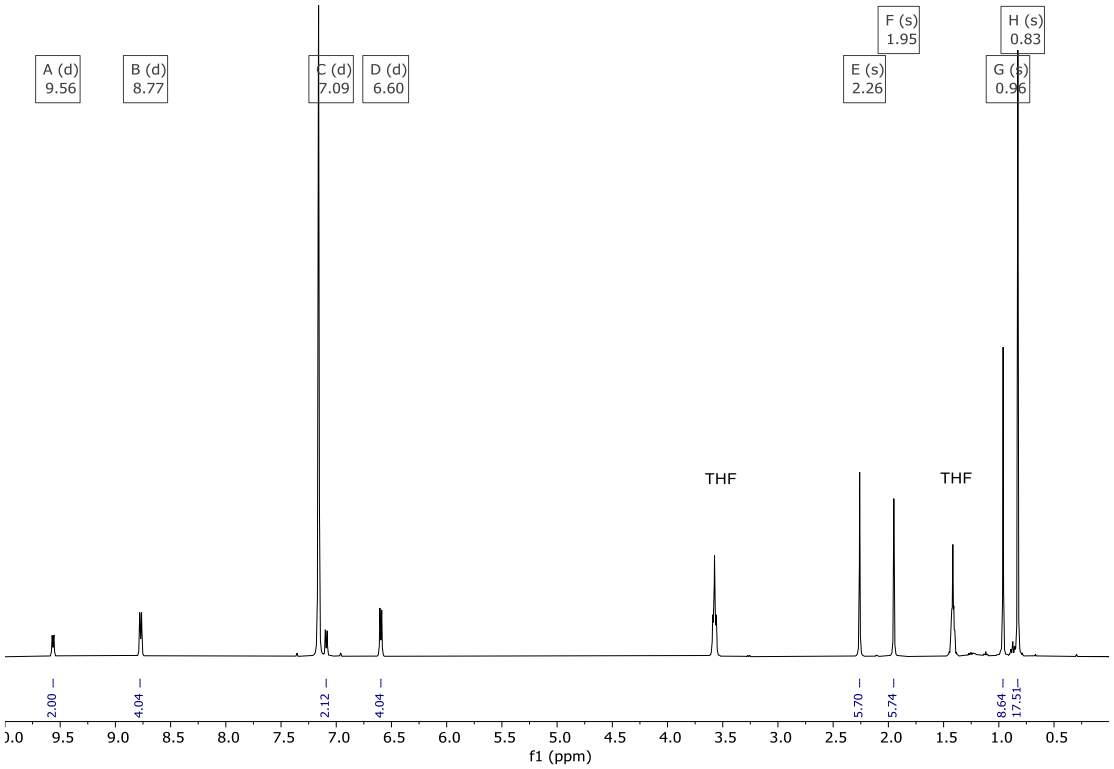
S6. ^{13}C{^{1}H} NMR spectrum of $OVCo_3O_4(OAc)_4$(*t*-Bupy)$_3$ (**VCo$_3$**) (125 MHz, acetonitrile-d_3)



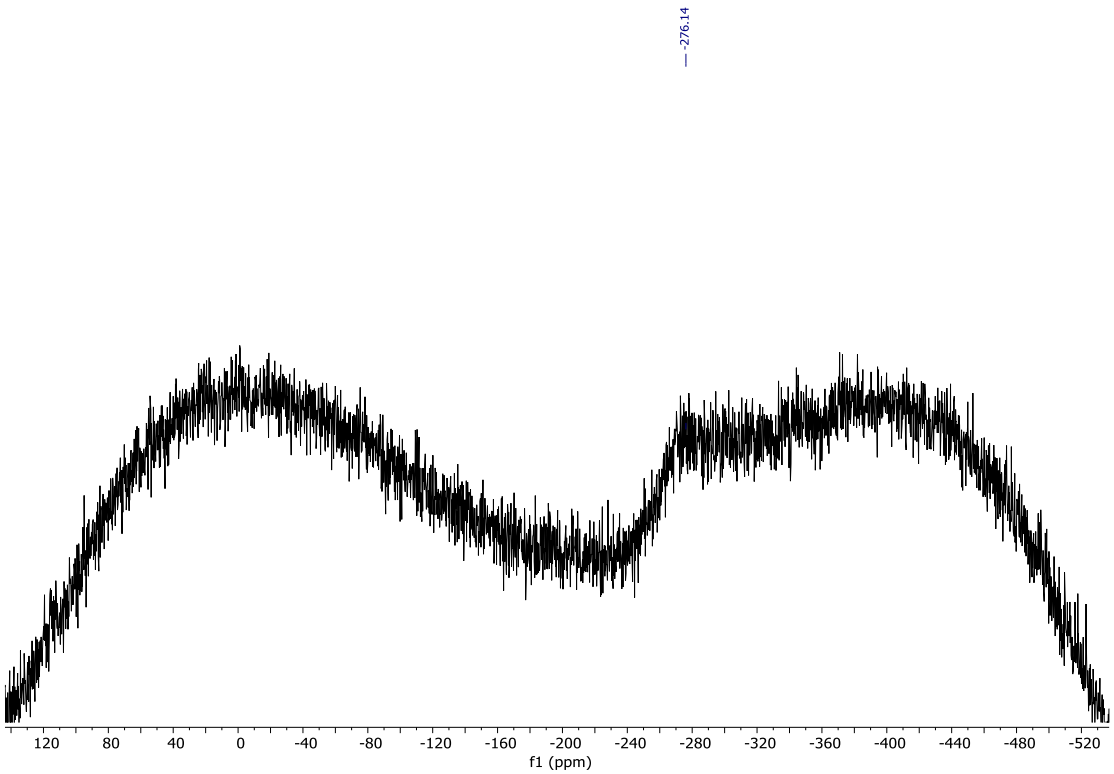
S7. ^{51}V NMR spectrum of $OVCo_3O_4(OAc)_4$(*t*-Bupy)$_3$ (**VCo$_3$**) (400 MHz, acetonitrile-d_3).



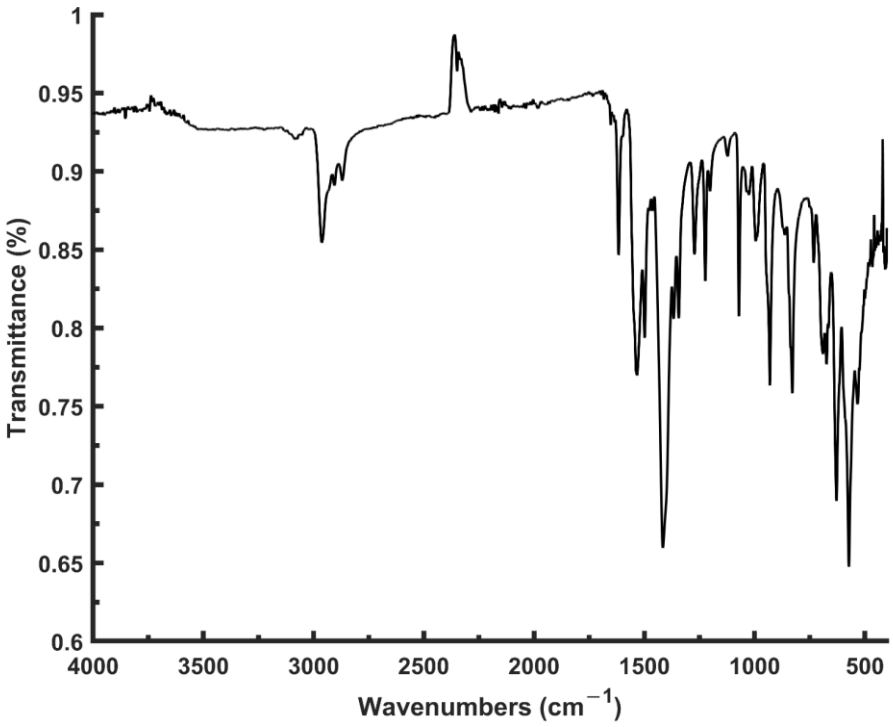
S8. ^{1}H NMR spectrum of $OVCo_3O_4(OAc)_4$(*t*-Bupy)$_3$ (**VCo$_3$**) (400 MHz, dichloromethane-d_2).



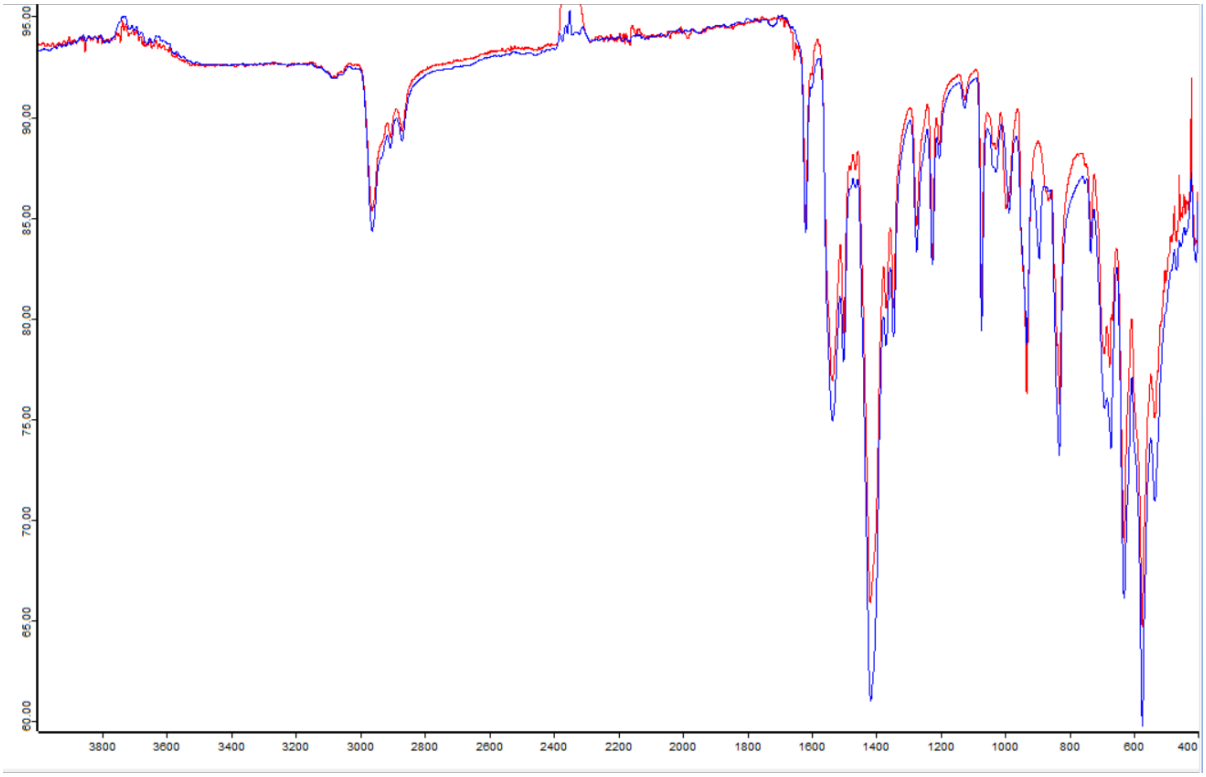
S9. ^{1}H NMR spectrum of $OVCo_3O_4(OAc)_4(^{t}Bupy)_3$ (400 MHz, benzene-d_6).



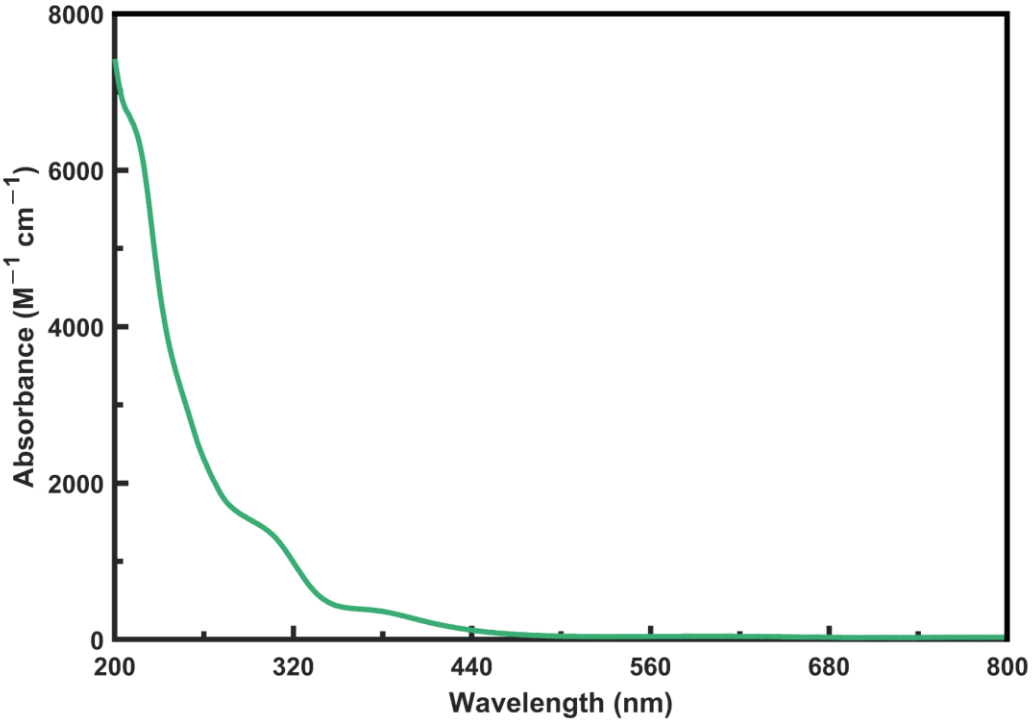
S10. ^{51}V NMR spectrum of $OVCo_3O_4(OAc)_4(^{t}Bupy)_3$ (105 MHz, benzene-d_6,).



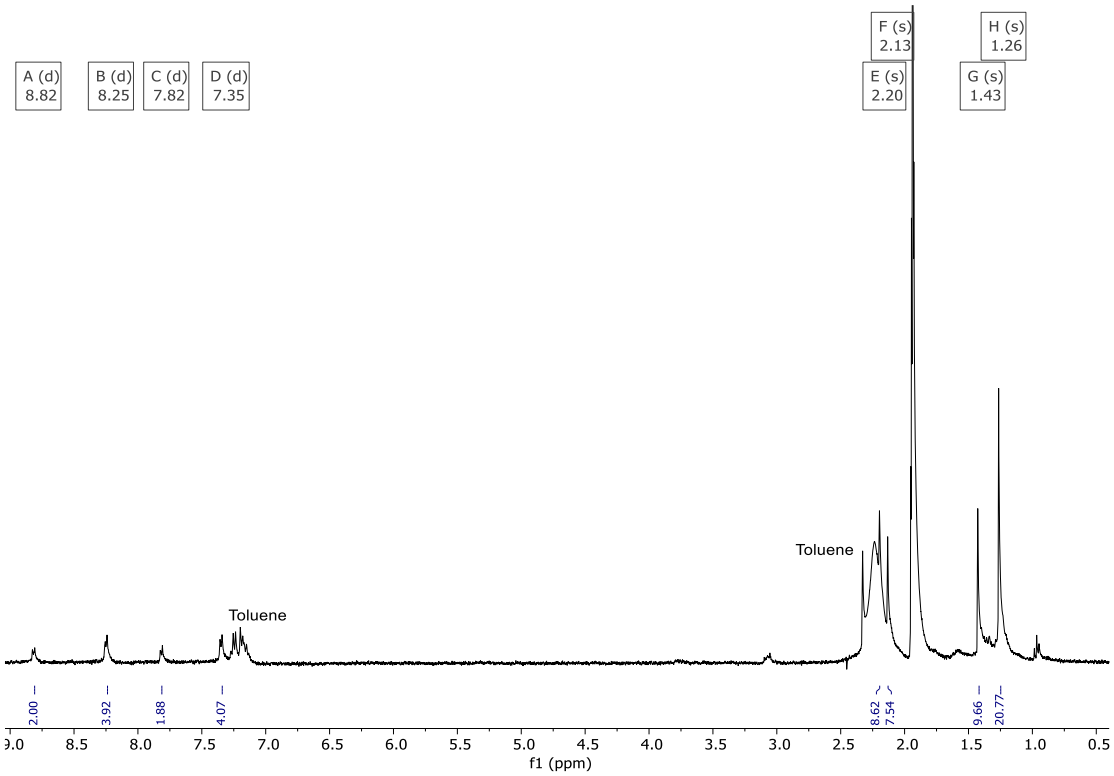
S11. FTIR spectrum of **VCo$_3$**.



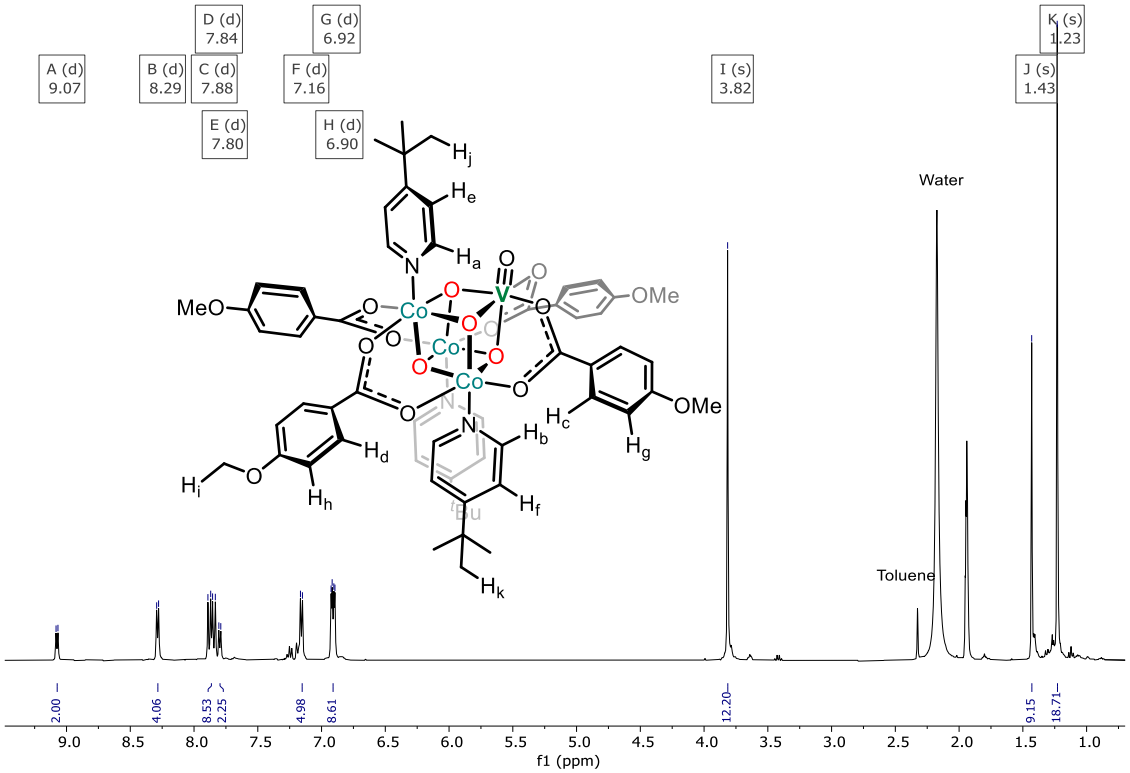
S12. FTIR Spectrum of **VCo$_3$** (red) and **VCo$_3$** enriched with ^{18}O (blue) demonstrating a new oxo stretch at 892 cm^{-1}, and absence of any shifts in the μ-oxo stretches between 800-400 cm^{-1}.



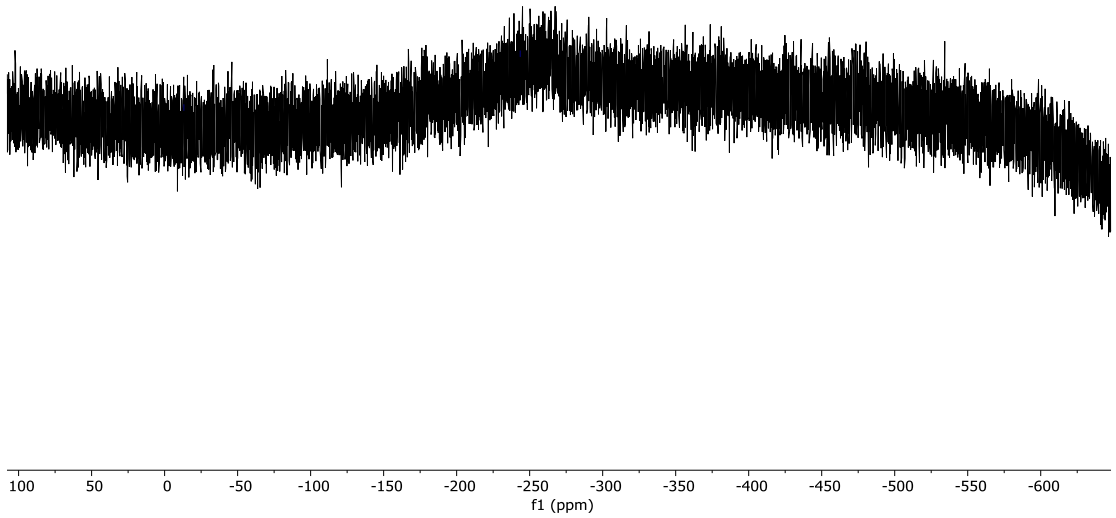
S13. Molar absorptivity of **VCo$_3$** in MeCN.



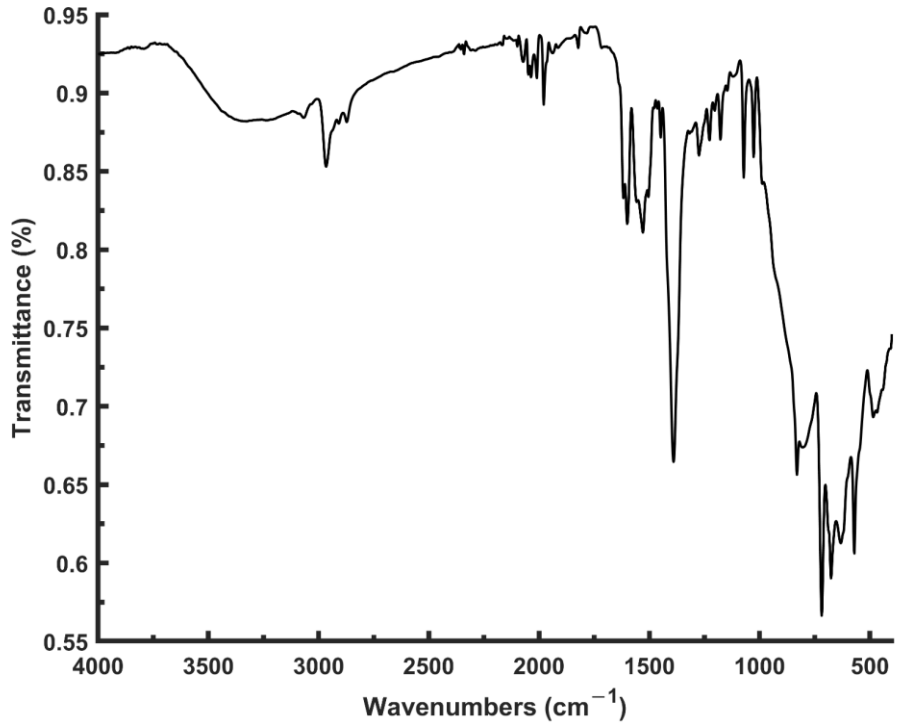
S14. ^{1}H NMR spectrum (400 MHz, acetonitrile-d_3) of [**HVCo$_3$**][**NO$_3$**].



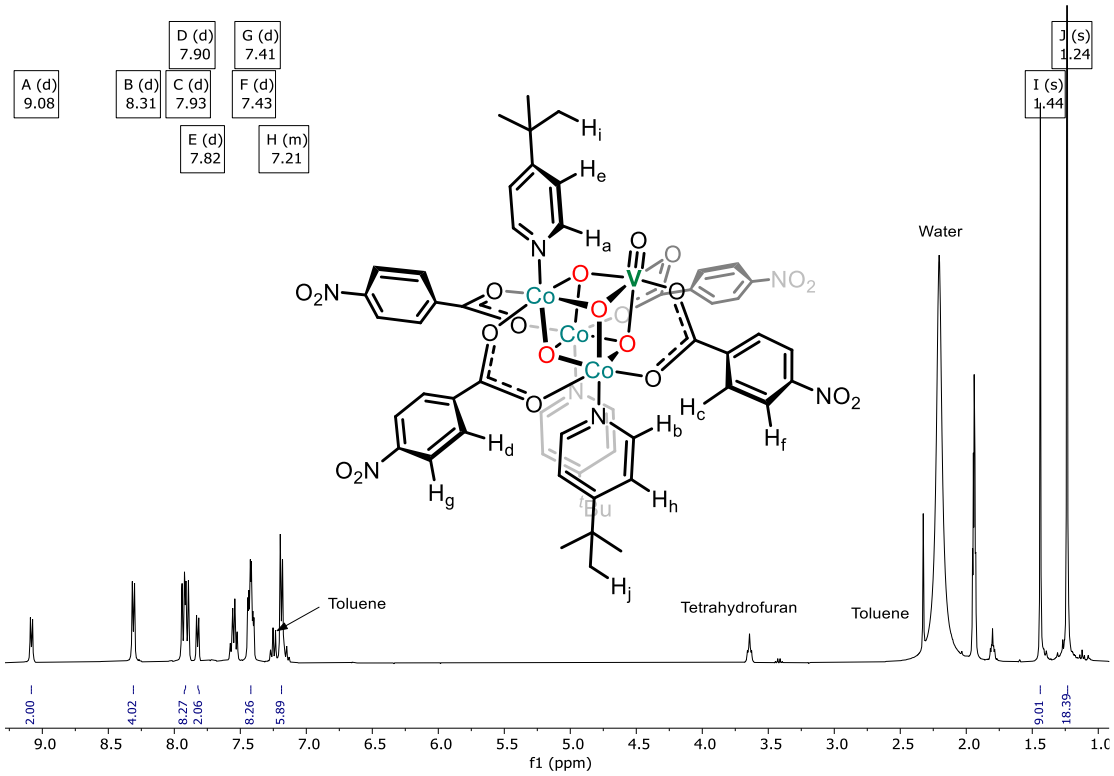
S15. ^{1}H NMR spectrum of **VCo_3(OBz-OMe)** (400 MHz, acetonitrile-d_3).



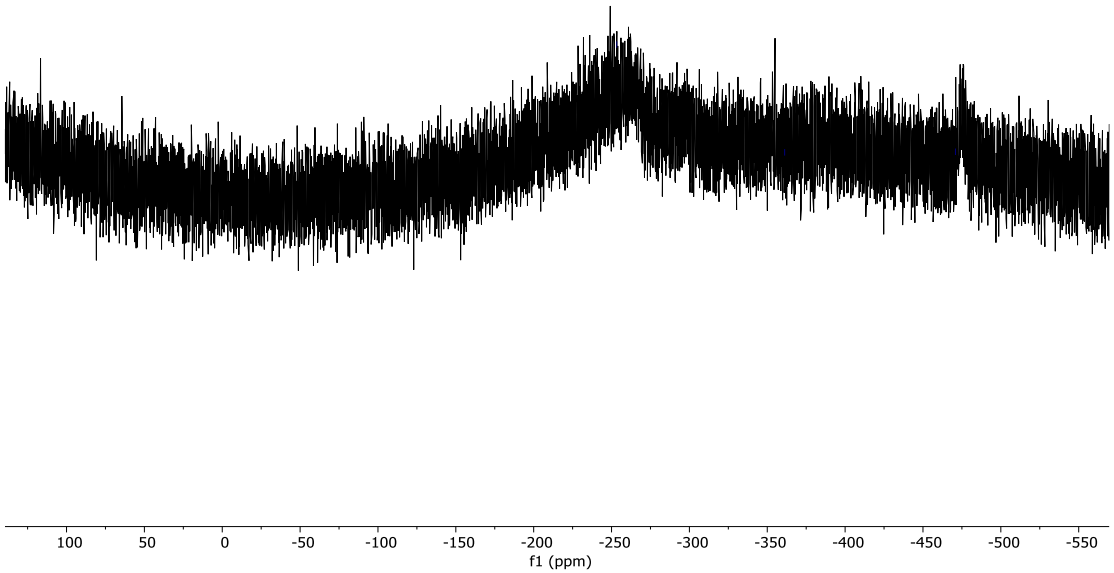
S16. ^{51}V NMR spectrum of **VCo_3(OBz-OMe)** (105 MHz, acetonitrile-d_3)



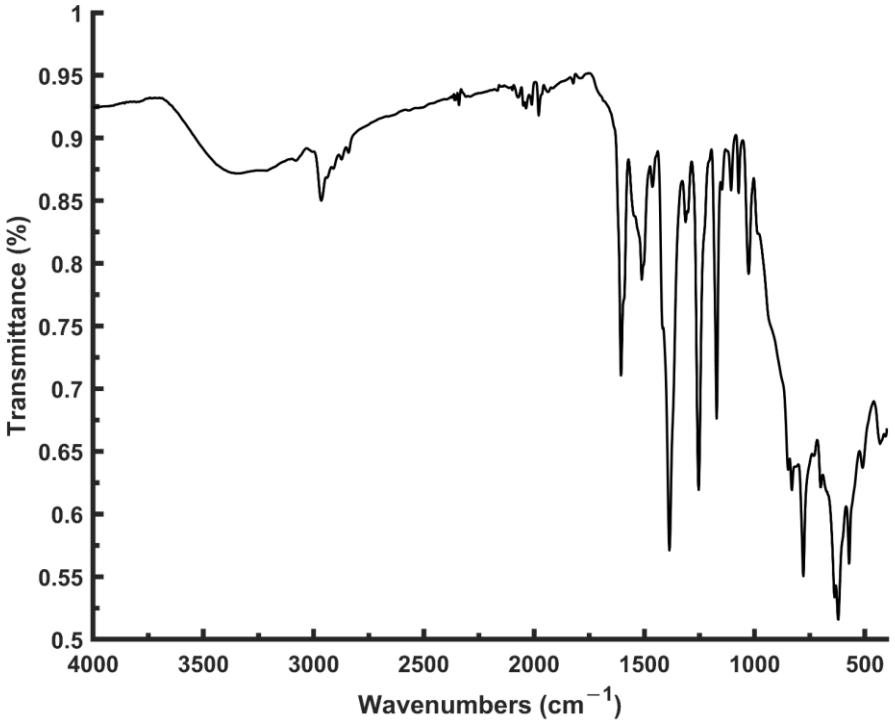
S17. FTIR spectrum of **VCo_3(OBz-OMe)**.



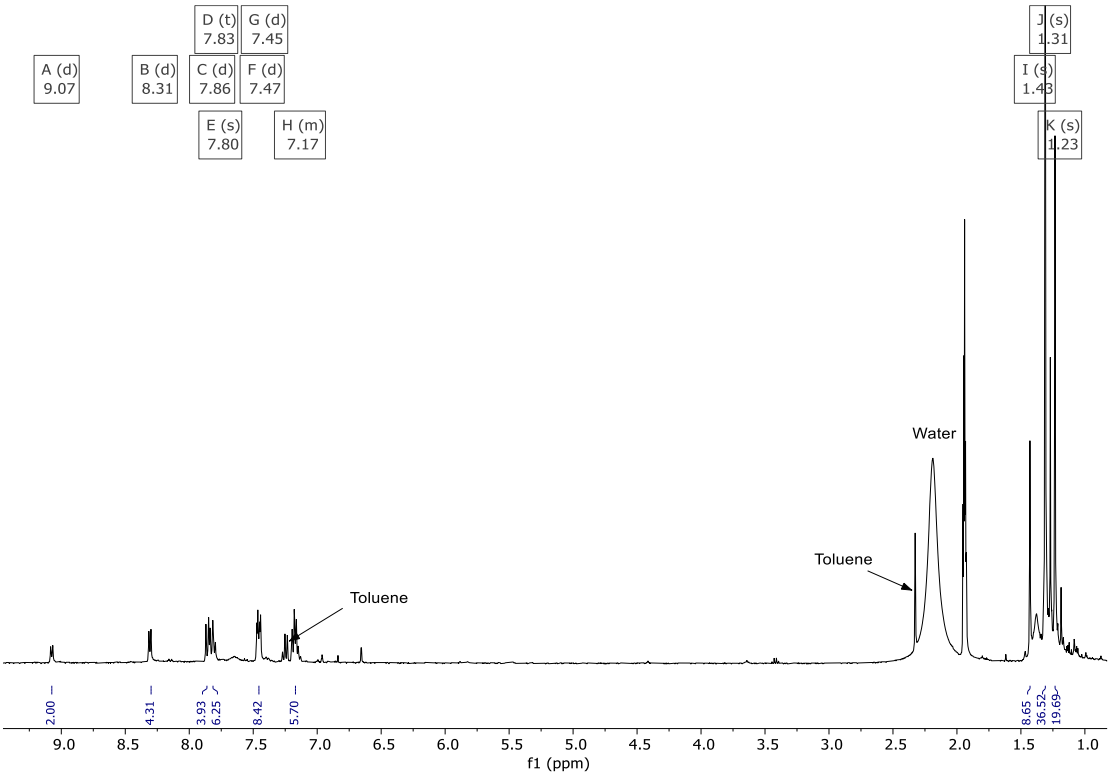
S18. ^{1}H NMR spectrum of **VCo_3(OBz-NO_2)** (400 MHz, acetonitrile-d_3).



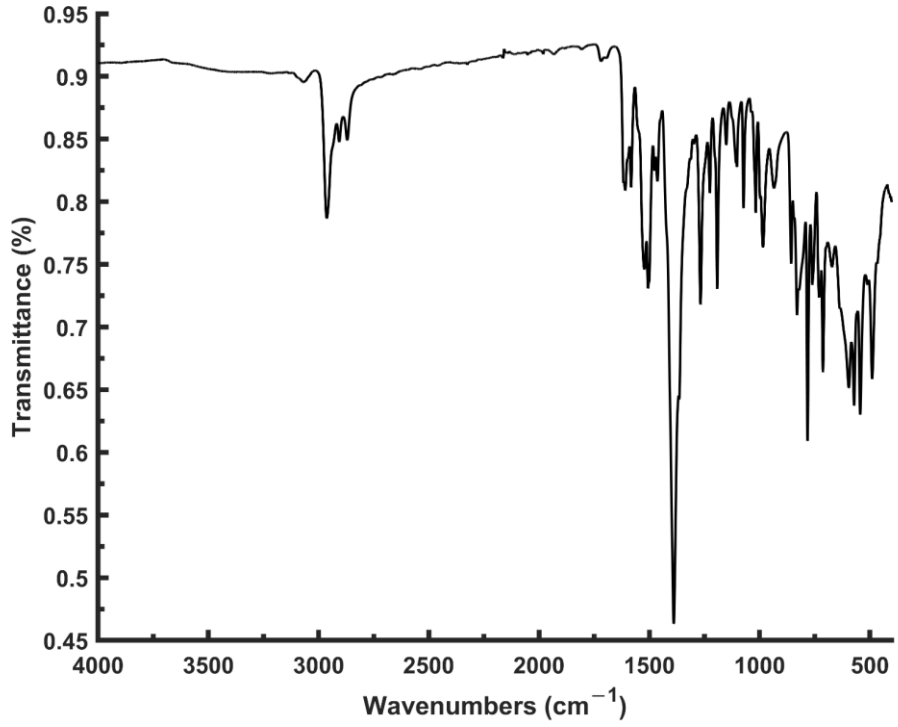
S19. ^{51}V NMR spectrum of **VCo_3(OBz-NO_2)** (105 MHz, acetonitrile-d_3). Peak at *ca* –490 ppm is a product of hydrolysis.



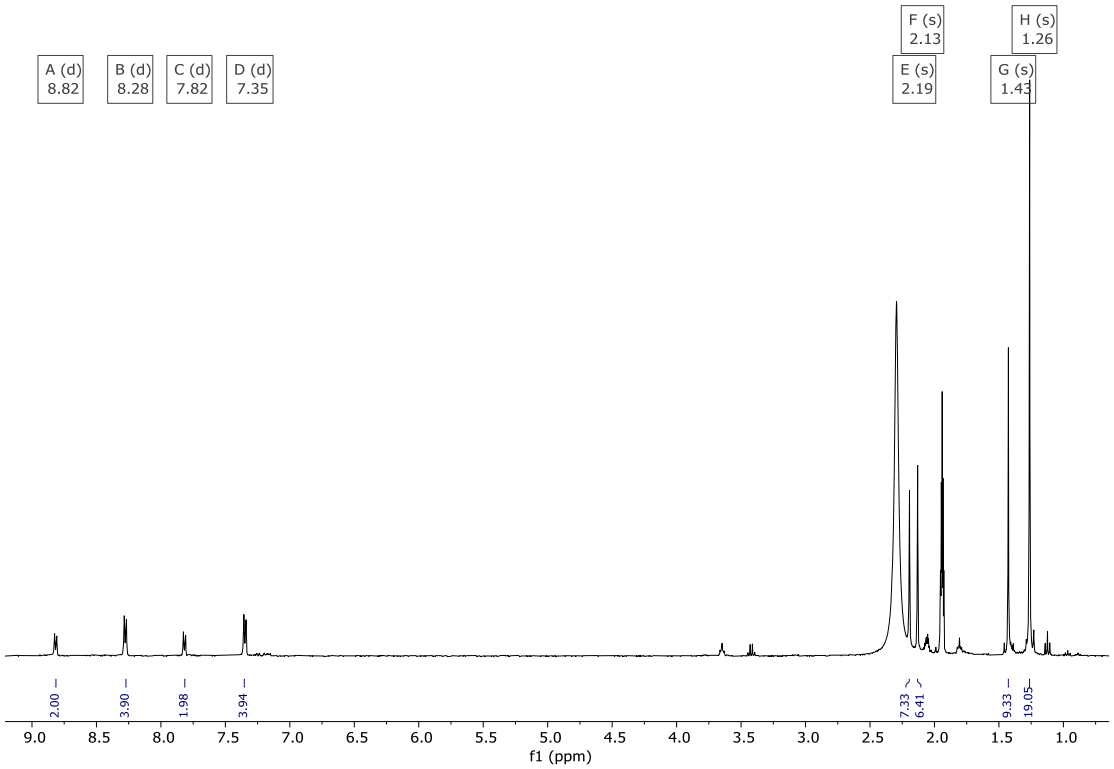
S20. FTIR spectrum of **$VCo_3(OBz\text{-}NO_2)$**.



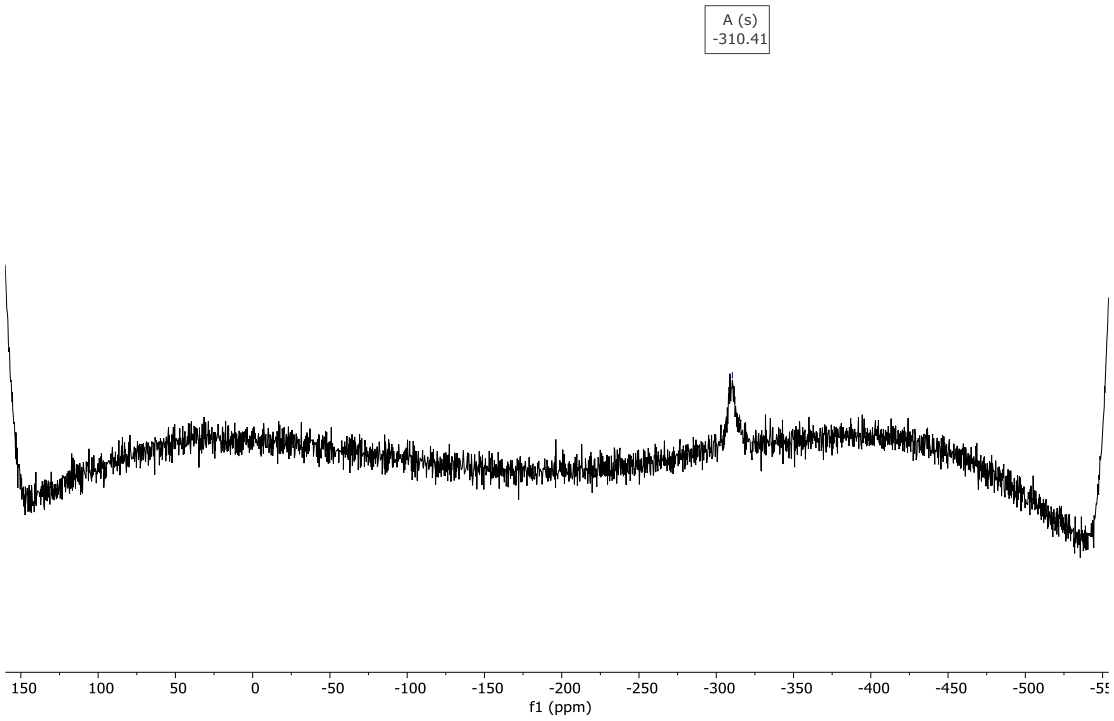
S21. ^{1}H NMR spectrum of **VCo$_3$(OBz-*t*Bu)** (400 MHz, acetonitrile-d_3).



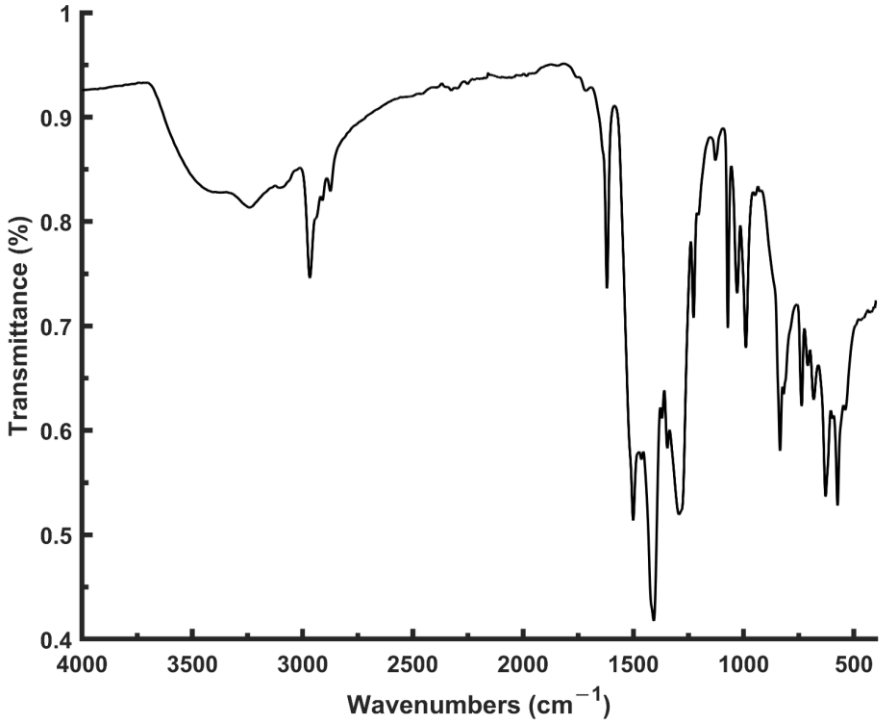
S22. FTIR spectrum of **Co$_4$(OBz-*t*Bu)**.



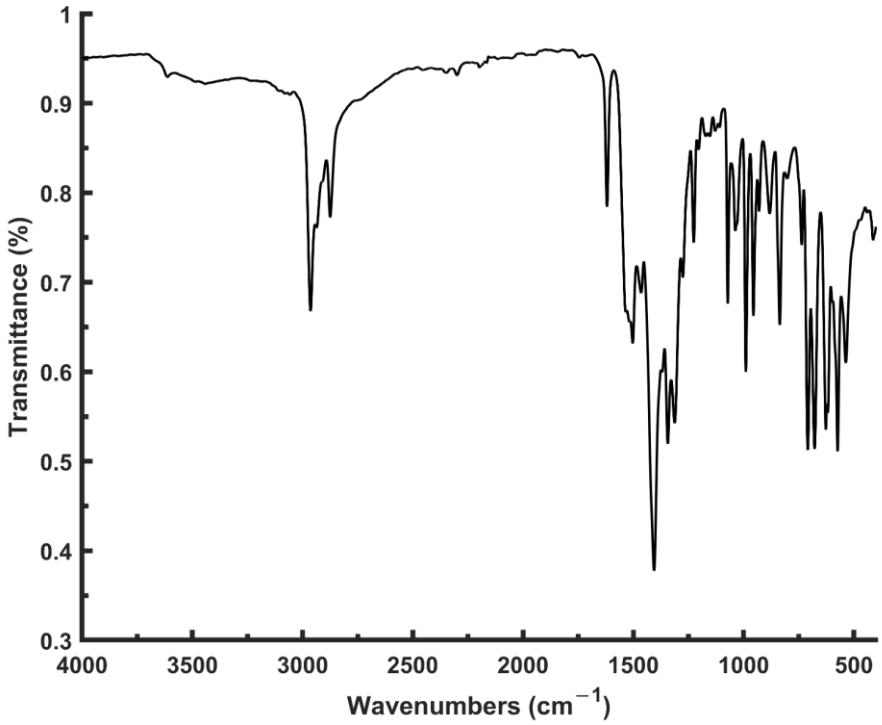
S23. ^{1}H NMR spectrum of **VCo$_3$H**$^{+}$[NO$_3$] (400 MHz, acetonitrile-d_3).



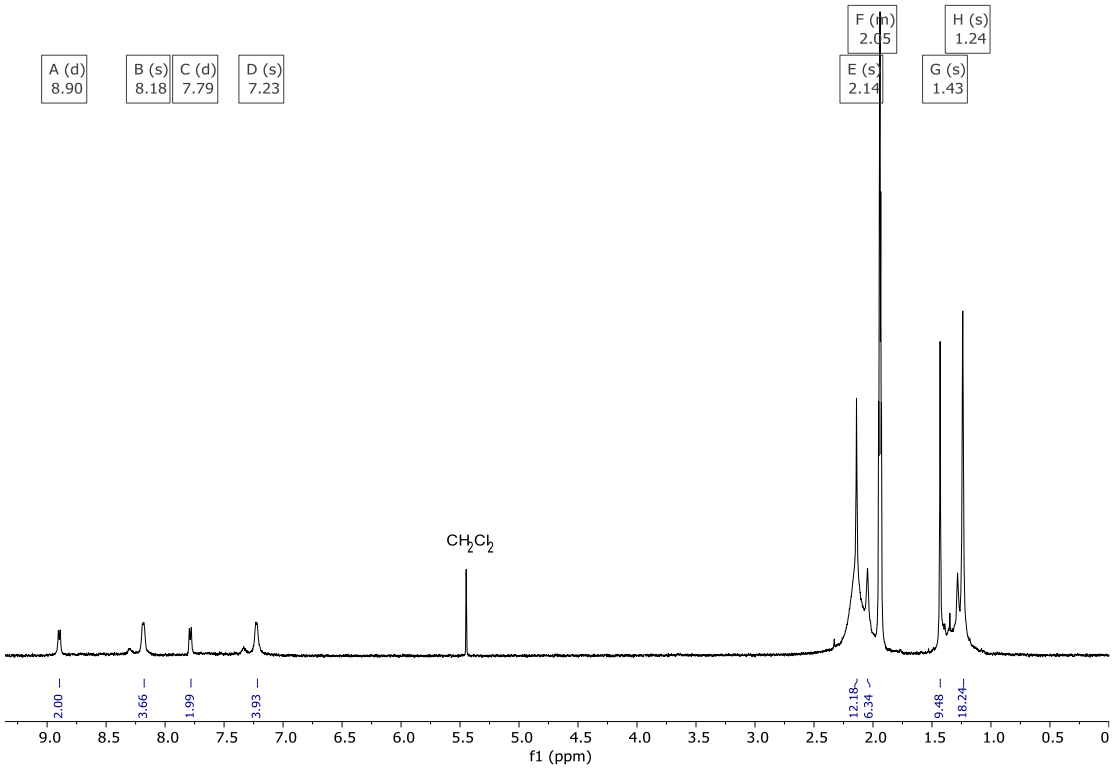
S24. ^{51}V NMR spectrum of **VCo$_3$H**$^{+}$[NO$_3$] (400 MHz, acetonitrile-d_3).



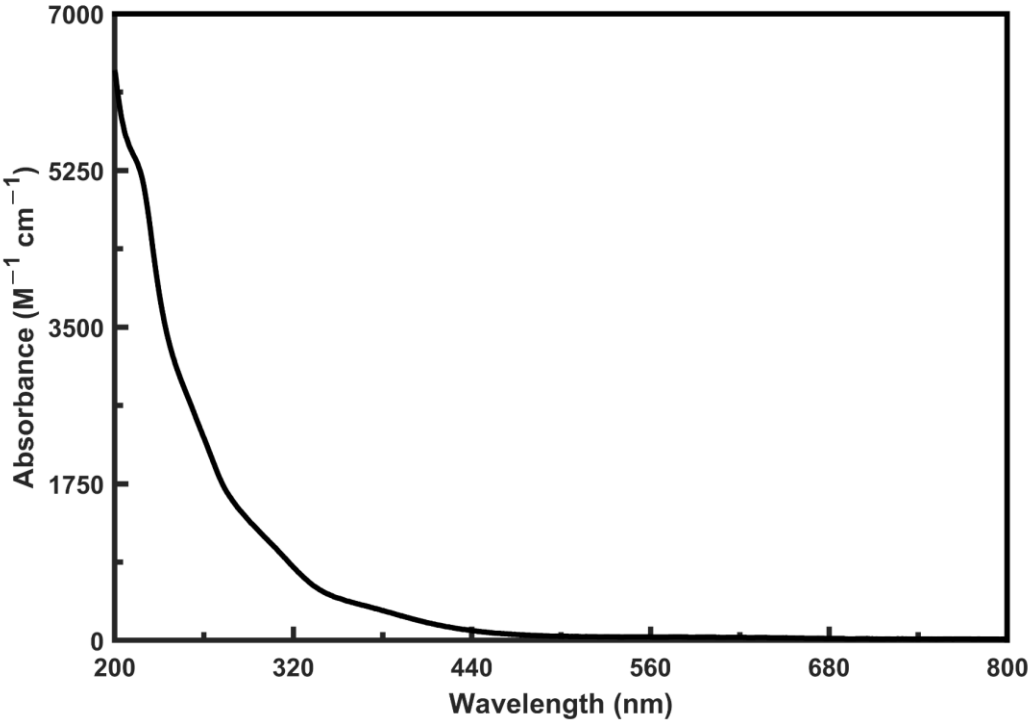
S25. FTIR spectrum of [**HVCo$_3$**$^+$][**NO$_3$**].



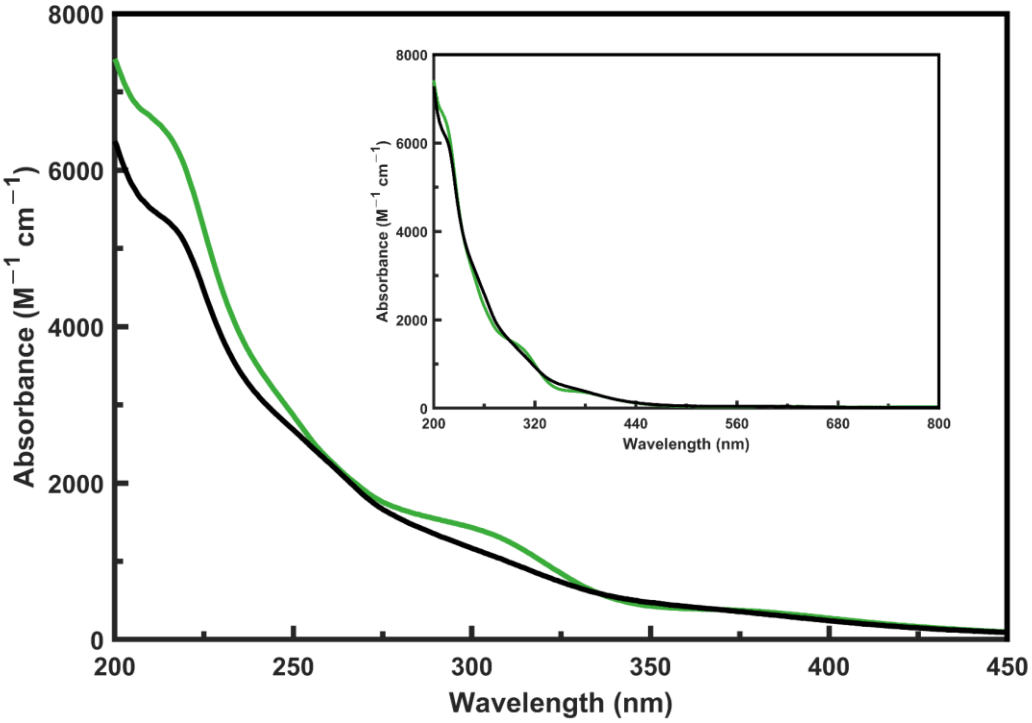
S26. FTIR spectrum of **VCo$_3$D**$^+$[NO$_3$] from reaction mixture from reaction between **VCo$_3$** and (^{n}Bu$_4$N)$_2$Ce^{IV}(NO$_3$)$_6$. Note the broad stretching frequency at 2720 cm^{-1} and absence of an O–H stretch.



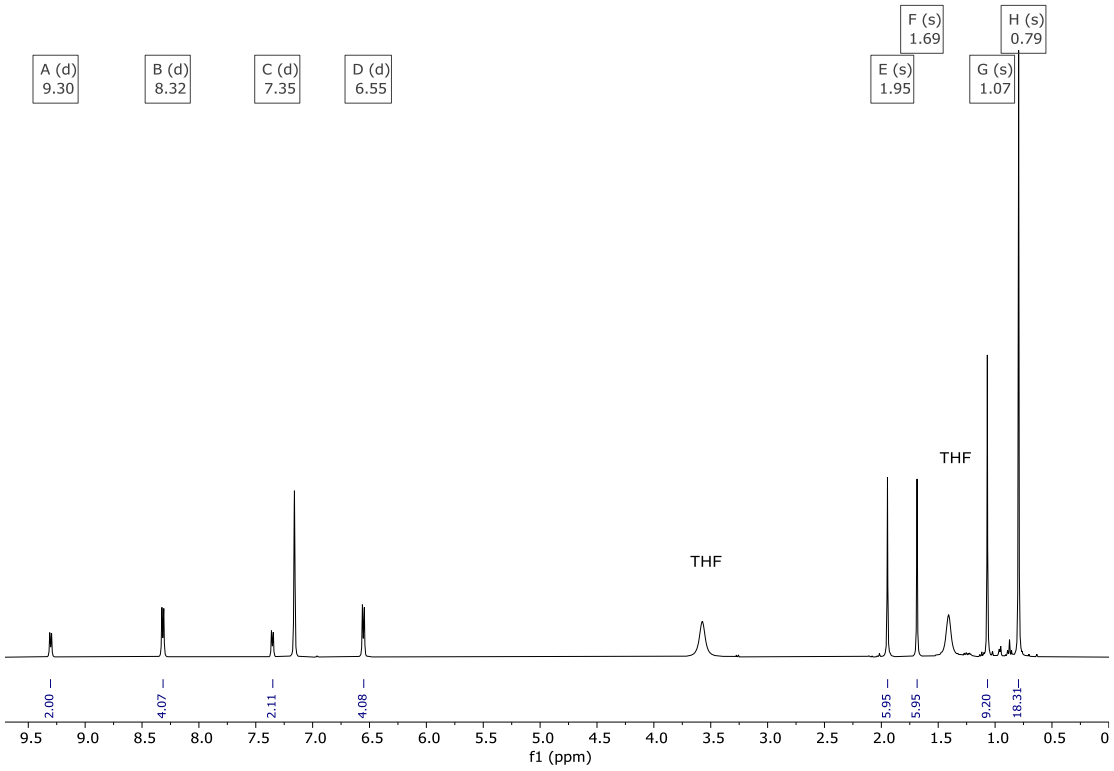
S27. ^{1}H NMR spectrum of **VCo$_3$H**$^{+}$[OTf] (400 MHz, acetonitrile-d_3).



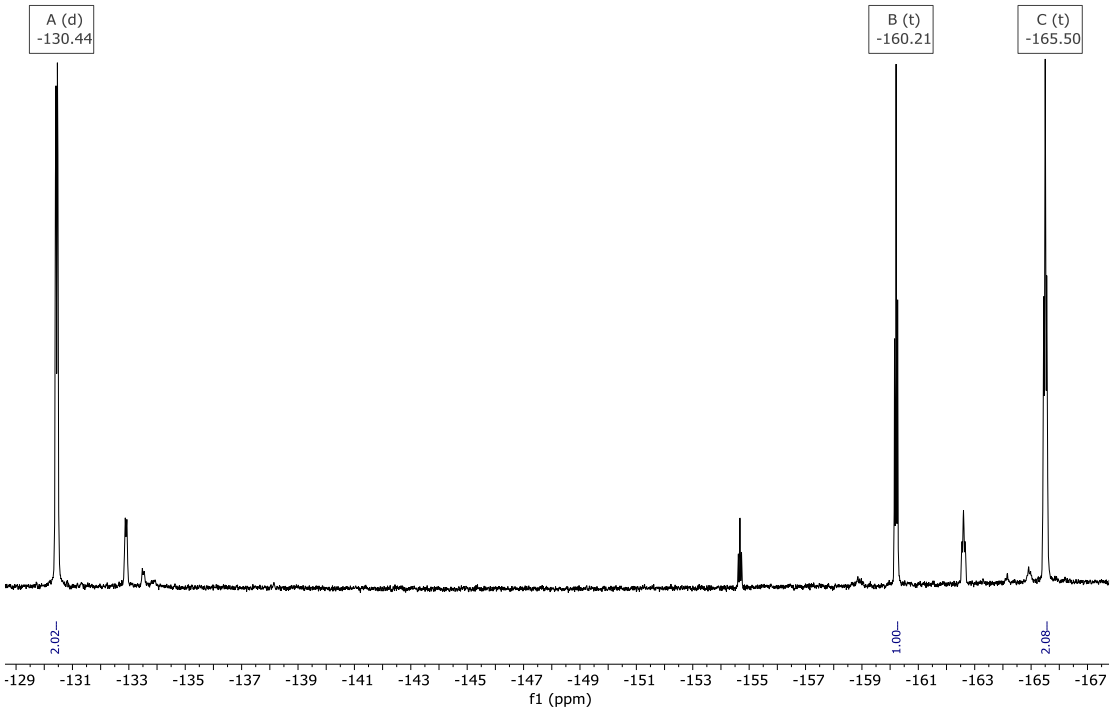
S28. Molar absorptivity of **VCo$_3$H**$^{+}$[OTf]



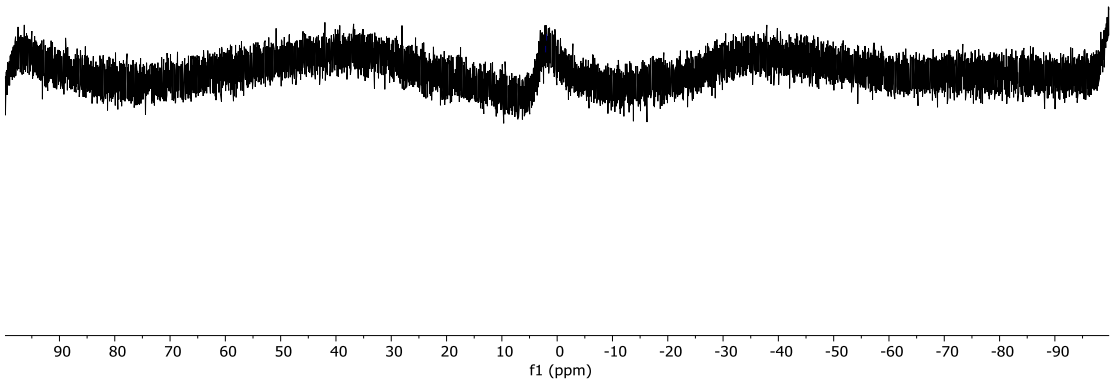
S29. Stacked molar absorptivity values of **VCo_3H^+**[OTf] (black) and **VCo_3** (green) from 200-450 nm, with 200-800 nm inset.



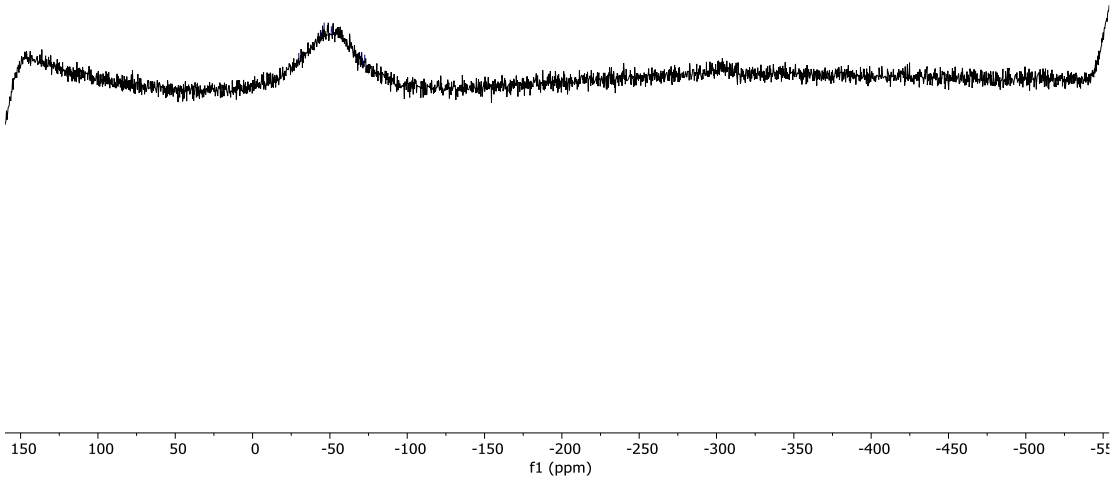
S30. ^{1}H NMR spectrum of **VCo_3(BCF)** (400 MHz, benzene-d_6).



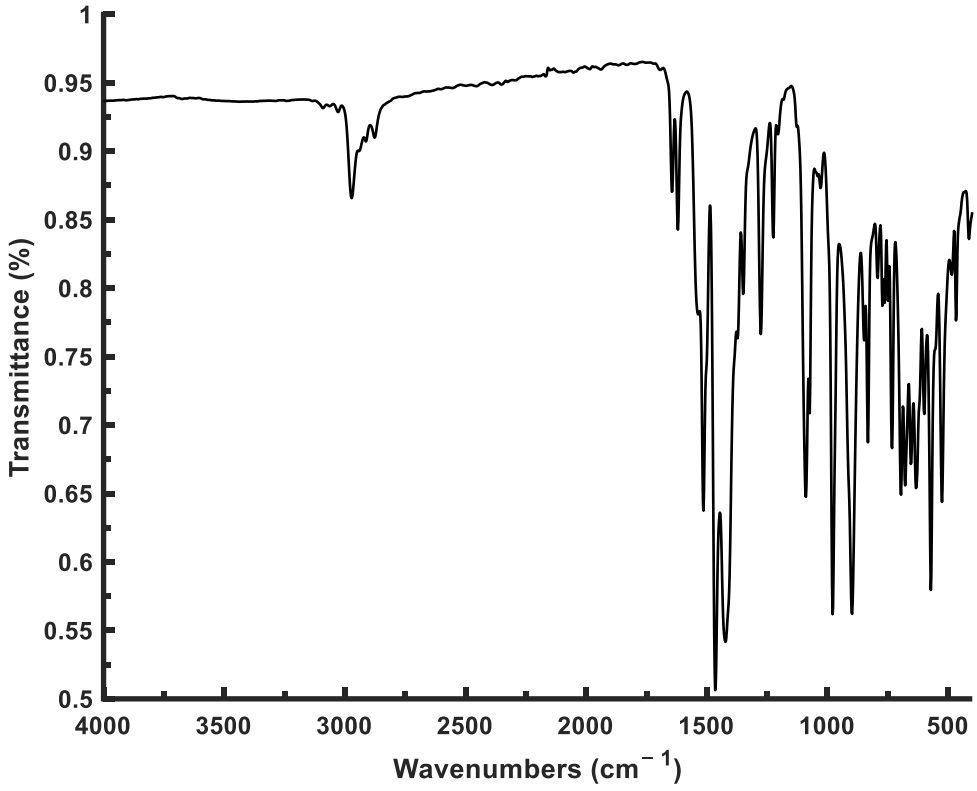
S31. ^{19}F{^{1}H} NMR of **VCo_3(BCF)** (376 MHz, benzene-d_6).



S32. ^{11}B NMR spectrum of **VCo$_3$(BCF)** (128 MHz, benzene-d_6).

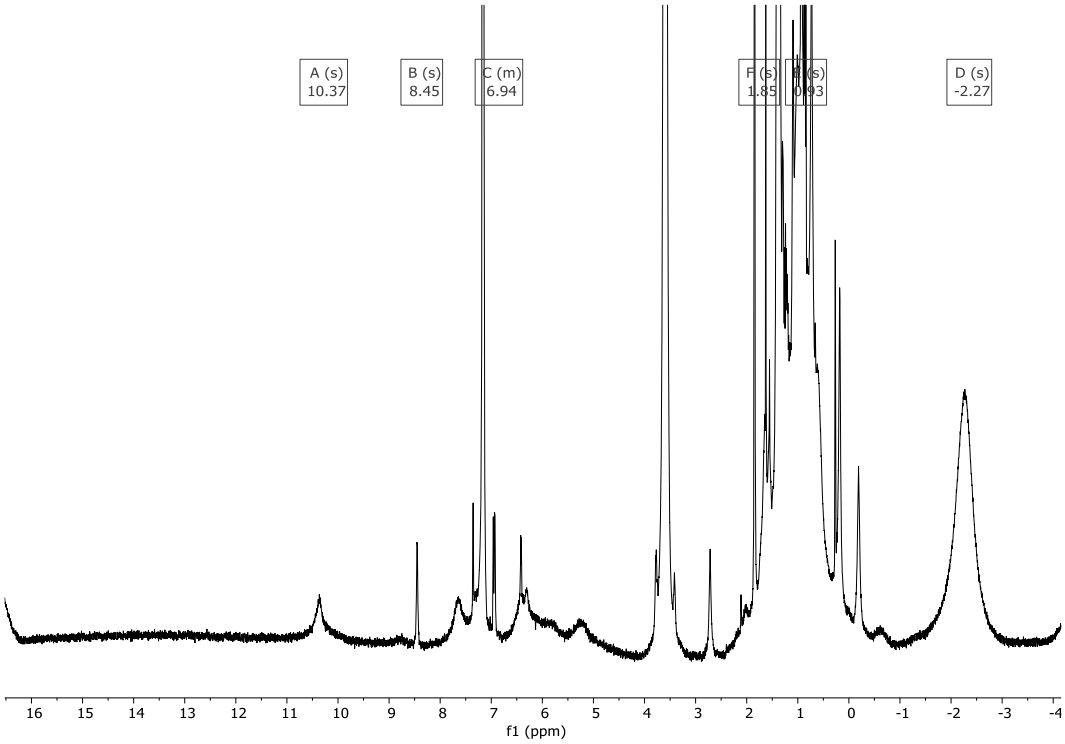


S33. ^{51}V NMR spectrum of **VCo$_3$(BCF)** (105 MHz, benzene-d_6).

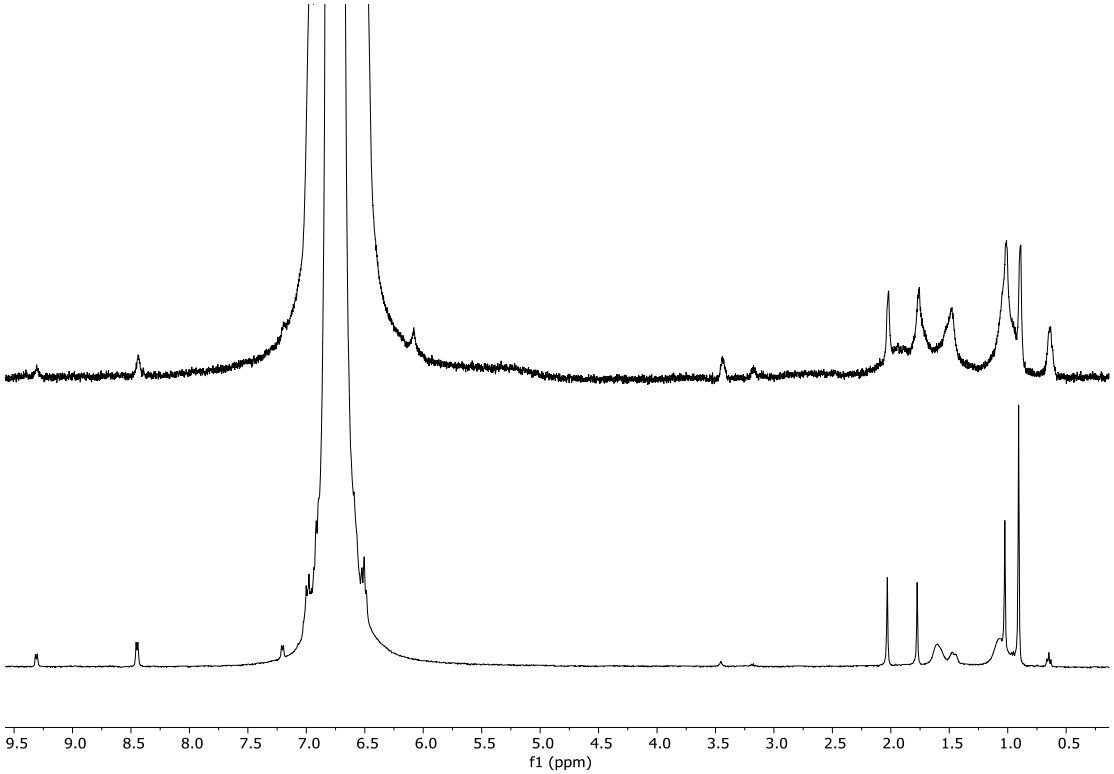


S34. FTIR spectrum of **VCo_3(BCF)**.

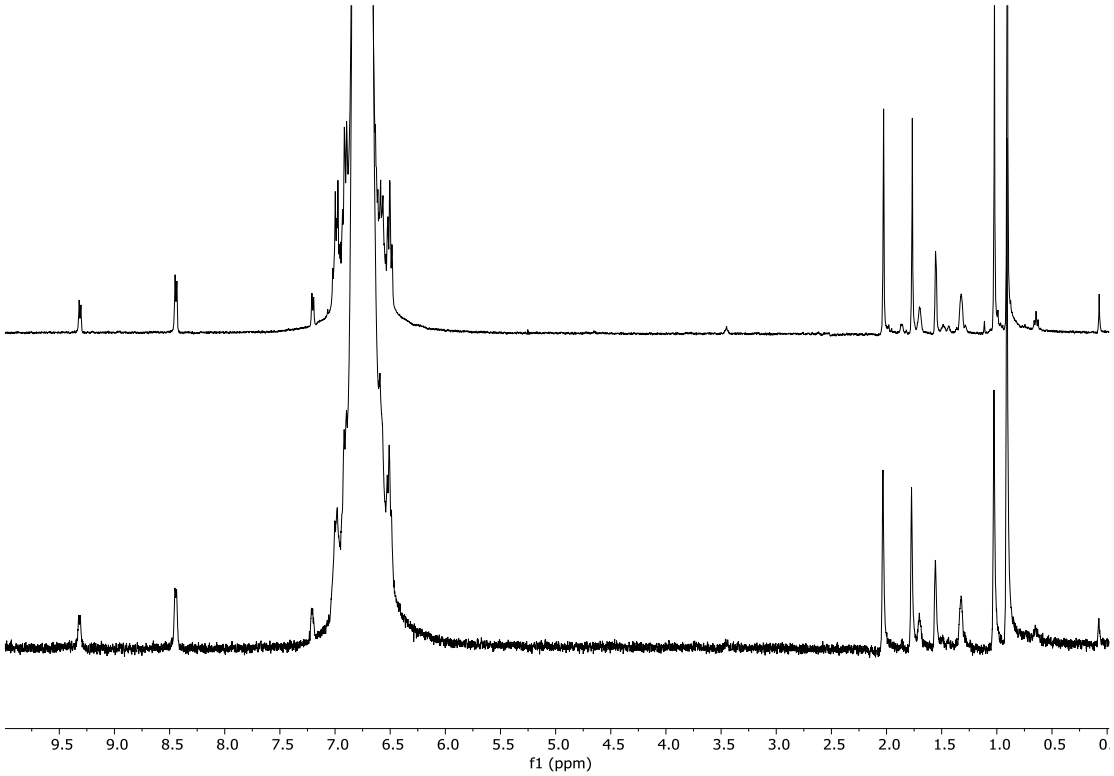
Reaction NMR Spectra:



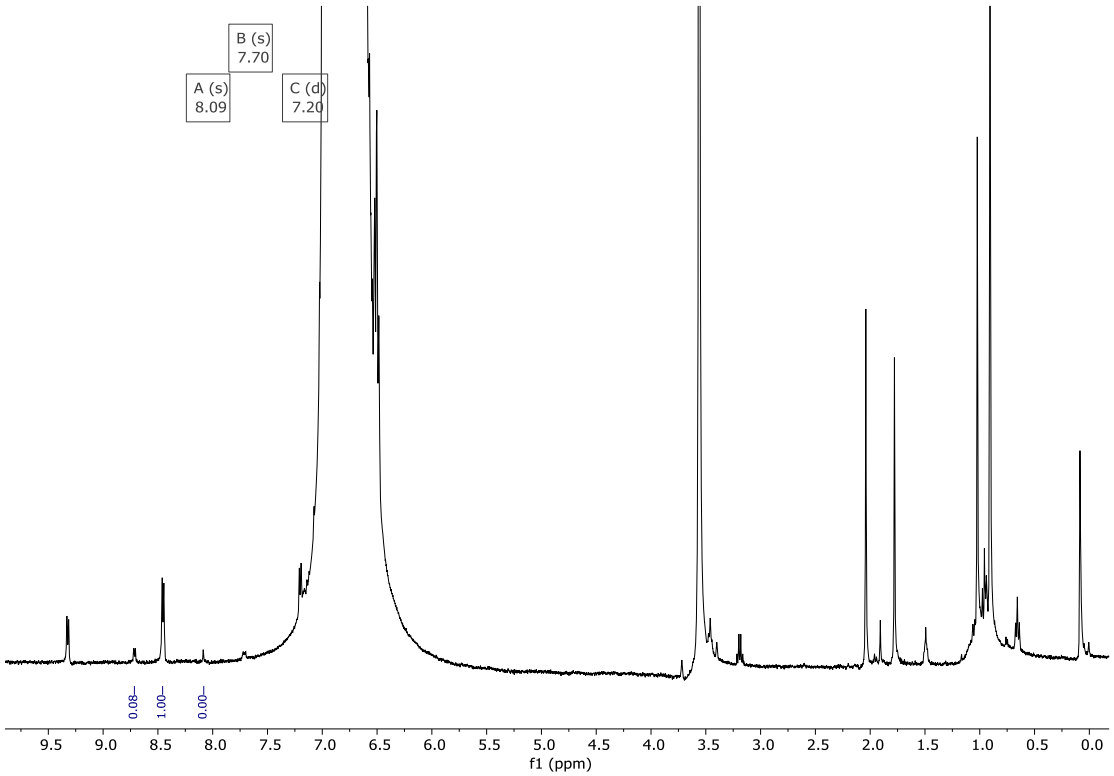
S35. ^{1}H NMR spectrum of an aliquot from the reaction of $VCl_4(THF)_2$ with **Co$_4$** (400 MHz, benzene-d_6).



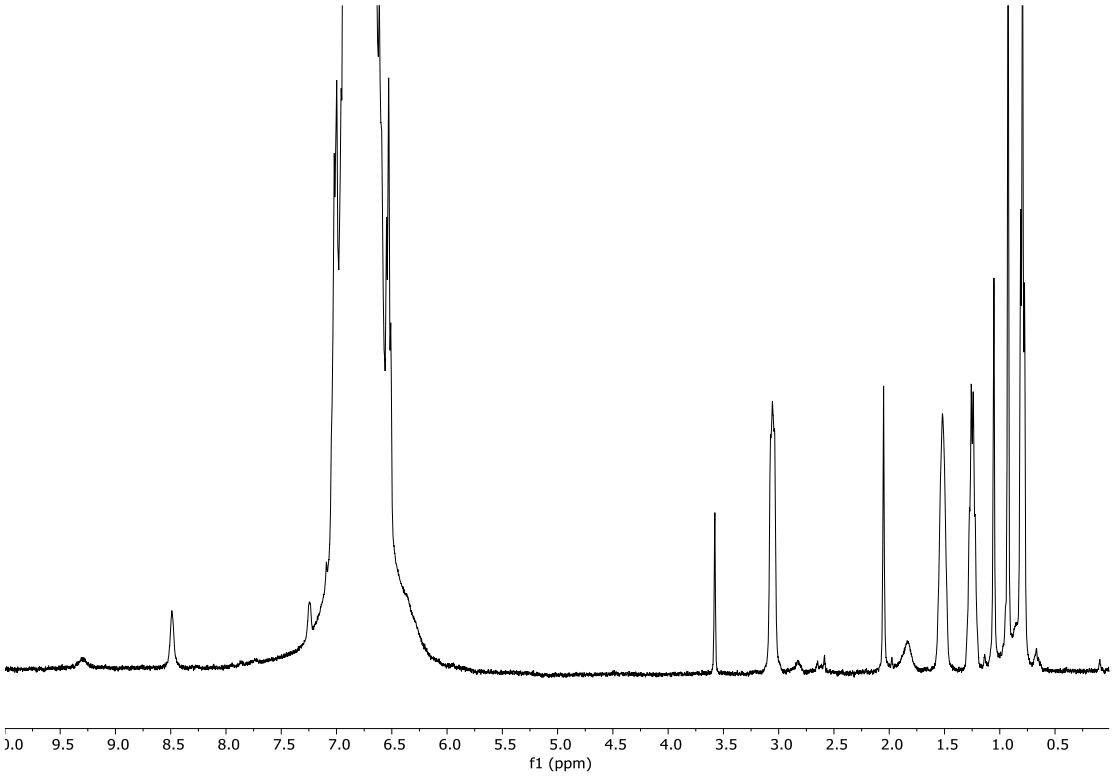
S36. ^{1}H NMR spectrum (400 MHz, *o*DFB-H$_4$) of the reaction of one equiv of P(Cy)$_3$ with **VCo$_3$** in *o*DFB.



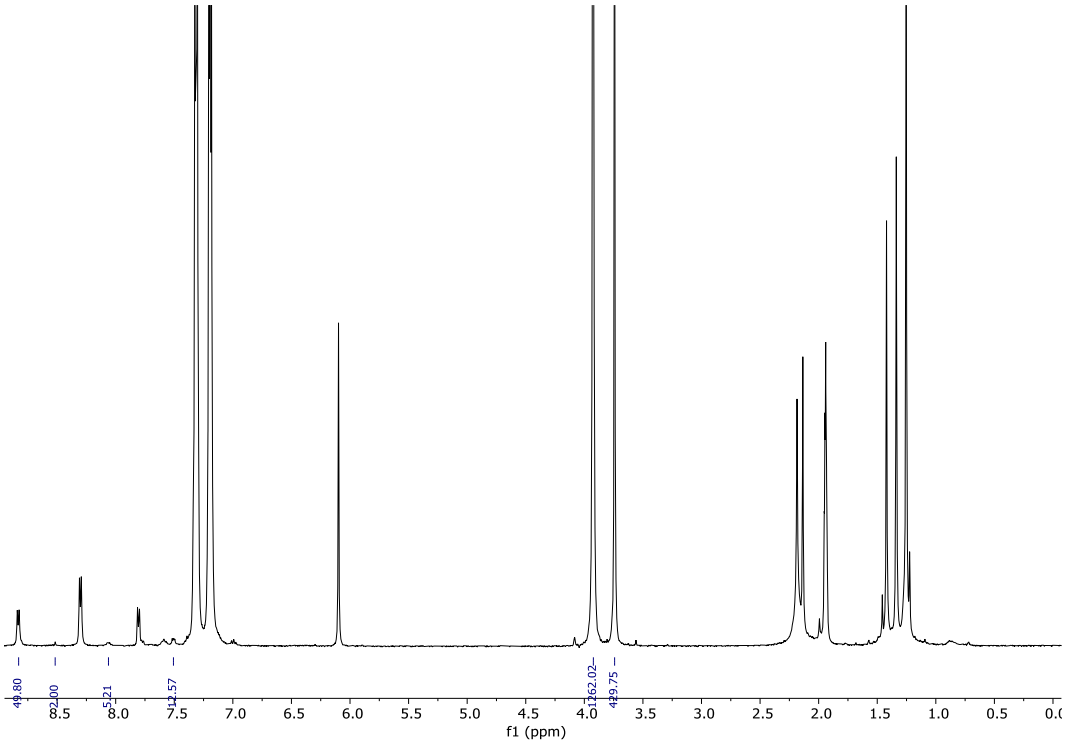
S37. [1]H NMR spectrum (400 MHz, *o*DFB-H_4) of reaction of one equiv of adamantylisocyanate with **VCo_3** in *o*DFB.



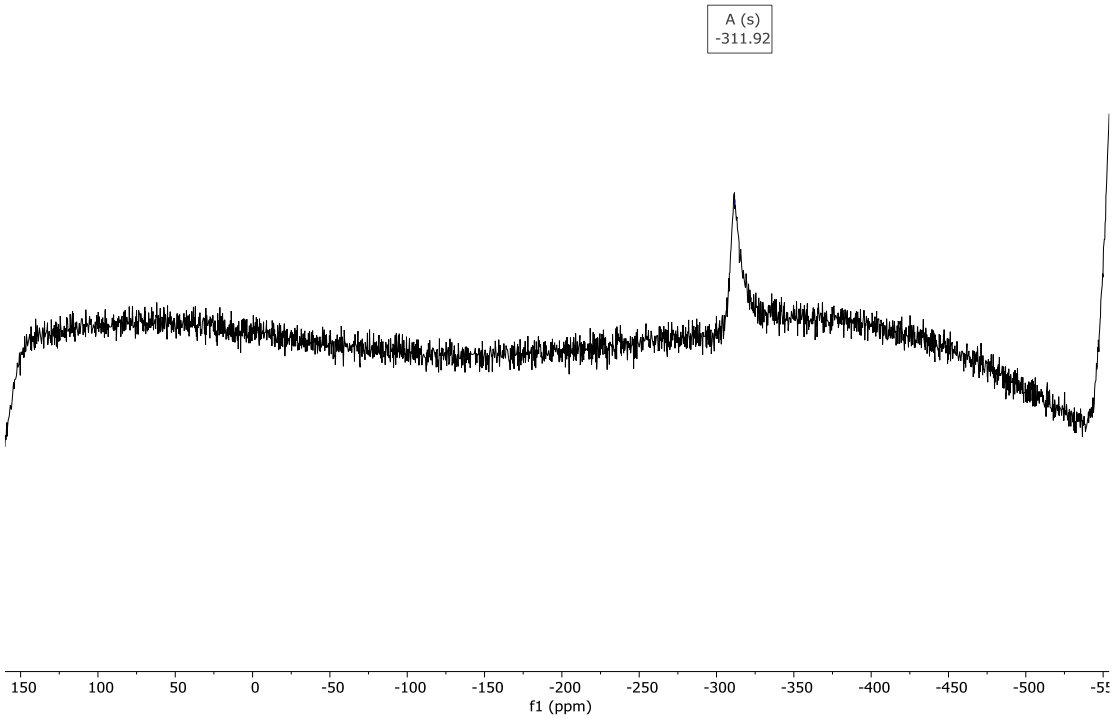
S38. [1]H NMR spectrum (400 MHz, *o*DFB-H_4) of the filtered attempted catalytic oxidation of 9,10-dihydroanthracene with 10 mol% **VCo_3**, with Ag_2O as tandem oxidant and base, a system which worked well in studies with $Co_4O_4(OAc)_4(py)_4$.[9]



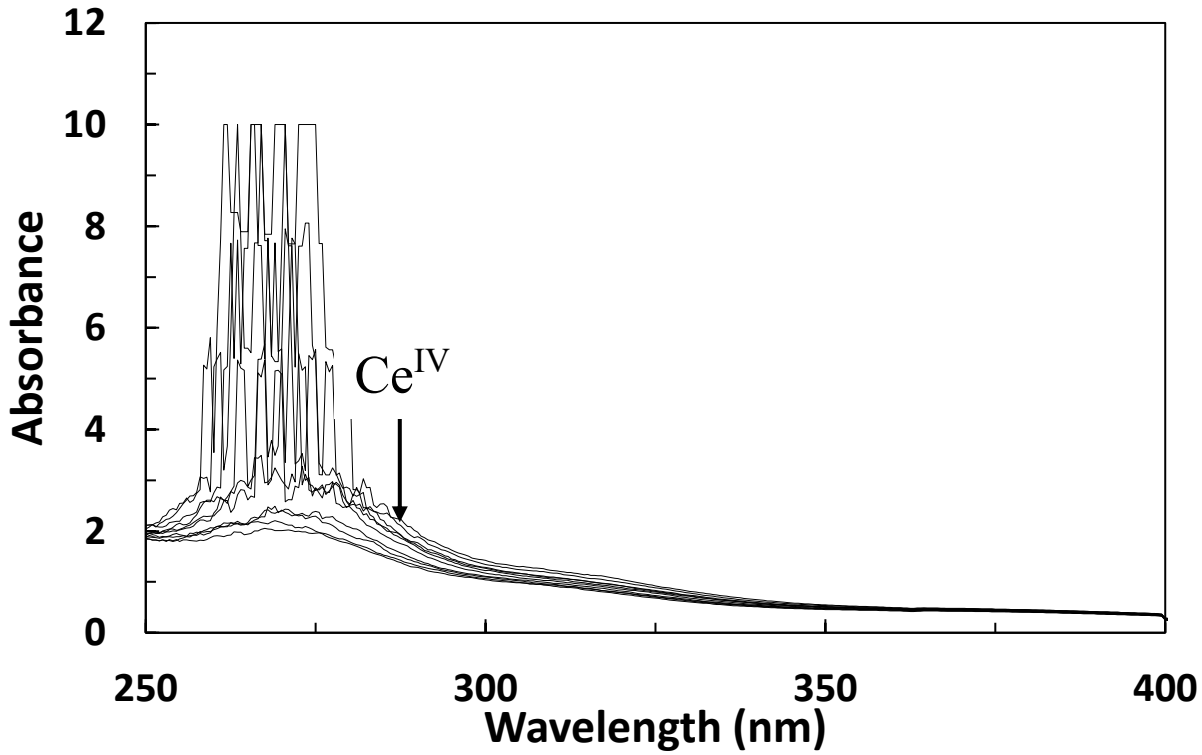
S39. ^{1}H NMR spectrum (400 MHz, *o*DFB-H$_4$) of attempted activation of 9,10-dihydroanthracene in by **VCo$_3$**$^{+}$ generated in situ with (^{n}Bu$_4$N)$_2$Ce(NO$_3$)$_6$. The peaks in the aromatic region outside correspond to **HVCo$_3$**$^{+}$; no evidence for formation of anthracene.



S40. ^{1}H NMR spectrum (400 MHz, acetonitrile-*d*$_3$) following filtration and removal of solvent from attempted catalytic reaction using 10 mol% **VCo$_3$**, 9,10-dihydroanthracene (DHA), 2,6-di*tert*butyl-4-methylpyridine, and (NH$_4$)$_2$Ce(NO$_3$)$_6$ in *o*DFB, with 1,3,5-trimethoxybenzene added as an internal standard. The DHA is 10% consumed, and **VCo$_3$** is converted to **HVCo$_3$**$^{+}$.



S41. ^{51}V NMR spectrum (105 MHz, acetonitrile-d_3) of the reaction solution from **S** demonstrating conversion to **HVCo$_3$**$^+$.

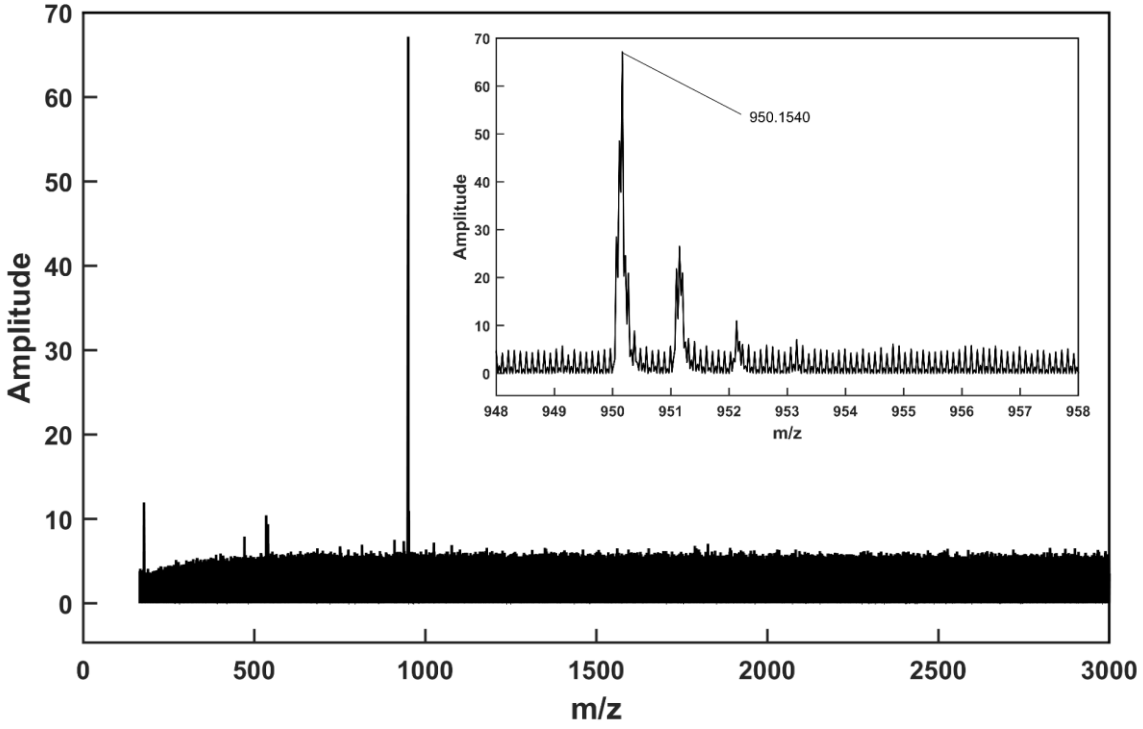


S42. Reaction of **VCo$_3$** and (^{n}Bu$_4$N)$_2$Ce(NO$_3$)$_6$ followed by UV-vis spectroscopy in CH_2Cl_2 at –93 °C, which was maintained with a Unisoku CoolSpeK UV USP-203 cryostat.[10] Spectra were collected every 75 s.

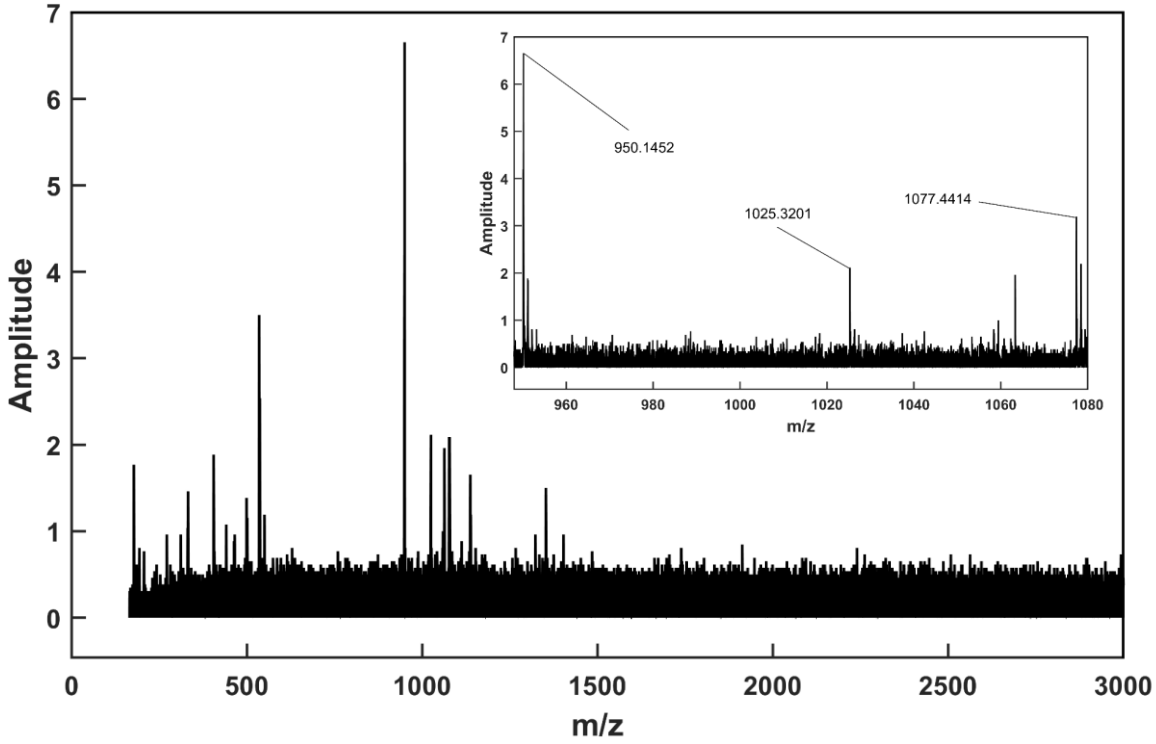
Table S1. Summary of Experimental Conditions for the Synthesis of **VCo_3**

Condition	Isolated Yield of **VCo_3** (%)	Observation
1 equiv $VCl_4(THF)_2$, dried reagents	0	**VCo_3** not observed by HR-ESI-MS
0.5 equiv H_2O	*Not isolated*	0.5:1 ratio of **VCo_3H**:**Co_4**
1 equiv H_2O	*Not isolated*	1:1 ratio of **VCo_3H**:**Co_4**
2 equiv H_2O	*Not isolated*	1.5:1 ratio of **VCo_3H**:**Co_4**
2 equiv $H_2{}^{18}O$	26	Up to one ^{18}O incorporated
Dry $^{32}O_2/^{34}O_2/^{36}O_2$ stat. mixture	*Not isolated*	No ^{18}O incorporation
2 equiv NaOAc or $^{n}Bu_4NOAc$	0	**$HVCo_3^+$** not observed by HR-ESI-MS
2 equiv Cs_2CO_3	0	**$HVCo_3^+$** not observed by HR-ESI-MS
1 equiv H_2NAd	0	**$HVCo_3^+$** not observed by HR-ESI-MS
1 equiv $NH_2C_6F_5$	20	
1 equiv vanadyl acetylacetonate	0	**$HVCo_3^+$** not observed by HR-ESI-MS
1 equiv VCl_3	0	**$HVCo_3^+$** not observed by HR-ESI-MS
2 equiv H_2O, –77 °C	30	
1.5 equiv 3,5-di*tert*butylphenol, –77 °C	25	
1 equiv pyridine-N-oxide	0	Appears to consume VCl_4

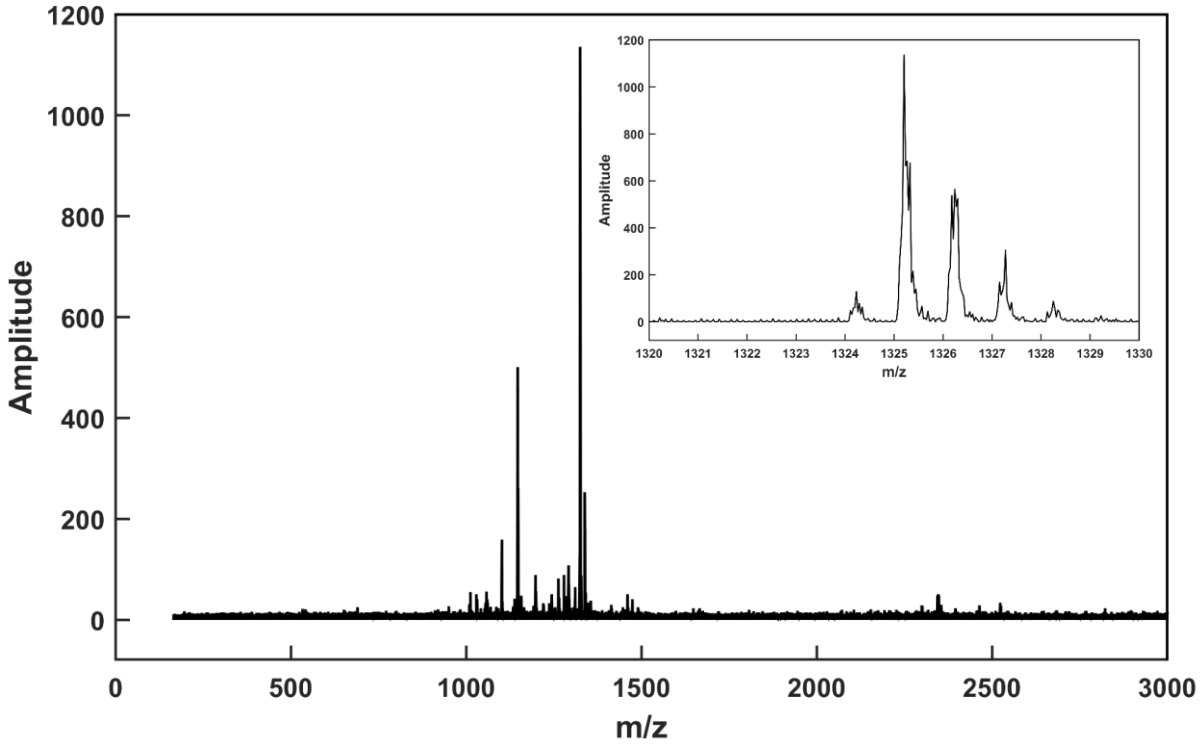
HR-ESI-MS:



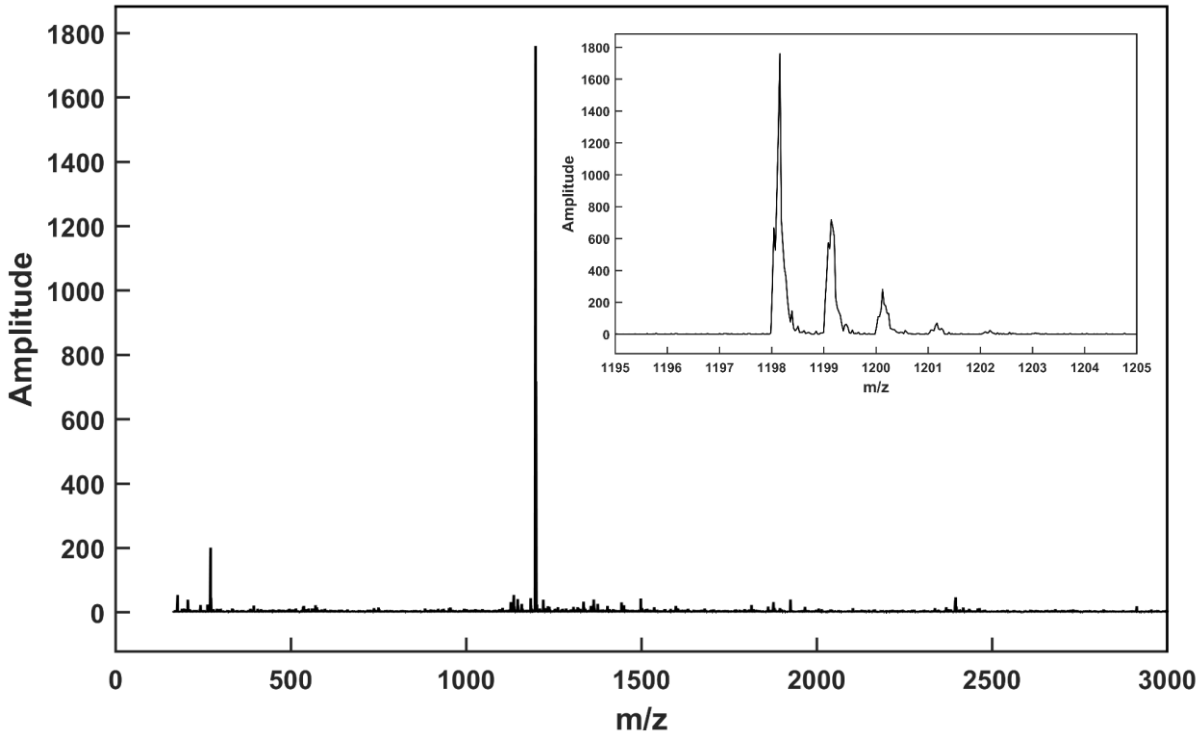
S43. HR-ESI-MS spectrum of **VCo$_3$**[Co].



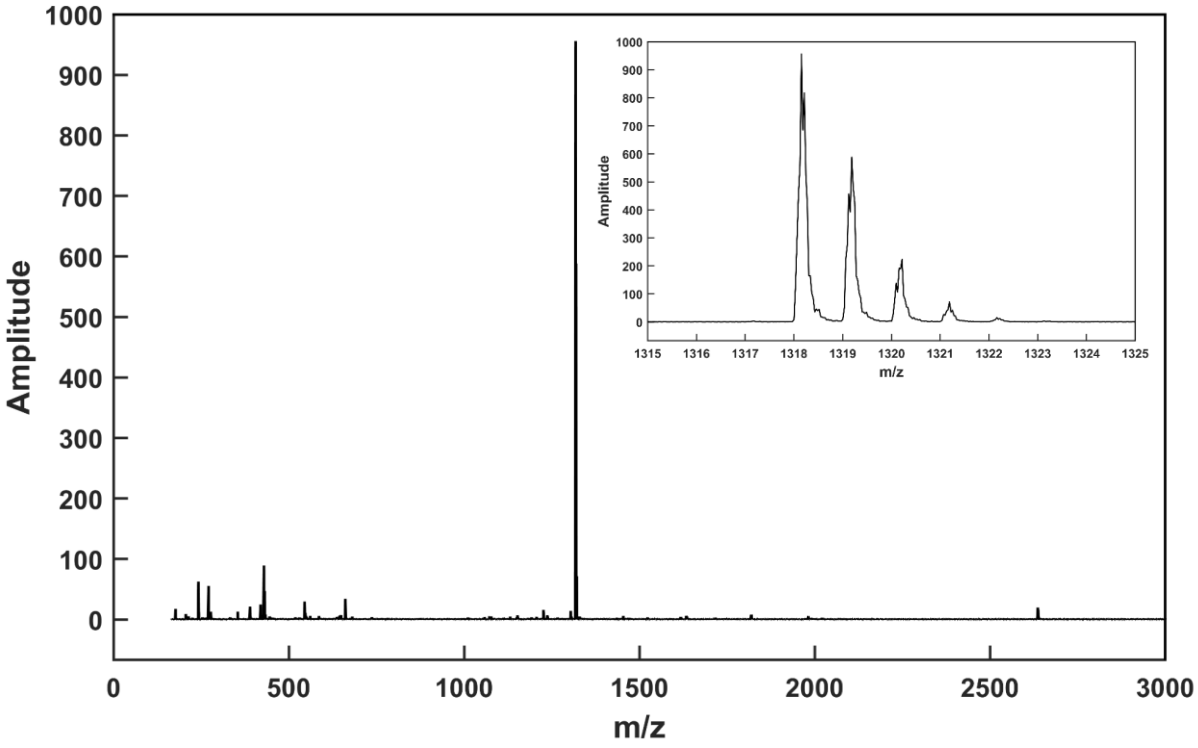
S44. HR-ESI-MS spectrum following purification in reaction of $H_2NC_6F_5$ of **VCo$_3$**[Co]



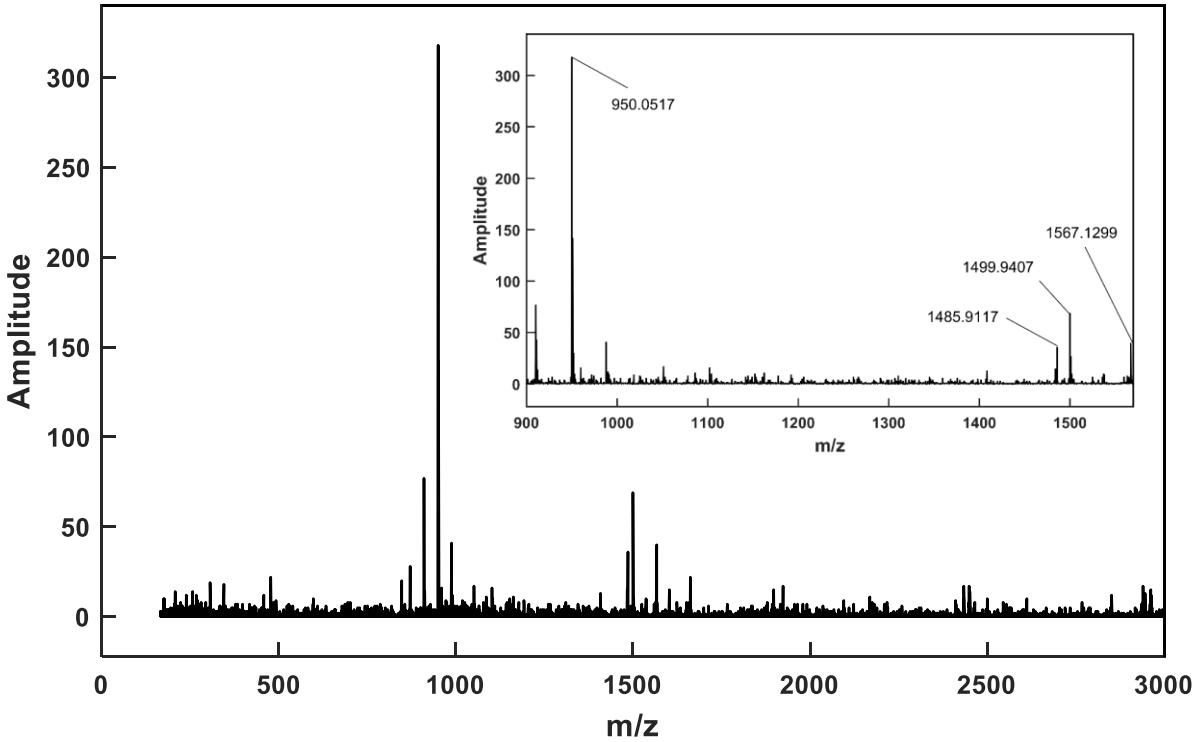
S45. HR-ESI-MS spectrum of **VCo_3(OBz-*t*Bu)**.



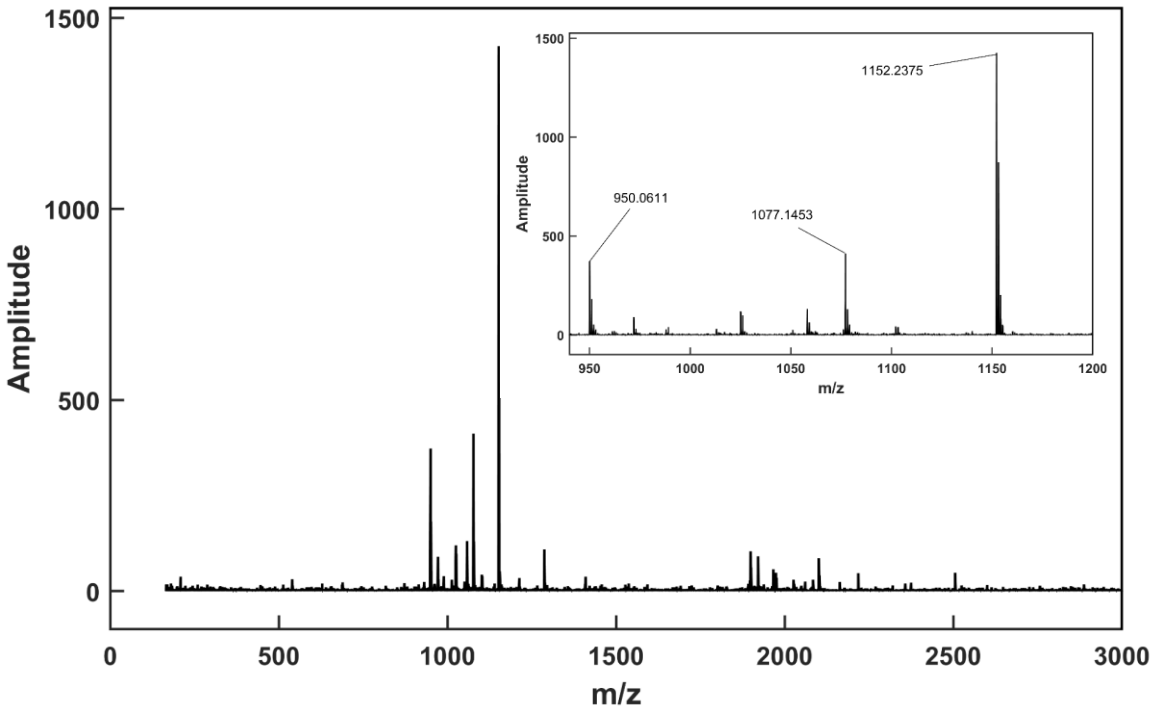
S46. HR-ESI-MS spectrum of **VCo_3(OBz-NO_2)**.



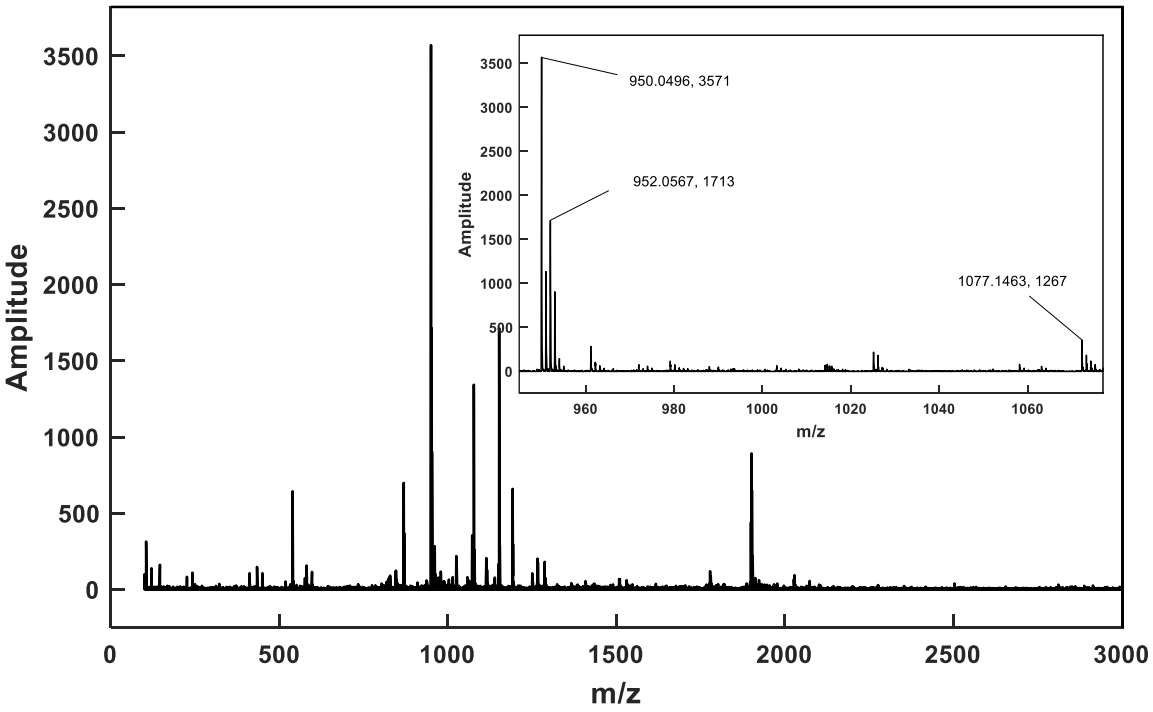
S47. HR-ESI-MS spectrum of **VCo_3(OBz-OMe)**.



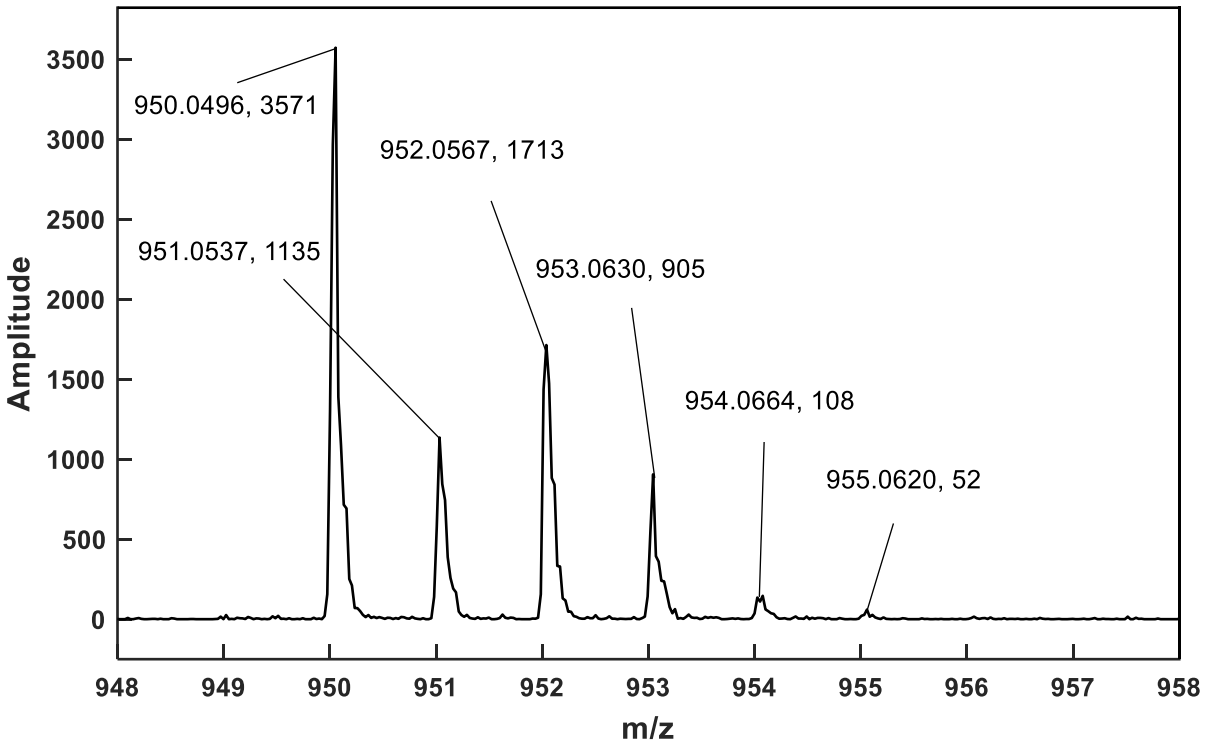
S48. HR-ESI-MS spectrum of **(BCF)VCo_3**.



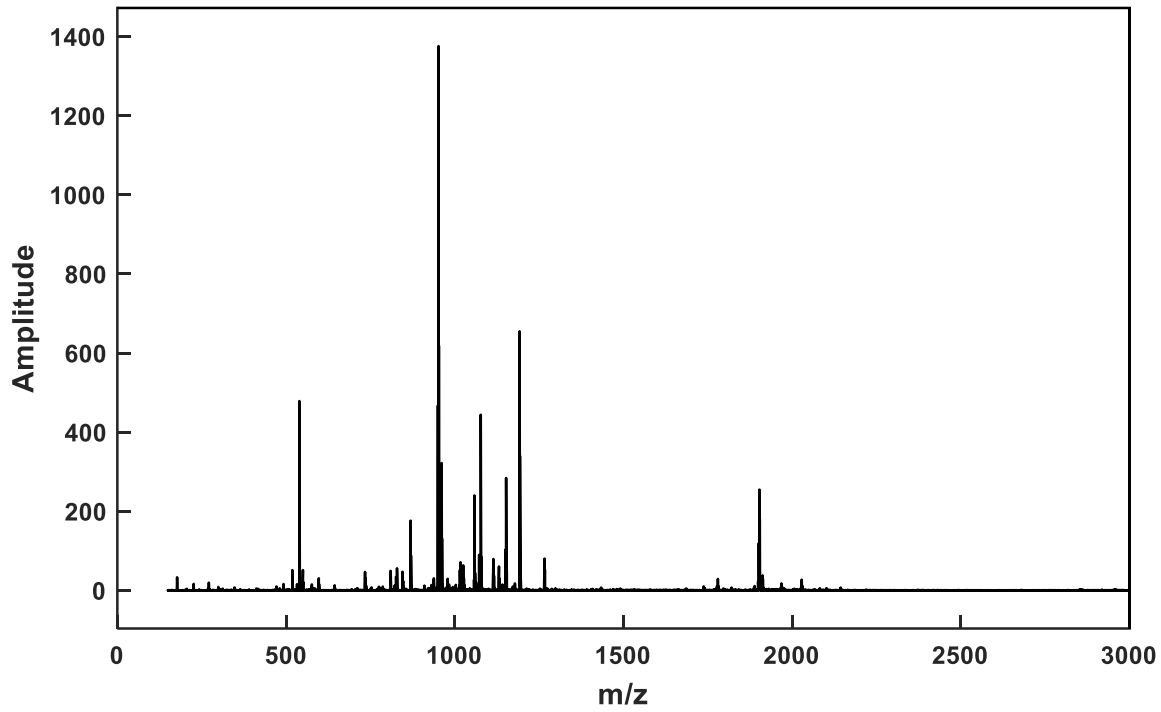
S49. HR-ESI-MS spectrum from the synthesis of **VCo$_3$**[Co] in the presence of $^{18}O_2$.



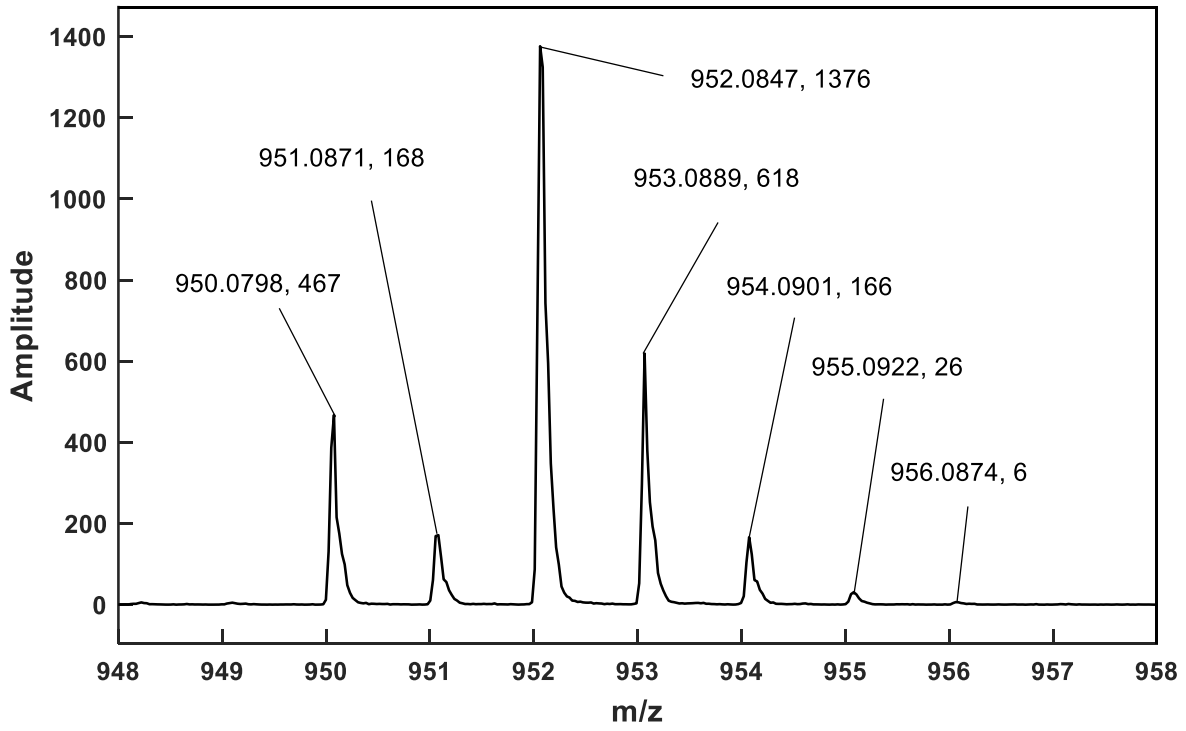
S50. HR-ESI-MS spectrum of the product isolated from synthesis of **VCo$_3$** with $H_2{}^{18}O$ in place of H_2O. Inset shows region between 945 and 1085; peaks shown correspond to [$C_{35}H_{52}Co_3N_3O_{13}VH^+$], [$C_{35}H_{52}Co_3N_3O_{12}(^{18}O)VH^+$], and **Co$_4$H**$^+$. The presence of the latter product indicates decomposition of the **VCo$_3$** cubane during the ionization process.



S51. Enhanced view of the region from between 948-958 from **S**. Observed peaks, followed by intensity, correspond to $[C_{35}H_{52}Co_3N_3O_{13}VH^+]$, $[C_{35}H_{52}Co_3N_3O_{12}(^{18}O)VH^+]$ and ^{13}C isotopologues. The observed distribution of isotopologues and intensities matches the predicted values, indicating that the presence of a doubly ^{18}O substituted cubane, $[C_{35}H_{52}Co_3N_3O_{11}(^{18}O)_2VH^+]$ is unlikely.

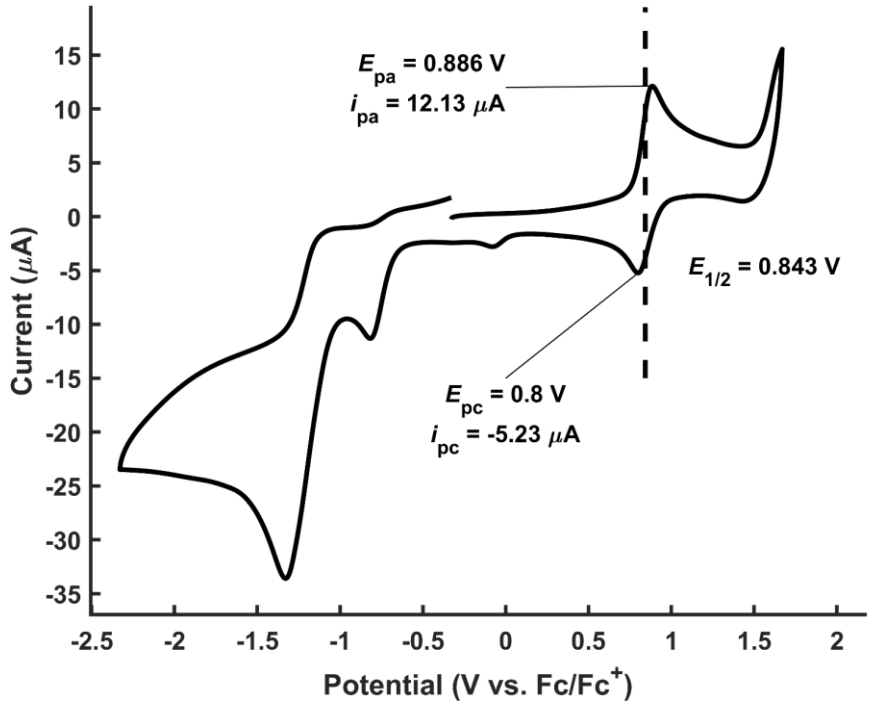


S52. HR-ESI-MS spectrum from the reaction of **VCo_3O_4** with 5 equiv of $H_2{}^{18}O$.

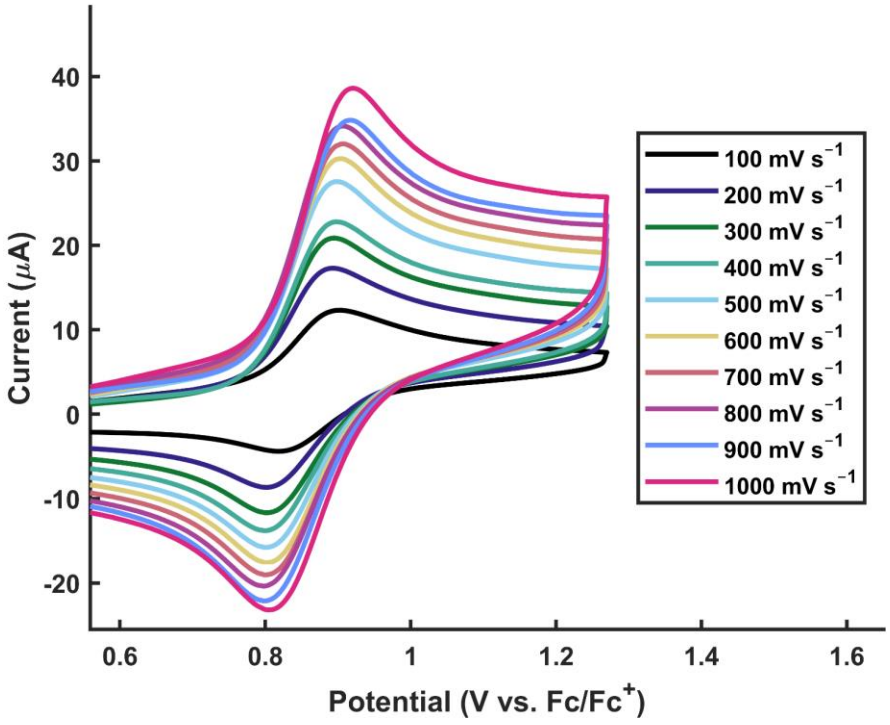


S53. HR-ESI-MS spectrum of the region between 948 and 958 from the reaction of **VCo_3O_4** with 5 equiv of $H_2{}^{18}O$ (**S**). Observed peaks, followed by intensity, correspond to $[C_{35}H_{52}Co_3N_3O_{13}VH^+]$, $[C_{35}H_{52}Co_3N_3O_{12}(^{18}O)VH^+]$ and ^{13}C isotopologues. The observed distribution of isotopologues and intensities matches the predicted values, indicating that the presence of a doubly ^{18}O substituted cubane, $[C_{35}H_{52}Co_3N_3O_{11}(^{18}O)_2VH^+]$ is unlikely.

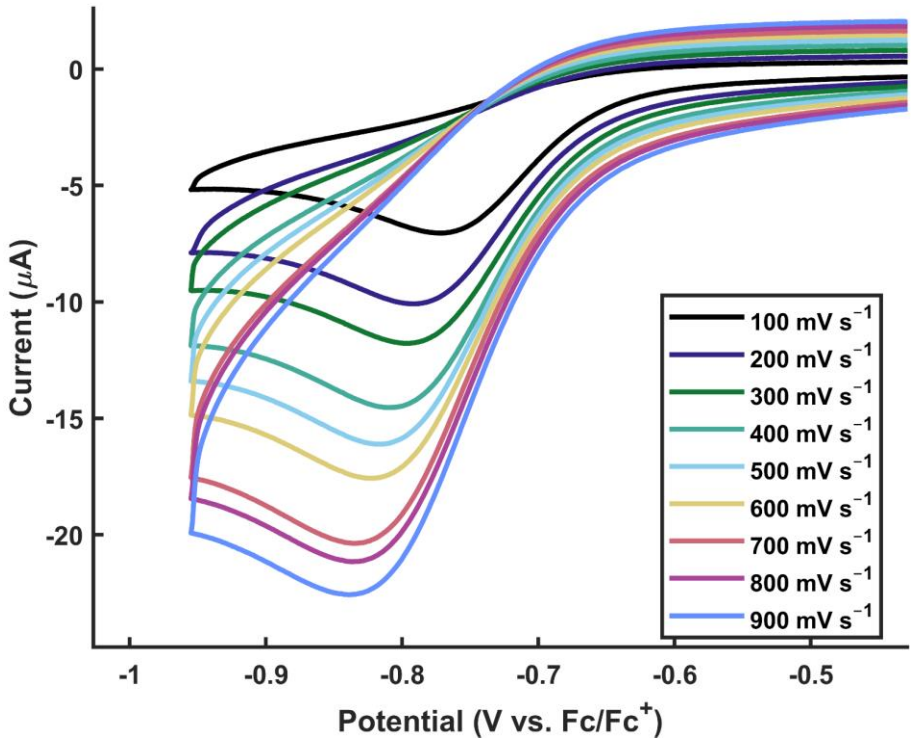
Cyclic Voltammetry:



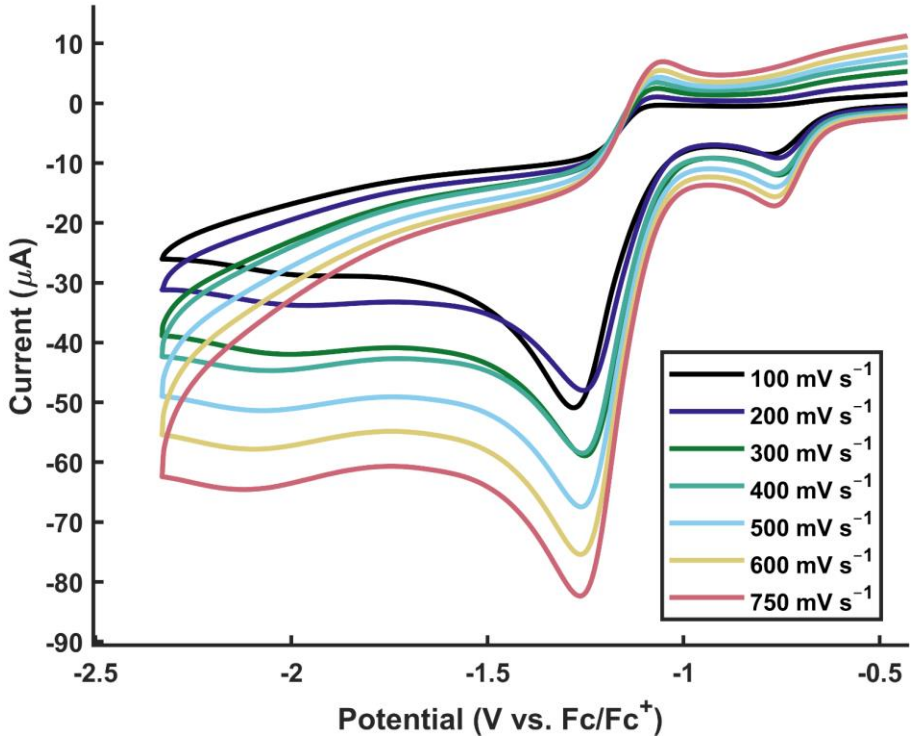
S54. Cyclic voltammogram of **VCo_3**.



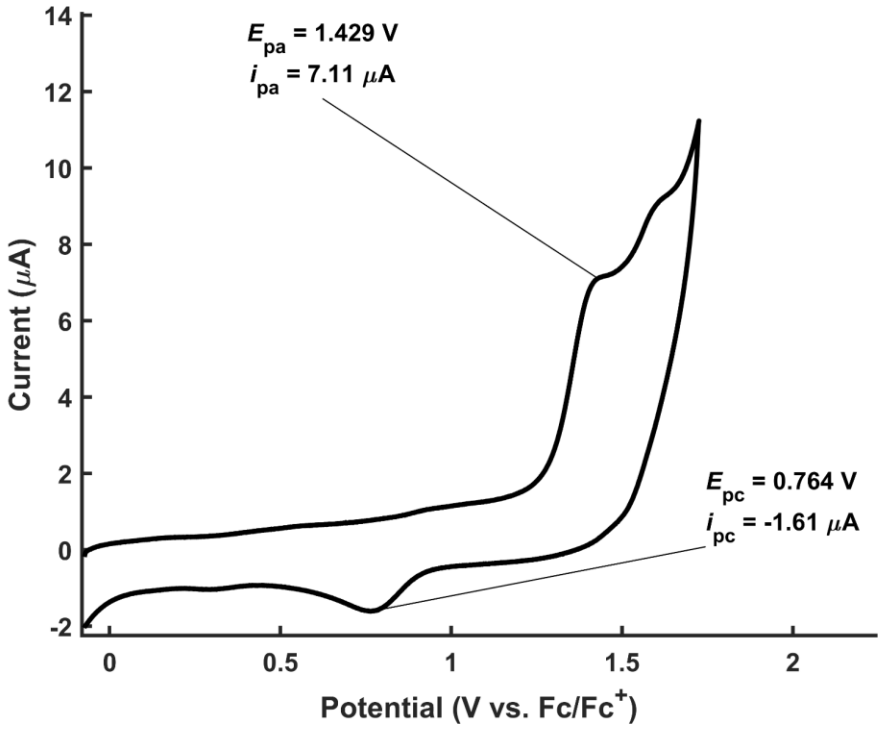
S55. Scan rate study of the oxidation of **VCo_3**.



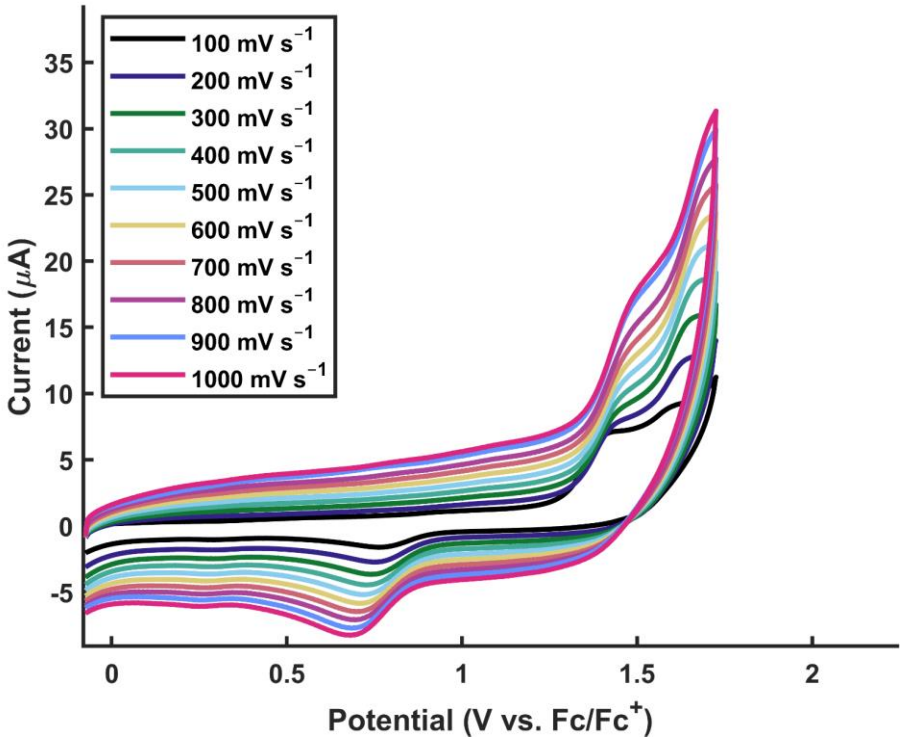
S56. Scan rate study of the first reduction of **VCo_3**.



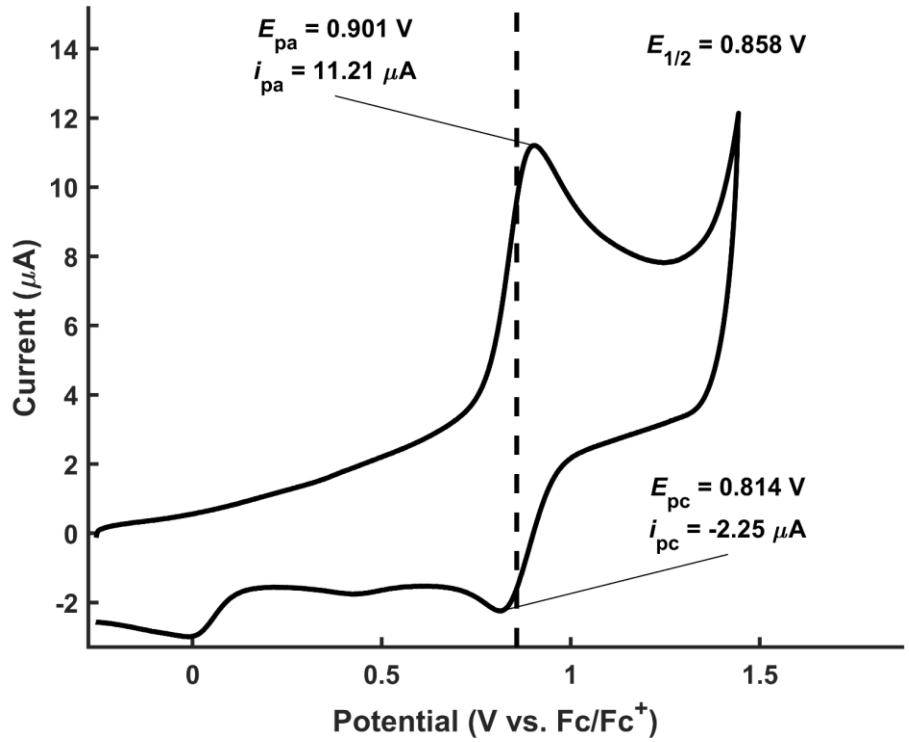
S57. Scan rate study of the second reduction of **VCo_3**.



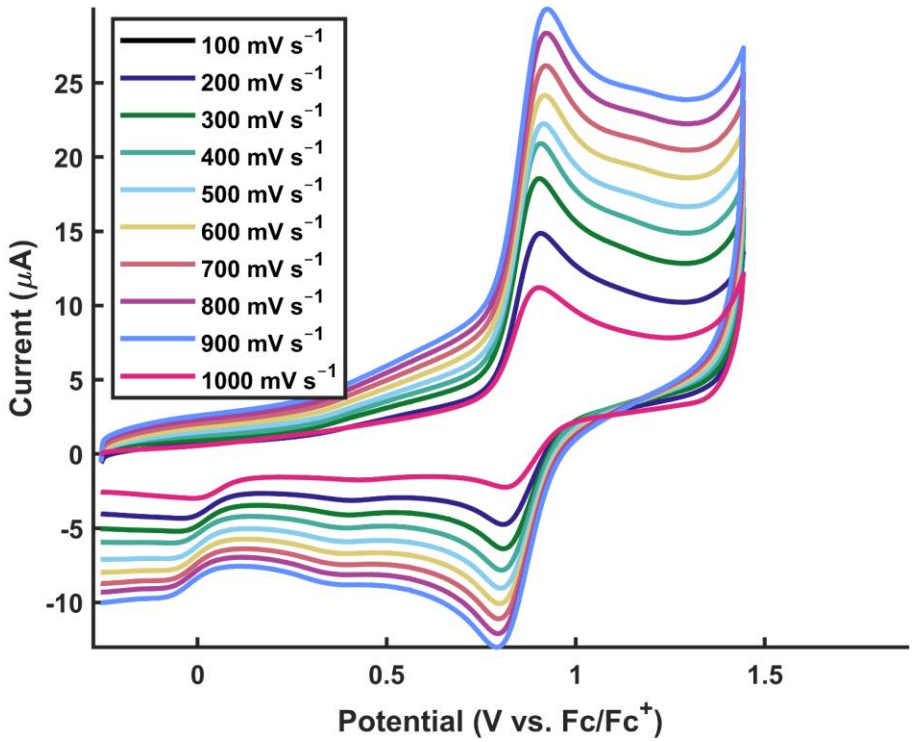
S58. Oxidation of **(BCF)VCo$_3$** in 0.2 M [^{n}Bu$_4$N][PF$_6$] *o*DFB solution. Glassy carbon electrode, Pt wire counterelectrode, silver wire floating pseudoreference internally referenced to Fc/Fc$^+$.



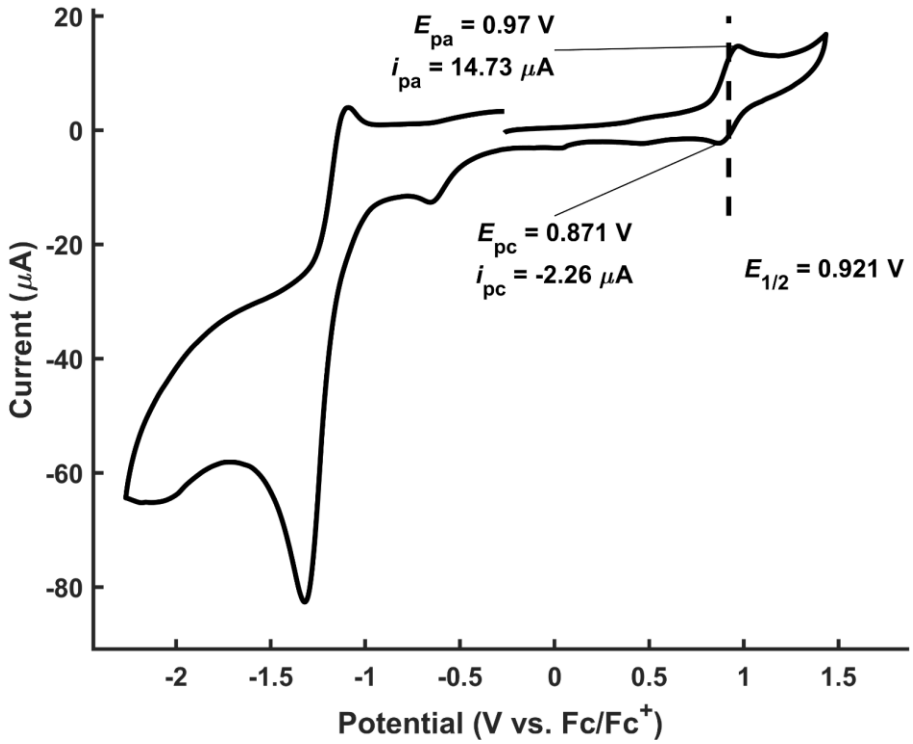
S59. Scan rate study of **(BCF)VCo$_3$**. See **S** for conditions.



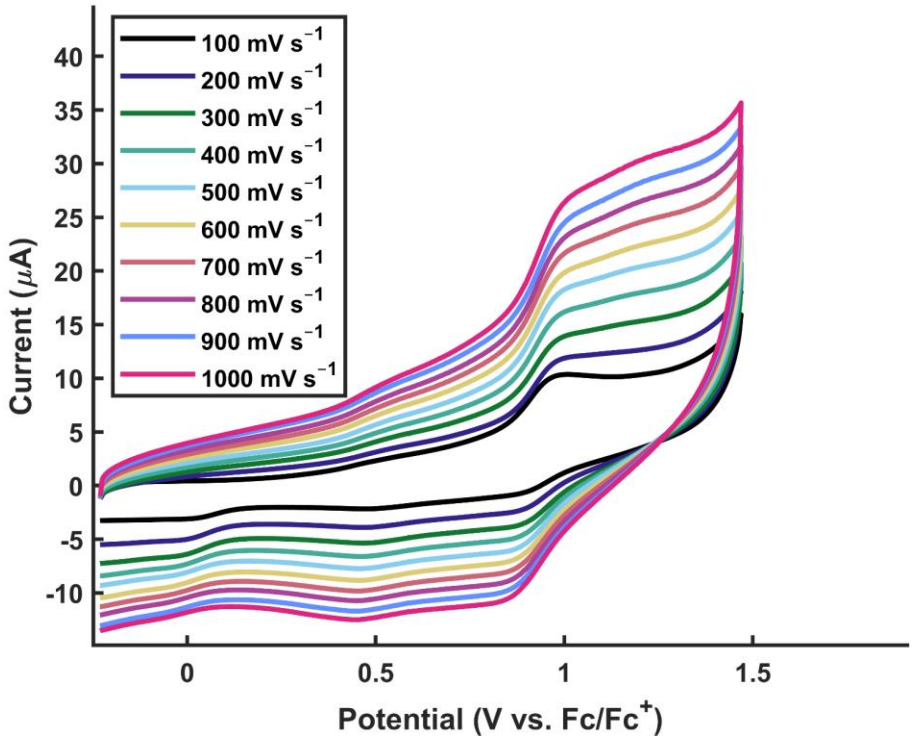
S60. Cyclic voltammogram of **VCo_3(OBz-OMe)**.



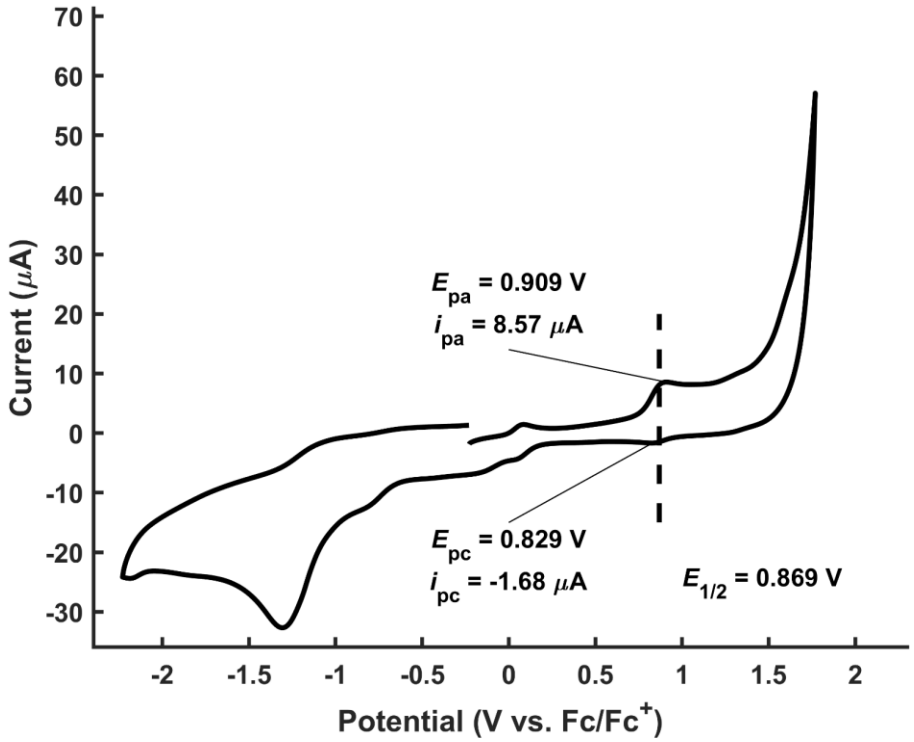
S61. Scan rate study of the oxidation of **VCo_3(OBz-OMe)**.



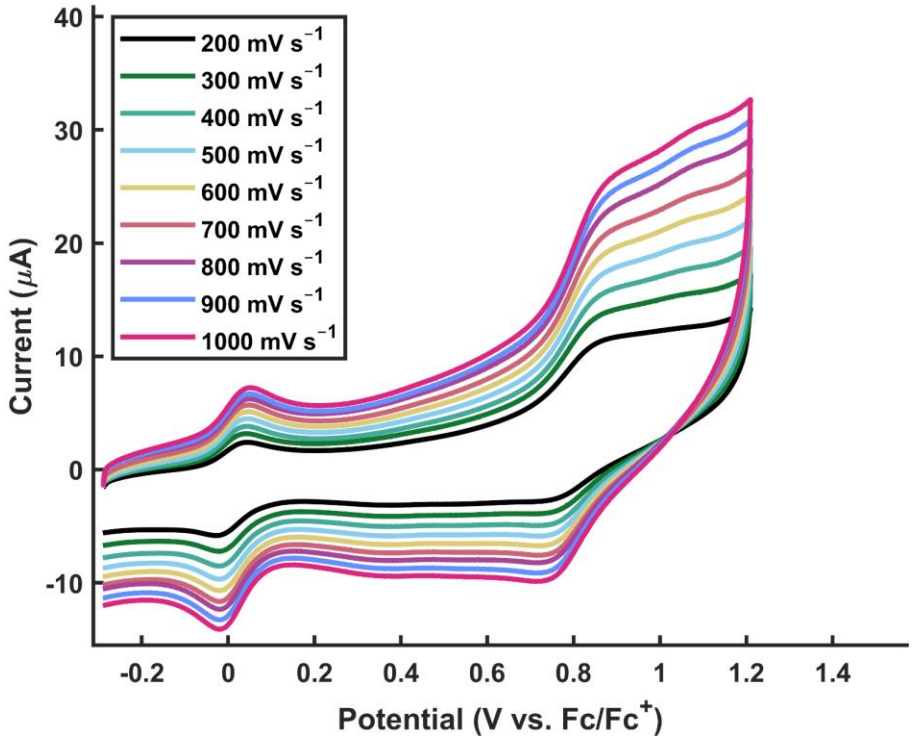
S62. Cyclic voltammogram of **$VCo_3(OBz\text{-}NO_2)$**.



S63. Scan rate study of **$VCo_3(OBz\text{-}NO_2)$**.



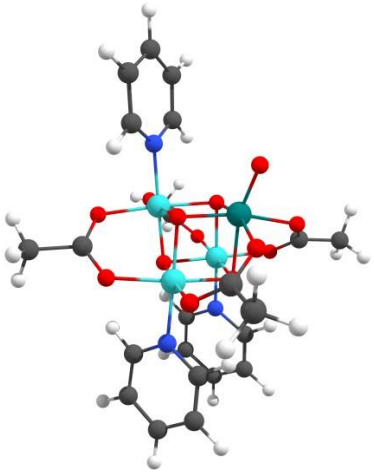
S64. Cyclic voltammogram of **VCo_3(OBz-*t*Bu)**.



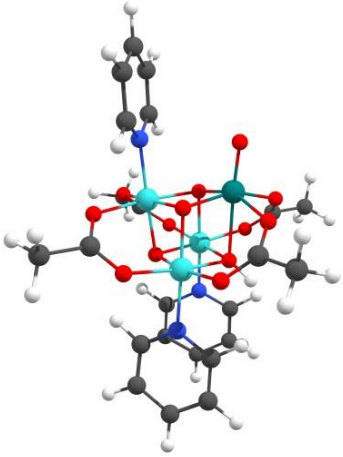
S65. Scan rate study of **VCo_3(OBz-*t*Bu)**. Peak centered at 0 corresponds to ferrocene.

Computational Details:

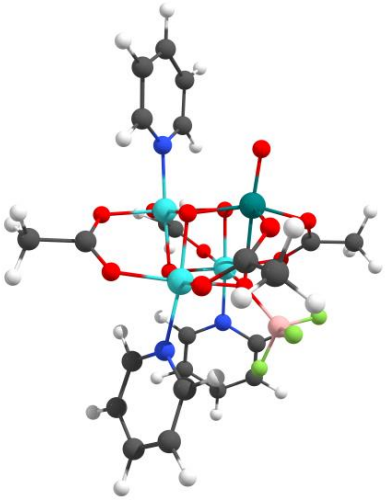
All calculations were performed in ORCA 5.4 and the calculated structures were rendered with ChemCraft 1.8, Wiberg bond indices (WBI) were analyzed using MultiWfn.[11-13] Geometry optimizations were performed at the TPSSh level of theory; these heterocubane systems were previously benchmarked and this functional was found to give the best performance.[14, 15] A mixed basis set consisting of the def2-SVP basis for light atoms (H, B, C, N, O_{OAc}, F), the def2-TZVP basis for the cubane core and heavy atoms (O_{oxo}, Co, V) and the RIJCOSX auxiliary basis was used for geometry optimizations and frequency calculations.[16] The dispersion effects were accounted for by the D3BJ dispersion correction, and the solvent modeled using a CPCM.[17, 18] All single-point calculations were performed with a full def2-TZVP basis. Imaginary frequencies <30 cm^{-1} associated with CH_3 group rotation were assumed to be inconsequential and possibly due to the use of the auxiliary basis approximation. The *tert*-butyl groups of the 4-*tert*-butylpyridine ligands were truncated to reduce computational costs. Comparison of the calculated truncated and untruncated structures revealed insignificant changes in the bonding metrics. Color scheme: H = white, B = pink, C = grey, N = blue, O = red F = green, V = dark green/blue, Co = teal.



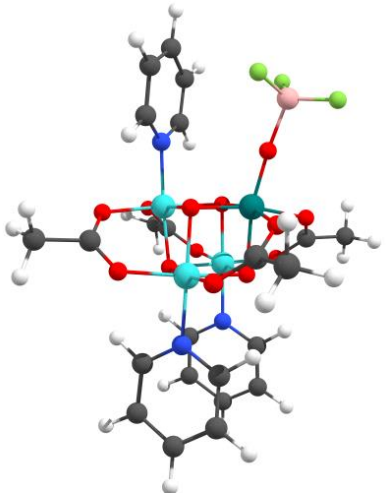
S66. Optimized solution-state (MeCN) molecular structure of **VCo_3**.



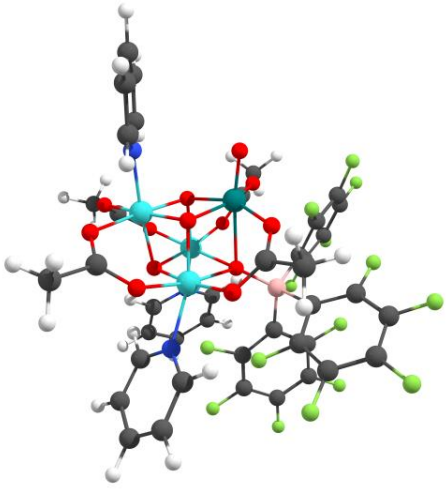
S67. Optimized solution-state (MeCN) molecular structure of **VCo_3H^+**



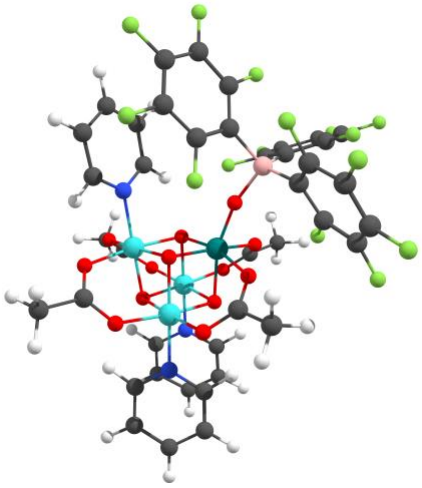
S68. Calculated solution-state (C_6H_6) molecular structure for **$VCo_3(BF_3)$**.



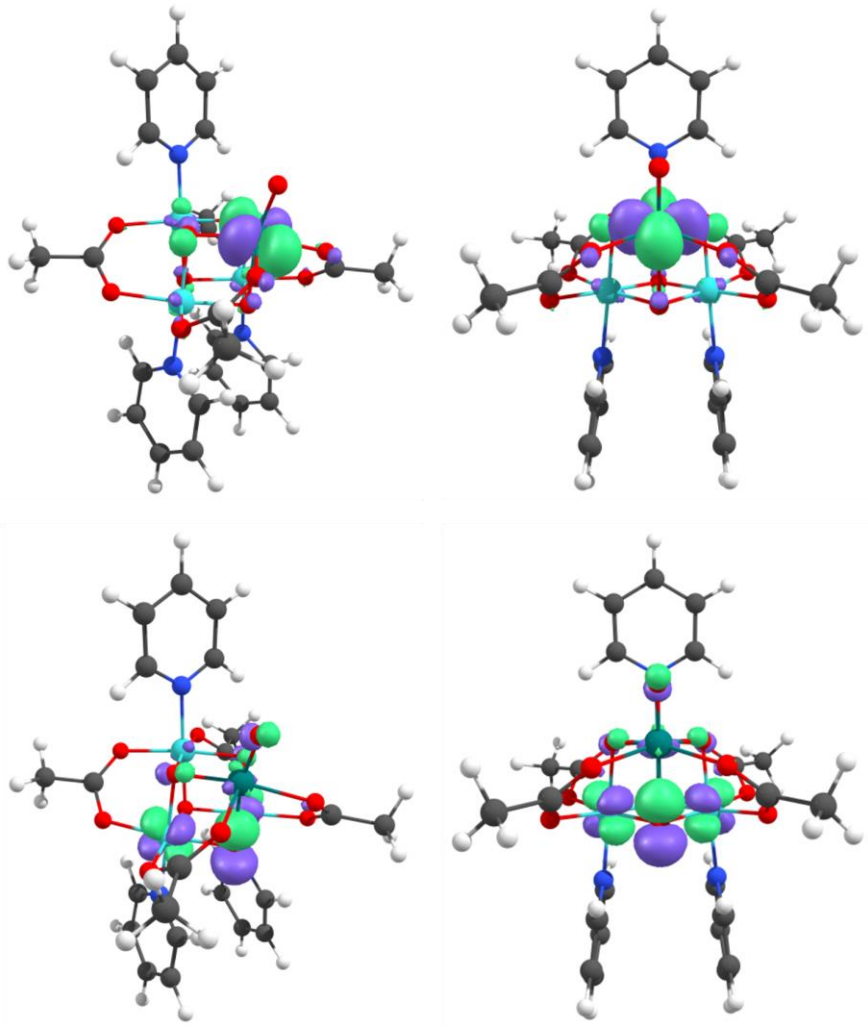
S69. Calculated solution-state (C_6H_6) molecular structure for **$(BF_3)VCo_3$**.



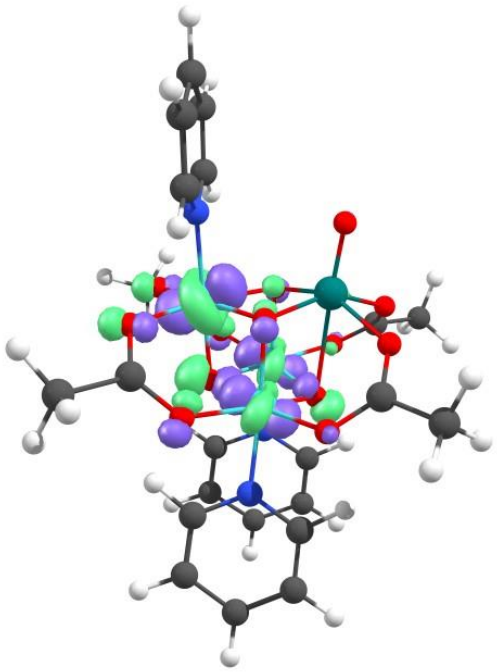
S70. Calculated solution-state (C_6H_6) molecular structure for **$VCo_3(BCF)$**.



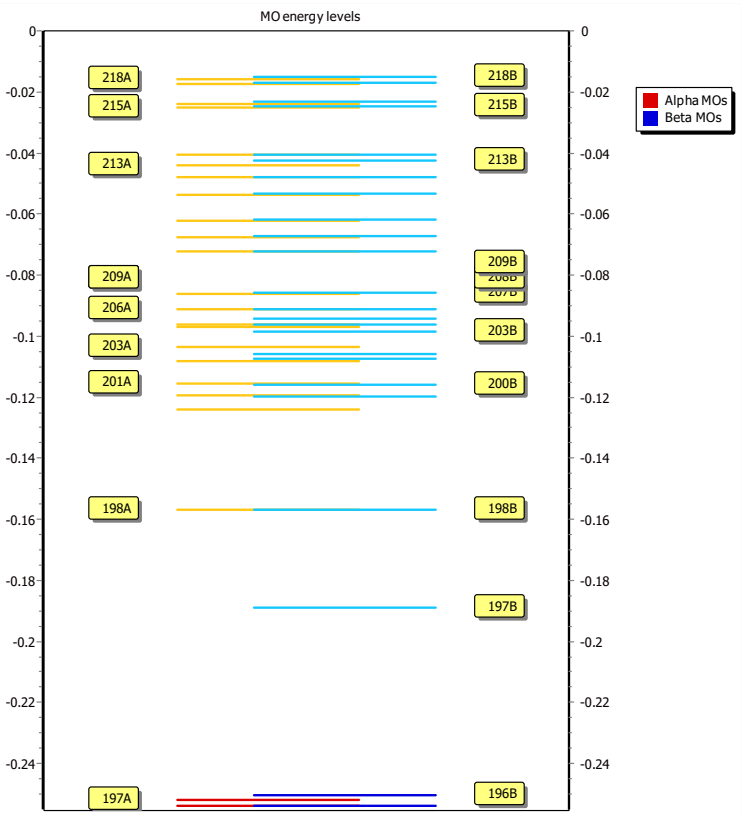
S71. Calculated solution-state (C_6H_6) molecular structure for **(BCF)VCo$_3$**.



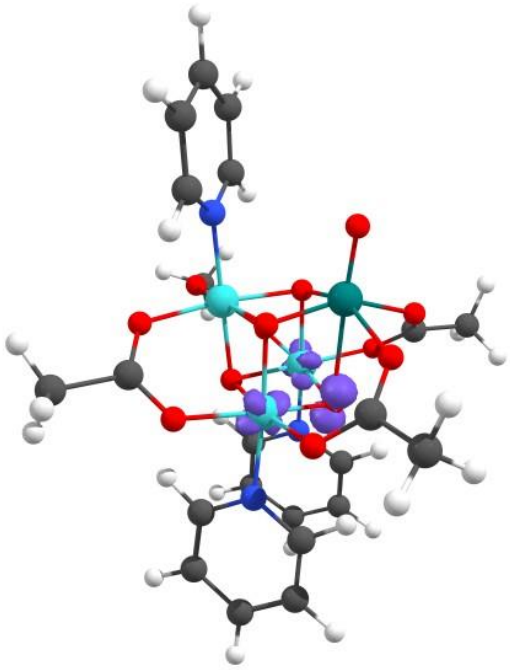
S72. Calculated canonical molecular orbitals of **VCo$_3$**. Top: lowest unoccupied molecular orbital (LUMO) from two different perspectives. Bottom: highest occupied molecular orbital (HOMO) from two different perspectives. Isosurface rendered with a contour value of 0.057870.



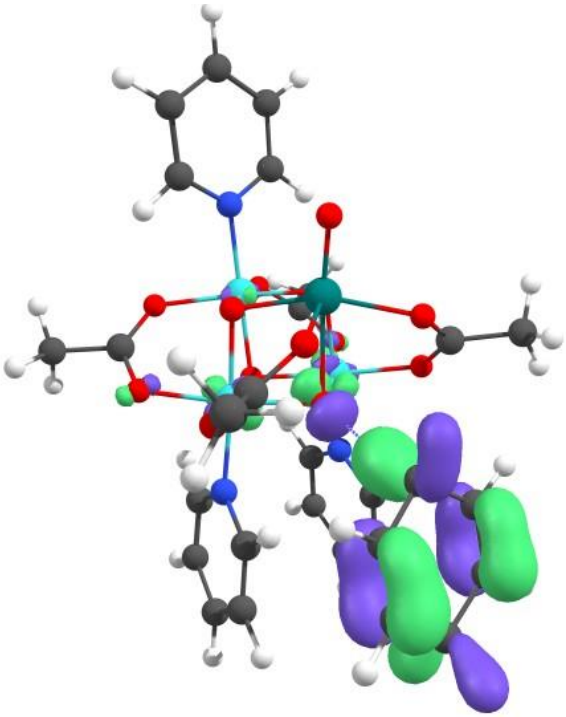
S73. Calculated canonical molecular orbital of $\mathbf{VCo_3^+}$. Shown is the highest SOMO. Isosurface rendered with a contour value of 0.057870.



S74. Orbital energy diagram for $\mathbf{VCo_3^+}$, with energy in Hartrees.



S75. Calculated spin-density plot of **VCo_3^+** rendered at an isovalue of 0.033.



S76. Calculated canonical molecular orbital of **VCo_3^+**. Shown is the highest SOMO. Isosurface rendered with a contour value of 0.057870.

Table S2. Calculated WBI for **VCo_3H^+**.

Atom 1	Atom 2	Bond Description	Wiberg Bond Order
V	O6	O≡V	2.59
V	O14	O_{trans}–V	0.27
V	O7	O_{cis}–V	1.11
V	O16	O_{cis}–V	1.11
Co3	O14	Co–O_{trans}–V	0.61
Co2	O14	Co–O_{trans}–V	0.61
Co2	O7	Co–O_{cis}–V	0.66
V	O	O≡V bond of $VOCl_3$	2.85

Table S3. Calculated WBI for **VCo_3**

Atom 1	Atom 2	Bond Description	Wiberg Bond Order
V	O5	O≡V	2.62
V	O15	O_{trans}–V	0.73
V	O6	O_{cis}–V	1.15
V	O16	O_{cis}–V	1.16
Co2	O30	Co–O_{trans}–V	0.91
Co2	O15	Co–O_{trans}–V	0.91
Co2	O6	Co–O_{cis}–V	0.76
V	O	O≡V bond of $VOCl_3$	2.85

Table S4. Calculated WBI for **BCF(VCo_3)**.

Atom 1	Atom 2	Bond Description	Wiberg Bond Order
V	O20	O=V	1.78
V	O30	O_{trans}–V	0.91
V	O21	O_{cis}–V	1.14
V	O31	O_{cis}–V	1.099
Co3	O15	Co–O_{trans}–V	0.70
Co2	O15	Co–O_{trans}–V	0.70
Co2	O21	Co–O_{cis}–V	0.64
V	O	O≡V bond of $VOCl_3$	2.85

Table S5. Calculated WBI for **VCo_3^+**

Atom 1	Atom 2	Bond Description	Wiberg Bond Order
V	O17	O≡V	2.74
V	O7	O_{trans}–V	0.24
V	O16	O_{cis}–V	1.17
V	O6	O_{cis}–V	1.17
Co1	O7	Co–O_{trans}–V	1.14
Co2	O7	Co–O_{trans}–V	1.15
Co1	O6	Co–O_{cis}–V	0.78

Table S6. Calculated WBI for transition state of $\mathbf{VCo_3^+}$

Atom 1	Atom 2	Bond Description	Wiberg Bond Order
V	O17	O≡V	2.56
V	O7	O_{trans}–V	0.37
V	O16	O_{cis}–V	1.11
V	O6	O_{cis}–V	1.12
Co1	O7	Co–O_{trans}–V	0.80
Co2	O7	Co–O_{trans}–V	0.79
Co1	O6	Co–O_{cis}–V	0.64

Table S7. Calculated spin density for $\mathbf{VCo_3^+}$.

Atom 1	Spin Population	Description
Co1	0.27	$\underline{Co_1}$–O_{trans}–V
Co2	0.28	$\underline{Co_2}$–O_{trans}–V
Co3	–0.00048	$\underline{Co}$— —V
V	–0.011	---
O5	–0.03438	---
O6	0.00913	$\underline{O}$≡V
O7	0.45	$\underline{O_{trans}}$–V
O16	0.00952	Co–$\underline{O_{cis}}$–V
O17	–0.00267	Co–$\underline{O_{cis}}$–V

Table S8. Calculated spin density for transition state of reaction of CHD $\mathbf{VCo_3^+}$.

Atom 1	Spin Population	Description
Co1	0.125	Co_1–O_{trans}–V
Co2	0.127	Co_2–O_{trans}–V
Co3	0.001328	Co—V
V	–0.011	---
O5	–0.007978	---
O6	0.00259	O≡V
O7	0.258	O_{trans}–V
O16	0.00262	Co–$\underline{O_{cis}}$–V
O17	0.00517	Co–$\underline{O_{cis}}$–V
C21	0.157	Vinylic carbon
C23	0.096	Vinylic carbon
C25	0.158	Allylic carbon
H51	0.03	Abstracted H

Table S9. Tabulated Calculated Energies for the Reaction of VCo_3^+ with Cyclohexadiene (CHD).

Species	E_{el}	$G^0 = G - E_{el} + E_{sp}$	ΔG (kcal mol^{-1})	H
CHD	–146393.9101	–146485.9283	---	–146313.8338
CHD (w/o disp)	–146385.1854	–146481.4908	---	
VCo_3^+	–4471846.615	–4473140.828	---	–4471501.138
VCo_3^+ (w/o disp)	–4471753.691	–4473047.364	---	
VCo_3^+ + CHD	---	–4619523.746	0	–4617814.972
VCo_3^+ + CHD (w/o disp)	–4618138.876	–4619528.855	97.90	
TS	–4617855.185	–4619622.542	4.21	–4617823.189
TS (w/o disp)	–4617855.185	–4619509.314	117.44 (19.54)	–4617430.957
CHD^+	–146002.7605	–146106.5052	---	–146002.7605
$HVCo_3^+$	–4472257.719	–4473546.137	---	–4471810.368
$HVCo_3^+$ + CHD^+	---	–4619652.642	–25.88	–4617741.448
VCo_3^+ (triplet)	–4471556.917	–4473125.773		–4471486.335
VCo_3^+ (Pentet)	–4471815.866	–4473128.547		–4471470.777

Table S10. Tabulated Calculated Energies for the Spin-States of VCo_3^+.

Species	E_{el} (kcal mol^{-1})	$G^0 = G - E_{el} + E_{sp}$ (kcal mol^{-1})	ΔG (kcal mol^{-1})
VCo_3^+ (doublet)	–4471846.615	–4473140.828	0
VCo_3^+ (quartet)	–4471830.644	–4473125.773	15.05
VCo_3^+ (sextet)	–4471815.866	–4473128.547	12.28

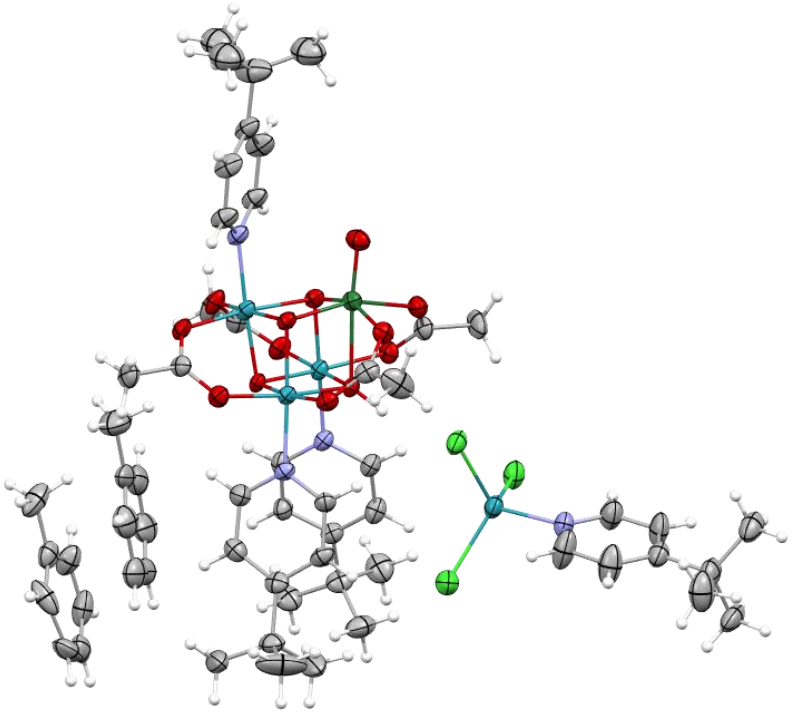
Table S11. Tabulated Calculated Energies for the Isomeric Adducts of BF_3 and $B(C_6F_5)_3$ with VCo_3.

Species	E_{el} (kcal mol^{-1})	$G^0 = G - E_{el} + E_{sp}$ (kcal mol^{-1})	ΔG (kcal mol^{-1})
$(BF_3)–O_{cubane}$	–4675498.233	–4677025.476	0
$(BF_3)–O_{terminal}$	–4675484.257	–4677020.487	4.98
$(BCF)–O_{cubane}$	–5856678.19	–5859492.283	0
$(BCF)–O_{terminal}$	–5856723.309	–5859546.446	–54.16 (!!)

Crystallographic Data:

General Comments: All structural data were collected at ALS beamline 12.2.1, and the authors acknowledge the advice and assistance of Simon Teat.

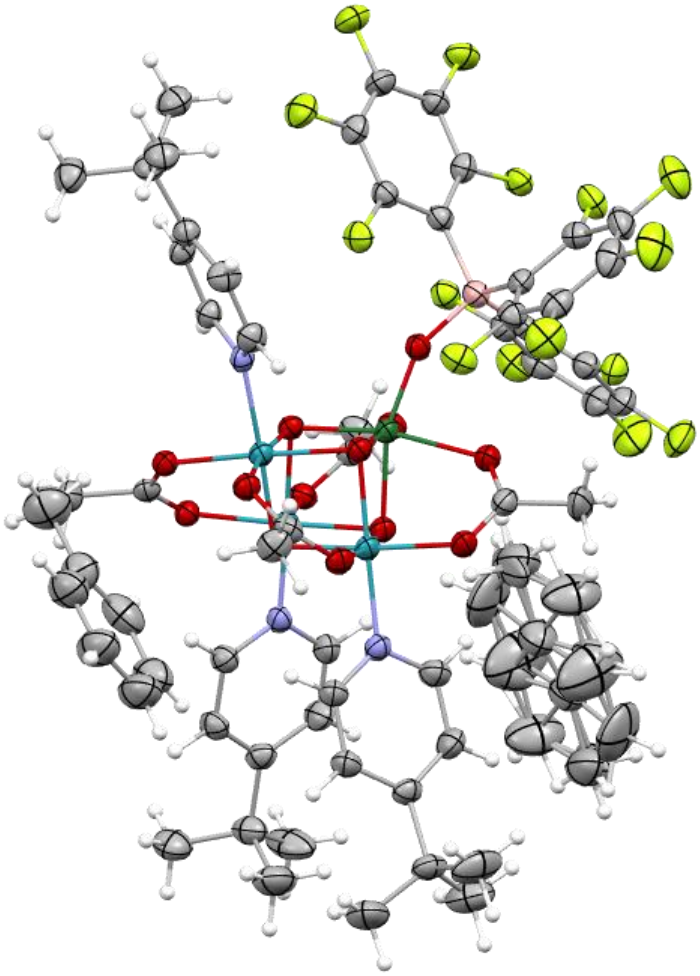
Color Scheme: H = white, B = pink, C = light gray, N = pale blue, O = red, F = light neon green, V = Dark green, Co = teal, Cl = dark neon green.



S77. Solid-state molecular structure of **VCo_3**[Co].

Table S12. Refinement data for **VCo_3**[Co].

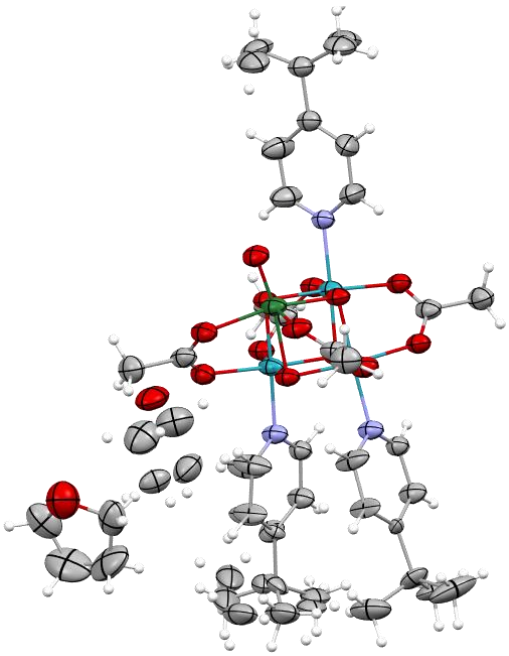
Identification code	WH_VCo3[Co]	**ρ_{calc}g/cm^3**	1.417
Empirical formula	$C_{54.5}H_{77}Cl_3Co_4N_4O_{13}V$	**μ/mm^{-1}**	1.401
Formula weight	1389.21	**F(000)**	2872.0
Temperature/K	100.15	**Crystal size/mm^3**	0.02 × 0.02 × 0.01
Crystal system	monoclinic	**Radiation**	? (λ = 0.7288)
Space group	$P2_1/n$	**2Θ range for data collection/°**	3.772 to 57.592
a/Å	13.299(2)	**Index ranges**	-17 ≤ h ≤ 17, -28 ≤ k ≤ 28, -30 ≤ l ≤ 30
b/Å	21.872(4)	**Reflections collected**	100622
c/Å	23.194(5)	**Independent reflections**	15665 [R_{int} = 0.0653, R_{sigma} = 0.0487]
α/°	90	**Data/restraints/parameters**	15665/31/766
β/°	105.172(4)	**Goodness-of-fit on F^2**	1.095
γ/°	90	**Final R indexes [I>=2σ (I)]**	R_1 = 0.0934, wR_2 = 0.2502
Volume/Å^3	6512(2)	**Final R indexes [all data]**	R_1 = 0.1107, wR_2 = 0.2596
Z	4	**Largest diff. peak/hole / e Å^{-3}**	1.40/-0.80



S78. Solid-state structure of **(BCF)VCo$_3$**.

Table S13. Refinement data for **(BCF)VCo$_3$**.

Identification code	WH_(BCF)VCo3	**ρ_{calc}g/cm^3**	1.570
Empirical formula	$C_{66}H_{67}BCo_3F_{15}N_3O_{13}V$	**μ/mm^{-1}**	1.164
Formula weight	1633.76	**F(000)**	1664.0
Temperature/K	100	**Crystal size/mm^3**	0.1 × 0.07 × 0.05
Crystal system	triclinic	**Radiation**	? (λ = 0.7678)
Space group	P-1	**2Θ range for data collection/°**	3.466 to 55.442
a/Å	14.6963(13)	**Index ranges**	-17 ≤ h ≤ 17, -18 ≤ k ≤ 18, -22 ≤ l ≤ 22
b/Å	14.9504(15)	**Reflections collected**	41274
c/Å	18.5417(17)	**Independent reflections**	12785 [R_{int} = 0.0717, R_{sigma} = 0.0830]
α/°	71.973(4)	**Data/restraints/parameters**	12785/140/954
β/°	87.659(4)	**Goodness-of-fit on F^2**	1.049
γ/°	63.866(4)	**Final R indexes [I>=2σ (I)]**	R_1 = 0.0489, wR_2 = 0.1152
Volume/Å^3	3456.1(6)	**Final R indexes [all data]**	R_1 = 0.0788, wR_2 = 0.1292
Z	2	**Largest diff. peak/hole / e Å^{-3}**	0.61/-0.48



S78. Solid-state structure of **VCo_3**.

Table S14. Refinement details for **VCo_3**.

Identification code	WH_VCo3	**ρ_{calc}g/cm^3**	1.374
Empirical formula	$C_{42}H_{65}Co_3N_3O_{14.25}V$	**μ/mm^{-1}**	1.233
Formula weight	1067.70	**F(000)**	2224.0
Temperature/K	100.15	**Crystal size/mm^3**	0.1 × 0.01 × 0.01
Crystal system	orthorhombic	**Radiation**	? (λ = 0.7228)
Space group	Pnma	**2Θ range for data collection/°**	4.036 to 53.98
a/Å	17.5153(16)	**Index ranges**	-21 ≤ h ≤ 21, -14 ≤ k ≤ 14, -31 ≤ l ≤ 31
b/Å	11.6326(11)	**Reflections collected**	65704
c/Å	25.324(2)	**Independent reflections**	5608 [R_{int} = 0.0594, R_{sigma} = 0.0298]
α/°	90	**Data/restraints/parameters**	5608/196/391
β/°	90	**Goodness-of-fit on F^2**	1.124
γ/°	90	**Final R indexes [I>=2σ (I)]**	R_1 = 0.0640, wR_2 = 0.1797
Volume/Å^3	5159.6(8)	**Final R indexes [all data]**	R_1 = 0.0745, wR_2 = 0.1857
Z	4	**Largest diff. peak/hole / e Å^{-3}**	0.72/-0.57

Special Refinement Details:

The crystallographic characterization of this complex was challenging due to the proclivity of this system to form extremely small plates that did not diffract past 1.0 Å even when using synchrotron radiation. Therefore, as the only attempt of many that diffracted to 0.80 Å, this sample was not recollected despite the disorder challenges. The final structure includes models for two independent molecules of THF, with one on an inversion center, and another on a mirror plane. These solvent models are heavily restrained, with RIGU, SIMU, and SADI, and two DFIX restraints; the bond lengths of both suggest that there is little preference for oxygen atom orientation. A third THF on an inversion center was located but all attempts to model this position

were unsuccessful. The electron density associated with this solvent was removed by way of SQUEEZE. The 4-*tert*-butylpyridine ligands were modeled across two slightly rotated positions, and the bond distances were restrained with SADI, and DFIX where required. EADP constraints were required for several of the overlapping atoms and some of the *tert*-butyl methyl groups.

References for Supporing Information for Chapter 4:

1. Mishra, A.; Tasiopoulos, A. J.; Wernsdorfer, W.; Abboud, K. A.; Christou, G., High-Nuclearity Ce/Mn and Th/Mn Cluster Chemistry: Preparation of Complexes with $[Ce_4Mn_{10}O_{10}(OMe)_6]^{18+}$ and $[Th_6Mn_{10}O_{22}(OH)_2]^{18+}$ Cores. *Inorg. Chem.* **2007,** *46*, 3105-3115.
2. Smith, P. D.; Martin, J. L.; Huffman, J. C.; Bansemer, R. L.; Caulton, K. G., Bimetallic Halides. Crystal Structure of and Ethylene Polymerization by Vanadium(II) Chloride-Zinc Chloride-tetrahydrofuran ($VCl_2.ZnCl_2.4THF$). *Inorg. Chem.* **1985,** *24*, 2997-3002.
3. Research, M., MestReNova.
4. Evans, D. F., The Determination of the Paramagnetic Susceptibility of Substances in Solution by Nuclear Magnetic Resonance. *Journal of the Chemical Society (Resumed)* **1959,**, 2003-2005.
5. Sheldrick, G., Crystal structure refinement with SHELXL. *Acta Cryst. C* **2015,** *71*, 3-8.
6. Sheldrick, G., SHELXT - Integrated Space-group and Crystal-structure Determination. *Acta Cryst. A* **2015,** *71*, 3-8.
7. Dolomanov, O. V.; Bourhis, L. J.; Gildea, R. J.; Howard, J. A. K.; Puschmann, H., OLEX2: a Complete Structure Solution, Refinement and Analysis Program. *J. Appl. Crystallogr.* **2009,** *42*, 339-341.
8. Hubschle, C. B.; Sheldrick, G. M.; Dittrich, B., ShelXle: a Qt graphical user interface for SHELXL. *J. Appl. Crystallogr.* **2011,** *44*, 1281-1284.
9. Amtawong, J.; Skjelstad, B. B.; Balcells, D.; Tilley, T. D., Concerted Proton–Electron Transfer Reactivity at a Multimetallic Co_4O_4 Cubane Cluster. *Inorg. Chem.* **2020,** *59*, 15553-15560.
10. Cryostat for Spectrometer USP-203 Series. https://www.unisoku.com/products/CryostatForSpectrophotometer.html.
11. Lu, T.; Chen, F., Multiwfn: A Multifunctional Wavefunction Analyzer. *J. Comput. Chem.* **2012,** *33*, 580-592.
12. Neese, F.; Wennmohs, F.; Becker, U.; Riplinger, C., The ORCA quantum chemistry program package. *The Journal of Chemical Physics* **2020,** *152* , 224108.
13. Chemcraft - Graphical Software for Visualization of Quantum Chemistry Computations. https://www.Chemcraftprog.com.
14. Staroverov, V. N.; Scuseria, G. E.; Tao, J.; Perdew, J. P., Comparative assessment of a new nonempirical density functional: Molecules and hydrogen-bonded complexes. *The Journal of Chemical Physics* **2003,** *119*, 12129-12137.
15. Nguyen, A. I.; Darago, L. E.; Balcells, D.; Tilley, T. D., Influence of a "Dangling" Co(II) Ion Bound to a $[MnCo_3O_4]$ Oxo Cubane. *J. Am. Chem. Soc.* **2018,** *140*, 9030-9033.
16. Weigend, F.; Ahlrichs, R., Balanced Basis Sets of Split Valence, Triple Zeta Valence and Quadruple Seta Valence Quality for H to Rn: Design and Assessment of Accuracy. *PCCP* **2005,** *7*, 3297-3305.
17. Barone, V.; Cossi, M., Quantum Calculation of Molecular Energies and Energy Gradients in Solution by a Conductor Solvent Model. *J. Phys. Chem. A* **1998,** *102*, 1995-2001.
18. Kelly, C. P.; Cramer, C. J.; Truhlar, D. G., Single-Ion Solvation Free Energies and the Normal Hydrogen Electrode Potential in Methanol, Acetonitrile, and Dimethyl Sulfoxide. *J. Phys. Chem. B* **2007,** *111*, 408-422.